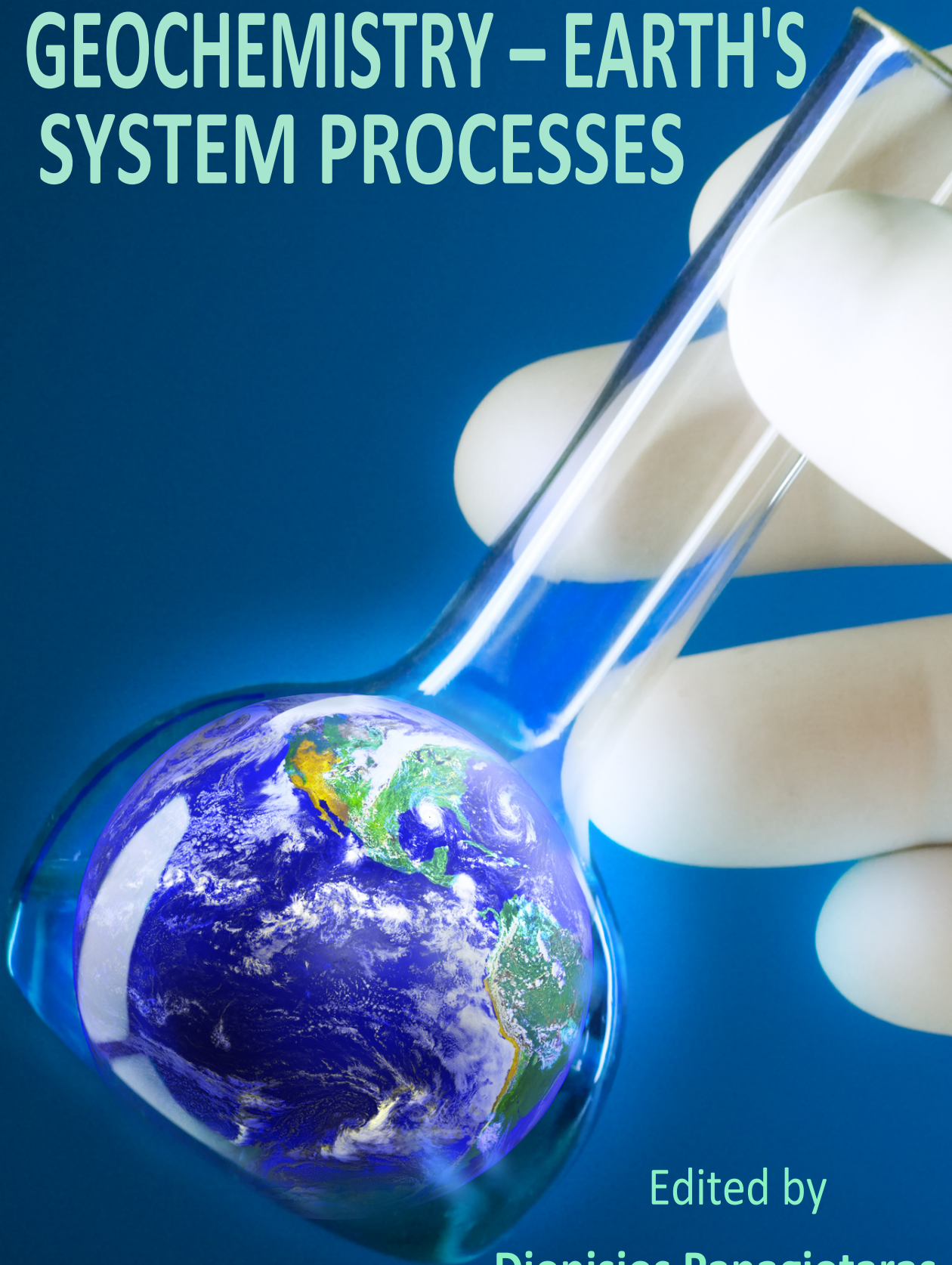


GEOCHEMISTRY – EARTH'S SYSTEM PROCESSES



Edited by

Dionisios Panagiotaras

GEOCHEMISTRY – EARTH'S SYSTEM PROCESSES

Edited by **Dionisios Panagiotaras**

Geochemistry – Earth's System Processes

Edited by Dionisios Panagiotaras

Published by InTech

Janeza Trdine 9, 51000 Rijeka, Croatia

Copyright © 2012 InTech

All chapters are Open Access distributed under the Creative Commons Attribution 3.0 license, which allows users to download, copy and build upon published articles even for commercial purposes, as long as the author and publisher are properly credited, which ensures maximum dissemination and a wider impact of our publications. After this work has been published by InTech, authors have the right to republish it, in whole or part, in any publication of which they are the author, and to make other personal use of the work. Any republication, referencing or personal use of the work must explicitly identify the original source.

As for readers, this license allows users to download, copy and build upon published chapters even for commercial purposes, as long as the author and publisher are properly credited, which ensures maximum dissemination and a wider impact of our publications.

Notice

Statements and opinions expressed in the chapters are those of the individual contributors and not necessarily those of the editors or publisher. No responsibility is accepted for the accuracy of information contained in the published chapters. The publisher assumes no responsibility for any damage or injury to persons or property arising out of the use of any materials, instructions, methods or ideas contained in the book.

Publishing Process Manager Mia Macek

Technical Editor Teodora Smiljanic

Cover Designer InTech Design Team

First published April, 2012

Printed in Croatia

A free online edition of this book is available at www.intechopen.com

Additional hard copies can be obtained from orders@intechopen.com

Geochemistry – Earth's System Processes, Edited by Dionisios Panagiotaras

p. cm.

ISBN 978-953-51-0586-2

Contents

Preface IX

- Chapter 1 **Geochemical and Sedimentation History of Neogene Lacustrine Sediments from the Valjevo-Mionica Basin (Serbia) 1**
Aleksandra Šajnović, Ksenija Stojanović,
Vladimir Simić and Branimir Jovančević
- Chapter 2 **Arsenic Geochemistry in Groundwater System 27**
Dionisios Panagiotaras, George Panagopoulos,
Dimitrios Papoulis and Pavlos Avramidis
- Chapter 3 **Geochemistry of Hydrothermal Alteration in Volcanic Rocks 39**
Silvina Marfil and Pedro Maiza
- Chapter 4 **Estimated Background Values of Some Harmful Metals in Stream Sediments of Santiago Island (Cape Verde) 61**
Marina M. S. Cabral Pinto, Eduardo A. Ferreira da Silva,
Maria M. V. G. Silva and Paulo Melo-Gonçalves
- Chapter 5 **The Relevance of Geochemical Tools to Monitor Deep Geological CO₂ Storage Sites 81**
Jeandel Elodie and Sarda Philippe
- Chapter 6 **Sm-Nd and Lu-Hf Isotope Geochemistry of the Himalayan High- and Ultrahigh-Pressure Eclogites, Kaghan Valley, Pakistan 105**
Hafiz Ur Rehman, Katsura Kobayashi, Tatsuki Tsujimori,
Tsutomu Ota, Eizo Nakamura, Hiroshi Yamamoto,
Yoshiyuki Kaneko and Tahseenullah Khan
- Chapter 7 **Geochemistry and Metallogenic Model of Carlin-Type Gold Deposits in Southwest Guizhou Province, China 127**
Yong Xia, Wenchao Su, Xingchun Zhang and Janzhong Liu

- Chapter 8 **Behaviors of Mantle Fluid During Mineralizing Processes 157**
Liu Xianfan, Li Chunhui, Zhao Fufeng, Tao Zhuan,
Lu Qiuxia and Song Xiangfeng
- Chapter 9 **Trace Metals in Shallow Marine Sediments from the Ría de Vigo: Sources, Pollution, Speciation and Early Diagenesis 185**
Paula Álvarez-Iglesias and Belén Rubio
- Chapter 10 **Organic Facies: Palynofacies and Organic Geochemistry Approaches 211**
João Graciano Mendonça Filho, Taissa Rêgo Menezes,
Joalice de Oliveira Mendonça, Antonio Donizeti de Oliveira,
Tais Freitas da Silva, Noelia Franco Rondon and
Frederico Sobrinho da Silva
- Chapter 11 **The Genesis of the Mississippi Valley-Type Fluorite Ore at Jebel Stah (Zaghuan District, North-Eastern Tunisia) Constrained by Thermal and Chemical Properties of Fluids and REE and Sr Isotope Geochemistry 249**
Fouad Souissi, Radhia Souissi and Jean-Louis Dandurand
- Chapter 12 **Potential and Geochemical Characteristics of Geothermal Resources in Eastern Macedonia 291**
Orce Spasovski
- Chapter 13 **Using a Multi-Scale Geostatistical Method for the Source Identification of Heavy Metals in Soils 323**
Nikos Nanos and José Antonio Rodríguez Martín
- Chapter 14 **Environmental Impact and Drainage Geochemistry of the Abandoned Keban Ag, Pb, Zn Deposit, Working Maden Cu Deposit and Alpine Type Cr Deposit in the Eastern Anatolia, Turkey 347**
Leyla Kalender
- Chapter 15 **Application of Nondestructive X-Ray Fluorescence Method (XRF) in Soils, Friable and Marine Sediments and Ecological Materials 371**
Tatyana Gunicheva
- Chapter 16 **Lanthanides in Soils: X-Ray Determination, Spread in Background and Contaminated Soils in Russia 389**
Yu. N. Vodyanitskii and A. T. Savichev
- Chapter 17 **Cu, Pb and Zn Fractionation in a Savannah Type Grassland Soil 413**
B. Anjan Kumar Prusty, Rachna Chandra and P. A. Azeez

- Chapter 18 **Characteristics of Baseline and Analysis of Pollution on the Heavy Metals in Surficial Soil of Guiyang** 429
Ji Wang and Yixiu Zhang
- Chapter 19 **Evaluating the Effects of Radio-Frequency Treatment on Rock Samples: Implications for Rock Comminution** 457
Arthur James Swart
- Chapter 20 **Evolution of Calciocarbonatite Magma: Evidence from the Sövite and Alvikite Association in the Amba Dongar Complex, India** 485
S. G. Viladkar

Preface

Geochemistry is the key to unlock the mysteries of planet Earth's origin and evolution

A better understanding of the fates and sources of chemical species can be reached through application of geochemistry. Geochemistry as a tool set is based on chemical rather than physical observations. Furthermore, it will assist us in explaining the functions of the natural environment. The Earth's crust and the oceans constitute major geological systems and their mechanisms can accordingly be sufficiently explained via geochemistry.

Geochemistry's area of interest has extended beyond the Earth's borders, coming to encompass the solar system in its entirety. In addition, it has made important contributions towards understanding a number of processes, including mantle convection, planets formation, as well as the origins of granite and basalt.

Cosmochemistry, isotope geochemistry, biogeochemistry, organic geochemistry, aqueous geochemistry, environmental geochemistry, exploration geochemistry (also called geochemical prospecting) and sedimentary geochemistry constitute primary subsets within the discipline of geochemistry.

The distribution of elements and their isotopes in the cosmos is the subject of cosmochemistry, while the study of the elements and their isotopes on the surface and within the Earth is the subject of isotope geochemistry. Furthermore, the effect of life on the Earth's chemical components is the main focus area of bio-geochemistry. The effect of components deriving from living matter on Earth and the use of chemical indicators associated with life forms to trace human habitation, as well as plant and animal activity on Earth, is the focus for organic geochemists. Organic geochemistry plays a vital role in the understanding of paleoclimate, paleoceanography, primordial life and its evolution. The distribution and role of elements in watershed and the way in which elemental fluxes are exchanged via atmospheric-terrestrial-aquatic interactions is the subject of aqueous geochemistry. Determining how mineral and hydrological exploration and environmental issues affect the Earth is the focus area for environmental geochemists. Various geochemical principles are applied when efforts are made towards locating ore bodies, mineral fields, groundwater supplies and oil and gas deposits. These principles derive from exploration geochemistry. The interpretation of what is known from hard rock geochemistry regarding soil and other

sediments, their erosion, deposition patterns and metamorphosis into rock, is the main aim of sedimentary geochemistry.

Geochemistry constitutes a relatively recent development since its growth was initiated and supported by proof in the early 19th century. Various issues and concerns in the areas of agriculture, environment, health and economics, related to the Earth's chemistry, attracted the interest of researchers. In the past, Germany and France have been countries with extensive mining activities, but it was not until the work performed by James Hutton, the so-called "Father of Geology" (1726-1797), that they constituted the forefront of research for earth sciences.

The French analytical chemistry laboratory (France *École des Mines*) was established in 1838 in order to cover the needs of French mining activities. The Clean Freshwater Society published chemical analyses results on drinking water in 1825, while the American geology began to develop rapidly in the first half of the 19th century. Lardner Vanuxem studied the chemical interaction between the atmosphere and the Earth's crust in 1827. The concept of metamorphism was introduced by James Dana in 1843, while the amount of carbon stored in rocks from the air was estimated by Henry D. Rogers in 1844. It was in that very period that geochemical achievements caught the attention of wider social and research communities.

The *"first report of a geological reconnaissance of the northern countries of Arkansas, made during the years 1857 and 1858...."* was authored and published in Little Rock, Arkansas in 1858 by David Dale Owen, M.D. who was the State geologist. In the same report, William Elderhorst M.D., who was the State Geologist's Chemical Assistant, wrote a chapter titled as "Chemical Reports of the Ores, Rocks, and Mineral Waters of Arkansas". At the same time, the State Geologist's Geological Assistant, Edward D. Cox performed chemical analysis mainly in water samples. There are numerous published reports illustrating the fact that chemistry is a well established aspect within the field of geology. These facts have constituted the starting point for an intensive study of the Earth's chemical composition and also for geochemistry's development as a discipline.

Furthermore, Wilhelm Ostwald, Jacobus Henricus Van't Hoff and Svante Arrhenius focused on reactions kinetics, equilibrium, chemical affinities and the conditions under which compounds are formed parallel to chemistry's growing development during the 19th century. In 1890s Arrhenius and Van't Hoff started applying their theories to rocks. More precisely, Van't Hoff tackled marine chemistry issues and Arrhenius studied the importance of the CO₂ content in the atmosphere for the climate. It was early in the 20th century when physical chemistry made an impact on metamorphic and igneous petrology and geochemistry, while the European geologists were resistant and hesitant towards the implementation of new ideas.

Well known American petrographers Joseph Paxson Iddings and Charles R. Van Hise linked the disciplines of physical chemistry and geology together. Iddings tried to explain magmatic differentiation by applying Van't Hoff's osmotic pressure theory

and also by considering C. Soret's findings stating that solute molecules tend to concentrate when the solution becomes cooler. On the other hand, Van Hise focused on the study of metamorphic rocks. However, both Iddings and Hise started laboratory experiments in a joined effort to connect physical chemistry and geology. With regard to Van't Hoff's theories, Arthur L. Day, E.T. Allen and Iddings studied the thermal properties of the albite-anorthite solid solution. Furthermore, Day and Allen published the fish-shaped equilibrium diagram in 1905. Two years later, in 1907 the Carnegie Institution in Washington DC established the Geophysical Laboratory to which Day was appointed its first director and Allen became the first chief chemist. The subject areas of geochemistry and petrology developed enormously as a result of the efforts put forward by the Allen and Day group.

However, modern geochemistry was based on Victor Moritz Goldschmidt's (1888-1947) ideas on the subject, explained in a series of publications from 1922 under the title "Geochemische Verteilungsgesetze der Elemente" (geochemical laws of distribution of the elements) and Vladimir Ivanovich Vernadsk's (1863-1945) book "*The Biosphere*" published in 1926, in which he inadvertently worked to popularize Eduard Suess' 1885 term biosphere, by hypothesizing that life is the geological force that shapes the Earth.

Geochemistry was assisted and came to a rise in the 21st century through technological revolution. The discipline of geochemistry was further advanced through developments in analytical chemistry and the manufacturing of tools and equipment such as microscopes, mass spectrometers and computers. Thus, by walking along the endless and infinite scientific pathway, geochemistry expands its boundaries via shifts towards disciplines like biology. As a result, new approaches rise up to explain the mysteries of life on our planet and in the universe.

Dr. Dionisios Panagiotaras

Department of Mechanical Engineering
Technological Educational Institute (TEI) of Patras
Greece

Geochemical and Sedimentation History of Neogene Lacustrine Sediments from the Valjevo-Mionica Basin (Serbia)

Aleksandra Šajnović¹, Ksenija Stojanović^{1,2},
Vladimir Simić³ and Branimir Jovančičević^{1,2}

¹University of Belgrade, Center of Chemistry, IChTM, Belgrade

²University of Belgrade, Faculty of Chemistry, Belgrade

³University of Belgrade, Faculty of Mining and Geology, Belgrade
Serbia

1. Introduction

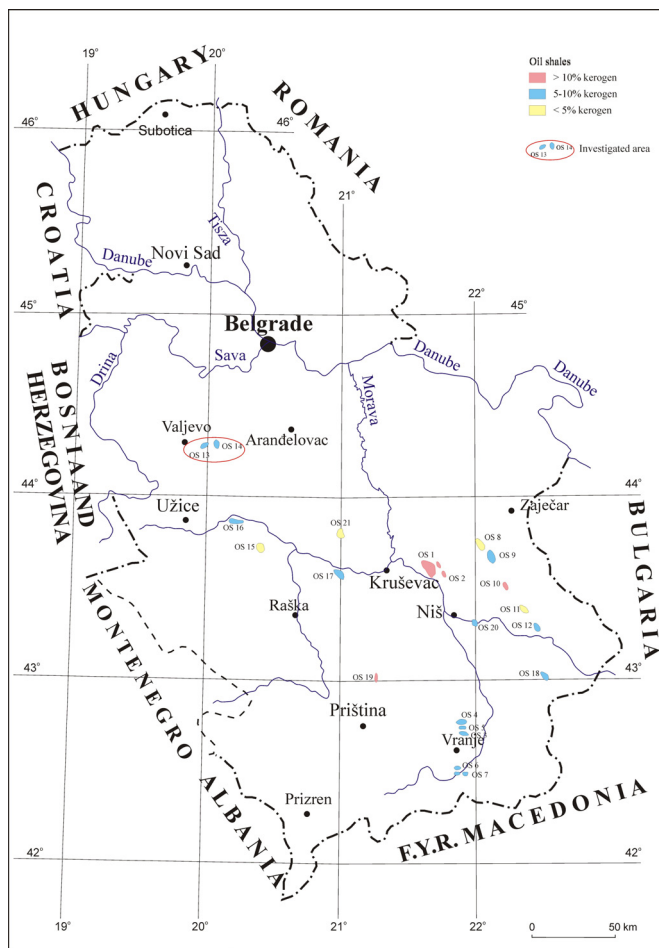
Valjevo-Mionica Basin is one of the numerous lacustrine Neogene basins in Serbia. After Aleksinac Basin, according to the quality and amount of oil shale, it is one of the main deposits of this raw material in Serbia. The most important oil shale deposits in Valjevo-Mionica Basin are located in the central part of the basin ("Bela stena series", Sušeočka and Radobička Bela Stena). The kerogen content in oil shales ranged from 8 - 16 %. The average oil yield of 6.3 % is of economical value.

Total of 62 samples of Neogene lacustrine sedimentary rocks to the depth of 400 m were investigated in this study. The first objective of the study was to reconstruct geological history (evolution) of the sediments i.e. to determine the palaeoconditions in depositional environment during its formation. For this purpose numerous geochemical methods and approaches were used. The second objective of the study was to determine the origin, type, maturity and liquid hydrocarbon potential of organic matter (OM). Aimed at detailed estimation of the oil shale OM potential, and prediction of the conditions necessary to become active oil generating source rock, pyrolytic experiments were performed on the bitumen-free sample. Bearing in mind that some metal ions (e.g. Al(III)-ion in clay minerals) (Jovančičević et al., 1993; Peters et al., 2005) have catalytic influence on most of the maturation processes, and that Pt(IV)- and Ru(III)- ions are often components of catalysts in many laboratory investigations and industrial procedures (Hu et al., 1994; Kawaguchi et al., 2005), the pyrolytic experiments of bitumen-free rock were performed also in the presence of simple inorganic compounds, $H_2[PtCl_6]$ and $RuCl_3$, to investigate if their presence changes the yield and hydrocarbon composition of liquid pyrolysates.

2. Geological characteristics of the investigated area

Valjevo-Mionica Basin is situated in the western part of Serbia, covering an area of 350 km². (Fig. 1). The Valjevo-Mionica Basin consists of lacustrine and marine sediments (Jovanović et al., 1994). The current investigations were focused on the lacustrine sediments from the

drillhole Val-1 at depth interval of 0-400 m. Interval from 15 to 200 m depth is made of sediments of the Mionica series which covers an area of approximately 40 km² (Dolić, 1984). Lithological characteristics of the Mionica series based on cores from the drillhole Val-1 down to depth of 200 m reflect transitions of oil shale, relatively rare thin beds or lenses of sandy siltstone and laminated shale, marlstone (dolomitic, sandy and clayey as well as tuffaceous), tuff, lenses enriched with searlesite and analcite and limestone with chert concretions. Another sedimentary interval underlying oil shale series is from 200 to 400 m depth. These sediments are represented by marlstone (dolomitic, sandy and clayey as well as tuffaceous), lenses of carbonates, siltstone, tuff and pyrite (Šajnović et al., 2008a).



OS 1. Aleksinac; OS 2. Bovan-Prugovac; OS 3. Goč-Devotin; OS 4. Vlase-G.Selo; OS 5. Stance;
 OS 6. Buštranje; OS 7. Klenike; OS 8. Vlaško polje-Rujište; OS 9. Vina-Zubetinac; OS 10. Podvis-G. Karaula;
 OS 11. Manojlica-Okoliste; OS 12. Miranovac-Orlja; OS 13 and OS 14. Valjevo-Mionica;
 OS 15. Pekčanica-Lazac; OS 16. Parmenac-Lazac; OS 17. Odzaci; OS 18. Raljin; OS 19. Rača;
 OS 20. Paljina; OS 21. Komarane-Kaludra.

Fig. 1. The most important deposits of oil shales in Serbia with kerogen content and location of investigated area

3. Methods

A total of 62 composite samples from drillhole Val-1 at depth to 400 m were prepared for investigation. From each plotted and cross-sectioned core of the drill hole, a quarter of core was taken for the preparation of composite samples.

The contents of SiO₂, Al₂O₃, Fe₂O₃, MgO, CaO, Na₂O, K₂O, TiO₂, as well as loss of ignition (LOI) were determined by X-ray fluorescence (XRF) spectrophotometry (Šajnović et al., 2008a, 2009). For X-ray fluorescence analysis, a sample powder was mixed with dilithium tetraborate (Li₂B₄O₇, Spectromelt from Merck), pre-oxidized with NH₄NO₃, and fused to glass beads in Pt crucibles. The contents of Sr, Li, B and As were determined by ICP-OES spectrophotometry after standard digestion (HNO₃:HCl = 1:3, v/v). These analytical methods were accredited in line with the ISO 9002 Standard. Reference samples were employed for calibration (CMLG, CS11, UXHG, IMV Gel for B content).

Qualitative composition of the mineral part was determined by X-ray powder diffraction method (Šajnović et al., 2008a, 2008b). The qualitative composition of the mineral part was determined by means of diffractometer Philips 1710 PW. The X-ray tube had following characteristics: Cu LFF, 40kV, 30 mA. Surveying was performed under the following conditions: $\lambda=1.54060-1.54438$ nm, step width 0.020 and time 0.50 s. The relative amount of the individual minerals was estimated qualitatively on the basis of the reflection of the most frequent peaks and comparison with the database (JCPDS-International Centre for Diffraction Data).

Elemental analysis was applied to determine the contents of carbon, sulphur and nitrogen. Organic carbon (Corg) was determined after removal of carbonates with diluted hydrochloric acid (1:3, v/v). The measurements performed using a Vario EL III, CHNOS Elemental Analyser, Elementar Analysensysteme GmbH. Rock-Eval pyrolysis was performed on the Rock-Eval II apparatus following the method JUS ISO/IEC 17025. The analysis included 50 mg of sample, and calibration 100 mg of standard IFP 160000.

Soluble organic matter (bitumen) was extracted from sediments using the Soxhlet extraction method with an azeotrope mixture of dichloromethan and methanol for 42 h. The saturated, aromatic, and NSO fractions (polar fraction, which contains nitrogen, sulfur, and oxygen compounds) were isolated from bitumen using column chromatography (Šajnović et al., 2008b, 2009, 2010). Elemental sulfur from the saturated fraction was removed by the method suggested by Blumer (1957).

Pyrolyses were performed on soluble organic matter (bitumen) free sample, which contained kerogen with native mineral matrix. The pyrolytic experiments also were performed on bitumen-free sample in the presence of H₂[PtCl₆] and RuCl₃ under the same conditions. The organic carbon in bitumen-free sample to catalyst mass ratio was 10:1. Pyrolyses were performed in an autoclave under nitrogen for 4 h at temperature 400 °C. Liquid pyrolysis products were extracted with hot chloroform. Gaseous products were not analyzed, although the production of gaseous products was indicated by the pressure change in the autoclave (Stojanović et al., 2009, 2010). Liquid pyrolysates were separated into saturated hydrocarbon, aromatic hydrocarbon, and NSO fractions using the same method as that applied for the fractionation of extracted bitumen.

Saturated and aromatic fractions isolated from the initial bitumen and pyrolysates were analyzed by gas chromatography-mass spectrometry (GC-MS). A gas chromatograph

Shimadzu GC-17A gas chromatograph (DB-5MS+DG capillary column, 30 m x 0.25 mm, He carrier gas 1.5 cm³/min, FID) coupled to a Shimadzu QP5050A mass selective detector (70 eV) was used. The column was heated from 80 to 290 °C, at a rate of 2 °C/min, and the final temperature of 290 °C was maintained for an additional 25 min. Saturated fractions were analyzed for *n*-alkanes and isoprenoids from the *m/z* 71, steranes from the *m/z* 217, and terpanes from the *m/z* 191 ion fragmentograms. Methyl-, dimethyl-, and trimethylnaphthalenes in the aromatic fractions were identified from the *m/z* 142, 156, and 170 ion fragmentograms, whereas phenanthrene, methyl-, and dimethylphenanthrene isomers were analyzed from the *m/z* 178, 192, and 206 ion fragmentograms. The individual peaks were identified by comparison with the literature data (Peters et al., 2005; Radke, 1987) and on the basis of the total mass spectra (libraries: NIST 107, NIST 121, PMW_tox3 and Publib/Wiley 229).

4. Results and discussion

4.1 Mineral composition

Mineral composition of sediments is characterized by predomination of dolomite and calcite, which were found in all samples. Contents of quartz, illite and chlorite were changeable. All samples from depth interval 15 to 200 m, which contain oil shale, are characterized by the presence of analcite (Fig. 2). Analcite is mainly linked with marine or lacustrine sediments which are formed in conditions of increased salinity and alkalinity (Remy & Ferrel, 1989). Feldspars, smectite and amphiboles were indicated by X-ray analyses, but they should be confirmed by detailed studies. According to certain specificities of the mineral composition, two important depth intervals were defined in the drillhole Val-1. The first interval is from 15 to 75 m depth. It is characterized by presence of searlesite (Fig. 2a), which is genetically linked to volcanogenic material. Another geochemically specific interval is at the depth of 360-400 m, and is characterised by interstratified clay minerals most probably of illite-smectite composition (lithium-bearing Mg-smectite) (Fig. 2b).

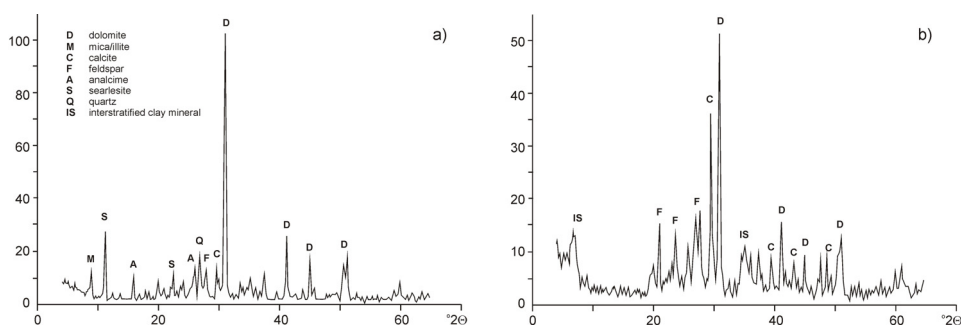


Fig. 2. Characteristic X-ray diffractograms of sediments from depth interval 15-75 m (a) and depth interval 360-400 m (b)

4.2 Geochemical parameters

Conditions which existed in the sedimentation environment, like water level, salinity, and climatic conditions, are reflected in the values of geochemical parameters (Ng & King, 2004).

For this purpose numerous group and specific geochemical parameters (Šajnović et al., 2008a, 2008b, 2009, 2010) were determined based on detailed investigation of inorganic part of sediments and its organic matter (kerogen and bitumen) (Tables 1 and 2). The differences in mineral composition and geochemical characteristics of the sediments indicate that the conditions in the sedimentation area changed over the time. That allowed defining four different depth intervals (Table 1).

Parameter	Depth interval (m)															
	15-75				75-200				200-360				360-400			
	Minimum	Maximum	Average	SD	Minimum	Maximum	Average	SD	Minimum	Maximum	Average	SD	Minimum	Maximum	Average	SD
SiO ₂ (%)	25.80	34.30	29.36	2.12	29.00	36.80	32.70	2.28	23.60	43.80	36.08	6.67	28.20	33.00	29.68	2.24
Al ₂ O ₃ (%)	7.35	12.70	9.29	1.19	9.70	13.60	11.52	1.18	6.58	15.40	11.93	2.78	7.07	8.17	7.52	0.49
Fe ₂ O ₃ (%)	3.10	4.93	3.84	0.41	3.97	5.01	4.51	0.31	2.64	7.39	5.19	1.43	3.02	3.56	3.19	0.25
MgO (%)	4.56	9.95	7.79	1.53	4.26	7.65	6.12	0.96	2.83	6.84	4.34	1.03	9.88	10.90	10.25	0.48
CaO (%)	9.78	19.40	14.19	2.33	10.70	17.90	14.81	2.24	7.66	30.20	15.34	6.66	15.40	19.20	17.83	1.80
Na ₂ O (%)	0.86	4.23	3.07	0.91	1.43	2.38	2.00	0.26	0.98	1.77	1.49	0.22	1.04	1.35	1.20	0.16
K ₂ O (%)	2.25	3.23	2.64	0.29	2.51	3.45	3.00	0.28	1.56	3.21	2.65	0.51	2.92	4.32	3.49	0.60
TiO ₂ (%)	0.26	0.42	0.32	0.04	0.34	0.48	0.39	0.04	0.24	0.64	0.46	0.13	0.26	0.28	0.27	0.01
LOI (%)	21.90	29.80	26.45	1.89	20.40	25.90	22.96	1.68	13.80	28.10	19.92	4.59	21.70	25.30	24.08	1.64
As (ppm)	20	93	57	18.95	20	54	29	9.60	20	31	26	3.41	10	37	11	14.00
Li (ppm)	120	390	252	64.68	140	560	269	106	130	370	180	53	890	1100	1000	116
Sr (ppm)	520	1600	1100	276	630	1100	881	139	390	11000	1700	2646	2700	7700	4025	2451
B (ppm)	120	7780	3811	2363	50	440	194	134	110	230	175	41	230	770	495	228
Corg (%)	1.39	4.75	3.32	0.86	0.68	3.63	2.42	0.82	0.51	1.96	1.10	0.41	0.47	1.51	1.07	0.44
S1	3.12	10.86	7.17	2.20	1.42	5.88	3.75	1.18	0.32	4.36	1.94	1.24	1.78	3.82	2.92	0.84
S2	16.66	71.40	47.77	13.11	7.02	46.26	29.18	10.70	0.96	21.12	8.14	6.24	3.66	20.04	12.98	6.96
HI	582	1044	695	98	544	745	661	55	126	603	359	151	369	672	542	131
Tmax (°C)	428	434	430	1.76	428	436	433	2.04	419	433	425	3.93	416	432	425	6.68

LOI - loss of ignition; Corg - organic carbon content from elemental analysis; S1 - free hydrocarbons in mgHC/g rock; S2 - pyrolysate hydrocarbons in mgHC/g rock; HI - hydrogen index = S2x100/TOC in mgHC/gTOC; HC - hydrocarbons; TOC - total organic carbon; Tmax - temperature corresponding to S2 peak maximum; SD - standard deviation

Table 1. Characteristical depth intervals and values of geochemical parameters

4.2.1 Depth interval 15-75 m

Relatively low values of the main inorganic geochemical parameters like SiO₂, Al₂O₃, Fe₂O₃, TiO₂ and CaO in this interval indicate that the share of aluminosilicate and carbonate fraction was low (Table 1). Change of contents of K₂O is similar to behaviour of SiO₂ and Al₂O₃, what indicates the connection between K₂O and aluminosilicates. This is confirmed by mineralogical analysis, that is presence of illite and rarely K-feldspar (Fig. 2a). Presence of potassium and terrigenous component is explained by the fact that potassium is mainly accumulated in clays by weathering and leaching processes as a result of syn- and post-depositional adsorption and ion exchange in salty or salted waters (Grim, 1968). Total iron (Fe₂O₃) may be found in crystal lattice of clay minerals, especially illite and chlorite. The

other possible connection is with colloid oxides and hydroxides of manganese (MnO) and titanium (TiO₂), which are, apart from clays, important constituents of recent sediments. The mentioned oxides and hydroxides may be found alone or in form of film on clay or other minerals. Contents of Li in depth interval 15-75 m is relatively low, whereas Sr content is relatively high and in positive correlation with LOI, indicating that it is connected with carbonate fraction (Table 1).

Parameter	Depth interval (m)															
	15-75				75-200				200-360				360-400			
	Minimum	Maximum	Average	SD	Minimum	Maximum	Average	SD	Minimum	Maximum	Average	SD	Minimum	Maximum	Average	SD
CPI	1.38	2.29	1.90	0.26	1.26	3.06	2.04	0.52	0.84	2.20	1.61	0.32	1.22	1.58	1.43	0.16
$n-C_{17}/n-C_{27}$	0.54	5.37	2.58	1.38	0.24	5.90	1.94	1.51	0.77	9.18	2.39	2.09	1.23	3.19	1.83	0.92
Pr/Ph	0.05	1.12	0.51*	0.33	0.02	0.53	0.14	0.12	0.06	0.67	0.31	0.18	0.45	0.85	0.63	0.18
Pr/ $n-C_{17}$	0.06	1.01	0.51	0.33	0.05	0.98	0.22	0.19	0.15	1.10	0.49	0.28	1.09	2.29	1.50	0.56
Ph/ $n-C_{18}$	0.91	7.89	2.20	1.55	0.52	25.0	5.50	5.25	0.62	8.76	4.31	2.49	3.01	13.29	6.24	4.75
Sq/ $n-C_{26}$	0.75	3.53	2.17	0.89	0.24	4.14	0.97	0.87	0.14	1.86	0.41	0.42	0.44	0.99	0.67	0.26
$i-25/n-C_{22}$	0.00	0.22	0.11	0.07	0.04	0.27	0.16	0.07	0.08	0.70	0.27	0.19	0.37	0.99	0.72	0.27
%C ₂₇	33.23	47.96	41.52	4.14	36.84	57.63	44.01	5.07	27.51	44.43	34.07	4.35	39.34	42.98	41.68	1.68
%C ₂₈	18.06	45.21	31.18	6.99	14.58	38.56	26.99	5.64	19.78	32.18	23.96	4.27	20.32	23.33	21.30	1.37
%C ₂₉	19.14	37.04	27.30	5.83	18.22	40.38	29.00	5.89	33.65	51.13	41.97	5.06	36.31	38.11	37.02	0.87
$C_{27}\alpha\alpha\alpha(R)/C_{29}\alpha\alpha\alpha(R)$	1.02	2.19	1.59	0.37	1.05	3.16	1.61	0.53	0.54	1.24	0.83	0.19	1.05	1.18	1.13	0.06
Gx100/ C ₃₀ H	11.11	57.14	30.86	13.09	14.71	56.25	30.81	10.90	14.10	84.31	45.93	19.20	6.67	37.50	17.69	14.51
C ₃₀ M/C ₃₀ H	1.47	10.64	7.05	2.35	1.49	11.92	4.56	2.70	0.49	1.55	0.86	0.33	0.73	1.30	1.08	0.26

*average value does not real, since it is increased due to relative high values of Pr/Ph ratio for samples at depths to 30 m; CPI – carbon preference index determined for full amplitude of *n*-alkanes (Bray & Evans, 1961); Pr – pristane; Ph – phytane; Sq – squalane; *i*-25 – C₂₅ regular isoprenoid; %C₂₇, C₂₈, C₂₉ regular sterane relative contents calculated from the peak areas of C₂₇-C₂₉ 5 α (H)14 α (H)17 α (H)20(R) isomers; C₂₇ $\alpha\alpha\alpha$ (R) – 5 α (H)14 α (H)17 α (H)20(R)-sterane; C₂₉ $\alpha\alpha\alpha$ (R) – 5 α (H)14 α (H)17 α (H)20(R)-sterane; G – gammacerane; C₃₀H – 17 α (H)21 β (H)-hopane; C₃₀M – 17 β (H)21 α (H)-moretane; SD – standard deviation

Table 2. Characteristical depth intervals and values of specific organic geochemical parameters

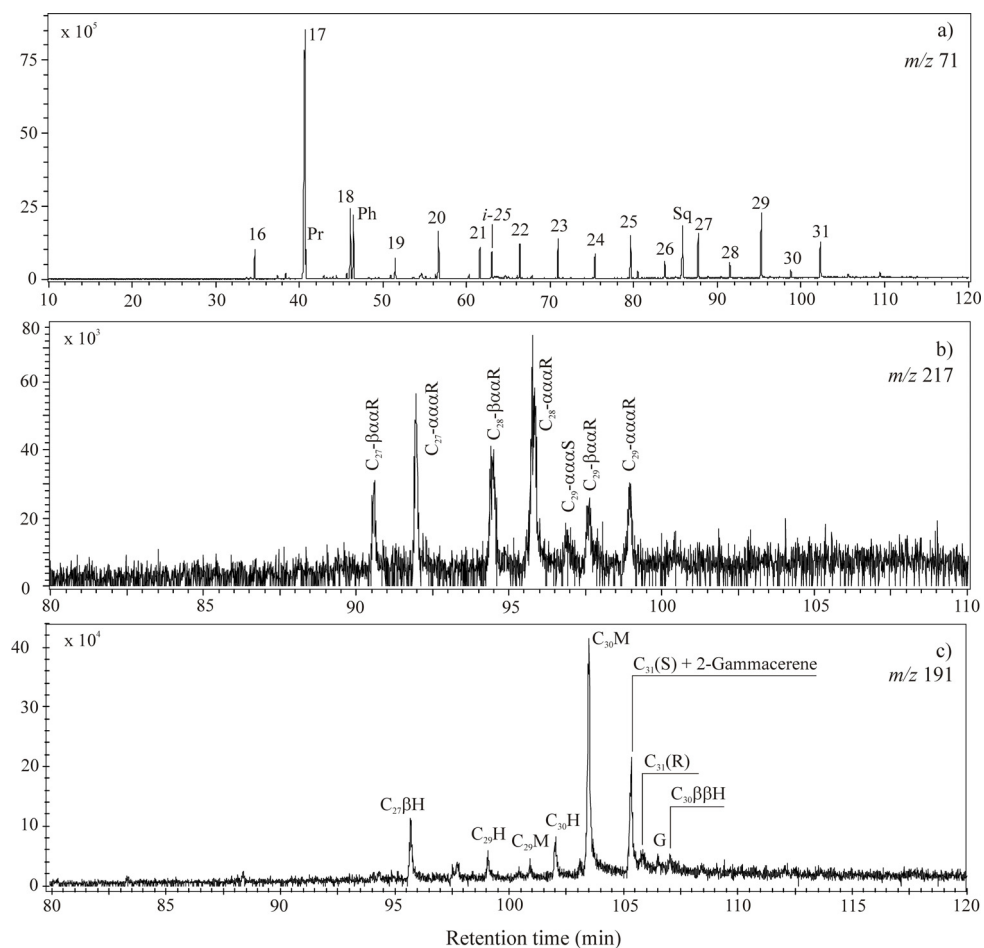
What makes this depth interval specific compared to the others is very high contents of Na₂O in main elements, B and As in the microelements (Table 1). It is well known that in comparison to other environments, Neogene lacustrine sediments are enriched in B and As (Alonso, 1999; Yudovich & Ketris, 2005). The contents of boron and arsenic in lacustrine sediments depend on: active volcanism, closed basin, arid to semi-arid climate, tectonic activity, pH, salinity, redox potential, temperature, type of the surrounding minerals in the depositional environment (Helvacı & Alonso, 2000; Kazancı et al., 2006; Valero-Garcés et al., 1999). The highest levels of boron in detrital sedimentary rocks are usually associated with argillaceous facies and are related to the amount and type of the mineral presents (Aggarwal

et al., 2000). Hydrated borate minerals accumulate as evaporate deposits in an arid, closed basin environment (Alonso, 1999; Floyd et al., 1998). Also, in arid areas, boron is likely to be co-precipitated with Mg and Ca hydroxides as coatings on the particles of the sediments, and it may also occur as Na-metaborate. Mineralogical analyses showed that dolomite and calcite were predominant in the investigated sediments and were found in all the examined samples (Fig. 2). Conditions of sedimentation, characterised by high salinity and pH and the presence of aluminosilicates and calcium and magnesium minerals, were suitable for boron accumulation. Therefore, sediments from this depth interval contained an order of magnitude higher amount of boron than sediments from other depth intervals (Table 1). Also, these sediments are characterised with increased contents of Na₂O and As compared to the other samples (Table 1) and the presence of the mineral searlesite (Fig. 2a), which is formed through the contact of sodium-rich alkaline saline waters with volcanic glass, which was the source of boron (Peng et al., 1998).

This interval is characterised by the highest average values of all bulk organic geochemical parameters (Corg, S1, S2, HI), with the exception of maturity parameter, temperature of maximum generation, Tmax (Table 1). Samples from depths 15-75 m contained relatively high amount of organic matter (Corg). This is also holds for the content of soluble OM expressed as S1 and for the content of hydrocarbons formed by pyrolysis, expressed through S2 (Table 1.) Relatively high values of hydrogen index (Table 1) show that OM of the samples consists predominantly of Type I and/or I/II kerogen, with a good potential for liquid hydrocarbons generation. The average value of Tmax indicates low maturity degree of OM, which is expected since at these depths OM was not exposed to more significant thermal stress.

The *n*-alkane distribution is characterised by domination of *n*-C₁₇ and relatively low proportion of longer chain *n*-alkane homologues (Fig. 3a, Table 2). In the immature samples, *n*-C₁₇ origin is associated to cyanobacteria and/or algae. Reducing conditions in saline lacustrine environments are caused by the high salinity of water and linked density stratification impeding vertical mixing of strata water body. This results in extremely anoxic conditions in the depositional environment (Peters et al., 1996), documented by very low Pr/Ph ratio of 0.05 (Table 2, see *).

In relatively immature sediments, pristane and phytane are presumed to originate from phytol, being a side chain in chlorophyll *a* structure of phototrophic organisms. However, there are other sources of phytane, like membrane lipids from *methanogenic* or *halophilic archaea* (Anderson et al., 1977; Volkman & Maxwell, 1988). Squalane is present in all of these sediments in relatively high quantities (Fig. 3a; Table 2). Squalane is presumed to originate from *Halophilic archaea* (Grice et al., 1998), and is interpreted as indicator for hypersaline depositional environment. Very high quantities of phytane, C₂₅ (*i*-25) and C₃₀ (squalane) regular isoprenoids were found in a numerous saline lakes of non-marine origin in China (Wang & Fu, 1997). In this contest, the Sq/*n*-C₂₆ ratio is often calculated, averaging a value of 2, indicating environments with very high salt content. Sediments from depth interval 15-75 m are characterized with high phytane and squalane contents (Sq/*n*-C₂₆ > 1, and in some samples even over 3), whereas *i*-25 was not identified, or was present in small quantity (Fig. 3a). This result shows that in the current study area such extremely saline anoxic conditions did not suitable for precursors of *i*-25.



n-alkanes are labelled according to their carbon number; Pr - pristane; Ph - phytane; *i*-25 - C_{25} regular isoprenoid; Sq - squalane; $\beta\alpha\alpha$ and $\alpha\alpha\alpha$ designate $5\beta(\text{H})14\alpha(\text{H})17\alpha(\text{H})$ and $5\alpha(\text{H})14\alpha(\text{H})17\alpha(\text{H})$ configurations, (R) and (S) designate configuration at C_{20} in steranes; $C_{27}\beta\text{H}$ - $C_{27}17\beta(\text{H})$ -22,29,30-trisnorhopane; $C_{30}\beta\beta\text{H}$ - $C_{30}17\beta(\text{H})21\beta(\text{H})$ -hopane; for other peak assignments, see legend, Fig. 7

Fig. 3. GC-MS ion fragmentogram of *n*-alkanes and isoprenoids, m/z 71 (a), steranes, m/z 217 (b) and terpanes, m/z 191 (c) representative for sediments from depth interval 15–75 m

C_{27} steranes in saturated lipid fraction of sediments in this depth interval accounts for over 40 %, and in some cases reaches even 50 %, whereas C_{28} sterane content accounts for approximately 30 % in total distribution of C_{27} – C_{29} regular sterane homologues (Fig. 3b; Table 2). Considering that distribution of regular steranes might serve even in classification of sediments or basins compared to the degree of salinity (Wang & Fu, 1997), the mentioned

data, apart from the high contents of isoprenoids squalane and phytane, represent another confirmation of hypersaline conditions of depositional environment in depth interval 15–75 m. The distribution of $14\alpha(H)17\alpha(H)20(R)$ C_{27} – C_{29} regular steranes is often used in the evaluation of the OM type (Peters et al., 2005; Volkman, 2003). Based on high contents of C_{27} and C_{28} steranes, distributions of n -alkanes dominated by C_{17} and high HI values (Tables 1 and 2) it might be concluded that the dominant source of OM during formation of sediments in this depth interval was from algal origin.

Concerning the distribution of terpane biomarkers, compounds with biological $\beta\beta$ -configuration and $\beta\alpha$ -moretanes are predominant in investigated samples representing immature microbial biomass (Fig. 3c). This agrees with the low level of thermal maturity. Gammacerane, which is most often considered as indicator of water column stratification and environments with high salinity (Sinninghe Damsté et al., 1995), is present in relatively small quantities (Fig. 3c). This confirms to the fact that extremely saline conditions are not suitable for its precursors e.g. protozoa *Tetrahymena* (Brassell et al., 1988; Šajnović et al., 2008b).

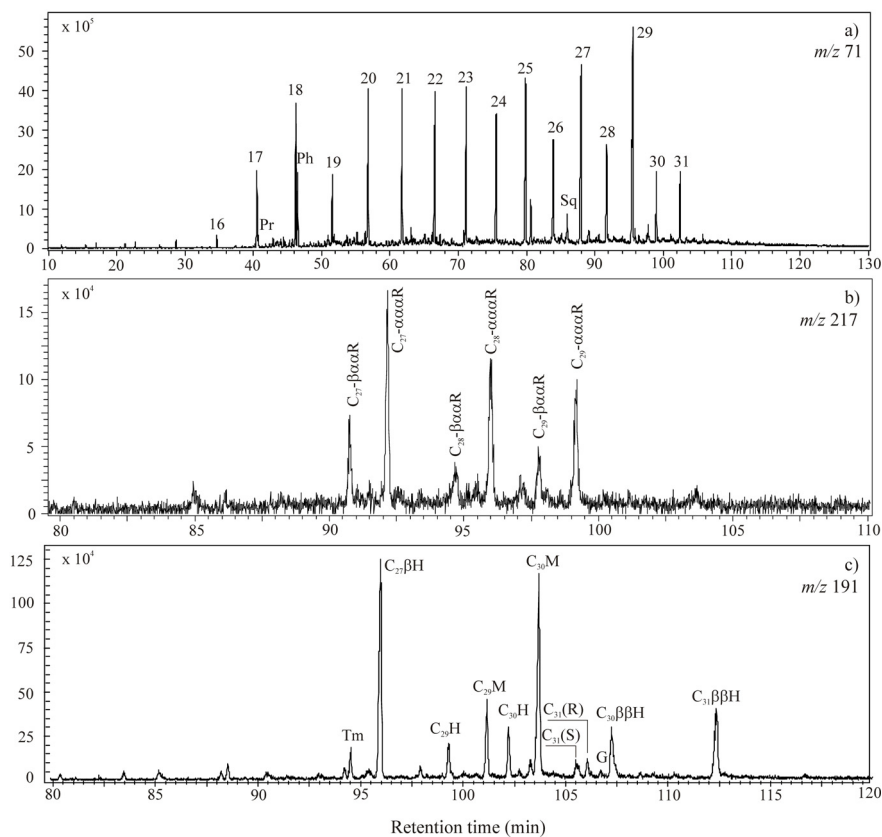
4.2.2 Depth interval 75-200 m

Contents of SiO_2 , Al_2O_3 , Fe_2O_3 and TiO_2 are higher, comparing to sediments from 15 to 75 m, whereas the contents of MgO , Sr and LOI are lower. Contents of Al_2O_3 and TiO_2 are the measure of clastic share of material (terrigenous origin), or erosion activity. In general, it may be said that in depth interval 75–200 m, due to increased erosion activity, aluminosilicate contents grows, and carbonate content falls. The greatest and most dramatic change was noticed in the reduction of the boron content (Table 1), what is mineralogically followed by absence of searlesite. In these sediments, lower contents of Na_2O and As were observed, although these changes are not that prominent as in content of boron (Table 1).

Sediments from this depth interval are characterised with lower values of all bulk organic geochemical parameters than in previous interval, especially those connected with the quantity of organic matter (Table 1). Lower HI values indicate that OM is composed of mixed terrestrial-algal precursor biomass (kerogen types II and mixture I/II; Table 1). The maturation degree of organic matter of the sediments is low.

n -Alkane distribution of the saturated fraction is characterized by relatively high proportions of n - C_{17} , and n - C_{27} , n - C_{29} , n - C_{31} long-chain odd n -alkanes (Fig. 4a). Decreasing of the n - C_{17}/n - C_{27} ratio indicates higher contribution of terrestrial precursor biomass (Table 2). Low value Pr/Ph ratio, in some cases of 0.07 (Table 2) suggests extremely anoxic conditions in the depositional environment (Peters et al., 1996). In addition, sediments from 75 to 200 m are characterized with low contents of i -25 and squalane (Fig. 4a; Table 2).

Sterane distribution with domination of C_{27} and C_{29} in similar proportions confirms mixed terrestrial algal precursor biomass, consistent with HI value and n -alkane distribution (Fig. 4b; Table 1). In distribution of terpane biomarkers, compounds with biological $\beta\beta$ -configuration and $\beta\alpha$ -moretanes are predominant, whereas gammacerane is present in relatively low quantity (Fig. 4c).



$C_{31}\beta\beta H - C_{31}17\beta(H)21\beta(H)$ -hopane; for other peak assignments, see legends, Figs. 3 and 7

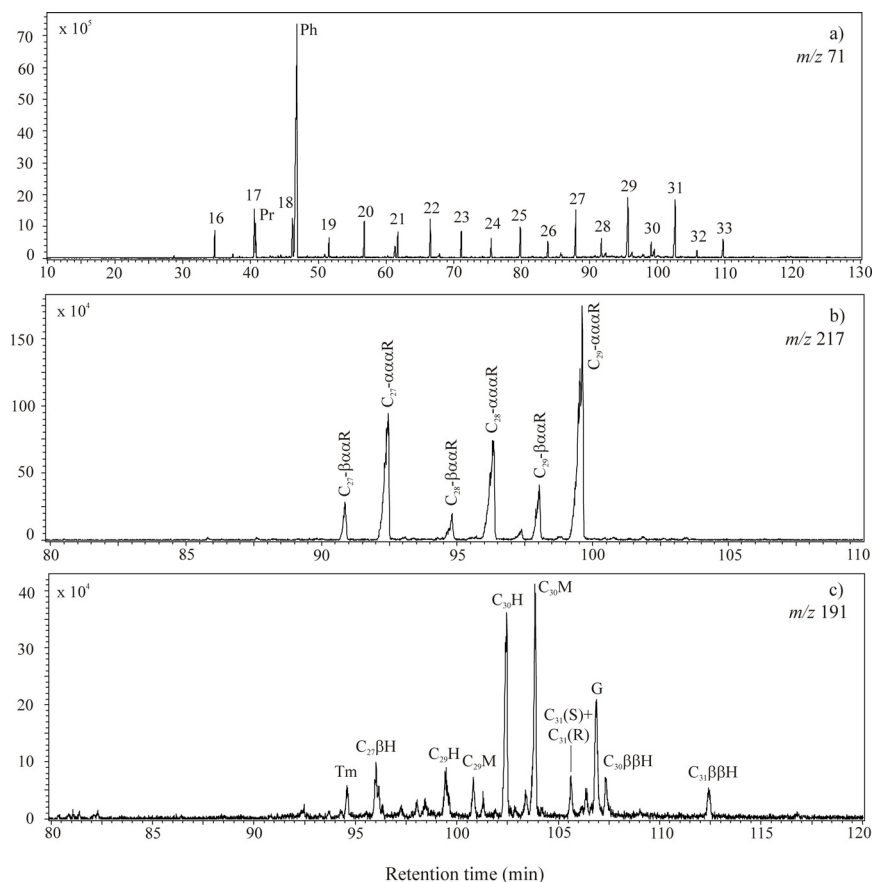
Fig. 4. GC-MS ion fragmentogram of *n*-alkanes and isoprenoids, m/z 71 (a), steranes, m/z 217 (b) and terpanes, m/z 191 (c) representative for sediments from depth interval 75–200 m

4.2.3 Depth interval 200–360 m

Contents of SiO_2 , Al_2O_3 , Fe_2O_3 and TiO_2 have the highest values; whereas the parameters connected with carbonate fraction (MgO and LOI) have the lowest values in sediments from this depth interval (Table 1). Obtained results indicate significant contribution of clastic material.

Sediments of this depth interval contain the least quantity of the organic matter in the whole vertical profile (Table 1). As values of both HI and parameter S2 are the lowest compared to the other intervals, it is obvious that the OM of these sediments is of the lowest quality, composed mainly from kerogen type III and II/III with a low potential for production of liquid hydrocarbons. These bulk data provide further indication that the terrestrial OM significantly contributed to samples from depth interval 200–360 m.

This is confirmed by biomarker distributions, which are characterized by domination of longer chain odd *n*-alkane homologues (C_{27} , C_{29} and C_{31}) and pronounced proportion of C_{29} regular sterane (Fig. 5a,b; Table 2). Moreover, the samples contain low content of squalane, whereas *i*-25 is absent (Fig. 5a; Table 2). All the mentioned changes in composition and quality of OM of sediments in depth interval 200-360 m are caused by expressed erosion activity which resulted in high contribution of clastic material. Relatively high values of gammacerane index (Table 2) could be explained by water stratification, which was most probably result of the temperature changes (Sinninghe Damsté et al., 1995).



for peak assignments, see legends, Figs. 3, 4 and 7

Fig. 5. GC-MS ion fragmentogram of *n*-alkanes and isoprenoids, m/z 71 (a), steranes, m/z 217 (b) and terpanes, m/z 191 (c) representative for sediments from depth interval 200–360 m

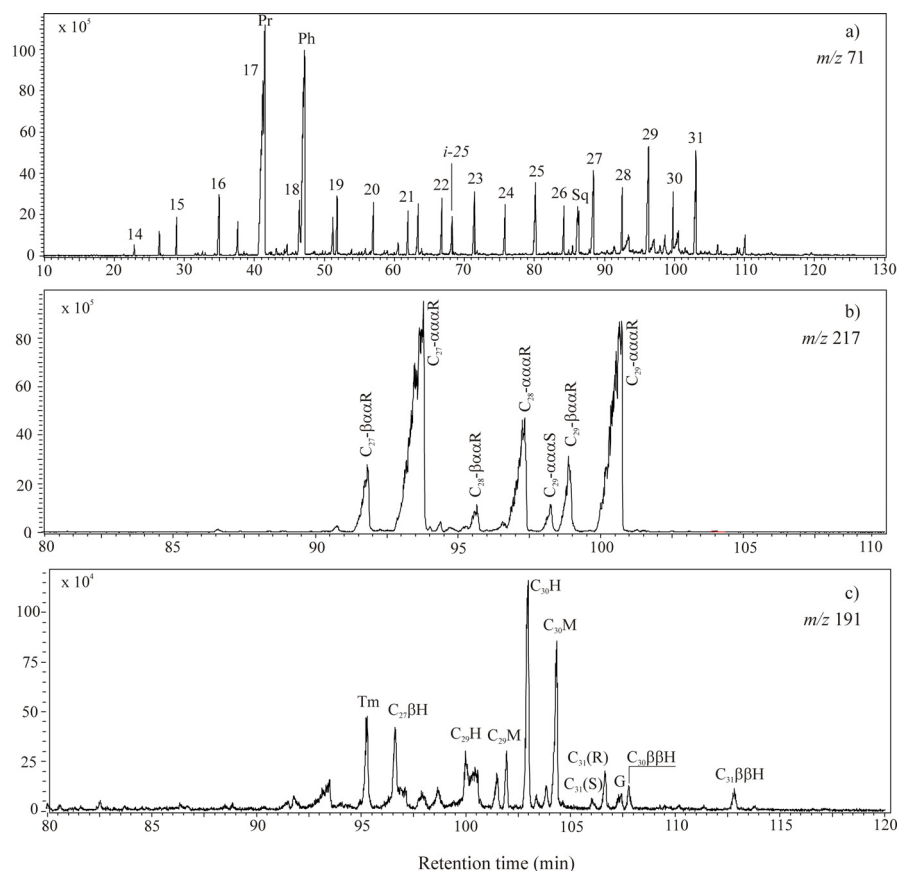
4.2.4 Depth interval 360-400 m

The last drilled interval is characterised by high share of dolomite and calcite, but also with presence of already mentioned lithium clay minerals. The most important geochemical link

in these sediments is related to the most likely presence of interstratified clay mineral type illite-saponite (lithium-bearing Mg-smectite). This is indicated by high concentrations of MgO, K₂O and Li and their mutual geochemical correlation (Table 1), as well as X-ray analysis (Fig. 2b).

In this depth interval the quantity of the OM is higher in comparison with previous depth interval, as well as the content of boron. However, this increase is not as pronounced as in depth interval 15–75 m. Value of HI indicates that the OM is composed of different types of kerogen, and that it is on relatively low degree of maturation (Table 1).

The saturated lipid fraction of these samples is characterized by relatively high proportions of *n*-C₁₇, phytane and pristane (Fig. 6a). The maximum in the short-chain length range (*n*-C₁₇) of the *n*-alkanes is higher than in the long-chain range, resulting in a *n*-C₁₇/*n*-C₂₇ ratio higher than 1 (Table 2). Odd homologues predominate among longer chain *n*-alkanes, and



for peak assignments, see legends, Figs. 3, 4 and 7

Fig. 6. GC-MS ion fragmentogram of *n*-alkanes and isoprenoids, *m/z* 71 (a), steranes, *m/z* 217 (b) and terpanes, *m/z* 191 (c) representative for sediments from depth interval 360–400 m

the maximum is at n -C₂₉ or n -C₃₁ (Fig. 6a). In sample 62 the relative proportion of pristane is highest among all investigated samples, causing the highest Pr/Ph and Pr/ n -C₁₇ ratios in the whole sample set. The isoprenoid alkane with 25 carbon atoms is present in relatively high quantity (Fig. 6a; Table 2). This indicates that the conditions with high pH values, i.e. alkaline environment are suitable for precursors of C₂₅ isoprenoid. Literature data show that the most frequent precursors of this isoprenoid alkane are *Archaea haloalkaliphiles*, for which, apart from the alkaline environment, suitable is the environment with increased salinity (de Rosa et al., 1986). However, in case of sediments of depth from 360 to 400 m, there is no indication of the increased salinity during their formation.

In some samples, C₂₇-steranes accounted for approximately 40 % (Table 2), and this observation was corroborated by high contents of n -C₁₇. The maturity of the organic matter of these samples being low, their high concentrations indicated a significant proportion of planktonic and cyanobacteric precursor organisms, which might have been favoured by increased alkalinity. Distributions of terpanes of the investigated samples are shown in figure 6c. The presence of thermodynamically less stable homologues with $\beta\alpha$ (moretane) and $\beta\beta$ configurations confirms that the OM of the investigated sediments has a low level of maturity. Sediment samples are additionally characterized by the presence of gammacerane. However, the values of gammacerane index for samples from this depth interval are low (Table 2). This data lead to the assumption that high alkalinity conditions were not very favourable for survival of gammacerane precursors e.g. protozoa *Tetrahymena* (Šajnović et al., 2008b; ten Haven et al., 1988).

4.3 Reconstruction of geological history based on geochemical and mineralogical parameters

The relatively low degree of OM maturity in all investigated samples (diagenetic phase), provides an opportunity to relate values of organic geochemical parameters with OM origin and palaeoconditions in sedimentation environment. Interpretation of those parameters, combined with mineralogical data and content of macro- and microelements allows reconstruction of the geological history of sediments in the drillhole Val-1. Obtained results showed that the conditions, and consequently sources of OM in the sedimentary environment changed significantly, based on which different geochemical intervals (zones) were defined. In certain periods sediments were deposited under very specific conditions.

Depth interval 360-400 m. Sediments from this interval were formed in alkaline conditions, with a variable bicarbonate to carbonate ratio. They are characterized by high content of magnesium, potassium and lithium, and also by presence of clay minerals of probably saponite, hectorite or interstratified illite-smectite types (Fig. 2b; Table 1), which needs further research. Results of elemental analysis and Rock-Eval pyrolysis indicate a moderately amount of immature OM (average organic carbon content, Corg, is 1.07 %; Table 1). Organic matter consists of kerogen types II and II/III. Biomarker distribution is characterized by domination of short chain over long chain n -alkanes, significant amount of phytane and regular isoprenoid C₂₅ (i -C₂₅), as well as by domination of C₂₇-homologue in the distribution of C₂₇-C₂₉ regular steranes (Fig. 6a,b; Tables 1 and 2). These results indicate significant contribution of algal biomass to OM in sediments (Peters et al., 2005). Therefore, it may be supposed that alkaline conditions are suitable for algae, and for some specific organisms such as *Archaea haloalkaliphile*, which is the main precursor of i -C₂₅ (de Rosa et al., 1986).

Depth interval 200-360 m. With time, environment is changed from calm to turbulent. Contents of magnesium, lithium and potassium in sediments decreased, whereas the contents of clastic material, SiO_2 , Al_2O_3 , Fe_2O_3 and TiO_2 are strongly increased, being the highest in the whole drillhole (Table 1). Mentioned changes resulted in decrease of OM content and quality (S1, S2 and HI; Table 1). Distribution of biomarkers, which is characterized by domination of odd homologues of long chain *n*-alkanes and high content of C_{29} sterane indicated significant contribution of terrestrial biomass to OM in sediments (Fig. 5a,b). Sedimentary OM from this interval consists predominantly of Type III kerogen, with a low generative liquid hydrocarbons potential.

Depth interval 200-75 m. Significant changes in the sedimentary environment occurred when the formation of sediments from the depth of 200 m, which belongs to Mionica series with oil shale, started. Those changes were primarily related to the increase in salinity, reflecting also in the increase of sodium content. The share of clastic sediments decreased, whereas the carbonate one increased (Table 1). Such conditions in sedimentary environment, followed by arid or semi-arid climate, allowed formation of analcite and better preservation of the OM, whose content increased in this depth interval (average, Corg, 2.42 %; Table 1). Biomarker distribution, which is characterized by high contents of *n*-alkanes (*n*- C_{17} , *n*- C_{27} , *n*- C_{29} , *n*- C_{31}) and phytane, uniform distribution of C_{27} - C_{29} regular steranes and also by low abundance of squalane, *i*-25 and pristane, indicates that sedimentary OM originates from mixed terrestrial/algal biomass, deposited under slightly anoxic conditions (Fig. 4a,b). It contains kerogen types II and I/II.

Depth interval 75-15 m. Salinity continues to increase in the sedimentation environment. Sediments from this interval were formed under the conditions of high salinity. The presence of clay minerals and calcium and magnesium minerals allows the accumulation of boron. Sediments from this interval have the highest content of boron, sodium and arsenic in the whole drillhole Val-1 and are characterized by the presence of searlesite (Fig. 2a; Table 1). Searlesite was probably formed by reaction of saline waters rich in sodium with thin beds of volcanic tuff. Such calm environment with high salt concentration and intensive evaporation, allowed increased bioproductivity of algal biomass and preservation of the deposited OM, due to pronounced stratification of water column. All that resulted in high content of the OM in sediments from this interval (average Corg is 3.32 %; Table 1), which consists of kerogen types I and I/II with good generative liquid hydrocarbons potential. Biomarker distribution is characterized by predominance of short chain over long chain *n*-alkanes, significant amount of phytane and squalane, as well as by domination of C_{27} -homologue in the distribution of C_{27} - C_{29} regular steranes (Fig. 3a,b).

4.4 Pyrolysis and catalyzed pyrolysis in the investigation of an oil shale potential

The generative potential of an oil shale from the Valjevo-Mionica Basin was investigated using conventional pyrolysis and pyrolysis in the presence of Pt(IV)- and Ru(III)-ions (Stojanović et al., 2010). Pyrolysis was performed on bitumen-free oil shale sample from the most interesting depth interval (15-75 m).

4.4.1 Characteristics of organic matter in the oil shale sample

Group organic geochemical parameters obtained by elemental analysis and Rock-Eval pyrolysis indicate the oil shale has significant generative potential with a total organic

carbon content (Corg) of 3.40 %, a Hydrogen Index (HI) of 600 mgHC/ gTOC, and a Tmax of 428 °C. These values are consistent with the presence of immature to marginally mature, oil-prone organic matter composed primarily of kerogens type I or I/II. Soxhlet extraction of the shale with an azeotrope mixture of dichloromethan and methanol yielded 5054 ppm of bitumen. The relatively high bitumen content in an immature sample may be explained by the presence of a significant amount of polar fraction (94.83 %), which is not readily expelled from the kerogen or did not incorporate into the kerogen matrix during late diagenesis (Stojanović et al., 2010; Šajnović et al., 2010).

The *n*-alkane distribution in bitumen extracted from the oil shale is characterised by pronounced *n*-C₁₇ domination, typical for organic matter of predominantly algal origin (Fig. 3a). CPI value for full amplitude of *n*-alkane range of 3.38 indicates low maturity, which has also been confirmed on the basis of the values of group organic geochemical parameters (Tmax and group bitumen composition). Pr/Ph ratio in bitumen extracted from the initial shale is 0.29, which indicates reducing conditions during deposition of the organic matter that contributed to its preservation.

Sterane distribution of saturated fraction of the extracted shale bitumen is characterised by the predominance of homologues with unstable ααα(R)- and βαα(R)-configurations (Fig. 3b), which again confirms a low maturity. Among them, C₂₇- and C₂₈-steranes are in higher proportions, which is in agreement with predominantly algal origin of the organic matter. Steranes with αββ(R)-, αββ(S)-configuration and typical geoisomers, βα- and αβ-diasteranes were not identified, and only C₂₉ sterane with ααα(S)- configuration is present in low amount (value of C₂₉ααα(S)/C₂₉ααα(S+R) ratio = 0.20).

Distribution of terpane biomarkers in bitumen isolated from the initial shale is characterised with domination of thermodynamically less stable βα- and ββ- isomers, the most abundant being C₃₀ βα-moretane (C₃₀M/C₃₀H ratio > 5; Fig. 3c). Terpanes typical for extracts of more mature source rocks and crude oils, such as, Tm, Ts, C₂₉Ts and series of 22(S)-homohopane isomers, were not identified with exception of C₃₁(S), which as minor component that coelutes with 2-gammacerene. C₂₉ and C₃₀ αβ-Hopanes are present in small quantity, as well as thermodynamically less stable epimer of C₃₁-homohopane with biological 22(R)-configuration (Fig. 3c).

Components of aromatic fraction, methyl- dimethyl- and trimethylnaphthalenes, as well as methyl- and dimethylphenanthrenes typical for more mature source rock bitumens and oils, were not identified or are present in traces in the shale extract, with exception of phenanthrene. The observation is consistent with the low maturity of the organic matter since the main quantity of alkylaromatics is generated during catagenesis.

4.4.2 Characteristics of liquid pyrolysates

Group organic geochemical parameters. Heated at 400 °C for 4 h, the sample generated a total liquid pyrolysate and hydrocarbons of 1700 ppm and 692 ppm, respectively (Table 3). The yields are consistent for source rock with good potential and support the assumption derived from an analysis of the immature oil shale. The presence of Pt(IV)- and Ru(III)-ions significantly increases the yields of liquid pyrolysate and hydrocarbons, with a bit more pronounced effect of Ru(III)-ion (Table 3).

Sample	Yield of liquid pyrolysates** (ppm)	Yields of hydrocarbons (HC)** (ppm)
S400	1700	692
SPt400	2700	1266
SRu400	2700	1376
Sample	p _o	p
S400	4.5	4.9
SPt400	4.5	5
SRu400	4.3	5.7

** relative to the bitumen-free sample; p_o, initial pressure; p, pressure at the end of pyrolysis; S400 – pyrolysate of bitumen-free oil shale at 400 °C; SPt400 – pyrolysate of bitumen-free oil shale at 400 °C + H₂[PtCl₆]; SRu400 – pyrolysate of bitumen-free oil shale at 400 °C + RuCl₃

Table 3. Values of group organic geochemical parameters in liquid pyrolysates

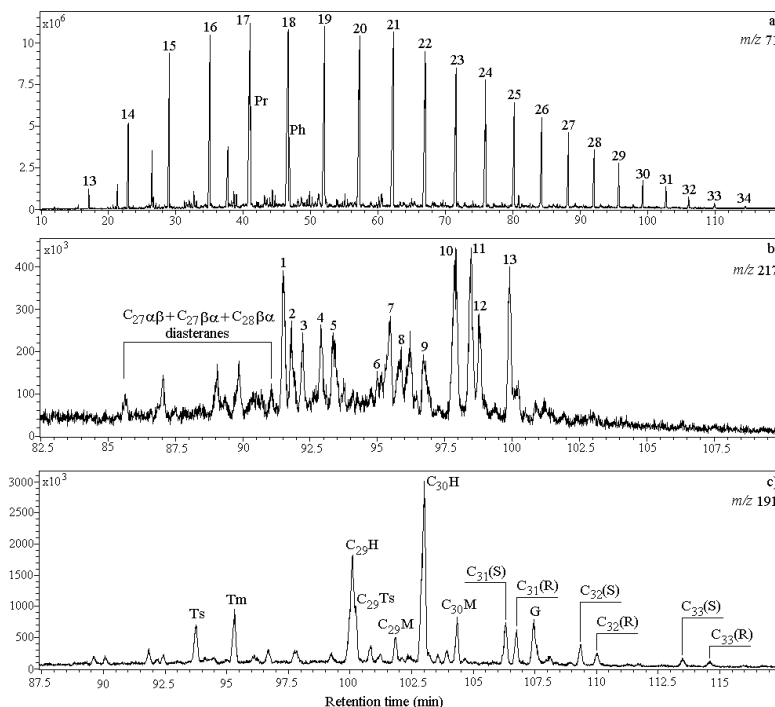
The catalytic effect of the used metal ions is based on them acting as Lewis acids and their high affinity for forming complexes with organic matter, both with the functional groups, such as carboxylic, hydroxyl, and amino groups, and the aromatic systems in the so-called sandwich compounds (Filipović & Lipanović, 1995; Hagen, 2006; Sheldon et al., 2007). Apart from the liquid pyrolysate, the pyrolytic experiments also produced gaseous products that may be generated by direct degradation of kerogen or as secondary products of the degradation of liquid hydrocarbons. Gaseous products were not analyzed. However, their presence is proved by measuring pressure in the autoclave at the end of pyrolysis in relation to the initial pressure, which typically was ~ 4.5 atm (Table 3). As in case of liquid products of pyrolysis, the increase of pressure/yield of gas products was somewhat more pronounced for Ru(III)-ion compared to Pt(IV)-ion. The more pronounced influence of Ru(III)-ion may be explained by the fact that the Ru(III)-ion forms exclusively octahedral complexes, while Pt(IV)-ion forms both octahedral and square planar complexes, because of which the Ru(III)-ion has greater capacity for forming complexes with organic substance (Filipović & Lipanović, 1995; Hagen, 2006; Sheldon et al., 2007).

Specific organic geochemical parameters based on biomarkers. All pyrolysates have similar *n*-alkane distributions in which *n*-alkanes C₁₇-C₂₃ are predominant (Fig. 7a), typical of organic matter of algal origin. CPI values for all the pyrolysates are close to 1, typical of a mature oil distribution (Table 4). Unlike bitumen in the immature oil shale, squalane is absent in the pyrolysates (Figs. 3a and 7a).

Values of Pr/Ph ratio are higher than in the initial bitumen, which may be explained by the fact that degradation of kerogen during laboratory simulations results in uniform formation of both pristane and phytane (Tables 2 and 4; Stojanović et al., 2009, 2010). Compared to the pyrolysate of sample alone, the pyrolysates obtained in presence of metal ions have greater relative contents of pristane and phytane, which is reflected through the increase in Pr/*n*-C₁₇ and Ph/*n*-C₁₈ ratios and have higher values of Pr/Ph ratios (Table 4). Ru(III)-ion exhibits a somewhat more pronounced catalytic effect on both *n*-alkanes and isoprenoids, which also is observed at interpretation of group organic geochemical parameters (Tables 3 and 4).

Sterane distributions in pyrolysates obtained at 400 °C are typical for oils, which confirms once again good potential of the investigated sediment and shows that catagenesis has been successfully simulated by pyrolysis. Apart from the regular ααα(R)-steranes, C₂₇-C₂₉ isomers with thermodynamically more stable ααα(S)-, αββ(R)-, and αββ(S)-configurations, as well

as, typical geoisomers, $\beta\alpha$ - and $\alpha\beta$ -diasteranes were present (Fig. 7b). All the three pyrolysates contain greater quantity of thermodynamically more stable C_{29} and C_{30} $\alpha\beta$ -hopanes, compared to corresponding $\beta\alpha$ -moretanes ($C_{29}M/C_{29}H$ and $C_{30}M/C_{30}H$ below 1; Table 4), whereas unstable $\beta\beta$ -hopanes and unsaturated hopenes were not identified. On the basis of mass spectra of corresponding peaks, the presence of Tm, Ts, $C_{29}Ts$ and 22(R and S)-epimers C_{31} - C_{33} homohopanes was determined in all pyrolysis (Fig. 7c).



- 1 - $C_{27}5\alpha(H)14\alpha(H)17\alpha(H)20(S)$ -sterane + $C_{28}13\alpha(H)17\beta(H)20(S)$ -diasterane;
 2 - $C_{27}5\alpha(H)14\beta(H)17\beta(H)20(R)$ -sterane + $C_{29}13\beta(H)17\alpha(H)20(S)$ -diasterane;
 3 - $C_{27}5\alpha(H)14\beta(H)17\beta(H)20(S)$ -sterane + $C_{28}13\alpha(H)17\beta(H)20(R)$ -diasterane;
 4 - $C_{27}5\alpha(H)14\alpha(H)17\alpha(H)20(R)$ -sterane; 5 - $C_{29}13\beta(H)17\alpha(H)20(R)$ -diasterane;
 6 - $C_{28}5\alpha(H)14\alpha(H)17\alpha(H)20(S)$ -sterane; 7 - $C_{28}5\alpha(H)14\beta(H)17\beta(H)20(R)$ -sterane +
 $C_{29}13\alpha(H)17\beta(H)20(R)$ -diasterane; 8 - $C_{28}5\alpha(H)14\beta(H)17\beta(H)20(S)$ -sterane;
 9 - $C_{28}5\alpha(H)14\alpha(H)17\alpha(H)20(R)$ -sterane; 10 - $C_{29}5\alpha(H)14\alpha(H)17\alpha(H)20(S)$ -sterane;
 11 - $C_{29}5\alpha(H)14\beta(H)17\beta(H)20(R)$ -sterane; 12 - $C_{29}5\alpha(H)14\beta(H)17\beta(H)20(S)$ -sterane;
 13 - $C_{29}5\alpha(H)14\alpha(H)17\alpha(H)20(R)$ -sterane;
 Ts - $C_{27}18\alpha(H)$ -22,29,30-trisnorneohopane; Tm - $C_{27}17\alpha(H)$ -22,29,30-trisnorhopane;
 $C_{29}H$ - $C_{29}17\alpha(H)21\beta(H)$ -30-norhopane; $C_{29}Ts$ - $C_{29}18\alpha(H)$ -30-norneohopane; $C_{29}M$ - $C_{29}17\beta(H)21\alpha(H)$ -
 moretane; $C_{30}H$ - $C_{30}17\alpha(H)21\beta(H)$ -hopane; $C_{30}M$ - $C_{30}17\beta(H)21\alpha(H)$ -moretane; $C_{31}(S)$ -
 $C_{31}17\alpha(H)21\beta(H)22(S)$ -hopane; $C_{31}(R)$ - $C_{31}17\alpha(H)21\beta(H)22(R)$ -hopane; G - gammacerane; $C_{32}(S)$ -
 $C_{32}17\alpha(H)21\beta(H)22(S)$ -hopane; $C_{32}(R)$ - $C_{32}17\alpha(H)21\beta(H)22(R)$ -hopane; $C_{33}(S)$ - $C_{33}17\alpha(H)21\beta(H)22(S)$ -
 hopane; $C_{33}(R)$ - $C_{33}17\alpha(H)21\beta(H)22(R)$ -hopane; for other peak assignments, see legend, Fig. 3

Fig. 7. GC-MS ion fragmentogram of *n*-alkanes and isoprenoids, *m/z* 71 (a), steranes, *m/z* 217 (b) and terpanes, *m/z* 191 (c) from saturated fraction of pyrolysate S400, typical for all pyrolysates

Values of the most used sterane maturation parameters based on the ratios of C_{29} sterane isomers, $C_{29}\alpha\beta\beta(R)/C_{29}(\alpha\beta\beta(R)+\alpha\alpha\alpha(R))$ and $C_{29}\alpha\alpha\alpha(S)/C_{29}\alpha\alpha\alpha(S+R)$ in pyrolysates are lower than equilibrium values. On the other hand, values for $C_{31}(S)/C_{31}(S+R)$ -homohopanes show that in isomerisation $22(R) \rightarrow 22(S)$ the equilibria has been achieved in all pyrolysates (Table 4). Based on these results, it may be assumed that during pyrolysis at 400 °C the investigated oil shale reached the value of vitrinite reflectance equivalence between 0.60 and 0.80 % (Peters et al., 2005). All pyrolysates obtained in presence of metal ions are characterised with higher values of $C_{29}M/C_{29}H$, $C_{30}M/C_{30}H$ ratios, and lower values of $C_{29}\alpha\alpha\alpha(S)/\alpha\alpha\alpha(S+R)$, $Ts/(Ts+Tm)$, $C_{29}Ts/C_{29}H$ ratios compared to pyrolysate of pure oil shale, especially in case of Ru(III)-ion (Table 4). The only exception among the sterane and terpene maturation parameters is the $C_{29}\alpha\beta\beta(R)/C_{29}(\alpha\beta\beta(R)+\alpha\alpha\alpha(R))$ ratio (Table 4). The reported observations lead to the assumption that metal ions, especially in case of Ru(III)-ion have greater impact on kerogen degradation, which directly reflects on the increase in the quantity of hydrocarbons, than on isomerisation reactions: moretanes \rightarrow hopanes, hopanes \rightarrow neohopanes and $C_{29}\alpha\alpha\alpha(R) \rightarrow C_{29}\alpha\alpha\alpha(S)$. This conclusion is not surprising since kerogen contains functional groups for which the used metal ions show much stronger affinity, compared to saturated hydrocarbons.

Sample	CPI	Pr/ Ph	Pr/ <i>n</i> -C ₁₇	Ph/ <i>n</i> -C ₁₈	C ₃₀ M/ C ₃₀ H	C ₂₉ M/ C ₂₉ H
S400	1.04	1.12	0.23	0.22	0.26	0.24
SPt400	1.03	1.29	0.46	0.37	0.31	0.35
SRu400	1.04	1.50	0.66	0.50	0.51	0.52
E.V.	/	/	/	/	0.05-0.15	/
Sample	$C_{31}(S)/$ $C_{31}(S+R)$	Ts/ (Ts+Tm)	Gx100/ C ₃₀ H	$C_{29}\alpha\alpha\alpha(S)/$ $C_{29}\alpha\alpha\alpha(S+R)$	$C_{29}\alpha\beta\beta(R)/C_{29}(\alpha\beta\beta(R)+\alpha\alpha\alpha(R))$	
S400	0.57	0.42	25.88	0.49	0.52	
SPt400	0.59	0.39	23.62	0.46	0.54	
SRu400	0.57	0.33	23.10	0.43	0.58	
E.V.	0.57-0.62	/	/	0.52-0.55	0.67-0.71	

for peak assignments, see legends, Figs. 3 and 7; E.V. – equilibrium value (Peters et al., 2005)

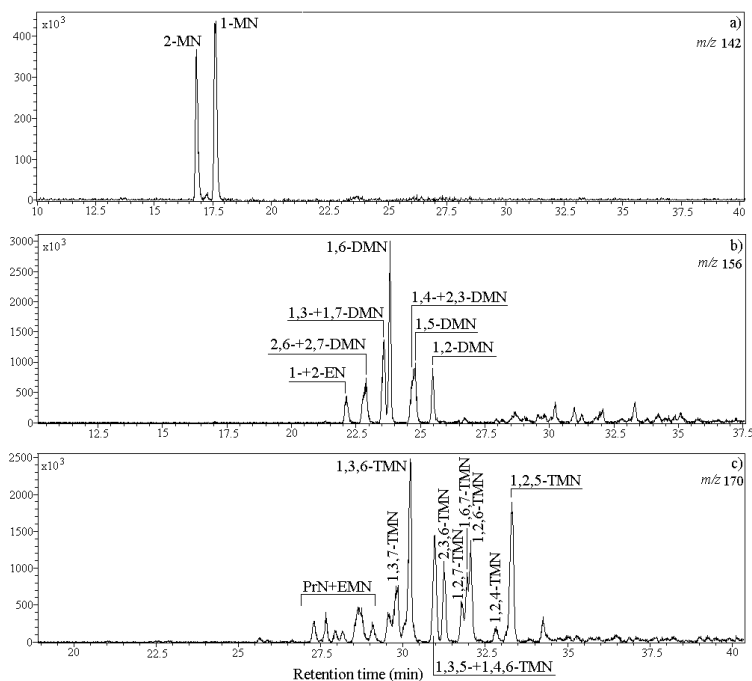
Table 4. Values of parameters calculated from distributions and abundances of biomarkers in pyrolysates

Specific organic geochemical parameters based on alkylaromatics. Liquid pyrolysis products have alkyl-naphthalene and phenanthrene distributions typical of mature oil (Figs. 8 and 9).

Values of the naphthalene maturation parameters in pyrolysates suggest that the metal ions have a catalytic effect on isomerisations of methyl groups that lead to the generation of more thermodynamically stable naphthalene isomers. Again, the Ru(III)-ion exhibits a somewhat more pronounced effect compared to Pt(IV)-ion (Table 5). Maturation parameters based on isomerisation of methyl phenanthrene groups from α - to β -positions, as well as on the reactions of methylation of phenanthrene ring are higher in pyrolysates obtained in the presence of Pt(IV)- and Ru(III)-ions, than in the pyrolysate of pure oil shale. Thus, Pt(IV)- and Ru(III)-ions have catalytic effect on both the processes (isomerisation $\alpha \rightarrow \beta$ and methylation)

at 400 °C. Ru(III)-ion showed more pronounced effect on the reactions of isomerisation of methylphenanthrenes (parameters MPI 1 and MPI 3), and Pt(IV)-ion on the methylation processes, especially in case of methylphenanthrenes to dimethylphenanthrenes transformation (parameters PAI 1, PAI 2 and DMR) (Table 5).

Applying the equation $Ro = 0.6 \times MPI\ 1 + 0.37$ (Radke & Welte, 1983), vitrinite reflectance equivalent of 0.70 % for pyrolysate of pure oil shale at 400 °C is calculated. This Ro value is in full agreement with the results obtained at interpretation of terpane and sterane biomarkers. In the presence of metal ions, under the same conditions, the organic matter of the analysed shale would attain the value of vitrinite equivalent of approximately 0.8 % (Table 5).



MN - methylphenanthrene; DMN - dimethylphenanthrene; TMN - trimethylphenanthrene;
PrN - propylphenanthrene; EMN - ethylmethylphenanthrene

Fig. 8. GC-MS ion fragmentograms of MN, m/z 142 (a), DMN, m/z 156 (b) and TMN, m/z 170 (c) from aromatic fraction of pyrolysate S400, typical for all pyrolysates

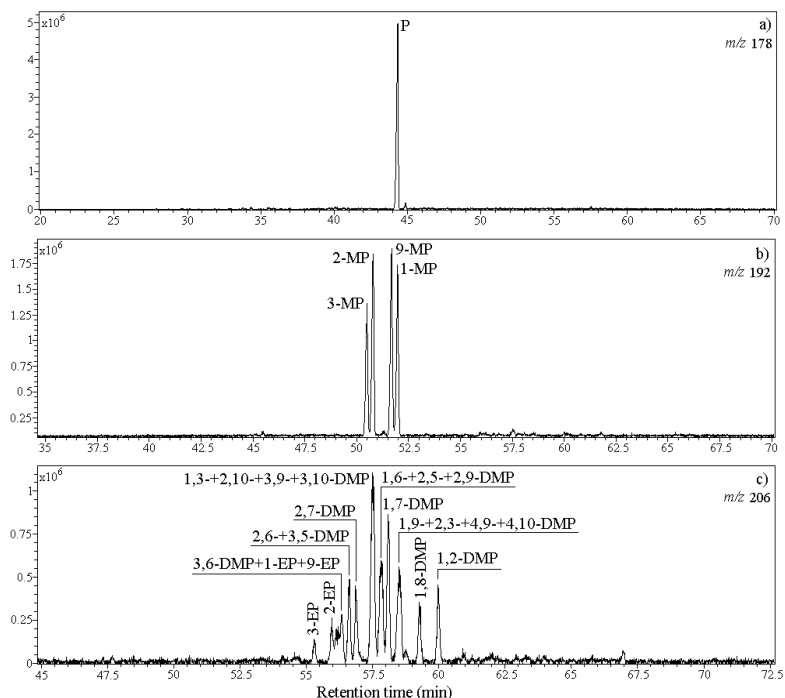
Differences in values of alkylaromatics maturity ratios obtained in the presence of metal ions in comparison to pyrolysate of the shale without metals are more pronounced in naphthalene, compared to phenanthrene parameters (Table 5). Comparing these results to maturation ratios calculated from distribution and abundance of saturated biomarkers, we conclude that Pt(IV)- and Ru(III)-ions have much greater influence on maturation changes on the planar systems (naphthalene and phenanthrene rings), than on isomerisations in the polycyclic alkanes, steranes and terpanes (Tables 4 and 5). The above observation is in agreement with the theoretical knowledge, as it is known that transition metal ions acting as

Lewis acids show an affinity for aromatic systems, and that they form stable complexes with aromatic ligands in the form of sandwich compounds (Hagen, 2006; Radke, 1987).

Sample	MNR	DNR 1	DN _x	α/βDN 1	TNR 3	α/βTN 1	TN _y
S400	0.63	1.44	2.28	1.61	1.14	0.82	2.27
SPt400	0.73	1.82	3.09	0.99	1.31	0.70	2.31
SRu400	0.77	2.35	2.95	1.07	1.67	0.57	2.44
Sample	MPI 1	MPI 3	Ro	DMPI 1	PAI 1	PAI 2	DMR
S400	0.49	0.91	0.70	0.41	1.07	0.57	0.53
SPt400	0.62	0.97	0.77	0.75	1.45	1.49	1.03
SRu400	0.63	1.01	0.78	0.70	1.43	1.40	0.98

MNR = 2-MN/1-MN; DNR 1 = (2,6-+2,7-DMN)/1,5-DMN; DN_x = (1,3-+1,6-+1,7-DMN)/(1,4-+1,5-+2,3-DMN); α/βDN 1 = (1,4-+1,5-+2,3-DMN)/(2,6-+2,7-DMN); TNR 3 = 1,3,6-TMN/1,2,5-TMN; α/βTN 1 = (1,2,4-+1,2,5-TMN)/(1,2,6-+1,2,7-+1,6,7-+2,3,6-TMN); TN_y = (1,3,6-+1,3,7-TMN)/(1,3,5-+1,4,6-TMN); MPI 1 = 1,5 x (2-+3-MP)/(P+1-+9-MP); MPI 3 = (2-+3-MP)/(1-+9-MP); Ro = 0.6 x MPI 1 + 0.37; DMPI 1 = 4 x (2,6-+2,7-+3,5-+3,6-DMP+1-+2-+9-EP)/(P+1,3-+1,6-+1,7-+2,5-+2,9-+2,10- +3,9- +3,10-DMP); PAI 1 = (1-+2-+3-+9-MP)/P; PAI 2 = ΣDMP/P; DMR = ΣDMP/ΣMP for peak assignments, see legends, Figs. 8 and 9

Table 5. Values of alkylaromatics maturation parameters in pyrolysates



P - phenanthrene; MP - methylphenanthrene; DMP - dimethylphenanthrene; EP - ethylphenanthrene

Fig. 9. GC-MS ion fragmentograms of P, *m/z* 178 (a), MP, *m/z* 198 (b) and DMP, *m/z* 206 (c) from aromatic fraction of pyrolysate S400, typical for all pyrolysates

Assessment of the conditions for achieving early catagenesis. Pyrolysis at 400 °C of the investigated oil shale achieved oil generation at a vitrinite reflectance equivalent of ~ 0.7 %. Applying a generalized diagram that relates Ro, depth and a regional geothermal gradient (Suggate, 1998) ranging between 40 and 50 °C/km (Kostić, 2010), the minimum depth of 2300-2900 m was estimated at which the shale would become a thermally mature source rock (Fig. 10). The minimum temperature necessary for catagenetic generation of hydrocarbons (temperature = depth x geothermal gradient + annual mean surface temperature; Suggate, 1998) was calculated at 103 °C ($t = 2.3 \times 40 + 11 = 103$ °C). Using the basin-independent equation $T = (\ln Ro + 1.68) / 0.0124$ (Barker & Pawlewicz, 1994), and Ro value of 0.70 % is estimated to be at 107 °C. Estimated temperature of hydrocarbons generation and necessary depth are in good agreement with corresponding data for the active source rocks in the region (Dragaš et al., 1991; Jovančičević et al., 2002; Kostić, 2010; Mrkić et al., 2011).

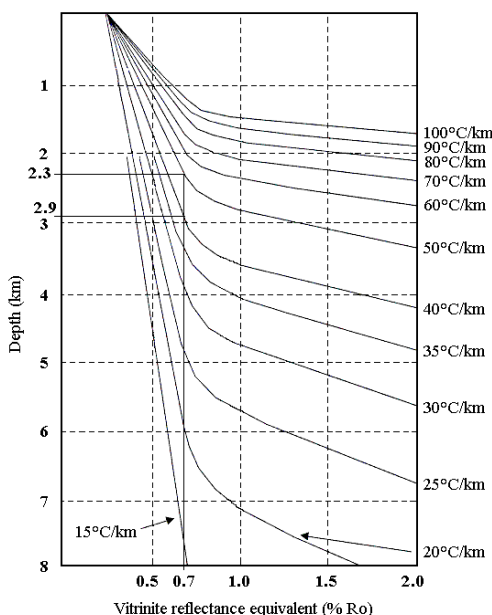


Fig. 10. Depth vs. vitrinite reflectance vs. geothermal gradient (according to Suggate, 1998); % of Ro value calculated in this study, and corresponding depth are indicated

5. Conclusions

The differences in geochemical and mineralogical characteristics of the sediments indicate that the palaeoconditions in the sedimentation area changed over the time, which allow defining four different depth intervals in the drillhole Val-1. In certain periods sedimentation occurred under very specific conditions. Sediments from 15-75 m depth interval were formed under the high salinity conditions, whereas sediments from depths 360-400 m were deposited in the conditions of the high alkalinity. Sediments from 15-75 m depths are characterized by the presence of searlesite and high amount of immature algal

OM with good generative liquid hydrocarbon potential, deposited under reducing environment. From the organic-geochemical point of view, depth interval 200-400 m is less interesting due to the lower OM content with low liquid hydrocarbons generation potential. Interval at depths from 360 to 400 m is significant, since sediments may contain lithium-bearing clay minerals.

Pyrolytic experiments showed that oil shale from depth interval 15 to 75 m in a catagenetic stage may be a source of liquid hydrocarbons. Pt(IV)- and Ru(III)-ions, demonstrated significant positive effects on the yields of total liquid pyrolysate and corresponding hydrocarbons. The used metal ions had much greater influence on maturity changes on planar systems (naphthalene and phenanthrene rings) than on isomerisations in the molecules of polycyclic alkanes. Values of terpane and sterane and phenanthrene maturation parameters indicate that through pyrolysis at 400 °C the investigated sample reaches the value of vitrinite reflectance equivalent of approximately 0.70 %.

It was estimated that the investigated oil shale should be found at depth of 2300-2900 m in order to become active source rock. The calculated minimum temperature necessary for catagenetic hydrocarbon generation is between 103 and 107 °C.

6. Acknowledgment

Investigations within this study were done in cooperation with the company Rio Tinto Exploration from Serbia. The study was partly financed by the Ministry of Science and Technological Development of the Republic of Serbia (Projects number 146008 and 176006).

7. References

- Alonso, R.N. (1999). On the origin of La Puna Borates. *Acta Geologica Hispanica*, Vol.34, No.2-3, (April-September 1999), pp. 141-166, ISSN 1695-6133
- Aggarwal, J.K.; Palmer, M.R.; Bullen, T.D.; Arnórsson, S. & Ragnarsdóttir, K.V. (2000). The boron isotope systematics of Icelandic geothermal waters: 1. meteoric water charged systems. *Geochimica et Cosmochimica Acta*, Vol.64, No.4, (February 2000), pp. 579-585, ISSN 0016-7037
- Anderson, R.; Kates, M.; Baedeker, M.J.; Kaplan, I.R. & Ackman, R.G. (1977). The stereoisomeric composition of phytanyl chains in lipids of Dead Sea sediments. *Geochimica et Cosmochimica Acta*, Vol.41, No.9, (September 1977), pp. 1381-1390, ISSN 0016-7037
- Barker, C.E. & Pawlewicz, M.J. (1994). Calculation of vitrinite reflectance from thermal histories and peak temperatures. A comparison of Methods, In: *Vitrinite Reflectance as a Maturity Parameter: Applications and Limitations*, Mukhopadhyay P.K & Dow, W.G. (Eds.), pp. 216-222, American Chemical Society, ISBN 0-8412-2994-5, Washington, USA
- Blumer, M. (1957). Removal of Elemental Sulfur from Hydrocarbon Fractions. *Analytical Chemistry*, Vol.29, No.7, (July 1957), pp. 1039-1041, ISSN 1520-6882
- Brassell, S.C.; Sheng, G.; Fu, J. & Eglinton, G. (1988). Biological markers in lacustrine Chinese oil shales. In: *Lacustrine and Petroleum Source Rocks*, Fleet, A.J., Kelts, K. & Talbot, M.R., (Eds.), pp. 299-308, ISBN 0-632-01803-8, London, UK

- Bray, E.E. & Evans, E.D. (1961). Distribution on *n*-paraffins as a clue to recognition of source beds. *Geochimica et Cosmochimica Acta*, Vol.22, No.1, (February 1961), pp. 2-15, ISSN 0016-7037
- de Rosa, M.; Gambacorta, A. & Gliozzi, A. (1986). Structure, Biosynthesis and physicochemical properties of archaeobacterial lipids. *Microbiological Reviews/Microbiology and Molecular Biology Reviews*, Vol.50, No.1, (March 1986), pp. 70-80, ISSN 0146-0749/1092-2172
- Dolić, D. (1984). Biostratigraphic contribution to the knowledge of the Middle Miocene lacustrine beds from Valjevo basin. *Protocol SGD*, Vol.1, pp. 63-67 (In Serbian with summary in German)
- Dragaš, M.; Opić, I. & Britvić, V. (1991). Temperature distribution analysis in INA - Naftaplin's exploration provinces based on the temperature measurements. *Nafta*, Vol.42, No.10, (October 1991), pp. 383-398, ISSN 0027-755X (in Croatian with summary in English).
- Filipović, I. & Lipanović, S. (1995). *General and Inorganic Chemistry* (9th edition), Školska knjiga, ISBN 953-0-30905-8, Zagreb, Croatia (in Croatian)
- Floyd, P.A.; Helvacı, C. & Mittwede, S.K. (1998). Geochemical discrimination of volcanic rocks associated with borate deposits: an exploration tool? *Journal of Geochemical Exploration*, Vol.60, No.3, (March 1998), pp. 185-205, ISSN 0375-6742
- Grice, K.; Schouten, S.; Nissenbaum, A.; Charrach, J. & Sinninghe Damsté, J. (1998). Isotopically heavy carbon in the C₂₁ to C₂₅ regular isoprenoids in halite-rich deposits from the Sdom Formation, Dead Sea Basin, Israel. *Organic Geochemistry*, Vol.28, No.6, (April 1998), pp. 349-359, ISSN 0146-6380
- Grim, R.E. (1968). *Clay Mineralogy* (2nd edition), McGraw-Hill Book Co, ISBN 978-0070248366, New York, USA
- Hagen, J. (2006). *Industrial Catalysis. A Practical Approach* (2nd edition), WILEY-VCH Verlag GmbH & Co. KGaA, ISBN 978-3-527-31144-6, Weinheim, Germany
- Helvacı, C. & Alonso, R.N. (2000). Borate Deposits of Turkey and Argentina; A Summary and Geological Comparison. *Turkish Journal of Earth Sciences*, Vol.9, No.1, (April 2000), pp. 1-27, ISSN 1300-0985
- Hu, J.; Venkatesh, K.R.; Tierney, J.W. & Wender, I. (1994). Reactions of aromatics and naphthenes with alkanes over a Pt/ZrO₂/SO₄ catalyst. *Applied catalysis A: General*, Vol.114, No.2, (July 1994), pp. L179-L186, ISSN 0926-860X
- Jovančičević, B.; Vučelić, D.; Šaban, M.; Wehner, H. & Vitorović, D. (1993). Investigation of the catalytic effects of indigenous minerals in the pyrolysis of Aleksinac oil shale substrates: Steranes, triterpanes and triaromatic steroids in the pyrolysates. *Organic Geochemistry*, Vol.20, No.1, (January 1993), pp. 69-76, ISSN 0146-6380
- Jovančičević, B.; Wehner, H.; Scheeder, G.; Stojanović, K.; Šajnović, A.; Cvetković, O.; Ercegovac, M. & Vitorović, D. (2002). Search for source rocks of the crude oils of the Drmno depression (southern part of the Pannonian Basin, Serbia). *Journal of the Serbian Chemical Society*, Vol.67, No. 8-9, (August-September 2002), pp. 553-566, ISSN 0352-5139

- Jovanović, O.; Grgurović, D. & Zupančić, N. (1994). The neogene sediments in Valjevomionica basin. *Geology, Series A, B (Hydrogeology and Engineering Geology)*, Vol.46, pp. 207-222 (In Serbian with Summary in English)
- Kawaguchi, T.; Sugimoto, W.; Murakami, Y. & Takasu, Y. (2005). Particle growth behavior of carbon-supported Pt, Ru, PtRu catalysts prepared by an impregnation reductive-pyrolysis method for direct methanol fuel cell anodes. *Journal of Catalysis*, Vol.229, No.1, (January 2005), pp. 176-184, ISSN 0021-9517
- Kazancı, N.; Toprak, Ö.; Leroy, S.A.G.; Öncel, S.; İleri Ö.; Emre Ö.; Costa, P.; Erturaç, K. & McGee, E. (2006). Boron content of Lake Ulubat sediment: A key to interpret the morphological history of NW Anatolia, Turkey. *Applied Geochemistry*, Vol.21, No.1, (January 2006), pp. 134-151, ISSN 0883-2927
- Kostić, A. (2010). *Thermal evolution of organic matter and petroleum generation modelling in the Pannonian basin (Serbia)*, University of Belgrade, Faculty of Mining and Geology & "Planeta print", ISBN 978-86-7352-221-0, Belgrade, Serbia (in Serbian with summary in English)
- Mrkić, S.; Stojanović, K.; Kostić, A.; Nytoft, H.P. & Šajnović A. (2011). Organic geochemistry of Miocene source rocks from the Banat Depression (SE Pannonian Basin, Serbia). *Organic Geochemistry*, Vol.42, No.6, (July 2011), pp. 655-677, ISSN 0146-6380
- Ng, S.L. & King, R.H. (2004). Geochemistry of lake sediments as a record of environmental change in a high Arctic watershed. *Chemie der Erde Geochemistry*, Vol.64, No.3, (September 2004), pp. 257-275, ISSN 0009-2819
- Peng, Q.; Palmer, M. & Lu, J. (1998). Geology and geochemistry of the Paleoproterozoic borate deposits in Liaoning-Jilin, northeastern China: evidence of metaevaporites. *International Journal of Salt Lake Research/Hydrobiologia*, Vol.381, No.1-3, (September 1998), pp. 51-57, ISSN 0018-8158
- Peters, K.E.; Cunningham, A.E.; Walters, C.C.; Jigang, J. & Fan, Z. (1996). Petroleum systems in the Jiangling-Dangyang area, Jiangnan basin, China. *Organic Geochemistry*, Vol.24, No.10-11, (October - November 1996), pp. 1035-1060, ISSN 0146-6380
- Peters, K.E.; Walters, C.C. & Moldowan, J.M. (2005). *The Biomarker Guide, Volume 2: Biomarkers and Isotopes in the Petroleum Exploration and Earth History*, Cambridge University Press, ISBN 978-0-521-83762-0, Cambridge, UK
- Radke, M. & Welte, D.H. (1983). The methylphenanthrene index (MPI): a maturity parameter based on aromatic hydrocarbons. In: *Advances in Organic Geochemistry 1981*, Bjørøy, M. et al. (Eds.), pp. 504-512, John Wiley & Sons Limited, ISBN 0 471 26229 3, Chichester, UK
- Radke, M. (1987). Organic geochemistry of aromatic hydrocarbons, In: *Advances in Petroleum Geochemistry*, Radke M. (Ed.), pp 141-205, Academic Press, ISBN 0-12-032009-9, London, UK
- Remy, R. & Ferrell, R. (1989). Distribution and origin of analcite in marginal lacustrine mudstones of the Green river formation, South-central Uinta basin, Utah. *Clays and Clay minerals*, Vol.37, No.5, (October 1989), pp. 419-432, ISSN 1552-8367
- Sheldon, R.; Arends, I. & Hanefeld, U. (2007). *Green Chemistry and Catalysis*, WILEY-VCH Verlag GmbH & Co. KGaA, ISBN 978-3-527-30715-9, Weinheim, Germany

- Sinninghe Damsté, J.S.; Keing, F.; Koopmans, M.P.; Koster, J.; Schouten, S.; Hayes, J.M. & de Leeuw, J.W. (1995). Evidence for gammacerane as an indicator of water column stratification. *Geochimica et Cosmochimica Acta*, Vol.59, No.9, (May 1995), pp. 1895-1900, ISSN 0016-7037
- Stojanović, K.; Jovančičević, B.; Šajnović, A.; Sabo, T.; Vitorović, D.; Schwarzbauer, J. & Golovko, A. (2009). Pyrolysis and Pt(IV)- and Ru(III)-ion catalyzed pyrolysis of asphaltenes in organic geochemical investigation of a biodegraded crude oil (Gaj, Serbia). *Fuel*, Vol.88, No.2, (February 2009), pp. 287-296, ISSN 0016-2361
- Stojanović, K.; Šajnović, A.; Sabo, T.; Golovko, A. & Jovančičević, B. (2010). Pyrolysis and Catalyzed Pyrolysis in the Investigation of a Neogene Shale Potential from Valjevo-Mionica Basin, Serbia. *Energy Fuel*, Vol.24, No.8, (August 2010), pp. 4357-4368, ISSN 1520-5029
- Suggate, R.P. (1998). Relations between depth of burial, vitrinite reflectance and geothermal gradient. *Journal of Petroleum Geology*, Vol.21, No.1 (January 1998), pp. 5-32, ISSN 0141-6421
- Šajnović, A.; Simić, V.; Jovančičević, B.; Cvetković, O.; Dimitrijević, R. & Grubin, N. (2008a). Sedimentation History of Neogene Lacustrine Sediments of Sušeočka Bela Stena Based on Geochemical Parameters (Valjevo-Mionica Basin, Serbia). *Acta Geologica Sinica - English Edition*, Vol.82, No.6, (December 2008), pp. 1201-1212, ISSN 1755-6724
- Šajnović, A.; Stojanović, K.; Jovančičević, B. & Cvetković, O. (2008b). Biomarker distributions as indicators for the depositional environment of lacustrine sediments in the Valjevo-Mionica basin (Serbia). *CHEMIE der ERDE GEOCHEMISTRY*, Vol.68, No.4, (September 2008), pp. 395-411, ISSN 0009-2819
- Šajnović, A.; Stojanović, K.; Jovančičević, B. & Golovko, A. (2009). Geochemical investigation and characterisation of Neogene sediments from Valjevo-Mionica Basin (Serbia). *Environmental Geology*, Vol.56, No.8, (February 2009), pp. 1629-1641, ISSN 1866-6280
- Šajnović, A.; Stojanović, K.; Pevneva, G.; Golovko, A. & Jovančičević, B. (2010). Origin, Organic Geochemistry, and Estimation of the Generation Potential of Neogene Lacustrine Sediments from the Valjevo-Mionica Basin, Serbia. *Geochemistry International*, Vol.48, No.7, (July 2010), pp. 678-694, ISSN 0016-7029
- ten Haven, H.L.; de Leeuw, J.W.; Sinninghe Damsté, J.S.; Schenk, P.A.; Palmer, S.E. & Zumberge, J.E. (1988). Application of biological markers in the recognition of paleohypersaline environment. In: *Lacustrine and Petroleum Source Rocks*, Fleet, A.J., Kelts, K. & Talbot, M.R., (Eds.), pp. 123-130, ISBN 0-632-01803-8, London, UK
- Valero-Garcés, B.L.; Grosjean, M.; Kelts, K.; Schreier, H. & Messerli, B. (1999). Holocene lacustrine deposition in the Atacama Altiplano: facies models, climate and tectonic forcing. *Palaeogeography, Palaeoclimatology, Palaeoecology*, Vol.151, No.1-3, (July 1999), pp. 101-125, ISSN 0031-0182
- Volkman, J.K. & Maxwell, J.R. (1988). Acyclic isoprenoids as biological markers, In: *Lacustrine and Petroleum Source Rocks*, Fleet, A.J., Kelts, K. & Talbot, M.R., (Eds.), pp. 103-122, Blackwell Scientific Publications, ISBN 0-632-01803-8, London, UK
- Volkman, J.K. (2003). Sterols in microorganisms. *Applied Microbiology and Biotechnology*, Vol.60, No.5, (January 2003), pp. 496-506, ISSN 0340-2118

Yudovich, Ya.E. & Ketris, M.P. (2005). Arsenic in coal: a review. *International Journal of Coal Geology*, Vol.61, No.3-4, (February 2005), pp. 141-196, ISSN 0166-5162

Wang, R. & Fu, J. (1997). Variability in biomarkers of different saline basins in China. *International Journal of Salt Lake Research/Hydrobiologia*, Vol.6, No.1, (March 1997), pp. 25-53, ISSN 0018-8158

Arsenic Geochemistry in Groundwater System

Dionisios Panagiotaras¹, George Panagopoulos²,
Dimitrios Papoulis³ and Pavlos Avramidis⁴

¹*Department of Mechanical Engineering, Laboratory of Chemistry, Technological Educational Institute (T.E.I.) of Patras, Patras*

²*Department of Mechanical and Water Resources Engineering, Technological Educational Institute (T.E.I.) of Messolonghi, Nea Ktiria, Messolonghi*

³*Department of Geology, University of Patras, Patras*

⁴*Technological Educational Institute (T.E.I.) of Mesolonghi, Laboratory of Geology for Aquatic Systems, Nea Ktiria Mesolonghi*

^{1,2,3,4}*Greece*

1. Introduction

Enormous population numbers from the global setting are known to have been affected by the adverse effects of arsenic. Further, soil and groundwater reserves have been contaminated. This has created the need for remediation. Treatment of arsenic has proved to be a difficult task to accomplish diachronically since it changes valence states and reacts towards the formation of species with varying toxicity and mobility [1].

The Maximum Contaminant Level (MCL) that provides the measurement for arsenic in drinking water was recently reduced by the United States Environmental Protection Agency (EPA) from 0.050 mg/l to 0.010 mg/l [2].

In the majority of the countries, the background values of arsenic in groundwater are less than 10 mg/l and sometimes even lower (USA values from Welch et al., 2000 [3]; UK values from Edmunds et al., 1989 [4]).

Arsenic shows variations from <0.5 to 5000 mg/l under natural conditions. Oxidising (under conditions of high pH) and reducing aquifers and areas affected by geothermal, mining and industrial activity provide a nurturing environment for high concentrations of Arsenic.

In the majority of the cases, natural sources have been found to contribute towards high level concentration of Arsenic. Meanwhile, mining activities result to high occurrence of arsenic locally. Furthermore, arsenic pollution increases at local levels due to industrial and agricultural activities.

Currently, there are reports on groundwater As problems from a magnitude of countries ranging from Argentina, Bangladesh, Chile, China, Hungary, India (West Bengal) to Mexico, Romania, Taiwan, Vietnam and many parts of the USA, particularly the southwest USA. The need for a rapid assessment of the situation in aquifers worldwide has been surfaced as a result of recent research discovery of As enrichment on a large scale [1, 2, 5].

Therefore, there is an imminent need from the side of the organisations that supply drinking water to provide new ways for treatment or to alter the existing treatment systems in order to meet the revised MCL. Relevant literature provides evidence on the fact that precipitation / co-precipitation is frequently used for purposes of treating arsenic-contaminated water. Furthermore, it is capable to treat influent arsenic concentrations in the revised MCL.

On the other hand, absorption and ion exchange for arsenic treatment is likely to be affected by characteristics and contaminants different to arsenic. Absorption and ion exchange appear to be used more often in cases where arsenic is the main and only contaminant to be subjected to treatment. This applies to smaller systems but also to larger systems as a polishing technology. The use of membrane filtering is less frequent due to the fact that it incurs higher costs and produces large residual volumes as compared to other technologies relative to the treatment of arsenic [1, 2, 6].

This chapter provides information needed to help meet the challenges of arsenic behavior in groundwaters. Clays, carbonaceous materials, and oxides of iron, aluminum and manganese are components that may participate in rock/soil-water interactions leading to enrichment or depletion with respect to arsenic.

2. Arsenic geochemistry

In nature arsenic occurs in air, soil, water, rocks, plants, and animals. Natural activities such as volcanic eruption, rocks erosion and forest fires, can release arsenic to the environment. The major arsenic minerals occurring in nature are presented in table 1 [5].

Mineral	Composition	Occurrence
Native arsenic	As	Hydrothermal veins
Nicolite	NiAs	Vein deposits and norites
Realgar	As ₂ S ₂	Vein deposits, often associated with orpiment, clays and limestones, also deposits from hot springs
Orpiment	As ₂ S ₃	Hydrothermal veins, hot springs, volcanic sublimation products
Cobaltite	CoAsS	High temperature deposits, metamorphic rocks
Arsenopyrite	FeAsS	The most abundant As mineral, dominantly in mineral veins
Tennantite	(Cu,Fe) ₁₂ As ₄ S ₁₃	Hydrothermal veins
Enargite	Cu ₃ AsS ₄	Hydrothermal veins
Arsenolite	As ₂ O ₃	Secondary mineral formed by oxidation of arsenopyrite native arsenic and other As minerals
Clauderite	As ₂ O ₃	Secondary mineral formed by oxidation of realgar arsenopyrite and other As minerals
Scorodite	FeAsO ₄ ·2H ₂ O	Secondary mineral
Anabergite	(Ni,Co) ₃ (AsO ₄) ₂ ·8H ₂ O	Secondary mineral
Hoernesite	Mg ₃ (AsO ₄) ₂ ·8H ₂ O	Secondary mineral, smelter wastes
Haematolite	(Mn,Mg) ₄ Al(AsO ₄)(OH) ₈	Secondary mineral
Conichalcite	CaCu(AsO ₄)(OH)	Secondary mineral
Pharmacosiderite	Fe ₃ (AsO ₄) ₂ (OH) ₃ ·5H ₂ O	Oxidation product of arsenopyrite and other As minerals

Table 1. Major arsenic minerals occurring in nature [5].

Anthropogenic activities such as farming, mining, uses of fossil fuels, pulp and paper production, cement manufacturing et.al., contributing as additional sources of arsenic in the environment [7].

Arsenic is generally distributed in more than 320 minerals [8], and it's commonly found in arsenopyrite (FeAsS) [9; 10; 11], orpiment (As_2S_3), realgar (As_2S_2), and pyrite solid solutions (FeS_2) [12; 13]. Arsenic is also present in sedimentary environments mainly adsorbed by Fe(III) and Mn(IV) after weathering of sulfide minerals [11; 14; 15; 16].

The major sources of arsenic in natural waters include arsenic minerals, together with a once widespread use of arsenic in pigments, insecticides and herbicides. About 70% of all arsenic uses are in pesticides [17].

Other important uses of arsenic and its compounds are in wood preservatives, glass manufacture, electronics, catalysts, alloys, feed additives and veterinary chemicals. Many studies document the adverse health effects in humans exposed to inorganic arsenic compounds [7], [18].

Arsenic can form both inorganic and organic compounds. It occurs with valence states of -3, 0, +3 and +5, nevertheless, the valence states of -3 and 0 occur only rarely in nature. This arsenic chemistry discussion focuses on inorganic species of As(III) and As(V). Inorganic compounds of arsenic include halides, hydrides (e.g., arsine), acids, oxides, and sulfides [19].

Arsenic's toxicity and mobility has been proved to vary with its chemical form and state of valence. In sea water and surface water, arsenite and arsenate constitute the dominant species. In addition, it is in natural gas and shale oil that organic arsenic species can be found. Varying degrees of toxicity and solubility can be evidenced in chemical compounds that contain arsenic [20].

The mobilization of arsenic in groundwater is controlled by several reactions i.e. dissolution/precipitation, adsorption / co-precipitation, and reduction/oxidation. Furthermore, numerous processes have given a rise to the existing global account for high levels of arsenic in natural water: The weathering of sulfide minerals provides for the reductive dissolution of arsenic rich iron oxyhydroxides [14; 15; 16; 21; 22; 23]; Arsenic-rich pyrite or arsenopyrite oxidative dissolution [10; 12; 13; 24]; Arsenic - bearing minerals that interact with water [10; 23].

Iron oxyhydroxides constitute the most common cause for the widespread contamination from arsenic. This is due to the post effect that evidenced following the reaction of iron oxyhydroxides with organic carbon release arsenic into solution [25; 26]. The oxidation of sulphide minerals such as pyrite is a major source of arsenic. It has also been found to constitute the primary source in aquifers located in Wisconsin and Michigan [26; 27].

3. Arsenic chemical reactions and speciation in water

Arsenic is a metalloid listed in group V_A of the periodic table. It exists in nature in the oxidation states +V (arsenate), +III (arsenite), 0 (arsenic) and -III (arsine). In aqueous systems, arsenic exhibits anionic behaviour. In case of oxygenated waters, arsenic acid predominates only at extremely low pH (< 2). In the pH range of 2 to 11, it is in the form of

H_2AsO_4^- and HAsO_4^{2-} . In mildly reduced conditions and low pH values, arsenious acid converted to H_2AsO_3^- as the pH increases. When the pH exceeds 12 HAsO_3^{2-} does appear (Fig.1).

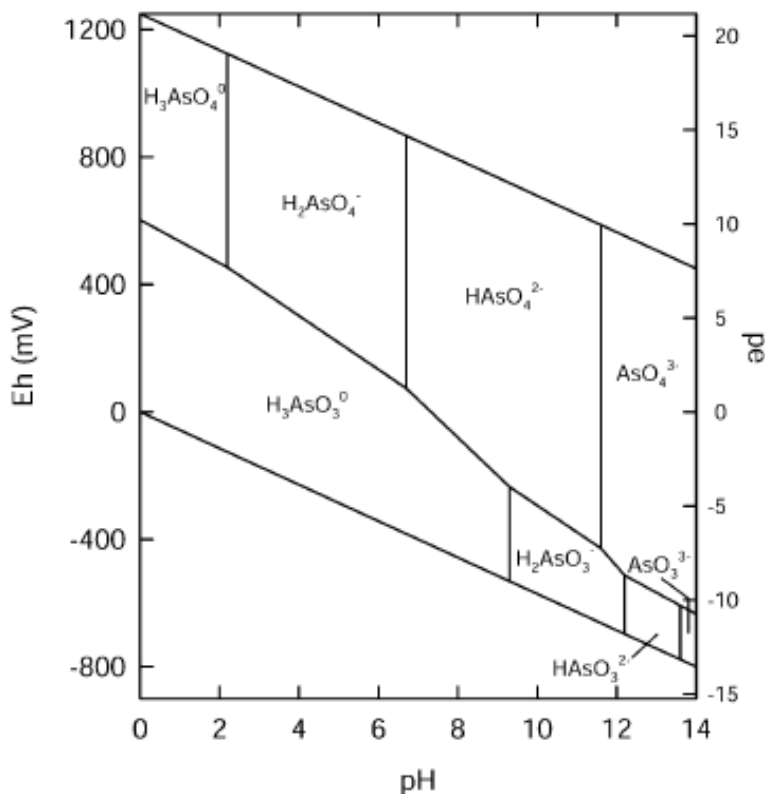


Fig. 1. Eh-pH diagram of aqueous arsenic species in water at 25°C and 1 bar total pressure [5].

In the presence of sulphide and in low pH conditions, HAsS_2 can form, arsine derivatives and arsenic metal can occur under extreme reducing conditions [27, 28]. Figure 1 shows the speciation of arsenic under varying pH and redox conditions [5].

In different environmental conditions arsenic readily changes its valence state and chemical form. Some conditions that may affect arsenic valence and speciation are presented: pH - in the pH range of 4 to 10, As(V) species are negatively charged in water, and the predominant As(III) species is neutral in charge; redox potential; the presence of complexing ions, such as ions of sulfur, iron, and calcium; microbial activity [29].

Adsorption-desorption reactions can also affect the mobility of arsenic in the environment. Geomaterials such as clays, carbonaceous materials, and oxides of iron, aluminum, and manganese are sediment components that may participate in adsorptive reactions with arsenic [29].

Studying the Mahomet aquifer, Illinois, U.S.A., Holms et al 2004 [30], constructed Eh-pH diagrams for arsenic speciation. The portion of the diagram that includes the pH and Oxidation-Reduction Potential (ORP) values of the Mahomet Aquifer was recalculated from Holms et al 2004 [30], for 14 °C, the approximate temperature of the aquifer (Figure 2). They used thermodynamic data for temperature adjustments from Nordstrom and Archer 2003 [31].

The diagonal lines separating the As(V) and As(III) species in Figure 2 were calculated as follows. The half-reaction for the reduction of As(V) to As(III) was given by equation 1.

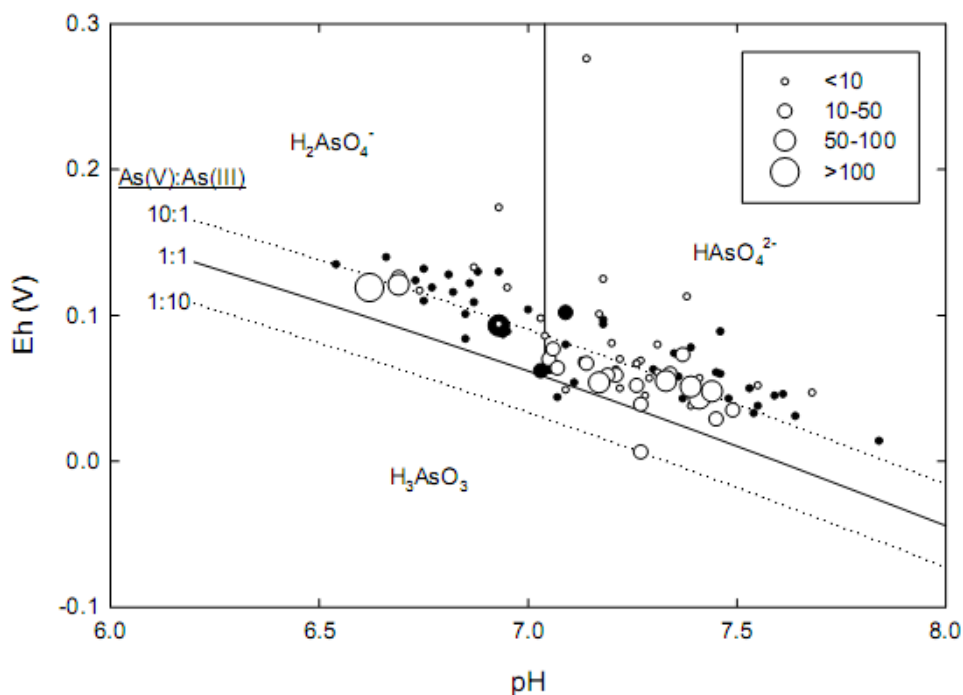
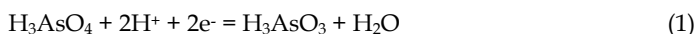


Fig. 2. Arsenic Eh-pH diagram, at 14 °C. Size of symbols indicates dissolved As concentration in $\mu\text{g}/\text{L}$. Filled symbols Champaign County, open symbols Tazewell County. Dotted lines indicate shift in stability fields for different As(V):As(III) ratios [30].

The Nernst equation (equation 2) relates the arsenic species concentrations at equilibrium.

$$E = E^0 + k \left(\text{Log}_{10} \left(\frac{\text{H}_3\text{AsO}_4}{\text{H}_3\text{AsO}_3} \right) - 2\text{pH} \right) \quad (2)$$

In equation 2, E^0 and k are a constant and a collection of constants, respectively. In the pH range of the Mahomet Aquifer, H_3AsO_4 makes up a small fraction of the As(V), which is given by equation 3 [32].

$$a^v = \frac{[H_3AsO_4]}{As(V)} = \frac{1}{1 + K_{a1}10^{pH} + K_{a1}K_{a2}10^{2pH} + K_{a1}K_{a2}K_{a3}10^{3pH}} \quad (3)$$

A similar equation can be derived for the fraction of As(III) in the H_3AsO_3 form (a^{III}). Essentially all of the As(III) is in the H_3AsO_3 form. Substituting equation 3 into equation 2 gives equation 4, which relates the equilibrium redox potential to the pH and concentrations of As(V) and As(III) (measured quantities [30; 32]).

$$E = E^0 + k \left(\text{Log}_{10} \left(\frac{As(V)a^v}{As(III)a^{III}} \right) - 2pH \right) \quad (4)$$

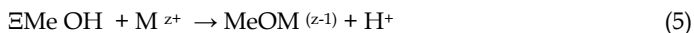
The lines labeled 1:1, 10:1, and 1:10 in Figure 2 are for the different ratios of As(V) to As(III) used in equation 4. The measured pH and ORP values, the points in Figure 2, plot in areas for which both As(III) and As(V) should be detectable and, indeed, both species were detectable in most samples [30; 32]. However, most of the points in Figure 2 lie in the As(V) field, the area in which As(V) makes up more than 50% of the total arsenic, whereas As(III) made up at least 85% of the arsenic in most of the samples analyzed in the present work [30; 32].

Other researchers have also found that their pH-ORP data plot completely in the As(V) field [33; 34; 35; 36; 37; 38]. Smedley 1996 [37], reported groundwater analyses for which As(III) made up 3-39% of the total arsenic, the ORP values were 221-469 mV, and the pH values were between 5.4 and 7.2. Although many of these data would be off the top of the scale of Figure 2, both arsenic species were detectable [30, 37].

The only As(III) species considered in equation 4 are H_3AsO_3 and $H_2AsO_3^-$, so the value of (a^{III}) was close to 1.0 for all measured pH values. However, there is evidence for complexation of As(III) by carbonate ions [39; 40]. The alkalinity values in the Mahomet Aquifer are fairly high (10 mmol/l), so if the As(III)- HCO_3^- stability constants are large enough, (a^{III}) could be significantly less than 1.0. An a^{III} value of 0.1 would shift the As(III)-As(V) boundary up approximately 30 mV and many more points would plot in the As(III) field [30; 32].

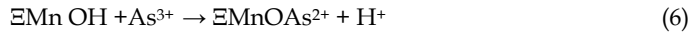
The shallow aquifers in Bangladesh and eastern India have attracted the focus of an array of studies regarding the source and fate arsenic in groundwater. The pollution of groundwater derives from organic-rich deltaic sediments. These sediments show highest concentrations in deeper and more reduced sections of the aquifers. As a result, different chemical correlations with arsenic have been reported by many investigators. Arsenic and iron have been found to be associated in the solid phase, and sometimes in solution but sometimes not [15; 16; 41; 42; 43].

The arsenic, either adsorbed to or co-precipitated with $FeOOH$, is released into solution. The adsorption of metal ions onto the surface of the metal oxides-hydroxides can be described by the equation 5, introduced by Stumm and Morgan 1996 [32]:



In order to explain the high positive loadings found between Mn and As concentrations in the groundwater of the Trifilia (Western Greece) karst aquifer, Panagopoulos and

Panagiotaras 2011 [44] rewritten equation 5 as equation 6 in the case of As and Mn-oxides/hydroxides phases:



In the case of oxidative weathering and dissolution of arsenic-containing minerals, they are primarily account for dissolved inorganic As(V) and As(III) ions in aquifers [10; 12]. This complex process can involve biological, chemical and electrochemical reactions and hydrodynamic factors. Subsequent mobility of the arsenic in groundwater depends on adsorption by mineral phases in soils and bedrocks, especially iron (III) hydroxides which have a high affinity for As(V) [14; 45; 46]. The processes can be depicted as in the following figure 3 [45]:

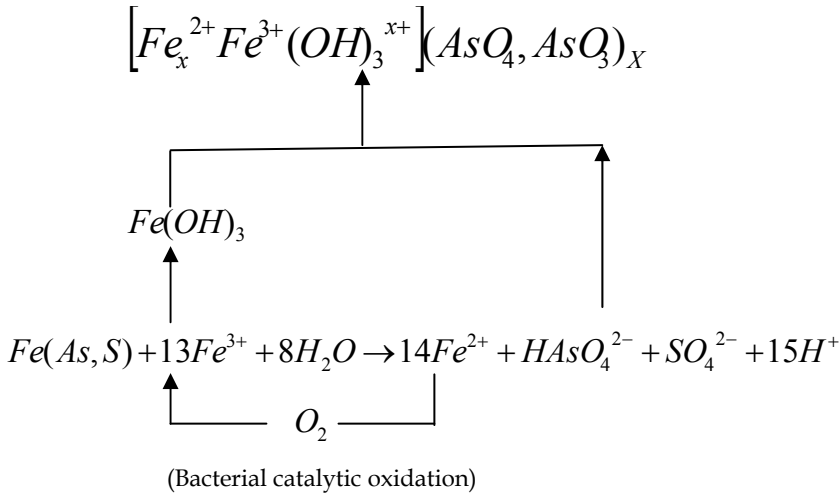
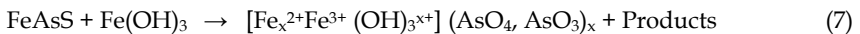


Fig. 3. Oxidative weathering and dissolution of arsenic-containing minerals in aquifers involving bacterial catalytic oxidation [45].

To some extent, the process can be regarded as the oxidation of arsenopyrite by amorphous ferric hydroxide. The oxy-anions of arsenic formed are quickly immobilized by the Fe(III) hydroxides due to equation 7 [45]:

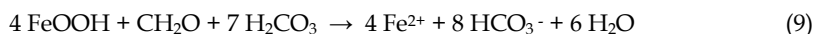
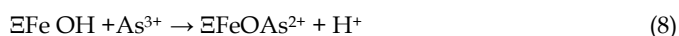


where x is less than one and the arsenic is adsorbed or co-precipitated with the ferrosferric hydroxides. The reaction is sustained by the shuttling of electrons between the oxidizing arsenopyrite surface and the ferric hydroxide, along chemical and biological pathways [45].

In other cases, arsenic correlated with HCO_3^- [15; 16; 41; 42]. The correlation with HCO_3^- was determined to be due to reductive dissolution of iron oxides-hydroxides coupled with oxidation of abundant organic matter in the sediments.

Significantly greater concentrations of HCO_3^- are likely due to CO_2^3 as a result of Organic Matter (OM) oxidation during reductive dissolution of ferric oxides-hydroxides.

The cycling of arsenic in such a case can be described by equations 8 and 9. Equation 8 delineates the adsorption of As onto the surface of Fe-oxides/hydroxides solid phases and introduced by Stumm and Morgan 1996 (equation 5) [32]. Equation 9 has been described by Nickson et al. 2000 [16] who proposed the release of As by the reductive dissolution of ferric oxides-hydroxides.



The vital role that microorganisms play in the release and/or immobilization of arsenic can be evidenced via the presence of significant amounts of organic matter and of viable populations of bacteria regarding arsenic reduction. [45].

Organic ligands can be bound with arsenic in solution and also decrease the amount of adsorption of arsenic coupled with reductive iron dissolution [47].

Due to the unstable nature of the arsenic species it might be rendered as difficult to treat wastes with unstable toxicity and mobility under certain environmental conditions. For long-term disposal and treatment purposes it is required that we understand the element's chemistry and the environment of its disposal.

Current research has expressed an increasing interest and has also shifted its focus on studies regarding the speciation of arsenic in both environmental and biological samples. A limitation is being posed alongside this research path and this is the low level of arsenic species in real samples. This implies that problems highly correlated with the element's speciation remain unresolved. Examples of these problems among others include: species instability during sampling, sample and storage treatment, partially complete recovery of all species, matrix interferences, lack of appropriate certified reference materials and of sensitive analytical methods [6; 17].

Analytical procedures through continuous development calls for an up-to-date knowledge of the recent publications for the purpose of coping successfully with these problems. Detection limits are provided for the majority of the methods. This takes place for the purpose of comparison affordability and for judging the possible applicability. Various researchers have approached these studies in a variety of ways that can lead to knowledge. Knowledge is the main determinant for the understanding of the environmental cycle regarding this element. Furthermore, it facilitates the understanding of its physiological and toxicological behaviour in the living organisms [6; 17; 45].

Arsenic does not form any complexes with simple anions like Cl^- and SO_4^{2-} as is the case with the cationic metals since it forms anions in solution. The behaviour of anionic arsenic resembles the behaviour of ligands in water. It furthermore forms bonds with nitrogen, carbon and the organic sulphur. As (III) has been found to react with sulphur and sulphhydryl groups i.e. cystine, organic dithiols, proteins, enzymes. It has not been found to react with amine groups or with organics with reduced nitrogen constituents [17].

On the opposite side, As (V) has been found to react with amines (reduced nitrogen groups but not with groups of sulphhydryl. Organoarsenicals in both trivalent and pentavalent forms can be formed by carbon. The complexation of arsenic III and V by dissolved organic

matter in natural environments has been found to prevent sorption and co-precipitation with both solid-phase organics and inorganics. Thus, it increases arsenic's mobility in both the soil and aquatic systems [48; 49].

It is possible for arsenic inorganic compounds to be methylated by bacteria, fungi, and yeasts to organic compounds. As such, it can be methylated into monomethylarsonic acid (MMA), dimethylarsinic acid (DMA), and gaseous derivatives of arsine.

The Bangladeshi samples were the ones that provided the correlation of arsenic with $\text{NH}_3\text{-N}$, methane (CH_4), Dissolved Organic Carbon (DOC), and Ca [41; 43]. The presence of Dissolved Oxygen (DO) or nitrates did not provide any evidence on the existence of arsenic [15; 16]. According to various observations arsenic and SO_4^{2-} tend to be mutually exclusive [41; 50]. Further on this path, Dowling et al. (2002) observed that SO_4^{2-} was absent from the samples received and observed, as well as, that arsenic was found to correlate with $\text{NH}_3\text{-N}$ and Total Organic Carbon (TOC) [43]. Various parts of the Mahomet Aquifer have provided evidence of methane existence. According to Meents (1960), CH_4 has been derived from the degradation of organic matter in the Sankoty sand found in the Mahomet Aquifer, Illinois [51]. He further reported buried soils, peats, and organic-rich silts associated with interglacial stages, especially the Sangamon soil, which overly the Mahomet aquifer as being additional CH_4 sources [30].

4. Conclusions

The distribution of arsenic species and chemistry in aquatic environments is a function of redox reactions, adsorption-desorption processes and dissolution of solid phases. In such a complex system the activity of bacteria must be considered in order to evaluate possible arsenic dissolution mechanisms. The concentrations of several ions and water quality parameters, and the relations between arsenic occurrence and other chemical components must be examined in order to better understand the correlation between them and gain the overall knowledge of arsenic geochemistry in groundwater system.

5. References

- [1] U.S. EPA. Arsenic Treatment Technologies for Soil, Waste, and Water. EPA-542-R-02 004. September 2002.
http://clu.in.org/download/remed/542r02004/arsenic_report.pdf.
- [2] U.S. EPA. National Primary Drinking Water Regulations; Arsenic and Clarifications to Compliance and New Source Contaminants Monitoring; Final Rule. Federal Register, Volume 66, Number 14, p. 6975-7066. January 22, 2001.
<http://www.epa.gov/sbrefa/documents/pnl14f.pdf>.
- [3] Welch, A.H., Westjohn, D.B., Helsel, D.R., Wanty, R.B., 2000. Arsenic in ground water of the United States: occurrence and geochemistry. *Ground Water* 38, 589-604.
- [4] Edmunds, W.M., Cook, J.M., Kinniburgh, D.G., Miles, D.L., Trafford, J.M., 1989. Trace-element Occurrence in British Groundwaters. Res. Report SD/89/3, British Geological Survey, Keyworth.
- [5] Smedley P. L. and Kinniburgh D. G. (2002) A review of the source, behaviour and distribution of arsenic in natural waters. *Applied Geochemistry* 17, 517-568.

- [6] U.S. EPA-542-R-02-004. Arsenic Treatment Technologies for Soil, Waste, and Water. September 2002. www.epa.gov/tioclu-in.org/arsenic.
- [7] U.S. EPA. National Primary Drinking Water Regulations; Arsenic and Clarifications to Compliance and New Source Contaminants Monitoring; Proposed Rule. Federal Register, Vol 65, Number 121, p. 38888. June 22, 2000. <http://www.epa.gov/safewater/ars/arsenic.pdf>.
- [8] Fleischer, M., 1983. Glossary of Mineral Species. The mineral record Inc, Tucson, Arizona.
- [9] Boyle, D.R., Turner, R.J.W., Hall, G.E.M., 1998. Anomalous arsenic concentrations in groundwaters of an island community, Bowen island, British Columbia. *Environ. Geochem. Health* 20, 199–212.
- [10] Smedley, P.L., Edmunds, W.M., Pelig-Ba, K.B., 1996. Mobility of arsenic in groundwater in the Obuasi gold-mining area Ghana: some implications for human health. In: Appleton, J.D., Fuge, R., McCall, G.J.H. (Eds.), *Environmental Geochemistry and Health*, vol. 113. Geological Society Special Publication, London, pp. 163–181.
- [11] Williams, M., Fordyce, F., Pajitprapapon, A., Charoensaisri, P., 1996. Arsenic contamination in surface drainage and groundwater in part of the southeast Asian tin belt, Nakhon Si Thammarat Province, southern Thailand. *Environ. Geol.* 27, 16–33.
- [12] Chowdhury, T.R., Basu, G.K., Mandal, B.K., Biswas, B.K., Samanta, G., Chowdhury, U.K., Chanda, C.R., Lodh, D., Roy, S.L., Saha, K.C., Roy, S., Kabir, S., Quamruzzaman, Q., Chakraborti, D., 1999. Arsenic poisoning in the Ganges delta. *Nature* 401, 545–546.
- [13] Mandal, B.K., Chowdhury, T.R., Samanta, G., Mukherjee, D.P., Chanda, C.R., Saha, K.C., Chakraborti, D., 1998. Impact of safe water for drinking and cooking on five arsenic-affected families for 2 years in West Bengal, India. *Sci. Total Environ.* 218, 185–201.
- [14] Acharyya, S.K., Chakraborty, P., Lahiri, S., Raymahashay, B.C., Guha, S., Bhowmik, A., 1999. Arsenic poisoning in the Ganges delta. *Nature* 401, 545.
- [15] Nickson, R., McArthur, J., Burgess, W., Ahmed, K.M., Ravenscroft, P., Rahman, M., 1998. Arsenic poisoning of Bangladesh groundwater. *Nature* 395, 338.
- [16] Nickson, R.T., McArthur, J.M., Ravenscroft, P., Burgess, W.G., Ahmed, K.M., 2000. Mechanism of arsenic release to groundwater, Bangladesh and West Bengal. *Appl. Geochem.* 15, 403–413.
- [17] M. Kumaresan and P. Riyazuddin (2001). Overview of speciation chemistry of arsenic. *Current Science*, Vol. 80, No. 7, 10, 837–846.
- [18] The Agency for Toxic Substances and Disease Registry (ATSDR): ToxFAQs™ for Arsenic (12). July, 2001. <http://www.atsdr.cdc.gov/tfacts2.html>.
- [19] Kirk-Othmer. "Arsenic and Arsenic Alloys." *The Kirk-Othmer Encyclopedia of Chemical Technology*, Volume 3. John Wiley and Sons, New York. 1992.
- [20] National Research Council. *Arsenic in Drinking Water*. Washington, D.C. National Academy Press. 1999. <http://www.nap.edu/catalog/6444.html>.
- [21] Korte, N., 1991. Naturally occurring arsenic in groundwaters of the Midwestern United States. *Environ. Geol. Water Sci.* 18, 137–141.
- [22] Matisoff, G., Khourey, C.J., Hall, J.F., Varnes, A.W., Strain, W.H., 1982. The nature and source of arsenic in northeastern Ohio ground water. *Ground Water* 20, 446–456.

- [23] Nimick, D.A., 1998. Arsenic hydrogeochemistry in an irrigated river valley—a reevaluation. *Ground Water* 36, 743–753.
- [24] Das, D., Samanta, G., Mandal, B.K., Chowdhury, T.R., Chanda, C.R., Chowdhury, P.P., Basu, G.K., Chakraborti, D., 1996. Arsenic in groundwater in six districts of West Bengal, India. *Environ. Geochem. Health* 18, 5–15.
- [25] Welch A. H., Westjohn D. B., Helsel D. R., and Wanty R. B. (2000) Arsenic in ground water of the United States: Occurrence and geochemistry [Review]. *Ground Water* 38(4), 589-604.
- [26] Schreiber M. E., Simo J. A., and Freiberg P. G. (2000) Stratigraphic and geochemical controls on naturally occurring arsenic in groundwater, eastern Wisconsin, USA. *Hydrogeology Journal* 8(2), 161-176.
- [27] Scow, K., Byrne, M., Goyer, M., Nelken, L., Perwak, J., Wood, M. and Young, S., Final Draft Report to the US Environmental Protection Agency, EPA Contract 68-01-6160, Monitoring and Data Support, Office of Water Regulations and Standards, Washington, DC, 1981.
- [28] Rai, D., Zachara, J., Schwabe, A., Schmidt, R., Girvin, D. and Rogers, J., Report, EA-3356 to EPRI by Pacific Northwest Laboratories, Battelle Institute, Richland, Wash, 1984.
- [29] Vance, David B. "Arsenic - Chemical Behavior and Treatment". October, 2001. <http://2the4.net/arsenicart.htm>.
- [30] Thomas R. Holm, Walton R. Kelly, Steven D. Wilson, George S. Roadcap, Jonathan L. Talbott, John W. Scott, (2004). Arsenic Geochemistry and Distribution in the Mahomet Aquifer, Illinois. Illinois Waste Management and Research Center. Division of the Illinois Department of Natural Resources. http://www.wmrc.uiuc.edu/main_sections/info_services/library_docs/RR/RR-107.pdf.
- [31] Nordstrom D. K. and Archer D. G. (2003) Arsenic thermodynamic data and environmental geochemistry. In *Arsenic in Ground Water* (ed. A. H. Welch and K. G. Stollenwerk), pp. 1-25. Kluwer.
- [32] Stumm W. and Morgan J. J. (1996) *Aquatic Chemistry: Chemical Equilibria and Rates in Natural Waters*, 3rd ed. Wiley.
- [33] Armienta M. A., Villasenor G., Rodriguez R., Ongley L. K., and Mango H. (2001) The role of arsenic-bearing rocks in groundwater pollution at Zimapan Valley, Mexico. *Environmental Geology* 40(4-5), 571-581.
- [34] Bottomley D. J. (1984) Origins of some arseniferous groundwaters in Nova Scotia and New Brunswick, Canada. *Journal of Hydrology* 69(1-4), 223-257.
- [35] Planer-Friedrich B., Armienta M. A., and Merkel B. J. (2001) Origin of arsenic in the groundwater of the Rioverde basin, Mexico. *Environmental Geology* 40(10), 1290-1298.
- [36] Robertson F. N. (1989) Arsenic in ground-water under oxidizing conditions, south-west United States. *Environ. Geochem. Health* 11(3-4), 171-185.
- [37] Smedley P. L. (1996) Arsenic in rural groundwater in Ghana. *J. African Earth Sciences* 22(4), 459-470.
- [38] Welch A. H., Lico M. S., and Hughes J. L. (1988) Arsenic in ground water of the western United States. *Ground Water* 26, 333-347.
- [39] Kim M. J., Nriagu J., and Haack S. (2000) Carbonate ions and arsenic dissolution by groundwater. *Environmental Science & Technology* 34(15), 3094-3100.

- [40] Lee J. S. and Nriagu J. O. (2003) Arsenic carbonate complexes in aqueous systems. In *Biogeochemistry of environmentally important trace metals* (ed. Y. Cai and O. C. Braids), pp. 33-41. American Chemical Society.
- [41] Harvey C. F., Swartz C. H., Badruzzaman A. B. M., Keon-Blute N., Yu W., Ali M. A., Jay J., Beckie R., Niedan V., Brabander D., Oates P. M., Ashfaque K. N., Islam S., Hemond H. F., and Ahmed M. F. (2002) Arsenic mobility and groundwater extraction in Bangladesh. *Science* 298(5598), 1602-1606.
- [42] McArthur J. M., Ravenscroft P., Safiulla S., and Thirlwall M. F. (2001) Arsenic in groundwater: Testing pollution mechanisms for sedimentary aquifers in Bangladesh. *Water Resources Research* 37(1), 109-117.
- [43] Dowling C. B., Poreda R. J., Basu A. R., Peters S. L., and Aggarwal P. K. (2002) Geochemical study of arsenic release mechanisms in the Bengal Basin groundwater - art. no. 1173. *Water Resources Research* 38(9), 12-1 - 12-18.
- [44] G. Panagopoulos and D. Panagiotaras (2011). Understanding the extent of geochemical and hydrochemical processes in coastal karst aquifers through ion chemistry and multivariate statistical analysis. *Fresenius Environmental Bulletin*, volume 20, No 12a, 3270-3285.
- [45] Myoung-Jin Kim, Jerome Nriagu, Sheridan Haack (2002). Arsenic species and chemistry in groundwater of southeast Michigan. *Environmental Pollution* 120, 379-390.
- [46] Welch, A.H., Lico, M.S., 1998. Factors controlling As and U in shallow ground water, southern Carson Desert, Nevada. *Appl. Geochem.* 13, 521-539.
- [47] Redman A. D., Macalady D. L., and Ahmann D. (2002) Natural organic matter affects arsenic speciation and sorption onto hematite. *Environmental Science & Technology* 36(13), 2889-2896.
- [48] Callahan, M. et al. Report, EPA-440/4-79-029a, EPA Contracts 68-01-3852 and 68-01-3867, Office of Water Planning and Standards, US Environmental Protection Agency, Washington, DC, 1979.
- [49] Ferguson, J. F. and Davis, J., (1972). A review of the arsenic cycles in natural waters. *J., Water Res.*, 6, 1259-1274.
- [50] Ravenscroft P., McArthur J. M., and Hoque B. A. (2001) Geochemical and Palaeohydrological Controls on Pollution of Groundwater by Arsenic. *Arsenic Exposure and Health Effects IV*, 1-20.
- [51] Meents W. F. (1960) *Glacial-Drift Gas in Illinois*, pp. 58. Illinois State Geological Survey.

Geochemistry of Hydrothermal Alteration in Volcanic Rocks

Silvina Marfil and Pedro Maiza
*Universidad Nacional del Sur – INGEOSUR- CIC de la
Provincia de Buenos Aires – CONICET
Argentina*

1. Introduction

Hydrothermal alteration is a chemical replacement of the original minerals in a rock by new minerals where a hydrothermal fluid delivers the chemical reactants and removes the aqueous reaction products. An understanding of hydrothermal alteration is of value because it provides insights into the chemical attributes and origins of ore fluids and the physical conditions of ore formation (Reed M. 1997).

Within a mineral deposit, the solution channelways are usually obvious because precipitated minerals and altered wallrocks remain as evidence. The direction in which the solutions flowed, especially in flat-lying deposits, is usually less obvious but in many cases can be inferred from mineral zoning or similar evidence (Skinner B. 1997).

The mobility of major, minor and rare-earth elements (REE) during alteration processes in different environments has been documented by numerous authors and has been used to discriminate the origin of kaolin deposits. (Sturchio et al., 1986; De Groot & Baker, 1992; Gouveia et al., 1993; van der Weijden & van der Weijden, 1995; Condie et al., 1995; Dill et al., 1997, 2000; Galán et al., 1998, 2007; Pandarinath et al., 2008, among others). Terakado & Fujitani (1998) studied the REE and other trace elements in silicstones, alunites and related rocks in order to examine the behaviour of trace elements in the acidic hydrothermal alteration of silicic volcanic rocks. They found that most of the elements such as Na, Fe, Ba and LREE were leached from the silicstones, while HREE, Th, Hf and Zr were retained in the rocks, even under strongly acidic hydrothermal processes. Alunite samples have LREE-enriched and HREE-depleted features. According to Dill et al. (1997), the ratios $TiO_2 + Fe_2O_3$ vs. $Cr + Nb$, Zr vs. TiO_2 and $Ba + Sr$ vs. $Ce + Y + La$ in kaolinities allow discrimination between hypogene and supergene kaolinization processes. The APS-bearing argillaceous zones that formed during supergene processes are significantly enriched in REE relative to hypogene equivalents (Dill, 2000).

Pandarinath et al. (2008) studied the effects of hydrothermal alteration on major, rare-earth, and other trace-element concentrations in rhyolitic rocks of the Los Azufres geothermal field, Mexico. They concluded that the hydrothermal alteration resulted in a decrease in MnO , P_2O_5 , Ta, Rb/Zr and Rb/Nb, and an increase in Zr, Nb and Nb/Y. The greater variances of Y, Ce, Pr, Nd, Sm, Lu and Pb in altered rocks are probably due to hydrothermal

processes, whereas smaller variances of CaO, Sr, Rb/Sr and Rb/Ba in altered rocks suggest that these processes led to more uniform chemical rock compositions. The concentrations of REE were not significantly different between fresh and altered rhyolitic rocks, which implies that either these elements remained immobile or were reincorporated into secondary minerals during the hydrothermal alteration of the rhyolitic rocks.

Papoulis & Tsolis-Katagas (2008) studied kaolin deposits in the western and southern parts of Limnos Island, northeast Aegean Sea, Greece, and they found two types of hydrothermal alteration zones: smectite-illite-halloysite and kaolinite-dickite-rich zones. Mineral assemblages reveal that temperatures ranged from <100°C (smectite-rich and halloysite rich zones) to ~270°C (kaolinite-dickite-rich zones). Limited supergene alteration was observed in the less hydrothermally altered rocks of the illite-rich zones as suggested by the presence of jarosite and pyrite. The development of the various assemblages depends not only on the temperature and composition of the hydrothermal fluids but also on the distance of the rock from the fault or the channel of the ascending hydrothermal fluids. Papoulis et al. (2004) used the K and Na content in a kaolin deposit from Greece to measure the degree of alteration of primary rocks. The positive correlation between Al₂O₃ and LOI and the large negative loadings between SiO₂-Al₂O₃ and SiO₂-LOI indicate that LOI and Al₂O₃ contents increase in the more altered samples.

Ece et al. (2008) studied acid-sulphate hydrothermal alteration in andesitic tuffs in the Biga Peninsula (Turkey), and concluded that changes in the chemical composition of geothermal waters through time and the chemistry of the intermediate products in clay deposits also control the formation of alunite. The main geothermal activity and acidsulphate alterations for the mineralizations of alunite and halloysite occurred after the onset of NAF-related faulting in the Biga Peninsula. The P₂O₅ enrichment in alunite nodules suggests a deep magmatic source for the geothermal waters that passed through the shallow-level granodiorite intrusions.

The minerals that constitute various alteration assemblages depend on: temperature, pressure, primary rock composition, primary fluid composition and the ratio of fluid to rock in the reaction that produced the alteration. (Reed M. 1997).

The aim of the study described in this chapter was to evaluate the relation between the chemical composition of major, minor and trace elements, the stable isotopes in kaolin (O and D) and the mineralogical alteration zonation to confirm the hydrothermal genesis of the deposits, working with volcanic rocks from Patagonia Argentina.

Knowing the genesis of such deposits is crucial in order to establish exploration criteria and evaluate reserves. These Patagonian deposits are derived from Mesozoic rhyolitic and andesitic rocks. There have been several studies aimed at discovering the origin of the primary deposits (Domínguez & Murray, 1995, 1997; Cravero et al., 1991, 2001; Domínguez et al., 2008, Marfil et al., 2005). Most of the studies deal with the mineralogy, chemical composition, the deposit structure and oxygen-deuterium isotopic data.

The deposits examined in this study are located in different areas of Patagonia in the Provinces of Río Negro and Chubut and they are studied by Cravero et al. (2010), Maiza et al. (2009) and Marfil et al. (2005, 2010).

Geologically, the area is characterized by the presence of a set of volcanic rocks and tuffs with minor clastic sediments that overlie a basement of Mesozoic age, essentially constituted by granites. At the base, the volcanic complex is composed of andesites, which is known as

Vera formation. This complex is followed by a succession of sandstone tuffs, rich in fossil plants (Dicroidium Flora formation) and finally by a suite of ignimbritic tuffs and flows known as the Sierra Colorada formation, deposited at the top of the series. The age of this volcano-sedimentary complex ranges from Triassic to Middle Jurassic. Kaolinite deposits are enclosed in rhyolitic tuffs of the Sierra Colorada formation. An important silicification, developed at the top of the formation, seems to have protected the altered areas from erosive processes giving rise to smooth elevations in the landscape.

The occurrence of hydrothermal events in the region is also proven by the presence of fluorite and Pb-Cu-Zn veins (Labudia & Hayase, 1975). Fluorite veins are hosted by rhyolites presenting an alteration mineralogy with sericite, carbonates, silica and kaolinite (Labudia & Hayase, 1975). According to Manera (1972) and Hayase & Manera (1973), homogenization temperatures of fluid inclusions in fluorite are between 150 and 240 °C (without correction for pressure). The presence of kaolinite and the formation temperatures of these veins suggest a possible relationship between fluorite-base metal veins and the studied kaolinite deposits of the area. In this case, kaolinite occurrences could be used as a prospecting tool for other types of mineral deposits in the region.

2. Geological setting

The deposits examined in this study are hydrothermal origin, located in the provinces of Río Negro (Blanquita, Equivocada and Loma Blanca mines) and Chubut (Estrella Gaucha mine) (Patagonia, Argentina) (Fig. 1).

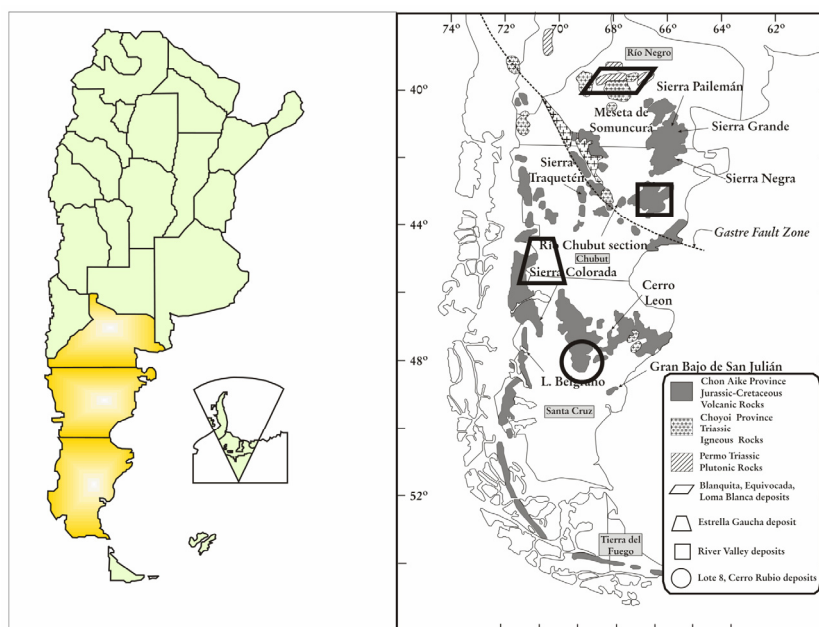


Fig. 1. Localization of the kaolin deposits in a sketch map of Patagonia (Cravero et al. 2010, modified).

In the provinces of Chubut and Santa Cruz there are many kaolin deposits, some of them very extensive, located in the Chubut river valley and lote 8, 18, 19 and Cerro Rubio respectively. These deposits are sedimentary and residual origin, formed from the alteration of volcanic materials, especially Jurassic rhyolitic tuffs.

In the province of Chubut there is another group of kaolin deposit related with hydrothermal alteration. Estrella Gaucha mine is one of them. It is situated in western Chubut Province, 70 km from Alto Río Senguer and 20 km from Aldea Apeleg. It is located at SW from Cerro Bayo at 1620 meters above sea level. Ploszkiewicz & Ramos (1977), found andesites and dacites of Ñirehuao Formation and dacitic ignimbrites of Gato Formation. These volcanic rocks are Cretaceous age. The outcropping rocks in the area studied are conglomeratic sandstones with moderate alteration and stratified. In their composition are common rhyolites, andesites and siliceous sandstones. These rocks are the base of the deposit. Iron oxides are abundant and they are chloritized. The lithic components are selectively altered related with the textures and mineralogical composition. It is possible to observe particles replaced pseudomorphologically by chlorite, kaolinite, alunite and quartz. Some grains conserve the original textures while in others the replacement is massive forming monomineral particles. The mineralization is developed from the alteration of rhyolitic tuffs of the Lower Cretaceous Payaniyeu Formation in contact with tuff sandstone of Apeleg Formation. The relation between both Formations is not clear because the alteration processes developed in the transition zone (Ploszkiewicz & Ramos 1977). The mineralogy consists mainly of dickite with rare alunite and variable amounts of quartz distributed in four alteration zones, from a silicified upper zone, grading downwards to an alunite zone, then a kaolinized zone and, finally, a sericite-chlorite zone (Hayase et al. 1971, Maiza 1972, 1981, Maiza & Hayase 1975 and Maiza et al. 2009). (Fig 2a)

The Chubut River Valley deposits and those of the Santa Cruz province are developed on Jurassic volcanic rocks which are predominantly rhyolitic and form one of the world's most voluminous silicic provinces (Pankurst & Rapela, 1995). It is called Chon-Aike Province (Pankurst et al., 1998), which ranges in age from Early Jurassic to Early Cretaceous. This province comprises several formations that, depending on the geographical locality, receive different names (Marifil and Chon-Aike, among others). In Chubut, the deposits were formed on the Marifil Formation (Malvicini & Llambias, 1974) and are found along the Chubut River in an area of ~60 km². In Santa Cruz, the primary deposits came from the alteration of rhyolitic ash-fall tuffs and ignimbrites of the Chon-Aike Formation which formerly belonged to the Bahía Laura Group) (Domínguez & Murray, 1997; Cravero et al., 2001). In both the Marifil and Chon-Aike rocks, the kaolinized areas have a wide horizontal extension, limited thickness (8-12 m at most) and a downward decreasing degree of alteration. The mineralogical composition is kaolinite with minor halloysite, illite and relict quartz and feldspars (Domínguez & Murray, 1997; Cravero et al., 2001; Domínguez et al., 2008). Table 1 synthesizes the geology and mineralogy of the deposits (Cravero et al. 2010).

Blanquita and Equivocada mines are situated 30 km SE of Los Menucos in the province of Río Negro (Fig. 1). The mineralized zone is distributed along a belt 5 to 8 km wide and 20 km long with an approximate area of 110 km². Kaolinite deposits are enclosed in rhyolitic tuffs of the Sierra Colorada Formation, Triassic to Middle Jurassic in age. Blanquita mine is characterized by the presence of kaolinite and alunite with scarce dickite and pyrophyllite,

whereas in the Equivocada mine, kaolinite is associated with dickite and traces of alunite (without pyrophyllite) (Marfil et al., 2005).

The rhyolitic tuffs, which host most of the kaolinized bodies, were deposited on top of the porphyritic rhyolites. The texture of the tuff is variable, from fine-grained up to agglomerate levels, and shows a microcrystalline matrix with abundant quartz, sanidine, plagioclase, hornblende and biotite. Alteration is moderate with sericitization and kaolinitization of feldspars and chloritization of amphiboles and biotites (Marfil et al. 2005) (Fig. 2b Blanquita Mine and Fig. 2c Equivocada Mine).

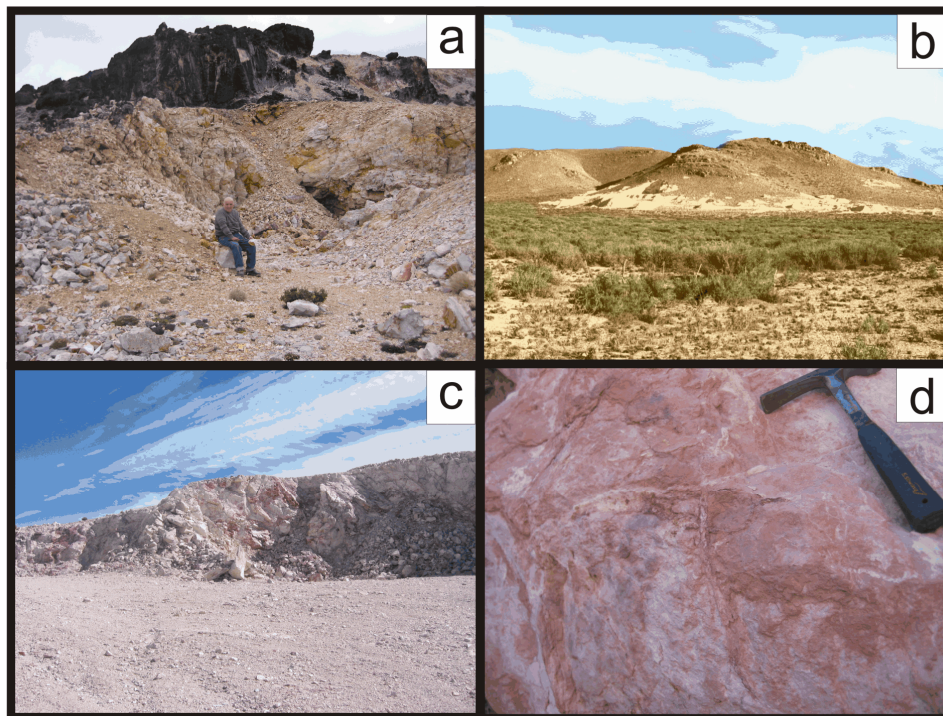


Fig. 2. a. Estrella Gaucha mine (kaolinized zone). b. Blanquita mine. c. Equivocada mine. d. Loma Blanca mine (Advanced argillic alteration zone)

Loma Blanca is situated 70 km NW of Los Menucos (Río Negro Province, Argentina) (Fig. 1). The parent rocks are andesites and their tuffs from the Vera Formation (Lower Triassic) (Los Menucos Group), which lie unconformably on the La Esperanza granite and Colo Niyeu metamorphites. 150 m to the northeast of the deposit there is an outcrop of granite intruded by aplitic dykes. Its geological importance arises from the mineralogy, structure and setting of the strongly mineralized area and its relationship with the different lithologic units (Fig 2d). Hayase & Maiza (1972a) studied the mineralogy of the Loma Blanca deposit using X-ray diffraction (XRD), thermogravimetric (TG) and differential thermal analysis (DTA), and microscopy. They concluded that the deposit was formed by the activity of an acid

Deposit	Host rocks	Mineral association	Age	Origin
Blanquita	Rhyolitic tuffs	Kaolinite ^{***} Alunite ^{**} Dickite [*] Pyrophyllite [*]	Triassic to Middle Jurassic	Hypogene
Equivocada	Rhyolitic tuffs	Kaolinite ^{***} Alunite [*] Dickite ^{**} Natroalunite ^{**}	Triassic to Middle Jurassic	Hypogene
Loma Blanca	Andesites and Andesitic tuffs	Kaolinite ^{***} Alunite ^{**} Dickite ^{**} Pyrophyllite ^{**} Diaspore [*] Illite ^{**} Montmorillonite [*] Chlorite [*]	Lower Triassic	Hypogene
Estrella Gaucha	Rhyolitic tuffs	Dickite ^{***} Alunite [*]	Lower Cretaceous	Hypogene
Chubut River Valley	Rhyolitic tuffs	Kaolinite ^{***} Quartz-Fd ^{**} Illite-halloysite [*]	Lower Jurassic- Lower Cretaceous	Supergene
Santa Cruz	Rhyolitic tuffs	Kaolinite ^{***} Quartz-Fd ^{**} Illite-halloysite [*]	Lower Jurassic- Lower Cretaceous	Supergene

*** Abundant

** Scarce

* Very rare

Table 1. Host-rock composition, alteration mineralogy, age and origin of the Patagonia kaolin deposits (Cravero et al. 2010, modified).

hydrothermal solution or superheated solfatara. They proposed a concentric zonation model. From the parent rock outward, different alteration patterns were recognized: a zone with sericite, chlorite and montmorillonite; a zone with kaolinite and dickite; a zone with dickite, pyrophyllite and alunite-natroalunite; and a zone with quartz, disseminated sulphides and diaspore (Fig. 3). (Marfil et al. 2010). The structure is not clearly exposed due to the scarce outcrops and smooth geomorphical topography covered by recent sediments. Geological evidence from the area indicates the development of tectonic fracturing and differential block movements affecting the heterogeneous volcanosedimentary pile that channelled the hydrothermal solutions responsible for the mineralization. The mineral assemblage, with high-temperature minerals (diaspore, pyrophyllite and dickite), the abovementioned sulphides, the areal structure and favourable lithology related to mineralization processes identify this zone as suitable for metallic mineral prospecting. The floor of the Loma Blanca mine consists of andesite that shows progressive alteration and development of a propylitic zone. Tuffaceous levels are transitionally interlayered; they are affected by tectonics and have developed breccias zones that, owing to their greater

permeability, provide pathways for mineralizing solutions. Towards the top of the mineralized zone, the texture is obliterated due to the intense silicification that has erased the lithological characteristics of the affected rocks (Maiza et al., 2009). The oldest formation in the area is Colo Niyeu, which is a low-grade metasedimentary basement. According to Labudia & Bjerg (1994), it could only be assigned a pre-Permian age. This unit was intruded by different plutonites of the so-called Complejo Plutónico La Esperanza. Close to the deposit, outcrops attributed to the Donosa granite, due to their mineralogical and textural characteristics, were recognized; the age of the intrusion, according to Pankurst et al. (1992), will be Late Permian. Over these formations lie the lithological components of the Los Menucos Group, of Triassic age; they are intruded by andesitic dykes of the Taquetren Formation. The field relations of these units have been obscured by tectonism, covered by recent sediments and masked by the mineralizing process (Marfil et al. 2010).

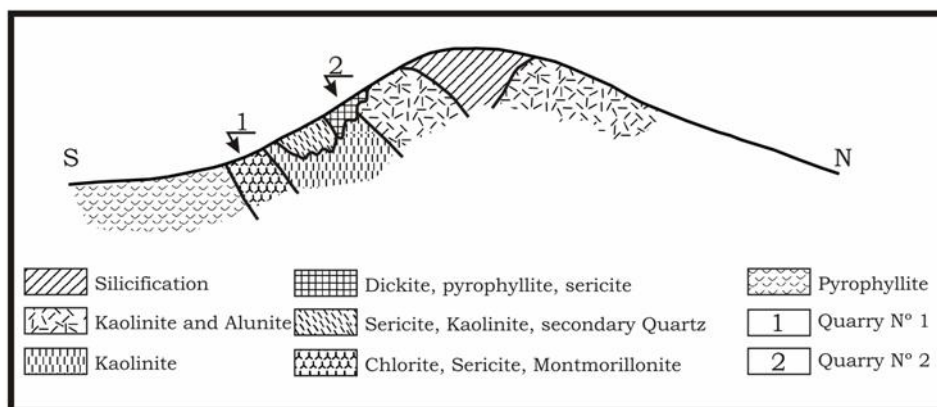


Fig. 3. Scheme of the Loma Blanca mine (Marfil et al. 2010).

3. Methods and instrumentation

The petrographic studies were carried out with an Olympus B2-UMA trinocular petrographic microscope with a built-in Sony 151A video camera, a high-resolution monitor and Image-Pro Plus image processing software were used. The mineralogical composition of bulk samples was determined by XRD, using a Rigaku D-Max III, with Cu-K α radiation and a graphite monochromator operated at 35 kV and 15 mA. The XRD patterns were recorded from 2° to 60° 2 θ . Chemical analyses of bulk samples for major, minor and trace elements were carried out by inductively-coupled plasma mass-spectrometry (ICP). Kaolin samples were selected for H and O isotope, SEM, IR and DTA-TG analyses. Isotope results are presented as % deviation with respect to SMOW. The reproducibility of results is better than $\pm 0.5\%$ for O and $\pm 10\%$ for H.

4. Mineralogical composition

4.1 Estrella Gaucha mine

The mineralogy of the kaolinized zone in this deposit is very simple. The mineral more abundant is dickite, with minor amount of alunite and quartz and scarce pyrophyllite and

diaspore. The presence of dickite was mentioned in other kaolin deposits: Tres Picos Mines (Province of Neuquen) (Hayase & Maiza 1970, Losada et al. 1975), Loma Blanca Mine (Province of Río Negro) (Hayase & Maiza 1972a) and Adelita Mine (Province of Río Negro) (Hayase & Maiza 1972b) but in any case the more abundant.

In Estrella Gaucha mine dickite is associated with fine size quartz. To the top of the mineralization the more abundant mineral is alunite, with relictic inclusions of dickite, in a 20-30 meters thickness zone. The deposit culminates with a silicified zone with quartz with saccharoidal texture. Massive dickite, constitutes tabular crystals of 200 microns (Fig. 4a). It has parallel extinction (to 4°) and very low birefringence (0.006 to 0.008).

4.2 Blanquita mine

The kaolinization processes have completely obliterated the original textures of the rock, leaving only quartz (Fig. 4b). The mineralogy includes dickite, kaolinite, pyrophyllite, variable amounts of quartz and scarce alunite (Marfil et al. 2005).

4.3 Equivocada mine

The alteration processes is similar to that mentioned in Blanquita mine. It has almost erased the original texture and mineralogy of the tuffs. Only quartz and some biotite remnants are still visible (Fig. 4c). The lithic particles have been pseudomorphically replaced by kaolinite and dickite. The alteration mineralogy consist of a core of alunite grading outwards to an association of kaolinite-illite, illite-zeolite and finally fresh rock (Hayase & Maiza 1970, Marfil et al. 2005). The whole mineralization was later discordantly overprinted by natroalunite (Maiza & Mas 1981).

4.4 Loma Blanca mine

In the propylitic alteration zone the original texture is preserved. Plagioclase (andesine) crystals are altered, mainly to illite and calcite. Chlorite pseudomorphically replaces the mafic minerals, and goethite is formed from the remaining Fe (Fig. 4d). Saccharoidal quartz is found as patches in the groundmass.

In sericitic alteration zone the groundmass is completely argillized with secondary quartz. Iron oxides stain the whole rock. Sericite is the main alteration product. Quartz forms saccharoidal textures where three or more anhedral crystals are grouped. No original minerals are preserved.

In the intermediate argillic alteration the andesitic tuff is completely kaolinized. There is a stockwork of pure dickite veins, where the area between the veins is composed of a quartz-dickite association with variable amounts of illite, and scarce diaspore (Fig. 4e). There are veins of dickite associated with bohemite crystals. Diaspore was identified in silicified zone and is closely related to dickite.

Advanced argillic alteration zone coincides with the greatest mineralization. The texture resembles that of tuff with lithic clasts replaced by natroalunite. There is no relict quartz. The groundmass is an association of quartz-kaolin and metallic minerals. Hydroxides of Al can be recognized in certain areas. Natroalunite is abundant in this area and is associated with dickite and pyrophyllite (Fig. 4f).

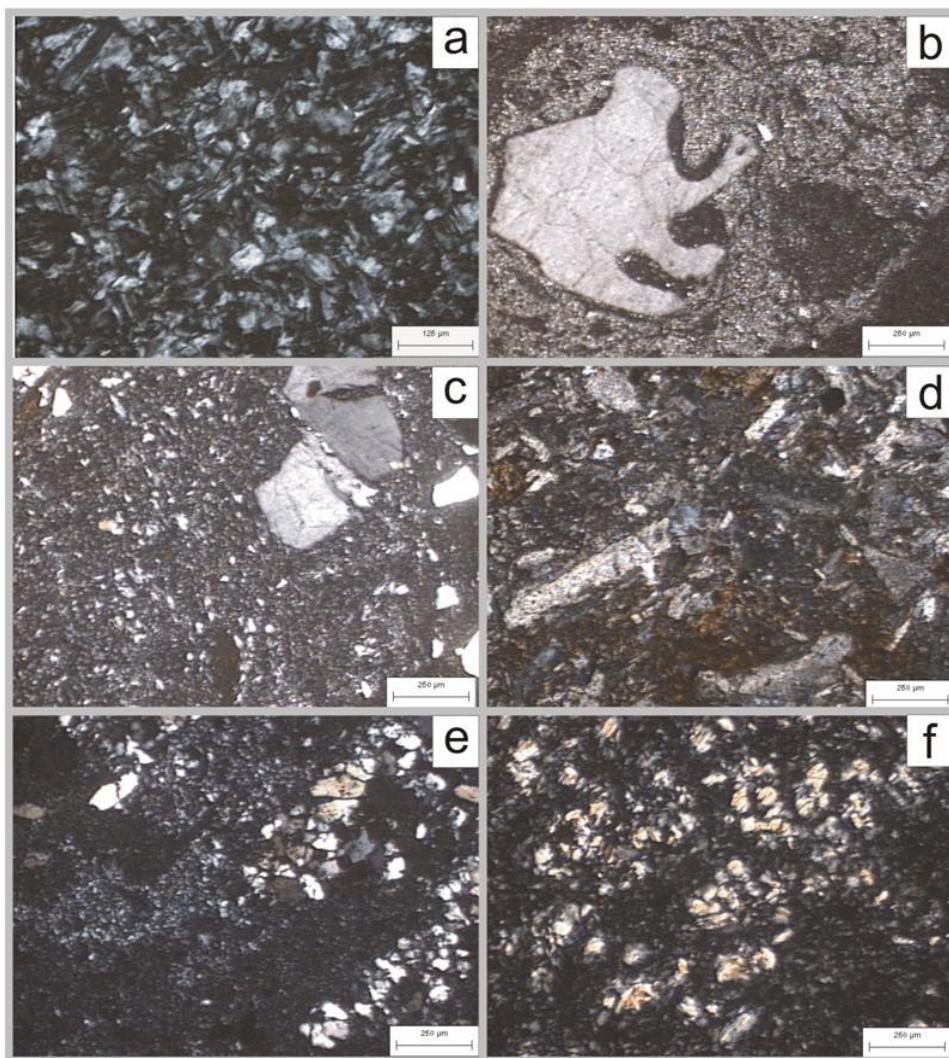


Fig. 4. a. Tabular crystals of massive dickite from Estrella Gaucha mine. b. Blanquita mine.: The kaolinization processes have completely obliterated the original textures of the rock, leaving only quartz. c. Equivocada mine: The original texture and mineralogy of the tuffs have almost erased. d. Propylitic alteration zone in Loma Blanca mine: The original texture is preserved. e. Intermediate argillic alteration: Andesitic tuff completely kaolinized. f. Advanced argillic alteration zone coincides with the greatest mineralization

5. XRD

When kaolinite and dickite are associated, it is very difficult to differentiate them by XRD. The two triplets located between 34° and $40^{\circ}2\theta$, were studied in detail. Dickite appears in

very small proportions compared with kaolinite in the samples Loma Blanca, Blanquita and Equivocada mines while in Estrella Gaucha mine dickite is the predominant mineral. In the last one, dickite with variable amounts of quartz (between 0 to 25 %) was determined. In some samples scarce alunite was identified.

In "Loma Blanca" in the advanced argillic alteration zone, besides alunite-natroalunite, diaspore at the top and pyrophyllite in the highest area of the profile were identified. These minerals are found in isolated masses within the area of greatest hydrothermal activity as relicts of a first stage of higher pressure and temperature. In the propylitic alteration zone, chlorite and scarce illite were identified. Feldspar from the andesitic rock is still present. The predominant alteration mineral is illite together with abundant quartz. In the intermediate argillic alteration zone, kaolinite and quartz reflections were identified. Natroalunite composition was determined by XRD using basal reflections (003, 006 and 009). Maiza & Mas (1980), synthesized the minerals of the series from sericite alteration in a H_2SO_4 solution with varying amounts of KCl and NaCl. They determined the c_0 values in each of the products obtained and checked them by chemical analysis. With these values they fitted a straight line by the least-squares method. The calculated value for natroalunite from Loma Blanca is 16.83 Å, which corresponds to 87% Na. The formula calculated on this basis is $(\text{Na}_{0.13}\text{K}_{0.87})\text{Al}_3(\text{SO}_4)_2(\text{OH})_6$. (Marfil et al. 2010).

6. Chemical composition

The kaolinite content in Blanquita, calculated from the mineralogical composition and major element analysis ranges between 27 and 73 % and between 40 and 97% in Equivocada. Samples with a greater silica content correspond to the silicified zone of the deposits. The alunite content, estimated from S concentration, varied from 0.3 to 2.1 % in both deposits, the larger contents being related to the more intense kaolinization. On the other hand, an increase in the alumina content can be related to an increase in the degree of alteration of the fresh rock, reaching values close to theoretical ones for pure kaolinite. In these samples, the alkali content is also small (Table 2). The concentration of MnO and MgO in the samples analysed are < 0.01 wt % (Marfil et al. 2005). The trace element contents of kaolinite helps to understand the origin. Kaolinites formed from hydrothermal alteration of acid-type igneous rock show enrichments in S, Ba and Sr, whereas Cr, Nb, Ti and the lanthanides tend to concentrate in kaolinites formed from meteoric processes (Dill et al. 1997). The S contents was determined to ranges from 0.03 to 0.36 wt %, this may reflect the presence of small amounts of alunite in the samples analysed. The Zr and Ti contents show a positive linear correlation with greater values of both elements found in samples from Equivocada mine. The (Ti + Fe) contents are less than 1 wt% and the (Cr + Nb) contents range from 0 and 174 ppm with no significant difference between samples from the two deposits. The (Sr + Ba) concentrations vary between 1000 and 10000 ppm, with the larger values probably related to the presence of trace amount of barite. The Ce + Y + La concentration is also variable (from 3 to 323 ppm). (Fig 5a, b, c and d) (Table 3). (Marfil et al. 2005). The chondrite-normalized REE diagrams are shown in figure 6a and 6b corresponding to Blanquita and Equivocada respectively.

In Loma Blanca mine Fe_2O_3 , CaO, Na_2O and K_2O contents decrease from propylitic to advanced argillic alteration zones, whereas Al_2O_3 and LOI increase in the kaolinite natroalunite zone (Table 2). The percentage of alunite, calculated from the S content, ranges

between 2% and 25%. The sulphur content in some samples is attributed to the sulphides present (covellite, sphalerite and pyrite). Sulphides were identified with a petrographic microscope on polished sections in almost all the samples, so the total percentage of natroalunite is considered to be slightly smaller than the calculated value. Relatively large Ba, Sr, V and Zr contents were observed, mainly in intermediate argillic and advanced argillic zones. Co, Ni, Cu, Zn and Rb are more common in the propylitic zone. Be, Ge, In, Sn, Mo, Nb and Ag are insignificant in all the samples (Table 3). Ba + Sr vs. Ce + Y + La, Fe₂O₃ + TiO₂ vs. Cr + Nb and Zr vs. TiO₂ plots are shown in Fig. 5.

Deposit/samples		SiO ₂	Al ₂ O ₃	Fe ₂ O ₃	CaO	Na ₂ O	K ₂ O	TiO ₂	P ₂ O ₅	S	LOI
Blanquita / 18	Average	66.08	22.74	0.28	0.73	0.15	0.06	0.16	0.20	0.16	9.39
	SD	10.31	7.21	0.23	1.78	0.09	0.03	0.07	0.14	0.09	2.97
	Minimum	46.28	10.84	0.11	0.02	0.00	0.01	0.25	0.05	0.03	14.60
	Maximum	84.78	37.21	0.80	6.28	0.23	0.12	0.05	0.64	0.36	4.22
Equivocada/13	Average	60.58	28.19	0.11	0.06	0.02	0.05	0.37	0.25	0.14	10.65
	SD	11.18	8.84	0.07	0.04	0.02	0.04	0.21	0.15	0.09	2.83
	Minimum	45.36	16.13	0.02	0.03	0.00	0.18	0.01	0.01	0.09	14.15
	Maximum	76.25	40.17	0.10	0.18	0.02	0.00	0.58	0.52	0.36	5.98
Loma Blanca/20	Average	58.49	22.20	2.54	0.50	1.22	0.69	0.80	0.28	1.13	11.28
	SD	8.67	7.57	3.02	0.75	1.88	0.76	0.20	0.15	1.49	4.73
	Minimum	34.02	16.25	0.04	0.05	0.09	0.00	0.10	0.17	0.04	5.16
	Maximum	69.18	37.82	9.45	2.86	5.42	3.01	1.12	0.80	3.68	23.03
Estrella Gaucha/9	Average	50.82	42.67	0.05	0.05	0.07	0.02	0.47	0.25	0.12	13.30
	SD	10.23	12.53	0.07	0.01	0.02	0.02	0.34	0.17	0.11	2.66
	Minimum	44.50	20.94	0.01	0.01	0.02	0	0.13	0.07	0.03	8.49
	Maximum	69.06	38.34	0.24	0.06	0.09	0.04	1.08	0.48	0.21	14.92

Table 2. Chemical analysis of major elements on whole rock samples (average weight %).

Deposit/samples		Ba	Sr	Y	Sc	Zr	V	Cr	Ga	Ge	As	Nb	Mo	Ag	La	Ce
Blanquita/ 18	Average	919	1660	4.8	8.9	74.4	107.4	80.3	18	4.7	390.9	5.7	5.8	7.1	35.7	62.4
	SD	2049	906	2.5	3.0	24.6	66.6	43.7	9	2.5	216.4	2.9	4.9	6.5	25.5	57.4
	Minimum	100	335	2	5	33	41	0	10	2	140	0	0	1	9	13
	Maximum	9041	4457	11	17	110	274	170	34	11	707	10	17	21	93	225
Equivocada/ 13	Average	610.4	1540	3.5	6	133.2	83.3	32.3	60.0	2.6	30.8	7.3	2.2	2.1	38.7	67.4
	SD	491.6	1056	1.9	2.2	73.6	59.2	28.9	29.7	1.6	36.4	5.0	2.6	2.0	16.3	32.3
	Minimum	56	32	0	3	11	20	0	0	1	0	0	0	0	1	2
	Maximum	1840	3160	6	11	235	212	90	77	7	107	15	6	6.9	60	118
Loma Blanca/ 20	Average	1122	1867	5.8	7.4	158.4	180.1	26.5	21.2	0.5	10.8	5.1	2.2	2.1	33.3	65.6
	SD	1282	1166	11.2	3.4	46.0	74.55	30.0	5.12	0.6	8.97	1.6	2.6	2.0	18.4	37.6
	Minimum	292	92	0	5	58	109	0	12	0	0	0	0	0	19	203
	Maximum	5990	4765	47	17	272	391	120	32	2	45	7	7	6.9	103	30.0
Estrella Gaucha/ 9	Average	282	1585	2.4	5.7	80.9	285.1	71.1	53.0	4.5	0	3.3	2.0	0	29.2	47.7
	SD	169	1200	2.0	3.1	50.3	128.1	76.7	25.9	1.7	0	2.4	2.4	0	16.5	33.9
	Minimum	72	447	0	2	27	102	0	17	2	0	0	0	0	5	10
	Maximum	563	3845	4	11	166	454	210	90	7	0	6	6	0	58	108

Table 3. Chemical analysis of trace elements (average ppm).

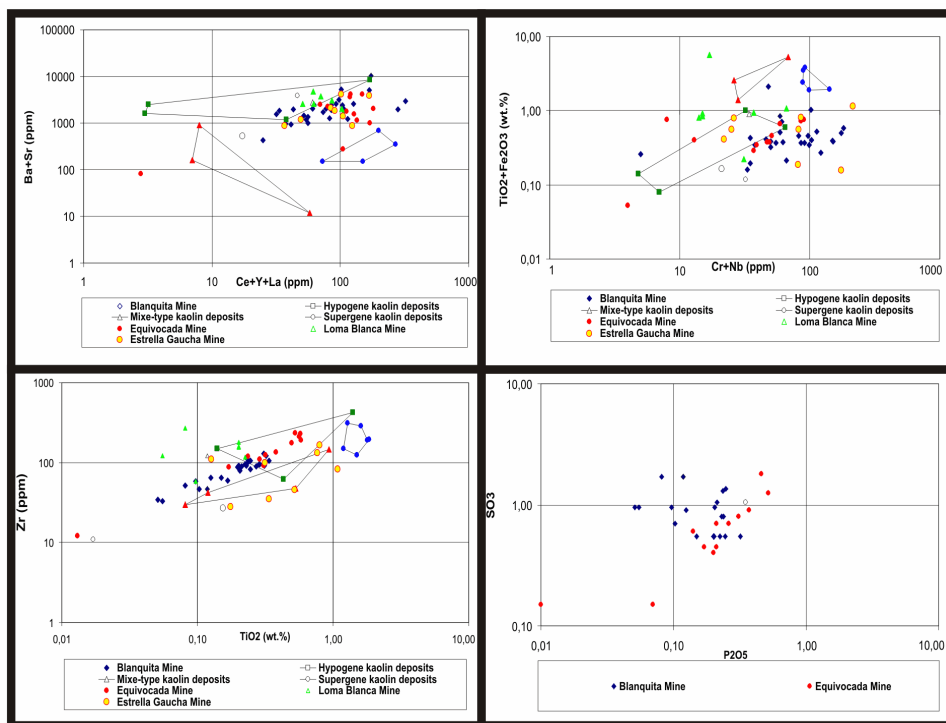


Fig. 5. Data plot from Blanquita, Equivocada, Loma Blanca and Estrella Gaucha mines. a. $(Ba + Sr)$ vs. $(Ce + Y + La)$. b. $(TiO_2 + Fe_2O_3)$ vs. $(Cr + Nb)$ c. Zr vs. TiO_2 . d. SO_3 vs. P_2O_5 from Blanquita and Equivocada mines.

The chondrite-normalized REE diagram according to Boynton, 1984 (in Rollinson, 1992), for the samples of the propylitic and sericitic alteration zones are shown in Fig. 6c and 6d for the samples of intermediate and advanced argillic alteration zones. In the latter, especially in pure kaolin samples, there is marked LREE impoverishment with respect to HREE, especially when compared with the less altered samples. There is no evidence of a positive Ce anomaly, which is typical of the deposits of residual and/or meteoric origin (Cravero et al., 2001). LREE are more abundant than HREE in the intermediate argillic alteration and advanced argillic alteration zones (Marfil et al. 2010).

The results of the chemical analysis of major elements in Estrella Gaucha mine, show that SiO_2 ranges from 44.50 to 69.06 % and Al_2O_3 38.34 to 21.70 %. The SO_3 content (between 0.08 and 0.93 %) was adjudicated to alunite. The alumina amount allowed determining kaolin content between 75 and 100 %. The MnO is less than 0.01 % (Table 2) (Maiza et al. 2009).

The results of trace element contents are shown in Table 3 and plotted in Fig. 5. The content of $TiO_2 + Fe_2O_3$ are lower than 1%wt, $Cr+Nb$ range between 1 and 214 ppm, $Sr+Ba$ between 1.000 and 10.000 while $Ce+Y+La$ is low (15 – 160 ppm). These results are closed with that determined in Blanquita, Equivocada and Loma Blanca mines. The content of As, Rb, Ag, In, Sn, Cs and Bi are insignificant.

In Fig. 6e the chondrite-normalized REE are shown for the samples from Estrella Gaucha. It is possible to observe a LREE impoverishment with respect to HREE, similar to that observed in Blanquita, Equivocada and Loma Blanca mines. Negative Eu anomaly was identified and Ce anomaly was no observed.

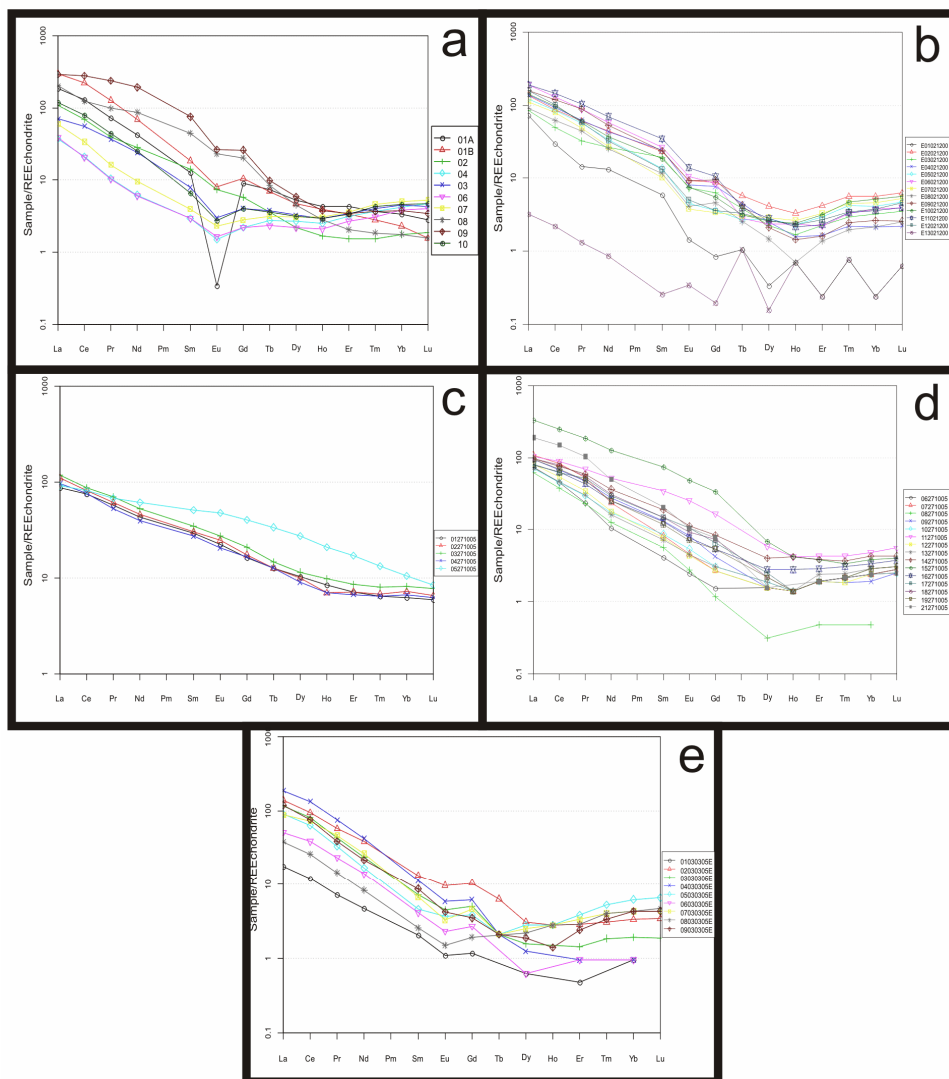


Fig. 6. Chondrite-normalized REE. a. Blanquita mine. b. Equivocada mine. c. Loma Blanca mine: Propylitic and sericitic alteration zones. (d) Loma Blanca mine: Intermediate argillic alteration and advanced argillic alteration zones. e. Estrella Gaucha mine.

7. O and H isotopes

The O and H stable isotope composition of kaolinites samples from the four mines studied are shown in Fig. 7. According to Savin & Lee (1988), the isotopic composition of kaolinite may reflect the geological conditions during its formation, provide the mineral did not suffer isotopic changes after its deposition. Thus, the O isotope composition in kaolinites of sedimentary origin usually varies from +19 to 23 ‰ and kaolinites from residual deposits has a $\delta^{18}\text{O}$ between +15 and +19‰ (Murray & Janssen, 1984). These values are compatible with a meteoric origin at temperatures between 20 and 25 °C. It is important to note than the $\delta^{18}\text{O}$ values of the analyzed samples from the four mines, are much lower than those assumed for kaolinite deposit formed under superficial conditions, thus suggesting a different origin for kaolinization fluids (Marfil et al. 2005).

$\delta^{18}\text{O}$ and δD values of kaolinites from Blanquita and Equivocada ranges from +4.8 to +10.3 ‰ and from -88 to -116‰ respectively (Table 4). While the O isotope composition is similar in both deposits, the δD values of Blanquite mine are slightly more negative. (Martil et al 2005). Both $\delta^{18}\text{O}$ and δD values are clearly different from those reported by Cravero et al (1991) in kaolinites from deposits of residual origin in the Santa Cruz and Chubut provinces ($\delta^{18}\text{O}$ from +16.5 to +18.8‰ and δD from -57.5 to -86.5‰). In a later paper, Cravero et al. (2001) presented additional data from Cerro Rubio and La Esperanza deposit in the province of Santa Cruz with kaolinites having $\delta^{18}\text{O}$ and δD values of +24‰ and -98‰ respectively.

Deposit/samples		$\delta^{18}\text{O}_{\text{SMOW}} \text{‰}$	$\delta\text{D}_{\text{SMOW}} \text{‰}$
Blanquita / 6	Average	7.3	-102.8
	SD	2.0	14.5
	Minimum	4.8	-116.6
	Maximum	9.6	-88
Equivocada/6	Average	8.1	-95.9
	SD	2.2	5.0
	Minimum	5.1	-105.1
	Maximum	10.3	-90.0
Loma Blanca/4	Average	11.6	-84
	SD	1.3	0.8
	Minimum	10.4	-85
	Maximum	13.2	-83
Estrella Gaucha/3	Average	15.9	-84.3
	SD	0.3	2.1
	Minimum	15.6	-86
	Maximum	16.1	-82

Table 4. $\delta^{18}\text{O}$ and δD ‰ average of kaolin samples from Blanquita, Equivocada, Loma Blanca and Estrella Gaucha mines.

In Loma Blanca mine $\delta^{18}\text{O}$ values in kaolinites range from 10.8 ‰ to 13.2 ‰ and δD from -83‰ to -85‰ (Table 4). Although these values are within the range of variation for hydrothermal kaolins (Murray & Janssen, 1984), they are larger than those determined for Blanquita and Equivocada mines.

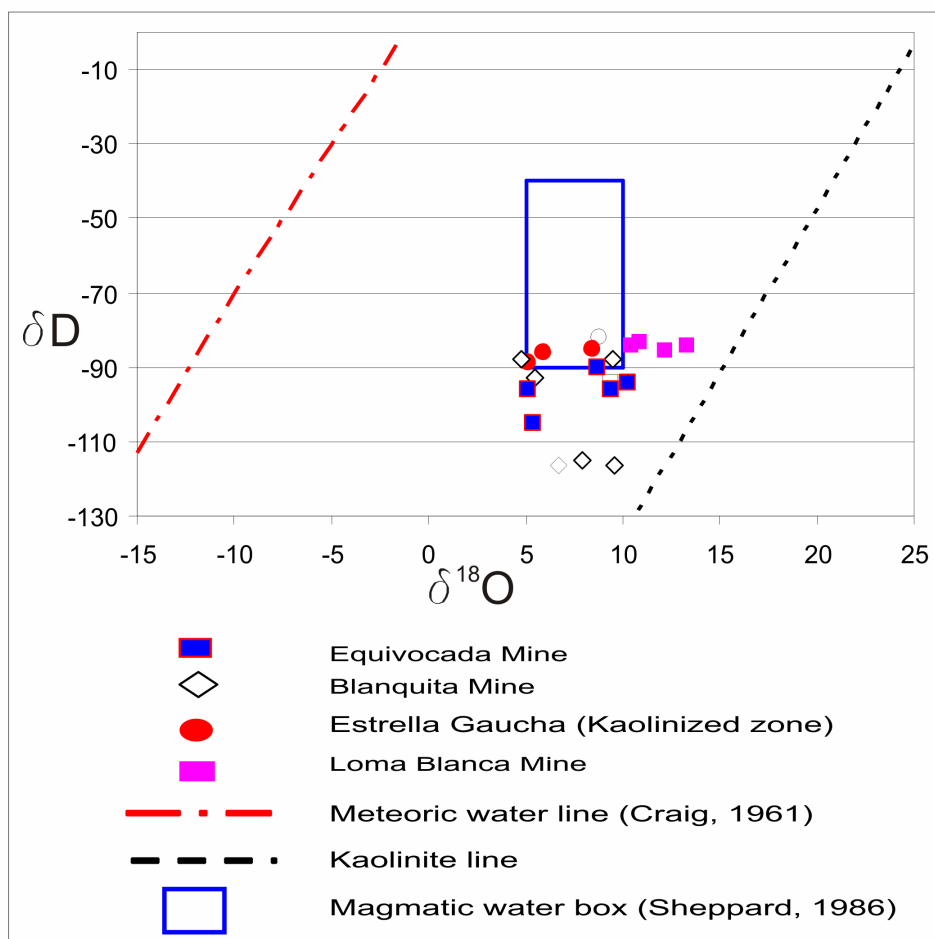


Fig. 7. $\delta^{18}\text{O}$ and δD values in Loma Blanca, Estrella Gaucha, Blanquita and Equivocada kaolins

$\delta^{18}\text{O}$ and δD values of kaolinites from Estrella Gaucha mine range from +5.1 to 8.8 ‰ and from -82 to -89‰ respectively (Table 4). They are similar to that obtained in Blanquita and Equivocada mines. The absence of primary minerals with fluid inclusions, not allowed determining the formation temperature of the deposit. However the presence of diaspore and pyrophyllite in the alteration minerals allows narrow the conditions between 250 and 350 °C, because they are the stability limits of those minerals.

8. Discussion

Dill et al.(1997) used the relationships between SO_3 vs. P_2O_5 , Zr vs. TiO_2 , Ti + Fe vs. Cr + Nb, and Ba + Sr vs. Ce + Y + La to discriminate between kaolin deposits of different origins in Peru. They found that S, Ba and Sr are enriched during hydrothermal alteration, whereas Cr, Nb, Ti and lanthanide elements are concentrated mainly during weathering.

The trace element content and P vs. S, Zr vs. Ti, (Cr + Nb) vs. (Ti + Fe) and (Ce + Y + La) vs. (Ba + Sr) ratios of kaolin samples from the four mines studied do not differ significantly. This suggests that all the deposits might have formed by the same genetic process. However, although the Ti + Fe and Sr + Ba contents indicate a hypogenic origin (Dill et al. 1997), the presence of large Cr + Nb and Ce + Y + La concentrations in some samples could indicate the presence of kaolinite of supergenic origin as well. Titanium may be released from a primary mineral in the parent rock (e.g. biotite) during either hypogenic or supergenic kaolinization. However, as supergenic alteration seems to be more efficient, the Ti content in kaolinite has been used to discriminate between the two processes (Dill et al. 1997). Because it behaves a geochemically immobile element in superficial conditions, Zr is also a good indicator of the degree of meteorization of the parent rock. Consequently, kaolin samples with high Ti and Zr contents point to a superficial environment of formation (Marfil et al. 2005).

Cravero et al. (2010) compared kaolin deposit from hypogene and supergene origin from Patagonia Argentina. In the hypogene deposits, S, Sr, Pb, V, P_2O_5 , and LREE are more abundant, whereas Fe_2O_3 , Y, Rb, U, Zr and HREE predominate in the supergene (weathered) deposits. It is important to consider that the samples are altered and the degree of alteration is not the same in all of them. The main alteration products in all the samples are clay minerals of the kaolin group. The approach adopted is to consider that the greater the LOI, the greater the resulting alteration degree. The concentrations of S, Pb and Sr, present only in the hypogene deposits, vary with the degree of alteration, indicating that these elements are mainly concentrated in the clay minerals. Zr does not show a clear behaviour; in the hypogene deposits it appears to be mobile during alteration, whereas under weathering conditions no clear relationship can be established. The V and U contents increase in both types of deposits with the degree of alteration; hence they can be considered to be immobile in both environments. P_2O_5 and S are only present in hypogene deposits and their contents increase with the alteration degree. Y shows no relation with the degree of alteration.

The greater content of HREE in the supergene deposits is more easily explained by considering that these elements are fractionated during alteration in the hydrothermal deposits and remain unchanged during weathering, thereby giving greater values in the supergene deposits, where no fractionation has occurred. Regarding the mobility of elements during hydrothermal alteration, other authors have found different behaviours. In rhyolitic rocks from Yellowstone drill cores, Ti, Al, Fe, Sc, Co, Y, Zr, REE, Hf, Ta and Th remained relatively immobile (Sturchio et al., 1986).

During the hydrothermal alteration of rhyolitic rocks of the Los Azufres geothermal field, Mexico (Pandarinath et al., 2008), REE concentrations were not significantly different between fresh and altered rocks. The immobile role of REE during hydrothermal processes in rhyolitic rocks has been reported by De Groot & Baker (1992). Nevertheless, in the advanced argillic alteration zone of Rangan area (Central Iran), composed mainly of alunite-jarosite and pyrophyllite, LREE are relatively immobile in the rocks of this zone and depleted in LREE and HREE (Parsapoor et al., 2009). These authors considered that this behaviour may be due to the entry of these elements into the lattice of alunite-jarosite. LREE can in fact substitute for K in the large-radius cations (A) of the alunite-jarosite formula. Alunite is a common component of the hypogene deposits studied here.

The samples from Patagonia studied by Cravero et al. 2010 have been taken as representative of the whole altered area, so the element contents do not come from a specific part of the weathering profile; therefore it can be considered that the conservative behaviour of the REE elements arises from the fact that they have fractionation could have occurred within the profile. Another characteristic of the REE that supports a supergene origin is the presence of a Ce anomaly, produced when Ce^{3+} is oxidized to Ce^{4+} . When these data are plotted in the graphical style of Dill et al. (1997, 2000), some of the relationships are not as clear as in their work, except for SO_3 vs. P_2O_5 . Their supergene deposits are characterized by much greater contents of Ce + Y + La than those formed under hypogene conditions, whereas in Patagonia, these values are dispersed. In Peru, supergene kaolins are characterized by large values of both TiO_2 and Zr, whereas in Patagonia only Zr shows the same behaviour. Cr + Nb also show the opposite trend, while in Peru the greatest contents are related to a supergene origin; in Patagonia they are associated with hydrothermal deposits. In both areas, the same behaviour is found for S, P_2O_5 , Ba and Sr, with the greater values being found in the deposits formed in the hypogene environment. The greater amounts of S and V in the hypogene deposits are explained by the presence of minerals such as alunite (sulphate) and mottramite (vanadate).

More information about the formation conditions of the studied deposits can be obtained from their mineralogy. Kaolin deposits of hydrothermal origin are constituted by kaolinite with dickite, alunite and pyrophyllite (Murray, 1984). However, in kaolin deposits of sedimentary origin only kaolinite is present. In the mines studied the presence of dickite, pyrophyllite with alunite and diasporite in Loma Blanca, indicate a hydrothermal origin. In order to estimate the isotopic composition of fluids responsible for the kaolinization process a temperature of 350 °C was assumed. Higher temperatures would not be reasonable as kaolinite coexists with pyrophyllite and lower values would not be compatible with the presence of pyrophyllite. Numerous authors have synthesized pyrophyllite at temperatures above 260°C (Grim, 1969; Roy & Osborn, 1954; Hemley, 1959; Reed & Hemley, 1967; Tzuzuki & Mizutani, 1971).

The coexistence of pyrophyllite and kaolinite allows us to estimate a maximum temperature of 350°C. Diasporite can be recognized frequently in kaolin deposits of hydrothermal origin. According to Roy & Osborn (1954), the bohemite-diasporite transformation temperature is between 270 and 300°C at 175-1500 atm. water pressure. (Marfil et al. 2010)

A schematic summary of the paragenetic sequence from Loma Blanca mine is given in Table 5. The main Al minerals of higher temperature occur predominantly in the central area below the silicified zone, which is responsible for protecting the deposit from subsequent erosion processes. Dickite and nacrite commonly occur in deposits of hydrothermal origin (Murray, 1984). Numerous authors have synthesized pyrophyllite at temperatures above 260°C (Grim, 1969; Roy & Osborn, 1954; Hemley, 1959; Reed & Hemley, 1967; and Tzuzuki & Mizutani, 1971). The coexistence of pyrophyllite and kaolinite allows us to estimate a maximum temperature of 350°C. Diasporite can be recognized frequently in kaolin deposits of hydrothermal origin. According to Roy & Osborn (1954), the bohemite-diasporite transformation temperature is between 270 and 300°C at 175-1500 atm. water pressure.

Thus, using the O isotope fractionation equation of Shepard & Gilg (1996) indicate that O and H isotope composition of the fluids involved in the kaolinization process are of

magmatic origin or of superficial origin but isotopically equilibrated with magmatic rocks at magmatic temperatures. (Marfil et al. 2005).

Mineral	Silicified Zone	Advanced argillic zone	Intermediate argillic zone	Sericitic zone	Propylitic zone
Quartz					
Diaspore					
Natroalunite					
Pyrophyllite					
Dickite					
Kaolinite					
Illite					
Chlorite					

Table 5. Summary of the paragenetic sequence. (Marfil et al. 2010)

9. Conclusions

- The deposits studied consist of a set of irregular bodies and veins developed on tuffs of rhyolitic and andesitic composition.
- The alteration minerals present include kaolinite, dickite, pyrophyllite, alunite, diaspore, illite and chlorite.
- The trace elements contents of the kaolin samples in all the deposits studied are very similar. Most of the comparative diagrams (P vs. S, Zr vs. Ti, (Cr + Nb) vs. (Ti + Fe) and (Ce + Y + La) vs. (Ba + Sr) suggest that kaolinite formed from hydrothermal alteration of volcanic rocks. However the high (Nb + Cr) and (Ce + Y + La) contents do not exclude the presence of kaolinite of residual origin.
- The mineral assemblage (dickite-natroalunitepyrophyllite-diaspore), the alteration zonation pattern, the geochemistry of trace elements, the relation between LREE and HREE and the small $\delta^{18}\text{O}$ values suggest that the deposits studied were formed by hydrothermal processes.
- Mineralization developed in two stages: the first stage, of higher temperature, led to the formation of dickite, pyrophyllite and diaspore. Then the temperature decreased due to contamination with meteoric water, and alunite and kaolinite developed.

- The mineral assemblage allows us to estimate a formation temperature between 270 and 350°C.
- The hypogene deposits are characterized by greater contents of Sr, Pb, V, S and P₂O₅, all of them, apart from V, increasing as alteration proceeds. REE, probably forming part of the alunite structure, are fractionated during alteration.
- The combination of chemical composition, mineralogical association and O and D isotopes data suggest that the deposits studied were formed because the circulation of hydrothermal fluids, discounting superficial processes at low temperatures.

10. Acknowledgments

The authors wish to thank the Geology Department of the Universidad Nacional del Sur, the Comisión de Investigaciones Científicas de la Provincia de Buenos Aires and CONICET - INGEOSUR for their helpful support during the research.

11. References

- Condie K.C., Dengate J. & Cullers R.J. (1995) Behavior of rare earth elements in a paleoweathering profile on granodiorite in the Front Range, USA. *Geochimica et Cosmochimica Acta*, 59, 279-294.
- Cravero M.F., Domínguez E. & Murray H.H. (1991) Valores $\delta^{18}\text{O}$ y δ^{D} en caolinitas, indicadores de un clima templado moderado durante el Jurásico Superior-Cretácico Inferior de la Patagonia, Argentina. *Revista Asociación Geológica Argentina*, 46, 20-25.
- Cravero F., Domínguez E. & Iglesias C. (2001) Genesis and applications of the Cerro Rubio kaolin deposit, Patagonia (Argentina). *Applied Clay Science*, 18, 157-172.
- Cravero F., Marfil S. and Maiza P. (2010). Statistical analysis of geochemical data: A tool to discriminate between kaolin deposits of hypogene and supergen origin. Patagonia, Argentina. *Clay Minerals*, 183-196.
- De Groot P. & Baker J.H. (1992) High element mobility in 1.9-1.86 Ga hydrothermal alteration zones, Bergslagen, central Sweden: relationships with exhalative Fe-ore mineralizations. *Precambrian Research*, 54, 109-130.
- Dill H., Bosse R., Henning H. & Fricke A. (1997) Mineralogical and chemical variations in hypogene and supergene kaolin deposits in a mobile fold belt the Central Andes of northwestern Peru. *Mineralium Deposita*, 32, 149-163.
- Dill H.G., Bosse H.R. & Kassbohm J. (2000) Mineralogical and chemical studies of volcanic-related argillaceous industrial minerals of the Central American Cordillera (western El Salvador). *Economic Geology*, 95, 517-538.
- Domínguez E. & Murray H.H. (1995) Genesis of the Chubut river valley kaolin deposits, and their industrial applications. Pp. 129-134 in: Proceedings of the 10th International Clay Conference, 1993 (G.J. Churchman, R.W. Fitzpatrick & R.A. Eggleton, editors) CSIRO Publishing, Melbourne, Australia.
- Domínguez E. & Murray, H.H. (1997) The Lote 8 Kaolin Deposit, Santa Cruz, Argentina. Genesis and paper industrial application. Pp. 57-64 in: Proceedings of the 11th International Clay Conference (H. Kodama, A.M. Mermut & J.K. Torrance, editors) Ottawa, Canada.

- Domínguez E., Iglesias C. & Dondi M. (2008) The geology and mineralogy of a range of kaolins from the Santa Cruz and Chubut Provinces, Patagonia (Argentina). *Applied Clay Science*, 40, 124-142.
- Ece O., Schroeder P.A., Smilley M.J. & Wampler J.M. (2008) Acid-sulphate hydrothermal alteration of andesitic tuffs and genesis of halloysite and alunite deposits in the Biga Peninsula, Turkey. *Clay Minerals*, 43, 281-315.
- Galán E., Aparicio P., González I. & Miras A. (1998) Contribution of multivariate analysis to the correlation of some properties of kaolin with its mineralogical and chemical composition. *Clay Minerals*, 33, 66-75.
- Galán E., Fernández-Caliani J.C., Miras A., Aparicio P. & Márquez M.G. (2007) Residence and fractionation of rare earth elements during kaolinization of alkaline peraluminous granites in NW Spain. *Clay Minerals*, 42, 341-352.
- Gouveia M.A., Prudencio M.I., Figueiredo M.O., Pereira L.C.J., Waerenborgh J.C., Morgado I., Pena T. & Lopes A. (1993) Behavior of REE and other trace and major elements during weathering of granitic rocks, Évora, Portugal. *Chemical Geology*, 107, 293-296.
- Grim H. (1969) *Clay Mineralogy*. 2nd Edition. McGraw Hill Book Co, New York, USA. 131-137.
- Hayase, K. & Maiza, P.J. (1970) Génesis del yacimiento de caolín Mina Equivocada, Los Menucos, Prov. de Río Negro, República Argentina. *Revista de la Asociación Argentina de Mineralogía Petrología y Sedimentología*, I, 1-2, 33-34.
- Hayase, K. & Maiza, P.J. (1972a) Génesis del yacimiento de caolín Mina Loma Blanca, Los Menucos, Prov. de Río Negro, Argentina. *5º Congreso Geológico Argentino*, Actas 2: 139-151.
- Hayase, K. & Maiza, P.J. (1972b) Presencia de dickita en yacimientos de caolín de la Patagonia, Argentina. *5º Congreso Geológico Argentino*, Actas 1: 153-170.
- Hayase K. & Manera T. (1973) A statistical analysis of experimental data on filling temperature of fluid inclusions in fluorite from fluorite deposits of Patagonia Argentina. *Mining Geology*, Japan, 23, 1-2.
- Hayase, K., Schincariol, O. & Maiza, P.J. (1971) Ocurrencia de alunite en cinco yacimientos de la Patagonia, Mina Equivocada, Mina Loma Blanca, Mina Estrella Gaucha, Mina Gato y Camarones, República Argentina. *Revista de la Asociación Argentina de Mineralogía, Petrología y Sedimentología*, 2, 49-72.
- Hemley J.J. (1959) Some mineralogical equilibria in the system $K_2O-Al_2O_3-SiO_2-H_2O$. *American Journal of Science*, 257, 241-70.
- Labudia C. & Hayase K. (1975) Relaciones entre las rocas y las mineralizaciones de Pb-Cu-Zn, fluorita y caolín de los alrededores de Los Menucos, Prov. de Río Negro, Argentina. *Sexto Congreso Geológico Argentino*, Actas, Bahía Blanca, III, 69-80.
- Labudia C. & Bjerg E. (1994) Geología del sector oriental de la hoja Bajo Hondo (39e), Provincia de Río Negro. *Revista de la Asociación Geológica Argentina*, 49, 284-296.
- Losada, O., Gelós, E., Maiza, P. y Bengochea, A. (1975) Geología de los afloramientos de caolín de la zona del arroyo Chilquirihuín, Prov. de Neuquén. *Revista de la Asociación Geológica Argentina* 30: 5-16.
- Maiza, P. (1972) Los yacimientos de caolín originados por la actividad hidrotermal en los principales distritos caoliníferos de la Patagonia, República Argentina. *Tesis Doctoral, Universidad Nacional del Sur, (inéedita)*. Bahía Blanca. Argentina. 136 pp.

- Maiza, P.J. (1981) Estudio de los yacimientos de caolín del oeste de la Provincia del Chubut, República Argentina, Minas Susana, Gato y Estrella Gaucha. 8° Congreso Geológico Argentino, Actas, 4, 471-484.
- Maiza, P.J. & Hayase, K. (1975) Los yacimientos de caolín de la Patagonia. República Argentina. 2° Congreso Ibero Americano de Geología Económica, Actas, 2, 365-383, Buenos Aires.
- Maiza, P.; S. Marfil; E. Cardellach & J. Zunino. (2009) Geoquímica de la zona caolinizada de Mina Estrella Gaucha (Prov. de Chubut, Argentina). *Revista de la Asociación Geológica Argentina* Vol 64. N° 3. ISSN 0004-4822, 426-432.
- Maiza P. & Mas G. (1980) Estudio de los sulfatos alunita-natroalunita. Síntesis de la serie. *Revista de la Asociación Argentina de Mineralogía, Sedimentología y Petrología*, 11, 32-41
- Maiza, P.J. & G. Mas (1981) Presencia de natroalunita en Muna Equivocada, río Negro. Su significado. VIII Congreso Geológico Argentino, San Luis. Actas, IV, 285-292.
- Malvicini L & Llambías E. (1974) In: Malvicini L. & Vallés J. M. (1984) Metalogénesis. Capítulo III-5. Geología y recursos naturales de la Provincia de Río Negro. Relatorio del IX Congreso Geológico Argentino, San Carlos de Bariloche. Río Negro, 649-662.
- Manera T. (1972) La mineralización de los yacimientos de fluorita de la Provincia de Río Negro. Tesis Doctoral, Universidad Nacional del Sur, Bahía Blanca, Argentina.
- Marfil S.A., Maiza P.J., Cardellach E. & Corbella M. (2005) Origin of kaolin deposits in the 'Los Menucos', Río Negro Province, Argentina. *Clay Minerals*, 40, 283-293.
- Marfil, S. A., Maiza, P. J. and Montecchiari, N. (2010) Alteration zonation in Loma Blanca Kaolin deposit, Los Menucos, province of Rio Negro, Argentina. *Clay Minerals*, 45, 157-169.
- Murray H. & Janssen J. (1984) Oxigen isotopes - indicators of kaolin genesis?. Proceedings of the 27th International Geological Congress, 15, 287-303.
- Pandarínath K., Dulski P., Torres Alvarado I.S. & Verma S.P. (2008) Element mobility during the hydrothermal alteration of rhyolitic rocks of the Los Azufres geothermal field, Mexico. *Geothermics*, 37, 53-72.
- Pankurst R.J.C., Rapela W., Caminos R., Llambías E. & Parica C. (1992) A revised age for the granites of the central Somoncuro Batholith, North Patagonian Massif. *Journal of South American Earth Sciences*, 5, 321-325.
- Pankhurst R.J. & Rapela W. (1995) Production of Jurassic rhyolite by anatexis in the lower crust of Patagonia. *Earth and Planetary Science Letters*, 134, 23-26.
- Pankhurst R.J., Leat P.T., Sruoga P., Rapela C.W., Márquez M., Storey B.C. & Riley T.R. (1998) The Con Aike province of Patagonia and related rocks in West Antarctica: A silicic large igneous province. *Journal of Volcanology and Geothermal Research*, 81, 113-136.
- Papoulis D. & Tsohis-Katagas P. (2008) Formation of alteration zones and kaolin genesis, Limnos Island, northeast Aegean Sea, Greece. *Clay Minerals*, 43, 631-646.
- Papoulis D., Tsohis-Katagas P. & Katagas C. (2004). Monazite alteration mechanisms and depletion measurements in kaolins. *Applied Clay Science*, 24. 271-285.
- Parsapoor A., Kahlili M. & Mackinzadeh H.A. (2009) The behaviour of trace and rare earth elements (REE) during hydrothermal alteration in the Rangan area (central Iran). *Journal of Asian Earth Sciences*, 34, 123-134.

- Ploszkiewicz, J.V. y Ramos, V.A. (1977) Estratigrafía y tectónica de la Sierra de Payaniyeu (Provincia del Chubut). *Revista Asociación Geológica Argentina* 32: 209-226.
- Reed, M. H. (1997) Hydrothermal Mineral Deposits: What we do and don't know. Chapter 1. In: *Geochemistry of hydrothermal ore deposit*. Third Edition. Ed. H. L. Barnes. 303-358.
- Reed B.L. & Hemley J.J. (1967) Occurrence of pyrophyllite in Kekiktuk Conglomerate. In: *Book Range, Northeastern Alaska*. U.S. Geological Survey, 162-166.
- Rollinson H. (1992) *Using Geochemical Data: Evaluation, Presentation, Interpretation*. University of Zimbabwe.
- Roy R. & Osborn E. (1954) The system $Al_2O_3-SiO_2-H_2O$. *American Mineralogist*, 39, 853-85.
- Savin, S.M & Lee, S. (1988) Isotopic studies of phyllosilicates. In: *Hydrous Phyllosilicates (Exclusive of Micas)*. (Bailey S.W.) Editor. Reviews in Mineralogy. Mineralogical Society of America, 19. Washington DC, 189-223.
- Shepard, S.M.F & Gilg h. A. (1996) Stable isotope geochemistry of clay minerals. *Clay Minerals*, 31, 1-24.
- Skinner, B. (1997) Hydrothermal alteration and its relationship to ore fluid composition. Chapter 7. In: *Geochemistry of hydrothermal ore deposit*. Third Edition. Ed. H. L. Barnes. 303-358.
- Sturchio N.C., Muehlenbchs K. & Meitz M. (1986) Element redistribution during hydrothermal alteration of rhyolite in an active geothermal system: Yellowstone drill cores Y-7 and Y-8. *Geochimica et Cosmochimica Acta*, 50, 1619-1631.
- Terakado Y. & Fujitani T. (1998) Behavior of the rare earth elements and other trace elements during interactions between acidic hydrothermal solutions and silicic volcanic rocks, southwestern Japan. *Geochimica et Cosmochimica Acta*, 62, 1903-1998.
- Tzuzuki Y. & Mizutani S. (1971) A study of rock alteration process based on kinetics of hydrothermal experiment. *Contributions to Mineralogy and Petrology*, 30, 15-33.
- van der Weijden C.H. & van der Weijden R.D. (1995) Mobility of major, minor and some redox-sensitive trace elements and rare-earth elements during weathering of four granitoids in central Portugal. *Chemical Geology*, 125, 149-167.

Estimated Background Values of Some Harmful Metals in Stream Sediments of Santiago Island (Cape Verde)

Marina M. S. Cabral Pinto^{1,2,3}, Eduardo A. Ferreira da Silva¹,
Maria M. V. G. Silva² and Paulo Melo-Gonçalves⁴

¹*University of Aveiro, Department of Geosciences, GeoBioTec Research Center, Aveiro*

²*Geosciences Center, University of Coimbra, Coimbra*

³*Department of Environmental Sciences, University Jean Piaget
Cidade da Praia, Santiago Island*

⁴*Department of Physics and Centre for Environmental and Marine Studies (CESAM)
University of Aveiro, Aveiro*

^{1,2,4}*Portugal*

³*Cape Verde*

1. Introduction

The aim of geochemical mapping programmes is to obtain regional background information for mineral exploration, planning and also to discriminate between anthropogenic pollution and geogenic sources. Resulting databases are multi-purpose basic tools with application in different areas, such as in environmental studies, agriculture, geomedicine, etc. (Darnley & Garret, 1990; Appleton & Ridgway, 1993; Darnley et al., 1995; Tarvained, 1996; Xie Xuejing et al., 1997; Plant et al., 2001; Albanese et al., 2007; Inácio, 2008) and national geochemical surveys became a priority for many countries.

In Santiago Island, Cape Verde, a total of 337 stream sediments samples were collected at a density of approximately 1 sample per 3 km² to compile an environmental geochemical atlas. The estimation of the background values is very important in countries like Cape Verde, where intervention limits for soils and stream sediments were not yet established.

There are two major methods used for assessing background concentrations (Matschullat et al., 2000): (1) direct (geochemical) and (2) indirect (statistical). The first method, also known as empirical method, consists of sampling locations not affected by industrial activities or relatively pristine sites, and usually use the mean or median to estimate the background concentrations. The indirect methods use more advanced statistical procedures to estimate the background concentrations. There are also other methods, the so called integrated methods, which combines both direct and indirect methodologies. Here we used a direct method and we will use the term Estimated Background Value (EBV) to refer to the estimates of the background concentrations. Our EBV is sometimes called Baseline Value by other authors. Note that “Baseline Value” is not a synonym of

“Background Value”, but a synonym of “Estimated Background Value”. The EBV or Baseline Value is an estimator of the real and unknown Background Value (Cabral Pinto et al., 2011).

In this work we present EBV maps of some harmful metals of stream sediments from Santiago Island and study their relationships with the defined geological formations. The geochemical survey was conducted, following the guidelines of the International Project IGCP 259 at the sampling stage, sample preparation, analysis, data treatment and mapping (Darnley & Garrett, 1990; Darnley et al., 1995). Levels were determined, in the fraction <2mm. Each sample was digested in aqua regia and analysed by ICP-MS.

Clear relationships between the EBV spatial distribution and the defined geological formations is difficult, since the chemical composition of each sample represents the chemical composition of the entire area upstream, covering different geological formations. However, we seek these relationships using the mineralogical composition of the stream sediments and the results of Principal Component Analysis (PCA).

The layout of this chapter is as follows: in section 2 we describe a brief presentation of the location and geology of Santiago Island. The methodologies used are presented in section 3 and the results and discussion can be found in section 4. Finally, the major conclusions are summarized in section 5.

2. Location and geology of Santiago Island

2.1 Location of Santiago Island

The archipelago of Cape Verde is located at the eastern shore of the Atlantic Ocean, 500 km west from Senegal's Cape Verde, in the African Western Shore. It is composed by 10 islands (Figure 1), with land areas that vary from 35 km² to 991 km² (Santiago Island). The Cape Verde Islands are located in the Macaronesia region, that spreads between the 39°45' and 14°49' latitude and the 31°17' and 13°20' West longitude, within an area of 14 473 km², that holds, beside Cape Verde (4033 km²), the Canary Islands (7542 km²), the Azores Islands (2344 km²) and Madeira Islands (4 km²) (Lousada-Lima 1987-88). The Santiago island is located in the southern part of the archipelago, between the 15°20'N and 14°50' N parallels and the 23°50'W and 23°20'W meridians. It is the biggest island in the Archipelago, representing 25% of the entire land area; it's elongated in the NNW – SSE direction, with a maximum length of 54.9 km and a maximum width of 29 km. This Island has a maximum altitude of 1.394 m. It has 215 km² of arable area, and an average precipitation of 321 mm.

2.2 Geological setting of the Santiago Island

The geological cartography of Santiago Island (Figure 2) was published by Serralheiro (1976) and, along with the works developed by Matos Alves et al. (1979), helped to establish the volcano-stratigraphic sequence of the island. It is possible to identify the periods of intense volcanic activity which caused the growth of the island, separated by erosion and sedimentation periods, recorded by sedimentary formations intercalated between the main volcanic episodes. After the initial phase of submarine volcanism the volcanic building emerged and the volcanism became subaerial.

Below we provide a brief description of the lithostratigraphic formations in Santiago, named as: Ancient Internal Eruptive Complex (CA), Flamengos (FL), Orgãos (CB), Eruptive Complex of Pico da Antónia (PA), Assomada (AS), Monte das Vacas (MV) and Quaternary (CC). A more detailed description was presented at Cabral Pinto et al. (2011).

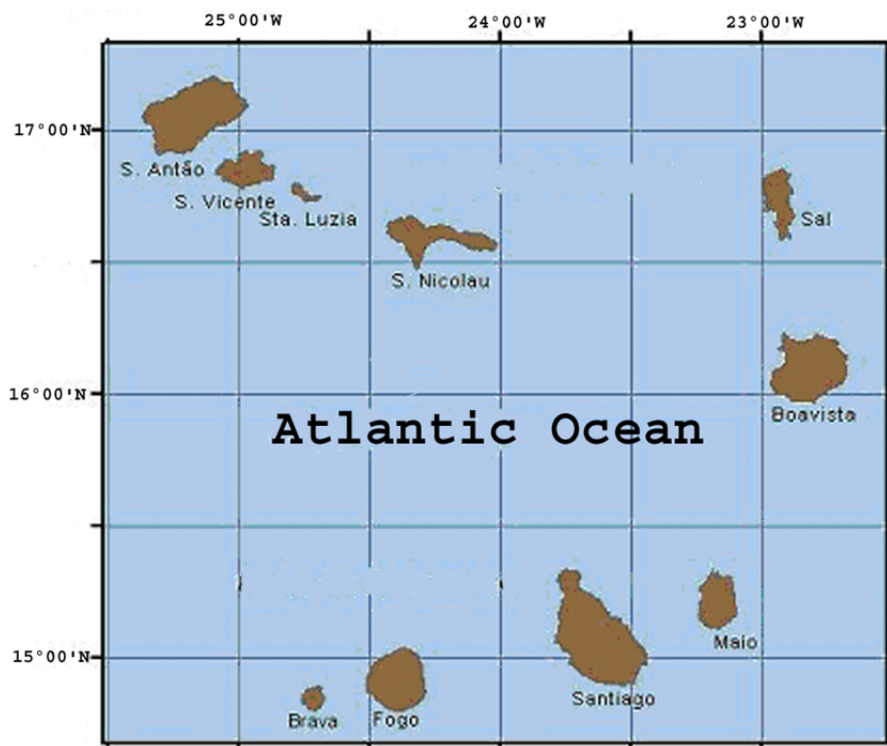


Fig. 1. Location of the Cape Verde Archipelago

2.2.1 Ancient Internal Eruptive Complex (CA)

There are a wide range of rock types in the Ancient Internal Eruptive Complex (CA), but they occupy small areas of the Santiago Island (Figure 2) and are always highly weathered.

The CA is essentially a dense, highly altered, dyke complex (Figure 3a) of basanite, ancartrites and limburgites (Serralheiro, 1976; Matos Alves et al., 1979). The rocks are fractured and display light colors due to intense alteration (Figure 3 a, b), with zeolites and carbonates filling the fissures. There are also some foid gabbroic and alkaline sienitic rocks, intravolcanic breccias (Figure 3 c), phonolite, trachytic trachytes (Figure 3 d), carbonatites, piroxenites, and ijolites-melteijites (Silva & Figueiredo, 1976; Serralheiro, 1976; Matos Alves et al., 1979; Silva, 1979). Carbonatite is extremely altered, with intense dissolution (Figure 3 b) and occurs as dykes and masses.

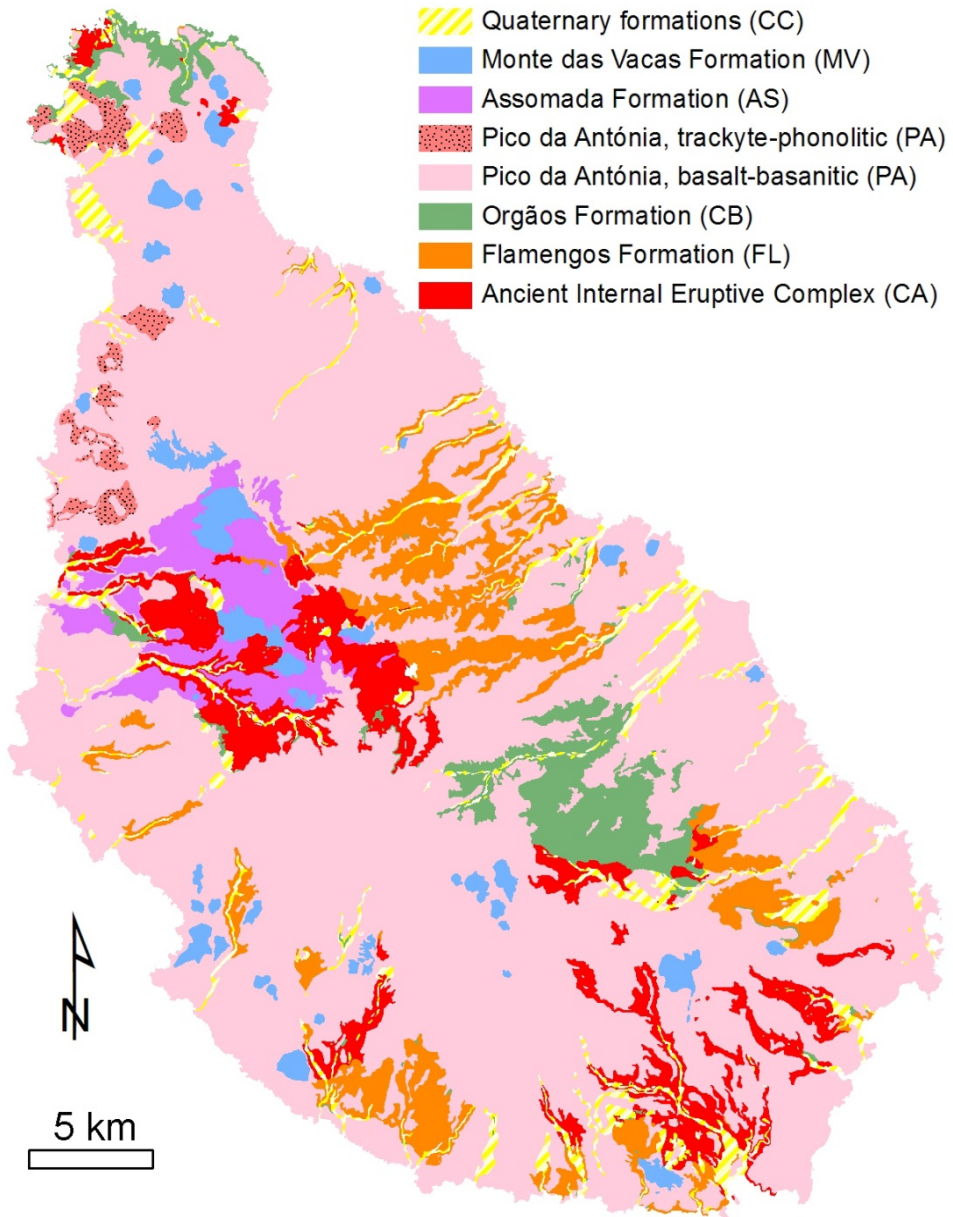


Fig. 2. Geological cartography of Santiago Island, Cape Verde, modified from Serralheiro (1976)

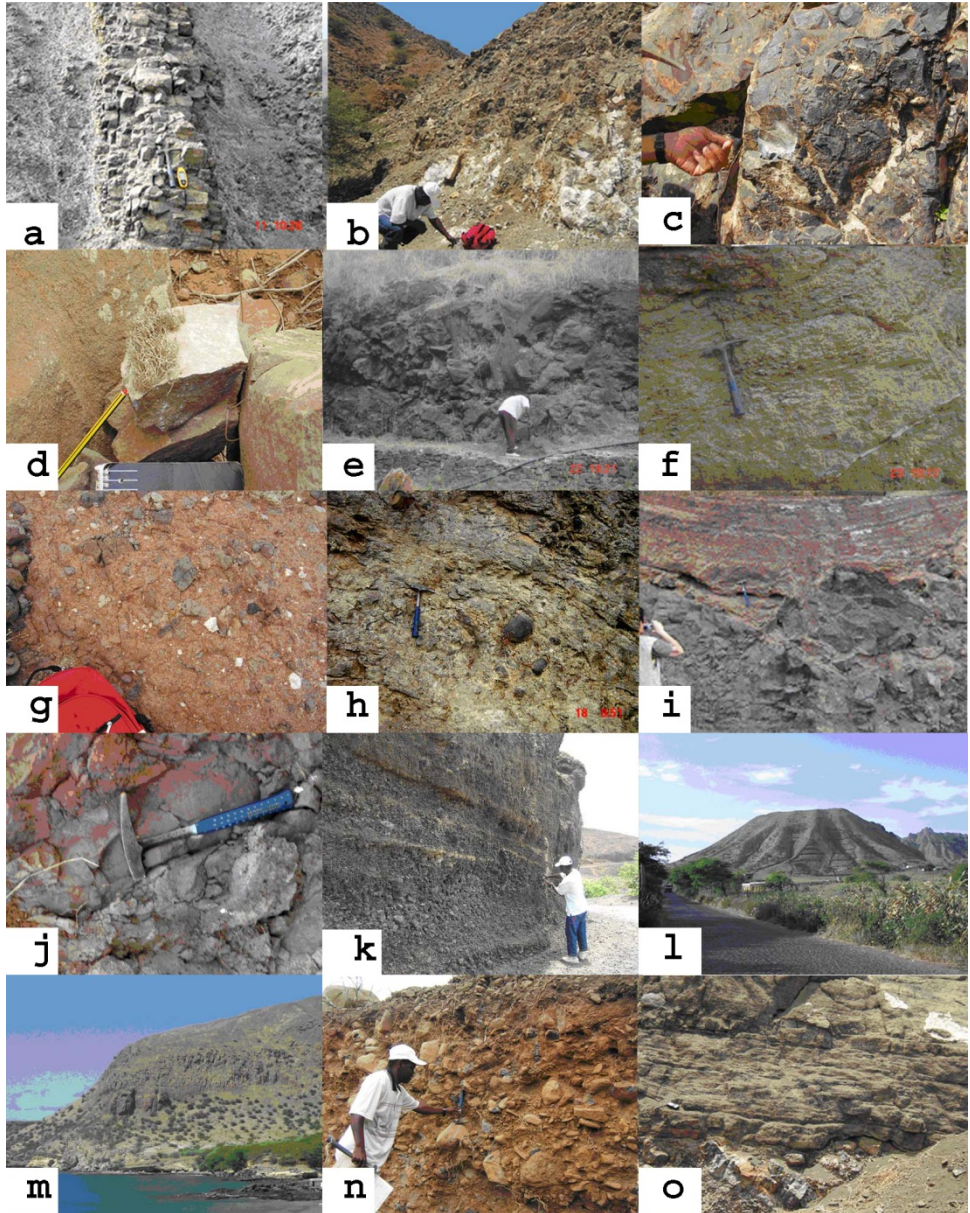


Fig. 3. Different geological formations

2.2.2 Flamengos Formation (FL)

The Flamengos Formation (FL) occurs essentially in the centre and south of the island, mainly at the northeast slope (Figure 2). It is of submarine nature and is constituted by

extended basaltic mantles, formed by the stacking of pillow-lavas (Figure 3 e), with subordinated breccias (Figure 3 e) and intercalated tuffs (Figure 3 f), which form compact deposits and are very altered. The rocks are limburgites, basanites and basanitoides, which are intensely altered into zeolites and carbonates.

2.2.3 Orgãos Formation (CB)

The Formation of Orgãos (CB) occurs mainly in the region of S. Lourenço dos Orgãos (Figure 2). The Formation of Orgãos (CB) is essentially a volcano-sedimentary unit, formed by a breccia/conglomerate with a sandstone matrix and may correspond to lahars. This formation is characterized by the high heterogeneity of materials (Figure 3 g, 3 h) and is generally weathered. The clasts are mostly of basalt, but also of phonolite and, not often, are of granular rocks derived from CA. The cement contains carbonated and zeolitic material. Beside the continental facies there are also marine and estuarine, fossiliferous deposits.

2.2.4 Eruptive Complex of Pico da Antónia (PA)

The PA is the geological formation more developed on the Santiago Island (Figure 2) and it is responsible for the high altitudes and the main structural platforms seen on the island. This unit is essentially formed by thick sequences of basaltic lava flows, intercalated by pyroclastic material (Figure 3i). The petrographic types are basanites, ancaratrites and limburgites and also nephelinites and olivine-melilitite (Matos Alves et al., 1979). PA also contains phonolites, trackytes and tuff-breccias. The phonolitic and trackytic rocks form dikes, chimneys, endogenous domes and pyroclastic formations. The PA Formation is constituted in its upper part by thick levels of pyroclasts, some lava flows and vertical dikes, which in certain cases have a glassy texture.

2.2.5 Assomada Formation (AS)

The Assomada Formation (AS) occupies a large depression, between the two largest elevations of the island, Pico da Antónia (1392 m) and Serra da Malagueta (1063m), (Figure 2). The Assomada Formation is constituted by basaltic mantles and some basaltic pyroclastes, originated exclusively from sub-aerial volcanic activity. The wide lavas flows, almost horizontal have reached the shore, flowing to west (Figure 2) and forming the plateau of Assomada. The rocks are essentially basanites, which are weathered in some places, presenting greyish and reddish colors (Figure 3 j).

2.2.6 Monte das Vacas Formation (MV)

The formation Monte das Vacas (MV) is the last volcanic episode in Santiago Island and it is represented by 50 cinder cones (Figures 2 and 3 k, 3 l) and small subordinated flows. The constituting materials are loosely aggregated (Figure 3 k) and are exploited for construction, originating gullies and landslides on the flanks due to erosive action of the water during intense rainfalls (Figure 3 l).

2.2.7 Quaternary Formations (CC)

The Quaternary Formations have a small spatial representation, occupying an area of 8.5% of the area of the Santiago Island above water (Figure 2). These sedimentary formations are

ancient and modern alluvium, torrent deposits, sand dunes and marine beaches (Figure 3 m, 3 n, 3 o). The terraces reach altitudes of about 100m and are formed by materials with dimensions ranging from clay to big blocks that reach 2 meters.

3. Methods

3.1 Sample collection and treatment

Sampling, sample preparation and analytical programme were performed according to the recommendations of the IGCP (International Geological Correlation Programme) Project 259 "International geochemical mapping" (Darnley et al. 1995). So, the sampling sites for stream sediments were randomly selected to represent small drainage basins and are evenly distributed within the study area. Composite samples of stream sediments were collected in 337 sites, representing stream sediments developed from all the geological formations in Santiago Island, at a density of approximately 0.3 site/km². To establish the sampling sites the guidelines of the IGCP 259 project were followed, which state that the stream sediments of these sites must be as pristine as possible. On each site the composite sample (~1kg) was obtained in collecting five points, spaced approximately 50 m along the water line. The sampling sites were selected to represent pristine sediments, therefore locations affected by pollution (near factories or heavy traffic roads) and arable soils were avoided. Duplicates samples were taken every 10 sites. The samples were dried at 35-40 °C, sieved to <2 mm through a plastic sieve, homogenized and quartered. Sub-samples of 50g each were obtained and crushed to < 75 µm for analysis.

3.2 Analysis and analytical quality control

The chemical analysis was performed in the ACME Analytical Laboratories, Ltd, Vancouver, Canada. Each sample was digested in aqua regia and analysed by inductively coupled plasma-mass spectrometry (ICP-MS) for Co, Cr, Cu, Fe, Mn, Ni, Pb, Th, U, and V. All the sub-samples were randomly numbered prior to analysis in order to remove any systematic relationship between the analysis order and geographic location. The data resulting from the chemical analysis of the elements was subjected to several data quality tests in order to determine which elements have reliable data to be analysed. The criteria used to select an element to subsequent statistical analysis were: (i) at least of 80% of the observations with a content greater than the detection limit; (ii) accuracy and precision (quantified by analytical duplicates) lower than 10%; and (iii) geochemical variance significantly representative (0.01 significance level) of the total observed variance (quantified by an Analysis of Variance using field duplicates). All above mentioned elements passed these quality tests. Table 1 shows the standard deviations (SD), asymmetry (Asy), curtosis (Kurt), coefficient of variation percent (CV%), minimum (Min), maximum (Max) and range of the concentrations of the elements analysed.

The mineralogical composition of the < 2mm fraction of 83 selected stream sediments samples, representing all geological formations of the island, was studied by X-ray diffraction (XRD). The XRD was performed at the Department of Geosciences, University of Aveiro. It was used the method of crystalline dust, and graphic mode register (post diffractometry technique). It was used a Philips X'Pert diffractometer, with a PW3050 goniometer, a PW 3040/60 microprocessor and a CuK α radiation with a Ni filter. The

operation conditions were 30 mA, 50 kV, between 2°-60°, a step size of 0.02 (2 θ) and a scan step time of 1.05 s and a JCPDS software.

	SD	Asy	Kurt	CV	Min	Median	Max	Range concentrations			Average
Co	13.86	1.21	10.65	0.31	3.1	44.70	139.9	3.1	-	139.9	45.1
Cr	68.03	1.48	7.39	0.55	8.0	114.00	463.1	8.0	-	463.1	123.7
Cu	17.99	0.51	5.33	0.37	3.2	48.80	141.6	3.2	-	141.6	48.6
Fe	1.65	0.35	4.09	0.24	1.61	6.64	13.53	1.61	-	13.5	6.8
Mn	441.65	2.06	11.72	0.35	197.00	1191.00	4210.0	197.0	-	4210.0	1259.9
Ni	76.02	0.50	4.10	0.47	0.0	155.20	0.4	0.0	-	0.4	160.5
Pb	6.61	7.50	72.21	1.26	1.2	3.90	25.8	1.2	-	25.8	5.2
Th	1.45	2.72	17.49	0.35	0.0	3.90	1.4	0.0	-	1.4	4.2
U	0.24	1.83	10.21	0.35	0.2	0.6	2.3	0.2	-	2.3	0.7
V	45.68	0.64	5.51	0.28	24.0	160.0	372.0	24.0	-	372.0	170.0

Table 1. Statistical parameters of the metals Co, Cr, Cu, Fe, Mn, Ni, Pb, Th, U and V, analyzed from the stream sediments of Santiago Island (n=337). Contents of metals in mg kg⁻¹ except for Fe (%). Min: minimum; Max: maximum, SD: standard deviation, Ass: asymmetry, Kurt: kurtosis, CV: coefficient of variation

3.3 Estimated background value for selected harmful elements

Policy makers usually prefer a single value representative of an entire country or region, although the background value of an element may present a considerable spatial variability, and, thus, are presented by distribution maps. So, we determined an EBV representative of the entire Santiago Island (EBV-S), and one EBV representative of each one of its geological formations (EBV-xx, where xx are the initials of a particular geological formation). The EBV-S was calculated as the median of the data set limited by the Tukey Range or also referred to as the Non-Anomalous Range (Tukey, 1977): $]P25-1.5*(P75-P25), P75+1.5*(P75-P25)[$. The Tukey Range filters out the outliers or the anomalous data. The EBV-xx were calculated as the EBV-S, with the difference that the data set used in the calculations consists of those sampling points that belong to the xx geological formation.

The degree of depletion or enrichment of each element in the stream sediments of Santiago in relation to the value for the upper crust (Rudnick & Gao, 1995), using the EBV-S of each element, was also quantified.

3.4 Statistical analysis and mapping

The spatial distribution of the content of a geochemical element sampled in stream sediment points (spatial locations) is not a spatially continuous field. The content of a particular point is representative of that point only, although it has also the contribution of the points located upstream of the stream sediment line. Since the field is not continuous (or is only along each stream sediment line) it makes no sense to perform a spatial interpolation between two points lying on two different stream sediment lines. Because of this, the spatial distribution of each element is mapped using dot points and not contour lines (isolines).

Spatial distributions of Co, Cr, Cu, Fe, Mn, Ni, Pb, Th, U, and V content were mapped using 337 samples of stream sediments, following the recommendations of Darnley et al. (1995). All the calculations and data visualization were made using Matlab which is a well-known and widely used general purpose programming language (<http://www.mathworks.com>). The size of the dot increases with increasing class levels. The diameter of the symbols were classified in 8 classes defined by the following intervals: [minimum -P10]; [P10-P25]; [P25-P50]; [P50-P75]; [P75-P90]; [P90-P95]; [P95-P97.5]; [P97.5-maximum], where Px is the xth percentile value. In each figure, it is also shown the histogram (blue bars) and corresponding empirical Cumulative Distribution Function (CDF) (red dots), because they provide an estimate of the probability distribution of the data. The histogram was constructed using the same classes of dot distribution maps. The boxplot, calculated according to Tukey (1977), is also included.

A Principal Component Analysis (PCA) was also performed, using the correlation matrix, and the first three Principal Components (PCs) are mapped using the same methodology used to map the content of selected harmful elements. The number of PCs to retain was objectively determined using the scree plot.

4. Results and discussion

4.1 Relative proportions of minerals in the stream sediments of the Santiago Island

The mineralogical composition of the stream sediments is primarily governed by the mineralogy of the bedrock, climatic conditions (precipitation, temperature, wind direction) and topography. Chemical weathering is not intense in Santiago, due to the semi-arid climatic conditions and the vigorous relief. The chemical alteration of rocks leads to the formation of phyllosilicate, hematite, calcite and quartz, that, together with the primary minerals, desegregated by physical alteration of the rock, are eroded and will form the stream sediments. Figure 4 shows the relative proportions of the various minerals identified in stream sediments in the different geological formations of Santiago Island.

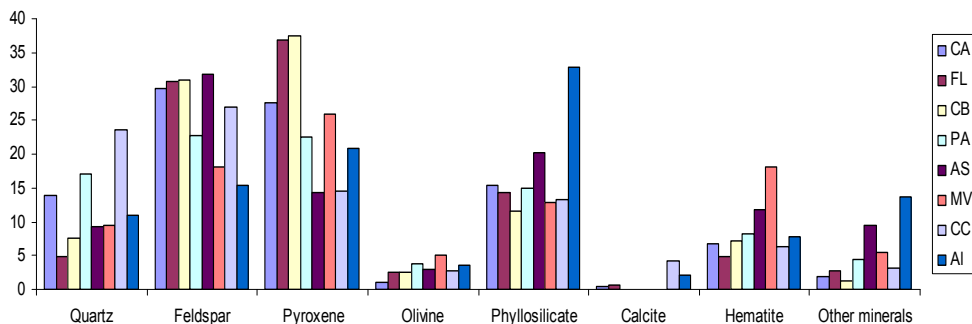


Fig. 4. Relative proportions, in percentage, of minerals in the stream sediments of Santiago Island. Geological formations: CA - Ancient Internal Eruptive Complex (n=5), FL- Flamengos Formation (n=23), CB- Órgãos Formation (n=13), PA - Pico da Antónia Formation (n=14), AS - Assomada Formation (n=5), MV - Monte das Vacas Formation (n=4), CC - Calcários e Cascalheiras Formation (n=4), AI: Alluvium (n=15)

The stream sediments associated with the CA Formation are composed mainly (in descending order of relative proportion) by plagioclase and K-feldspar (30.4%), pyroxene (28.3%), phyllosilicate (15.8%) (smectite, mica / illite), quartz (14.1%), hematite (6.8%), "other minerals" (1.8%) (such as larnite, siderite, leucite, apatite, magnetite, aragonite), olivine (1.1%) and calcite (0.4%) (Figure 4).

The stream sediments occurring in the FL, CB and PA formations consist mainly of pyroxene (36.8%, 37.4% and 23.9%, respectively), plagioclase and K-feldspar (30.8%, 30.9% and 24.0%, respectively), and phyllosilicate (14.3%, 11.6% and 15.9%, respectively). They differ by the proportions of different phyllosilicate and by the relative proportions of the other minerals identified. In descending order, in stream sediments of the FL it occurs (smectite+ interstratified, mica / illite), quartz (4.8%), hematite (4.9%), olivine (2.6%) and "other minerals" (2.8%) (magnetite, chromite, larnite, siderite, leucite, apatite, aragonite, opal, barite, halite); in stream sediments of CB formation it occurs (smectite and traces of mica / illite and kaolinite), quartz (7.5%), hematite (7.2%), olivine (2.4%), and "other minerals" (1.2%) (chromite, larnite, siderite, garnet, opal, barite, dolomite), and in the stream sediments of PA Formation it occurs (kaolinite, mica, illite and smectite), quartz (18.0%), hematite (8.7%), "other minerals" (4.7%) (larnite, siderite, zeolite, dolomite, garnet) and olivine (4.0%) (Figure 4).

The stream sediments associated with the AS Formation consist of plagioclase and K-feldspar (31.7%), phyllosilicate (20.3%) (mica / illite and smectite), pyroxene (14.3%), hematite (11.9%), "other minerals" (9.5%) (magnetite, zeolite, larnite, siderite), quartz (9.4%) and olivine (3.0%). These stream sediments have the highest proportion of phyllosilicate (with the exception of the alluvium) because the rocks of this formation are very weathered.

The stream sediments that occur on the MV Formation are composed by pyroxene (27.1%), plagioclase and K-feldspar (18.9%), hematite (18.8%), phyllosilicate (13.5%) (mainly kaolinite), quartz (9.9%), "other minerals" (5.6%) (magnetite, chromite, larnite, siderite) and olivine (5.3%). The stream sediments that occur on the CC Formation have plagioclase and K-feldspar (28.5%), quartz (24.8%), phyllosilicate (13.0%) (kaolinite, smectite), pyroxene (15.2%), and in lesser proportions calcite (4.3%), hematite (6.6%), olivine (3.9%) and "other minerals" (3.3%) (magnetite, larnite, siderite). The alluvium is distinct from the other stream sediments because it is richer in phyllosilicate (13.6%), "other minerals" (4.1%) (mainly magnetite, zeolite, siderite) and have very little feldspar (23.9%) (Figure 4).

The minerals that occur in higher proportions in the stream sediments are feldspars and pyroxene, which are the principal primary components of rocks forming the island and so they and were eroded from the volcanic rocks. So the mineralogy of stream sediments is essentially conditioned by the lithology and erosion, while the alluvium is conditioned by relief, as it is located in areas of flattened valleys, where the deposition of clay minerals occurs.

4.2 Estimated background values of Santiago Island and of its geological formations

Although the background value of an element may present a considerable spatial variability, and, thus, is presented by distribution maps, policy makers usually prefer a single value representative of an entire country or region. The chemical background of an element has been estimated in different statistical ways in the literature, either by interval

estimation or by point estimation. Table 2 presents four interval estimators (Observed Range, P₅-P₉₅ Range, Tukey Range and Expected Range) and one point estimator (Estimated Background Value for Santiago stream sediments, EBV-S).

	Min	-	Max	P ₅	-	P ₉₅	Tukey Range		Dudka Range		EBV-S		
Co	3.1	-	139.9	26.4	-	66.1	15.8	-	73.4	20.5	-	89.0	44.7
Cr	8.0	-	463.1	20.0	-	251.5	8.0	-	264.0	26.8	-	401.2	111.0
Cu	3.2	-	141.6	17.6	-	77.8	9.4	-	87.6	17.3	-	114.5	48.7
Fe	1.61	-	13.53	4.47	-	9.64	2.65	-	10.70	3.87	-	11.13	6.60
Mn	0.2	-	4.2	0.3	-	1.3	0.1	-	1.5	0.3	-	1.7	0.6
Ni	0.0	-	0.4	0.1	-	0.3	0.0	-	0.3	0.1	-	0.4	0.16
Pb	1.2	-	25.8	3.7	-	15.3	1.2	-	16.4	3.3	-	18.3	7.7
Th	0.0	-	1.4	0.3	-	0.9	0.0	-	1.0	0.2	-	1.2	0.5
U	0.2	-	2.3	0.4	-	1.1	0.5	-	1.25	0.3	-	1.2	0.6
V	24.0	-	372.0	92.4	-	237.3	50.5	-	262.5	81.6	-	290.7	159.0

Table 2. Background concentrations of metals from the stream sediments of Santiago Island estimated by five different estimators. Contents of metals in mg kg⁻¹ except for Fe and Mn (%)

The difficulty of establishing a single value of background level is well illustrated in Table 2, given the ranges of variation in their natural concentrations. The range values contained between P₅ and P₉₅ is, in most cases, narrower than that obtained in the Non-Anomalous Range, calculated by the Tukey method (Tukey, 1977). The range values calculated by the Expected Range (Dudka, 1995), presents, usually, higher upper limits, while the Tukey Range (Tukey 1977) comprises lower bottom limits.

The EBV-S of the studied metals in Santiago stream sediments are compared with the values estimated for the upper crust (UC, Rudnick & Gao, 1995) in Figure 5, where the Tukey Range is also shown. Figure 6 shows the enrichment or impoverishment in metal content of Santiago stream sediments relative to the values of the upper crust (Holland & Turekian, 2005 in Rudnick & Gao, 1995).

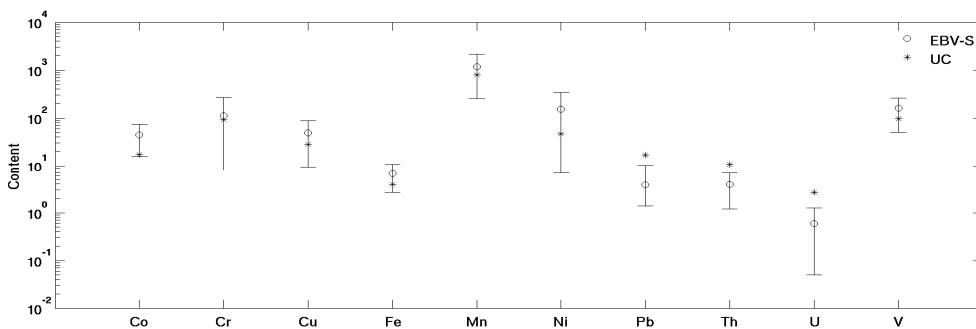


Fig. 5. EBV-S (circles) and Tukey Range of metals in Santiago stream sediments, and upper crust reference values (UC, asterisks), according to Rudnick & Gao, 1995

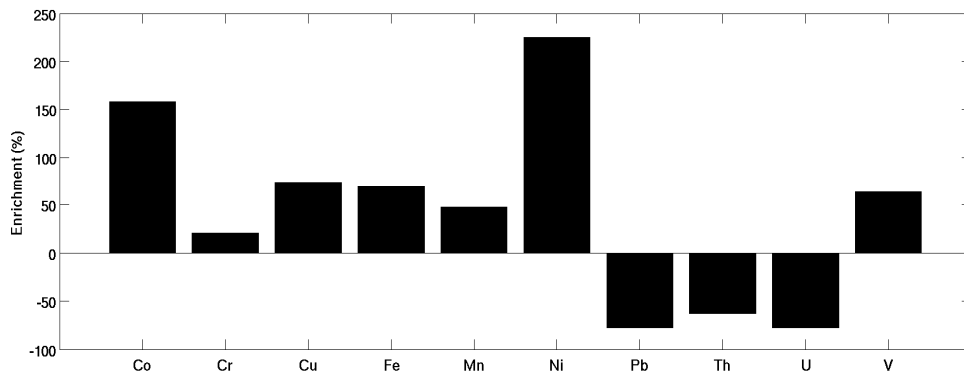


Fig. 6. Enrichment (%) in metal content of Santiago stream sediments relatively to the upper crust reference values (UC, Holland & Turekian, 2005 in Rudnick & Gao, 1995), determined by $100(EBV-UC)/UC$

Stream sediments of Santiago Island have higher contents in Co, Cr, Cu, Fe, Mn, Ni and V than those on the upper crust (UC) (Figures 5 and 6). Volcanic rocks of Santiago Island, which occupy the majority of the area of the Island, are mainly basanites, alkaline basalt and trachytic-phonolitic rocks, rich in siderophile elements (Fe, Mn, Co, Cr, Ni). This agreement suggests that the metal composition of the stream sediments is controlled by the chemical composition of the parent rock. The results shows also that the stream sediments of Santiago are impoverished in Pb, Th, and U. Furthermore, the UC values of these metals are higher than the upper limit of the Tukey range (Figure 5). This is due to the fact that the upper crust has a granodioritic composition, and is therefore rich in these elements.

In order to further explore the relationship of the spatial distributions of the EPVs and the geological formations, we show in Table 3 the estimated background values (EBV-xx) of the studied metals in the stream sediments collected from the different geological formations of the Island. Stream sediments derived from Ancient Complex (CA) have high Cr and V. Stream sediments from Flamengos formation (FL) have low Pb and high Cu. Órgãos formation (CB) have stream sediments with high Cu, and low Fe, Mn, Th and U. Stream sediments derived from Pico da Antónia (PA) formation have high Co, Cr, Fe, Ni and V. Stream sediments derived from Assomada (AS) and Monte das Vacas (MV) formations have high Fe, Mn (as sediments from CA formation) and Pb, and low Co, Cr, Cu and Ni. Stream sediments samples collected in MV formation distinguish from the other sediments samples by its high Th and low V contents. Finally, stream sediments from CC formation have low Th and U.

4.3 Maps of estimated background values

Figure 7 presents the dot distribution maps of studied harmful metals. Is also presented for each element the boxplot, calculated according to Tukey (1977), the histogram (blue bars) and the corresponding empirical CDF (red dots).

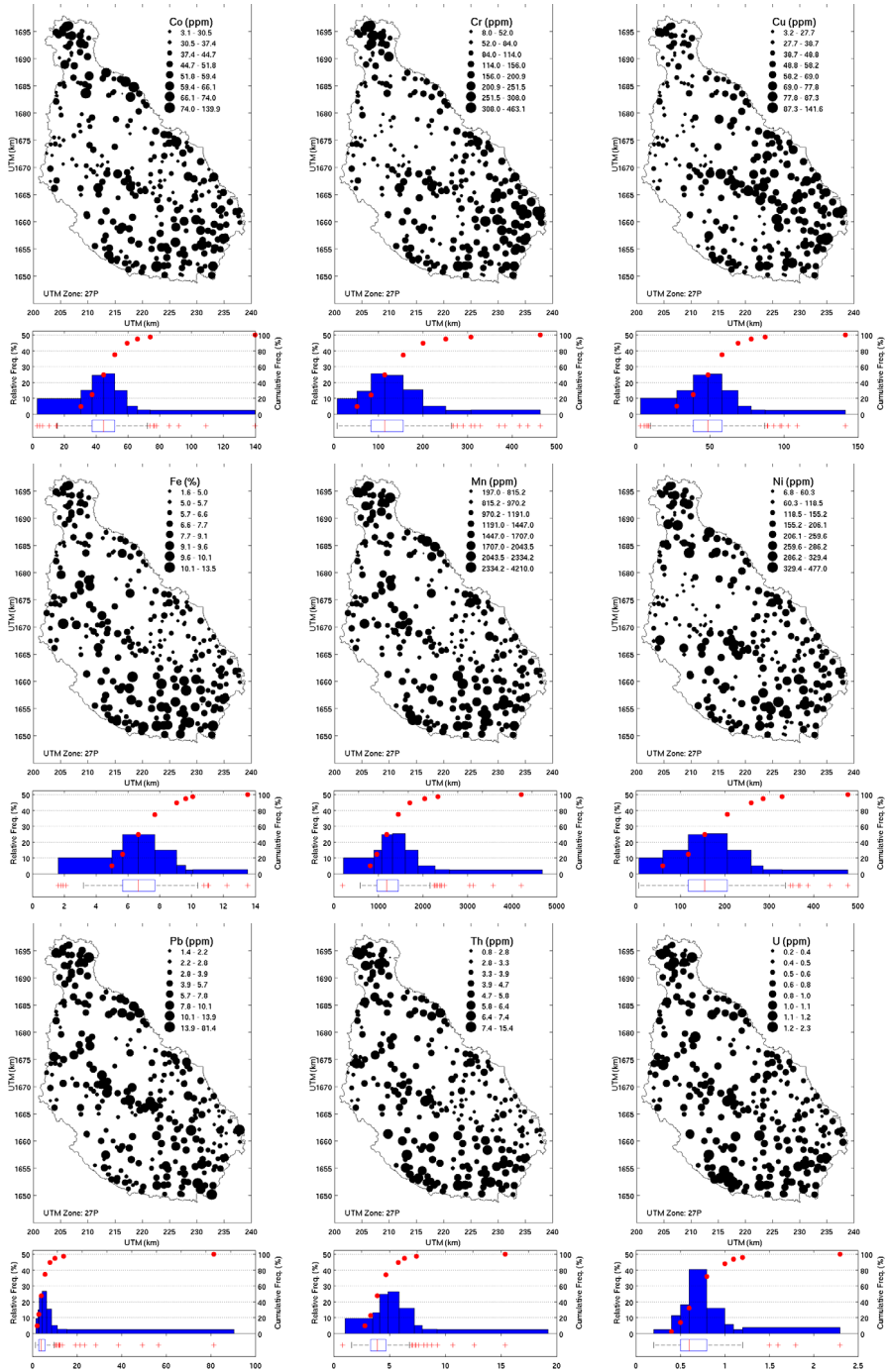
	EBV-CA	EBV-FL	EBV-CB	EBV-PA	EBV-AS	EBV-MV	EBV-CC	EBV-AL
Cd	0.1	0.1	0.1	0.1	0.2	0.2	0.1	0.1
Co	43.6	41.3	40.3	48.8	35.8	42.6	42.2	44.9
Cr	116.0	112.5	99.0	122.5	20.5	76.0	93.5	119.3
Cu	53.8	57.6	56.7	46.6	26.4	34.2	47.4	48.9
Fe	7.04	6.12	5.99	7.03	8.12	6.90	5.97	6.54
Mn	1199.0	1035.5	980.0	1328.0	1612.0	1423.0	1026.5	1157.0
Ni	126.7	139.1	145.1	168.1	20.1	104.1	148.9	164.1
Pb	3.6	2.5	3.3	4.7	6.6	6.0	4.1	3.4
Th	4.0	3.6	3.4	3.9	4.0	4.1	3.7	3.8
U	0.7	0.7	0.5	0.6	0.7	0.7	0.5	0.7
V	166.0	157.5	148.0	167.0	153.0	131.0	147.0	156.0

Table 3. Comparison of the Estimated Background Values (EBVs) between the different geological formations of the stream sediments of Santiago Island, Cape Verde. Concentration of Fe expressed in % and Co, Cr, Cu, Mn, Ni, Pb, Th, U and V in mg kg⁻¹

The comparison of the Co, Cr, Cu, Fe, Mn, Ni, Pb, Th, U and V dot maps with the geological map shows that a clear chemical characterization of stream sediments in different geological formations is difficult, since the chemical composition of each sample represents the chemical composition of the entire area upstream, covering different geological formations. However, it seems that same associations between the geological formation and stream sediments composition can be identified.

Lead, Mn, U and Th appear to be highly correlated to phonolitic-trachytics rocks of Pico Antónia (PA) and Ancient Internal Eruptive Complex (CA), and also with pyroclastic deposits of Monte das Vacas and Assomada formations. Contrarily, the Órgãos and Flamengos formations are depleted in these metals. Assomada and Monte das Vacas formations are depleted in Ni, Co, Cr, Cu, and Flamengos and Órgãos formations are depleted in Fe. Stream sediments derived from CC formation is depleted in V and Fe. Cobalt, Cr, Ni, and V appear to be highly correlated to basaltic-basanite rocks of Pico Antónia formation.

In order to try to establish the association between the Co, Cr, Cu, Fe, Mn, Ni, Pb, Th, U, and V, spatial distribution and the geology, a correlation-based PCA was conducted. Using the scree plot it was decided to retain three Principal Components (PCs - Figure 8).



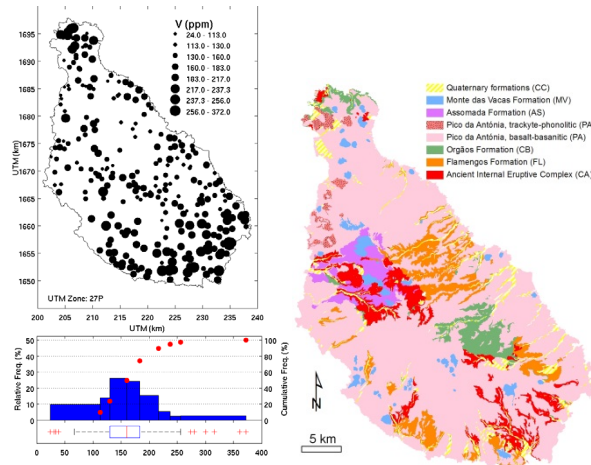


Fig. 7. Spatial distribution, histogram and associated empirical CDF, and boxplot of the EBV of Co, Cr, Cu, Fe, Mn, Ni, Pb, Th, U and V. Geological map is presented for comparison

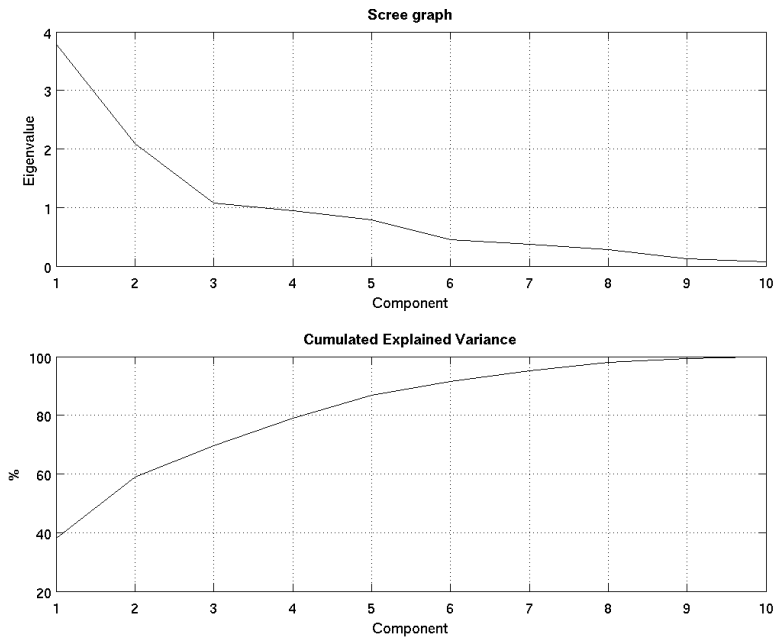


Fig. 8. Eigenvalue (upper panel) and Cumulative Explained Variance (lower panel) of the first ten PCA mode

The first three PCs represent 69.6% of total variability (37.96% + 20.87% + 0.77%). The loadings of these PCs are shown in the plots of PV1 vs PV2 and PV1 vs PV3 (Figure 9).

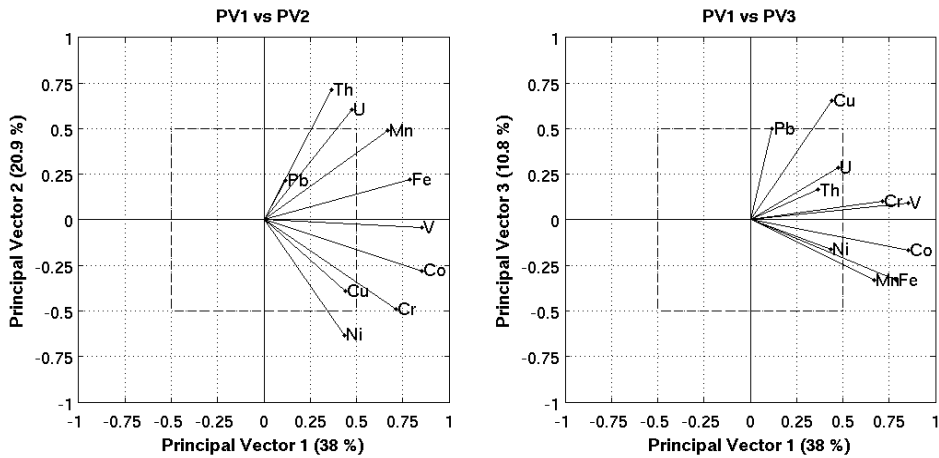


Fig. 9. PV1 versus PV2 (left) and PV1 versus PV3 (right)

The elements whose loadings in each PC have an absolute value greater than 0.5 are:

- PC1: Co, Cr, Fe, Mn and V
- PC2: Th and U oppose in sign to Ni
- PC3: Cu and Pb.

The association in PC1 clearly shows the influence of a rich lithology in siderophile elements (Co, Cr, Fe), typical of basic rocks and the presence of minerals such pyroxene (Fe, V), amphibole, olivine and magnetite (Fe), serpentine (Co, Cr, Ni). The metal association in PC2 represent crustal elements, typical of acid rocks, and show the presence of zircon (U, Th), oppose in sign to Ni, which enters in the structure of minerals typical of basaltic rocks, such as serpentine (Co, Cr, Ni). The PC scores are presented in Figure 10.

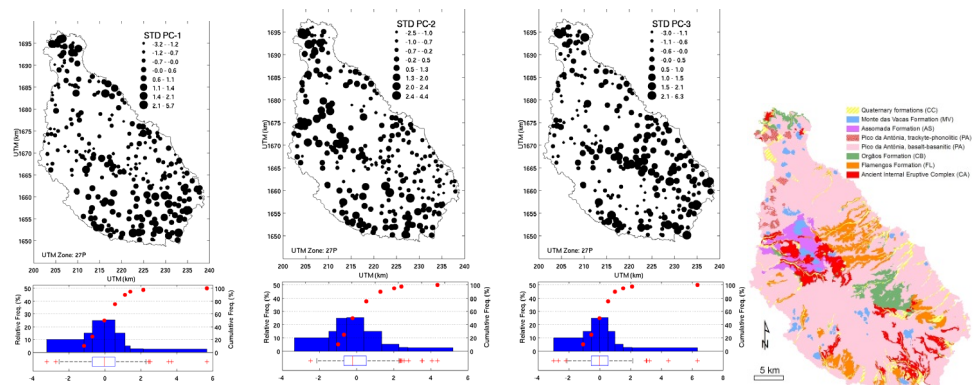


Fig. 10. Spatial distribution, histogram and associated empirical CDF, and boxplot of PC1, PC2 and PC3. Geological map is presented for comparison

When comparing the spatial distribution of the PCs (Figure 10) with the geological formations, it not clear a relationship between them. For example, PC1 is associated with basaltic-basanite rocks of the PA formation, contrarily to the Flamengos formation (FL); however, the AS formation is depleted in Co, Cr, but is the richest in Fe and Mn; PC2 is associated to phonolitic-trachytics rocks of Pico Antónia (PA), Assomada (AS) and Monte das Vacas (MV). PC3 is associated probably to anthropogenic origin.

5. Conclusions

A clear chemical characterization of the stream sediments in different geological formations is difficult, since the chemical composition of each sampling point represents the chemical composition of the entire area upstream, covering different geological formations. Despite this constraint, the results of PCA distinguished three associations of key variables. The first (Co, Cr, Fe, Mn, V) consists of elements enriched in basic rocks, and compatible elements. These elements are related to pyroxene, amphibole, and olivine minerals. The second association of variables, Th and U, as opposed to variable Ni, appears to be strongly controlled by the composition of alkaline volcanic rocks and pyroclastic rocks. The K-feldspar, zircon, pyroxene, amphibole, olivine are examples of minerals that are causing this association. The third association (Cu and Pb) consists of elements of anthropogenic origin.

The minerals present in stream sediments from Santiago Island are a combination of minerals inherited from the original lithology, minerals resulting from alteration of these primary minerals, and probably also wind-transported, largely from the Sahara desert (quartz and phyllosilicates).

The mineralogical composition of stream sediments of Santiago are dominated by primary silicate minerals, such as feldspar, pyroxene and olivine, and also quartz. The main secondary minerals are phyllosilicates (smectite, kaolinite, mica / illite), calcite and hematite. Thus the stream sediments have a high relative proportion of primary minerals, reflecting the mineralogical signature of the igneous rocks that support the island. In the "other minerals" group were identified leucite, apatite, nepheline, magnetite, titanomagnetite, ilmenite, chromite, garnet, zeolites, siderite, opal, barite, sphene, zircon, halite, aragonite, dolomite, brucite and chlorite, most of them are primary. The existence of quartz must result fundamentally of wind-transported from Saara desert, but also from the weathered of rocks;

The mineralogical composition of the stream sediments results mainly from the composition of the rocks upstream;

In terms of the relation between stream sediments composition and geological formation we can be concluded that:

- a. the stream sediments that occur on the PA formation have the highest background values for the variables Co, Cr, Ni, V, which explains the enrichment seen in association Co-Cr-Fe-Mn, which is consistent with mineralogical analysis. They consist mainly of pyroxene, plagioclase, potassium feldspar, and phyllosilicates, and may also experience other minerals such as hematite, olivine, magnetite, chromite, larnite, siderite, leucite, apatite, garnet, aragonite, brucite, opal, barite, halite;

- b. the stream sediments collected associated with the CB formation show depletion in Th-U and Mn, which is consistent with the results obtained for the analysis of rocks (Cabral Pinto et al. 2011a). The sediments associated with this formation are composed mainly of pyroxene, plagioclase, potassium feldspar, and phyllosilicates (smectite, mica / illite), hematite, quartz, olivine and chromite, larnite, sidereite, opal, barite, and garnet, dolomite, brucite;
- c. the majority of the samples of stream sediments that occur associated with the AS formation is enriched in Th-U and in the elements Fe, V, Mn and impoverished in Co-Cr-Cu-Ni association, probably because this geological formation is significantly weathered and consequently impoverished in primary minerals such as pyroxene and olivine, and enriched in weathered minerals, such as hematite, phyllosilicates, serpentine and zeolite. Chemical analysis of this formation the rocks show higher levels of Fe (Cabral Pinto et al. 2011a).
- d. the stream sediments associated with the Monte das Vacas formation are impoverished in Co-Cr-Ni-V. They consist of pyroxene, hematite, plagioclase and potassium feldspar, phyllosilicates, quartz, magnetite, chromite, barite, larnite, siderite and olivine;
- e. the alluvium samples are distinguished from other stream sediments because they are rich in phyllosilicates, other minerals, and are poor in feldspar. Its mineralogical composition is conditioned by weathering and relief, as the alluvium is located in areas of flattened valleys where the deposition of clay minerals occurs;

The spatial distribution of the selected elements allowed to establish relationships between the concentrations and the geological formations. These relationships were confirmed by the results of PCA. Firstly, the metals with higher loadings in PC1 clearly show the influence of a rich lithology in siderophile elements (Co, Cr, Fe), typical of basic rocks and the presence of minerals such as pyroxene (Fe, V), amphibole, olivine and magnetite (Fe), serpentine (Co, Cr, Ni) and opaque minerals (Cu). Secondly, the metals with higher loadings in PC2 represent crustal elements, typical of acid rocks, and show the presence of zircon (U, Th). Furthermore, the spatial distribution of the first two PCs also allowed us to distinguish associations between chemical elements, essentially of geogenic origin.

The determination of a single EBV for the entire Santiago Island (EBV-S) showed that, in general, stream sediments from this Island have higher contents in Co, Cr, Cu, Fe, Mn, Ni and V than those of the upper crust. Stream sediments from Santiago are impoverished in Pb, Th, and U, relatively to the upper crust.

Finally, the determination of an EBV for each geological formation (EBV-xx) gave us even more confidence on the dependence of the spatial distribution of the EPVs from the geological formations.

6. Acknowledgments

This work was supported by the grant SFRH/BD/24791/2005 provided by the Portuguese Foundation for Science and Technological (FCT). The authors acknowledge Dr. Oliveira Cruz, Professor Dr. Jorge Brito and Doctor Luis Filipe Tavares for the logistic support in Santiago Island through the University Jean Piaget of Cape Verde. The authors also acknowledge with great affection the field support provided by Ricardo Ramos.

7. References

- Albanese, S., De Vivo, B., Lima, A. & Cicchella, D. (2007). Geochemical background and baseline values of toxic elements in stream sediments of Campania region (Italy). *Journal of Geochemical Exploration* Vol.93, pp. 21-34
- Appleton, J.D. & Ridgway, J. (1993). Regional geochemical mapping in developing countries and its application to environmental studies. *Applied Geochemistry* Vol.2, pp. 103-110
- Cabral Pinto, M.M.S., Ferreira da Silva, E.A., Silva, M.M.V.G., Melo-Gonçalves, P., Hernandez, R., Reis, A.P., Inácio & M.M., Rocha, F.J. (2011). Maps of Estimated Geochemical Background Values of some metals in Santiago Island, Cape Verde. In: *Progress on Heavy Metals in the Environment*. Maralthe Books. Accept, in press.
- Cabral Pinto, M.M.S., Ferreira da Silva, E.A., Silva, M.M.V.G., Prudêncio, M.I., Marques, R. & Melo-Gonçalves, P. (2011a). Geochemical Background Values of chemical elements in Stream Sediments of Santiago Island, Cape Verde. *Proceedings of VIII Congresso Ibérico de Geoquímica, VII Semana de Geoquímica*, 6pp, Castelo Branco, Portugal, September 24-28, 2011. Accept, in press
- Darnley, A. & Garrett, R.G. (eds). International Geochemical Mapping Special Issue. *Journal of Geochemical Exploration* (1990), Vol. 39
- Darnley, A.G., Björklund, A., Bølviken, B., Gustavsson, N., Koval, P.V., Plant, J.A., Steinfeld, A., Tauchid, M. & Xie Xuejing. (1995). *A Global Geochemical Database For Environmental and Resource Management. Recommendations for international geochemical mapping*. Final report of IGCP project 259, UNESCO Publishing
- Dudka, S., Piotrowska, M., Chlopecka, A. & Wittek, T. (1995). Trace metal contamination of soils and crop plants by minning and smelting industry in Upper Silesia, South Poland. *Journal of Geochemical Exploration*, Vol.52, pp.237-250
- Inácio, M., Pereira, V. & Pinto, M. (2008). The soil Geochemical Atlas of Portugal: Overview and applications. *Journal of Geochemical Exploration*, Vol.98, pp.22-33
- Losada-Lima, A. (1987-88). Algunas consideraciones sobre la brioflora macaronésica. *Lazaroa* Vol.10, pp.213-218
- Matschullat, J., Ottenstein, R. & Reimann, C. (2000). Geochemical background—can we calculate it? *Environ Geol* Vol.39, pp.990- 1000
- Matos Alves, C.A., Macedo, J.R., Celestino Silva, L., Serralheiro, A. & Peixoto Faria, A.F. (1979). Estudo geológico, petrológico e vulcanológico da ilha de Santiago (Cabo Verde). *Garcia de Orta, Serv Geol*, Vol.3, pp.47-74
- Plant, J.A., Smith, D., Smith, B. & Williams, L. (2001). Environmental geochemistry at the global scale. *Applied Geochemistry* Vol.16, pp.1291-1308
- Rudnick, R.L. & Gao, S. (2005). Composition of the Continental Crust. Elsevier. In RL Rudnick (Ed.) *The Crust, Treatise on Geochemistry*
- Serralheiro, A. (1976). A Geologia da ilha de Santiago (Cabo Verde). *Boletim Museu Laboratório Mineralógico Geológico Faculdade de Ciências de Lisboa* Vol.14, n.º2
- Silva, L.C. (1979). Considerações geológicas e estudos preliminares sobre inclusões primárias, fluídas e sólidas, em apatites de rochas carbonatíticas e ijolíticas da ilha de Santiago (República de Cabo Verde). *Comunicações dos Serviços Geológicos de Portugal* Vol.LXIV, pp.261-268

- Silva, L.C. & Figueiredo, M.O. (1976). Alkaline-calcic metasomatic undersaturated rocks associated alkaline-carbonatitic complexes of Santiago (Cape Verde Islands). *Garcia de Orta, Sér Geol* Vol.1 n.º4, pp.133-142
- Tarvainen, T. (1996). Environmental Applications of Geochemical Databases in Finland. Synopsis. *Geological Survey of Finland*, Espoo. Academic Dissertation
- Tukey, J.W. (1977). *Exploratory data analysis*. Addison-Wesley, Reading
- Xie Xuejing, X., Xuzhan, M. & Tianxiang, R. (1997). Geochemical mapping in China. *Journal of Geochemical Exploration* Vol.60, n.º3, pp.99-113

The Relevance of Geochemical Tools to Monitor Deep Geological CO₂ Storage Sites

Jeandel Elodie¹ and Sarda Philippe²

¹*European Institute for Energy Research*

²*Université Paris-Sud, UMR IDES*

¹*Germany*

²*France*

1. Introduction

Combined with an increase in energy efficiency and production of more renewable energy, Carbon Capture and Storage (CCS) is a promising technological chain that aims to prevent climate change by reducing anthropogenic CO₂ emissions into the atmosphere. The three steps of this technology are (i) capturing large-scale CO₂ emissions produced by industrial activities using fossil fuels (coal-fired power plants, factories, steelworks, refineries), by post or pre-combustion methods, (ii) transporting the captured CO₂ to a storage site through pipelines, (iii) storing the CO₂ deep underground. Potential underground storage targets are (i) deep saline aquifers containing a high concentration of dissolved salts, (ii) depleted oil and gas fields (abandoned or used to perform Enhanced Oil Recovery (EOR) or Enhanced Gas Recovery (EGR)), (iii) coal seams, used to perform Enhanced Coal Bed Methane recovery (ECBM). Another possible solution for CO₂ storage would be to chemically fix CO₂ into the carbonated minerals in mafic and ultramafic rocks. Other geological media proposed as storage for CO₂ are oil or gas rich shales, salt caverns and abandoned mines (IPCC, 2005). According to the International Energy Agency (IEA), CCS could contribute up to 19% in the reduction of global emissions in 2050. Measuring Monitoring and Verification (MMV) is an important part of each CCS project. As stated in the European directive on the geological storage of carbon dioxide, “monitoring is essential in order to assess whether injected CO₂ is behaving as expected, whether any migration or leakage occurs, and whether any identified leakage is damaging the environment or human health...” Various monitoring methods, i.e. geophysics and geochemistry, can be used to fulfil such requirements, assess the efficiency of geological storage and ensure the containment of the storage system. In this chapter, we focus particularly on geochemical methods, and discuss their assets and relevance in monitoring CO₂ geological storage sites. At first, a classification is proposed based on a literature review. The role of geochemical methods to identify fluids sources and physicochemical processes is explained, and some examples of applications to deep geological CO₂ storage monitoring are described. Key elements of a relevant spatial use of geochemical methods during the lifecycle of a CCS project are also given, as well as general guidelines and recommendations for the integration of geochemical tools into a monitoring programme.

2. Assets and relevance of the geochemical methods in the framework of deep geological CO₂ storage

2.1 Geochemical tools classification

Geochemical methods used in the framework of CO₂ geological storage can be classified based on the chemical nature of the measured species and include a broad spectrum of chemical and isotopic parameters. The measurements traditionally performed on liquids, gases or solids are (non-exhaustive list): (i) pH measurements and total alkalinity; (ii) ions concentrations, such as Ca, Mg, Mn, K, Na, Li, Fe, Si, Cl, Sr, Ba, SO₄, NH₃, S₂... and Total Dissolved Solid (TDS); (iii) isotopic compositions ($\delta^2\text{H}$, $\delta^{13}\text{C}(\text{CO}_2)$, $\delta^{13}\text{C}(\text{C}_1\text{-C}_5)$, $\delta^{13}\text{C}(\text{HCO}_3^-)$, $\delta^{13}\text{C}(\text{CO}_3^{2-})$, $\delta^{13}\text{C}(\text{CaCO}_3)$, $\delta^{18}\text{O}(\text{H}_2\text{O})$, $\delta^{18}\text{O}(\text{CaCO}_3)$, $\delta^{34}\text{S}(\text{SO}_4)$, $\delta^{34}\text{S}(\text{H}_2\text{S}(\text{aq}))$, $\delta^{34}\text{S}(\text{H}_2\text{S}(\text{g}))$, $\delta^{15}\text{N}$, $^3\text{He}/^4\text{He}$, $^{20}\text{Ne}/^{22}\text{Ne}$, $^{21}\text{Ne}/^{22}\text{Ne}$, $^{38}\text{Ar}/^{36}\text{Ar}$, $^{40}\text{Ar}/^{36}\text{Ar}$, $^{87}\text{Sr}/^{86}\text{Sr}$); (iv) isotopic elementary ratios ($^{20}\text{Ne}/^{36}\text{Ar}$, $^4\text{He}/^{40}\text{Ar}$, $^{84}\text{Kr}/^{20}\text{Ne}$, $^{130}\text{Xe}/^{20}\text{Ne}$...); (v) molar concentrations (CO₂, C₁-C₅, H₂, O₂, Dissolved Inorganic Carbon (DIC) = [H₂CO₃] + [HCO₃⁻] + [CO₃²⁻], noble gases); (vi) measurements of the organic contents and use of organic tracers; (vii) SF₆ and perfluorocarbons concentrations; (viii) ^3H , ^{14}C , CD₄, ^{36}Cl , ^{125}I , ^{129}I , ^{131}I . Tracers and chemical compounds used to measure and verify the presence of the injected CO₂ can be native (indigenous), while others can be exogenous and added as an exotic species.

2.2 Powerful identification of the fluid source

2.2.1 Principles

The identification of crustal-fluid sources is based on knowledge of the isotopic compositions of different end-members (for example, the atmosphere, the crust and the mantle), which could present unique isotopic fingerprints. For example, the isotopic compositions of CO₂ produced by different processes in the geosphere (magma degassing, regional metamorphism of carbonate rocks, contact metamorphism of carbonate rocks, dissolution of marine carbonates, biodegradation of hydrocarbons, maturation and metamorphism of coal) each shows an expected range of $\delta^{13}\text{C}(\text{CO}_2)$ (Figure 1).

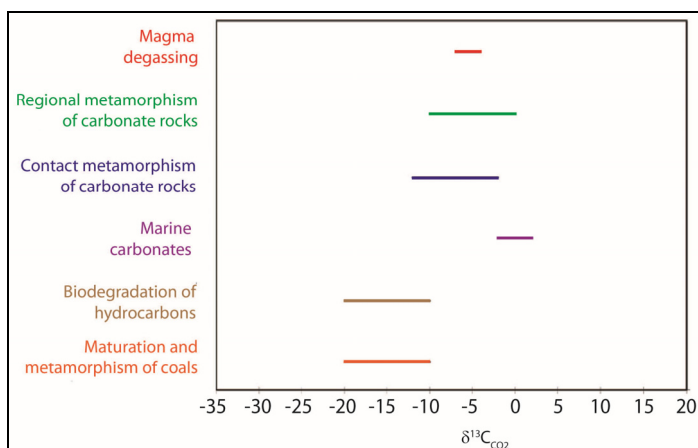


Fig. 1. $\delta^{13}\text{C}(\text{CO}_2)$ values for CO₂ derived from different processes occurring in the geosphere (Holloway et al., 2005).

The source of carbon cannot be unequivocally identified by the $\delta^{13}\text{C}(\text{CO}_2)$ ratios, as there is an overlap in the $\delta^{13}\text{C}(\text{CO}_2)$ of both crustal and mantle origins for CO₂ (e.g. Ballentine, 1997; Jenden et al., 1993; Sherwood Lollar et al., 1994, 1997; Wycherley et al., 1999). Isotopic compositions of mantle-derived carbon are indeed contained between -3 and -8‰ Pee Dee Belemnite (PDB) and isotopic compositions of bulk crustal carbon correspond to a range of -5 to -7‰ PDB. Noble gases can then be used to distinguish between decarbonation/magmatic sources, by comparing for example the measured CO₂/³He ratios in the gas phase with the known values of the crustal and mantle ranges (Sherwood Lollar et al., 1997; Ballentine et al., 2001; Gilfillan et al., 2008; Jeandel et al., 2010).

2.2.2 Applicability to deep geological CO₂ storage monitoring

Isotopic methods can be employed to determine the origin of pre-existing fluids in the reservoir, identify the injected CO₂ based on its isotopic fingerprint and resolve the origin of potentially leaking CO₂.

2.2.3 Examples

If the isotopic fingerprint of the injected CO₂ is sufficiently distinct from that of the background CO₂ in the reservoir, the injected CO₂ can easily be identified. This is notably the case in the International Energy Agency Greenhouse Gas (IEA GHG) Weyburn-Midale CO₂ Monitoring and Storage Project (Saskatchewan) and the Pembina Cardium CO₂ Monitoring Project (Alberta) (Johnson et al., 2009). Fluid and gas samples were regularly collected and analyzed for geochemical and isotopic compositions ($\delta^{13}\text{C}(\text{CO}_2)$, $\delta^{18}\text{O}(\text{H}_2\text{O})$, CO₂ concentrations, DIC). After the CO₂ injection began, even though only a small increase in the CO₂ concentrations was observed in some wells, the $\delta^{13}\text{C}(\text{CO}_2)$ values began to trend towards the value of the injected CO₂. Isotopic monitoring can thus be used to identify and monitor CO₂ breakthrough migration and behaviour.

2.3 Powerful identification of the physicochemical processes

2.3.1 Principles

Geochemical measurements are particularly suitable tools to identify and quantify the physicochemical processes that occur during CO₂ storage. This methodology is based on the knowledge of the physical properties of geochemical tracers and can be used to quantify CO₂/fluids/rocks interactions and fluids partitioning (gas/liquid and possibly oil). The tracers can be reactive (¹⁴C, for example) and be used to monitor chemical reactions. Or they can be un-reactive and conservative (noble gases, perfluorocarbons) and be used to track physical processes, as they are not involved in chemical and biological reactions. The main methodologies applied are based on isotope and mass balance calculations, and the evolution of the chemical and isotopic compositions, and/or the evolution of elementary ratios over time.

2.3.2 Applicability to deep geological CO₂ storage monitoring

The effectiveness, safety and security of geological CO₂ storage depends on a combination of trapping mechanisms such as (i) stratigraphic trapping; (ii) structural trapping; (iii) residual

trapping; (iv) solubility in brine; and (v) mineral trapping. As previously explained, geochemical tools play a key role in detecting the arrival of CO₂ at the observation wells, and are helpful in the quantification of stratigraphic and structural trapping. Mixing curves allow quantifying the respective percentage of background and injected CO₂ over time. Some quantifications of solubility trapping (formation of H₂CO₃ when CO₂ dissolves into water) and ionic trapping (formation of HCO₃⁻) are also documented in the literature, using carbon and/or noble gas isotopes (Gilfillan et al., 2009; Myrntinen et al., 2010). The quantification of mineral trapping, i.e. the formation of carbonate minerals due to the reaction of the dissolved CO₂ with the host rocks, can be similarly performed.

2.3.3 Example

Raistrick et al. (2006) and Myrntinen et al. (2010) introduced and used the following carbon isotope balance calculation to determine the percentage of DIC from CO₂ dissolution in the water phase, and thus to quantify the geochemical trapping of injected CO₂:

$$\frac{\delta^{13}\text{C}_{\text{DICafterinj.}} - \delta^{13}\text{C}_{\text{DICbaseline}}}{\delta^{13}\text{C}_{\text{CO}_2(\text{g})\text{inj.}} - \delta^{13}\text{C}_{\text{DICbaseline}}} \times 100 = \% \text{DIC} \quad (1)$$

from CO₂ dissolution

The percentage of DIC from CO₂ dissolution was corrected for isotope fractionation (−1‰) between CO₂ (g) and CO₂ (aq) at the given reservoir temperature. It should be noted that the trapping quantification is only feasible if the composition of the injected CO₂ is isotopically constant. Moreover, the newly formed DIC from the injected CO₂ and the pre-existing DIC should have different isotopic compositions. Using the geochemical signatures of gas samples taken from different natural CO₂ reservoirs, Gilfillan et al. (2009) have assessed the coherent change in CO₂/³He ratios and δ¹³C(CO₂), for different pH values and dissolution/precipitation processes. In the case of precipitation, there is zero ³He loss from the CO₂ phase and CO₂/³He changes in proportion to the fraction of the remaining CO₂ phase. In the case of dissolution, the change in the CO₂/³He ratio is calculated following the Rayleigh equation. Changes in δ¹³C(CO₂) are calculated using the Rayleigh fractionation equation. They highlighted that in seven gas fields with carbonated or siliciclastic reservoirs, dissolution at a pH of 5-5.8 is the sole major sink for CO₂. CO₂ loss through precipitation as carbonated minerals cannot be ruled out for two siliciclastic reservoirs, but appears minor. Some examples with oxygen isotopes are also reported in the literature (Mayer et al., 2011). Changes of δ¹⁸O values of produced water are due to oxygen isotope exchange between CO₂ and H₂O following CO₂ injection and allow a quantitative assessment of CO₂ dissolved in the fluids and of free phase CO₂ in the pore space of the reservoir.

2.4 Tracer tests and CO₂ plume spreading

Conservative tracers to be injected are extensively used to monitor migration of the CO₂ plume during the CO₂ injection period. Tracers are required to be “chemically inert, environmentally safe, nontoxic, persistent, and stable for purposes of the desired monitoring time scale” (Stalker et al., 2009a). Examples of noble gas, perfluorocarbons, SF₆ and carbon isotopes usage are reported in the literature. They allow for the identification of

single or multiple CO₂ breakthroughs. Their travel time may also validate subsurface flow paths and directions and strengthen the flow modeling of the field test.

2.4.1 Principles

Tracer tests consist of injecting a tracer, generally gaseous and not already present in the reservoir system, into a hydrological system and monitoring its arrival, over time, at various observation points such as monitoring wells. Phase partitioning tracers (non-condensable gases (O₂, CO₂, CH₄), noble gases, SF₆ and other volatile organic chemical compounds), that are both water soluble and volatile, can also give information on the volume fractions of the different fluid phases along the CO₂ migration paths. Due to partitioning into an immobile phase, tracer migration is slowed relative to the inert tracers. This is governed by the Henry law. The retardation factor, expressed as the local ratio of total tracer inventory to the tracer inventory in the mobile phase, depends on the solubility of the tracer in water. For example, more water-soluble tracers are more retarded than fewer soluble tracers. The use of simplifying assumptions (local equilibrium partitioning, absence of diffusion and sorption on solids...) can result in the interpretation of tracer data not being unique, so using several different tracers can reduce ambiguities and uncertainty (Pruess et al., 2005).

In the field, different types of sequence tests can be performed. Prior to CO₂ injection, dual tracer single-well push-pull tests and dual tracer inter-well circulation tests can be carried out to determine fluid-rock interface densities, the connectivity of the hydrologic system and the presence of reservoir heterogeneities. These tests also assess the fluid residence time (Ghergut et al., 2011). For example, tracers can be injected into the aquifer and pushed away by a continuous injection of water. The tracer is then pulled back into the borehole, where a breakthrough curve is measured which is directly dependent on the residual gas saturation. During the CO₂ injection, single well push-pull experiments and dipole flow experiments can be carried out for a dynamic characterisation of CO₂/brine/rock interfaces, and an assessment of the residual saturation.

2.4.2 Examples

Observations from two monitoring wells at the Ketzin CO₂ injection pilot site (Germany), indicated the arrival of nitrogen and krypton gas tracers prior to CO₂ breakthrough (Figure 2) (Martens et al., 2011; Zimmer et al., 2009, 2011). The gases were detected by high temporal resolution Gas Membrane Sensors (GMS), permanently installed at both observation wells (Ktzi 200 (OW1) and Ktzi 202 (OW2)). The first breakthrough was detected after about 530 tons of injected CO₂ in Ktzi 200, which is 50 m away from the injection well. The arrival of the gas at the second observation well (Ktzi 202, 112 m lateral distance to the injection well) was recorded after about 11,000 tons of CO₂ was injected.

The Frio Brine Pilot test (Texas) was another opportunity to test a combination of tracers (perfluorocarbons, SF₆, Kr) and to compare their transport times and to test the efficiency of anticipating a CO₂ breakthrough (Pruess et al., 2005). Tracer tests have been successfully used to monitor migration of the CO₂ plume, after their introduction at given times alongside the injected CO₂ stream and their movement through the formation (Figure 3).

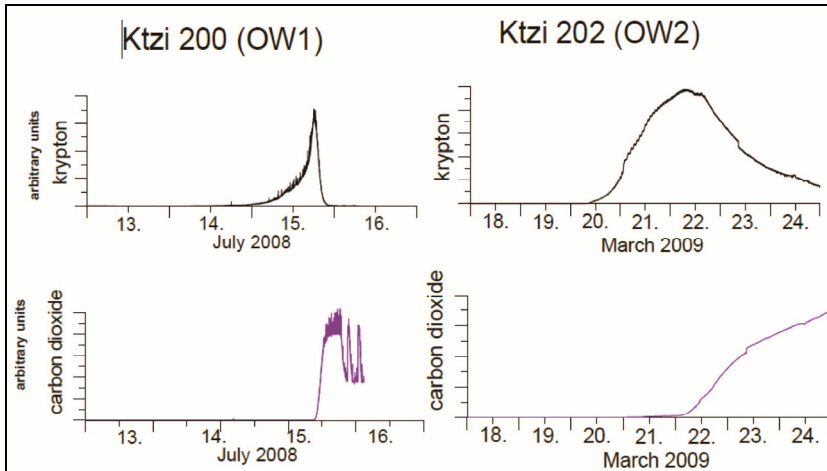


Fig. 2. CO₂ and Kr Arrival in Ktzi 200 (OW1) and Ktzi 202 (OW2). After Zimmer et al., 2011.

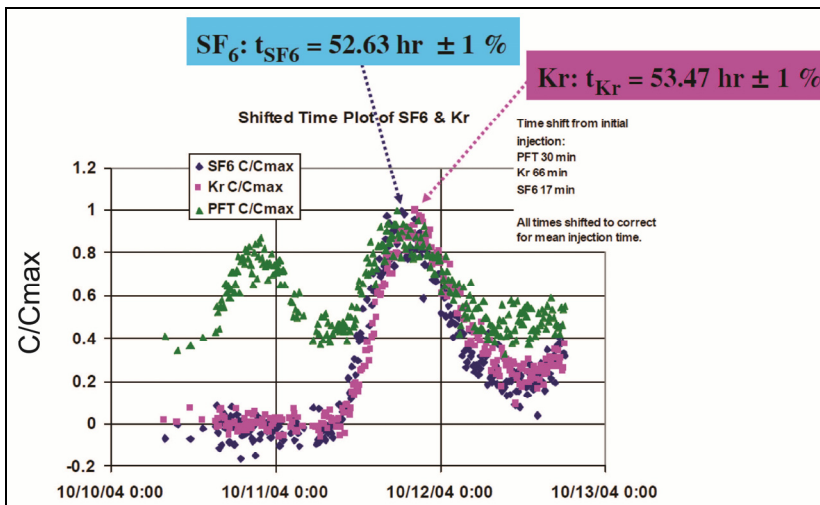


Fig. 3. C/C_{max} of SF₆, Kr and PerFluoroTracers (PFTs) versus time for the Frio brine Pilot test. As Kr is more soluble in water than SF₆, it is retarded relative to less soluble SF₆. After Pruess et al., 2005.

Similar tracer tests (with SF₆ and Kr) were performed at the Cooperative Research Centre for Greenhouse Gas Technologies (CO₂CRC) Otway project (Australia), which was also an opportunity to test perdeuterated methane (CD₄) injection in the depleted Naylor gas field (Stalker et al., 2009b). As the stored gas consists of 75% CO₂ and 20% CH₄, it was hoped that CD₄ would highlight the exchange between native methane (both in the gas cap and the residual gas saturation below) and the injected CO₂/CH₄ gas stream. The new and innovative **Kinetic Interface Sensitive Tracers (KIS-Tracer)** can also be used to assess the interfacial area between supercritical (sc) CO₂ and brine and to survey its development over

time. After the dissolution of the KIS-Tracer in scCO₂, a hydrolysis reaction of the tracer with brine occurs at the scCO₂/brine interface that can be quantified by measuring the concentrations of the reaction products over time at the monitoring wells (Fagerlund et al., 2011).

2.5 Identification and quantification of potential CO₂ leakage from deep geological CO₂ storage sites

Because the detection and quantification of small and diffuse leaks is generally considered to be particularly difficult, the potential role of geochemical methods for such purposes must be scrutinized.

2.5.1 Principles

CO₂ concentrations vary widely in the Earth's crust, so detecting very small releases is difficult. Because of their unique compositions, isotopic fingerprints are particularly useful in identifying and quantifying mixing processes between different sources of CO₂. This geochemical monitoring can be applied to both overlying freshwater aquifers and at the surface.

2.5.2 Examples

Noble gas geochemistry was used to investigate the possible impact of CO₂ migration on groundwater chemistry in the Montmiral natural CO₂ field (France). In plotting the distance between the Montmiral area wells (SL₁, SL₂, VMO₂) and the water sample locations against the measured ⁴He/(²⁰Ne+²²Ne) ratios, an increase in the ⁴He/(²⁰Ne+²²Ne) ratios, associated with a decrease in the distance between SL₁ and the sampling points, was observed. This increase was attributed to a deep gas input (Lafortune et al., 2009), linked to the absence of cement in the abandoned SL1 well. Isotopic compositions can also help to identify the origins of the CO₂ leaks at the surface which were previously detected through flux and concentration measurements. In the Rangely oil field (Colorado), isotopic measurements have shown that loss of injected CO₂ by microseepage into the atmosphere is a fraction of natural biogenic methane seepage (Klusmann 2003). This allowed re-evaluating the deep CO₂ seepage rate.

2.6 Costs and deployment methods

The criteria of an efficient and cost-effective use of tracers should be as follows: sensitivity to detection by analytical methods, low usage volume, and easy handling. For example, Nimz & Hudson (2005) have calculated the quantity of tracers per mass unit of CO₂ needed to detect an increase of 1% of the present natural soil CO₂ (Table 1).

According to Stalker et al. (2009a), application methods (pulsed or continuous injection) also play a role in cost. Analytical costs are seen as the most prohibitive costs overall (specialist tracers, precise measurements by specialized equipment or methods, etc.). Compared to the other methods generally used for CCS monitoring, geochemical methods are by far the least expensive on-site measurements tools to track CO₂ (Benson & Cole, 2008).

Tracer	Atmospheric Concentration (cm ³ /cm ³ air)	Minimum Detectable Variation	Required Tracer Concentration in Stored CO ₂ (cm ³ /cm ³ CO ₂ , STP)	Required Tracer Per 10 ⁶ m ³ CO ₂ (liters, STP)	Tracer Cost (\$US/l)	Tracer Cost/Metric Ton CO ₂ (\$US)	Required Tracer Per Year (liters, STP)
³ He	7.2E-12	300%	2.17E-09	2.2	\$100	\$0.40	1532
²² Ne	1.7E-06	0.1%	1.68E-07	168	\$50	\$15.67	118629
³⁶ Ar	3.2E-05	0.1%	3.16E-06	3161	\$1,000	\$5,904	2234515
¹²⁴ Xe	8.7E-11	0.2%	1.75E-11	0.02	\$20,000	\$0.65	12
¹²⁹ Xe	2.5E-08	0.05%	1.25E-09	1.2	\$1,000	\$2.33	883
¹³⁶ Xe	8.7E-09	0.10%	8.70E-10	0.9	\$300	\$0.49	615
SF ₆	1.0E-11	1000%	1.00E-08	10	\$1	\$0.02	7070
¹⁴ C	1.0E-14	300%	3.00E-12	0.003	\$5,000	\$0.03	2

Table 1. Comparison of different tracers used to detect CO₂ leakage (Nimz & Hudson, 2005).

2.7 Relevance of geochemical methods to fulfill the requirements of the european CCS directive

The European Directive on geological CO₂ storage (Directive 2009/31/EC, 2009), published in 2009, provides a regulatory framework for permanent storage (above 100 kilotonnes of CO₂) and gives details for the practical implementation and permitting of this storage. The Directive recognises that monitoring is essential in assessing whether (i) injected CO₂ is behaving as expected, (ii) whether any migration or leakage occurs, and (iii) whether any identified leakage is damaging the environment or human health. Among the monitoring tasks required by the European Directive, geochemical tools can be relevant for: (i) detecting significant irregularities (Article 13); (ii) detecting migration of CO₂ (Article 13); (iii) detecting leakage of CO₂ (Article 13); (iv) detecting significantly adverse effects on the surrounding environment, particularly drinking water; (v) assessing the effectiveness of any corrective measures; and (vi) updating the short and long term safety and integrity assessment of the storage complex. Geochemical data (mainly dissolution and mineralisation rates) are also included in the list of data collected for the characterisation and assessment of the potential storage complex and its surrounding area (Step I, Annex I). The data are needed to build a three-dimensional static geological earth model of the reservoir and its overburden (Step II, Annex I), and play a key role in assessing the reactive processes and the dissolution rate of CO₂ in water (Step III, Annex I). The characterisation of the storage dynamic behaviour implies a quantification of the trapping rates and an assessment of changes in formations fluid chemistry and subsequent reactions (pH change, mineral formation) (Step III.I, Annex I). A part of the risk assessment (III.III) also concerns the magnitude of leakage in identified leakage pathways (flux rates), and the displacement of formation fluids, as well as the new substances created by CO₂ storage. Consequently, geochemical monitoring methods are central to the monitoring plan (Annex II).

3. Relevant spatial use of geochemical methods in a CCS project

An integrated Measurement Monitoring and Verification (MMV) program must include technologies to track CO₂ through the entire CO₂ storage complex. Benson (2007) schematically describes the different monitoring targets of the bio- and geosphere, for both

offshore and onshore CO₂ storage sites (Figure 4): (i) reservoir rock, (ii) cap rock, (iii) well(s), (iv) overlying aquifers, (v) vadose zone, terrestrial and aquatic ecosystems, (vi) the surface and the atmosphere.

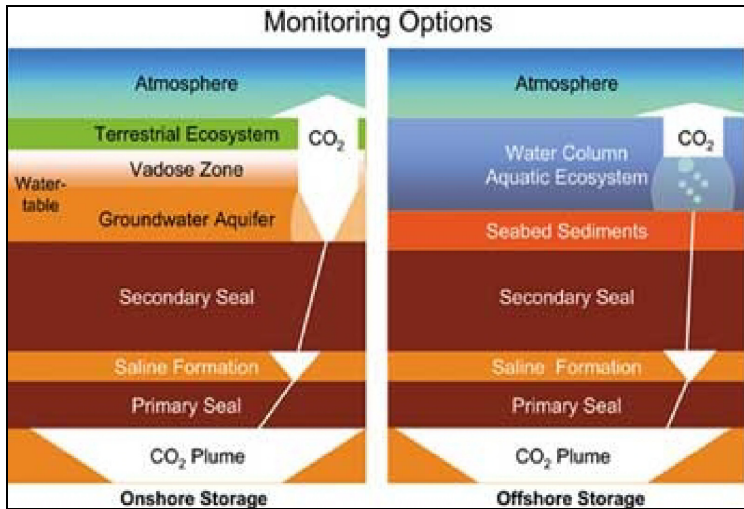


Fig. 4. Main monitoring targets of a CO₂ storage project in the bio- and geosphere (Benson , 2007).

Depending on targeted geological levels, an effective, fully integrated monitoring programme should be implemented, for operational, verification and environmental purposes (Figure 5).

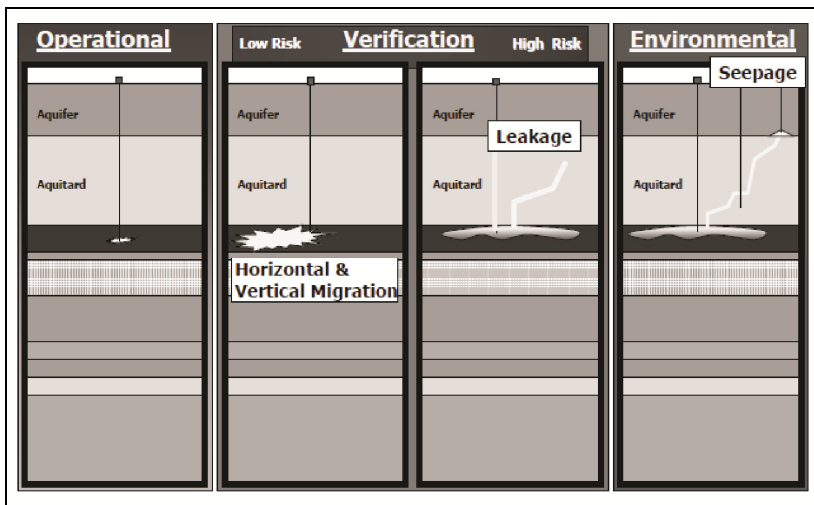


Fig. 5. Monitoring objectives, as a function of the monitored geosphere targets (Chalaturnyk & Gunter, 2005).

3.1 Reservoir monitoring

Produced down-hole fluids sampling and analysis are the main geochemical methods focusing on the CO₂ reservoir. Sampling systems like U-Tube (Freifeld et al., 2005) are of great value in obtaining minimally altered samples of subsurface fluids, preserved from formation contamination and degassing. Different analyses can be performed on the sampled fluid: aqueous chemistry, dissolved gas chemistry, isotopic composition, etc. For instance, geochemical reservoir monitoring of the IEA GHG Weyburn-Midale EOR field (Saskatchewan, Canada) showed that these data are particularly helpful in identifying and quantifying CO₂/fluid/rock interactions, like the dissolution of carbonate minerals and the production of alkalinity (Emberley et al., 2005) (Figure 6).

3.2 Cap rock integrity monitoring

The integrity of long-term cap rock sealing is a critical issue in guaranteeing and demonstrating efficiency, safety and security of CO₂ storage. The following different mechanisms for the loss of cap rock integrity have been identified: (i) reactivated faults in the cap rock: local pressure near a fault during injection reduces effective normal stress and thus reduces the shear strength of the fault; (ii) induced shear failure of cap rock; (iii) hydraulic fracture (prior to injection and during injection); (iv) exceeded capillary membrane seal pressure; and (v) dissolved CO₂ diffusion through cap rock (Shukla et al., 2010). Such processes can lead to concomitant geochemical alteration and geomechanical deformation of the cap rock, as well as to a modification of crucial petrophysical parameters such as porosity and permeability, which play a key role in sealing capacity (Johnson et al., 2004). Both static (batch) and dynamic (flow-through) experiments that permit the reproduction of reservoir conditions (P, T, brine salinity, chemistry, and flow rates in the case of reactive percolation experiments) are performed to investigate the evolution of a fractured cap rock during leakage of CO₂-acidified brine. These experiments also study the geochemical reactivity of cap rocks exposed to CO₂-rich brine injection (Andreani et al., 2008, Ellis et al., 2011). Fluid chemistry (cation concentrations) is monitored during these experiments (which are also applied on reservoir rocks) to identify the dissolution/precipitation reactions occurring in the rock plug and to realize mass-balance calculations (Luquot and Gouze, 2009).

3.3 Well integrity monitoring

One of the main risks identified in geological CO₂ storage is the potential for CO₂ leakage through, or along wells. One of the reasons for the loss of well integrity is the degradation of cement and carbon steel casings through acid attack due to CO₂ dissolution in groundwater and the resulting significant pH decrease (Bachu & Bennion, 2009). Experiments with CO₂-brine-cement and CO₂-cement interactions bring solutions to the problems of understanding and quantifying reactions occurring in the near-well environment. Some authors note that a carbonate layer can be formed at the interface between the CO₂-rich brine and the cement, which forms a barrier to further cement degradation (Kutchko et al., 2007, 2008).

3.4 Overlying aquifer monitoring

In the case of leakage and/or seepage, deep CO₂ storage may potentially impact on the quality and availability of groundwater resources and thus create potential risks for human

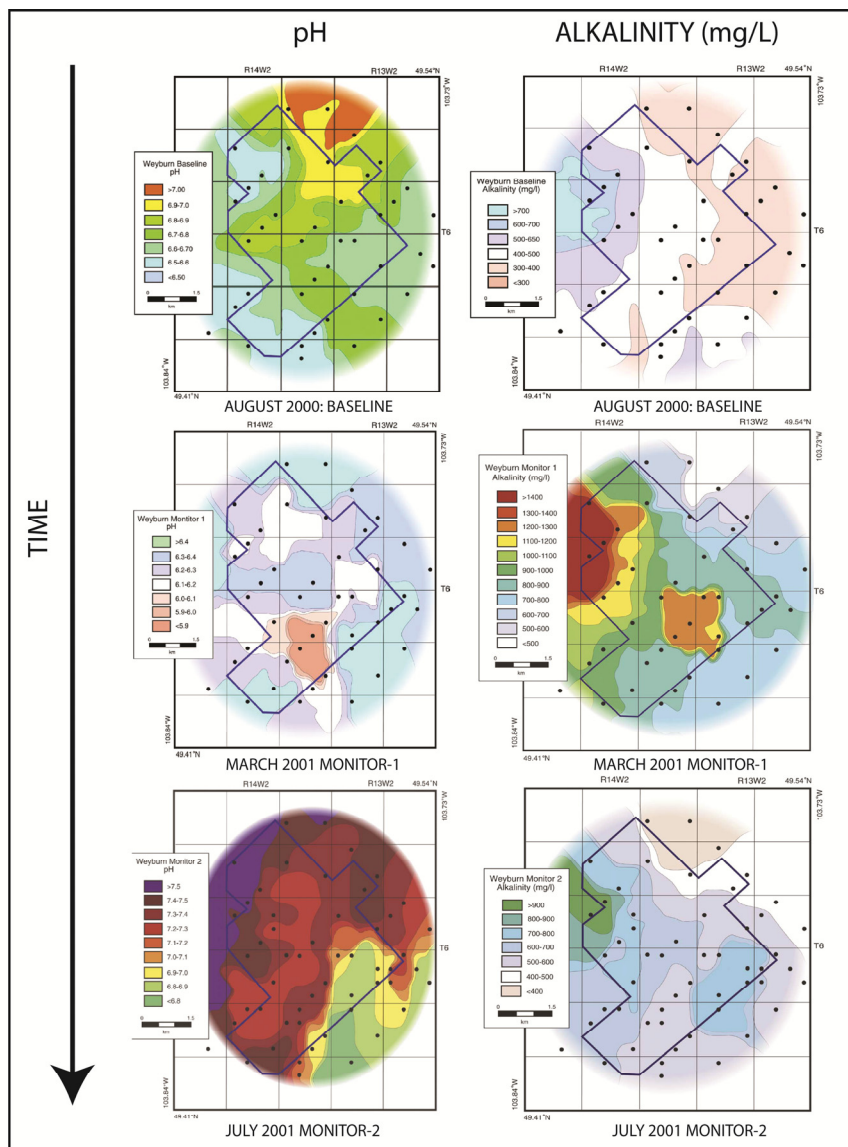


Fig. 6. pH and alkalinity monitoring at the Weyburn CO₂-injection enhanced oil recovery site, Saskatchewan, Canada (modified, after Emberley et al., 2005). AUGUST 2000: Baseline. MARCH 2001: MONITOR-1: the pH has decreased compared to the baseline (between 0.5 and 0.6). Absolute values of alkalinity have increased. JULY 2001: MONITOR-2: the pH has generally increased in comparison to the baseline and Monitor-1 data, indicating reaction with carbonate minerals in the reservoir. The alkalinity is higher than the baseline alkalinity, but has decreased in comparison to the Monitor-1 data, which also suggests a reaction with carbonate minerals in the reservoir.

health and ecosystems. The geochemical effects of CO₂ injection on water quality (for aquifers receiving the CO₂ injection and/or overlying and nearby aquifers that can contain drinking water) have been listed by Norton et al., 2009 as: (i) effects of physical displacement of groundwater by CO₂; (ii) effects of CO₂ injection on pH and alkalinity; (iii) effects of solution and mineral trapping; (iv) effects of CO₂ on soluble organic compounds; (v) effects of CO₂ injection on redox conditions; (vi) effects of CO₂ on microbial populations. Some geochemical clues are indicative of saline water migration into adjacent aquifers, such as an increase of TDS and alkalinity through reactions with host minerals and a possible increase in organic compounds. Furthermore, changes in the relative concentration of cations and anions in drinking water aquifers would occur, depending on the chemistry of the contaminating saline brines (notably through mixing and enrichment in Na-Cl and Na-Cl-SO₄). Saline water and CO₂ migration may also increase some common and trace metals concentrations (Al, Fe, Mn, As, Se, Zn), by leaching due to the pH decrease caused by elevated CO₂ partial pressures (Norton et al., 2009; Wang & Jaffe, 2004). This would depend on the redox conditions, or the buffering capacity of the host rock, that is closely linked to the abundance and type of minerals. Zheng et al. (2009) reported and modelled some secondary effects induced by pH changes. These include the significant mobilization of lead and arsenic, contaminating groundwater both near the CO₂ intrusion and further downstream. Laboratory experiments have also demonstrated that some geochemical parameters (pH, manganese, iron and calcium contents) can serve as early leakage indicators, because their concentrations increase within 2 weeks of exposure to CO₂ (Little and Jackson, 2010). Geochemical parameters can thus act as a warning for potential CO₂ leaks that might affect overlying aquifers.

3.5 The vadose zone and the terrestrial ecosystems

The vadose and soil zone is the final layer underground that could be affected by potential CO₂ leaks from deep reservoirs. Vadose and soil zone monitoring is particularly challenging because it requires the distinction between naturally occurring CO₂ and deep CO₂ leaks. CO₂ is naturally abundant and reactive in the near-surface, and as its concentrations are spatially and temporally variable. Its vulnerability reinforces the importance of soil gases monitoring to protect natural resources and to address landowner concerns. Oldenburg et al. (2003) described the different soil CO₂ sources and sinks, as: (1) exchange with the atmosphere; (2) production from decay of organic matter such as leaf litter; (3) uptake by plants; (4) production by root respiration; (5) deep degassing; (6) release from groundwater due to depressurization; and (7) production by oxidation of organic carbon in groundwater at the water table (Figure 7).

The measurement of natural “background” CO₂ concentrations for at least one year before CO₂ injection is paramount when determining the range of seasonal and diurnal CO₂ variations, which depend on soil temperature, moisture, and soil aeration, substrate quality and pH (Oldenburg et al., 2003). Leak detection is based on changes in soil gases concentration and on the isotopic composition of different CO₂ contributions. One proposed method for identifying deep CO₂ input is to predict gas relationships because an enrichment in deep CO₂ may result in the relative depletion of other existing gases such as CH₄, O₂, N₂ (Romanak et al., 2011). Furthermore, as explained in Yang (2011), carbon isotopes ($\delta^{13}\text{C}$ & $\delta^{14}\text{C}$) in soil gas have been particularly useful in detecting CO₂ leakage in recent years, since the $\delta^{13}\text{C}$ in the gas from fossil-fuel-driven sources is very different from the $\delta^{13}\text{C}$ in shallow soil gas, and $\delta^{14}\text{C}$ is basically absent in fossil CO₂ (Johnson et al., 2009; Klusmann, 2003, Van Alphen et al., 2009).

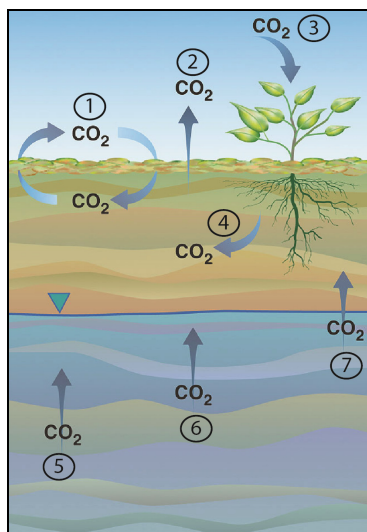


Fig. 7. Soil sources and sinks (modified, after Oldenburg et al., 2003). The significance of the number 1 to 7 is described in the text.

3.6 The aquatic ecosystems

Monitoring techniques for the detection of underwater CO₂ seepage have been recently and extensively developed in parallel with specific underwater methods to identify the CO₂ effects on the marine environment (Caramanna et al., 2005, 2010). These techniques have been notable in the framework of the CO₂GEONET and CO₂Remove projects. PH, dissolved CO₂ and CH₄ concentrations are key geochemical parameters to provide an assessment of water quality. According to Annunziatellis et al., (2009), the corrosive nature of seawater, the potentially high hydrostatic pressures, and the fact that these sites are likely to be isolated and far from the onshore infrastructures or power supplies explain why offshore monitoring is particularly challenging.

3.7 Surface and atmospheric monitoring

The earth's surface and atmosphere offer opportunities to measure gaseous CO₂ concentrations and fluxes; these measurements demonstrate the need for CO₂ to be stored with respect to the atmosphere. One of the most common techniques used for surface measurement is an Infrared Gas Analyser (IRGA) that can be installed on an accumulation chamber to measure CO₂ fluxes. IRGA can also be used with Eddy covariance towers to measure atmospheric CO₂ concentrations at specific heights above the ground, taking into account micrometeorological parameters such as wind speed, humidity and temperature (Oldenburg et al., 2003). Other techniques like Light Detection And Ranging (LIDAR), mobile open path lasers, Fourier Transform InfraRed (FT-IR) spectrometers, and micro gas-chromatographs have also been successfully tested in natural analogues (Gal et al., 2010; Jones et al., 2009; Pironon et al., 2009). However, it seems particularly important to combine the different techniques to increase the possibility of detecting significant anomalies.

Geochemical monitoring at Latera (Italy) by Jones et al. (2009) showed, for example, that some vents cannot be detected and measured by Eddy covariance tower at heights greater than 10 cm (Figure 8). This indicates that geochemical methods may only be able to sample and analyse at individual locations; very small leaks are particularly difficult to detect and larger leaks can also be missed. The detection capability will thus depend on the coincidence of the leaks and the location of sensors deployed in the area.

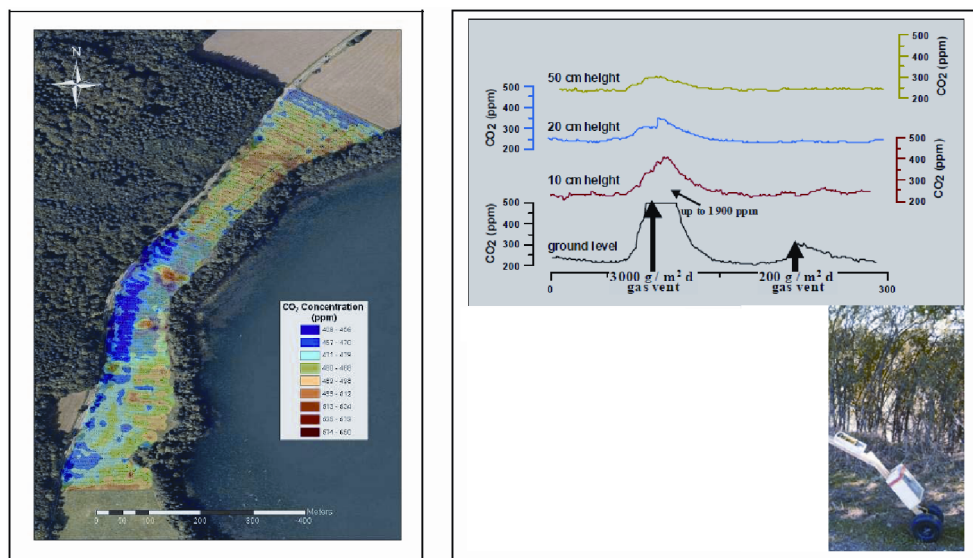


Fig. 8. Ground surface CO₂ concentrations at Latera, obtained using an IRGA measurement system. The weaker CO₂ vent is not seen at heights greater than 10 cm (Jones et al., 2009).

A baseline for soil gas values for CH₄, N₂, O₂, light hydrocarbons, sulphur species, helium, uranium, thorium and radon can also be established by using grid sampling and profiling. This can be used to evaluate natural variations, including seasonal effects. The comparison of the baseline dataset with a dataset obtained after CO₂ injection allows for the identification of anomalies with higher gas fluxes, that may indicate deep gas escape, and for the calculation of upward gas velocity. Such calculation has been performed at Weyburn using long term radon and helium measurements and CO₂ fluxes (Strutt et al., 2002). When CO₂ abundances in soils cannot be distinguished from the biological baseline and when the stable isotopic composition of carbon is insufficient to track CO₂ surface leaks, noble gases measurements can be used as powerful leak detectors and discriminators, as shown by Magnier et al. (2011) in the Buracica EOR-CO₂ field on-shore (Brazil).

4. Relevant use of geochemical methods during the lifetime of a CCS project

Schlumberger distinguishes different parts in a CO₂ storage injection workflow, as the pre-operation phase, the operation phase, and the post-operation phase (Figure 9).

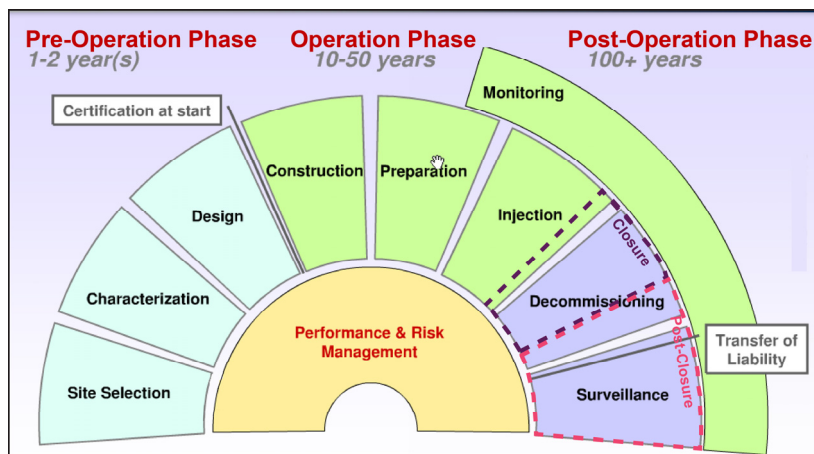


Fig. 9. Life cycle of a CCS project (Modified, after Marquette, 2010).

The pre-operation phase includes site characterization, risk assessment and the establishment of a monitoring baseline. The operation phase deals with verification of the injection rate, tracking the plume location, detection and prevention of any environmental impact. The post operation phase can be divided into two periods: the closure and the post closure. The closure phase implies the end of CO₂ injection, the decommissioning of the injection wells and surface facilities and the confirmation of the long-term storage security. The post closure phase aims to decommission the monitoring wells and complete the records given to regulatory authorities. Long term monitoring may only be needed if long term storage security is not established. During the following steps: (i) site selection and characterisation, as input data for the modelling, (ii) baseline and pre-injection period, (iii) injection period, (iv) post-injection period, (v) abandonment period (closure and post closure phases), geochemical tools can be integrated into the monitoring programmes and applied throughout the lifetime of the CCS project.

4.1 Site selection and characterization

The geochemical properties of the reservoir, the reservoir overburden (cap rock, seals, porous and permeable horizons) and surrounding formations (overlying aquifers) constitute some of the input data required to build both static and dynamic geological models. A simplified geochemical reactivity model is generally associated with building a detailed 2D or 3D fluid flow reservoir model, while a detailed description of the CO₂/fluid/rock interactions with complex mineralogical assemblages and reaction kinetics is required for batch modelling (Gaus et al., 2008). Even though many kinetic data and rate laws are described in the literature (Plummer et al., 1978; Lasaga et al., 1994), the complexity of the system makes it difficult to acquire accurate data. Moreover, kinetics vary widely depending on the minerals and their reactions. For example, the kinetics of aluminosilicates mineral reactions are for instance slower than dissolution kinetics of carbonates and sulphates. The physical and physicochemical properties (density, solubility, viscosity, enthalpy) of the CO₂-brine system are also integrated into the solute transport model. This is achieved via equations of state describing these properties and their P-T evolution (for example, the Equation Of State (EOS) given in Duan et al., 1992).

4.2 Baseline and pre-injection period

Baseline MMV aims to determine the initial hydrological, geochemical and environmental conditions prior to CO₂ injection. For geochemical methods, measuring the baseline consists of analysing fluid properties of the reservoir (fluid and gas compositions, pressures and temperatures), overlying potable aquifers (pH, elemental compositions of the fluid and dissolved gases, isotopic signatures). Soil gas (fluxes, chemical and isotopic fingerprint measurements) and ecosystems properties have also to be determined (Simone et al., 2009). The chemical and isotopic composition of the proposed injected CO₂ should also be measured prior to injection. Chemical analyses of samples must take place in a laboratory, and are labour intensive and time consuming. Therefore, measurements of background concentrations must be limited and cannot be taken from locations throughout the storage complex. A sampling strategy is generally defined, and focuses on high-risk features, such as structural lineaments, that are potential pathways for CO₂ migration and leakage. The monitoring installations can also be deployed along a systematic grid around the injection point. The reliability, resolution, and repeatability of each measurement are key to establishing a high-quality baseline database, which is paramount for detecting and quantifying small rates of leakage. Furthermore, it appears that one year of baseline acquisition is generally not sufficient to capture the full seasonal and annual variation of the natural release of CO₂ from soil. Thus, in every instance, special attention should be paid to baseline acquisition.

4.3 Injection period

After injection has begun, monitoring surveys are repeated at specified time intervals to build up images of site properties and to establish how the geochemical parameters change through time. Hovorka et al. (2005) reported that geochemical monitoring was particularly successful one year after the 2004 injection of 1,600 tons of CO₂ at the Frio field test (Texas). Noteworthy success was achieved in following the evolution of the CO₂ plume, detecting CO₂ breakthrough at the observation well, identifying CO₂/fluid/rocks interactions (a significant pH drop, an increase in alkalinity, dissolved Fe, Mg and Ca contents, indicated dissolution reactions) and quantifying CO₂ saturation and dissolution. Two-phase fluid samples were also obtained during CO₂ injection using a U-Tube. The mobilization of minor amounts of organic compounds was also revealed by an increase in dissolved organic contents concentrations in brine, 20 days after injection.

4.4 Post-injection period

After CO₂ injection is finished, reservoir, groundwater, soil gas, and atmospheric monitoring surveys, continuous or intermittent, should be continued for verification and environmental monitoring and to develop the understanding of long term CO₂ behaviour. For example monitoring results from the Japanese pilot CO₂ injection site of Nagaoka, into which 10,400 tons of CO₂ was injected from July 2003 to January 2005, indicate that solubility and residual trapping are in progress in the reservoir sandstone (Mito & Xue, 2011). Similarly, for the CO₂ CRC Otway project (Australia), geochemical sampling at the Naylor-1 observation well has shown that injected gas migrated into the Naylor structure, as predicted in numerical simulations (Underschultz et al., 2009). Geochemical data obtained during the post-injection period will help to calibrate and update the dynamic model in an

iterative manner, and to calculate the reservoir's trapping mechanisms over time. The observed and predicted results will be compared and any discrepancies should be identified. In case of significant deviation, the model would be recalibrated based on the observed behaviour.

4.5 Abandonment period

The monitoring data obtained during the post-closure period, which can last for decades, should prove that stored CO₂ behaves as predicted. The data should also demonstrate the absence of any detectable leaks. Evolution towards long term stability of the CO₂ plume is also required and is indicated by a small, and declining, rate of change in monitored parameters. Geochemical changes are key parameters for assessing the evolution towards long-term stability and for showing that CO₂ will remain stored within the complex through various trapping processes. All the measured geochemical parameters should be stable and consistent with the results of the CO₂/fluid/rocks interactions models, and should ensure that there is no significant risk of compromising cap rock and well integrity in the future. Geochemical methods play a key role in leakage detection and quantification and in assessing that no sources of drinking water are endangered. These methods can help to increase confidence in the long- term stability of the CO₂ storage complex.

5. Guidelines and recommendations for the integration of geochemical tools into a monitoring programme

5.1 Integration of geochemical data into monitoring programmes

The toolbox available for designing MMV programmes is particularly impressive and comprises geophysical (seismic and non-seismic, electrical), geomechanical, atmospheric, diagraphic, microbiological and geochemical methods. Methodological tools, like the "Monitoring Selection Tool" decision support system from IEA GHG, are particularly useful. The selection of an appropriate multi-disciplinary monitoring package for a particular CO₂ storage project depends on site-specific geological conditions as well as project objectives. The overall monitoring strategy may be improved by using tools of complementary sensitivity, spatial resolution and sampling characteristics, and by combining continuous and/or intermittent, local and/or extended measurements, based on various physical principles. A combined interpretation may lead to a better processes understanding. For instance, geophysical, geochemical monitoring and modelling R&D programmes have been successfully integrated in the IEA GHG Weyburn-Midale monitoring and storage project (Saskatchewan, Canada) (White & Johnson, 2009). According to the authors, the geochemical dataset provides a strong value-added history matching resource for reservoir simulation and reactive transport studies. In the Latera caldera (Italy), a natural analogue site, various geophysical tools were applied to track CO₂ migration from the storage complex and were combined with CO₂ flux measurements and soil gas sampling (Arts et al., 2009). The geochemical data confirmed and validated the geophysical results, reinforcing the conclusion that no single method is sufficient to clearly understand the processes driving CO₂ migration. Jones et al. (2009) have also shown that environmental monitoring can be optimised by combining the use of mobile open path laser measurements and ground surface IRGA measurements over a large area with more detailed

investigations, in order to verify CO₂ migration pathways and leakage extent. When seismic monitoring methods cannot be used for technical and economical reasons, geochemical monitoring can give insights into CO₂ saturation over time. Dissolved CO₂ is unlikely to be detected by any seismic method because of the low acoustic contrast between brine saturated with CO₂ and brine without CO₂. However, geochemical measurements, direct (total inorganic carbon, bicarbonate) and indirect (pH, alkalinity), can be particularly useful. They can also help to identify CO₂ and residual hydrocarbon contact for EOR applications. In fact, seismic monitoring methods are more appropriate for use in deep saline aquifer storage.

5.2 Identification of gaps and research & development perspectives

Future geochemical research into CO₂ storage must touch on different aspects, such as (i) modelling, (ii) experimental studies, (iii) investigations on organic chemistry and on secondary geochemical effects (redox, microbial reaction), (iv) technological development to improve data quality. As the co-injection of impurities (i.e. SO₂) can lead to extremely low pH (Knauss et al., 2005), experimental and modelling studies investigating their geochemical effects could be particularly useful. As pointed out by Gaus et al. (2008), the lack of basic thermodynamic and kinetic data at reservoir temperature and pressure conditions is also a major gap; this is particularly the case for CO₂-brine systems integrating co-injected gases (O₂, N₂, NO, SO₂, H₂S). Coupled reactive transport and geomechanical modelling remain challenging as well. Moreover, few experimental studies have been performed reproducing in situ conditions (P, T, salinity, flow rates). Flow-through experiments are particularly useful in assessing relationships between the chemical changes of the rock and fluids composition, and porosity and permeability evolution induced by mass transfers during percolation (Luquot & Gouze, 2009). Recently, isotopic monitoring has also been performed during flow-through experiments, consolidating the interpretation of cation concentrations evolution and allowing quantification of trapping (Jeandel et al., 2011; Myrtilinen et al., 2011). Emissions quantification technologies that measure dissolved CO₂ in the water column and free CO₂ at the surface, are in development, along with specific down-hole and seabed fluid sampling systems. These technologies will require further testing, especially in the marine environment, in which there is a gap in quantification and detection of CO₂. Guidelines for establishing sampling strategies (frequency, spacing, gridding, influence of the climate and meteorological regimes) would also be useful for the environmental monitoring of terrestrial ecosystems. More generally, permanently installed systems with fast-response sensors for monitoring pH, temperature, O₂ and CO₂ would counterbalance the fact that most geochemical measurements are intermittently performed. The coupling of geochemical and microbiological data could also be interesting in assessing the potential environmental CO₂ impact on both aquatic and terrestrial ecosystems.

6. Conclusion

Geochemical methods are extensively used for operational, verification and environmental monitoring because they can be applied to different monitoring targets that could be surveyed in the framework of a CO₂ geological storage project. They play a major role in providing information on fluid sources, which enable a unique identification of injected

CO₂, and on the physicochemical processes occurring within the storage complex. The migration of the CO₂ plume, as well as the distribution of the CO₂ phases (gas or dense versus dissolved), also represent key data that can be provided by geochemical measurements, which complement the other types of data. Geochemical methods provide essential input data for the calibration, validation and development of static and dynamic geological models for characterizing and predicting CO₂/fluid/rocks interaction. Moreover, they are important elements in the risk management process because they can identify the possible contamination of potable groundwater by toxic trace metals and/or organic compounds mobilized by the chemical interactions induced by CO₂ reactivity. Due to their high sensitivity, they also aim to directly detect any CO₂ leakage, which is crucial to ensure that stored CO₂ will be completely and permanently contained. Geochemical methods represent a significant step to improve public and regulatory confidence in geological storage of CO₂.

7. References

- Andreani, M.; Gouze, P.; Luquot, L. & Jouanna, P. (2008). Changes in seal capacity of fractured claystone cap rocks induced by dissolved and gaseous CO₂ seepage. *Geophysical Research Letters*, Vol.35, L14404, doi:10.1029/2008GL034467.
- Annunziatellis, A.; Beaubien, SE.; Ciotoli, G.; Finoia, M.G.; Graziani, S. & Lombardi, S. (2009). Development of an innovative marine monitoring system for CO₂ leaks: system design and testing. *Energy Procedia*, Vol.1, pp. 2333-2340.
- Arts, R. J.; Baradello, L.; Girard, J. F.; Kirby, G.; Lombardi, S.; Williamson, P. & Zaja, A. (2009). Results of geophysical monitoring over a "leaking" natural analogue site in Italy. *Energy Procedia*, Vol.1, No.1, pp. 2269-2276.
- Bachu, S. & Bennion, D.B. (2009). Experimental assessment of brine and/or CO₂ leakage through well cements at reservoir conditions. *International Journal of Greenhouse Gas Control*, Vol.3, No.4, July 2009, pp. 494-501, doi:10.1016/j.ijggc.2008.11.002.
- Ballentine, C. J. (1997). Resolving the mantle He/Ne and crustal ²¹Ne/²²Ne in well gases. *Earth and Planetary Science Letters*, Vol.152, No.1-4, pp. 233-249.
- Ballentine, C.J.; Schoell, M.; Coleman, D. & Cain, B.A. (2001). 300-Myr-old magmatic CO₂ in natural gas reservoirs of the west Texas Permian basin. *Nature*, Vol.409, pp. 327-331.
- Benson, S. M. (2007). Monitoring Geological Storage of Carbon Dioxide, Carbon Capture and Geologic Sequestration: Integrating Technology, Monitoring, and Regulation, Wilson, E.J. & Gerard, D., Blackwell Scientific Publishing, Ames, Iowa.
- Benson, S.M. & Cole, D.R. (2008). CO₂ Sequestration in Deep Sedimentary Formations. *Elements*, Vol.4, No.5, October 2008, pp. 325-331; DOI: 10.2113/gselements.4.5.325.
- Caramanna, G.; Volattorni, N.; Caramanna, L.; Cinti, D.; Galli, G.; Pizzino, L. & Quattrocchi, F. (2005). Scientific Diving Techniques applied to the geomorphological and geochemical study of some submarine gas vents (Aeolian Islands - Southern Tyrrhenian Sea - Italy). Diving for Science, *Proceeding of the American Academy of Underwater Sciences*, pp. 217-227, Groton, Connecticut, March 2005.
- Caramanna, G.; Espa, S. & Bouché, V. (2010). Study of the environmental effects of submarine CO₂- rich emissions by means of scientific diving techniques (Panarea Island -Italy). *International Journal of the society for Underwater Technology*, Vol.29, No.2, pp. 79-85.

- Chalaturnyk, R. & Gunter, W.D. (2005). Geological storage of CO₂: Time frames, monitoring and verification, *Proceedings of the 7th International Conference on Greenhouse Gas Control Technologies (GHGT-7)*, Vancouver, Canada, September 5–9, 2004.
- Directive 2009/31/EC of the European parliament and of the council of 23 April 2009 on the geological storage of carbon dioxide.
<http://eur-lex.europa.eu/LexUriServ/LexUriServ.do?uri=OJ:L:2009:140:0114:0135:EN:PDF>.
- Duan, Z.; Moller, N. & Weare, J.H. (1992). An equation of state for the CH₄-CO₂-H₂O system: 1. Pure systems from 08 to 1000 8C and 0 to 8000 bar. *Geochimica et Cosmochimica Acta*, Vol.56, pp. 2605–2617.
- Ellis, B.R.; Bromhal, G.S.; McIntyre, D.L. & Peters, C.A. (2011). Changes in cap rock integrity due to vertical migration of CO₂ -enriched brine. *Energy Procedia*, Vol.4, pp. 5327–5334.
- Emberley, S.; Hutcheon, I.; Shevalier, M.; Durocher, K.; Mayer, B.; Gunter, W.D. & Perkins, E.H. (2005). Monitoring of fluid–rock interaction and CO₂ storage through produced fluid sampling at the Weyburn CO₂-injection enhanced oil recovery site, Saskatchewan, Canada. *Applied Geochemistry*, Vol.20, pp. 1131–1157, doi:10.1016/j.apgeochem.2005.02.007.
- Fagerlund, F.; Tong, F.; Rasmusson, M.; Niemi, A.; Licha, T. & Sauter, M. (2011). Modelling of novel tracers in a two-phase flow system for characterization of geologically stored CO₂ in deep saline formations. *Proceeding of the European Geosciences Union (EGU), General Assembly*, May 3-8, 2011.
- Freifeld, B.M.; Trautz, R.C.; Kharaka, Y.K.; Phelps, T.J.; Myer, L.R.; & S.D. Hovorka (2005). The U-Tube: A Novel System for Acquiring Borehole Fluid Samples from a Deep Geologic CO₂ Sequestration Experiment. Lawrence Berkeley National Laboratory: Lawrence Berkeley National Laboratory. *LBNL Paper LBNL-57317*.
- Gal, F.; Le Pierres, K.; Brach, M.; Braibant, G.; Beny, C.; Battani, A.; Tocqué, E.; Benoît, Y.; Jeandel, E.; Pokryszka, Z.; Charmoille, A.; Bentivegna, G.; Pironon, J.; de Donato, P.; Garnier, C.; Cailteau, C.; Barrès, O.; Radilla, G. & Bauer, A. (2010). Surface Gas Geochemistry above the Natural CO₂ Reservoir of Montmiral (Drôme, France), Source Tracking and Gas Exchange between the Soil, Biosphere and Atmosphere. *Oil Gas Sci. Technol. – Rev. IFP*, Vol.65, No.4, pp. 635–652.
- Gaus, I.; Audigane, P.; André, L.; Lions, J.; Jacquemet, N.; Durst, P.; Czernichowski-Lauriol, I. & Azaroual A. (2008). Geochemical and solute transport modelling for CO₂ storage, what to expect from it? *International Journal of Greenhouse Gas Control*, Vol.2, pp. 605–625.
- Ghergut, I.; Bensabat, J.; Niemi, A.; Licha, T.; Nottebohm, M.; Schaffer, M. & Sauter, M. (2011). Single-well and inter-well tracer test design for CCS pilot site assessment (Heletz, Israel), *Proceedings of the 6th Trondheim CCS Conference (TCCS-6)*, June 14–16, 2011.
- Gilfillan, S.M.V.; Sherwood Lollar, B.; Holland, G.; Blagburn, D.; Stevens, S.; Schoell, M.; Cassidy, M.; Ding, Z.; Zhou, Z.; Lacrampe-Couloume, G. & Ballentine, C.J. (2009). Solubility trapping in formation water as dominant CO₂ sink in natural gas fields. *Nature*, Vol.458, No.7238, pp. 614–618.
- Gilfillan, S.M.V.; Ballentine, C.J.; Holland, G.; Blagburn, D.; Sherwood Lollar, B.; Stevens, S.; Schoell, M. & M. Cassidy, M. (2008). The noble gas geochemistry of natural CO₂

- gas reservoirs from the Colorado Plateau and Rocky Mountain provinces, USA. *Geochimica et Cosmochimica Acta*, Vol.72, No.4, pp. 1174-1198.
- Holloway, S.; Pearce, J.M.; Ohsumi, T. & Hards, V.L. (2005). A review of natural CO₂ occurrences and releases and their relevance to CO₂ storage. *British Geological Survey External Report*, CR/05/104, 117 pp.
- Hovorka, S.; Sakurai, S.; Kharaka, Y.; Nance, H.; Doughty, C.; Benson, S.; Freifeld, B.; Trautz, R.; Phelps, T. & Daley, T. (2005). Monitoring CO₂ Storage in Brine Formations: The Frio Field Test One Year Post Injection, *Proceedings of the 4th Annual Conference on Carbon Capture and Sequestration*, Alexandria, Virginia, May 2-5, 2005.
- IPCC (2005). *IPCC Special Report on Carbon Dioxide Capture and Storage*. Metz, B.; Davidson, O.; de Coninck, H.C.; Loos, M. & Meyer, L.A. (eds.), Cambridge University Press, Cambridge, United Kingdom and New York, NY, USA, 442 pp.
- Jeandel, E.; Dimier, A.; Myrtilinen, A.; Ukelis, O. & Zorn, R. (2011). Presentation of the new ICARE 4 set-up: principle and first results on the reactive-percolation experiments and modelling. *Proceeding of the European Geosciences Union (EGU), General Assembly*, May 3-8, 2011.
- Jeandel, E.; Battani, A. & P. Sarda (2010). Lessons learned from natural and industrial analogues for storage of carbon dioxide. *International Journal of Greenhouse Gas Control*, Vol.4, No. 6, pp. 890-909.
- Jenden, P.D.; Hilton, D.R.; Kaplan, I.R. & Craig, H. (1993). Abiogenic hydrocarbons and mantle helium in oil and gas fields, In: *The future of energy gases*, Howell, D.G. (eds.), U.S. Geological Survey Professional Paper 1570, Washington, D.C., U.S. Government Printing Office, pp. 31-56.
- Johnson, J.W.; Nitao, J.J. & Knauss, K.G. (2004). Reactive transport modeling of CO₂ storage in saline aquifers to elucidate fundamental processes, trapping mechanisms and sequestration partitioning, In: *Geological Storage of Carbon Dioxide*, Baines and Worden (eds.), Special Publication, Vol.233, pp. 107-128, Geological Society of London.
- Johnson, G.; Raistrick, M.; Mayer, B.; Shevalier, M.; Taylor, S.; Nightingale, M. & Hutcheon, I. (2009). The use of stable isotope measurements for monitoring and verification of CO₂ storage. *Energy Procedia*, Vol.1, pp. 2315-2322.
- Jones, D. G.; Barlow, T.; Beaubien, S. E.; Ciotoli, G.; Lister, T. R.; Lombardi, S.; May, F.; Möller, I.; Pearce, J. M. & Shaw, R. A. (2009). New and established techniques for surface gas monitoring at onshore CO₂ storage sites. *Energy Procedia*, Vol.1, No.1, pp. 2127-2134.
- Klusmann, R.W. (2003). A geochemical perspective and assessment of leakage potential for a mature carbon dioxide-enhanced oil recovery project and as a prototype for carbon dioxide sequestration; Rangely field, Colorado. *American Association of Petroleum Geologists Bulletin*, Vol.87, pp. 1485-1507.
- Knauss, K.G.; Johnson, J.W. & Steefel, C.I. (2005). Evaluation of the impact of CO₂ co-contaminant gas, aqueous fluid and reservoir rock interactions on the geologic sequestration of CO₂. *Chemical Geology*, Vol.217, pp. 339-350.
- Kutchko, B. G.; Strazisar, B. R.; Dzombak, D. A.; Lowry, G. V. & Thaulow, N. (2007). Degradation of well cement by CO₂ under geologic sequestration conditions. *Environmental Science & Technology*, Vol.41, No.12, pp. 4787-4792.

- Kutchko, B. G.; Strazisar, B. R.; Lowry, G. V.; Dzombak, D. A. & Thaulow, N. (2008). Rate of CO₂ attack on hydrated ClassHwell cement under geologic sequestration conditions. *Environmental Science & Technology*, Vol.42, No.16, pp. 6237–6242.
- Lafortune, S.; Moreira, M.; Agrinier, P.; Bonneville, A.; Schneider, H. & Catalette, H. (2009). Noble gases as tools for subsurface monitoring of CO₂ leakage. *Energy Procedia*, Vol.1, No.1, pp. 2185-2192.
- Lasaga, A.C.; Soler, J.M.; Ganor, J.; Burch, T.E. & Nagy, K.L. (1994). Chemical weathering rate laws and global geochemical cycles. *Geochimica et Cosmochimica Acta*, Vol.58, pp. 2361–2386.
- Little, M.G. & Jackson, R.B. (2010). Potential Impacts of Leakage from Deep CO₂ Geosequestration on Overlying Freshwater Aquifers. *Environmental Science & Technology*, Vol.44, No.23, pp 9225–9232.
- Luquot, L. & Gouze, P. (2009). Experimental determination of porosity and permeability changes induced by massive injection of CO₂ into carbonate reservoirs. *Chemical Geology*, Vol.265, No.1-2, pp. 148-159.
- Magnier, C.; Rouchon, V.; Bandeira, C.; Goncalves, R.; Miller, D. & Dino, R. (2011). Surface and Subsurface Geochemical Monitoring of an EOR-CO₂ Field: Buracica, Brazil. *Proceedings of the Goldschmidt Conference*, Prague, Czech Republic, August 14-19, 2011.
- Marquette, G. (2010). Monitoring and Verification of CO₂ Geological Storage Sites. *IEF-GCCSI Symposium on CCS*, 31st May, 2010.
- Martens, S.; Liebscher, A.; Möller, F.; Würdemann, H.; Schilling, F.; Kühn, M. and Ketzin Group (2011). Progress Report on the First European on-shore CO₂ Storage Site at Ketzin (Germany) – Second Year of Injection. *Energy Procedia*, Vol.4, pp. 3246–3253.
- Mayer, B.; Johnson, G.; Shevalier, M.; Nightingale, M. & Hutcheon, I. (2011). Accounting for Injected CO₂ at the Pembina Cardium CO₂ Monitoring Project, Alberta, Canada. *Proceeding of the European Geosciences Union (EGU), General Assembly*, May 3-8, 2011.
- Mito, S. & Xue, Z. (2011). Post-Injection Monitoring of Stored CO₂ at the Nagaoka Pilot Site: 5 Years Time-Lapse Well Logging Results. *Energy Procedia*, Vol.4, pp. 3284-3289.
- Myrtilinen, A.; Becker, V.; van Geldern, R.; Würdemann, H.; Morozova, D.; Taubald, H.; Blum, P. & Barth, J.A.C. (2010). Carbon and Oxygen isotope indications 1 for CO₂ behavior after injection: first results from the Ketzin Site. *International Journal of Greenhouse Gas Control*, Vol.4, Nr.6, pp. 1000-1006.
- Myrtilinen, A.; Jeandel, E.; Ukelis, O.; Dimier, A.; Becker, V.; Van Geldern, R. & Barth, J.A.C. (2011). Geochemical monitoring of reactive percolation experiments using carbon stable isotopes. *Proceedings of the Goldschmidt Conference*, Prague, Czech Republic, August 14-19, 2011.
- Nimz, G.J. & Hudson, G.B. (2005). The use of noble gas isotopes for monitoring leakage of geologically stored CO₂. Carbon Dioxide Capture for Storage in Deep Geologic Formations – Results from the CO₂ Capture Project, In: *Geologic Storage of Carbon Dioxide with Monitoring and Verification*, Benson, S.M. Elsevier Science, London.
- Norton, J.; Petersen, C.; Berard, T.; Parker, T.K.; Eary, L.E.; Largey, J.; Duguid, A.; Lamei, A.; Roulet, C.; Mills, S.K.; Johnson, N.; Picard, G. & Couselan, M. (2009). Potential Groundwater Quality Impacts Resulting from Geologic Carbon Sequestration. ISBN: 978-1-60573-060-8.

- Oldenburg, C. M.; Lewicki, J.L. & Hepple, R.P. (2003). Near-Surface Monitoring Strategies for Geologic Carbon Dioxide Storage Verification. Berkeley, CA, USA., Earth Science Division, Ernesto Orlando Lawrence Berkeley National Laboratory, pp. 1-54.
- Pironon, J.; de Donato, Ph.; Barrés, O.; Garnier, Ch.; Cailteau, C.; Vinsot, A. & Radilla, G. (2009). On-line greenhouse gas detection from soils and rock formations. *Energy Procedia*, Vol.1, No.1, pp. 2375-2382.
- Plummer, L.N.; Parkhurst, D.L. & Wigley, T.M.L. (1978). The kinetics of calcite dissolution in CO₂-water systems at 5-60 C and 0.0-1.0 atm CO₂. *American Journal of Science*, Vol.278, pp. 176-216.
- Pruess, K.; Freifield, B.; Kennedy, M.; Oldenburg, C.; Phelps, T.J. & van Soest, M.C. (2005). Use of gas phase tracers for monitoring CO₂ injection at the Frio Test Site, *Proceedings of the National Energy Technology Laboratory Fourth Annual Conference on Carbon Capture and Sequestration*, Alexandria, Virginia, May 2-5, 2005.
- Raistrick, M.; Mayer, B.; Shevalier, M.; Perez, R.J.; Hutcheon, I.; Perkins, E. & Gunter, B. (2006). Using chemical and isotopic data to quantify ionic trapping of injected carbon dioxide in oil field brines, *Environmental Science & Technology*, Vol.40, No.21, pp. 6744-6749.
- Romanak, K.; Bennett, P.; Yang, C. & Hovorka, S. (2011). New Approach to Soil Gas Monitoring, *Proceedings of the 6th Trondheim CCS Conference*, Trondheim, Norway, June 14-16, 2011.
- Shukla, R., Ranjith, P., Haque, A. & Choi, X. (2010). A review of studies on CO₂ sequestration and cap rock integrity. *Fuel*, Vol.89, No.10, pp. 2651-2664.
- Simone, A.; Mackie, E. & Jenvey, N. (2009). CO₂ Geological Storage Field Development - Application of Baseline, Monitoring and Verification Technology. *Energy Procedia*, Vol.1, pp. 2219-2226.
- Sherwood Lollar, B.; Ballentine, C. J. & O'Nions, R.K. (1997). The fate of mantle-derived carbon in a continental sedimentary basin: Integration of C/He relationships and stable isotope signatures. *Geochimica et Cosmochimica Acta*, Vol.61, No.11, pp. 2295-2308.
- Sherwood Lollar, B.; O'Nions, R.K. & Ballentine, C.J. (1994). Helium and neon isotope systematics in carbon dioxide-rich and hydrocarbon-rich gas reservoirs. *Geochimica et Cosmochimica Acta*, Vol. 58, No. 23, pp. 5279.
- Stalker, L.; Boreham, C. & Perkins, E. (2009a). A Review of Tracers in Monitoring CO₂ Breakthrough: Properties, Uses, Case Studies, and Novel Tracers. *American Association of Petroleum Geologists Special Volumes*, pp. 595-608.
- Stalker, L.; Boreham, C.; Underschultz, J.; Freifeld, B.; Perkins, E.; Schacht, U. & Sharma, S. (2009b). Geochemical monitoring at the CO₂CRC Otway Project: tracer injection and reservoir fluid acquisition. *Energy Procedia*, Vol.1, pp. 2119-2125.
- Strutt, M.H.; Beaubien, S.E.; Baubron, J.C.; Brach, M.; Cardellini, C.; Granieri, R.; Jones, D.G.; Lombardi, S.; Penner, L.; Quattrocchi, F. & Voltatoni, N. (2002) - Soil gas as a monitoring tool of deep geological sequestration of carbon dioxide: preliminary results from the Encana EOR project in Weyburn, Saskatchewan (Canada). *Proceedings of the 6th International Conference on Greenhouse Gas Control Technologies (GHGT-6)*, Vol. I, Gale, J. and Kaya, Y. (Eds), p. 391-396, Kyoto, Japan, Oct. 1st-4th 2002, Elsevier Science Ltd.

- Underschultz, J.R.; Freifeld, B.; Boreham, C.; Stalker, L. & Kirste, D. (2009). Geochemical and hydrogeological monitoring and verification of carbon storage in a depleted gas reservoir: examples from the Otway Project, Australia, *Proceedings of the SPE Hedberg Conference*, Vancouver, Canada, August 16-19, 2009.
- Van Alphen, K.; Hekkert, M.P. & Turkenburg, W.C. (2009). Comparing the development and deployment of carbon capture and storage technologies in Norway, the Netherlands, Australia, Canada and the United States – An innovation system perspective. *Energy Procedia*, Vol.1, pp. 4591–4599.
- Wang, S. & Jaffe, P.R. (2004). Dissolution of a mineral phase in potable aquifers due to CO₂ releases from deep formations: effect of dissolution kinetics. *Energy Conversion and Management*, Vol.45, No.18-19, pp. 2833-2848.
- White, D.J. & Johnson, J.W. (2009). Integrated geophysical and geochemical research programs of the IEA GHG Weyburn-Midale CO₂ monitoring and storage project. *Energy Procedia*, Vol.1, pp. 2349–2356.
- Wycherley, H.; Fleet, A. & Shaw, H. (1999). Some observations on the origins of large volumes of carbon dioxide accumulations in sedimentary basins. *Marine and Petroleum Geology*, Vol.16, pp. 489–494.
- Yang, Y.M. (2011). Statistical Methods for Integrating Multiple CO₂ Leak Detection Techniques at Geologic Sequestration Sites. *Dissertations*. Paper 25. <http://repository.cmu.edu/dissertations/25>.
- Zheng, L.; Apps, J.A.; Zhang, Y.; Xu, T. & Birkholzer, J.T. (2009). On mobilization of lead and arsenic in groundwater in response to CO₂ leakage from deep geological storage. *Chemical Geology*, Vol.268, No.3-4, pp. 281-297, doi:10.1016/j.chemgeo.2009.09.007.
- Zimmer, M.; Erzinger, J.; Kujawa, C. & CO₂SINK Group (2009). *In situ* Down Hole Gas Measurements During Geological Storage of CO₂ at Ketzin, Germany. *Proceeding of the European Geosciences Union (EGU), General Assembly, 2009*.
- Zimmer, M.; Erzinger, J.; Kujawa, C. & CO₂-SINK Group (2011). The Gas Membrane Sensor (GMS): a new method for gas measurements in deep boreholes applied at the CO₂ SINK Site. *International Journal of Greenhouse Gas Control*.

Sm-Nd and Lu-Hf Isotope Geochemistry of the Himalayan High- and Ultrahigh-Pressure Eclogites, Kaghan Valley, Pakistan

Hafiz Ur Rehman et al.*

*Graduate School of Science and Engineering, Kagoshima University
Japan*

1. Introduction

Eclogites are generally considered as derived from basaltic or gabbroic rocks which have either been intensely metamorphosed during subduction-obduction related processes or, associated with continental crust and affected by major crustal thrusting. The advantage of petrological, geochemical, and geochronological study of eclogitic rocks is twofold. First, metabasic rocks are capable of preserving the original magmatic characteristics of igneous formations. Second, the study of eclogites enables us to appreciate the behaviour of isotopic tracers during high-grade metamorphism.

In this chapter we report Sm-Nd and Lu-Hf isotope compositions of whole rock and their constituent minerals (garnet, clinopyroxene, phengite, and epidote) from the Himalayan high-pressure (HP) and ultrahigh-pressure (UHP) eclogites which are exposed in the Kaghan Valley of Pakistan (Fig. 1). These eclogites were formed when the Indian Plate slab subducted beneath the Asian Plate to greater depths and experienced UHP metamorphism. The Kaghan Valley eclogites have been discussed previously by several authors (e.g. Greco et al., 1989; Pognante & Spencer, 1991; Tonarini et al., 1993; Spencer et al., 1995; Lombardo & Rolfo, 2000; O'Brien et al., 2001; Kaneko et al., 2003; Parrish et al., 2006; Rehman et al., 2008). Spencer et al. (1995) carried out geochemical work (major and trace elements and Sr isotope) on the Kaghan Valley whole rock eclogites. They interpreted based on their geochemical results that the protolith for these eclogites was the Permian Panjal Trap basalts. Similarly, Tonarini et al. (1993) reported an Sm-Nd isochron age of 49 and a Sm-Nd isochron age of 49 ± 6 Ma representing the eclogite facies event in the Himalayan region. They calculated the above age from a garnet-clinopyroxene pair. Spencer & Gebauer (1996) reported a U-Pb zircon SHRIMP age of 44 Ma for the eclogite facies event. In addition, Kaneko et al. (2003)

* Katsura Kobayashi², Tatsuki Tsujimori², Tsutomu Ota², Eizo Nakamura², Hiroshi Yamamoto¹, Yoshiyuki Kaneko³ and Tahseenullah Khan⁴

¹Graduate School of Science and Engineering, Kagoshima University, Japan

²The Pheasant Memorial Laboratory, Institute for Study of the Earth's Interior, Okayama University, Misasa, Tottori, Japan

³Department of Education, Meisei University, Hodokubo, Hino-shi, Tokyo, Japan

⁴Department of Earth and Environmental Sciences, Bahria University, Islamabad, Pakistan

reported 46 Ma as the peak time for the UHP event in the Himalayan region. Their result was based on the U-Pb age dating on the coesite-bearing zircon from felsic gneisses which surround the UHP eclogites in Kaghan Valley. Parrish et al. (2006) also reported similar age results deduced from the U-Pb zircon age dating. Recently, Wilke et al. (2010a) elaborated the multi-stage history of the Kaghan Valley eclogites based on the major and trace element geochemistry of the eclogites, and a U-Pb zircon and rutile geochronology from the felsic gneisses. Most of the above mentioned researchers and references therein elaborate the metamorphic history of the eclogites and surrounding felsic gneisses. However, (i) details on the protolith environment of these eclogites, (ii) fluids infiltration effects on these rocks during their subduction to mantle depths, and (iii) element mobility during eclogite facies and late-stage metamorphism remained unclear. To discuss the above problems we reinvestigated the Kaghan Valley eclogites by examining carefully petrological and textural features, and extending our work to multi-isotope (Sm-Nd and Lu-Hf) systematic. Our results enabled us to (i) differentiate between the types of eclogites, (ii) evaluate their source rock, and (iii) effect of fluid infiltration on these eclogites during subduction and later stages of exhumation. Our results provide significant evidence of isotopic disequilibrium during and after the eclogite facies metamorphism.

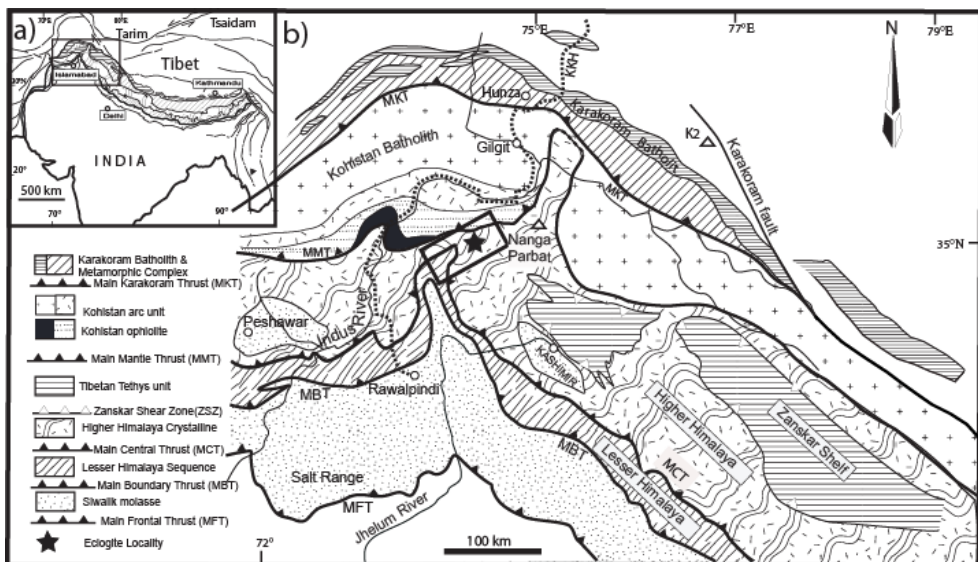


Fig. 1. (a) Geographical location of the Himalayan range. (b) An enlarged portion of the boxed area shown in the upper left, representing main tectonic units of the Indian Plate, the Kohistan arc, and the southern margin of the Asian Plate. Black star and a rectangle surrounding it represent location of the eclogites in the Kaghan Valley transect (see Fig. 2 for details).

2. Geological background

Eclogites of the Himalayan chain are the products of continental basaltic flows and their preceding feeder dikes of Permian to Lower Triassic Panjal Trap (e.g. Honegger et al., 1982;

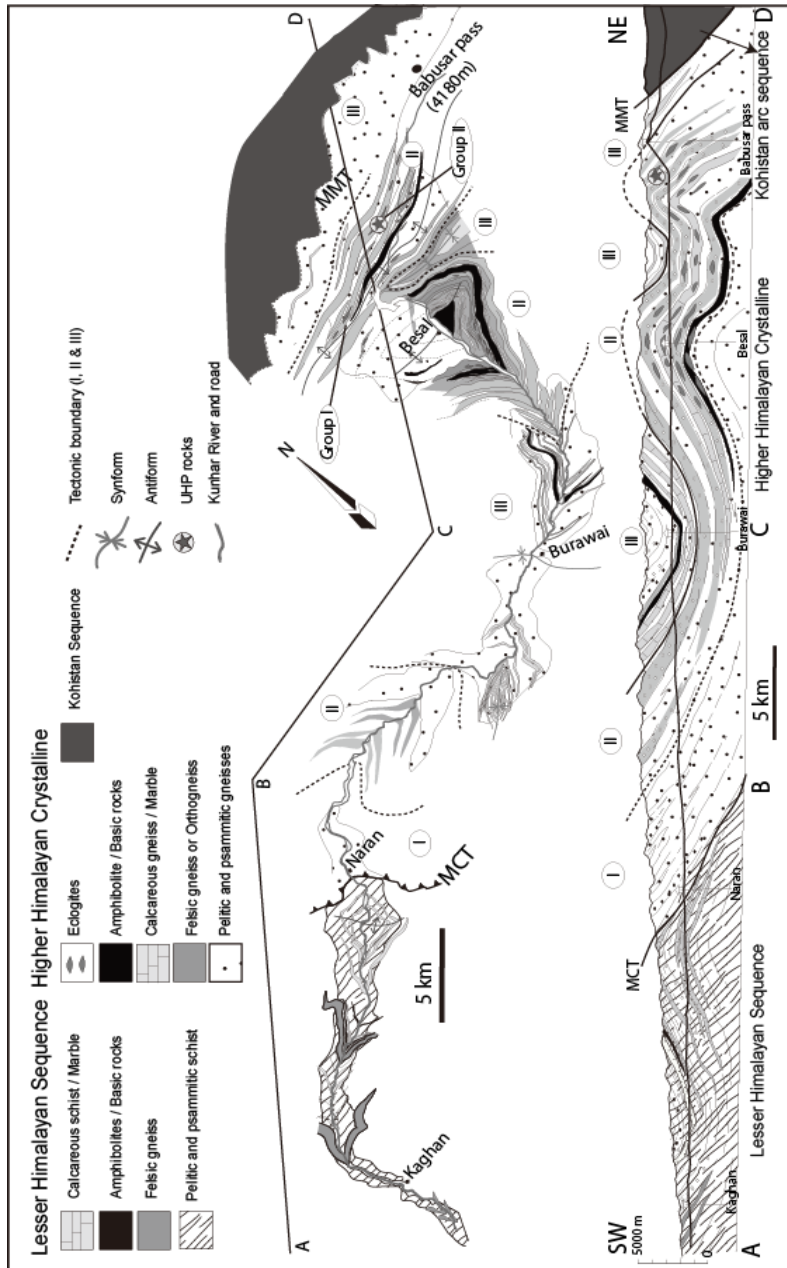


Fig. 2. A geological map with cross-section of the Himalayan metamorphic belt along the Kaghan Valley transect. Abbreviations used in map are; MCT: Main Central Thrust; MMT: Main Mantle Thrust (for further details on the rock types and structures, see Rehman et al., 2007, 2008). The map is modified after Kaneko et al. (2003).

Spencer et al., 1995). These basaltic extrusions at the northern margin of the Indian Plate mark start of the Himalayan cycle (Honegger et al., 1982). During the Himalayan cycle the volcanic activity began in the Upper Carboniferous, with the climax in Lower Permian, producing several hundred meters of intermediate to acid pyroclastic and welded tuffs overlying Carboniferous shales and shallow water limestone (Honegger et al., 1982). The onset of India-Asia collision ranging from 65 Ma to 40 Ma resulted in deep subduction of the Indian Plate beneath the Asian Plate (e.g. Patriat & Achache, 1984; Beck et al., 1995; Guillot et al., 2003). This subduction and related metamorphism resulted in a large-scale thrusting and piling up of the oceanic crust and sediments in the form of the Lesser Himalayan sequence, the Higher Himalayan crystalline and the Tethyan sediments as well as the ophiolitic mélanges along the suture zone between the Indian Plate and the Kohistan island arc (Greco et al., 1989; Spencer et al., 1995; Rehman et al., 2007) (Fig. 2).

In the Kaghan Valley transect a geological section is exposed which comprises the Lesser Himalayan sequence, the Higher Himalayan Crystalline, and the basement rocks of the Kohistan island arc (Fig. 2). Information on petrological, geochemical, and structural geology of the above sequences are explained in detail elsewhere (e.g. Rehman et al., 2007; 2008 and references therein). In this session, we will explain mafic rocks mainly. The mafic sheets exposed in the Higher Himalayan Crystalline in the Kaghan Valley, range in size from a few meters to few tens of meters within pelitic gneisses and marbles. Greenschist and amphibolite facies overprint on earlier eclogite facies assemblages. Coesite-bearing UHP eclogite is found as an isolated block (for locations see Rehman et al., 2007, 2008). The presence of coesite pseudomorphs in omphacite in eclogites, and in zircon from gneisses (Kaneko et al., 2003) indicate that these rocks reached a depth exceeding 100 km when the leading edge of the Indian Plate subducted beneath the Asian Plate.

3. Field occurrence and petrography of eclogites

Eclogites in the Kaghan Valley occur as massive and extend for a few tens of meters (Fig 3a, b) and as an isolated boudines or lenses 2 to 3 m in diameter (Fig. 3c, d). They are hosted by felsic gneisses, marbles and amphibolite sheets. These eclogites were subdivided into Group I and II (Fig. 4). Both groups of eclogites are differentiated from each other on the basis of occurrence, mineralogy, and geochemistry. Group I eclogites are composed of garnet, clinopyroxene, quartz, amphibole with rare epidote and phengite. They contain rutile, ilmenite, apatite, and abundant zircons as accessory minerals. Group II eclogites are composed of garnet, clinopyroxene, quartz/coesite, phengite, epidote, and amphibole with accessory rutile, ilmenite, apatite, and rare zircon.

Group I eclogites are HP and record pressure-temperature conditions at 704 ± 92 °C and 2.2 ± 0.3 GPa, whereas, Group II eclogites are UHP and recorded pressure-temperature conditions between 2.7 and 3.2 GPa and 757 and 786 °C respectively (Rehman et al., 2007).

Based on petrographic features and mineral inclusion study three apparent stages of metamorphism have been reported in the Himalayan eclogites of Kaghan Valley (Rehman et al., 2008). The first stage represented a prograde garnet growth stage (jadeite + quartz + albite inclusions in garnet core). The second stage represented peak UHP stage (deduced from the presence of coesite inclusion in clinopyroxene and pressure-temperature conditions estimated from the chemical composition of the rim portions of adjacent garnet, clinopyroxene and phengite). The third stage was a decompression/retrogressive stage

represented by the common occurrence of symplectitic augite, amphibole, and quartz after clinopyroxene. The third stage recorded texturally late-stage amphibolite facies overprint. Reaction textures and phase relations indicate that the metamorphic overprint was largely under hydrous conditions.

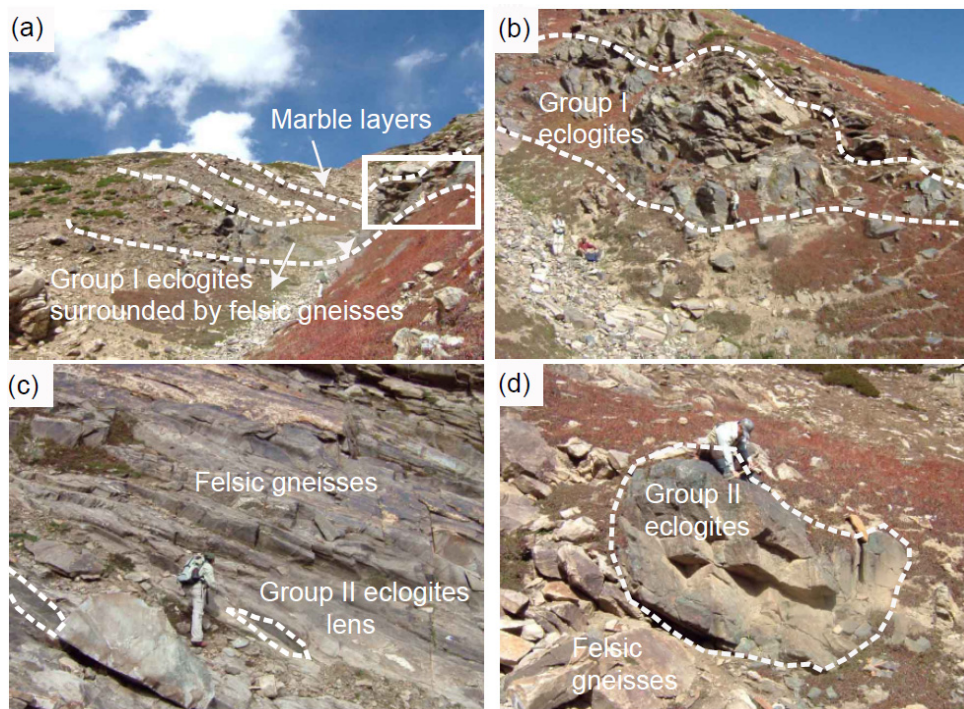


Fig. 3. Field photographs of eclogite types exposed in the Kaghan Valley. (a) Group I (massive) eclogite exposed in the northwest of Lulusar lake (for location see Fig. 4). (b) Closer view of the boxed area shown in the upper right in photograph on the left. (c) Group II (lens type) eclogite exposed in the northwest of Giti das (for location see Fig. 4). (d) Group II (boudine) eclogite exposed in the same gorge located northwest of Giti das (for location see Fig. 4).

4. Analytical methods

Geochemical analytical procedures were performed at the Pheasant Memorial Laboratory (PML), Institute for the Study of the Earth's Interior (ISEI), Okayama University at Misasa, Japan, following the procedures of Nakamura et al. (2003), Lu et al. (2007), and Makishima & Nakamura (2007). Basaltic standard (JB3) from the Geological Survey of Japan was used as a standard. Five eclogite samples (whole rock powders of two samples from the Group I and three samples from the Group II eclogites) and 15 mineral separates of the same five eclogite samples from both groups were decomposed and analyzed for their Sm-Nd and Lu-Hf isotopic ratios and abundances. Garnet and clinopyroxene separates from Group I and II eclogites and epidote and phengite from Group II eclogites were handpicked (Group I

did not contain phengite and epidote). To remove surface contamination, garnet and clinopyroxene were washed using ultrasonic bath, with 6 M HCl till the yellow color faded away, whereas epidote and phengite were washed with 2 M HCl for 30–40 minutes, and rinsed with distilled water few times. Then distilled water was added to all mineral separates and put for washing in an ultrasonic bath for overnight for complete removal of any contamination. After drying, the separated mineral fractions were further pulverized using agate mill and mortar. The powdered fractions were further leached with 0.1 N HCl till the yellow color faded away. Then rinsed with distilled water few times to remove any remaining contamination and dried at 70 °C. Powdered samples were decomposed in Teflon Bombs added with concentrated HF and HClO₄ at 245 °C for 4 days to get complete digestions. The solutions were then transferred to Teflon beakers, added with 0.1, 0.6 and 0.3 ml of HF, HClO₄ and HNO₃ respectively and put for agitation in ultrasonic bath for 8 hours to get complete homogenous solution. Fluoride residues produced by the initial acid attack were removed by repeated redissolution in HClO₄ following the procedures of Yokoyama et al. (1999).

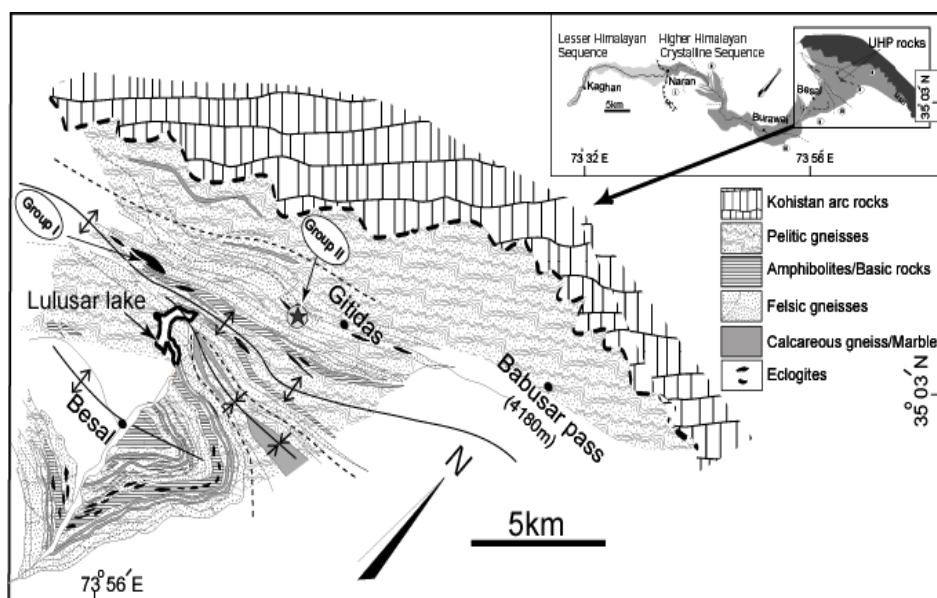


Fig. 4. Location of the Group I and II eclogites. The location map is zoomed area of the box shown on the upper right, which is a reduced/modified form of the geological transect map shown in Fig. 2 (modified from Kaneko et al., 2003; Rehman et al., 2007).

The analytical procedures for mass spectrometry following Yoshikawa & Nakamura (1993) for Nd isotopic ratios and abundances of Sm and Nd, employing Thermal Ionization Mass Spectrometer (TIMS: Finnigan MAT262) in static multi-collection mode. To determine the isotopic ratios and abundances of Sm and Nd, a fraction of decomposed sample solution was successively separated from each of the whole rock and separated minerals, using a multi-ion exchange column chemistry approach modified after Nakamura et al. (2003). In each sequence JB3 standard was decomposed which yields typical analytical reproducibility

of less than 0.005% Nd isotopic ratio, respectively, and < 1% for Sm and Nd abundances. Chemical separation procedures for Lu-Hf follow after Lu et al. (2007) using multi-ion exchange column chemistry. Lutetium was successively separated from the same solution as those used for Sm and Nd. Hf isotopic ratios, and Hf and Lu abundances were determined using multi-sector ICP-MS (Neptune) at the PML following the method of Makishima & Nakamura (2007). Accuracies of the isotopic ratio and element concentrations were confirmed by repeated measurement of JB3 standard solutions. Isotopic fractionation during analysis was corrected using $^{146}\text{Nd}/^{144}\text{Nd} = 0.7219$ as normalizing factors. Instrumental mass discrimination of TIMS analyses was corrected by the $^{143}\text{Nd}/^{143}\text{Nd}$ (La Jolla) values of standards (0.511874 ± 0.000020 , $n=10$). The Hf isotope ratios were normalized to JMC 475=0.282160. Total procedural blanks for digestion and column chemistry were < 12, < 2, < 2, and < 10 pg for Lu, Hf, Sm and Nd respectively; sample sizes were sufficiently large so that blanks were negligible and blank corrections were unnecessary, however, for Sm and Nd we used blank corrected values.

Values used for age calculations and initial isotope compositions are based on the decay constants $\lambda^{176}\text{Lu} = 1.865 \times 10^{-11} \text{ year}^{-1}$ (Scherer et al., 2001) and $\lambda^{147}\text{Sm} = 6.54 \times 10^{-12} \text{ year}^{-1}$ (Lugmair & Marti, 1978 and references therein). The chondritic uniform reservoir (CHUR) parameters used for calculating initial ϵHf and ϵNd values are $^{176}\text{Hf}/^{177}\text{Hf}=0.282818$ (White, 2011), $^{176}\text{Lu}/^{177}\text{Hf} = 0.0334$ and $^{143}\text{Nd}/^{144}\text{Nd}=0.512638$ recalculated using $^{146}\text{Nd}/^{144}\text{Nd} = 0.7219$ to correct for mass fractionation, and $^{147}\text{Sm}/^{144}\text{Nd} = 0.1967$ (Faure, 1986). Age calculations (Sm-Nd and Lu-Hf isochrones) were made using Isoplot 3.6 (Ludwig, 2009).

5. Results

Major and trace element compositions of the Himalayan Group I and II eclogites in the Kaghan Valley have been reported elsewhere (Rehman et al., 2008) in which all the eclogitic samples have basaltic compositions with 42 ~ 50 wt. % SiO_2 , and display tholeiitic differentiation trends. Group I eclogites are FeO-TiO₂ rich (FeO: 15 to 18 wt. %, and TiO₂: 2 to 5 wt. %), whereas Group II eclogites are comparatively less enriched in FeO and TiO₂. Present paper focuses on the Sm-Nd and Lu-Hf isotope compositions and in the following sections we will describe the isotopic results only.

5.1 Sm-Nd isotope geochemistry

The Sm-Nd isotopic compositions of five whole rock eclogite samples (2 samples from Group I and 3 samples from Group II eclogites) were determined (Table 1). In addition, we also determined the Sm-Nd compositions of 15 mineral separates (garnet, clinopyroxene, epidote and phengite) from the above mentioned five whole rock eclogites.

5.1.1 Group I eclogites

Sm and Nd contents, $^{147}\text{Sm}/^{144}\text{Nd}$ and $^{143}\text{Nd}/^{144}\text{Nd}$ ratios for the whole rock eclogites (Sample Ph380 and Ph381) and for garnet and clinopyroxene from the above two samples have been analysed. Results are plotted in Fig. 5 and are shown in Table 1.

In sample Ph380 the Nd contents are 4.69 ppm in garnet, 10.99 ppm in 41 clinopyroxene and 39.77 ppm in whole rock. Similarly the Sm contents are 3.93 ppm in garnet, 3.48 ppm in clinopyroxene and 10.85 ppm in whole rock.

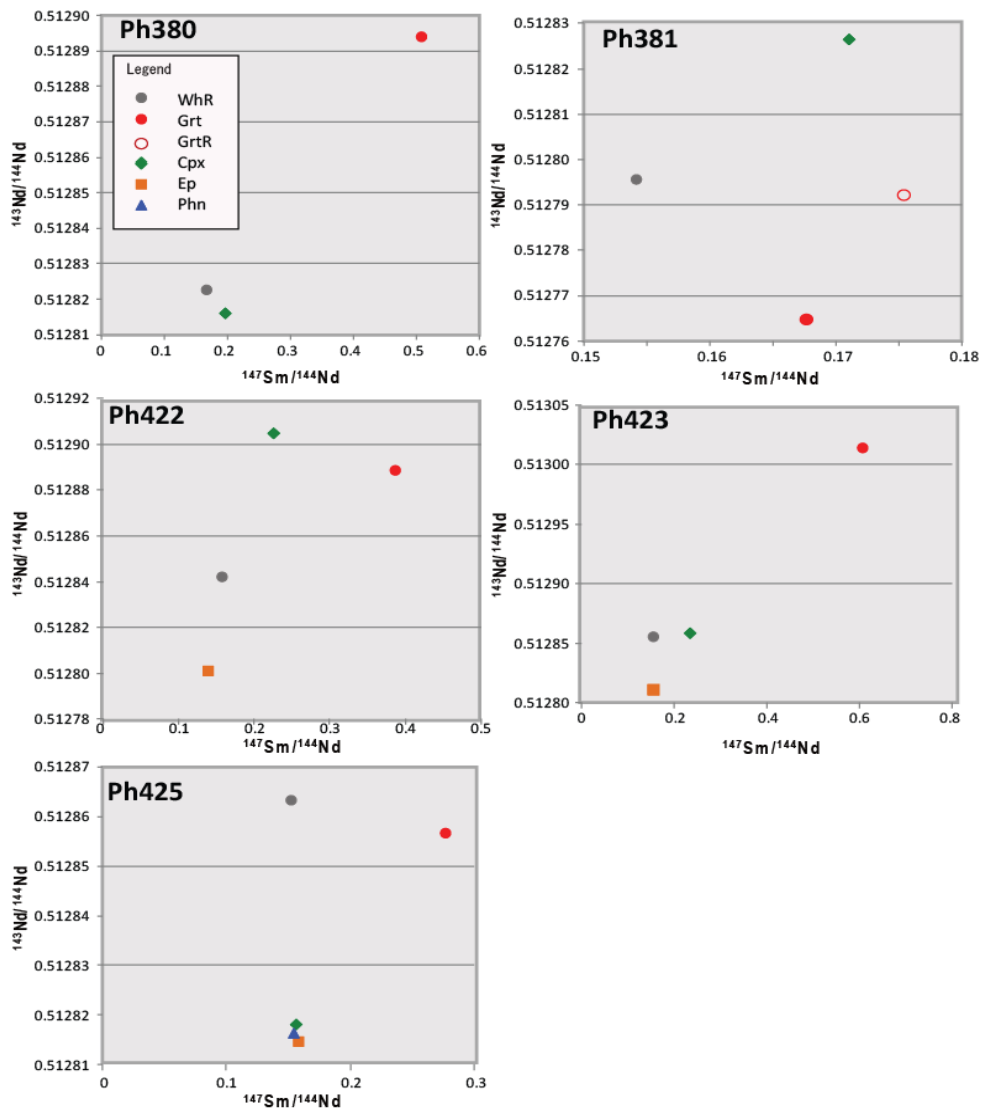


Fig. 5. $^{147}\text{Sm}/^{144}\text{Nd}$ versus $^{143}\text{Nd}/^{144}\text{Nd}$ diagrams for group I and II ecolites. Samples Ph380 and Ph381 represent Group I, whereas samples Ph422, Ph423, and Ph425 represent Group II ecolites. Abbreviations used are WhR: whole rock, Cpx: clinopyroxene, Ep: epidote, Grt: garnet, and Phn: phengite. GrtR is a repeat analysis of the same garnet fraction. Note the $^{147}\text{Sm}/^{144}\text{Nd}$ and $^{143}\text{Nd}/^{144}\text{Nd}$ ratios of garnet in sample Ph381, and in sample Ph422 which are lower than the ratios of clinopyroxene indicating isotopic disequilibrium for garnet.

The Nd contents in clinopyroxene have intermediate values between those of garnet and whole rock values however, the Sm contents in garnet and clinopyroxene are almost same. The resulting $^{147}\text{Sm}/^{144}\text{Nd}$ ratios vary from 0.1650 in whole rock to 0.1914 in clinopyroxene to 0.5077 in garnet, whereas the $^{143}\text{Nd}/^{144}\text{Nd}$ ratios range from 0.512816 in clinopyroxene to 0.512823 in whole rock to 0.512894 in garnet. Clinopyroxene and whole rock have somewhat similar $^{147}\text{Sm}/^{144}\text{Nd}$ and $^{143}\text{Nd}/^{144}\text{Nd}$ ratios however the $^{143}\text{Nd}/^{144}\text{Nd}$ ratios in clinopyroxene are slightly lower than those in whole rock (Fig. 5), and garnet has the highest $^{147}\text{Sm}/^{144}\text{Nd}$ and $^{143}\text{Nd}/^{144}\text{Nd}$ ratios. The isotopic data plot in a regression line with a positive slope. Although, three-point isochron cannot be calculated, however the garnet-clinopyroxene pair resulted in an isochron with age value of 37.9 ± 6.2 Ma (Fig. 6a).

In sample Ph381 the Nd contents are 12.18 ppm in garnet, 16.18 ppm in clinopyroxene and 73.79 ppm in whole rock. The Sm contents are 3.37 ppm in garnet, 4.58 ppm in clinopyroxene and 18.81 ppm in whole rock. In this sample also the Nd contents in clinopyroxene have intermediate values between those of garnet and whole rock values. The resulting $^{147}\text{Sm}/^{144}\text{Nd}$ ratios vary from 0.1542 in whole rock to 0.1711 in clinopyroxene to 0.1677 in garnet, whereas the $^{143}\text{Nd}/^{144}\text{Nd}$ ratios range from 0.512827 in clinopyroxene to 0.512796 in whole rock to 0.512765 in garnet (Fig. 5). Clinopyroxene has highest $^{147}\text{Sm}/^{144}\text{Nd}$ and $^{143}\text{Nd}/^{144}\text{Nd}$ ratios, whereas garnet has the highest $^{147}\text{Sm}/^{144}\text{Nd}$ ratios exhibits the lowest $^{143}\text{Nd}/^{144}\text{Nd}$ ratios. These results in a regression line with a negative slope, no isochron can be calculated among whole rock and mineral pairs. However, when we calculated all data points of Group I, an isochron or regression line with a 42 ± 29 Ma was constructed (Fig. 6b).

5.1.2 Group II eclogites

Similar to Group I eclogites we also analysed Sm and Nd contents, $^{147}\text{Sm}/^{144}\text{Nd}$ and $^{143}\text{Nd}/^{144}\text{Nd}$ ratios from the whole rock eclogites of Group II (Sample Ph422, Ph423, and Ph425) and their constituent minerals (garnet, clinopyroxene, phengite, and epidote). Results are plotted in Fig. 5 and are shown in Table 1.

In sample Ph422 the Nd contents are 1.49 ppm in garnet, 1.39 ppm in clinopyroxene, 2.26 in phengite and 19.88 ppm in whole rock. The Sm contents are 0.95 ppm in garnet, 0.52 ppm in clinopyroxene, 0.66 ppm in phengite and 5.19 ppm in whole rock. The Nd and Sm contents in epidote in this sample are extremely high i.e. Nd contents are 565 ppm and Sm contents are 129 ppm. The resulting $^{147}\text{Sm}/^{144}\text{Nd}$ ratios range from 0.1579 in whole rock to 0.2266 in clinopyroxene to 0.1761 in phengite to 0.3856 in garnet, whereas the $^{143}\text{Nd}/^{144}\text{Nd}$ ratios range from 0.512905 in clinopyroxene to 0.512843 in whole rock to 0.512801 in phengite to 0.512889 in garnet. In this sample also, garnet has lower $^{143}\text{Nd}/^{144}\text{Nd}$ ratios than clinopyroxene (Fig. 5) and results in a regression line with negative slope, thus no isochron can be defined.

In sample Ph423 the Nd contents are 0.51 ppm in garnet, 0.70 ppm in clinopyroxene and 16.87 ppm in whole rock. The Sm contents are 0.51 ppm in garnet, 0.27 ppm in clinopyroxene and 4.24 ppm in whole rock. The Nd and Sm contents in Epidote in this sample are also high i.e. Nd contents are 374 ppm and Sm contents are 95 ppm. The resulting $^{147}\text{Sm}/^{144}\text{Nd}$ ratios range from 0.1521 in whole rock to 0.2318 in clinopyroxene to

0.6045 in garnet, whereas the $^{143}\text{Nd}/^{144}\text{Nd}$ ratios range from 0.512859 in clinopyroxene to 0.512857 in whole rock to 0.513 in garnet. Whole rock, clinopyroxene and garnet show a large range in $^{147}\text{Sm}/^{144}\text{Nd}$ and $^{143}\text{Nd}/^{144}\text{Nd}$ ratios with garnet having the highest $^{147}\text{Sm}/^{144}\text{Nd}$ and $^{143}\text{Nd}/^{144}\text{Nd}$ ratios (Fig. 5). Three-point isochron yields no geological meaningful age. However the regression line drawn from the garnet-whole rock pair plots with a positive slope and gives an isochron of 53 ± 14 Ma.

Sample No.	$^{147}\text{Sm}/^{144}\text{Nd}$	$2\delta(\text{m})$	$^{143}\text{Nd}/^{144}\text{Nd}$	$2\delta(\text{m})$	Nd (ppm)	Sm (ppm)	Sm/Nd
Group I eclogites							
Ph380WhR	0.1650	0.0007	0.512823	6.33E-06	39.77	10.85	0.27
Ph380Grt	0.5077	0.0007	0.512894	9.72E-06	04.69	03.93	0.84
Ph380Cpx	0.1914	0.0014	0.512816	8.64E-06	10.99	03.48	0.32
Ph381WhR	0.1542	0.0005	0.512796	6.47E-06	73.79	18.81	0.25
Ph381Grt	0.1677	0.0019	0.512765	1.09E-05	12.17	03.37	0.28
Ph381Grtr	0.1754	0.0017	0.512792	8.35E-06	12.18	03.53	0.29
Ph381Cpx	0.1711	0.0007	0.512827	5.92E-06	16.18	04.58	0.28
Group II eclogites							
Ph422WhR	0.1579	0.0011	0.512843	7.93E-06	19.88	5.19	0.26
Ph422Grt	0.3856	0.0009	0.512889	7.80E-06	1.49	0.95	0.64
Ph422Cpx	0.2266	0.0008	0.512905	4.55E-05	1.39	0.52	0.37
Ph422Ep	0.1381	0.0006	0.512801	6.76E-06	565	129	0.23
Ph422Phn	0.1761	0.0011	0.512837	8.21E-06	2.26	0.66	0.29
Ph423WhR	0.1521	0.0010	0.512857	8.00E-06	16.87	4.24	0.25
Ph423Grt	0.6045	0.0005	0.513014	4.13E-05	0.51	0.51	1.00
Ph423Cpx	0.2318	0.0008	0.512859	2.38E-05	0.70	0.27	0.38
Ph423Ep	0.1542	0.0017	0.512812	8.88E-06	375	95	0.25
Ph425WhR	0.1522	0.0008	0.512863	7.08E-06	20.64	5.19	0.25
Ph425Grt	0.2780	0.0007	0.512857	1.41E-05	0.62	0.28	0.46
Ph425Cpx	0.1562	0.0009	0.512818	1.64E-05	1.27	0.33	0.26
Ph425Ep	0.1573	0.0008	0.512815	6.71E-06	156	41	0.26
Ph425Phn	0.1550	0.0006	0.512816	1.12E-05	7.37	1.89	0.26

Table 1. Sm-Nd concentrations and isotopic ratios of the whole rock Group I and II eclogites and their constituent minerals. Mineral abbreviations used in the table are same as shown in Fig. 5.

In sample Ph425 the Nd and Sm contents are in the same range as discussed above. The $^{147}\text{Sm}/^{144}\text{Nd}$ ratios range from 0.1522 in whole rock to 0.1562 in clinopyroxene to 0.1550 in phengite to 0.1573 in epidote to 0.2780 in garnet, whereas the $^{143}\text{Nd}/^{144}\text{Nd}$ ratios range from 0.512818 in clinopyroxene to 0.512863 in whole rock to 0.512816 in phengite to 0.512815 in epidote to 0.512857 in garnet (Fig. 5). A three-point isochron (garnet-clinopyroxene-phengite) can be defined with an age values of 50 ± 21 Ma (Fig. 6c). When we pooled all the Sm-Nd data for whole rock and minerals from both groups of eclogites for isochron calculation, we obtained an internal isochron of 51 ± 18 Ma (Fig. 6d).

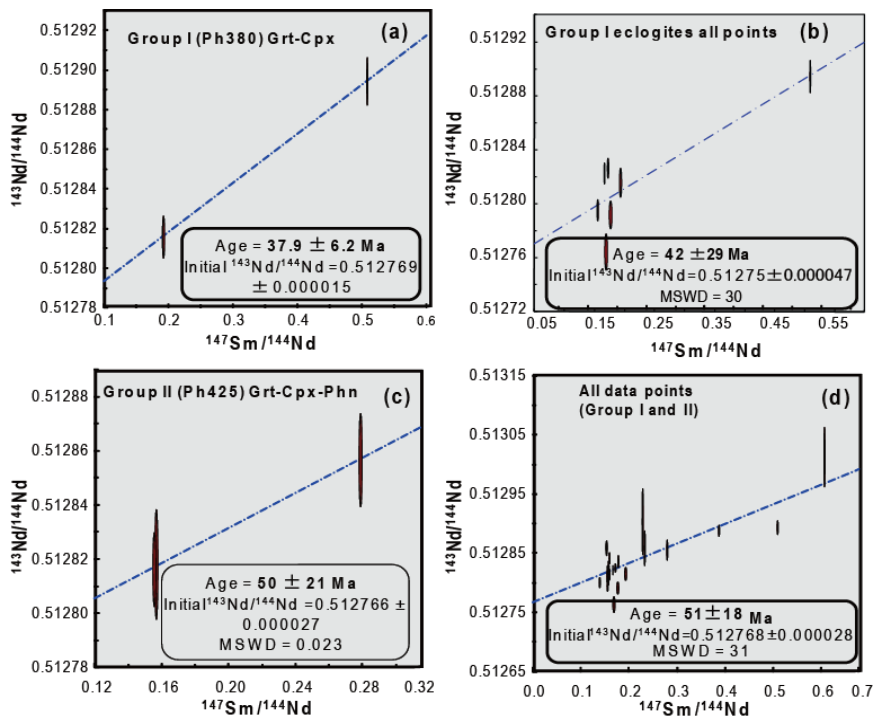


Fig. 6. Sm-Nd isochrones (mixing lines) for the Himalayan Group I and II eclogites. Plots a and b show data from Group I eclogites. Plot c shows three-point isochron from Group II eclogite (sample Ph425). Plot d shows combination of all data pooled as a single system. Data-point error ellipses are 2σ . Isochrones were calculated using Isoplot 3.6 (Ludwig, 2009).

5.2 Lu-Hf isotope geochemistry

The same five eclogitic whole rock samples and their constituent minerals (garnet, clinopyroxene and epidote) were analyzed for Lu and Hf contents, and $^{176}\text{Lu}/^{177}\text{Hf}$ and $^{176}\text{Hf}/^{177}\text{Hf}$ ratios (Table 2). Phengite was not analyzed because of its extremely low Hf concentrations. The whole rock samples and separated minerals show large variation in Lu and Hf concentration and Lu/Hf ratio for separated minerals (Table 2).

5.2.1 Group I eclogites

Lu and Hf contents, $^{176}\text{Lu}/^{177}\text{Hf}$ and $^{176}\text{Hf}/^{177}\text{Hf}$ ratios for the whole rock eclogites (Sample Ph380 and Ph381) and for garnet and clinopyroxene from the above two samples have been analysed. Results are plotted in Fig. 7 and are shown in Table 2.

Sample No.	$^{176}\text{Lu}/^{177}\text{Hf}$	$2\delta(\text{m})$	$^{176}\text{Hf}/^{177}\text{Hf}$ corrected	$2\delta(\text{m})$	Lu (ppm)	Hf (ppm)	Lu/Hf
Group I eclogites							
Ph380WhR	0.005532	2.8E-06	0.282844	4.69E-06	0.67	17.22	0.04
Ph380Grt	0.404834	2.0E-04	0.283273	1.22E-05	1.33	0.47	2.85
Ph380Cpx	0.004485	2.2E-06	0.282895	5.05E-06	0.06	1.90	0.03
Ph381WhR	0.008481	4.2E-06	0.282871	3.70E-06	0.78	13.13	0.06
Ph381Grt	0.095139	4.8E-05	0.282944	5.25E-06	1.93	2.89	0.67
Ph381Cpx	0.007200	3.6E-06	0.282908	6.35E-06	0.22	4.37	0.05
Ph381Cpxr	0.007055	3.5E-06	0.282898	3.38E-06	0.22	4.46	0.05
Group II eclogites							
Ph422WhR	0.011174	5.6E-06	0.282898	7.03E-06	0.28	3.52	0.08
Ph422Grt	0.024751	1.2E-05	0.282925	1.34E-05	0.67	3.82	0.17
Ph422Cpx	0.003276	1.6E-06	0.282902	6.64E-06	0.04	1.89	0.02
Ph422Ep	0.008019	4.0E-06	0.282847	1.68E-05	0.14	2.57	0.06
Ph423WhR	0.010787	5.4E-06	0.282900	8.96E-06	0.32	4.25	0.08
Ph423Grt	0.032721	1.6E-05	0.282917	5.30E-06	0.70	3.05	0.23
Ph423Cpx	0.002681	1.3E-06	0.282905	5.76E-06	0.04	1.94	0.02
Ph423Ep	0.030260	1.5E-05	0.282764	4.99E-05	0.12	0.58	0.21
Ph425WhR	0.010889	5.4E-06	0.282909	7.63E-06	0.33	4.27	0.08
Ph425Grt	0.035713	1.8E-05	0.282927	4.96E-06	0.72	2.86	0.25
Ph425Cpx	0.001502	7.5E-07	0.282900	6.21E-06	0.02	1.91	0.01
Ph425Ep	0.023419	1.2E-05	0.282970	3.51E-05	0.09	0.55	0.16

Table 2. Lu-Hf concentrations and isotopic ratios of the whole rock Group I and II eclogites and their constituent minerals. Mineral abbreviations are same as explained earlier.

In sample Ph380 the Lu and Hf contents range from 1.33 ppm in garnet, 0.06 ppm in clinopyroxene to 0.67 ppm in whole rock, respectively, and 0.47 ppm in garnet, 1.90 ppm in clinopyroxene to 17.22 ppm in whole rock, respectively. The resulting $^{176}\text{Lu}/^{177}\text{Hf}$ ratios vary from 0.005532 in whole rock to 0.004485 in clinopyroxene to 0.404834 in garnet, whereas the $^{176}\text{Hf}/^{177}\text{Hf}$ ratios range from 0.282895 in clinopyroxene to 0.282844 in whole rock to 0.283273 in garnet. The $^{176}\text{Lu}/^{177}\text{Hf}$ ratios in whole rock and clinopyroxene have almost same values however with different $^{176}\text{Hf}/^{177}\text{Hf}$ ratios as shown in Fig. 7 and it is difficult to have a three-point isochron for them. However, a two point mixing line (garnet-clinopyroxene) from this sample defines a slope of 50.6 ± 1.7 Ma (Fig. 8a).

In sample Ph381 the Lu and Hf contents range from 1.93 ppm in garnet, 0.22 ppm in clinopyroxene to 0.78 ppm in whole rock, respectively, and 2.89 ppm in garnet, 4.46 ppm in clinopyroxene to 13.13 ppm in whole rock, respectively. The resulting $^{176}\text{Lu}/^{177}\text{Hf}$ ratios are 0.008481 in whole rock, 0.0072 in clinopyroxene, and 0.095139 in garnet, whereas the

$^{176}\text{Hf}/^{177}\text{Hf}$ ratios are 0.282908 in clinopyroxene, 0.282871 in whole rock, and 0.282944 in garnet. Same pattern of the isotopic ratios were observed in this sample i.e. similar $^{176}\text{Lu}/^{177}\text{Hf}$ ratios in whole rock and clinopyroxene (even we repeated analysis for clinopyroxene) and lower $^{176}\text{Hf}/^{177}\text{Hf}$ ratios in whole rock and slightly higher in clinopyroxene (Fig. 7). Garnet from this sample with considerably high Lu/Hf ratio (> 2) yielded a two-point (garnet-whole rock) isochron of 45.3 ± 3.9 Ma (Fig. 8b). However, when data for three points (garnet-whole-rock-clinopyroxene) were used, no isochron was obtained.

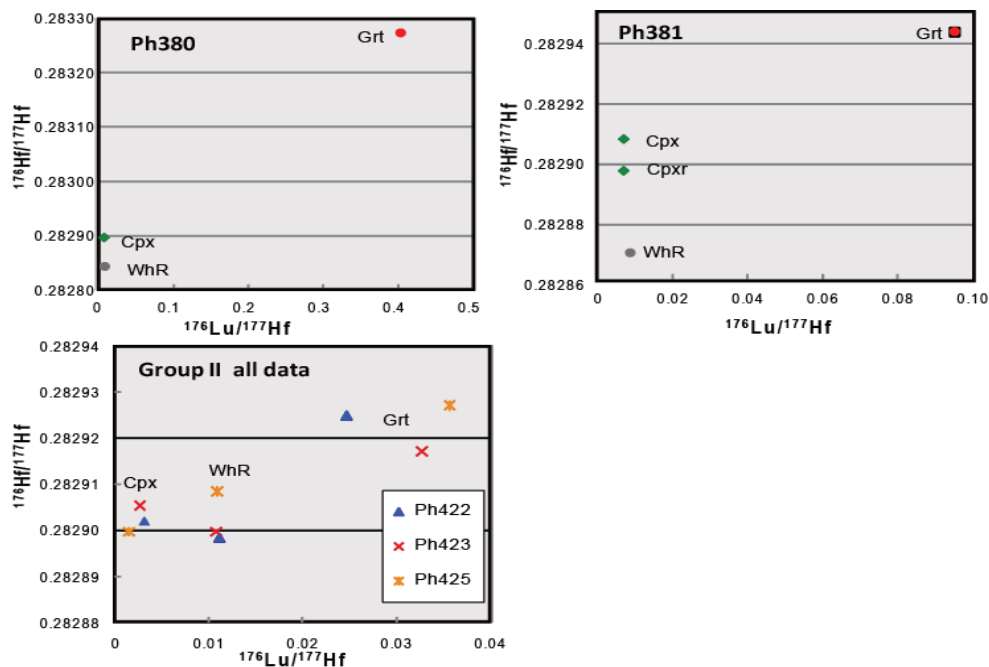


Fig. 7. $^{176}\text{Lu}/^{177}\text{Hf}$ versus $^{176}\text{Hf}/^{177}\text{Hf}$ diagrams for group I and II eclogites. Samples Ph380 and Ph381 represent Group I and the lower diagram represents a combined data from the three samples (Ph422, Ph423, and Ph425) of Group II eclogites. Abbreviations used are same as explained above.

5.2.2 Group II eclogites

In sample Ph422 the Lu and Hf contents range from 0.67 ppm in garnet, 0.04 ppm in clinopyroxene, 0.14 ppm in epidote to 0.28 ppm in whole rock, respectively, and 3.82 ppm in garnet, 1.89 ppm in clinopyroxene, 2.57 ppm in epidote to 3.52 ppm in whole rock, respectively. The resulting $^{176}\text{Lu}/^{177}\text{Hf}$ ratios are 0.011174 in whole rock, 0.003276 in clinopyroxene, 0.008019 in epidote, and 0.024751 in garnet, whereas the $^{176}\text{Hf}/^{177}\text{Hf}$ ratios are 0.282902 in clinopyroxene, 0.282898 in whole rock, 0.282847 in epidote, and 0.282925 in garnet.

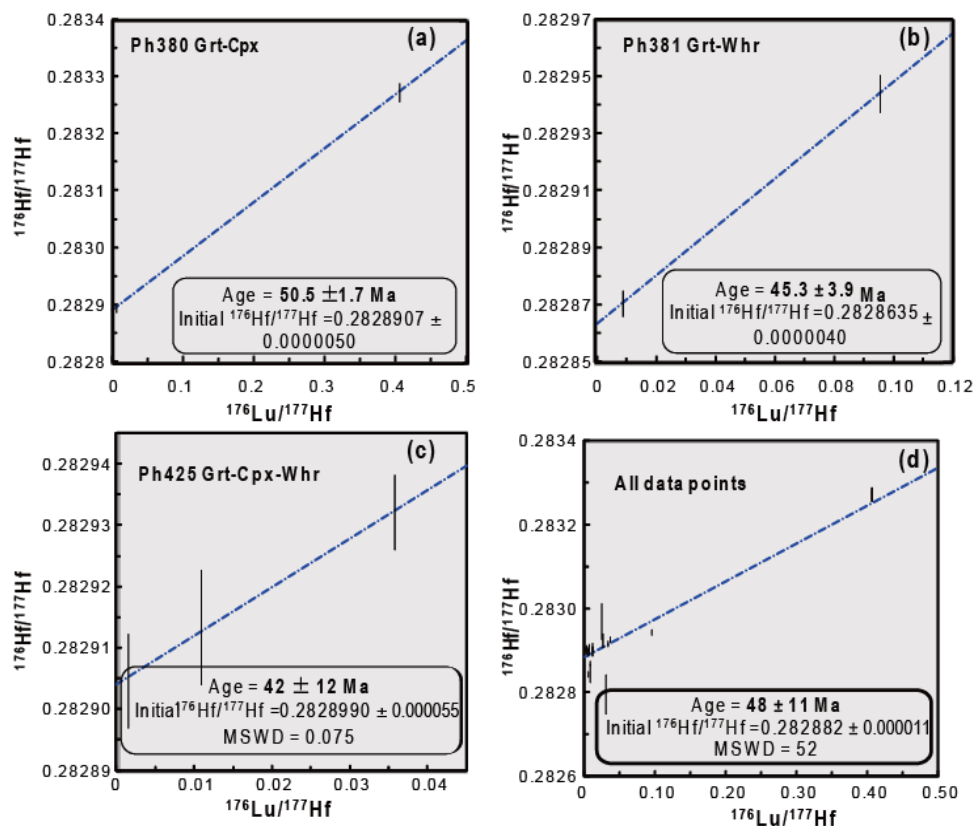


Fig. 8. Lu-Hf garnet-clinopyroxene (a), garnet-whole rock (b), and garnet-clinopyroxene-whole rock isochrones (c) for the Himalayan Group I and II eclogites. Plots a-b show data from Group I eclogites and plot c represents data from one sample in Group II eclogites. Plot d displays combined result for all data and yielded an internal isochron of 48 ± 11 Ma. Data-point error ellipses are 2σ . Isochrones were calculated using Isoplot 3.6 (Ludwig, 2009).

Similar results (Lu and Hf contents, and $^{176}\text{Lu}/^{177}\text{Hf}$ and $^{176}\text{Hf}/^{177}\text{Hf}$ ratios) were observed in other samples of Group II eclogites (i.e. sample Ph423 and Ph425). The whole rock Lu/Hf ratio from Group II eclogites are very much identical, thus, may indicate complete isotopic equilibration, however, the separated minerals show large scatter in Lu/Hf ratio, as well as, in the $^{176}\text{Lu}/^{177}\text{Hf}$ and $^{176}\text{Hf}/^{177}\text{Hf}$ isotope results (Table 2 and Fig. 7). Garnet from Group II eclogites bears very low Lu/Hf ratio (< 3) which may indicate isotopic disequilibrium or the effect of micro-inclusions. When various data points (garnet-clinopyroxene, garnet-whole rock or garnet-whole rock-clinopyroxene) were used to calculate isochrones, the age values obtained from these mixing lines show an age range between 50 and 30 Ma. In contrast when we utilised the Lu-Hf data of sample Ph425 (fresh eclogite) for three-point isochron (garnet-clinopyroxene-whole rock), an age value of 42 ± 12 Ma (with smaller values of MSWD: 0.075) was obtained (Fig. 8c). Since, the Himalayan eclogites of the Kaghan Valley are derived from the Panjal Trap volcanics and they were metamorphosed during the

subduction of the Indian Plate slab beneath the Asian Plate, therefore, we could pool all the analysed samples (whole rock and separated minerals as a single system) and an internal isochron of 48 ± 11 Ma (MSWD=52) was obtained (Fig. 8d). These results are consistent with the previously reported Sm-Nd isochron results for the Kaghan Valley eclogites by Tonarini et al. (1993).

6. Interpretation of results

6.1 Multistage mixing

The Rb-Sr isotope results (Spencer et al., 1995) and Sm-Nd isotopic results (this study) from the whole rock did not yield isochron, however, in situ zircon U-Pb isotope yielded age values between 254 and 267 Ma (Spencer & Gebauer 1996; Parrish et al., 2006; Rehman et al., 2010; Wilke et al., 2010a) show evidence of magmatic activity in Permian. From the available reference data and the present results of multi-isotope systems, we interpret that the Himalayan eclogites were originated from a wide range magmatic activity throughout the Himalayan region in the Permian to Carboniferous time. The eclogites found as lenses and sheets in the Kaghan Valley indicate Panjal Trap basaltic volcanism and intrusive diking. The presence of abundant zircons and the Fe-Ti rich chemical composition of Group I eclogites (Rehman et al., 2008) indicate probably a gabbroic protolith for some of these eclogites. The large time span from the initiation of volcanic activity in the Permian (ca. 267 Ma to 254 Ma; obtained from the protolith-related zircon U-Pb age-dating by Rehman et al 2010) to the subduction-related metamorphism in the Eocene (ca. 50 to 40 Ma; obtained from the Sm-Nd and Lu-Hf isotopes during this study, and the U-Pb zircon age-dating from felsic gneisses which surround these eclogites by Kaneko et al., 2003) reveal multistage mixing of these eclogites. The volcanic activity started primarily at 267 Ma followed by the probable mixing of the sediment component during magmatic assimilation and periodic volcanic events in the later stages as indicated by the U-Pb zircon ages (Rehman et al. 2008).

Furthermore, the India-Asia collision before and after 50 Ma and the subduction-related metamorphic event between 50 and 40 Ma suggest an open system where elemental exchange occurred when the Indian Plate slab was subducting to mantle depths. The whole rock $^{176}\text{Lu}/^{177}\text{Hf}$ and $^{176}\text{Hf}/^{177}\text{Hf}$ ratios from selected eclogite samples when used for internal isochron yielded an isochron of 569 ± 180 Ma (MSWD = 3.4), rather defines a mixing line and hence giving values older than the protolith age. This result indicates that a crustal component (most probably sediment flux) incorporated in the eclogite source rock.

Moreover, the ϵNd verses ϵHf plot for the Kaghan Valley eclogites (Fig. 9) also indicates that these eclogites were derived from ocean-island-basalts with a significant mixing trend of sediments component (as shown in Fig. 9 with ϵ (t 267, t 46, and t 0). The large variations in the Sm-Nd isotope ratios strongly suggest that the precursor rocks of these eclogites assimilated a sediment component during volcanic activity with further possible fluid influx during subduction of the Indian Plate slab after it's collision with the Asian Plate.

6.2 Low Sm/Nd and Lu/Hf ratios: Effect of inherited micro-inclusions

The use of separated or in situ minerals (e.g. garnet, clinopyroxene, phengite, zircon, monazite, and hornblende etc.) as a chronometer, mostly provides exact time information of history of the rocks, however, the strong preference of the garnet lattice for the heavy rare

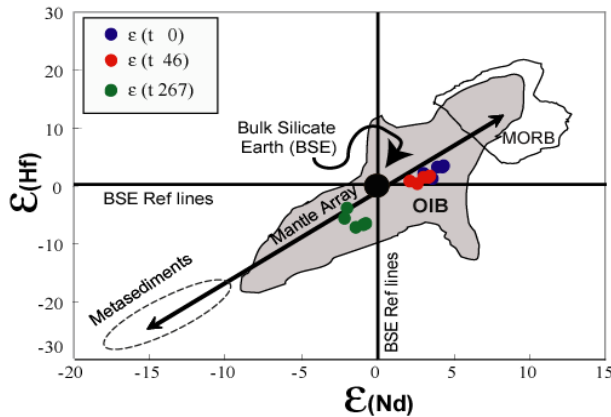


Fig. 9. Plot displaying the Hf-Nd isotopic compositions of the Himalayan eclogites at 267 Ma (protolith age; green circles), at 46 Ma (UHP eclogite facies metamorphic stage; red circles), and at 0 Ma (present time; blue circles) relative to the terrestrial Hf-Nd mantle array. Fields for the mid-ocean-ridge-basalts (MORB) and ocean-island-basalts (OIB) are modified from John et al. (2004) and references therein. Field for metasediments was adopted from Kempton et al. (2002). Bulk Silicate Earth (BSE) is assumed to be chondritic with respect to Lu-Hf and Sm-Nd.

earth elements over light rare earth elements makes this mineral highly suitable for Sm-Nd dating (relatively less mobile) (Thöni, 2002). Moreover, the Lu-Hf system (relatively immobile) has been argued to be superior to the Sm-Nd method in some respects (e.g. Blichert-Toft et al., 1999; Blichert-Toft & Frei, 2001; de Sigoyer et al., 2000). Particularly, the immobile nature of the Lu-Hf dating (Blichert-Toft et al., 1999; White, 2009) is considered to be the best used for metamorphic rocks. When applying Sm-Nd and Lu-Hf isotope systems, using separated minerals, for geochronological research, the problem of the influence of high-light rare earth element inclusions is strong (Thöni, 2002).

In case of the Kaghan Valley eclogites (both Group I and II) it is clear that the above factor played a vital role. The possible presence of micro-inclusion (zircon and/or allanite?) even in the optically clean mineral separates could have affected the isotopic ratios. Also, the very low Sm/Nd ratio (< 0.6) and Lu/Hf ratio (< 0.3) and concentration in garnet and the negative correlation of Sm-Nd isotope ratios (Fig. 5) in garnet and clinopyroxene in sample Ph381 (Group I eclogites) indicate abnormal behaviour which caused the isotopic disequilibrium. That is why no isochron relationship was constructed between garnet and clinopyroxene or garnet and whole rock. Even if an isochron was calculated for a single pair (i.e. garnet-clinopyroxene) a two-point mixing line was always obtained with more or less identical age values for the metamorphic event the Himalayan eclogites have experienced. However, a two-point isochron calculation may not always yield geologically meaningful ages. Same pattern is observed in the present research. The age values obtained from various mineral-mineral pairs and mineral-whole rock pairs fall in the metamorphic age range for the Himalayan eclogite facies event but the scatter in age values and the errors are large. This scatter in isochrones/mixing lines and their large errors or no isochron relationship among various minerals indicate presence of optically invisible micro-

inclusions, which could have disturbed the concentrations of the heavy rare earth elements over light rare earth elements. In contrast, for samples having no effect of micro-inclusions, a three-point isochron was obtained which yielded geologically meaningful age (Fig. 6c) if we assume that the isotopic equilibrium was reached in those samples.

6.3 Isotopic disequilibrium

Rocks under eclogite facies conditions usually show disequilibrium amongst major and trace elements and therefore isotopic systems very often do not remain in equilibrium (Vidal & Hunziker, 1985). The Kaghan Valley eclogites display large variations in major and trace element geochemistry (Rehman et al., 2008), and are in partial disequilibrium; for example Rb-Sr (Spencer et al., 1995) and Sm-Nd (Samples Ph381 and Ph422; this study). In the work of Spencer et al. (1995; Fig. 4, p. 98), it is clear that the analyzed eclogite samples align poorly along the reference isochron of 270 Ma. This indicates (i) either an addition of a crustal component to the protolith after their emplacement but before their subduction or (ii) a fluid infiltration to the eclogite protolith during the subduction of the Indian Plate slab. Moreover, additional remobilization of trace elements and rare earth elements must have occurred to produce the observed isotopic disequilibrium during eclogite facies metamorphism and late-stage retrogression. The isotopic disequilibrium can be seen in two of the eclogite samples (Ph381:Group I, and Ph422; Group II) in which garnet show either $^{147}\text{Sm}/^{144}\text{Nd}$ ratios lower than the whole rock or $^{143}\text{Nd}/^{144}\text{Nd}$ ratios lower than whole rock for higher $^{147}\text{Sm}/^{144}\text{Nd}$ ratios (Fig. 5). Also, it is important to note that the timing of eclogite facies metamorphism at 49 Ma (Tonarini et al., 1993) was adopted from a single garnet-clinopyroxene pair of the two analyzed samples, a second garnet-clinopyroxene pair (sample 90/181 of Tonarini et al., 1993) resulted in an isochron of 89 ± 4 Ma. This implies that the Sm and Nd, and presumably other trace elements underwent remobilization during subduction of the eclogite protolith, and/or later fluid infiltration, resulting in incomplete equilibration.

The reason for disequilibrium can be the incomplete recrystallization of garnet either during an UHP eclogite facies event or during retrogression (Mørk & Mearns, 1986; Luais, et al., 2001). The Sm-Nd mineral equilibria of eclogites have been used to estimate a Sm-Nd closure temperature of 600–800 °C in garnets from various tectonic settings (Mezger et al., 1992; Hensen & Zhou, 1995; Luais et al., 2001). The Himalayan eclogites of the Kaghan Valley have a temperature range of 650–780 °C, within the closure temperature range for the Sm-Nd isotopic system. However, due to an amphibolite facies overprint and subsequent retrogression, volume diffusion or elemental remobilization might have occurred under fluid-rich conditions, resulting in isotopic disequilibrium. Garnet crystallizes partly from pre-existing plagioclase, with contrasting rare earth element patterns (low Sm/Nd ratio of 0.2). This reaction implies the transfer of major elements between igneous and metamorphic minerals. The isotopic ratio of the plagioclase could be preserved during garnet growth, provided that trace elements such as rare earth elements are less mobile than major elements during mineral reactions (Luais et al., 2001). The high Sm/Nd ratio of 1.25 in garnet from sample Ph381Grt is in disequilibrium, compared to the low Sm/Nd ratios of 0.37 in garnet from sample Ph425Grt, and Sm/Nd ratios of 0.79 in garnet from sample Ph380Grt, which is in equilibrium (See table 1 for sample numbers). Our data indicate that the garnets are in disequilibrium, as reflected by the extremely low $^{143}\text{Nd}/^{147}\text{Nd}$ ratios, variable Sm and Nd

concentrations, and negative correlation (Fig. 5), thus no isochron was defined. Similarly, low Lu/Hf ratios (< 0.3) and concentrations in garnets also support our conclusion of isotopic disequilibrium even in the case of immobile elements. Therefore, several mineral-mineral pairs and mineral-whole rock pairs when applied for Lu-Hf isochron calculations, no geologically meaningful age was obtained. However when all data was pooled as one system, an internal isochron with identical age values representing the Himalayan eclogite facies event was obtained (Fig. 8d).

7. Conclusion

1. Eclogites from the Himalayan mountain chain (Kaghan Valley) are classified into two groups on the basis of field occurrence, petrology, and multi-isotope data. Group I eclogites are massive and they record high-pressure metamorphism. Group II eclogites appear as thin lenses or boudines, and they record ultrahigh-pressure metamorphism.
2. Their geochemical characteristics (Sm-Nd and Lu-Hf isotope ratios) are fairly similar to within-plate-basalts or ocean-island-basalts. The U-Pb zircon age dating (254 ~ 267 Ma) from the protolith-related magmatic zircons indicate that the magmatic activity occurred in Permian when the Panjal Trap basalts were extruded. Thus during their extrusion a significant sediment component mixing could have occurred, that is why the initial ϵ_{Nd} versus ϵ_{Hf} values shows the composition of eclogite protolith (at t 267 Ma) close to the metasediments field. Our results of multi-isotope systems indicate that the Himalayan eclogites were probably originated from a wide range magmatic activity in which a sediment component mixed significantly. Moreover, the Fe-Ti enriched pattern and the presence of abundant magmatic zircons in Group II eclogites indicate probably a gabbroic protolith for some of these eclogites. In contrast, the lens- or boudine-type Group II eclogites were derived from basaltic volcanism with some intrusive diking.
3. The Sm-Nd and Lu-Hf isotope systems applied for the Kaghan Valley eclogites did not yield isochron age for the whole rock samples. However, the calculated isochrones from various mineral-mineral and mineral-whole rock pairs exhibited slightly different results. Group II eclogites have higher $^{147}\text{Sm}/^{144}\text{Nd}$ and $^{143}\text{Nd}/^{144}\text{Nd}$ ratios, and lower Sm-Nd concentrations. The Sm and Nd concentration and Sm/Nd ratio among same minerals but in different samples with contrasting differences indicates that even optically clean mineral separates, particularly garnet, may contain high-light rare earth element micro-inclusions such as allanite, epidote/zoisite, apatite or zircon. Therefore, the extremely low concentrations and low Sm/Nd ratios in garnet from Group II eclogite are probably controlled by the presence of allanite/epidote micro-inclusions. The Sm-Nd mixing lines show values ranging from 51 Ma to 38 Ma, using two- to three-point isochrones. Some of the pseudo-isochrones gave values close to those which were published by earlier workers. The Sm-Nd data from all five whole rock samples and their constituent minerals defined an internal isochron of 51 ± 18 Ma, which is consistent with the previous results but with large error and a large value of MSWD.
4. Multi-isotope ratios and compositions from both whole-rocks and their constituent minerals indicate considerable trace element mobilization during subduction of the Indian Plate. The large scatter in Sm-Nd and Lu-Hf isotopic ratios in same minerals of different samples and the large difference in isochron/mixing lines within same group eclogites in this and previous studies indicate that the Sm-Nd and Lu-Hf isotope

systems experienced remobilization with other trace elements during their subduction to deeper crustal levels. In addition, they may have been disturbed by later fluid infiltration that produced isotopic disequilibrium among some rock samples.

8. Acknowledgement

Thanks to A. Makishima, T. Moriguti, and C. Sakaguchi for their support in analytical work. First author is thankful for comments and scientific discussion by H. Kitagawa and several other researchers of the PML. This study was carried out under the Visiting Researcher's Program of the ISEL, Okayama University. Part of this project was supported by the Ministry of Education, Culture, Sports, Science and Technology to H.Y. (KAKENHI 22540472).

9. References

- Beck, R. A., Burbank, D. W., Sercombe, W. J., Riley, G. W., Barndt, J. K., Berry, J. R., Afzal, J., Khan, A. M., Jurgen, H., Metje, H., Cheema, A., Shafique, N. A., Lawrence, R. D. & Khan, M.A. (1995). Stratigraphic evidence for an early collision between northwest India and Asia. *Nature*, Vol. 373, (January, 1995), pp. 55-58, ISSN: 0028-0836
- Blichert-Toft, J., Albarede, F. & Komprobst, J. (1999). Lu-Hf isotope systematics of garnet pyroxenites from Beni Bousera, Morocco: implications for Basalt origin. *Science*, Vol. 283, (February, 1999), pp. 1303-1306, ISSN: 0036-8075
- Blichert-Toft, J. & Frei, R. (2001). Complex Sm-Nd and Lu-Hf isotope systematics in metamorphic garnets from the Isua supracrustal belt, West Greenland. *Geochimica et Cosmochimica Acta*, Vol. 65, (September, 2001), pp. 3177-3189, ISSN: 0016-7037
- de Sigoyer, J., Chavagnac, V., Blichert-Toft, J., Villa, I. M., Luais, B., Guillot, S., Cosca, M. & Mascle, G. (2000). Dating the Indian continental subduction and collisional thickening in the northwest Himalaya: multichronology of the Tso Moriri eclogites. *Geology*, Vol. 28, (June, 2000), pp. 487-490, ISSN: 0091-7613
- Faure, G. (1986). *Principles of Isotope Geology (2nd Edition)*. John Wiley and Sons, ISBN: 0-471-62986-3, Singapore
- Greco, A., Martinotti, G., Papritz, K., Ramsay, J.G. & Rey, R. (1989). The Himalayan crystalline rocks of the Kaghan Valley (NE-Pakistan). *Eclogae Geologicae Helvetiae*, Vol. 82, (n. d.), pp. 603-627, ISSN: 0012-9402
- Guillot, S., Garzanti, E., Baratoux, D., Marquer, D., Mahéo, G. & de Sigoyer, J. (2003). Reconstructing the total shortening history of the NW Himalaya. *Geochemistry Geophysics Geosystems* 4(1): XXXX, doi:10.1029/2002GC000484, ISSN: 1525-2027
- Hensen, B. J. & Zhou, B. (1995). Retention of isotopic memory in garnets partially broken down during an overprint granulite facies metamorphism: implications for Sm-Nd closure temperature. *Geology*, Vol. 23, (March, 1995), pp. 225-228, ISSN: 0091-7613
- Honegger, K., Dietrich, V., Frank, W., Gansser, A., Thöni, M. & Trommsdorf, V. (1982). Magmatism and metamorphism in the Ladakh Himalaya (the Indus-Tsangpo suture zone). *Earth and Planetary Science Letters*, Vol. 60, (September, 1982), pp. 253-292, ISSN: 0012-821X
- John, T., Scherer, E. E., Haase, K. & Schenk, V. (2004). Trace element fractionation during fluid-induced eclogitization in a subducting slab: trace element and Lu-Hf-Sm-Nd isotope systematics. *Earth and Planetary Science Letters*, Vol. 227, (November, 2004), pp. 441-456, ISSN: 0012-821X

- Kaneko, Y., Katayama, I., Yamamoto, H., Misawa, K., Ishikawa, M., Rehman, H. U., Kausar A.B. & Shiraishi, K. (2003). Timing of Himalayan ultrahigh-pressure metamorphism: sinking rate and subduction angle of the Indian continental crust beneath Asia. *Journal of Metamorphic Geology*, Vol. 21, (August, 2003), pp. 589-599, ISSN: 1525-1314
- Kempton, P. D., Pearce, J. A., Barry, T. T., Fitton, J. G., Langmuir, C. & Christie D. M. (2002). Sr-Nd-Pb-Hf Isotope Results from ODP Leg 187: Evidence for Mantle Dynamics of the Australian-Antarctic Discordance and Origin of the Indian MORB Source. *Geochemistry Geophysics Geosystems*, Vol. 3, 1074, doi:10.1029/2002GC000320, ISSN: 1525-2027
- Lombardo, B. & Rolfo, F. (2000). Two contrasting eclogite types in the Himalaya: implications for the Himalayan orogeny. *Journal of Geodynamics*, Vol. 30, (February, 2000), pp. 37-60, ISSN: 0264-3707
- Lu, Y., Makishima, A. & Nakamura, E. (2007), Purification of Hf in silicate materials using extraction chromatographic resin, and its application to precise determination of $^{176}\text{Hf}/^{177}\text{Hf}$ by MCICP-MS with ^{179}Hf spike. *Journal of Analytical Atomic Spectrometry*, Vol. 22, (n. d.), pp. 69-76, ISSN: 02679477
- Luais, B., Duchêne, S. & de Sigoyer, J. (2001). Sm-Nd disequilibrium in high-pressure, low-temperature Himalayan and Alpine rocks. *Tectonophysics*, Vol. 342, (December, 2001), pp. 1-22, ISSN: 0040-1951
- Ludwig, K. R. (2009). Isoplot 3.6, A Geochronological Toolkit for Microsoft Excel, Berkeley Geochronology Center Special Publication No. 4, Berkeley, CA, USA, revised April 8, 2008.
- Lugmair, G. W. & Marti, K. (1978). Lunar initial $^{143}\text{Nd}/^{144}\text{Nd}$; differential evolution of the lunar crust and mantle. *Earth and Planetary Science Letters*, Vol. 39, (May, 1978), pp. 349-357, ISSN: 0012-821X
- Makishima, A. & Nakamura, E. (2007). Determination of Major, Minor and Trace Elements in Silicate Samples by ICP-SFMS Applying Isotope Dilution-Internal Standardisation (ID-IS) and Multi-Stage Internal Standardisation. *Geostandards and Geoanalytical Research*, Vol. 30, (November, 2006), pp. 245-271, ISSN: 1751-908X
- Mezger, K., Essene, E. J. & Halliday, A. N. (1992). Closure temperatures of the Sm-Nd system in metamorphic garnets. *Earth and Planetary Science Letters*, Vol. 113, (October, 1992), pp. 397-409, ISSN: 0012-821X
- Mørk, M. B. E. & Mearns, E. W. (1986). Sm-Nd isotopic systematic of gabbro-eclogite transition. *Lithos*, Vol. 19, (October, 1986), pp. 255-267, ISSN: 0024-4937
- Nakamura, E., Makishima, A., Moriguti, T., Kobayashi, K., Sakaguchi, C., Yokoyama, T., Tanaka, R., Kuritani, T. & Takei, H. (2003). Comprehensive geochemical analyses of small amounts (<100 mg) of extraterrestrial samples for the analytical competition related to the sample-return mission, MUSES-C. *The Institute of Space and Astronomical Science Report*, Vol. 16, (n. d.), pp. 49-101, ISSN: 0288-433X
- O'Brien, P. J., Zotov, N., Law, R., Khan, M. A. & Jan, M. Q. (2001). Coesite in Himalayan eclogite and implications for models of India-Asia collision. *Geology*, Vol. 29, (May, 2001), pp. 435-438, ISSN: 0091-7613
- Parrish, R. R., Gough, S. J., Searle, M. P. & Waters, D. J. (2006). Plate velocity exhumation of ultrahigh-pressure eclogites in the Pakistan Himalaya. *Geology*, Vol. 34, (November, 2006), pp. 989-992, ISSN: 0091-7613

- Patriat, P. & Achache, J. (1984). India-Eurasia collision chronology has implications for crustal shortening and driving mechanism of plates. *Nature*, Vol. 311, (October, 1984), pp.615-621, ISSN: 0028-0836
- Pognante, U. & Spencer, D. A. (1991). First record of eclogites from the High Himalayan belt, Kaghan Valley (northern Pakistan). *European Journal of Mineralogy*, Vol. 3, (Month, year), pp. 613-618, ISSN: 0935-1221
- Rehman, H.U., Yamamoto, H., Kaneko, Y., Kausar, A. B., Murata, M. & Ozawa, H. (2007). Thermobaric Structure of the Himalayan Metamorphic Belt in Kaghan Valley, Pakistan. *Journal of Asian Earth Sciences*, Vol. 29, (February, 2007), pp. 390-406, ISSN: 1367-9120
- Rehman, H.U., Yamamoto, H., Khalil, M.A.K., Nakamura, E., Zafar, M. & Khan, T. (2008). Metamorphic history and tectonic evolution of the Himalayan UHP eclogites in Kaghan Valley, Pakistan. *Journal of Mineralogical and Petrological Sciences*, Vol. 103, (August, 2008), pp.242-254, ISSN: 1345-6296
- Rehman, H.U., Kobayashi, K., Tsujimori, T., Nakamura, E., Yamamoto, H. & Khan, T. (2010). Ion microprobe U-Pb geochronology and trace element geochemistry of the zircon from the Himalayan high- and ultrahigh-pressure eclogites, Kaghan Valley of Pakistan. *Eos Trans. AGU*, 91(26), *Western Pacific Geophysics Meeting 2010*. Supplementary Abstract V44A-03, Taipei, Taiwan, June, 2010
- Scherer, E., Münker, C. & Mezger, K. (2001). Calibration of the lutetium-hafnium clock. *Science*, Vol. 293, (July, 2001), pp. 683-687, ISSN: 0036-8075
- Spencer, D. A., Tonarini, S. & Pognante, U. (1995). Geochemical and Sr-Nd isotopic characterisation of Higher Himalayan eclogites (and associated metabasites). *European Journal of Mineralogy*, Vol. 7, (n. d.), pp. 89-102, ISSN: 0935-1221
- Spencer, D. A. & Gebauer, D. (1996). SHRIMP evidence for a Permian protolith age and a 44 Ma metamorphic age for the Himalayan eclogites (Upper Kaghan, Pakistan): Implication for the subduction of the Tethys and the subdivision terminology of the NW Himalaya. *Himalayan-Karakoram-Tibet Workshop*, 11th, (Flagstaff, Arizona, USA), Abstract Volume, pp. 147-150.
- Thöni, M. (2002). Sm-Nd isotope systematics in garnet from different lithologies (Eastern Alps): age results, and an evaluation of potential problems for garnet Sm-Nd chronometry. *Chemical Geology*, Vol. 185, (May, 2002), pp. 255-281, ISSN: 0009-2541
- Tonarini, S., Villa, I. M., Oberli, F., Meier, M., Spencer, D. A., Pognante, U. & Ramsay, J. G. (1993). Eocene age of eclogite metamorphism in Pakistan Himalaya: Implications for India-Eurasia collision. *Terra Nova*, Vol. 5, (January, 1993), pp. 13-20, ISSN: 1365-3121
- Vidal, P. & Hunziker, J.C. (1985). Systematics and problems in isotope work on eclogites. *Chemical Geology*, Vol. 52, (July, 1985), pp. 129-141, ISSN: 0009-2541
- Wilke, F.D.H., O'Brien, P.J., Gerdes, A., Timmerman, M.J., Sudo, M. & Khan M.A. (2010a). The multistage exhumation history of the Kaghan Valley UHP series, NW Himalaya, Pakistan from U-Pb and $40\text{Ar}/39\text{Ar}$ ages. *European Journal of Mineralogy*, Vol. 22, (October, 2010), pp. 703-719, ISSN: 0935-1221
- Wilke, F.D.H., O'Brien, P.J., Altenberger, U., Konrad-Schmolke, M. & Khan M.A. (2010b). Multi-stage reaction history in different eclogite types from the Pakistan Himalaya and implications for exhumation processes. *Lithos*, Vol. 114, (January, 2010), pp.70-85, ISSN: 0024-4937

- White, W. M. (2011). *Geochemistry*, In: *An on-line text book of geochemistry to be published by John-Hopkins University Press*, Aug, 22, 2011, Available from: <URL: <http://www.imwa.info/white-geochemistry.html>>
- Yokoyama, T., Makishima, A. & Nakamura, E. (1999). Evaluation of the coprecipitation of incompatible trace elements with fluoride during silicate rock dissolution by acid digestion. *Chemical Geology*, Vol. 157, (May, 1999), pp. 175-187, ISSN: 0009-2541
- Yoshikawa, M. & Nakamura, E. (1993). Precise isotope determination of trace amounts of Sr in magnesium-rich samples. *Journal of Mineralogy Petrology and Economic Geology*, Vol. 88, (June, 1993), pp. 548-561, ISSN: 0091-7613

Geochemistry and Metallogenic Model of Carlin-Type Gold Deposits in Southwest Guizhou Province, China

Yong Xia, Wenchao Su, Xingchun Zhang and Janzhong Liu
*State Key Laboratory of Ore Deposit Geochemistry, Institute of Geochemistry
Chinese Academy of Sciences, Guiyang
China*

1. Introduction

Carlin-type gold deposits, also known as sediment-hosted gold deposits are among the largest hydrothermal gold deposits in the world, currently being sought and mined in the United States and China (Tretbar et al., 2000; Hu et al., 2002). The region of southwestern Guizhou (SW Guizhou), which is a region where the Carlin-type gold deposits were found for the earliest time in China, is an important component of the Yunnan-Guizhou-Guangxi “gold triangle” province. Carlin-type gold deposits in SW Guizhou, China, are hosted in late Paleozoic and early Mesozoic sedimentary rocks along the southwest margin of the Precambrian Yangtze craton. They can be classified as two types, i.e., the fault type and the strata-bound type, on the basis of their occurrence, shape and structural controls (Zhang et al., 2003; Xia, 2005). The former type includes the Lannigou, Yata, Banqi, Zhimudang (the upper orebodies), etc. with gold ores mostly occurring in high-angle compresso-shear faults. The ore-hosted strata are generally Middle and Lower Triassic in age, ore-bearing rocks are dominated by muddy siltstones and silty mudstones. The strata-bound gold deposits include the Shuiyindong, Taipingdong, Zhimudang (the lower orebodies), Getang, Nibao, etc. Gold ores are hosted mainly in the interbedded rupture zone at the karst discontinuity surface of the Upper-Lower Permian and the Upper Permian strata. The deposits are mostly concealed ones at depth, the orebodies occur as stratiform, stratoid and lenticular ones and are developed along the strata, characterized by multi-layer distribution. Ore-hosted rocks are mainly impure bioclastic limestones and carbonate rocks in organic-rich coal series formations, with obvious anticline ore-controlling features. They have characteristics similar to Carlin-type gold deposits in Nevada, including notable enrichment in As, Sb, Hg, and Tl (Hu et al., 2002; Xia, 2005). Typical characteristics include impure carbonate or calcareous and carbonaceous host rock that contains disseminated pyrite and arsenopyrite. Gold occurs either as submicrometer-sized particles or invisibly as solid solution in As-rich rims of pyrite and arsenopyrite. Late stibnite, realgar, and orpiment fill fractures on the periphery of gold mineralization. Hydrothermal alteration caused decarbonation, silicification, argillization, and sulfidation, similar to Carlin-type gold deposits in Nevada (Hofstra and Cline, 2000; Emsbo et al., 2003; Kesler et al., 2003). Detailed studies in recent years have shed much light on the geochemistry and metallogenic mechanisms of the Carlin-type gold deposits in the

region, promoted metallogenic prognosis and exploration, thus making the Shuiyindong gold deposit become a typical super-large Carlin-type gold deposit. On the other hand, a great breakthrough has been made in metallogenic prognosis and exploration of Carlin-type gold deposits on a regional scale.

2. Regional geologic setting

2.1 Stratigraphy in SW Guizhou

The Carlin-type gold mineralization area in southwestern SW Guizhou Province (Fig.1) lies on the southwestern edge of the Yangtze Paraplatform which is composed of crystalline rocks of Proterozoic age overlain mainly by shallow-marine platform deposits of Devonian through Triassic age. After the Caledonian tectonism, from Devonian to Triassic, this area subsided and formed a large sedimentary basin filled with thick sedimentary strata. Outcrops of Devonian, Carboniferous, Permian and Triassic strata occur in the area with sporadic outcrops of Jurassic and Cretaceous strata in this area.

The Carlin-type gold in SW Guizhou are located in sedimentary rocks of Permian and Triassic age, and the environment of sedimentation changed from continental, to marine platform to marine basin facies across the area from the northwest, to the central and to the southeastern part.

The Permian strata are mainly limestones of the Lower Permian with EW-trending facies distribution, and clastic sediments and thinly-bedded limestones of the Upper Permian with NS-trending facies distribution. Late Permian strata change from the northwest to the southeast across the line of Anshun-Anlong-Xingyi. On the northwest side of the line, there are interbedded continental margin facies, where the Getang deposit is located on the palaeokarst surface which separates Early and Late Permian sequences. On the southeast side, there are mainly platform carbonates, and reef facies along the platform margin. Further to the southeast, sedimentation took place in a deep-sea trough-like basin near Ceheng-Zhenfeng-Ziyun-Wangmo and shingle fine-grained clastic sediments of the marine basin were deposited.

Triassic strata were developed extensively in the area. The Late Permian framework of sedimentation continued into the Early Triassic period. The Early Triassic platform facies, mainly marl and claystone interbedded with bioclastic limestone, in which the Zimudang deposit is located, is situated on the northwest side of the Anshun-Zhenfeng-Ceheng line. However, a slope facies of platform margin, mainly calcirudite and micritic limestone, occurs on the southeast side, and the marine basin facies, micritic limestone and shale, occurs further to the southeast. The Banqi and Ceyang deposits are located in slope facies which surrounded the Permian island reef.

The pattern of sedimentation of the Early Triassic continued through the Middle Triassic. The Middle Triassic slump deposits of conglomerate/psephite which crop out in the belt between the platform margin and the deep-sea trough-like basin further indicate that it was an active fault-trough basin. The Lannigou and Yata deposits are located on the boundary between that belt and deep-sea facies. There were Middle Triassic platform facies on the northwest side of the platform margin along the line of Anshun-Zhenfeng-Ceheng, and marine basin facies on the southeast side.

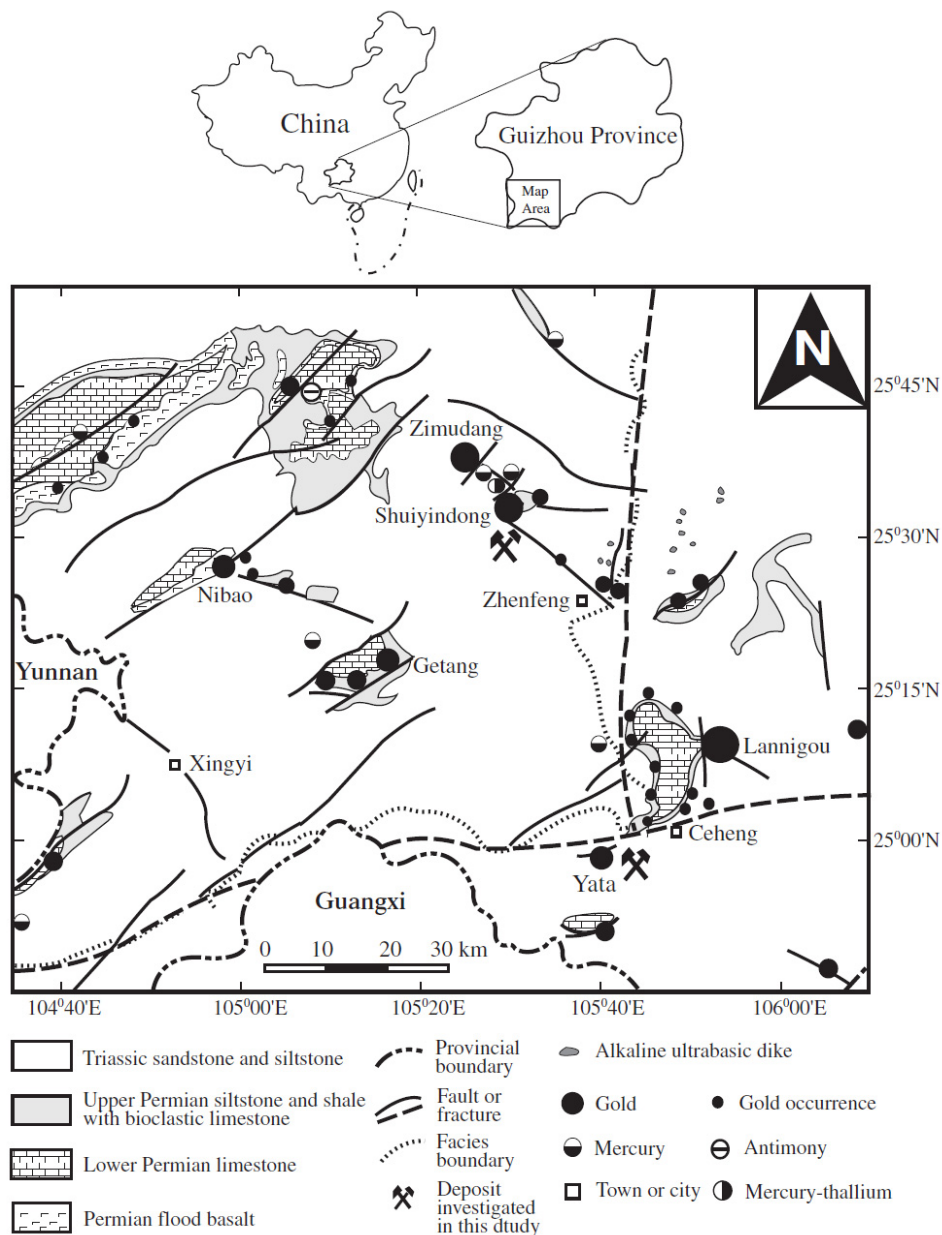


Fig. 1. Simplified geologic map of southwestern Guizhou (modified after Zhang et al., 2003), showing the locations of the major Carlin-type gold (e.g., Shuiyindong and Yata) and antimony and mercury deposits.

2.2 Igneous rocks in SW Guizhou

Outcrops of both intrusive and extrusive igneous rocks including basalts, diabase, vitric tuff and meta-alkaline ultrabasic rocks occur in the area (Fig.2). Several sequences of basalts from Carboniferous to Late Permian are exposed in the northwest corner of the area. Explosion-type basalts of Early Carboniferous and Early Permian only crop out locally in shallow marine environment, whereas Late Permian Emeishan basalts of the continental flood-type are widely exposed on the northwest corner of the area with the thickness of the basalt sequence decreasing from west (500-1250m in Panxian/Puan) to east (<150m in Anshun/Qinglong) (Bureau of Geology and Mineral Resources of Guizhou Province, 1987; Yang et al., 1992; Li et al., 1989). From the results of petroleum exploration drilling, it is known that a thick sequence of Late Permian Emeishan basalts, reaching one thousand metres, lies buried several hundred metres beneath the western area of Xingyi and Luoping (Huang, 1986). Late Permian diabbases are generally exposed as sills and dykes in limited areas (Mei, 1973, 1980). Thin seams of Late Permian acidic vitric tuffs are locally distributed within Triassic dolomite and claystone. Small pipes and dykes of meta-alkaline ultrabasic rocks are exposed in the belt of transitional sedimentary facies along the line of Zhenfeng-Ziyun (Mei, 1973). It is believed that the Puding-Ceyang Fracture provided a pathway for their intrusion (Yang et al., 1992).

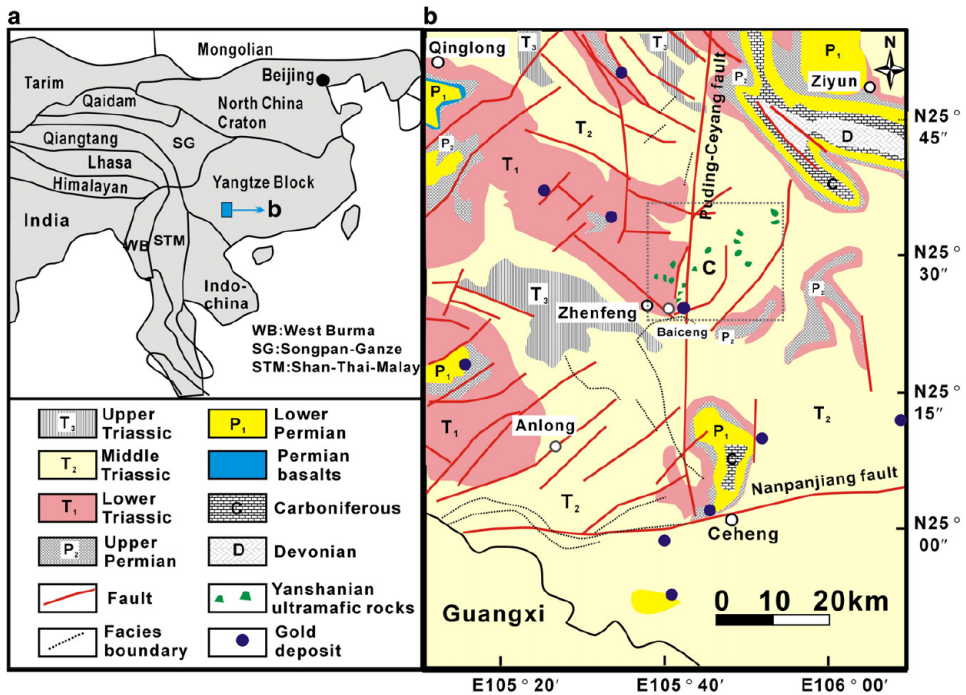


Fig. 2. (a) Distributions of the major terranes in China (modified after Chung and Jahn, 1995); (b) geological map of the SW Guizhou area and the distribution of the sedimentary rocks, Permian basalts, tectonic elements, ultramafic dykes and gold deposits.

2.3 Regional structures in SW Guizhou

The SW Guizhou lies on the southwestern edge of the Yangtze Paraplatform. The adjacent southeast area (mainly northwestern Guangxi) belongs to Youjiang geosyncline which is believed to be the northwest part of the South China Fold System. However, with the discovery of characteristic Yangtze paraplatform-type sedimentary associations, fossils and Caledonian folds in covering strata, it is believed that the Youjiang geosyncline was developed on the southwestern edge of the Yangtze Paraplatform by continental rifting activation during the Variscan cycle (Lu, 1986).

Several deep fractures or fracture zones cut through the area (Fig.1, Fig.2). The movements on these fractures provided an important control on geological development including sedimentation and folding in this area from Late Palaeozoic to Triassic time (Li et al., 1989, Yang et al., 1992, Hou and Yang, 1989). The NE-trending Mile-Shizhong Fracture cut through the northwestern part of the area and separates the outcrop of Upper Proterozoic sediments and Permian continental flood basalts on its northwest side from the Triassic sediments on its southeast side. The NW-SE-trending Shuicheng-Ziyun-Bama Fracture Zone (Hezhang-Ziyun) cut through the northeast part of the area. The NEE-trending Nanpanjiang Fracture (Kaiyuan-Pingtang) cut through the southern part of the area with the character of different Triassic sedimentary facies on its two sides. The NS-trending Puding-Ceyang Fracture is believed to be a concealed fracture with the characteristic outcrop of meta-alkaline ultrabasic pipes and the characteristic sedimentary transition of Permian and Triassic strata along the line (Yang et al., 1992). However, Wang et al. (1994) indicated that the boundary between clastic rocks and carbonates along the line of Anshun-Zhenfeng-Ceyang-Nidang was not a real sedimentary transition boundary but a SW Guizhou Thrust formed by thrusting of the shallow-water carbonates onto the clastic sediments from northwest to southeast after the main gold mineralization, with possible maximum thrusting distance of 80 km at peak of the thrust arc near Ceyang.

As a result of the reactivation of these fractures during the Yanshanian orogeny from Middle Triassic to the end of the Cretaceous, a series of subsidiary fractures were formed. It was with these that the gold, mercury, antimony and arsenic mineralization were associated. According to the characteristic sedimentary associations, the structural deformation of the sedimentary cover and the distribution of regional deep fracture zones in this area, two structural units are identified by the Bureau of Geology and Mineral Resources of Guizhou Province (1987). The Puan Rotational-Shear Deformation Area, which is bordered by the Nanpanjiang Fracture to the south, the Puding-Ceyang Fracture to the east and the Shuicheng-Ziyun Fracture to the northeast, mainly has rotational-shear folds associated NW-, NE- and NNE-trending structures, carbonates and calcareous clastic sediments with coal seams of carbonate platform facies in which the gold deposits of Getang, Zimudang, Sanchahe, Xiongwu, the Lamuchang mercury-thallium deposit and the Dachang antimony deposit are located. The Wangmo Deformation Area, which is bordered by the Ziyun-Bama Fracture to the northeast and the Puding-Ceyang Fracture on the west, mainly has NW-trending shear structures and EW- and NS-trending compressive structures, turbidites of marginal slope facies and marine basin facies in which the gold deposits of Banqi, Yata, Baidi, Lannigou, Daguan are located.

3. Geology of the gold deposits

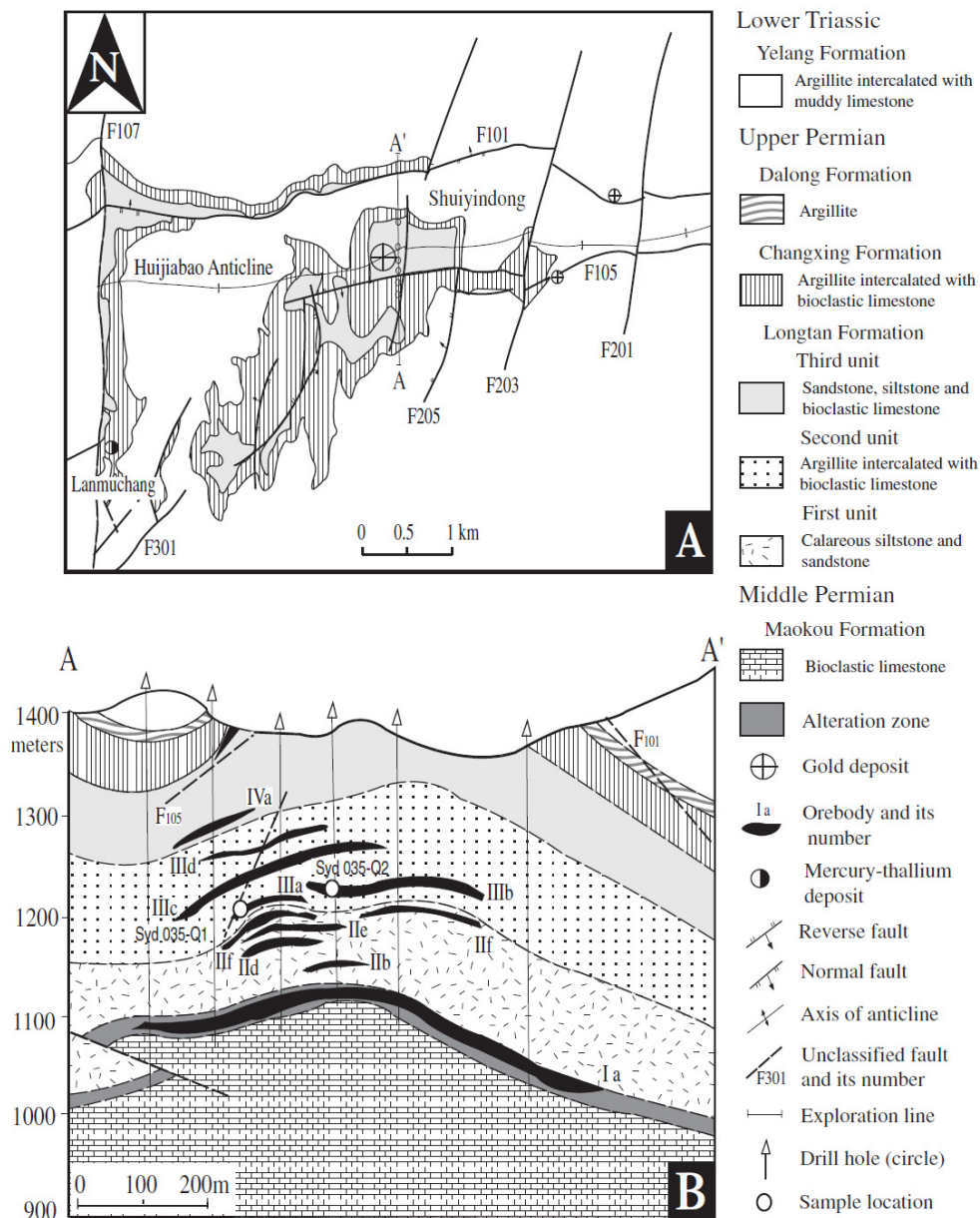
There are two kinds of Carlin-type gold deposits: stratabound and fault-controlled in the southwestern Guizhou Province. The stratabound Carlin-type gold deposits such as Shuiyindong, Taipingdong, Zimudang (lower orebodies), Getang, Nibao gold deposits, etc. are controlled by anticlines and hosted in silty bioclastic limestones of Upper Permian (e.g., Shuiyindong). The fault-controlled Carlin-type gold deposits such as Lannigou, Yata, Banqi, Zimudang (upper orebodies) gold deposits, etc. are localized at the compressive shear faults and hosted in siltstones and silty mudstones of Middle or Lower Triassic (e.g., Yata).

3.1 Geology of the Shuiyindong (Stratabound Carlin-type gold deposit)

The Shuiyindong deposit is located about 20 km northwest of the town of Zhenfeng in southwestern Guizhou (Fig. 3). It lies on the eastern limb of the Huijiabao anticline (Fig. 3A), which also hosts a cluster of deposits on its western limb, including the Zimudang deposit. Recent exploration and mining at Shuiyindong has proven gold reserves of 55 metric tons (t) Au (1.8 Moz), with average gold grades from 7 to 18 g/t (Xia, 2005). All of the gold is refractory, occurring in arsenian pyrite and arsenopyrite (Xia, 2005; Su et al., 2008).

Sedimentary rocks in the district consist of bioclastic limestone, siltstone, and argillite of the Middle and Upper Permian and Lower Triassic. The Middle Permian Maokou Formation, a massive bioclastic limestone, is overlain by the Upper Permian Longtan, Changxing, and Dalong and Lower Triassic Yelang Formations. The Longtan Formation is about 300 m thick in the Shuiyindong district and has been divided into three stratigraphic units (Liu, 2001). The lowest unit consists of calcareous siltstone, which grades into fine-grained sandstone at the top. The second unit consists of silty argillite intercalated with bioclastic limestone and coal seams. The third unit includes calcareous siltstone, sandstone, and muddy and bioclastic limestone. Gold mineralization is preferentially disseminated in bioclastic limestone and calcareous siltstone of the first and second units of the Longtan Formation at depths of 100 to 300 m below the surface (Fig. 3B). These rocks were deformed into an east-trending anticline with limbs that dip 10° to 20°. Strata-bound gold orebodies are located mainly on the flanks of the anticline (Fig. 3B). The limbs of the anticline are cut by reverse faults F101 and F105, respectively, which strike east-west and dip steeply to the north and south, respectively (Fig. 3A). The reverse faults host small orpiment and realgar bodies with low-grade gold mineralization and are cut by a series of near north-south-trending normal faults with steep dips (70°–80°). The normal faults contain mercury-thallium deposits, such as Lanmunchang (Fig. 3A).

The three main orebodies at Shuiyindong (IIIa, IIIb, IIIc; Fig. 3B) contain approximately half of the gold reserves. They are 100 to 400 m long, 50 to 350 m wide, 1.7 to 1.9 m thick, and have an average gold grade of 16 g/t (Xia, 2005). A lower grade orebody (Ia) is hosted in silicified, brecciated argillite and limestone at the unconformity between the Maokou Limestone and the first unit of the Longtan Formation. This unconformity controlled the distribution of other gold deposits regionally in the southwestern Guizhou, such as Getang and Nibao (Fig. 1), suggesting that it may have been a feeder conduit for gold mineralization.



Note the stratiform nature of the numbered orebodies.

Fig. 3. Simplified geologic plan (A) and cross section (B) along the A-A' exploration line of Shuiyindong (modified from Liu, 2001).

Wall-rock alteration at Shuiyindong caused decarbonation, silicification, sulfidation, and dolomitization. Of the alterations, silicification, dolomitization, pyritization (associated with arsenopyritization) are most closely connected with gold mineralization. In the ores metallic minerals include pyrite, arsenopyrite, hematite, stibnite (occasionally seen), cinnabar (occasionally seen), realgar (occasionally seen), and native gold (occasionally seen, found for the first time in this study) (Su Wenchao et al., 2006). Gangue minerals are quartz, dolomite, calcite, hydromica, sericite, kaolinite, and organic carbon. As viewed from the compositional characteristics of ore minerals and phase analyses, it is known that pyrite and arsenopyrite are the carrier minerals of gold.

3.2 Geology of the Yata (Fault-controlled Carlin-type gold deposit)

The Yata gold deposit is located about 15 km southwest of the town of Ceheng in southwestern Guizhou (Fig. 1). The deposit had been mined for arsenic (realgar) at a small scale for many years. Gold mineralization was discovered as a result of reconnaissance sampling around the old realgar pits in the early 1980s. Intensive exploration was carried out by the Guizhou Bureau of Geology and Mineral Resources in the late 1980s. This resulted in the definition of more than 10 t of gold reserves, with an average gold grade of 3 to 5 g/t (Tao et al., 1987). Geologic descriptions of the deposit were given by Zhang et al. (2003).

Sedimentary rocks exposed in the district are mainly siltstone, sandstone, argillaceous limestone, and shale of the Middle Triassic Xuman Formation, which is divided into four members based on sand grain size and bedding thickness (Tao et al., 1987). Gold mineralization occurs in Member 2, which is composed of interbedded sandstone, fine-grained sandstone, siltstone, and mudstone. Unmineralized carbonaceous shale in this formation contains quartz, biotite, ferroan dolomite, illite, calcite, and minor fine-grained diagenetic pyrite.

Gold mineralization (Fig.4) occurred along a narrow easttrending zone and comprises more than 40 orebodies. Most of them occur along high-angle and strike-slip faults that cut the south limb of the east-trending Huangchang anticline and subsidiary folds. Limbs of the anticline dip at 35° to 70°, contain chevron folds and mesoscopic compressive fracture zones. Faults F1, F2, F3, and F6 controlled mineralization within the zone. The F2 and F3 faults, which have easterly trends and dip south at 65° to 85°, controlled the largest mineralization zone (M1) in the district. The M1 zone is 1,500 m long, 40 to 60 m wide, and 200 m thick, with average gold grades varying from 1 to 3 g/t (Zhang et al., 2003). Smaller orebodies with average gold grades of 3 to 5 g/t occur as lenticular zones, veins, and vein stockworks within the larger envelope of mineralization. Gold orebodies are preferentially hosted in altered calcareous siltstone and shale at intersections with high-angle faults that focused fluid flow during gold mineralization.

Despite the stronger structural control than at Shuiyindong, wall-rock alteration at Yata is similar and extends well away from faults and fractures along more reactive or permeable clastic strata or calcareous shale and siltstone. Carbonate dissolution mostly occurred in carbonate strata. In proximal zones of carbonate dissolution, disseminated irregular or euhedral crystals of orpiment or realgar formed locally in porous decarbonated rocks. Silicification typically produced small bodies of jasperoidal quartz within the larger areas of altered rocks. Coarser quartz crystals occur in veins and veinlets. Argillization has mainly

produced illite or illite-quartz veinlets, many of which contain pyrite and arsenopyrite. The dominant primary ore minerals at Yata are arsenian pyrite, arsenopyrite, marcasite, stibnite, orpiment, and realgar (Zhang et al., 2003). Trace amounts of sphalerite, galena, and chalcopyrite also occur. Gangue minerals include quartz, dolomite, calcite, and clay minerals (e.g., illite). Pyrite is the dominant sulfide in the ores (3–5 vol %). It occurs disseminated in the host rocks as rounded pentagonal, dodecahedral, octahedral, and cubic

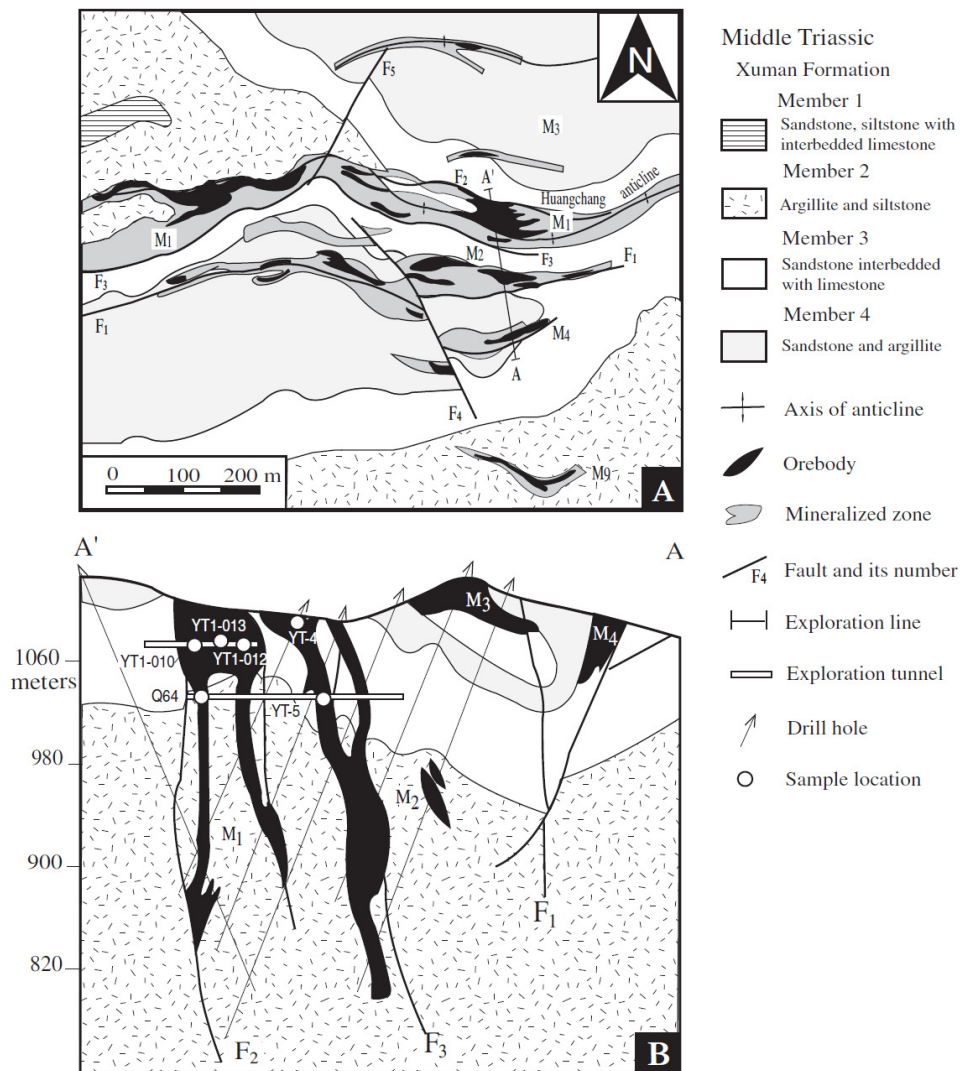


Fig. 4. Simplified geologic plan (A) and cross section (B) along the A-A' exploration line of Yata (after Zhang et al., 2003). Note the vertical (\pm fault-controlled) orientation of the orebodies.

crystals, or as aggregates of all morphologies. EMPA showed that gold is predominantly in arsenian pyrite (540 ppm Au, 10.73 wt % As: Ye et al., 1994), but a few gold grains (0.3–0.8 μm) have been observed in arsenian pyrite using scanning electron microscopy (Ye et al., 1994). Arsenopyrite is generally disseminated in the ore as tiny acicular to prismatic crystals. Some arsenopyrite occurs as rims on pyrite. Marcasite occurs as rare, tiny grains surrounding pyrite grains. Some stibnite formed early, although later than the gold-bearing pyrite, because stibnite crystals have overgrown on gold-bearing pyrite crystals at their margins. Most of the stibnite formed euhedral crystals filling fractures on the periphery of gold mineralization, local overgrowths of realgar and orpiment (Fig. 4B). Orpiment and realgar are also commonly observed in open cavities with euhedral quartz crystals (Fig. 4K) and fractures in the ore zones or their vicinities. Some calcite-orpiment-realgar veinlets cut pyrite-arsenopyrite-jasperoidal quartz veinlets.

4. Geochemistry of elements and isotope

4.1 Geochemistry of elements

The mineralized rocks in gold deposits in SW Guizhou, are chiefly bioclastic limestone, fine-grained sandstone, siltstone and shale. The gold concentrations are variable for different rock types in different deposits, even within sedimentary rocks of similar type. Generally, siltstones contain higher concentrations of gold than sandstones and shales. As, Sb, Hg, Pb and Zn are generally enriched in weakly mineralized rocks compared to the country rocks in SW Guizhou. However, not only As, Sb and Hg, but also Tl, Mo, and Ag are highly enriched in gold-rich ores compared to the country rocks (Zhang et al., 2003). This phenomenon is particularly noticeable for the ore rocks at Shuiyindong.

Weakly altered or unaltered samples in Shuiyindong were selected from various types of rocks for trace element analysis and comparisons were made between their trace element compositions with those of the same type of rocks in the ore-bearing series (Table 1).

As can be seen clearly, the contents of Au, As, Cu, Sb, Tl and Pb in the ore-bearing series are remarkably increased relative to those of unaltered rocks of the same type, reflecting that the trace elements had been brought in by mineralizing hydrothermal solutions. Ti, Sc, Nb, Ta, Zr, Hf, V, Cr, Co, Sn, Ga, Ge, Cd, Rb, Cs, Ba, Mn, Zn, Th and REE showed a little variation in their contents. According to the element geochemical analysis, the former elements belong to the relatively inert elements without having been reworked by hydrothermal solutions, while the latter elements were affected by hydrothermal solutions, slightly influenced by hydrothermal superimposition and reworking processes.

There is no significant difference in primary contents of Au, As, Cu, Sb and Tl for various types of rocks (with unaltered rock samples for reference), and their variation is much less obvious than what was caused by mineralization alteration. As can be seen more clearly from the values of Table 1, the average contents of Au, As, Cu, Sb and Tl in various types of mineralized rocks are several tens to one hundred times those of the elements in the normal rocks of the same type. Of those elements, the contents of Au, As and Tl are the highest. It may be considered that the contents of these elements in the mineralized rock series were generally affected by mineralizing hydrothermal activities. Relatively speaking, their primary contents in the protoliths can be ignored. These elements are the basic hydrothermal elements in the Shuiyindong gold deposit. Their ratios can be used as the

basic parameters for measuring the hydrothermal alteration intensity. As, Cu, Sb and Tl, especially As, can be employed as the indicator elements for ore exploration.

Element	Average value of ore-bearing rocks/normal rocks				Element	Average value of ore-bearing rocks/normal rocks			
	Limestone	Muddy limestone	Claystone	Muddy siltstone		Limestone	Muddy limestone	Claystone	Muddy siltstone
Au	79.80	55.14	69.33	82.50	Zr	1.15	1.34	1.32	0.70
Sc	1.06	1.14	1.15	0.50	Nb	1.32	1.42	1.29	0.68
TiO ₂	1.25	1.04	1.19	0.62	Mo	1.59	6.56	1.42	1.48
V	0.65	1.46	1.23	0.66	Cd	1.87	2.76	2.67	6.31
Cr	0.55	2.32	1.01	0.54	Sn	0.57	2.20	1.79	0.97
MnO	1.25	1.69	0.45	1.20	Sb	2.91	7.95	11.73	32.80
Co	1.30	1.41	1.86	0.62	Cs	1.94	1.39	1.05	0.32
Ni	1.22	1.12	1.06	0.72	Ba	1.01	0.73	1.14	3.07
Cu	3.74	2.27	2.47	1.57	Hf	0.95	1.29	1.29	0.73
Zn	2.07	1.92	1.04	0.82	Ta	1.17	1.29	1.28	0.73
Ga	1.32	1.18	1.38	0.63	Tl	109.0	53.27	69.07	34.92
Ge	0.50	1.17	1.20	0.71	Pb	1.53	1.52	1.62	1.30
As	22.00	19.39	94.26	63.08	Th	0.96	1.04	1.21	0.79
Rb	1.60	1.14	1.51	0.87	U	0.70	3.34	1.47	2.01
Sr	0.25	0.60	0.51	0.86	ree	0.95	1.52	1.42	0.72
Y	0.84	1.61	1.31	0.74					

Table 1. Average values of elements in ore-bearing rock series and content ratios of elements of normal rocks of the Shuiyindong gold deposit (unit: wt% for TiO₂, MnO, and 10⁻⁶ for the others).

The result of elements analysis of rocks and ores indicates that the contents of Au, As, Cu, Sb, Tl in rocks are similar and original differences of their contents in rocks is much smaller than the differences caused by hydrothermal alteration. The average contents of these elements in mineralized rocks are tens times even hundred times higher than nonmineralized rocks. So, the contents of these elements are controlled by action of ore-forming fluids. These elements are most basic elements representing action of ore-forming fluids and indicator elements of prospecting.

4.2 Stable Isotopes

The sulfur isotopic composition of pyrite in the ore varies significantly, with $\delta^{34}\text{S}$ values varying within the range of +27.17‰– -8.64‰, with a range value of 35.81‰, indicating a high measure of dispersion. There would be shown the characteristics of sulfur of sedimentary origin and the involvement of other sources of sulfur. Electron microscopic analysis of pyrite monomineral (Fig. 5) indicated that pyrite in the ore contains framboid (irregular) pyrite powder crystals and zonal pyrite with arsenopyrite surface (hydrothermal origin) and framboid (irregular) pyrite core (primary sedimentary origin). The sulfur isotope values can only represent those of pyrite of primary sedimentary origin and hydrothermal origin. In most cases the volume of pyrite inner core (petrogenesis) is much larger than that of the girdles of arsenopyrite formed during the metallogenic period. Therefore, the sulfur isotope values obtained mainly represent the sulfur isotopic composition of pyrite of petrogenic origin, but can not fully represent the sulfur isotopic composition of ore-forming fluids (Zhang et al., 2010).

However, the $\delta^{34}\text{S}$ values of realgar range from 0.81‰ to 3.03‰ and close to the value of mantle with the range 2.22‰, mean value 1.6‰, indistinctive variation and high homogenization, indicating that the ore-forming substance was probably derived mainly from the deep place (Zhang et al., 2010).

The $\delta^{13}\text{C}_{\text{V-PDB}}$ values of calcite which is the main gangue mineral vary from -8.473~0.866‰, with two main distribution from -4~-9‰ and around 0‰. According to the previous literatures, carbon derived from the mantle and the formation (Zhang et al., 2010).

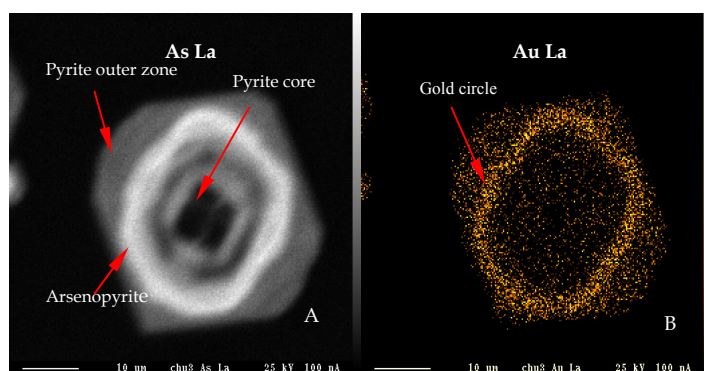


Fig. 5. Scan images of As La(A) and Au La(B) compositions of fine-grained pyrite by electron microprobe spectral scanning.

5. The Sm-Nd isotopic composition of the Shuiyindong gold deposit and its ore-forming geochronological study

In the Carlin-type gold deposits there are usually no minerals suitable for traditional dating, so the problem of metallogenic time has not yet been solved. In the past the fission track method, the quartz fluid inclusion Rb-Sr method and the pyrite Pb-Pb method were used to

constrain the metallogenic ages, giving a larger age range of 80–170 Ma (Hu et al., 2002). Studies by researchers from the Institute of Ore Deposits Geology showed that there are usually developed carbonate veins or realgar (orpiment)-stibnite-carbonate veins in the fault zones exposed on the surface or the hanging-wall of orebodies in the Carlin-type gold mining districts of SW Guizhou. The extensive development of such carbonate veins may imply that there had occurred such geochemical processes as interactions between Au-bearing hydrothermal solutions and Fe-bearing carbonate strata or cements (decarbonation) and they would be the most direct macroscopic geological manifestation of decarbonation during gold metallogenesis.

REE analyses indicated that there are significant differences between the calcite veins closely associated with gold metallogenesis and those with no connection with gold metallogenesis on a regional scale (Table 2, Figs. 6 and 7). The analytical results of Sm-Nd isotopic composition for calcite veins which have close genetic connections with gold mineralization are listed in Table 4 and the calculated results of Sm-Nd isotopic ages are shown in Fig.8. All the results showed that the considerably reliable mineralization age of the super-large Shuiyindong strata-bound Carlin-type gold deposit is 134–136 Ma (Early Cretaceous), just corresponding to the tectonic background of the regional lithosphere expansion (Su Wenchao et al., 2009).

Sample No.	La	Ce	Pr	Nd	Sm	Eu	Gd	Tb	Dy	Ho	Er	Tm	Yb	Lu
Cal-08	0.43	1.77	0.45	3.33	2.38	1.08	3.99	0.7	3.07	0.49	1.05	0.1	0.57	0.07
Cal-11	0.73	3.08	0.73	5.58	3.82	1.89	5.85	0.96	4.32	0.65	1.3	0.14	0.72	0.09
Cal-16	0.18	0.68	0.15	1.05	0.48	0.19	0.57	0.1	0.44	0.08	0.21	0.02	0.14	0.02
Cal-03	6.54	17.1	3.1	16.06	3.81	1.87	3.46	0.46	1.96	0.3	0.61	0.06	0.29	0.04
Cal-17	0.63	2.1	0.4	2.4	0.95	0.41	1.51	0.26	1	0.14	0.22	0.02	0.12	0.02
Cal-10	0.64	1.58	0.38	2.26	0.85	0.28	1.2	0.2	1.02	0.2	0.5	0.05	0.31	0.04
Cal-05	1.66	3.96	0.71	3.5	0.85	0.6	0.95	0.12	0.51	0.09	0.21	0.02	0.1	0.01
Cal-20	1.28	4.18	0.67	3.4	1.04	0.34	1.06	0.18	0.75	0.13	0.3	0.04	0.21	0.03
Cal-21	0.99	3.46	0.59	3.16	1	0.37	1.16	0.18	0.89	0.15	0.35	0.04	0.23	0.03
Cal-12	0.09	0.32	0.07	0.46	0.22	0.09	0.32	0.06	0.29	0.05	0.12	0.01	0.07	0.01
Cal-14	0.67	0.25	0.2	0.99	0.21	0.07	0.24	0.03	0.16	0.03	0.07	0.01	0.05	0.01
ZK1648-14	0.45	0.89	0.17	0.95	0.3	0.12	0.46	0.08	0.36	0.07	0.14	0.02	0.09	0.01
ZK3101-22	0.17	0.55	0.12	0.81	0.81	0.17	0.43	0.07	0.31	0.05	0.1	0.01	0.05	0.01
ZK2002-31	0.21	0.7	0.16	1.23	0.32	0.47	2.72	0.64	3.37	0.55	1.02	0.09	0.47	0.07
NN-03	2.06	3.1	0.49	2.357	0.565	0.182	0.961	0.171	1.009	0.221	0.609	0.085	0.5	0.074
NN-04	0.63	1.26	0.22	1.13	0.339	0.0178	0.45	0.064	0.361	0.068	0.149	0.018	0.087	0.011
NN-05-1	2.3	4.41	0.71	3.368	0.795	0.227	1.018	0.18	0.971	0.203	0.569	0.078	0.449	0.071
NN-05-2	1.49	2.47	0.34	1.234	0.2	0.046	0.192	0.032	0.189	0.036	0.103	0.015	0.087	0.013

Table 2. REE data ($\times 10^{-6}$) for calcite samples in the orebodies and wall rocks of the Shuiyindong gold deposit.

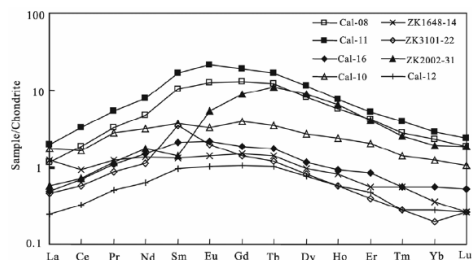


Fig. 6. The chondrite-normalized REE patterns for the calcite veins associated with Au mineralization in the Shuiyindong gold deposit. All data are normalized according to the chondrite REE values of Sun and McDonough (1989).

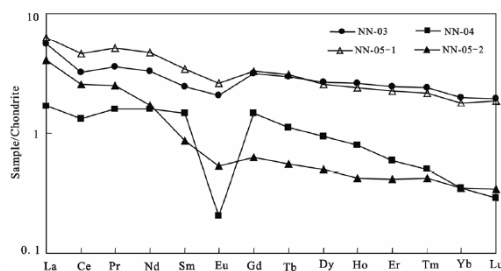


Fig. 7. The chondrite-normalized REE patterns for the calcite veins which have no genetic connection with gold mineralization. All the data are normalized according to the chondrite REE values of Sun and McDonough (1989).

Sample No.	Sm	Nd	$^{147}\text{Sm}/^{144}\text{Nd}$	$^{143}\text{Nd}/^{144}\text{Nd}(2\sigma)$	$^{87}\text{Sr}/^{86}\text{Sr}(2\sigma)$
	($\times 10^{-6}$)	($\times 10^{-6}$)	(atomic)	(atomic)	
Cal-08	2.3002	3.0752	0.4522	0.512762 \pm 6	0.707083 \pm 10
Cal-11	3.8689	5.5334	0.4227	0.512735 \pm 5	0.707203 \pm 21
Cal-16	0.4683	1.0775	0.2628	0.512593 \pm 9	0.707482 \pm 13
Cal-03	3.6978	14.5286	0.1539	0.512496 \pm 7	0.707251 \pm 25
Cal-17	0.9178	2.2416	0.2475	0.512579 \pm 6	0.707991 \pm 11
Cal-10	0.8437	2.1825	0.2337	0.512567 \pm 8	0.707217 \pm 13
Cal-05	0.8203	3.2117	0.1544	0.512497 \pm 8	0.707152 \pm 16
Cal-20	0.9776	3.2226	0.1834	0.512523 \pm 12	0.707125 \pm 13
Cal-21	0.9602	2.8964	0.2004	0.512537 \pm 7	0.707143 \pm 10
Cal-12	0.2227	0.457	0.2946	0.512064 \pm 6	0.707729 \pm 8
Cal-14	0.2044	0.9306	0.1328	0.511922 \pm 15	0.707614 \pm 10
ZK1648-14	0.2869	0.8801	0.1971	0.511978 \pm 20	0.708003 \pm 24
ZK3101-22	0.812	0.9904	0.4957	0.512241 \pm 18	0.707610 \pm 11
ZK2002-31	0.39	0.9459	0.2493	0.512024 \pm 7	0.706620 \pm 18

Table 3. Sm, Nd and Sr isotopic compositions of calcite veins from the Shuiyindong gold deposit.

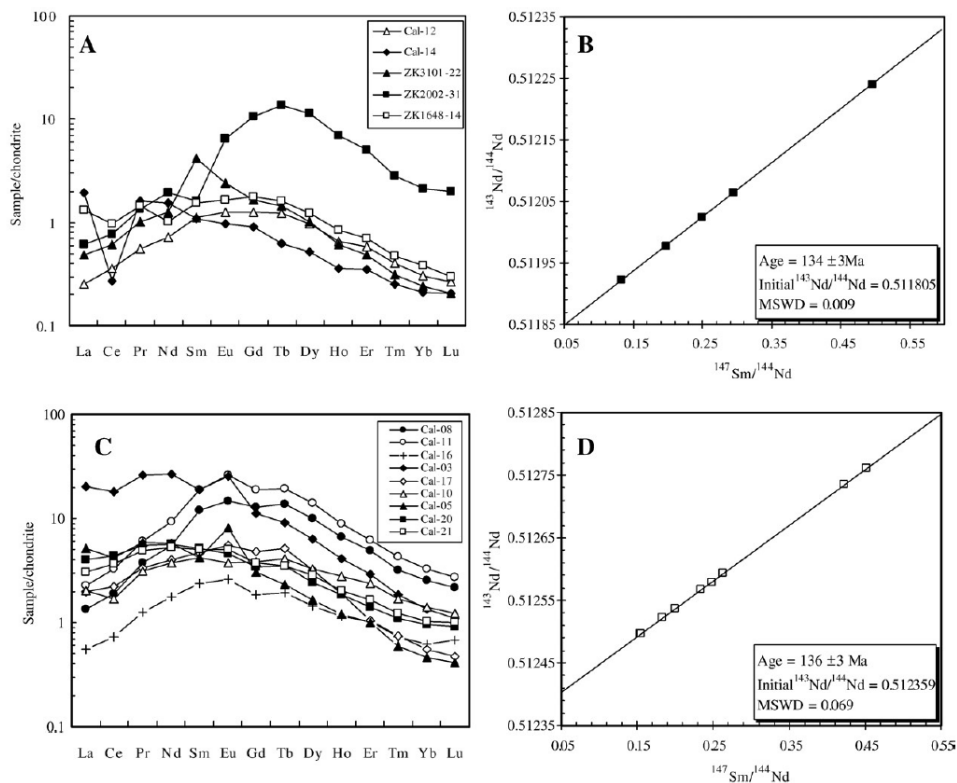


Fig. 8. The chondrite-normalized REE patterns (A and C) and corresponding Sm-Nd isochron ages (B and D) for the calcite veins from the Shuiyindong deposit. All data are normalized using the chondrite REE values of Herrmann (1970).

6. Geochemistry of fluid inclusions

6.1 Fluid inclusion types and petrographic relationships

Eight samples used in this study were collected from the main orebodies in the Shuiyindong and Yata deposits (Figs.3B, 4B). Three are barren milky quartz veins that have early horizontal dips in the ore zones at Shuiyindong and fill fractures at Yata. Some of the milky quartz veins are colored orange or gray by inclusions of realgar or stibnite or are cut by stibnite-realgar-orpiment-quartz veinlets. A sample (YT-5) from Yata contains arsenian pyrite, arsenopyrite, and quartz; other samples from Yata contain stibnite, realgar, orpiment, calcite, and quartz, filling in fractures on the periphery of gold mineralization.

Fluid inclusions observed in this study have negative crystal, elongate, or irregular shapes (Fig. 9). Fluid inclusion types were classified based on their appearance at 25°C and by their Raman spectra and occur in successive stages of the vein and alteration paragenesis.

Type Ia inclusions are two-phase, liquid-rich aqueous inclusions with 10 to 20 vol percent of a low-density vapor bubble at room temperature. They occur in early barren milky quartz veins at Shuiyindong and Yata. Primary inclusions of this type occur along growth zones of quartz and have negative crystal shapes, generally less than 25 μm in diameter (Fig. 9B, E). Secondary inclusions are elongate or irregular and occur along trails crosscutting quartz grains or grain boundaries (Fig. 9C, F). Raman spectroscopy analysis has failed to accurately determine the composition of the vapor phase of this type of inclusion because the bubble moved as the laser beam was focused on it. Raman peaks of CO_2 , N_2 , and CH_4 have, however, been detected.

Type Ib inclusions are two- or three-phase aqueous-carbonic inclusions with a dominant aqueous liquid phase and a relatively constant carbonic (vapor + CO_2 liquid) fraction of 15 vol percent (Fig. 9H). They are commonly observed in quartz veinlets with arsenian pyrite and arsenopyrite of the main stage of gold mineralization at Yata and in jasperoidal quartz of the main stage at Shuiyindong. Primary inclusions are typically 20 μm in diameter, occur along growth zones of quartz, and have negative crystal shapes (Fig. 9G, H). Some inclusions along microfracture planes within quartz grains are pseudosecondary based on their spatial relationship to the growth zones and healed fractures. Both microthermometry and Raman spectroscopy analyses have revealed that the main component of the volatile phase of the inclusions is CO_2 , with minor N_2 and trace CH_4 .

Type II inclusions are rare, two-phase, aqueous-carbonic inclusions with variably high proportions of a carbonic phase ranging from 45 to 90 vol percent (Fig. 9K). In samples from Yata, they occur in late drusy quartz with realgar, stibnite, and calcite.

Type III inclusions are monophasic carbonic inclusions (Fig. 9L) and generally less than 15 μm in diameter. They are restricted to late quartz-realgar veins or veinlets at Yata and occur along trails crosscutting quartz grains. Both microthermometry and Raman spectroscopy have revealed that the volatile phase is mainly composed of CO_2 and N_2 , with trace CH_4 . Petrographic relationships indicate that CO_2 -poor aqueous inclusions of type Ia can be interpreted to approximate the mineralizing fluid, which was responsible for precipitation of early ore minerals in veins but predates the deposition of the bulk of disseminated gold-bearing arsenian pyrite and arsenopyrite deposition in both deposits. CO_2 -rich fluids of type Ib are interpreted to correspond to the main gold-bearing fluid in both deposits. The same aqueous-carbonic fluids also occur together with type II and III carbonic fluids in the late quartz-realgar veins at Yata. Type II and III fluids are interpreted to represent the waning or outflow stage of economic gold mineralization.

6.2 Quantitative fluid inclusion results

6.2.1 Microthermometry and Raman data

Microthermometric measurements were made on primary, pseudosecondary, and secondary inclusions in quartz crystals from milky quartz veins, replacement-style quartz veinlets, and late drusy quartz. Three distinctive fluid compositions are interpreted to be

representative of the different mineralization stages. Microthermometric data and Raman spectroscopy analyses of representative fluid inclusions are given in Table 4.

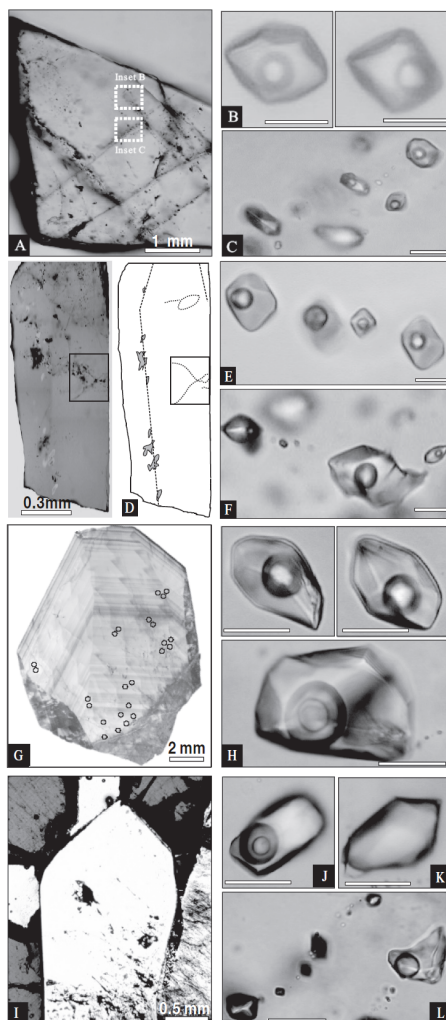


Fig. 9. Microphotographs of fluid inclusions in quartz. A. Early milky quartz (thin section) from Shuiyindong. B. Primary and C. Secondary type Ia aqueous inclusions in the milky quartz from Shuiyindong. D. Photograph and sketch of early milky quartz from Yata. E. Primary and F. Secondary type Ia aqueous inclusions in the milky quartz from Yata. G. SEM-CL image of a main ore-stage quartz crystal, and H. Photographs of type Ib aqueous-carbonic inclusions from Yata. Circles denote the positions of inclusions analyzed by LA-ICP-MS. I. to L. Late drusy quartz crystal with types Ib, II, and III aqueous-carbonic and carbonic-rich inclusions from Yata, respectively. Note that two end-member fluid inclusion assemblages are cogenetic in (L). Scale bar is 20 μ m unless defined otherwise.

Stage	Quartz type	Inclusion	Microthermometry				Raman data				
			Tm (CO ₂) (°C)	Th(CO ₂) (°C)	Mode	Tm(cl) (°C)	Th (°C)	Mode	CO ₂	N ₂	CH ₄
Main-stage	Veinlet quartz crystals	41	-56.7	20.5	L	9.4	228	L	97.5	1.5	1.0
		42	-57.7	17.6	L	9.3	227	L	95.7	3.3	1.0
		55	-56.7	21.6	L	9.4	220	L	97.0	3.0	n.d.
		60	-56.8	22.2	L	8.8	215	L	96.8	2.0	1.2
		61	-56.6	22.9	L	9.4	210	L	99.5	0.5	n.d.
		65	-56.9	21.4	L		238	L	96.0	3.5	0.5
		66	-56.8	22.3	L		217	L	97.0	3.0	n.d.
		76	-56.7	23.4	L	9.6	223	L	96.8	2.5	0.7
		80	-56.7	23.3	L		206	L	98.2	1.8	n.d.
		93	-56.6	24.8	L	8.6	225	L	98.7	1.3	n.d.
		94	-56.7	24.5	L	9.4	210	L	97.5	1.8	0.7
		99	-56.7	17.9	L	9.0	247	L	96.5	2.7	0.8
	107	-56.7	20.8	L	9.8	216	L	97.2	1.9	0.9	
Late stage	Veinlet quartz crystals	34	-58.7	6.3	L	9.5	232 ¹		86.5	13.5	n.d.
		35	-58.6	7.8	L	9.3	228 ¹		89.2	10.0	0.8
		11	-60.5	-24.3	L				71.0	27.2	1.8
		12	-60.3	-24.0	L				73.0	27.0	n.d.
		14	-60.2	-23.3	L				75.0	25.0	n.d.
		15	-60.2	-23.2	L				77.0	23.0	n.d.

(Notes: Tm (CO₂) = final melting temperature of CO₂, Th(CO₂) = homogenization temperature of CO₂, Tm = melting temperature of ice, Tm(cl) = final melting temperature of clathrate, Th = homogenization temperature; L = homogenize to liquid; ¹ Decrepitation temperature; n.d. = not detected; Composition is given in mol percent)

Table 4. Chemical Compositions of Representative Aqueous–Carbonic and Carbonic–Rich Inclusions Obtained by Raman Spectroscopic Analysis and Corresponding Microthermometric Data from Yata.

Type Ia primary and secondary aqueous inclusions (Fig. 9B-C, E-F) have initial ice-melting temperatures (Te) from -22.2° to -21.0°C, which is similar to the eutectic melting temperature in the NaCl-H₂O system (Hall et al., 1988) but does not exclude more complex systems such as the NaCl-KCl-H₂O system (Sterner et al., 1988). Final ice-melting temperatures (Tm) of primary aqueous inclusions range from -3.0° to -4.3°C, corresponding to salinities of 5.0 to 6.9 wt percent NaCl equiv (Bodnar, 1993) with an average of 6.0 wt percent NaCl equiv (Fig. 10B, D). Homogenization of these fluid inclusions was to the liquid phase at temperatures ranging from 190° to 258°C with a mode around 230°C (Fig. 10A, C). The Tm of secondary inclusions range from -1.2° to -4.5°C, corresponding to salinities of 2.1 to 7.2 wt percent NaCl equiv (Fig. 10B, D). Secondary inclusions of type Ia also homogenized into the liquid phase at temperatures ranging from 151° to 261°C with a mode around 190°C (Fig. 10C). No evidence of other phases, such as clathrate, liquid, or solid CO₂ were observed, suggesting that this type of inclusion may contain as much as 2.4 mol percent CO₂ dissolved in the aqueous phase without developing a separate CO₂ liquid phase at room temperature (Bodnar et al., 1985).

Type Ib primary and secondary aqueous-carbonic inclusions (Fig. 9H, J) always develop a vapor phase in the carbonic bubble, even if they are two-phase at room temperature. The melting temperature of CO₂ (Tm (CO₂)) ranges from -58.1° to -56.6°C with the majority of

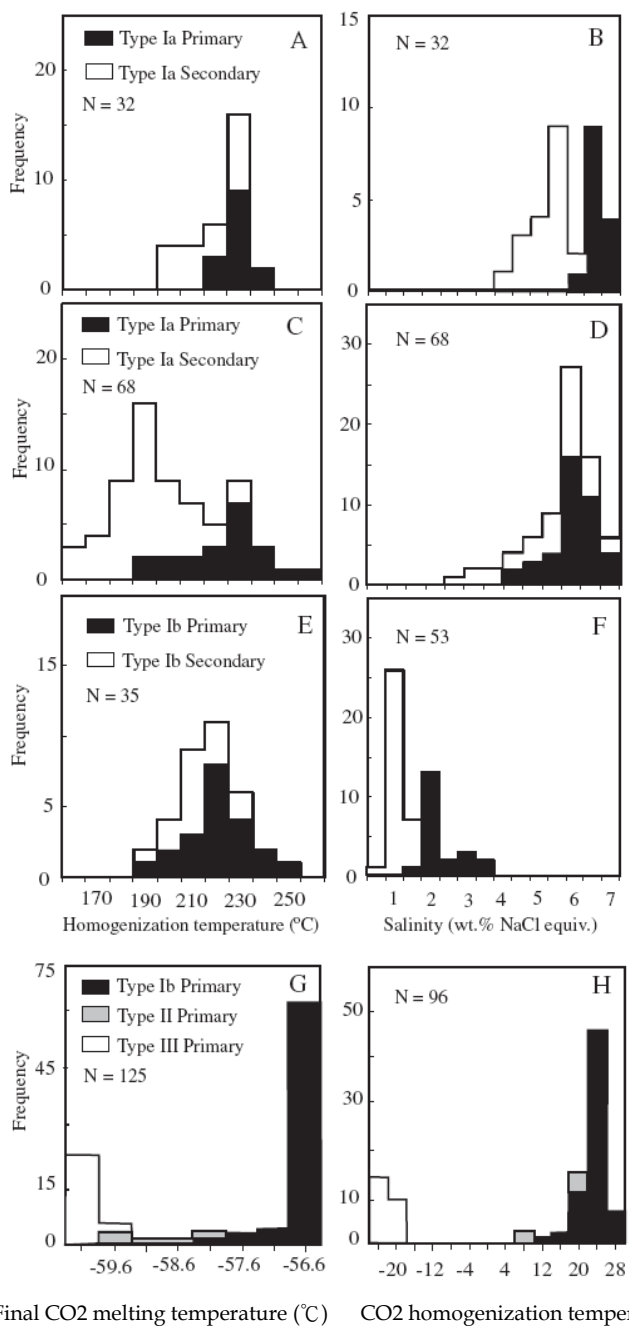


Fig. 10. Histogram of homogenization temperature, final CO₂ melting temperature, and salinity of fluid inclusions from Shuiyindong (A-B) and Yata (C-H).

CO₂ melting occurring at -56.6°C (Fig. 10G). The carbonic phase always homogenized to the liquid (Th (CO₂)) at temperatures ranging from 10.2° to 26.1°C with a mode around 24.0°C (Fig. 10H). Clathrate observed in these inclusions exhibits a typical Q2 melting behavior (Bakker and Brown, 2003). The clathrate melting temperatures (T_m(cl)) of primary inclusions range from 8.3° to 9.2°C, corresponding to salinities of 1.6 to 3.3 wt percent NaCl equiv (Diamond, 1992), with an average of 2.3 wt percent NaCl equiv (Fig. 10F), which is two to three times lower than the salinity of the type Ia aqueous inclusions. The T_m(cl) of secondary inclusions range from 9.4° to 9.8°C, corresponding to salinities of 0.4 to 1.2 wt percent NaCl equiv (Fig. 10F). These inclusions commonly decrepitated at temperatures below 200°C, before total homogenization was attained.

The 35 inclusions that did not decrepitate homogenized into the liquid phase at temperatures from 190° to 245°C, with a mode around 220°C (Fig. 10E). Raman spectroscopy of the carbonic phase in individual fluid inclusions showed that CO₂ is the dominant volatile (>96 mol %), N₂ is always detected (0.5–3.5 mol %), and CH₄ has been detected (up to 1.2 mol %) in a few inclusions (Table 4).

Type II aqueous-carbonic inclusions (Fig. 9K) also always develop a vapor phase in the carbonic bubble during cooling runs. Their T_m(CO₂) ranged from -59.6° to -58.1°C (Fig. 10G). Homogenization of the CO₂ was always to the liquid phase between 6.3° to 20.9°C. The T_m(cl) range from 9.5° to 10.7°C, corresponding to salinities of 0 to 8.9 wt percent NaCl equiv (Bakker and Brown, 2003). Total homogenization temperatures were not obtained because these inclusions decrepitated when heated to above 200°C. Raman spectroscopy revealed that their volatile phases contain major CO₂ (87–89 mol %), minor N₂ (10–14 mol %), and trace CH₄ (0.8 mol %; Table 4).

In the process of freezing (down to -180°C) and subsequent heating, type III carbonic inclusions (Fig. 9L) underwent the following sequence of phase transitions: S + V → L + V → L. The T_m(CO₂) range from -60.5° to -59.6°C with the majority at -60.1°C (Fig. 10G). The Th(CO₂) of this type of inclusion range from -24.3° to -22.5°C (Fig. 10H) and were always into the liquid phase. Total homogenization temperatures could not be measured reliably owing to optical limitations (Diamond, 2003). Raman spectroscopy showed that the volatile phase of type III inclusions contains major CO₂ (71–77 mol %), minor N₂ (23–27 mol %), and trace CH₄ (up to 1.8 mol %; Table 4).

6.2.2 Bulk compositions of aqueous-carbonic and carbonic-rich fluids

Aqueous-carbonic inclusions in the main stage of pyrite-arsenopyrite-quartz veins and late stage of stibnite-realgar-orpiment-quartz veins at Yata have 10 to 15 vol percent volatile phase (nearly pure CO₂), regardless of the sample localities. Calculated density of the volatile phase varies from 0.72 to 0.82 g/cm³, with an average of 0.75 g/cm³. Calculated bulk compositions showed that the fluids are dominated by H₂O (91–92 mol %) and CO₂ (6.3–8.4 mol %, with an average of 7.6 mol %). Their bulk densities range from 0.97 to 0.99 g/cm³. Their average salinities vary from 0.9 to 2.3 wt percent NaCl equiv. Calculated bulk compositions of carbonic-rich inclusions in the late stage of stibnite-realgar-orpiment-quartz veins at Yata are dominantly CO₂ (58–64 mol %), N₂ (19.2–23.7 mol %), and H₂O (12.5–22.8 mol %), and trace CH₄ (up to 1.6 mol %), with volatile phase densities and bulk densities of 0.75 to 0.80 and 0.77 to 0.82 g/cm³, respectively.

6.3 Pressure and temperature estimation

The compositions of type Ib inclusions plot close to the solvus of the H₂O-CO₂ system at 1.0 kb in Figure 8A. It is possible that the fluids of these inclusions may represent one end member produced by unmixing of H₂O-CO₂ fluids. The compositions of a few type II inclusions plot in the two-phase field in Figure 11A. These inclusions may represent mechanical mixtures of two immiscible fluid phases. The local occurrence of type II inclusions at Yata indicates that the hydrothermal fluid reached a state of immiscibility at some time in its history (Diamond, 1990). Type III inclusions plot close to the 1.0 kb solvus in Figure 8A. If they coexisted with type Ib inclusions, then these inclusions may represent another end member produced by unmixing of H₂O-CO₂ fluids.

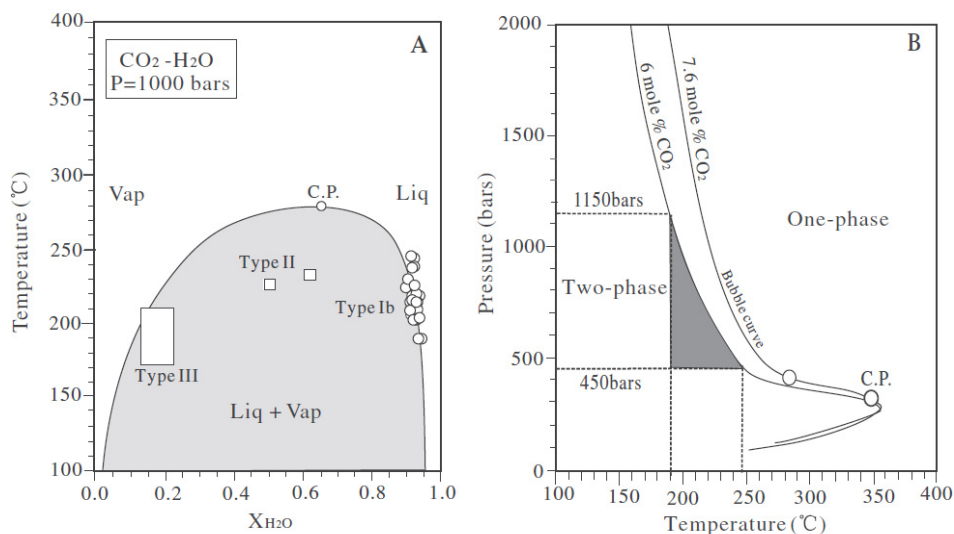


Fig. 11. A. T-X diagram of the H₂O-CO₂ system at 1.0 kbar based on experimental data from Tödheide and Franck (1963) and Takenouchi and Kennedy (1964). B. P-T diagram showing the range of possible P-T conditions during mineralization at Yata. The miscibility boundaries for fluids with 6 and 7.6 mol percent CO₂ are from experimental data of the H₂O-CO₂ system of Tödheide and Franck (1963) and Takenouchi and Kennedy (1964).

The minimum P-T conditions of inclusion entrapment are constrained by intersecting points using the range of homogenization temperatures of type Ib inclusions (190°–245°C) and the minimum of the bubble curves of 6 mol percent CO₂ (Fig. 11B). The defined area in Figure 8B (shaded) ranges from 450 to 1,150 bars, corresponding to a depth of 1.7 to 4.3 km under lithostatic load, using the average density of sedimentary rocks in southwestern Guizhou (2.67 g/cm³; Wang et al., 1995) and 4.5 to 11.5 km assuming hydrostatic pressure. As Yata was controlled by a fault, the estimated pressure may have been fluctuating between hydrostatic and lithostatic pressures. Decompression associated with episodes of faulting may have caused the immiscibility in the late stage of stibnite-realgar observed in this deposit. Zhang et al. (2003) previously estimated pressures for the Lannigou deposit ranging from 600 to 1,700 bars based on the CO₂-bearing fluid inclusions, corresponding to a depth of 2.2 to 6.3 km under lithostatic conditions or an unlikely 6 to 17 km under hydrostatic

load. CO₂ contents of fluid inclusions at Yata (6–8 mol %) are somewhat lower than those of many orogenic lode gold deposits (10–25 mol % CO₂; Ridley and Diamond, 2000) but higher than those of Carlin-type gold deposits in Nevada (2–4 mol % CO₂; Hofstra and Cline, 2000). It is, therefore, reasonable to infer that the Yata deposit may have formed at depths intermediate between orogenic-type gold deposits and those of the Carlin trend in Nevada.

6.4 Source of fluids

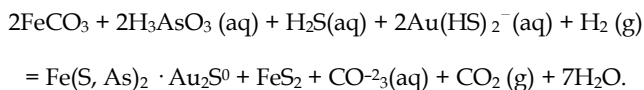
Oxygen and hydrogen isotope compositions of early barren milky quartz veins and clay minerals (<2 μm) in the mineralized rock from Shuiyindong have been reported by Hofstra et al. (2005). The milky quartz veins have a narrow range of high δ¹⁸O values (21–27‰). Calculated δ¹⁸O(H₂O) values for fluids in these samples vary from 10.5 to 16.5 per mil, using a homogenization temperature of 230°C from this study and the quartz-water isotopic equilibrium fractionation equation of Friedman and O'Neil (1977). Calculated δ¹⁸O(H₂O) and δD(H₂O) values for fluids in equilibrium with clay minerals in the mineralized rocks at Shuiyindong range from 4 to 10 and –56 to –68 per mil, respectively (Hofstra et al., 2005). Similar fluid calculations for clay minerals in the mineralized rocks from the Zimudang deposit, located 15 km west of Shuiyindong on the same large-scale dome structure, indicate δ¹⁸O(H₂O) and δD(H₂O) values from 13 to 16 and –35 to –40 per mil, respectively (Hofstra et al., 2005).

Li et al. (1989) and Zhu et al. (unpub. data) reported oxygen for the main ore quartz and the late ore calcite from Yata. The main ore quartz has a narrow range of δ¹⁸O values (20.9–26.1‰), similar to milky quartz veins at Shuiyindong. The calculated δ¹⁸O(H₂O) values for the main ore fluids from Yata vary from 9.9 to 15.1 per mil at 220°C. The δ¹⁸O(H₂O) values of late ore fluids (8.1–10.9‰) were calculated from measured δ¹⁸O calcite values (18.2–20.8‰), the minimum homogenization temperature of 190°C for CO₂-bearing fluid inclusions within calcite (Zhang et al., 2003) and the calcite-water isotopic equilibrium fractionation equation of Friedman and O'Neil (1977). The δD(H₂O) values of water extracted from inclusion fluids in the main ore quartz at Yata range from –51.1 to –78.8 per mil (Li et al., 1989), significantly higher than the average δD(H₂O) value of local meteoric water during the Jurassic and Cretaceous (–85‰; Han et al., 1999). The δ¹⁸O(H₂O) and δD(H₂O) values plot within or close to the metamorphic-water box (Hofstra et al., 2005, fig. 3), suggesting that the ore fluids are characterized by a predominantly metamorphic component. There is no evidence for meteoric water involvement, but a deep magmatic component cannot be excluded.

6.5 Processes of gold deposition

Recent studies of Carlin-type deposits in Nevada have concluded that gold-rich arsenian pyrite precipitated from H₂S rich fluids, which sulfidized iron-bearing minerals in the host rocks (Hofstra et al., 1991; Hofstra and Cline, 2000). The chemical reaction of cooling H₂S-rich fluids in contact with iron-poor carbonate-bearing sedimentary rocks has been calculated from thermodynamic data by Heinrich (2005). An important prediction is that Au solubility may remain high to temperatures as low as 150°C, provided that an excess of H₂S over Fe is maintained in a moderately oxidized hydrothermal fluid, the pH of which is kept close to neutral by carbonate dissolution (Heinrich, 2005, fig. 6). This fluid-chemical evolution path can equally apply to fluids of magmatic or metamorphic origin but clearly

matches the low Fe contents of fluids measured in the inclusions from the Shuiyindong and Yata deposits. At the strata-bound Shuiyindong deposit, there is no evidence for significant phase separation during the main mineralization stage. At the fault-controlled Yata deposit, phase separation was minor during gold mineralization and common in the late stibnite-realgar stage. This fluid inclusion evidence suggests that phase separation was not the key process for deposition of gold and arsenian pyrite. The low Fe contents in the ore fluids (below 400 $\mu\text{g/g}$) measured by LA-ICPMS of fluid inclusions and many relict inclusions of ferroan carbonate (with up to 7.0 wt % Fe determined by EMPA: Su et al., 2008) enclosed in the jasperoidal quartz crystals suggest that iron in sulfide minerals was probably derived from dissolution of ferroan carbonate in the host rocks, as has been documented in Carlin-type gold deposits in Nevada by litho-geochemistry of ores (Hofstra et al., 1991; Hofstra and Cline, 2000). Sulfidation of ferroan carbonate-rich host rocks by H_2S -rich ore fluids containing $\text{Au}(\text{HS})^{-2}$ or $\text{Au}(\text{HS})^0$ (Seward, 1973, 1991), along with arsenic as H_3AsO_3 (aq) complex (Heinrich and Eadington, 1986; Pokrovski et al., 2002), would have effectively extracted gold from solution and transformed primary ferroan carbonate to secondary gold-bearing arsenian pyrite, possibly by a coupled reaction such as the following:



Any loss of CO_2 by fluid phase separation would further promote the formation of gold-bearing arsenian pyrite by such a reaction. This is consistent with petrographic observations that gold-bearing arsenian pyrite and arsenopyrite occur together with Fe-poor hydrothermal dolomite (Fig. 4C). Moreover, it can explain the covariance of Au, As, Sb, and Sr contents of the ore fluids (Fig. 9). The reaction involves reduction of As (+III) and Au (+I) by consumption of H_2 (g), which can be provided by reaction of the metal-transporting fluids with the local organic-rich sediments. This situation is likely to occur where fluids are channeled into a fluid conduit (e.g., along the unconformity between the Maokou Limestone and the Longtan Formation at Shuiyindong or the reverse faults at Yata). Here, they reacted with carbonate and Fe carbonate-rich host rock, or were mixed with Fe^{+2} - and CH_4 -bearing pore fluids previously equilibrated with the reduced host-rock package, to deposit arsenian pyrite and arsenopyrite that host most of the gold in the deposits. The generation of secondary pervasive permeability and porosity by carbonate dissolution from the host rocks favors fluid focusing and the formation of strata-bound orebodies (Heinrich, 2005), as is the case in the Shuiyindong. Therefore, fluid reduction and sulfidation of wall-rock iron by H_2S -rich ore fluids are proposed to be the most important mechanism of gold deposition as auriferous arsenian pyrite in the Chinese Carlin-type gold deposits.

Genetic models previously proposed for Carlin-type deposits in Nevada fall into three groups involving magmatic (Radtke et al., 1980; Ressel et al., 2000), metamorphic (Groves et al., 1998; Hofstra and Cline, 2000), and deeply or shallowly circulated meteoric waters (Ilchik and Barton, 1997; Emsbo et al., 2003). Our study of Carlin-type deposits in Guizhou indicates that the ore fluids are of low salinity but rich in high-density CO_2 , and stable isotope data are consistent with a dominant metamorphic fluid source. The ore-forming fluids have extremely high contents of the characteristic ore elements (As, Sb, and Au), and the mineralogical characteristics and high gold grade of the deposits can be explained by interaction of such fluids with chemically reactive carbonate-, iron-, and carbon-rich

sedimentary host rocks. The deposits formed at similar temperatures as epithermal gold deposits, but at significantly higher pressure and greater depths (4–6 km), consistent with regional-metamorphic temperature gradients. Their thermal regime and ore fluid characteristics are similar to those of the broad group of orogenic gold deposits, raising the possibility that the Carlin-type deposits in Guizhou might be the basin-hosted and relatively cool end member of the crustal continuum of orogenic gold deposit formed from fluids liberated by deep metamorphic dehydration or magmatism (Groves, 1993; Groves et al., 1998; Pettke et al., 2000).

7. Metallogenic model

Through comprehensive geological-geochemical studies and discussion on the problems concerning metallogenesis, the metallogenic model of the Shuiyindong gold deposit can be summarized as follows (Xia 2005; Zhang et al., 2010):

Late Indosinian to Early Yanshanian tectonic movements put the end to the history of basin evolution in this region. Development of strata folds, faults, deep giant faults and magmatism, abnormally high geothermal temperature, and deeper burial resulted in the formation of ore fluids with abundant volatile elements in the deep interior of the crust and upper mantle. In addition, the fluids also became the overpressured fluids after extracting ore-forming elements in the Au-, Hg-, Sb-, As- and Tl-rich rocks in the basement and at great depth.

At that time, as the crust was in the compressive sealed stress state, the overpressured ore fluids were sealed at depth and were in strong equilibrium with the lithosphere. During the Yanshanian period this region was in the extensional state. With the injection of alkaline ultrabasic dykes (tubes), resurival of the faults had occurred at the basement, which, together with cover-strata faults, cut through the crust. As a result, the sealing conditions of overpressured ore fluids were destroyed, the fault system, like a pump, made ore fluids find their way into the upper crust. Gold in the ore fluids would be rapidly precipitated and accumulated as gold deposits in the favorable loci where metallogenic conditions changed suddenly. Meanwhile, Hg, Sb, As, Tl and other ore-forming elements would be precipitated as ores in the proper locations. All these led to what we see today in Southwest Guizhou, where the Carlin-type gold deposits are characterized by close Au-Hg-Sb-As-Tl paragenesis or association on a regional scale, while various gold deposits show the phenomenon of differentiation. At that time, as for the Shuiyindong gold deposit, due to the formation of the Huijiabao short-axis anticline and that of the favorable Upper Permian Longtan Formation assemblage of claystone→bioclastic limestone→claystone, volatiles with abundant CH₄, N₂ and CO₂, which found their way into the anticline core along the karst and non-karst unconformability at the bottom of the Longtan Formation, and gold overpressured ore fluids were gathered. The fluids contained no iron (Su Wenchao et al., 2006), gold can exist in the form of Au-S coordination compound (Seward, 1973; Hofstra and Cline, 2000; Zhang Jun et al., 2002). Relatively high pressure and high volatiles made ore fluids move laterally and infiltrate to some extent in bioclastic sandy limestones in the favorable lithologic assemblage. Sometimes, the overpressured ore fluids would hydrodynamically destroy the country rocks. With the structural development, the faults destroyed the traps constituted by the anticline and favorable lithologic assemblage, making volatiles in the fluids escape out rapidly. As a result, the fluid pressure dropped suddenly, followed by the

decrease of reductivity and the local or partial involvement of iron, some other components and meteoric water in the strata, leading to significant differences in ore-forming conditions. The ore-forming conditions thus rapidly turned favorable for gold deposition, and gold would be rapidly precipitated with the crystallization of arsenopyrite (partly in the inner core of pyrite of sedimentary origin) or fine-grained cinnaba.

Run-through of the faults and the repeated occurrence of favorable lithologic assemblages led to the multi-layer orebody occurrence of the Shuiyindong gold deposit (Fig. 14). And Hg and Tl in metallogenic hydrothermal solutions possess much higher mobility, thus forming ore deposits in high-angle tensional-shear faults in the priphery of the gold deposit. Therefore, there appeared anticline core and low-angle compresso-shear fault strata-bound gold deposits and slightly later high-angle tensional-shear strata-bound Hg and Hg-Tl deposits.

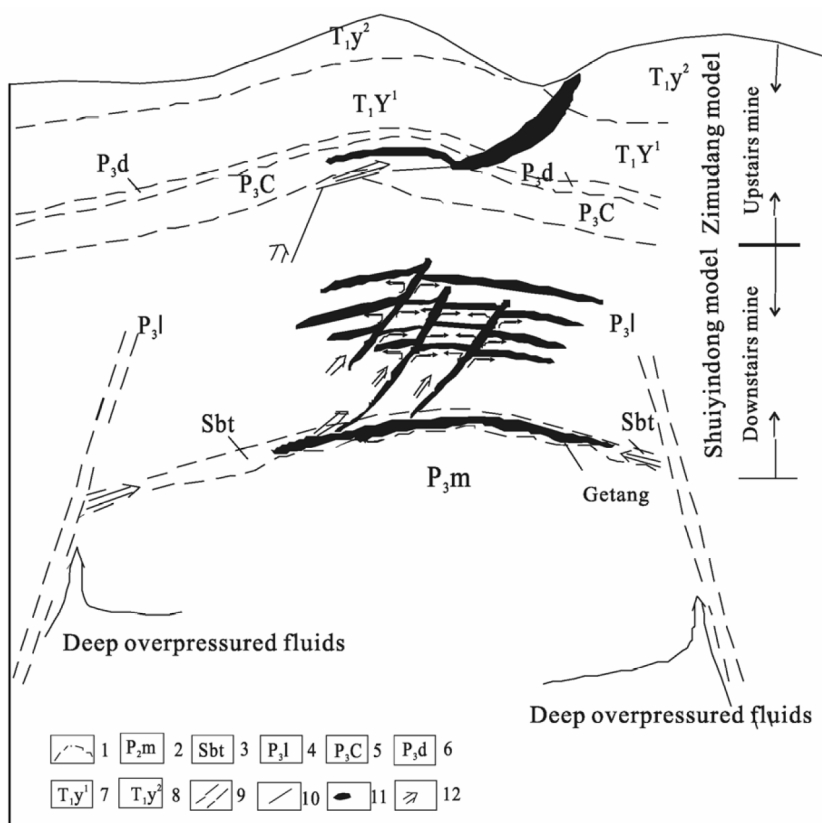
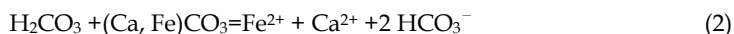


Fig. 11. The "two-stories" gold orebodies distribution and metallogenic model of the Carlin-type gold deposit in SW Guizhou (after Xia, 2005). 1. Stratum boundary; 2. Maokou Formation; 3. alteration zone; 4. Longtan Formation; 5. Changxin Formation; 6. Dalong Formation; 7. the first member of the Yelang Formation; 8. the second member of the Yelang Formation; 9. deep giant fault; 10. fault; 11. gold orebody; 12. migration direction of ore-forming fluid.

Studies showed (Su Wenchao et al., 2006) that the mineralization experienced decarbonation, gold and sulfur precipitation and the formation of carbonate veins, The chemical reactions involved in these three processes are presented as follows:

1. Decarbonation:



2. Precipitation of gold and sulfides:



3. Formation of carbonate veins:



a. Weak acidity of Au-bearing hydrothermal solutions made Fe-carbonate minerals in ore-hosted wall rocks dissolve, followed by the release of Fe and Ca into the hydrothermal system [Reactions (1) and (2)], i.e., decarbonation. b. $\text{Au}(\text{HS})_2^-$ in hydrothermal solutions was decomposed under relatively reducing conditions, making H_2S and HS^- enter into the hydrothermal system [Reaction (3)], both of them together with Fe-carbonate minerals were dissolved, releasing Fe^{2+} -bound pyrite (sulfidation) and producing H^+ [Reactions (4) and (5)].

The acidic environment resultant from sulfidation may further promote Fe-carbonate minerals in the wall rocks to dissolve, followed by the release of a large amount of Fe^{2+} into the hydrothermal system. Sulfidation would finally lead to the over-saturation of Au in hydrothermal solutions and its precipitation as native gold grains and accumulation on the surface of arsenopyrite grains or their margins. c. Dissolution of Fe-carbonate minerals led to the release of Ca [Reaction (6)], which would be involved in the formation of late calcite veins, accompanied by Au pyrite veinlets or cutting through the latter. Therefore, high-grade Fe-carbonate ore-hosted wall rocks are one of the important factors for the formation of large-sized Carlin-type gold deposits. Carbonate veins associated with decarbonation may be one of the important indicators for search of large-sized Carlin-type gold deposits.

8. Acknowledgments

The project was supported jointly by the State Science and Technology Supporting Program (2006BAB01A13), the self-research project funded by the State Key Laboratory of Ore Deposit Geochemistry (Ore Deposit Special Research Project), and Guizhou Provincial Bureau of Geology and Mineral Resource Exploration and Development [Qian Di Kuang Ke (2009) No. 11].

9. References

- Bakker, R.J. & Brown, P.E. (2003). Computer modelling in fluid inclusion research, Mineralogical Association of Canada Short Course Series, Vol. 32, pp. 175-212
- Bodnar, R.J. (1993) Revised equation and table for determining the freezing point depression of H₂O-NaCl solutions. *Geochimica et Cosmochimica Acta*, Vol. 57, (February 1993), pp. 683-684, ISSN 0016-7037
- Bodnar, R.J., Reynolds, T.J. & Kuehn, C.A. (1985). Fluid inclusion systematics in epithermal systems. *Reviews in Economic Geology*, Vol. 2, pp. 73-79, ISSN 0741-0123
- Bureau of Geology and Mineral Resources of Guizhou Province (1987), *Regional Geology of Guizhou Province: Geological Memoirs S.1, No. 7*, pp. 1-698, Geological Publishing House Beijing (in Chinese)
- Diamond, L.W. (1990). Fluid inclusion evidence for P-V-T-X evolution of hydrothermal solutions in late-alpine gold-quartz veins at Brusson, Val D' Ayas, northwest Italian Alps. *American Journal of Science*, Vol. 290, (October 1990), pp. 912-958, ISSN 0002-9599
- Diamond, L.W. (1992). Stability of CO₂ clathrate + CO₂ liquid + CO₂ vapour + aqueous KCl-NaCl solutions: Experimental determination and application to salinity estimates of fluid inclusions. *Geochimica et Cosmochimica Acta*, Vol. 56, No. 1, (January 1992), pp. 273-280, ISSN 0016-7037
- Diamond, L.W. (2003). Introduction to gas-bearing aqueous fluid inclusions: Mineralogical Association of Canada Short Course Series, Vol. 32, No. 1-8, pp. 101-158
- Emsbo, P., Hofstra, A.H., Lauha, E.A., Griffin, G.L. & Hutchinson, R.W. (2003). Origin of highgrade gold ore, source of ore fluid components and genesis of the Meikle and neighboring Carlin-type deposits, north Carlin Trend, Nevada. *Economic Geology* · Vol. 98, (September 2003), pp. 1069-1105, ISSN 0361-0128
- Friedman, I. & O'Neil, J.R. (1977). Compilation of stable isotope fractionation factors of geochemical interest, U.S.G.S. Prof. Paper, 440-kk, pp.1-12
- Geophysical & Geochemical Prospecting Team of the Bureau of Geology & Mineral Resources of Guizhou Province (1988). A regional magnetic and gravity investigation in southwestern Guizhou Province: Scale 1:200000, Unpub. Internal Report.
- Groves, D.I. (1993). The crustal continuum model for late-Archaeon lodegold deposits of the Yilgarn Block, Western Australia. *Mineralium Deposita*, Vol. 28, No. 6, pp. 366-374, ISSN 0026-4598
- Groves, D.I., Goldfarb, R.J., Gebre-Mariam, M., Hagemann, S.G. & Robert, F. (1998). Orogenic gold deposits: A proposed classification in the context of their crustal distribution and relationships to other gold deposit types. *Ore Geology Reviews*, Vol. 13, (April 1998), pp. 7-27, ISSN 0169-1368
- Hall, D.L., Sterner, S.M. & Bodnar, R.J. (1988). Freezing point depression of NaCl-KCl-H₂O solutions. *Economic Geology*, Vol. 83, (February 1988), pp. 197-202, ISSN 0361-0128
- Heinrich, C.A. (2005). The physical and chemical evolution of low-salinity magmatic fluids at the porphyry to epithermal transition. A thermodynamic study. *Mineralium Deposita*, Vol. 39, No. 8, (February 2005), pp. 864-889, ISSN 0026-4598
- Heinrich, C.A. & Eadington, P.J. (1986). Thermodynamic predictions of the hydrothermal chemistry of arsenic, cassiterite-arsenopyrite-base metal sulfide deposits. *Economic Geology*, Vol. 81, No. 3, (May 1986), pp. 511-529, ISSN 0361-0128

- Herrmann, A.G. (1970). Yttrium and Lanthanides. In: Wedepohl, K.H. (Ed.), *Handbook of Geochemistry*, Vol. II/2. Springer-Verlag, Berlin, pp. 57-71. Section 39
- Hofstra, A.H., Levethal, J.S., Northrop, H.R., Landis, G.P., Rye, R.O., Birak, D.J. & Dahl, A.R. (1991). Genesis of sediment-hosted disseminated-gold deposits by fluid mixing and sulfidation. Chemical-reaction-path modeling of ore-depositional processes documented in the Jerritt Canyon district, Nevada. *Geology*, Vol. 19, No. 1, (January 1991), pp. 36-40, ISSN 0091-7613
- Hofstra, A.H., Zhang, X.C., Emsbo, P., Hu, R.Z., Su, W.C., Christiansen, W.D., Fu, S.W. & Theodorakos, P. (2005). Source of ore fluids in Carlintype gold deposits in the Dian-Qian-Gui area and West Qinling belt, P.R. China: Implications for genetic models, in Mao, J.W., and Bierlein, F.P., eds., *Mineral deposits research: Meeting the global challenge: Heidelberg*, Springer-Verlag, Vol. 1, pp. 533-536
- Hofstra, H. & Cline J.S. (2000). Characteristics and models of Carlin-type gold deposits. *Reviews in Economic Geology*, Vol. 13, pp. 163-220, ISSN 07410123
- Hou, Z.L. & Yang, Q.D. (1989). Discussion on metallogenic condition and model for micro-fine disseminated gold ore in the triangle area of Yunnan, Guizhou and Guangxi Province. *Dizhi Zhaokuang Rencong*, Vol. 4, No. 3, pp. 1-13 (in Chinese)
- Huang, K.N. (1986). The petrological and geochemical characteristics and the tectonic setting of the Emeishan basalts in Kangdian craton and adjacent areas. unpub. PhD thesis (in Chinese)
- Hu, R.Z., Su, W.C., Bi, X.W., Tu, G.Z. & Hofstra, A.H. (2002). Geology and geochemistry of Carlin-type gold deposits in China. *Mineralium Deposita*, Vol. 37, No. 3-4, (december 2001), pp. 378-392, ISSN 0026-4598
- Ilchik, R.P. & Barton, M.D. (1997). An amagmatic origin of Carlin-type gold deposit. *Economic Geology*, Vol. 92, No. 3, (May 1997), pp. 269-288, ISSN 0361-0128
- Kesler, S.E., Fortuna, J., Ye, Z.J., Alt, J.C., Zohar, D.P., Borhauer, J. & Chryssoulis, S.L. (2003). Evaluation of the role of sulfidation in deposition of gold, Screamer section of the Betze-Post Carlin-type deposit, Nevada. *Economic Geology*, Vol. 98, No. 6, (September 2003), pp. 1137-1157, ISSN 0361-0128
- Li, W.K., Jiang, X.S., Ju, R.H., Meng, F.Y. & Zhang, S.X. (1989). The geological characteristics and metallogenesis of impregnated gold deposits in southwestern Guizhou, China, In: *Collected Works of Regional Ore-forming Condition of Main Gold Deposit Styles in China, V.6 Southern Guizhou*. Geological Publishing House Beijing, pp.1-86 (in Chinese)
- Liu, J.Z. (2001). The geology of the Yanshang gold deposit, Zhenfeng county, Guizhou. *Guizhou Geology*, Vol. 18, pp. 174-178, ISSN 1000-5943(in Chinese with English abstract)
- Lu, Z.M. (1986). The activation of southwestern bordering of Yangtze paraplatform and the forming of Youjiang Geosyncline. *Geology of Guizhou*, Vol. 3, No. 1, pp. 9-27, ISSN 1000-5943(in Chinese)
- Mei, H.J. (1973). Petrochemical characteristics of two deep-derived trap in southwestern China and its relationship with iron and nickel mineralization. *Geochemica*, Vol. 1, No. 4, pp. 219-253(in Chinese)
- Pettke, T., Diamond, L.W. & Kramers, J.D. (2000). Mesothermal gold lodes in the north-western Alps: A review of genetic constraints from radiogenic isotopes. *European*

- Journal of Mineralogy, Vol. 12, No. 1, (January,February 2000), pp. 213–230, ISSN 0935-1221.
- Pokrovski, G.S., Kara, S. & Roux, J. (2002). Stability and solubility of arsenopyrite, FeAsS, in crustal fluids. *Geochimica et Cosmochimica Acta*, Vol. 66, No. 13, (July 2002), pp. 2361-2378, ISSN 0016- 7037
- Radtke, A.S., Rye, R.O. & Dickson, F.W. (1980). Geology and stable isotope studies of the Carlin gold deposit, Nevada. *Economic Geology*, Vol. 75, No. 5, (August 1980), pp. 641-672, ISSN 0361-0128.
- Ressel, M.W., Noble, D.C., Henry, C.D. & Trundel, W.S. (2000). Dikehosted ores of the Beast deposit and importance of Eocene magmatism in gold mineralization of Carlin trend. *Economic Geology*, Vol. 95, No. 7, (November 2000), pp. 1417–1444, ISSN 0361-0128
- Ridley, J.R. & Diamond, L.W. (2000). Fluid chemistry of orogenic lode gold deposits and implications for genetic models. *Reviews in Economic Geology*, Vol. 13, pp. 141–162, ISSN 0361-0128
- Seward, T.M. (1973) Thio-complexes of gold in hydrothermal ore solutions. *Geochimica et Cosmochimica Acta*, Vol. 37, No. 3, (March 1973), pp. 379–399,ISSN 0016-7037
- Sterner, S.M., Hall, D.L. & Bodnar, R.J. (1988). Synthetic fluid inclusions, V. Solubility relations in the system NaCl-KCl-H₂O under vapor-saturated conditions. *Geochimica et Cosmochimica Acta*, Vol. 52, No. 5, (May 1988), pp. 989–1005, ISSN 0016-7037
- Sun S.-S. & McDonough W.F. (1989). Chemical and isotopic systematics of oceanic basalts: Implication for the mantle composition and process. In *Magmatism in the Ocean Basins* (eds. Saunder A.D. and Norry M.J). Geological Society of London Special Publication, London, Vol. 42, pp. 313–345
- Su, W.C., Hu, R.Z., Xia, B., Xia, Y. & Liu, Y.-P. (2009). Calcite Sm-Nd isochron age of the Shuiyindong Carlin-type gold deposit, Guizhou, China. *Chemical Geology*, Vol. 258, No. 3-4, (January 2009), pp. 269–274, ISSN 0009-2541
- Su,W.C., Xia, B., Zhang, H.T., Zhang, X.C. & Hu, R.Z. (2008). Visible gold in arsenian pyrite at the Shuiyindong Carlin-type gold deposit. Guizhou, China: implications for the environment and processes of ore formation. *Ore Geology Reviews* , Vol. 33, No. 3-4, (June 2008), pp. 667–679, ISSN 0169-1368
- Su,W.C., Heinrich, C.A., Pettke, T., Zhang, X.C., Hu, H.R., Xia, B., (2009). Sediment-hosted gold deposits in Guizhou, China: products of wallrock sulfidation by deep crustal fluids. *Economic Geology*, Vol. 104, pp. 73–93, ISSN 0361-0128
- Su W.C, Zhang H.S, Xia B, Zhang X.C, Hu R.Z, Zhou G.F. & Xia Y. (2006). The first discovery of sub-micro and micro visible native gold grains in the Shuiyindong Carlin-type gold deposit in Guizhou. *Acta Mineralogica Sinica*, Vol. 26, No. 3, (September 2006), pp. 257–260, ISSN 1000- 4734(in Chinese with English abstract)
- Tao, C.G., Liu, J.S. & Dan, G. (1987). On the gold ore deposit geological characteristics and genesis of Yata, Ceheng. *Geology of Guizhou*, Vol. 4, No. 2, pp. 135-150, ISSN 1000-5943(in Chinese)
- Takenouchi, S. & Kennedy, A.C. (1964). The binary system H₂O-CO₂ at high temperatures and pressures. *American Journal of Science*, Vol. 262, (November 1964), pp. 1055–1074, ISSN 0002 -9599

- Tödheide, K. & Franck, E.U. (1963). Das Zweiphasengebiet und die kritische Kurve im System Kohlendioxid-Wasser bis zu Drucken von 3500 bar. *Zeitschrift für Physikalische Chemie Neue Folge*, Vol. 37, pp. 387–401
- Tretbar, D.R., Arehart, G.B., Christensen, J.N. (2000). Dating gold deposition in a Carlin-type gold deposit using Rb/Sr methods on the mineral galkhaite. *Geology*, Vol. 28, No. 10, (October 2000), pp. 947–950, ISSN 0091-7613
- Wang, Y.G., Suo, S.T. & Zhang, M.-F. (1994). Tectonics and Carlin-Type gold deposits in southwestern Guizhou. Geological Publishing House Beijing, pp. 115 (in Chinese)
- Wang, Y.G., Wang, L.T., Zhang, M.F. & Wang, L.L. (1995). Texture of the Upper crust and pattern of the disseminated gold deposits distributed in Nanpanjiang area. *Guizhou Geology*, Vol. 12, No. 2, pp. 91–183, ISSN 1000-5943 (in Chinese with English abs.)
- Xia Y. (2005). Study on the Metallogenic Characteristics and Gold Abnormal Enrichment Mechanism of the Shuiyindong Gold Deposit at Zhenfeng, Guizhou. Doctoral Dissertation of Post-graduate School of the Chinese Academy of Sciences
- Yang, K.W. (1992). A preliminary discussion on the genesis of Getang gold deposit and its prospecting significance. *Guizhou Geology*, Vol. 9, No. 4, pp. 299–305, ISSN 1000-5943 (in Chinese)
- Yang, K.Y., Chen, F., Mei, H.J., Yang, K.W., Su, W.C., Zhang, X.C., Chen, S.M. & Feng, X.X. (1992). The investigation of ore-forming conditions and exploration for micro-grained disseminated gold deposits in southwestern Guizhou. Unpub. report of IGCAS Guiyang, pp. 96 (in Chinese)
- Ye, X.X., Wan, G.Q., Sun, Z.-Y., Liu, Y.-K., Zhou, L.-D., Liu, S.-R., Xue, D.-J., Rivers, L. & Jones, K.W. (1994). Microbeam analysis of gold in Carlin-type gold deposits, southwestern Guizhou, China. *Science in China (series B)*, Vol. 24, No. 8, pp. 883–889, ISSN 1674-7224 (in Chinese)
- Zhang, J., Lu, X.B., Yang, F.Q., Liao, Q.A., Wang, P., Wang, K.Y., Zhang, X.J., Wang, Q.W., Wang, H.M., Chen, K.L. & Fu, S.H. (2002). *Geology of Gold Deposits in Northwest China and Metallogenic Prognosis*. Chinese University of Geology Press, Wuhan
- Zhang, X.C., Spiro, B., Halls, C., Stanley, C. & Yang, K.Y. (2003). Sediment-hosted disseminated gold deposits in southwest Guizhou, PRC: Their geological setting and origin in relation to mineralogical, fluid inclusion, and stable-isotope characteristics. *International Geology Review*, Vol. 45, No. 5, pp. 407–470
- Zang Yu, Xia Yong, Su Wenchao, Tao Yan, Zhang Xingchun, Liu Jianzhong & Deng Yiming. (2010). Metallogenic model and prognosis of the Shuiyindong super-large strata-bound Carlin-type gold deposit, southwestern Guizhou Province, China. *Chinese Journal of Geochemistry*, Vol. 29, (June 2010), pp. 157–166, ISSN 1000-9426.
- Zhang Yu, Xia Yong, Wang Zepeng, Yan Baowen, Fu Zhikang & Chen Ming. REE and stable isotope geochemical characteristics of Bojitian gold deposit, Guizhou Province. *Earth Science Frontiers*, Vol. 17, No. 2, (March 2010), pp. 385–395, ISSN 1005-2321. (in Chinese with English abstract)

Behaviors of Mantle Fluid During Mineralizing Processes

Liu Xianfan, Li Chunhui, Zhao Fufeng, Tao Zhuan,
Lu Qiuxia and Song Xiangfeng
*Chengdu University of Technology
People's Republic of China*

1. Introduction

In this chapter detailed discussions are given about the behavior of mantle fluid during mineralizing process. Several topics are covered to make it clear and comprehensible, which include its definition, evolvments and the contributions to mineralizing or ore forming process.

Former studies show that mantle metasomatism is universal among mantle xenoliths and related rocks. Metasomatism processes always are caused by some kind of fluid, mantle metasomatism included. However, the relationship between mantle fluid and mineralizing process is amphibious. So, in the first place it is really needed to make it clear what mantle fluid is and what mantle fluid metasomatism is, any difference between mantle metasomatism and mantle fluid metasomatism. The nature of the mantle fluid is a key window to look into its contributions to ore forming process.

Another question followed is the difference between mantle fluid and magmatic fluid. Luo et al., (2006, 2007a, 2007b and 2008) put forward a metallogenic theory on the transmagmatic fluids and classify the relationship between metallogenic fluid and atransmagmatic fluid in to three kinds. What we suggest is that mantle fluid is one of the most important transmagmatic fluids. His thoughts make up of our theoretic foundation.

2. Concepts of mantle fluid metasomatism

Studies show that the elevation of temperature and changes of oxygen fugacity drive the degas process of mantle (C and H₂ et al.) (Spera, 1987). Water in the mantle was mainly brought in during the process of ocean crust-underthrustion, as well as the normal elements and volatile (Peacock,1990; Philippot,1991; Su Genli et al.,1998). Mixture of mantle gas exhaustion and water dissolving CH₄ and CO₂ formed a mantle fluid, which was a supercritical fluid being of great ability of abstraction and transportation. The fluid, which led to the richment of high temperature silicate-alkali-volatile and ore-elements, was named as mantle ichors by Du (1998), who emphasized volatile, thermal and alkali in the fluid and regarded the mantle fluid metasomatism as one kind of alkali metasomatism; Shmulovich et al., (1998) treated the fluid as a system of supercritical volatile (mantle CO₂, chnoricitles and

deep water) and enriching in recycling original compositions in crust; Cao Ronglong et al (1995) reckoned that is rich in primal earth inner gases (such as ^3He and ^{36}Ar) and volatiles (such as mantle CO_2 , meteorolite S, deep seated H_2O et al) which form alkali-rich silicate melt. Liu et al., (2004) recognizes that the mantle C-H-O fluid is a high temperature-density supercritical fluid with volatile of H_2O and CO_2 , as well as Cl, F, S and P, being capable of dissolution huge amount of rare and normal elements. Trough experiments, Schracder et al (1994) found that mantle fluid various, it could be melt (e.g. carbonatite melt) or water-rich fluid.

Sun et al., (1995) thought that there are two fluid reservoirs in the upper mantle. The one is at the depth of 300 km-66 km. In where, a great amount of K_2O , SiO_2 and Al_2O_3 are dissolved and in equilibrium with phlogopite peridotite phase, and the fluid appears as a persalic property. The other locates between 53km and the M-boundary. In where, there are of little solutions but rich in Na and alkali and in equilibrium with amphibole peridotite. The patent metasomatism characteristic of Na-rich alkali mantle fluid metasomatism is expressed by the replaced minerals assembly of domain hornblende concomitant with interstitial phlogopite.

Based on the analysis above, Sun et al., (1995) summarizes the relationship between the mantle metasomatism and in-contencial metallogenism and its significance.

1. In favor of the formation of diamond-bearing kimberlita and lamprey.
2. Transport mantle-derived ore-elements into crust to enrichment.
3. Reconstruct crustal material and activate, transport and enrich ore-elements.
4. Provide with plenty of silicate and alkali for the hydrothermal deposits.
5. Cause high geothermal gradient to accelerate the mixing between deep recycle of ground water and mantle-crust-derived until the formation of low temperature hydrothermal deposits.

Yu Xuehui et al., (1995, 2006) suggested that mantle fluid process is connected with the mantle magma process, and alkali-rich magma originates from Enriched mantle where mantle fluid process developed; during alkali-rich magma crystallization, mantle fluid metasomatise alkali-rich porphyry and xenoliths in it (Liu Xianfan et al., 2006a; 2009). Xie Rongjv(1998) discovered that mantle fluid is able to escape from the magmatic rocks, flow along the deep faults and rifts to replace the wallrocks and form ore deposits in suitable spaces. This brings on a high temperature→low temperature mineralizing processes from magmatic rocks to wall rocks (Liu X F et al., 2002).

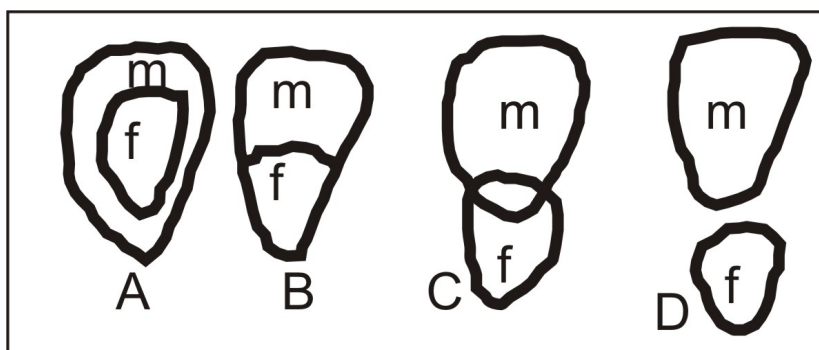
From the above all, we could conclude that the mantle fluid is a ligamerment among deep process, fluid and telescoped mineralization. Referencing to other scholars' views (including Zhu (1998)), we can conclude that generalized mantle fluid process is a synthetic impact for mantle-derived melt, supercritical fluid and the thermal from the melt or the fluid's evolution. This process can be documented as follows:

1. Mantle metasomatism is defined as a metasomatism which occurs within the mantle accompanying the mantle gas exhaustion. During the formation of enrichment mantle, alkali magma was formed and the stronger the metasomatism, the more alkali.
2. Mantle fluid metasomatism is defined as a metasomatism in the ascent of fluid from enriched mantle. The mantle fluid could be contained in the alkali-rich magma and

move synchronically. And it is possible to depart from the magma and move independently. In this process, the characteristics of the mantle fluid change from melt→supercritical fluid→liquid, company with the change of depth and environment corresponding with the changes of physical and chemical condition. It could carry, activate and enrich ore-material into suitable place, accelerate the crust-mantle material overprinting mineralization , and be in favor of deep ore-forming and large-super large deposit. Company with the formation of alkali-rich magma, the original mantle evolved from impoverished to enhancement (Liu X F et al., 2006). The process resulted in the enrichment of LILE (large ion lithophile elements), HFSE (high field strength elements) and some ore-elements, and prepared materials base for the mantle fluid metasomatic mineralization.

3. Deep fluid metallization and its relation to magma

Existing studies show that fluid is vital to metallogenesis, especially endogenesis metal deposits (Luo Z H et al., 2007; Mao J W et al., 2005 and Yang L et al., 2001). Yang et al. reckon that deep fluid is what comes from the under-base of basins, including mantle fluid and deep crust fluid, while Luo et al., (2007) recognize the fluid as transmagmatic fluid, in particular to metallogenic fluid, could be independent from magmatic fluid, and classifies the relationship between metallogenic fluid and magmatic fluid in to three kinds (Fig.1).



m-magmatic system; f- metallogenic fluid system (from Luo et al.,2007a)

Fig. 1. Evolution sketch map of transmagmatic fluid metallogenic system

1. If the magmatic system and metallogenic fluid system move synchronically, and cool as rapidly as possible, major of the latter will be preserved in the former , then orthomagmatic deposits are formed inside the magmatic body, constituting an orthomagmatic metallogenic system (Fig.1 A and B) .
2. If the magma emplaces deeply to some extent, the rate of consolidation will be slow. Then the most metallogenic fluid may overflow to contact zones, forming contact deposit and constituting a contact metallogenic system. (Fig.1 C) .
3. If the magma emplaces shallower, as well as the volatile is abundant and circulation conditions are well provided, the metallogenic fluid may escape from the magmatic body, and move along passageway for ore fluid to the space which is in favor of mineral enrichment, such as secondary fractures or rock interface, forming

high→middle→low temperature hydrothermal deposits and constituting a long-distance hydrothermal metallogenic system (Fig.1 D) .

Therefore , magma could be the media to schlep metallogenic fluid ascending, while deep metallogenic fluid may push magma upward. This is because of that , on the one hand, the fluid dilates the magma and enlarge its bulk with a bigger buoyancy; on the other hand, with the pressure upward, volumetric expansion of fluid makes a push power to the magma.

- Scoates and Michell (2000) take the independent metallogenic fluid system and unmixing magma or fluid injecting into the felsic magma as a kind of deep fluid. However , what this independent metallogenic fluid system is? Magma fluid, crust fluid, thermal fluid or mantle fluid?. Most previous studies are strong in geochemical analysis and theoretical derivation, but weak in providing petrographical evidences. It is the complexity of the mantle fluid that makes it hard to learn what its true color is, and then many researches slide over the significance of mantle fluid unintentionally or deliberately and reckon them generally as deep fluid.
- Studies suggest that there are plentiful deep fluid under the Qinghai-Tibet Plateau (Huang W C et al., 2000 and Unsworth M J et al., 2005). The $^3\text{He}/^4\text{He}$ proved that main body of the Tibet Plateau is influenced by the iacking of the asthenosphere material flow, and the contribution of the mantle fluid can not be ignored; and the Cenozoic magmatism and metallogenesis are both controlled by the Indian- Eurasian continental collision, delamination and large Strike-slip faults. It is obviously that polymetallic mineralization in the Sanjiang- Tethy orogen and mantle fluid are closely related

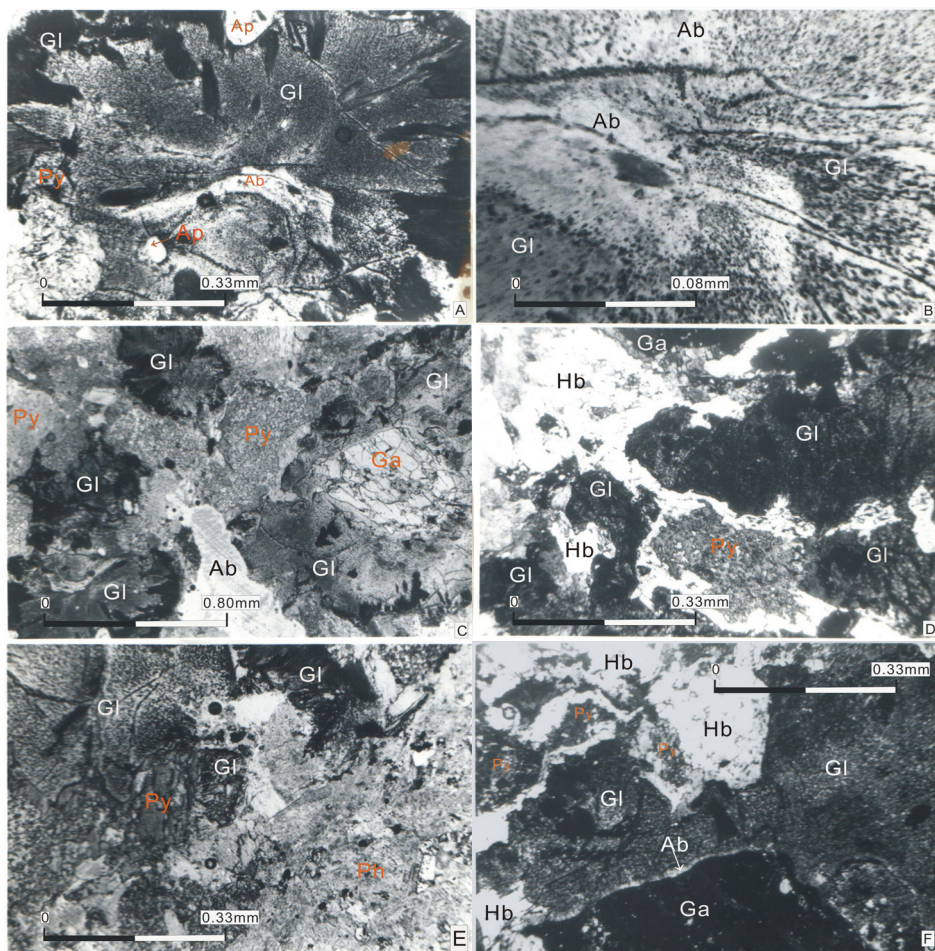
Apparently, alkali-rich prophyries and their deep xenoliths are assumed to have a close relationship to the deep fluid, especially the mantle fluid. Xenoliths are usually classified into two catagories. The one is called accidental inclusion, and the other is cognate xenolith resulting from unmixing process of different magmas or fluids, such as femic magma and felsic magma Physical process of magma or fluid unmixing is expressed as following (Luo Z H et al., 2007).

1. the viscosity of mafic magma is always lower than felsic magma.
2. as temperature reduction during magma migration, viscosity of mafic magma becomes higher than felsic magma due to femic magma crystallization early.
3. Mafic magma crystallize earlier than felsic magma results in the formation of accidental xenoliths or inclusions, especially when emperature variation is remarkable or felsic magma accounts for a larger proportion.

4. Actual traces of mantle fluid process and its compositions characteristics

4.1 Na-rich microlite-glass in deep mafic xenoliths

A kind of Na-rich glass in the ablitization garnet-phlogopite pyroxenite from aegerine syenite porphyry was discussed at Liuhe, western Yunnan province. Under the microscope, the Na-rich glasses are shown as microlite and embryonic crystal. Its color changes with the compositions from light gray to light black. Light black microlite glasses appear as arcauate, pitting, linear, and radical or sheet along the margin (Fig.2A-B). Light gray-white microlite glasses penetrate or round the pyroxene and garnet in veins or interpartical infilling of various shapes and sizes(Fig.2C-D). Most margins of white microlite glasses are straight or irregular,



A. In the process of transformation of Na-rich glass into microlite, iron (black), along which an edge was formed irregularly distributed consisting of infinitely small granular microlite-glass. Apatite (Ap) was include in Na-rich glass (Gl). (-) 10×4

B. In the process of transformation of Na-rich glass (Gl) into microlite, iron (black) and micro-albite (Ab) (grayish-white) released from Na-glass and highly irregularly distributed in worm-like, ring or more or less oriented fluid patterns. (-) 10×16

C. Na-rich glass (Gl) in irregular veinlets in interstices among pyroxene (Py) and garnet (Ga) and albite (Ab). (-) $\times 15$

D. Na-rich glass (Gl) in irregular veinlets in interstices between pyroxene (Py) and garnet (Ga); amphiboles (Hb) enclosing pyroxene (Py) and glass veinlets. (+) 10×4

E. The veinlet-like Na-rich glass (Gl) in the xenoliths does not extend beyond the contact between the xenoliths and the host rock (Ph) (Aegirinite-augite orthophyre in photograph of below-right -angle). (-) 10×4

F. Na-rich glass (Gl) in irregular veinlets in interstices among pyroxene (Py) and garnet (Ga); microlites albite (Ab) in the glass is in a circular fingers around garnet (Ga) (in extinction); Amphibolites (Hb) enclosing pyroxene (Py). (+) 10×4 . (Note: (+): crossed nicols; (-): plainlight).

Fig. 2. Microscope characters of Na-rich microlite-glass from albitized garnet-mica-pyroxenite

and account for 18% of the total volume of the xenolith, 8% of which has crystallized into albite. Microlite glasses, penetrating the xenoliths in veins, interrupt the contact surface of xenoliths and host rocks (aegerine syenite porphyry) (Fig.2E), indicating that microlite glasses formed before alkali-rich porphyry and after xenoliths. Under the electric microprobe, microlites are mainly acicular rimmed garnets (Fig.2F) or dispersed embryonic albites (Fig.2B,E,F); hornblende appears as the rim of pyroxene and veined glass (Fig.2D,F), and ilmenite, magnetite and rutile are distributed sporadically in black microlite glasses.

The main chemical compositions of Na-rich glass as shown in the table 1, include high SiO₂ (39%-65%), Al₂O₃ (14%-21%), Na₂O (7%-16%) and FeO (2%-23%), with low K₂O(0.1%-1.0%), CaO (1%-5%) and MgO (0.2%-6%). It is anisotropic that light gray glass shows high Si and low Fe (compared among samples), as well as high Ca and low Mg (compared among samples). This is in contrast to the dark gray glass. Further more, from light gray glass to dark gray glass, EMPA total amount increases, indicating that volatility is gradually lost in the involution of Na-rich glass.

- Now, it is believed that there are three possible origins of glass in xenoliths (Girod M et al., 1981 and Jones A P et al., 1983).
 1. from the fractional melt of basaltic magma.
 2. from the escaping melt of rapidly ascending xenoliths (Rong J S et al., 1995)
 3. from upper mantle fluid (melt or segregate melt) which injects the alkaline magma derived from enrichment mantle.

From the comparison between table 1 and table 2, we can see there is an obvious difference of chemical composition between the Na-rich glass and basalt, aegerine syenite porphyry, albite garnet anthrophyllite pyroxenite, and the host rocks. So, there is hardly a possibility that Na-rich glass derives from the rock-forming minerals of host rocks; in particular to the markable difference from the pyroxene, mica and garnet, and a similarity to the albite, especially the light gray Na-rich glass's SiO₂ is lower than albite, while FeO is higher than it. Enrichment of SiO₂ and impoverishment of FeO from the black→dark gray→light color microlite glass→albite indicates that formation of crystallized albite in garnet-anthrophyllite pyroxenite goes with the Si-Fe segregation from the Na-rich glass. At the end of Si, albite crystallized. At the end of Fe, magnetite, ilmenite and rutile crystallized. EMPA shows that segregates and concentrates of TiO₂ going with the one of Fe. From the analysis above, we could conclude that Na-rich glass derives from upper mantle fluid with the natures of melt, volatile-saturated and low solidus temperature before the alkali-magma captures xenoliths. With the transportation of upper-mantle fluid, the rapid changes of temperature and pressure of the environment led to a sharp increase of solidus temperature driving the formation of glass before it has time to crystallize. During this process, material differentiation within the fluid or between the fluid and magma led to the formation of Na-rich glass behaving as high Si, Al, Na, Fe and low K, Ca Mg, Ti. The evolution includes early Na-metasomatism and late K-metasomatism going with the crystallization of albite, results in the formation of rimmed hornblende between the pyroxene and microlite glass (Fig.2D,F). The result indicates the diversity and polystage of the upper-mantle fluid evolution going with the change of the fluid's chemical compositions. There are differences of chemical compositions of Na-rich glass because of varying areas, bodies and occurrence contrasting to publishing data (Francis D M et al., 1976, Maaloe S et al., 1979, Girod M et al., 1981, Jones A P et al., 1983, Zheng H F et al., 1987 and Lin C Y et al., 1994). Generally speaking, magma

originating directly from the upper-mantle is alkali-rich, such as Na-rich (Girod M et al., 1981), K-rich or Na-K-rich. Composition of glasses derived from mantle xenoliths depends on melt rocks and minerals, not ensuring high alkali content (Maaloe S et al., 1979 and Zheng H F et al., 1987). High Na content of microlite glasses in the xenolith from Liuhe may be an important sign of mantle origin. Recently, experiments prove that it is possible that alkali-rich fluid exits in the upper mantle (Schneider M E et al., 1986). Domestic researches on fluid inclusions from mantle xenoliths also proved that upper mantle metasomatic fluid is marked by being rich in volatile (H_2O or CO_2) and alkaline(Na_2O or K_2O).

	color	SiO ₂	TiO ₂	Al ₂ O ₃	CaO	MgO	MnO	Na ₂ O	K ₂ O	Cr ₂ O ₃	FeO	Total
1	white	61.62	0.04	19.89	2.06	0.85	0.05	8.42	0.86	0.01	2.74	96.52
2	white	62.48	0.04	20.77	2.93	1.03	0.10	8.38	0.34	0	1.29	96.82
3	white	59.16	0.02	23.68	1.14	1.69	0.18	9.50	0.96	0	2.12	98.45
4	white	62.96	0.58	17.77	5.20	0.20	0.11	8.13	0.09	0.03	2.42	97.49
5	white	61.92	0.05	18.44	2.11	0.72	0	8.68	0.29	0.02	3.15	95.37
6	white	60.85	0.09	19.31	3.87	1.95	0.08	7.53	0.47	0	3.78	97.93
7	darkgray	47.88	0.79	17.96	5.08	0.39	0.04	16.39	0.14	0.06	7.04	95.76
8	darkgray	57.11	0.02	20.71	1.21	0.33	0.01	13.61	0.20	0.01	2.64	95.85
9	darkgray	65.35	0.23	18.16	2.57	0	0.15	8.42	0.20	0	3.37	98.45
10	darkgray	59.74	0.42	19.78	2.98	0.39	0	9.76	0.07	0.03	6.75	99.96
11	darkgray	62.62	0.18	18.85	2.79	1.57	0.13	8.79	0.38	0.02	3.43	98.76
12	black	38.84	0.10	13.96	5.49	6.65	0.29	10.23	0.49	0	23.19	99.24
13	black	48.68	0.18	17.85	4.66	5.51	0	6.59	0.53	0.04	13.91	97.95
14	black	51.51	0.08	15.69	1.00	1.77	0	9.53	1.23	0.02	18.04	98.86
15	black	49.74	0.13	14.86	2.15	3.32	0.12	8.15	1.16	0	19.61	99.24
16	black	46.82	0.16	17.23	2.87	3.53	0.22	8.82	1.91	0.07	18.15	99.78

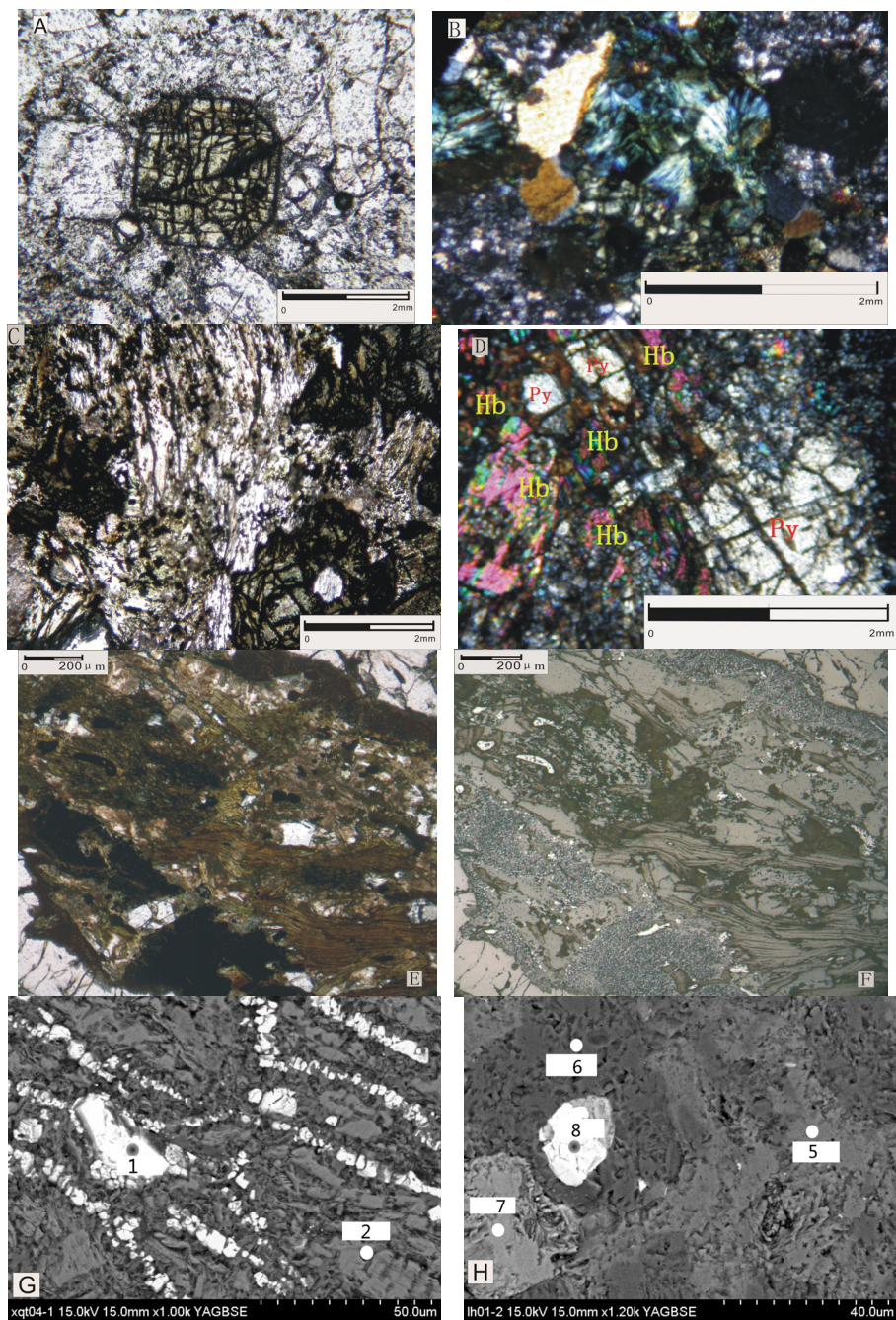
Table 1. Chemical composition of the Na-rich glass in deep xenoliths from Liuhe ($\omega_B/\%$)

Rocks	Mineral	SiO ₂	TiO ₂	Al ₂ O ₃	CaO	MgO	MnO	Na ₂ O	K ₂ O	FeO	Fe ₂ O ₃	Total
Aegirine orthophyre	bulk	58.04	0.62	16.39	4.50	2.20	0.10	3.53	5.30	2.01	2.59	95.28 ^(a)
Basalt (Yunnan)	bulk	52.74	1.73	12.22	7.36	5.47	-	2.84	1.63	11.99	4.27	100.25
	bulk	43.13	2.13	15.90	10.80	5.50	0.35	2.42	0.97	9.17	5.43	95.80 ^(a)
Albitization garnet	(5) pyroxene	51.13	0.32	2.04	24.10	12.32	0.12	0.58	0.03		9.59	100.24
phlogopite	(3) phlogopite	34.65	3.62	15.80	0.06	15.86	0.26	0.70	8.69		15.62	95.26 ^(a)
pyroenite (xenolith)	(2) garnet	38.28	0.16	20.89	8.36	5.48	2.38	0.09	0.01		24.19	99.84
	(4) albite	66.80	0.01	20.19	0.93	0.02	0.04	11.53	0.12		0.21	99.85

Table 2. Chemical composition of host rock and rock-forming mineral in xenoliths

4.2 Alkali-rich porphyry and Fe-rich glass in xenoliths

Petrographic studies show that Fe-rich glasses inject, penetrate or envelope the minerals along the intergranular or cleavage crack (Fig.3A-D). Those opaque materials under transmitted microscope were simply treated as charcoal, ferrum or dissemination of metallic minerals. EMPA, scanning electron microscope and energy spectrum studies affirm this kind of Fe-rich glasses being made up of nonmetal minerals such as microlite silicate and



A. Egyrinaugite in the aegyrine syenite porphyry from Jinhe intrusive body, with cleavage cracks of aegyrine full of Fe-rich glass (-).

- B. Eyrinaugite in the aegirine syenite porphyry from Xiaoqiaotou intrusive body, with partly developed chloritization and silicatization, Fe-rich glass are found all over the phenocrysts and quasi-matrix. (+)
- C. Hornblende in xenoliths from Xiaoqiaotou intrusive body is replaced by epidote and chlorite or uralite, Fe-rich glass are of reticulate or star-spot distribution. (-)
- D. Amphibole(Hb) replacing pyroxene(Py), and Fe-rich glass existent as disseminated replacement in xenoliths from Jinhe intrusive body. (+)
- E. (Plainlight under transmission condition) and
- F. (Plainlight under reflex condition), twain maps' field of view is same. F. Wrapped margin of Fe-rich glass at garnet(Ga) from xenoliths in Liuhe aegirine syenite porphyries, and biolite, especially hornblende is replaced disseminately by Fe-rich glass. The phenomena of disport dissolve (or: differentiation by liquation) between metal and nonmetal is expressed by plainlight under reflex condition in Fe-rich glass.
- G. Specularite(white) and silicate(dimgrey) unmixing intergrowth texture in Fe-rich glass from Xiaoqiao xenoliths is expressed by back scattered electrons, graph of SEM. H. Specularite(white) and quartz and silicate(dimgrey) unmixing intergrowth texture in Fe-rich glass from Liuhe xenoliths is expressed by back scattered electrons graph of SEM (Scanning Electronic Microscopy). (Label point at Fig.G and Fig.H are corresponding with the data of Table4)

Fig. 3. Microscope characteristics of Fe-rich glass in the alkali-rich porphyries and xenoliths from western Yunnan

quartz. The phenomena of liquating or unmixing intercrescence texture (Fig.3E, F) for fine metal metariel in disseminatedly and microlite nonmetal mineral were observed (under the condition of high-power reflected light of polarizing microscope). In the Fe-rich glasses, especially, we found mantle typomorphic minerals such as moissanite, native iron, ilmenite, titanium iron glance et al., and exceed microlite liquating or unmixing intercrescence texture (Fig.3G and H, table3 and 4) to be made up of mantle typomorphic minerals and rock-forming minerals-silicate and quartz.

We could get the characteristics and rules from Figure 4, table 3 and table 4:

1. Figure.3A-F exhibit the basic matter phases and characters for rock-forming minerals and Fe-rich glasses penetrating the alkali-rich porphyry and xenoliths. Fluid metasomatism (alteration) between the host rocks and xenoliths held a close association with the Fe-rich glasses. The metasomatic alteration expressed as a retrograde reaction in order of pyroxeney→amphibole→biotite→chlorite, at the same time resulting in siliconizing. Therefore, the Fe-rich glasses were an important power and material provider to the alteration of alkali-rich porphyry and xenoliths.
2. Figure.3G and H represent two different parts for Fe-rich glasses under the scanning electric microscope back distribution scatter, the white part constitution of microlite minerals of heavy elements while the black part of the less heavy elements. Their compositions are determined by the electric microprobe and energy spectrum (table 3 and 4), the white part is various compositions metallic mineral microlite, and the black part is nonmetal microlite, such as silicate and quartz. So the Fe-rich glasses, as black opaque material under transmitted microscope, is a microlite solid. Its composition is mainly of nonmetallic minerals-silicate and quartz, and contains some special metallic minerals.
3. What should be give great attention is the date of measuring point 5,9 and 10 in table 3. Total weight of some mineral in Fe-rich glass of alteration pyroxenite xenoliths is obviously over 100%. The existence of dominating element compound. SiO_2 is

Point	alkali-rich porphyry	Xenoliths	SiO ₂	TiO ₂	Al ₂ O ₃	FeO	MnO	MgO	CaO	Na ₂ O	K ₂ O	Cr ₂ O ₃	Total	Mineral
1	Xiaoqiaotou	alteration amphibolite	33.81	0.20	21.95	14.29	0.39	14.30	0.03	0.16	9.78	0.03	94.59	alike biotite
2		banded migmatite	63.19	0.02	20.59	0.37	0.02	0.09	4.29	9.20	0.64	0.02	98.43	alike albite
3		alteration biotite garnet gabbro	55.26	0.04	26.88	0.90	0.02	0.02	9.63	5.95	0.26	0.01	98.96	alike labradorite
4		alteration biotite garnet gabbro	50.21	0.07	3.05	23.59	0.44	22.66	0.32	0.06	-	0.29	100.68	hypersthene
5		amphibolization gabbro	156.36	0.004	0.19	0.39	0.02	0.04	0.15	0.02	0.01	0.01	157.19	moissanite
6	Jinhe	alteration biotite pyroxenite	37.97	3.38	12.92	6.03	0.04	21.90	0.01	0.43	12.94	1.01	96.63	magnesian biotite
7		alteration biotite gabbro	91.89	0.05	4.16	0.13	0.00	0.05	0.23	1.26	2.25	-	100.02	quartz
8		alteration biotite gabbro	51.31	0.34	1.50	8.64	0.52	14.42	22.13	0.78	0.01	0.01	99.66	clinopyroxene
9		alteration biotite pyroxenite	1.05	0.05	0.10	99.97	0.96	0.02	0.11	-	0.26	27.86	130.38	chromium-bearing ferrite
		Fe, Cr				77.71						19.06	96.77	
10	Lituhe	alteration biotite pyroxenite	3.80	0.17	0.78	87.07	0.70	0.16	0.49	0.08	1.25	24.47	118.97	chromium-bearing ferrite
		Fe, Cr				67.68						16.74	84.42	
		alteration biotite gabbro	0.27	9.77	1.18	81.41	0.52	0.85	-	0.02	-	0.21	94.23	titaniferous specularite
11		alteration peridot gabbro	0.03	4.99	0.57	81.63	1.05	2.15	-	0.03	0.01	0.17	100.25	
		Fe ₂ O ₃		9.77		90.48							90.63	
12	Lituhe	alteration peridot gabbro	0.03	4.99	0.57	81.63	1.05	2.15	-	0.03	0.01	0.17	90.63	titaniferous specularite
		Fe ₂ O ₃		4.99		90.72							95.71	
		alteration diabase	59.83	0.03	23.81	0.64	-	0.06	4.87	10.03	0.38	0.02	99.68	alike albite
14		alteration garnet biotite	39.45	0.09	9.84	30.06	0.20	12.42	0.84	0.36	0.38	0.05	93.69	alike chlorite
15		alteration biotite pyroxenite	54.19	0.17	4.53	2.47	0.03	13.82	15.91	2.24	0.12	0.24	93.71	alike amphibole
16	alteration garnet biotite	0.01	78.96	0.11	18.71	0.10	1.65	0.05	0.03	-	0.06	99.65	ilmenite	

Table 3. EMA of Fe-rich glass in deep xenoliths from alkali-rich porphyries

Point	Alkali-rich porphyry	Xenolith	Si	Al	Fe	Mg	Ca	Na	K	O	Total	Mineral	Note
1	Xiaoqiaotou	alteration amphibolite			65.09					34.91	100	specularite	Corresponding to Fig.4G
2		alteration amphibolite	16.52	10.55	9.05	7.85			6.80	49.23	100	alike biotite	Corresponding to Fig.4G
3		alteration biotite pyroxenite		3.53	53.51	2.55				40.40	99.99	specularite	
4	Jinhe	alteration biotite pyroxenite	23.16	13.50			6.52	4.22		52.60	100	alike plagioclase	
5		alteration garnet pyroxenite	29.26	9.19					12.47	49.08	100	K-feldsparoid	
6	Liuhe	alteration garnet pyroxenite	44.61							55.39	100	Quartz	
7		alteration garnet pyroxenite	23.93	1.12	7.44	6.13	14.18	0.98		46.22	100	alike amphibole	Corresponding to Fig.4H
8		alteration garnet pyroxenite				70.26				29.74	100	specularite	

Table 4. Energy spectrum analyses of Fe-rich glass in deep xenoliths from alkali-rich porphyry and zircon. All of these further prove that Fe-rich melt xenoliths are of mantle characteristics.

expressed as measuring point 5 in table 3, other compositions content to neglect. The result suggests principal part of silicon, which atom mass fraction at 73.13%, in the matter. Apparently, the matter could not be simple substance silicon but exist undetected missing material. Based on the most common simple silicide under deep circumstance, we may presume the missing material to be C. By the way of calculating the proportion of SiC, we get that C atom mass fraction at 31.23%, and both (Si and C) total weight percentage at 104.36%. The data is near to the standard total weight percentage (100%). Therefore, microlite mineral of measuring point 5 should be carborundum. Microlite mineral of measuring point 9 and 10 in table 3 may be Fe-Cr alloy or chrome native iron. By conversion, we get the each weight percentage of atomic iron (77.71% and 67.08%) and corresponding weight percentage of atomic chrome (19.06% and 16.74%). Hereby, corresponding total weight percentage (96.7% and 84.42%) is near to the standard total weight. Due to atomic weight similarities of Fe and Cr, iron-chrome alloy could not match the data above. Therefore, microlite mineral of measuring point 9 and 10 should be chrome-bearing native iron. Chrome is isomorphism element in native iron.

4. as shown data of measuring point 11 and 12 in table 3, there are still titanium iron-oxide in Fe-rich glass. FeO conversion of according to Fe_2O_3 based on weight percentage of atom, we get the total weight percentage of Fe_2O_3 and TiO_2 reaches almost 100%. So the microlite mineral should be titanium-bearing specularite. Titanium is isomorphism element in specularite. Standard ilmenite (point 16 in table 3) is detected in alteration garnet diopsidite in Liuhe rock-body, referring to the existence of chrome native iron and titanium specularite, we could conclude that Fe and Ti behave in different ways as special metal mineral in Fe-rich glass.
5. Although the data in table 4 are only semiquantitative, composition species and data characteristics are corresponding to data of table 3. So total weight percentage obvious deficiency of measuring point 1, 6, 14 and 15 in table 3, which reason is that hydrogen couldn't be detected by EMA, is proved that there is no key or important composition missing.

The reason of total weight deficiency of measuring point 11 and 12 is mass fraction vacancy caused by treating actual Fe_2O_3 as FeO. The reason of total weight overfillment of measuring point 9 and 10 is treating actual iron-chrome element compound as oxide.

6. From Figure.3G-H and table 3 and 4, we could draw such a conclusion that the light gray part of Fe-rich glass are constitutes of metal microlite minerals of Fe, Cr and Ti in various status, while the dark black part is of nonmetal microlite minerals, such as silicate, quartz and moissanite. The two parts formed unmixing texture. From the above, we recognize that Fe-rich glass is a microlite solid to be mainly constituted of nonmetal minerals---silicate, quartz and so on, liquating some mantle typomorphic mineral, such as native iron, ilmenite, titanium-specularite and moissanite and so on.

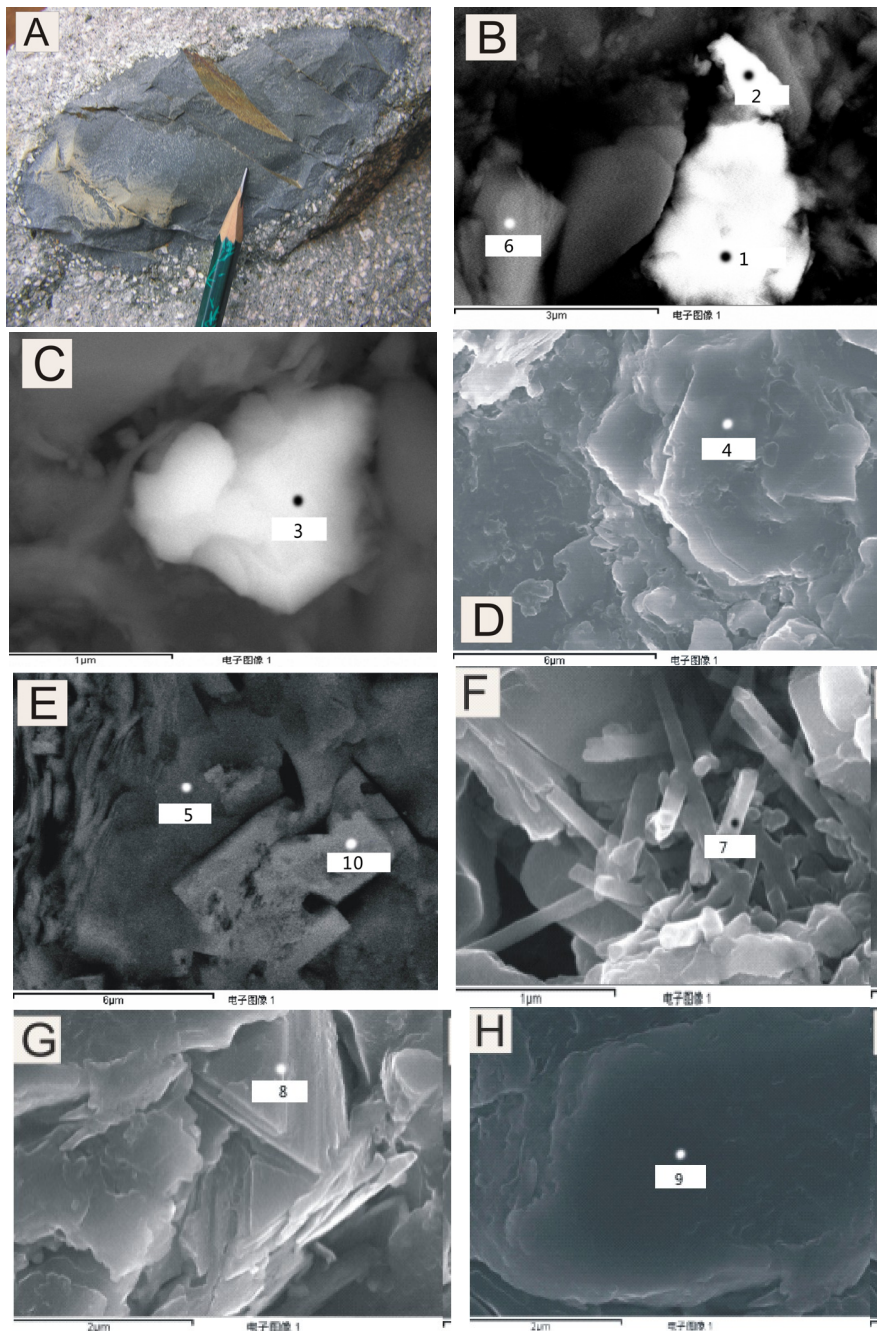
4.3 Fe-rich melt xenolith in alkali-rich porphyry

Recently, a special xenolith was discussed in the Liuhe aegirine syenite porphyry. As exhibited in Fig.4A, the xenolith, in long-ellipse shapes with a longest radius of 14cm and a

shortest radius of 6cm, has a clear contact boundary with the host rocks without an roasted or chilled border - only a narrow contaminated transition zone is observed under the magnifying glass. The black xenolith is of microlite-cryptocrystal texture and compact block structure. Owing to its very fine particles, there is hardly any optical character under transmission and reflection microscope. The petrography character suggests that this special xenolith is a microlite-cryptocrystal Fe-rich melt xenolith with some special compositions and natures other than common olcanic glass.

Preliminary study is documented as follows:

1. As shown in table 5, the domain compositions are SiO₂, FeO and Al₂O₃, and SiO₂ content for as high as 57%, while CaO and MgO content are low. Thinking about silicon isotope for the xenolith. $\delta^{30}\text{Si}=-0.8$ (this paper data), we could conclude that compositions and origin of Fe-rich melt xenoliths have a certain connection with mantle.
2. As shown in table 5 and 6, besides domain mineral assemblage---silicate and quartz, there are still special mantle typomorphic minerals---moissanite and iron---as well as accessory minerals to be formed in mantle, such as apatite
3. Analysis of moissanite in table 5 is similar to that of Fe-rich glass in Xiaoqiaotou rock body. As with the microlite iron in table 6, data of measuring point 1 is nearest to the standard one. The matter cannot be ferrous silicate with ferrous content for 84.02% and little Si, Al and O. Comparing figure 4B and C with measuring point 2 and 3 in table 6 indicates that the increase (15.95→32.75) of Si, Al and O corresponding to the decrease (2.50 μm →0.63 μm) of microlite iron diameter. Therefore, we regard the reason for Si, Al and O increasing, as well as emergence of Mg as touched microlite silicate, which encircled the iron, increase by ray spot., There is no doubt that the microlite of measuring point 1-3 is iron.
4. Fe-rich microlite rodshaped-sheet silicates (Figure 4F-G) corresponding to measuring point 7 and 8 in table 6, which do not have similarity to any known common silicate, suggest that there is more Fe-rich silicate, which formed in the mantle, in Fe-rich melt xenolith.
5. Mineral chemical compositions and species are identical to the bulk-rock analysis of Fe-rich melt xenolith. The conformity indicates that domain minerals, which detected by electric microprobes and the energy spectrum, could represent basic mineral characteristics of Fe-rich melt xenolith. While iron and moissanite are opaque minerals, the others (including Fe-rich silicate) are transparent minerals, those content are much more than opaque minerals. The phenomenon of its black color, opaque and no optic property is caused by its exceed microlite property of particles diameter ranging from 1-6(μm).
6. As shown in figure 5, identify icon of X-ray crystal powder diffraction for Fe-rich melt xenolith shows that there are still many exceed microlite-amorphous material, which could not cause X-ray to diffract, besides quartz, clinocllore, illite and albite. The icon further confirmed the result of electric microprobe and energy spectrum analyse. Why are not there the mantle typomorphic minerals in the icon? two reasons as following: The mantle typomorphic minerals are few and dispersed, and they are exceed microlite or amorphous. The xenolith is electric-microscope grade microlite Fe-rich silicate melt solid.



A. Fe-rich melt xenoliths in aegirine syenite porphyry (photograph of hand specimen from Hedong hamlet, Liuhe village, Heqing county, Yunnan Province); B. The iron (points 1 and 2) and chlorite (point 6)

in the Fe-rich melt xenolith; C.The iron (point 3) in the Fe-rich melt xenolith; D.Microcrystalline quartz (point 4) in the Fe-rich melt xenolith; E.Chlorite (point 5) and apatite (point 10) in the Fe-rich melt xenolith; F. Columnar iron-rich silicate mineral (point 7) in the Fe-rich melt xenolith; G. Sheet-shaped iron-rich silicate mineral (point 8) in the Fe-rich melt xenolith; H.Microcrystalline zircon (point 9) in the Fe-rich melt xenolith.

Fig. 4. Characteristics of hand specimen and its composition of micro-minerals for Fe-rich melt xenolith

Point	SiO ₂	Al ₂ O ₃	FeO	Fe ₂ O ₃	Na ₂ O	K ₂ O	MgO	CaO	TiO ₂	Cr ₂ O ₃	MnO	CO ₂	SO ₂	H ₂ O ⁻	H ₂ O ⁺	Total	Mineral
	57.04	11.58	13.81	4.53	0.08	0.14	3.66	1.43	0.46	SO ₂ 0.01	P ₂ O ₅ 1.38			5.63		99.75	whole rock
	57.44	11.38	11.65	4.31	0.08	0.24	3.24	2.83	0.23	P ₂ O ₅ 2.25	0.06	0.98	0.13	5.13	0.72	100.67	
1	164.08	0.10	0.47		—	0.02	0.02	0.04	0.04	-	0.04					164.79	moissanite
	SiC: Si-76.73; C-30.77;															106.50	
2	150.50	1.44	1.72		0.13	0.16	0.20	0.46	0.04	0.02	0.04					154.70	moissanite
	SiC: Si-70.37; C-30.05;															100.42	
3	83.38	4.96	0.06		0.06	0.16	1.53	1.07	0.04	-	0.05					97.31	microlite quartz
4	30.88	18.22	31.10		0.04		5.31	0.60	0.03	0.03	0.04					86.25	microlite chlorite
5	27.56	25.45	32.12		0.03	0.02	7.72	0.22	0.03	0.10	0.01					93.26	microlite chlorite

Table 5. Whole-rock chemical composition and electron microprobe analyses (EMPA) of micro-minerals in the Fe-rich melt xenolith

Piont	Si	Al	Fe	Mg	Ca	P	O	Total	Mimeral
1	4.95	2.07	84.02				8.97	100	iron (Fig.5B)
2	8.76	5.16	67.22	1.59			17.27	100	iron (Fig.5B)
3	13.36	0.92	74.96				10.76	100	iron (Fig.5C)
4	40.66			Br 1.50			57.84	100	microlite quartz (Fig.5D)
5	13.29	10.55	17.33	5.46	Ti 1.62		51.75	100	microlite chlorite (Fig.5E)
6	14.91	8.78	16.61	3.31	0.86	0.80	54.74	100	microlite chlorite (Fig.5B)
7	30.43	11.81	23.85				33.91	100	Fe-rich columnar silicate (Fig.5F)
8	17.81	10.16	30.74	3.61	1.25		36.43	100	Fe-rich sheet silicate (Fig.5G)
9	15.75			Zr 53.43			30.84	100	zircon (Fig.5H)
10			1.16	F 4.65	35.32	19.83	39.03	100	apatite (Fig.5E)

Table 6. Energy spectral analyses of minerals in the Fe-rich melt xenolith

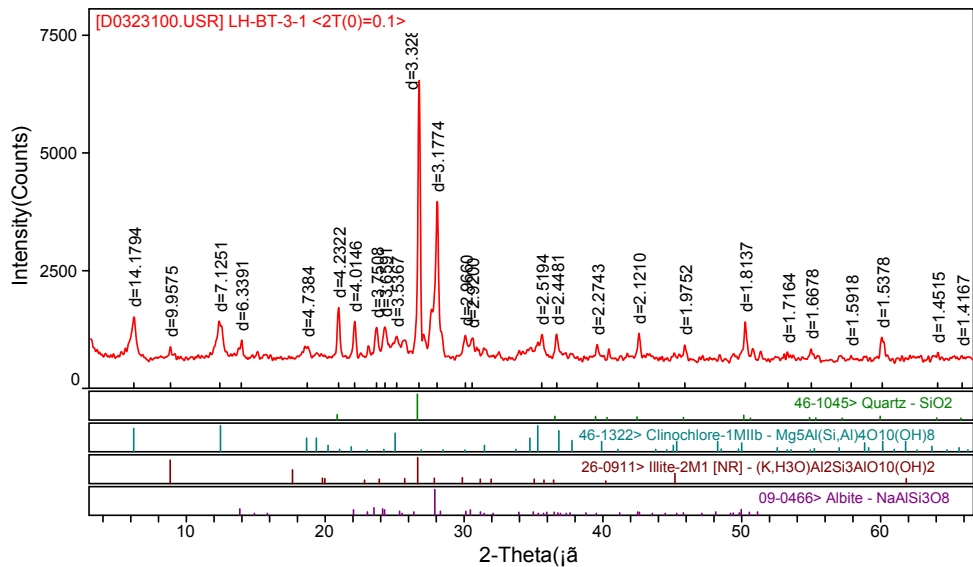


Fig. 5. Checkup icon of X-ray crystal power diffraction for the Fe-rich melt xenolith

5. Geological significances of the mantle fluid actual microcosmic traces

As discussed above, microcosmic traces and existing modality of the mantle fluid from alkali-rich porphyry and xenoliths can be directly manifested as following :

1. Na-rich glasses, which appear as microlite and embryonic crystal under optical microscope, interpenetrated and altered, nervatedly and disseminatedly, in garnet-mica-pyroxenite. The glass has the characteristics of colour change with its composition variation, high Si, Al, Na and Fe, low K, Ca, and Mg, and the assemblage of albite, amphibole, magnetite(specularite) and ilmenite. The microlite glass is an upper mantle fluid that was formed before alkali-rich magma caught it.
2. Fe-rich glasses interpenetrated and altered, nervatedly, agglomeratedly and disseminatedly, host rocks and various xenoliths.
3. Black microcrystalline iron-rich melt xenoliths as a special independence in aegirine syenite porphyry.

Both matters of (2) and (3), as black opaque materials, are of submicroscopic crystalline texture under the electron microscope, but almost no optical properties (transmitted and reflected light). Their chemical compositions are expressed as high Si, Al and Fe, low Ca, Mg, Na and K. Their main mineral compositions are silicate and quartz, as well as moissanite, native iron with chromium, specularite with titanium, ilmenite and apatite et al. The unmixing texture, which is assumed by immixing of minerals between micro-metal and nonmetal, indicates the mantle fluid's melt property and immixing with alkali-rich magma. Widely developed alteration, such as amphibolization, silification and chloritization et.al., and corresponding retrograde reaction in order of pyroxeny→amphibole→biotite→chlorite resulted in the mantle fluid disseminating and replacing the host rocks and xenoliths. Na-

rich glass, which was characterized by microlite-embryonic-crystal, originates from upper-mantle fluid before being captured by alkali-rich magma. However, what fluid property was expressed by the Fe-rich glasses and Fe-rich melt xenolith?

5.1 Solid for crystallize ? Cryptocrystalline? Submicrolite ? Or amorphous ?

It is well known that these are possible materials appearing as black-opaque under the transmitted microscope---black glass, char matter, metal mineral or crystallized minerals smaller than 10 μ m. As detected by an electron scanning microscope, electric microprobe and energy spectrum, as well as being exhibited in a background-scattering electron photograph(Fig 4G and H and 5B-H), the domain mineral of Fe-rich melt xenoliths is silicate, with some quartz, metal minerals and mantle typomorphic minerals. The majority of the minerals are smaller than 10 μ m., most of which are 5 μ m and of a crystal shape. Therefore it cannot be black glass or char matter.

5.2 Melt fluid or thermal fluid?

As mention above, Fe-rich melt glass is found in host rocks and deep xenoliths as veins, net-veined, scattering dissemination and lump. The characters themselves are results of fluid process but differ to general hydrothermal fluid:

1. The domain mineral of Fe-rich glass is silicate, together with some quartz metal and minerals, and mantle typomorphic minerals. The mineral assemblage is different from the composition of hot brine.
2. Crystallized minerals are reconstructed by hydrothermal fluid to form new crystallized minerals through solid-solid direct metasomatism, except for cryptocrystal or amorphous solids. So the matter facies of cryptocrystal- amorphous were formed in the rapid cooling process of melt fluid.
3. Differentiation by liquation structures among the metal minerals and silicate minerals are exhibited in Fig.4G, and H, Fig.5B and C.The characters are similar to Bea et al., (2001) study suggesting the compositional unmixing structure developed in alkali magma during the rapid cooling process.

According to the discussion above, we could conclude that Fe-rich glass is a kind of crytocystal-amorphous solid forming in the metasomatic process of mantle fluid in host rock and xenoliths going with the changes of temperature and pressure, resulting in a decrease of volatility and increase of solidus temperature. Pertofacies and compositions of Fe-rich melt xenolith are similar to those of Fe-rich glass.

5.3 Mantle fluid or magmatic fluid?

Generally speaking, magmatic fluid is regarded s a recapitulate for magma and postmagmatic thermal fluid. Magma has the ability to self-crystallize, while postmagmatic thermal fluid derives from magmatic fractional crystallization. The melt fluid defined in this paper approaches the basic properties of mantle fluid, evidence as following:

1. Nowadays, one is inclined to think that mantle fluid is a kind of high temperature and density supercritical alkali-rich silicate melt. The melt can concentrate rarity gas elements(³He , ³⁶Ar) and volatiles (mantle CO₂, meteorite sulfur, deep H₂O) in inner-

earth and dissolve and carry a great lot of major, trace amount and metal element (Cao R L et al., 1995, Liu C Q et al., 2004, Sun F Y et al., 1995 and Shmulovich K I et al., 1995). Schrauder's experiment (1994) suggests that mantle fluid, as a kind of media, could be a melt (carbonate melt) or H₂O-rich fluid of great diversity. Therefore, mantle fluid metasomatism has a close connection with mantle magmatism. Aegirine syenite porphyry is the product (Deng W M et al., 1998, Liu X F et al., 2009 and Yu X H et al., 2006) of alkali-rich magma derived from enrichment mantle. Ascending alkali-rich magma captures mantle fluid, which has melt property and is unmixing with magma, or xenoliths. The mantle fluid replaced or disseminated host rocks and xenoliths in the diagenetic stage of alkali-rich magma.

2. Moissanite, Cr-native iron and Ti-specularite are detected in Fe-rich glass and Fe-rich melt xenoliths (Table 3, 4, 5, 6 and Fig. 3G and H, Fig. 4B and C). The three minerals are reckoned as typical mantle typomorphic mineral, demonstrating as following:
 - a. Moissanite occurring mainly in kimberlite and lamproite, especially in podiform chromites in serpentine, has a close genetic relation with diamond; more importantly, Bai, et al., (2001, 2004) discovered fine mantle mineral inclusions, such as native silica, calc-aluminosilicate, and accrete alloy Fe₃Si₇ as interlocking crystals in moissanite. Yajima, et al., (1998) compound β-moissanite and α-moissanite at 1500°C and 2400°C respectively. Taking pressure related to the temperature and geothermal gradient into account, moissanite's forming depth was at least as upper-mantle. Therefore, moissanite could be treated as mantle typomorphic mineral.
 - b. Native iron was first discovered in diamond inclusion, and then in kimberlite at the North China Platform. It is acknowledged that native iron forms in a deacidizing environment. Addition chrome as a mantle typomorphic element, Cr-bearing native iron could be treated as mantle typomorphic mineral. In accordance with the Si-Fe binary phase diagram, Zhao, et al., (1993) suggests that the crystalline temperature of native iron in kimberlite is 1528°C. If the Si-Fe binary diagram could be applied to Fe-rich melt xenoliths, taking Zhang's experiment phase diagram (1981) of girdle orthoclase from alkali rock in Western Yunnan into account, the crystallizing temperature of native iron in Fe-rich glass and Fe-rich melt xenoliths is higher than the diagenetic temperature of aegirine syenite porphyry. The characters suggest that it is time for the alkaline magma crystallized, volatiles abruptly lost in the alkali magma diagenetic stage and lead to a solidus temperature correspondence increase of Fe-rich silicate melt. Under this circumstance, going with mantle melt fluid disseminating and replacing host rock and xenoliths, electric microscope-grade microlite solids were formed.
 - c. Although specularite, which may originate from like micaceous hematite to be formed in metamorphic process, is an iron-oxidization, it could mostly originate from the transform of relative deacidizing magnetite to be formed in the endogenic hydrothermal fluid process. The fact for symbiosis in both of Ti-specularite and Cr-native iron indicates that Ti-specularite is an evolution product of Ti-magnetite going with mantle fluid changes from deacidizing to oxidation. Previous studies show that magnetite forms in an endogenic-deoxidize environment. Addition, Ti as a mantle element, it is reasonable to conclude that Ti-magnetite (specularite) is a mantle typomorphic mineral. Zircon and apatite (measuring point 9 in Fig 5H and measuring point 10 in Fig 5E) in clear crystal form are detected, as well as ilmenite and rutile, The four accessory minerals are commonly considered deriving from mantle.

Based on the discussion above, we can conclude that compositions of Fe-rich glass penetrating host rock and xenoliths as vein and disseminated stockwork are almost identical to independent Fe-rich melt xenoliths. Both (Fe-rich glass and Fe-rich melt xenoliths) of them are electronic microscope-grade cryptocrystalline-sunmicrolite- amorphous solid derived from mantle melt and supercritical fluid. The mantle fluid was captured and moved synchronously by alkali-rich magma, at one time disseminated and replaced host rock and xenoliths going with volatile loss and alkali-rich magma diagenesis. This kind of cryptocrystalline-sunmicrolite- amorphous solid is an important microcosmic modality of mantle fluid which causes silication, kalium matter alter, albitization and retrograde reaction of dark minerals, as well as in favor of various mineralizations.

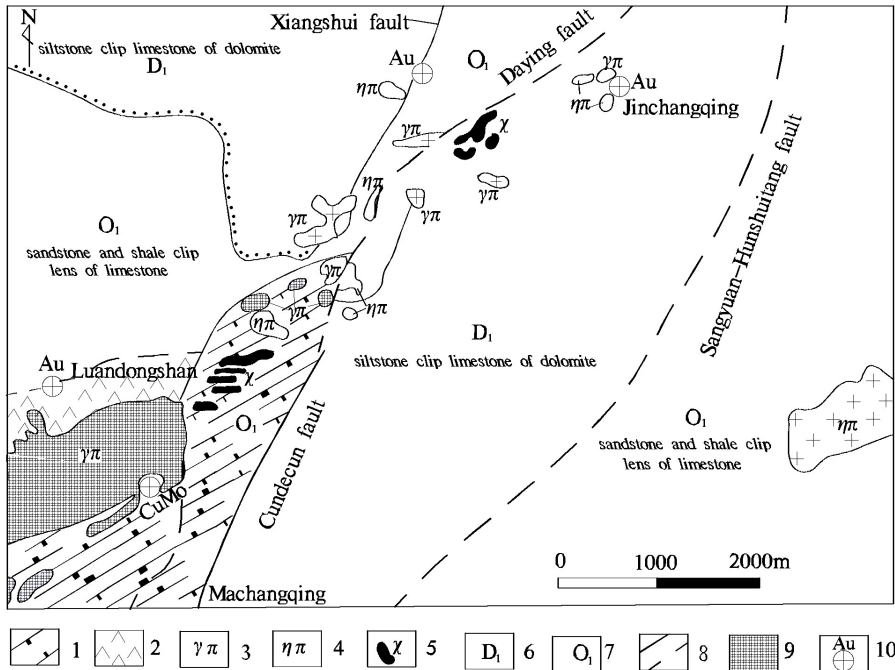
6. Metallogenic significance of mantle fluid metasomatism

Many studies suggest that large-scale fluid migration is necessary for mineralization, since there are wide and intensive wall-rock alterations in endogenic metal ores. Therefore, it is of great importance to study the properties, origins, effects and migration of fluid, as well as reasons and spaces for metallogenic elements sink (Luo Z H et al., 2007).

It is well known that the polymetal deposits in Western Yunnan have a close relation with alkali-rich porphyry. Preliminary studies show the intrinsical unified mechanism is an effective combination of mantle fluid metasomatism, deep faults transporting and controlling metallogenic elements, and sub-faults and wall-rock or strata as a host space. The mechanism is represented as the effect of series metallogenesis in western Yunnan (Liu X F et al., 2002).

Both alkali-rich magma and mantle fluid, which is shown as three microcosmic modalities, coexist and migrate together, but unmixed because of the differences of composition and properties. On the basis of synthesis analyses in combination with theory of metallogenesis by transmagnetic fluid, the following conclusions are drawn: the alkali-rich porphyries were synchronically self-replaced and altered by the mantle fluid accompanying the process of alalkali-rich magma crystallizing while the fluid and magma was trapped well, and the otrthomagmatic deposit was formed in the magma body or its depths, and the typical deposit of otrthomagmatic metallogenic system is Machangqing porphyry Mo-deposit; that if perturbation of tectonization happened in the process of diagenesis and metallogeneis, the mantle fulid would enter into the contact zone between magma bodies and wall rocks or strata next to the contact zone, and replacing and altering took place to form the contact-metasomatic system, and the typical deposit of the contact-metasomatic metallogenic system is Machangqing porphyry Cu-deposit in skarn-marble zone, and porphyry Au-deposit mainly in atrsta rocks; if the Au-deposit exists in a porphyry body, it is commonly controlled by the fractures after diagenesis; if the deep fractures, as magma and fluid channels, are well developed, and the environment is relatively open, the ore-bearing mantle fluid will flow far from alkali-rich magma along branch fractures and enter into different strata and rocks, and the replacing and altering occurred along with diagenesis process, and the typical deposit of epithermal metallogenic system is Lanping Jinding supper-large Pb-Zn deposit. In this process, the mantle fluid's properties were changed from magma→supercritical fluid→liquid by the changes of depth and environment, and corresponding to the changes of physical and chemical conditions, and the moving fluid carried, activated and enriched ore-material at suitable places; It is the

deep process and the action of fluid that accelerated crust-mantle materials overlapping, facilitated the deep ore-forming and benefited the formation of large and super-large deposits.



1. skarn-marble zone; 2.horn zone; 3.granite porphyry; 4.monogranite porphyry; 5.lamprophyre; 6. siltstone clip limestone of dolomite quality from lower Devonian series;7.fleet turn sandstone and shale clip lens of limestone from lower Ordovician series;8.fault or inferred fault;9.high-grade Mo-Cu orebody in granite porphyry;10.site and type of ore deposits.

Fig. 6. Sketch geological map of Machangqing Mo-Cu-Au deposits area (base map from gold unit thirteenth detachment,brief simplification and modification)

The Machangqing Mo-Cu deposit is located at northern block of the Jinshajiang- Ailaoshan gold zone, and on the intersection of the Jinshajiang-Ailaoshan deep fault and the Cehngnai-Binchuan fault. The main strata(Fig.6) are siltstone clip limestone of dolomite quality from low Devonian series,fleet turn sandstone and shale clip lens of limestone from low Ordovician series. The ore body is controlled by trunk faults trending northwest to southeast andnorth to south, which develop with secondary faults and anticline of various types and scales tending northeast to southwest, east to west, northwest to southeast and southeast. The main intrusive rocks are granite porphyry, monzonitic granite porphyry, and sills and typhoons, forming during Himalayan period. There are still some lamprphyre, agabbro and dolerite as dikes and veins. Contact zones of intrusive rocks and wall-rocks are hornstone and sharn-marble. From south to north there are three ore blocks - Machangqing Cu-Mo ore block occurrences in porphyry, Luandongshan Cu-Mo-(Au) ore blocks in sharn-

marle, and Jinchangqing Au ore block in wall rocks (O1&D1). There are still some Au-Ag ore spots in the faulted fracture zone which cuts porphyry and contact zones. Mo-Cu-Au ores and alkali-rich porphyry are of concordant ages (34-45Ma). The forming ages of independent Au-(Ag) ore spots may be 15Ma later than the diagenetic age of alkali-rich porphyry (Peng J T et al., 2005 and Liu X F et al., 2000). Besides that Cu-Mo-Au ores occurrence in porphyry and contact zones, they are also found in sharn, altered gabbro, dolerite and lamprophyre, which indicates that mineralization is unified control of structures and mantle fluid processes. Geochemical and Pb, Si, Sr, Nd stable isotopic researches of alkali-rich porphyry and its typical minerals suggested that source of alkali-rich magma appear to be low partial melted EM II enriched mantle; while metallogenic mantle fluid is HIMU mantle with high U/Pb. At the same period of alkali-rich magma transportation and crystallization, mantle fluid self metasomates and alters the alkali-rich porphyry, which makes metallogenic material, carried in alkali-rich magma and mantle fluid, mineralized at suitable spaces. He-Ar studies of pyrite fluid inclusions in mineralized porphyry indicate the existence of mantle fluid (Hu R Z et al., 1997).

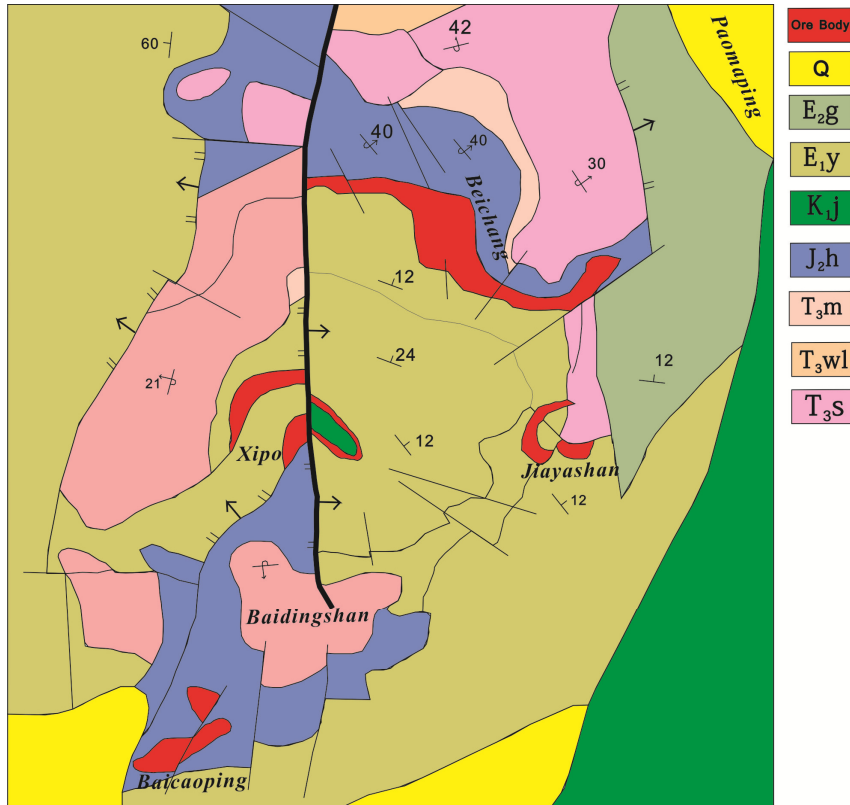
The Jinding super-large Pb-Zn deposit is located in the northern part of Lanping Basin, at the junction of Indian and China continental plates. The tectonic zone at which Jinding is located was active during the Mesozoic and reached its peak in the Himalayan period. Studies of host rocks, isotopes and metallogenic fluid suggest that the ages of ore-forming are 27-34Ma (Li Z M et al., 2006).

Structures controlling the deposit consist of a top broad dome and a napped fault. The Jinding deposit is made of seven ore blocks - Jiayashan, Beichang, Nanchang, Xipo, Beicaoping, Paomaping and Fengzishan et al, which are zones circling the core of the dome. The napped fault separates the strata into two different systems - (a) the foreign system-upfaulted block includes inverted strata T_{3sr} , T_{3wl} , T_{3mv} , J_{2h} and K_{1j} (from old to new), the lithology of which is a varicolored fine-clastic rock of interbedded carbonate; (b) the proto system-downfaulted block includes normal strata E_{1y} and E_{2gr} , the lithology of which is dark red siltstone and thick bedded sandstone interbedded olistostrome. Pb-Zn ore body occurrence in napped fault and its secondary faults.

There are two different kinds of ores, (a) sandstone, which is mainly found in Beichang, Jiayashan, Fengzishan and Xipo; (b) breccia, which is found in Jiayashan, Nanchang and Paomaping et al.

What should be given great attention is that metallogenic elements are in the conditions of microlite sulfide (galena and sphalerite) and carbonate (siderite) which occur in black opaque cements (Fig.8A, 8B). In sandstone ores, black opaque material partially disseminates, replacing primary cements (98). In breccia ores, black opaque material is siliceous cryptocrystal-microlite and other sunmicroscopic cements. Obviously, this phenomenon inhibits characteristics of fluid injection metasomatism. Electron microprobe analysis shows that, besides microlite sulfides, there are still great amounts of carbonate minerals, including microlite calcite, dolomite, smithsonite and siderite. Preliminary studies suggested that black opaque material derives from mantle carbonatite melt mixing sulfides and crystallizing in the overcooling process. Evolution and tectonic settings of this mantle carbonatite fluid are similar to the mantle fluid which forms the Na-rich glass, Fe-rich glass and Fe-rich melt xenoliths. The mantle fluid escapes from alkali-rich magma and enters into

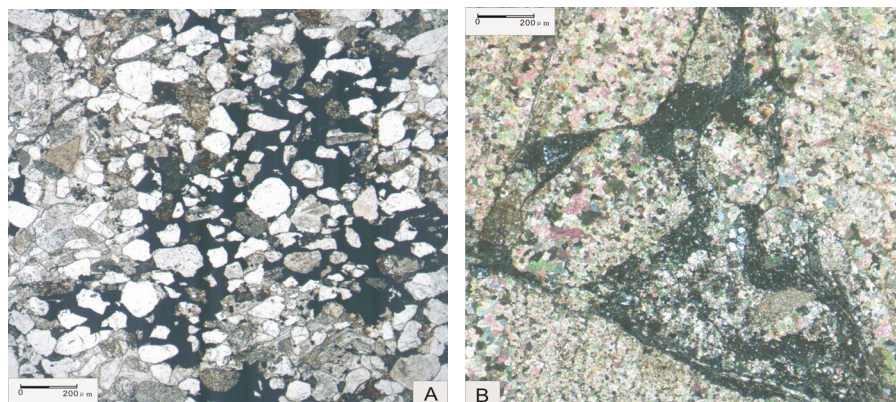
wall-rocks mixing with crustal fluid in a relatively open environment. We propose that the sulfides and microlite carbonate are products of supercritical-melt mantle fluid which escapes from alkali-rich magma, extracts metallogenic materials along the way and alters wall-rocks.



1.thrusting fault;2.normal fault;3.character incertitude fracture; 4.line of geological limitation; 5.surface of unconformity; 6.normal strata occurrence; 7.inversion strata occurrence; 8.Pb-Zn orebody; 9.Quaternary Sytem; 10.Eocene series guolang group;11.Paleocene Series Yunlong group; 12.low Cretaceous Series Jingxing group;13.middle Jurassic Series Huakaizuo group;14.upper Triassic Series Maicuqin group;15.upper Triassic Series Waluba group;16.upper Triassic Series Sanhedong group.

Fig. 7. Geological sketch of the Jinding lend-zinc ore deposit (area) (from Li et al.,2006)

A great deal of research proposes that carbonatite is the product of mantle magma. Fan H R et al., (2001) proposed that the intrusion of magma is associated with crust thinning. Liu et al., (1999) discussed the mantle upthrust and crust thinning processes of West Yunnan province. Yang X M (1998) pointed out that carbonatite is a fingerprint rock of lithosphere and mantle metasomatism. Although no carbonatite has been discovered in the Jinding deposit, the carbonatite melt could be regarded as a direct actual trace of mantle fluid.



A. Sandstone type ore with sand shape texture and basement type cementation, there are thereinto some cement to be replaced disseminatedly by black opaque materials. (plainlight under transmission condition) B. Limestone debris type ore with brecciform structure, there is cement, which is composition of tocryptocrystal- microcrystal kiesel and super-minuteness crystalline, to be injected to among debris. (crossed nicols under reflex condition)

Fig. 8. Microscope characters of cement in two type ores from Jinding Pb-Zn deposit.

Due to the fact that Jinding deposit occurs in sedimentary rocks, for a time it was treated as a typical strata-bound (sediment-reformation) deposit. However, present studies make a breakthrough about the genesis of this deposit. Based on the studies of REE, Wang J B et al., (1991) proposed that the metallogenic material derives from CO₂-rich fluid. After study of the Pb isotope, Zhang Q (1993) found that after syndeposition and reformation, Jinding was overprinted by mantle Pb. Zhu S Q et al., (2000) pointed out that some signs indicate that mantle fluid was part of the mineralization process. Based on the spot survey and the fact that asphalt is rich in brecciola ores, Gao L et al., (2005) suggested that the brecciola is a kind of emplaced brecciola of hervidero, which brought the metallogenic materials from depth. Our research shows that cements of the two kinds of ores are of emplacement characteristics, and the emplaced fluid is carbonatite melt which irregularly immixes sulfides. The carbonatite melt injects and cements the sedimentary rocks through the channel of large scale napped faults. Researches regarding the black opaque material in the ores inhibit a new way of mantle metasomatism and mineralization.

7. Conclusion

Formation and evolution of plentiful alkali-rich porphyries with deep-xenoliths have an inevitable connection to Cenozoic continental deformations, tectonisms, mantle magmas, anatectic fluids, and associated abundant polymetallic deposits. Study of petrographical, petrochemical, electron microprobe, scanning electron microscopy and energy spectrum analysis indicate that the connection is brought about by deep geological processes and ore-bearing mantle fluids action. Microcosmic traces and existing modality of the processes and the action can be directly manifested as following :

Na-rich glasses, which is showed as microlite and embryonic crystal under optical microscope, interpenetrated and altered , nevatedly and disseminatedly, deep-xenoliths.

The glass have the characteristics of colour change with its composition variation, high Si, Al, Na and Fe, low K, Ca, and Mg, and the assemblage of andesine, amphibole, magnetite (specularite) and ilmenite. The microlite glass is a upper mantle fluid hat was formed before alkali-rich magma caught it. (2) Fe-rich glasses interpenetrated and altered, nevededly, agglomeratedly and disseminatedly, host rocks and various xenoliths. (3) Black microcrystalline iron-rich melt xenoliths as independent in aegerine syenite porphyry. Both matters of (2) and (3) are of submicroscopic crystalline texture under the electron microscope, but almost no optical properties (transmitted and reflected light) as black opaque materials are seen under the optical microscope. Their chemical compositions are expressed as high Si, Al and Fe, low Ca, Mg, Na and K. Their main mineral compositions are silicate and quartz, as well as moissanite, native iron with chromium, specularite with titanium, ilmenite and apatite et al. The unmixing texture, which is assumed by unmixing of minerals between micro-metal and nonmetal, indicates the mantle fluid's properties of magmatic melt and unmixing with alkali-rich magma. Widely developed alteration, such as hornblendication, silification and chloritization et al., and corresponding retrograde reaction in order of pyroxene \rightarrow amphibole \rightarrow biotite \rightarrow chlorite resulted in the mantle fluid disseminating and replacing the host rocks and xenoliths.

Both alkali-rich magma and mantle fluid, which are shown as three microcosmic modalities, coexist and migrate in step, but unmix due to the differences of compositions and properties. On the basis of synthesis analyses in combination with metallogeny theory by transmagmaic fluid and demonstration in this paper, the following conclusions are reached: the alkali-rich porphyries were synchronically self-replaced and altered by the mantle fluid going with the process of alkali-rich magma crystallizing while the fluid and magma was trapped well, and the orthomagmatic deposit was formed in magma body or its deep-seat, and the typical deposit of orthomagmatic metallogenic system is Machangqing porphyry Mo-deposit; if perturbation of tectonization was happened in the process of diagenesis and metallogenesis, the mantle fluid would enter into the contact zone between magma body and wall rock or strata next to the contact zone replacing and altering to form contact-metasomatic deposit, and the typical deposit of the contact-metasomatic metallogenic system is Machangqing porphyry Cu-deposit, which exists in skarn-marble zone, and porphyry Au-deposit, which exists mainly in strata rocks; if the Au-deposit exists in porphyry body, it is commonly controlled by the fractures after diagenesis; if the deep fractures, as magma and fluid channels, are well developed, and environment is relatively open, the ore-bearing mantle fluid will flow far from alkali-rich magma along branch fractures and enter into different strata and rocks, replacing and altering to go with the process of diagenesis, and the typical deposit epithermal metallogenic system is Lanping Jinding super-large Pb-Zn deposit. In this process, the mantle fluid's properties were changed from magma \rightarrow supercritical fluid \rightarrow liquid going with the changes of depth and environment, and corresponding the change of physical and chemical condition. Moving fluid carried, activated and enriched ore-material at suitable places. It is the deep process and the fluid action to accelerate crust-mantle materials overprinting mineralization and profit to deep ore-forming and large and super-large deposits.

8. Acknowledgement

The study is jointly supported by National Natural Science Foundation of China grant 40473027 and 40773031, Foundation of Open Subjects of the State Key Laboratory of

Geological Processes and Mineral Resources of the China University of Geosciences grant GPMR0509 and GPMR200705, and the Project of the State Key (Preparation Support) Disciplines of Mineralogy, Petrology and Mineral Deposit Geology of Sichuan Province. We owe a debt of gratitude to friends, Carlos Villaseca and Sixto Rafael FERNANDEZ LOPEZ of Universidad Complutense de Madrid for their kindly help.

9. References

- Bai W J, Yang J S, Fang Q S, Yan B G and Zhang Z M. Study on a storhouse of ultrahigh pressure mantle minerals: podiform chromite deposits[J]. *Earth Science Frontiers*, 2001, 8(3): 111-121(in chinese).
- Bai W J, Yang J S, Fang Q S, Yan B G, Zhang Z M, Ren Y F, Shi N C, Ma Z S and Dai M Q. Some nature metals from ophiolitic chromitites in Tibet[J]. *Earth Science Frontiers*, 2004, 11(1): 179-187(in chinese).
- Bea F, Arzamastsev A and Montero P, Anomalous alkaline rocks of Soustov, Kola: Evidence of mantle-derived metasomatic fluids affecting crustal materials[J]. *Contribution to Mineralogy and Petrology*, 2001, 140(5): 554-566.
- Bi X W, Hu R Z, Peng J T, Wu K X, Su W C and Zhan X Z. Geochemical characteristics of the Yao'an and Machangqing alkali-rich intrusions[J]. *Acta Petrologica Sinica*, 2005, 21(1): 113-124(in chinese).
- Cao R L and Xia L Q. Characters and dynamics of upper mantle[C]. China, Beijing: Earthquake Press, 1989: 14-22(in chinese).
- Cao R L and Zhu S H. The mantle fluid and metallogeny [J]. *Advance in Earth Science*, 1995, 10(4): 323-329(in chinese).
- Deng W M, Huang X and Zhong D L. The alkali-rich porphyries of the northern Jinshajiang River in Western Yunnan and its relationship with intraplate deformation[J]. *Science in China (Series D)*, 1998, 28(2): 111-117(in chinese).
- Du L T. Mantle fluids, and magma origin of basalts and alkaline rocks[J]. *Earth Science Frontiers*, 1998, 5(3) : 145-157(in chinese).
- Dowson J B. Contasting types of upper-mantle metasomatism[A]. In: Kompobst J ed. *Kimberlites II: The mantle and crust-mantle relationships*[C]. Amsterdam: Elsevier, 1984: 289-294
- Fan H R, Xie Y H, Wang K Y and Yang X M. Carbonatitic fluids and REE mineralization [J]. *Earth Science Frontiers*, 2001, 8(4): 289-295(in chinese).
- Francis D M. The origin of amphibole in lherzolite xenoliths from Nunivak Island ,Alaska[J]. *J. Petrol.*, 1976, 17(3): 357-378.
- Gao L, Wang A J, Liu J L, Xiu Q Y, Cao D H and Zhai Y F. New progress in study of superlarge Jinding Pb-Zn deposit: Discovery of intrusive breccias and its geological implications[J]. *Mineral Deposit*, 2005, 24(4): 457- 461(in chinese).
- Hoke L, Lamb S and Hilton D R. Southern limit of mantle-derived geothermal helium emissions in Tibet : implications for lithospheric structure[J]. *Earth and Planetary Science Letters*, 2000, 180: 297-308.
- Hu R Z, Bi X W, Turner G ,et al. System for He-Ar isotope of fluid inclusion of pyrite form Machangqing Cu deposit[J]. *Science in China (Series D)*, 1997, 27(6): 503-508(in chinese)
- Huang W C ,Ni J F, Tilmann F, et al. Seismic polarization anisotropy beneath the central Tibetan Plateau[J]. *J. Geophysical Research*, 2000, 105(B12): 27979-27989.
- Jones A P, Smith J V and Dawson J B. Glasses in mantle xenoliths from Olmali, Tanzania[J]. *J. Geol.*, 1983, 91 (2): 167-198.

- Girod M, Dautria J M and De Girvanni R. A first insight into the constitution of the upper mantle under the hoggar area(Southern Algeria): the lherzolite xenoliths in the alkali–basalts[J]. *Contrib . Mineral. Petrol*, 1981, 77: 66-73.
- Li Z M, Liao Z T, Liu J J, Qin J Z and Zhang C J. The metallogenic age of Jinding superlarge scale Pb-Zn deposit in Lanping basin[J]. *Contributions to Geology and Mineral Resources Research*, 2006, 21(1) : 23-27(in chinese).
- Liang H Y, Xie Y W, Zhang Y Q and Ian Campbell. The constrains of formation and evolution of K-rich alkaline rock to copper ore-forming: Example of Machangqing copper deposit[J]. *Advance in Natural Science*, 2004, 14(1): 116-120(in chinese).
- Lin C Y, Xu Y G, Shi L B, et al., K- and Na-rich glass in mantle xenoliths: evidence of upper mantle fluid[J]. *Chinese Science Bulletin*, 1994, 39(9): 820-823(in chinese).
- Liu C Q, Huang Z L, Xu C, Zhang H X, Su G L, Li H P and Qi L. Mantle fluids and their metallogeny [M]. Beijing: Geology Publishing House, 2004: 3-98(in chinese).
- Liu X F, Zhan X Z, Gao Z M, Liu J J, Li C Y and Su W C. Deep xenoliths in alkalic porphyry, Liuhe, Yunnan, and implications to petrogenesis of porphyry and associated mineralizations[J]. *Science in China (Series D)(English edition)*, 1999, 42(6): 627-635.
- Liu X F. A study for the characteristics of the alkali-rich porphyries and their geochemical mechanism on diagenesis and metallogenesis. Post-doctor research thesis, Guiyang, Institute of Geochemistry, CAS, 1999: 24-51(in chinese).
- Liu X F, Gao Z M, Liu J J, Zhan X Z and Su W C. Primary discuss on chronology for mantle metasomatism and associated mineralizations of the alkali-rich porphyries[C], *Annals of Open Laboratory of Ore Deposits Geochemical Research*, Institute of Geochemistry, Chinese Academy of Sciences, Guizhou Technology Press, 2000: 103-105(in chinese).
- Liu X F, Liu J D, Zhang C J, Yang Z X, Wu D C and Li Y G. Effect of series mineralization of mantle fluid metasomatism[J]. *Mineral Deposits*, 2002, 21(supp.): 1002-1004(in chinese).
- Liu X F, Yang Z X, Liu J D, Zhang C J, Wu D C and Li Y G. Mineralogical features of ultramafic hypoxenoliths in alkali-rich porphyry[J]. *Geotectonica et Metallogenia*, 2003, 27(1-2): 81-90.
- Liu X F, Song X F, Lu Q X, Tao Z and Long X R. Mantle fluids action in the processes of petrogenesis of alkali porphyry and associated mineralizations, western Yunnan[J]. *Journal of Jilin University (Earth Science Edition)*, 2006a, 36(4): 503-510(in chinese).
- Liu X F, Tao Z, Lu Q X, Song X F and Long X R. An approach to mantle fluid mineralization in the superlarge Jinding Pb-Zn deposit, Yunnan Province[J]. *Mineral Deposits*, 2006b, 25 (Supp): 79-82
- Liu X F, Song X F, Lu Q X, Tao Z, Long X R and Zhao F F. Special Xenoliths in an Aegirine-Augite Syenite Porphyry in Liuhe, Yunnan, China : Discovery and Implications[J]. *Acta Geologica Sinica(English Edition)*, 2009, 83(2): 258-265.
- Liu X F, Zhao F F, Tao Z, Song X F, Cai Y W and Cai F Y. Mantle fluid metasomatism in Jinhe intrusive body of Jianchuan, Yunnan Province, and its ore-forming implication[J]. *Mineral Deposit*, 2009, 28(2): 185-194(in chinese).
- Luo Z H, Mo X X, Hou Z Q, Deng W M, Wang J H, Zhao Z D, Yu X H and Li J P. An integrated model for the Cenozoic evolution of the Tibetan Plateau: constraints from igneous rocks[J]. *Earth Science Frontiers*, 2006, 13(4): 196-211(in chinese).
- Luo Z H, Mo X X, Lu X X, Chen B H, Ke S, Hou Z Q and Jiang W. Metallogeny by transmagmatic fluids – theoretical analysis and field evidence[J]. *Earth Science Frontiers*, 2007a, 14(3): 165-183(in chinese).

- Luo Z H, Liang T, Chen B H, Xin H T, Ke S, Zhang Z L and Cheng S H. Intraplate orogenesis and its implications in metallogenesis[J]. *Acta Petrologica Sinica*, 2007b, 23(8): 1945-1956(in chinese).
- Luo Z H, Lu X X, Guo S F, Sun J, Chen B H, Huang F and Yang Z F. Metallogenic sytem on the trans-magmatic fluid theory.*Acta Ptrologica Sinica* , 2008,24(12): 2669-2678(in chinese).
- Maaloe S and Printzclau I. Natrual partial melting of spinel lherzolite[J]. *J.Petrol.* 1979, 20(4): 727-741
- Mao J W, Li X F, Zhang R H, et al. Deep-derived fluid -related ore-forming system[M].Beijing: China Land Publishing House, 2005 : 365(in chinese).
- Moore R O and Gurney J J. Mineral inclusions in diamond from the Monastery Kimberlite, South Africa[A]. Ross J, et al. Kimberlite and Relate Rocks[M]. *Geol. Society of Australia, Special Publication*, 1995, 2(14): 1029-1041.
- Peacock S M. Fluid processes in subduction zones[J]. *Science*, 1990, 248: 329-337.
- Peng J T, Bi X W, Hu R Z, Wu K X and Sang H Q. Determination of ore and rock-forming time of the Machangqing porphyry Cu(Mo) deposit, western Yunnan[J]. *Acta Mineralogica Sinica*, 2005, 25(1): 69-74(in chinese).
- Philippot P. Trace-element rich brines in eclogite veins: Implications for fluid composition and transport during subduction[J].*Contribution to Mineralogy and Petrology*, 1991, 106: 417-430.
- Rong J S and Du L T. Godization of Orthopyroxene in Mantle Xenoliths[J].*Acta Petrologica Sinica*,1995, 11(1): 28-42(in chinese).
- Schneider M E and Eggler D H. Fluids in equilibrium with peridotite minerals: Implications for mantle metasomatism[J]. *Geochim. Cosmochim. Acta*, 1986, 50(5): 711-724.
- Schrauder M and Navon O. Hydrous and carbonatitic mantle fluids in fibrous diamonds from Jwaneng , Botswana. *Geochmica et Cosmochimca Acta*, 1994,58(2): 761-771
- Scotes J S and Mitchell J N.The evolution of troctolitic and high Al basaltic magmas in Proterzoic anorthosite plutonic suites and implications for the Voisey's Bay massive Ni-Cu sulfide deposit. *Economic Geology*[J], 2000, 95: 677-710.
- Shmulovich K I, Yardleyb W D and Conchar G G. Fluids in the crust[M]. Moscow: Chapman and Hall Press, 1995.
- Shmulovich K I and Churakov. Natural fluid phases at high temperatures and low pressures [J]. *Journal of Geochemical Exploration*, 1998,62(1-3): 183-191.
- Song X F,Liu X F, Tao Z , Lu Q X and Long X R. The characteritis of the mantle fluid metasomatism of the alkali-rich porphyries and its xenoliths in western Yunnan[J].*Jounal of Mineralogy and Petrology*,2006, 26(4): 19-25(in chinese).
- Song X F,Liu X F, Tao Z , Lu Q X and Long X R. Mantle fluid metasomatism: Evidence from alkali syenite and its deep xenoliths[J]. *Acta Petrologica et Mineralogica*, 2007,26(4): 310-314(in chinese).
- Spera F J.Dynamics of translithospheric migration of metasomatic fluid and alkaline magma[A]. Menzies M A,et al, eds. *Mantle Metasomatism*[C]. London: Academic Press *Geology Series*,1987: 1-20.
- Su G L, Xie H S and Ding D Y. Physicochemical properities of supercritical water and their significance[J]. *Geology-Gelchemistry*, 1998, 26(2) : 83-89(in chinese).
- Sun F Y and Shi Z L. Discussion of some geologic processes between mantle C-H-O fluids and hedreocraton [J]. *Earth Science Frontiers*, 1995, 2(1-2): 167-174(in chinese).
- Unsworth M J, Jones A G, Wei W B,et al. Crustal rheology of the Himalaya and Southern Tibet inferred from magnetotelluric data[J]. *Nature*, 2005, 438: 78-81.

- Wang J B and LI C Y. REE geochemistry of the Jinding upper large Pb-Zn deposit [J]. *Geochimica*, 1991, 19(4): 359-365 (in chinese).
- Wei Q R and Wang J H. Study on petrology and mineralogy of mafic deep-derived xenoliths in Liuhe-Xiangduo area, Eastern Tibet [J]. *Mineral Petrol*, 2004, 24(1): 17-28 (in chinese).
- Xie R J and Peng S L. K₂O content, K-metasotism of rock and metallogenesis [J], *Geotectonica et Metallogena*, 1998, 22(3): 271-279 (in chinese).
- Yajima L and Doi Ms. Sinterability of submicron β -SiC Pounder synthesized by carbothermal reduction of silica [J]. *Silican Carbide Ceramics-2*, 1988: 39-49.
- Yang L and Jin Z J. The effect of hydrogen from deep fluid on hydrocarbon generation [J]. *Earth Science Frontiers*, 2001, 8(4): 337-341 (in chinese).
- Yang X M, Yang X Y and M. J. LeBas. Carbonatite: A probe rock for the tectonic settings of continental lithosphere and mantle metasomatism [J]. *Chinese Journal of Geophysics*, 1998, 41(Supp.): 228-235 (in chinese).
- Yu X H. Mantle metasomatism: Progresses, Problems and Countermeasure [J]. *Advance in Earth Science*, 1995, 10 (4): 330-335 (in chinese).
- Yu X H, Mo X X, Zeng P S, Zhu D Q and Xiao X N. A study on the mantle xenoliths in the Cenozoic volcanic rocks from Maguan Area, Yunnan Province [J]. *Acta Petrologica Sinica*, 2006, 22(3): 621-630 (in chinese).
- Zeng P S, Mo X X and Yu X H. Nd, Sr and Pb isotopic characteristics of the alkaline-rich porphyrics in weastern Yunnan and its compression strike-slip setting [J]. *Acta Petrologica et Mineralogica*, 2002, 21(3): 231-241 (in chinese).
- Zhang A D, Xie X L, Guo L H, et al. Study on mark minerals for searching diamond and its database [M]. Beijing: Science Press, 1991: 122 (in chinese)
- Zhang Q. Pb isotopic composition of Jinding super-large Pb-Zn deposit in Yunnan province and discussion on the source of Lead . [J]. *Geology and Prospecting*, 1993, 29(5): 21-28 (in chinese).
- Zhang Z Z . The zonal texture of orthoclase in alkaline rock from Yaoan country, Yunnan Province [J]. *Chinese Journal of Geology*, 1981, 16(2): 171-175 (in chinese).
- Zhao L, Lu F X, Ren Y X, Zheng J P and Zhang H F. The recent discovery of several minerals in kimberlites of the north China platform and its significance [J]. *Acta Petrologica et Mineralogica*, 1993, 12(3): 284-288 (in chinese).
- Zhao X, Yu X H, Mo X X, Zhang J and Lv B X. Mineralogical characteristics and petrogenesis of deep-derived Cenozoic syenite-porphyry in Liuhe, western Yunnan Province [J]. *Earth Science Frontiers*, 2003, 10(3): 93-104 (in chinese).
- Zhao X, Yu X H, Mo X X, Zhang J and Lv B X. Petrological and geochemical characteristics of Cenozoic alkali-rich porphyries and xenoliths hosted in western Yunnan province [J]. *Geoscience*, 2004, 18(2): 217-228 (in chinese) .
- Zheng H F and Feng J L. Microlite-glass in basalt xenoliths at Hannoba and their significance [J]. *Geological Review*, 1987, 33(1) : 12-21 (in chinese).
- Zhu S Q, Qin G J, Wen C Q, e tal. The Jinding superlarge landfacies clastic rock type Pb-Zn deposit [A]. Tu G C ed. *Superlarge deposits in China (I)* [M], Beijing, Science Press, 2000: 56-87 (in chinese).
- Zhu Y F. Mantle fluid and earth degassing [J]. *Earth Science Frontiers*, 1998, 5(supp.): 71-75 (in chinese).

Trace Metals in Shallow Marine Sediments from the Ría de Vigo: Sources, Pollution, Speciation and Early Diagenesis

Paula Álvarez-Iglesias and Belén Rubio
Universidad de Vigo, Vigo (Pontevedra)
Spain

1. Introduction

The maintenance of the environmental quality of coastal environments requires a good knowledge on them, identifying their potential problems and considering the different anthropogenic activities that take place in these settings. A great proportion of the suspended material that arrives to these environments is incorporated to the bottom sediments. Sedimentation is favoured due to the abrupt changes that are produced in the physico-chemical parameters (pH, Eh, salinity, etc.) by the confluence of continental and marine waters. Their sediments constitute environmental archives, recording trace element inputs to the marine environment. Metal concentrations in these sediments usually surpass in several orders of magnitude those existing in the adjacent water column and in the interstitial waters (Tessier & Campbell, 1988). Their analysis allows covering different objectives, such as studying the spatial and temporal history of pollution of a particular place (Zwolsman et al., 1993), detecting pollutant sources (Dassenakis et al., 1996) and evaluating their potential effects to the organisms (Fichet et al., 1998). Sediments can act as a secondary source of pollution by resuspension or dissolution (early diagenesis) processes. Their study needs a multidisciplinary approach, taking into account the different physico-chemical processes operating in the study area and considering the relationships between metal concentration, mineralogy, grain-size and metal sources. All these variables are reviewed in this chapter, showing examples of sediments from a shallow transitional environment: the Ría de Vigo (NW Spain).

The Ría de Vigo is the southernmost ría of the Galician Rías Baixas (Fig. 1) with approximately 30 km in length. At its mouth the Cíes Islands are located, which act as a barrier against storms. It can be differentiated the outer and middle ría sectors from the inner sector of the ría (the Bay of San Simón). The central axis of the former runs NE-SW, while the axis of the inner sector is NNE-SSW oriented. This last sector, separated from the rest of the Ría by the Rande Strait (depth > 30 m), is very shallow (average depth of 7 m, in front of ~20 m in the remaining ría). It is a low energy area, where hydrodynamic conditions are ruled by tides, whereas water circulation in the middle and outer ría sectors is conditioned by waves and littoral drift and exhibits a two-layered positive residual circulation pattern (Álvarez-Salgado et al., 2000). Rivers are relatively small and mostly

discharge in the southern margin and in the inner sector (Pérez-Arlucea et al., 2005). They run on a watershed mainly composed by granites, schist and gneiss (IGME, 1981). Surface sediment distribution is conditioned by hydrodynamic conditions: coarse-grained particles of fluvial origin concentrate close to the river inputs, whilst fine-grained particles are located in the central axis and in the inner sector of the ría, and biogenic sands are located at the northern margin of the outer ría (Vilas et al., 2005). The area is subjected to seasonal processes of upwelling/downwelling (Álvarez-Salgado et al., 2000). Upwelling events contribute to the ecological richness of the ría, where marine organisms (fish, shellfish) are exploited, some of them in rafts (floating platforms) (Freire & García-Allut, 2000). This high productivity explains the high organic matter contents observed in the ría sediments (Rubio et al., 2000a; Vilas et al., 2005), which are maxima toward the inner ría (up to 15%; Álvarez-Iglesias et al., 2003, 2006, 2007) and are positively correlated with the fine-grained particles content. Carbonate content is inversely correlated with these variables. Its percentage is negligible in inner ría sediments (Álvarez-Iglesias et al., 2003) and maximum towards the ría mouth (Rubio et al., 2000a). The main industrial activities in the ría are shipbuilding, automobile manufacture, ceramic manufacture and canned food (González-Pérez & Pérez-González, 2003). The Vigo harbour, which concentrates many of the industrial activities, is located in the middle ría sector, and the wastewater plant of the city of Vigo (the biggest settlement in the ría), is located in the middle-outer ría sector, close to the mouth of the Lagares River (Fig. 1).

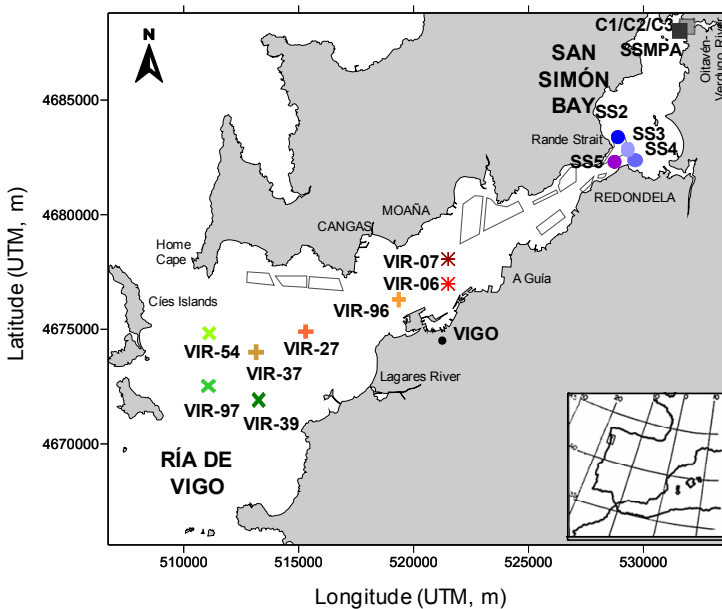


Fig. 1. Study area. Location of sampling points considered in the present study: inner ría (squares and circles), middle ría (double crosses), middle-outer ría (crosses) and outer ría (vanes) cores. Note that location for intertidal cores C1, C2 and C3 is showed by a single symbol due to the map scale, although they have been recovered at different points. Polygonal areas represent current mussel raft areas.

2. Sources of metals to coastal sedimentary environments

Metal content in marine sediments reflects both natural and anthropogenic components. Inputs from weathering of soils, rocks and ores from the watershed, constitutes the lithogenic natural component (background level, see subsection 5.1 for details). The natural component has also inputs from biogenic production, that are going to dilute both lithogenic and anthropogenic inputs. The anthropogenic component is constituted by those metals released to the environment as a consequence of different human activities.

Metal inputs to the marine environment can be direct or indirect. Direct inputs come from urban sewage, industrial wastes (metallic, chemical, building and shipping industries) and metal production and recycling. Indirect inputs come from atmosphere and from rivers as dissolved or suspended load (Salomons & Förstner, 1984). Most of the inputs consist of a group of trace elements (As, Cd, Cu, Co, Fe, Mn, Pb and Zn, among others) usually known as heavy metals. This term, according to Moore (1991) refers to a group of persistent metals and semimetals with relatively high density and that are usually toxic or poisonous at low concentrations. Nevertheless, according to Duffus (2002), the term heavy metal has not a precise definition, it is outdated and it should be substituted for another more adequate such as trace element or trace metal depending on the context.

Once trace elements arrive to the marine environment they are going to be distributed between the different compartments by association with dissolved organic and inorganic ligands or with particulate matter, and by ingestion by organisms.

In the particular case of the Ría de Vigo some metal enrichments have been detected for particular areas in several works on surficial sediments: around the harbour area (Cu, Pb, Zn, Fe), the outflow of the Lagares River (Pb, Zn) and the inner ría sector (Pb) (for details see the review by Prego & Cobelo, 2003). Metal ranges of concentrations and metal speciation will be considered in the following sections.

3. Metal concentration vs grain size

Trace metals in the marine environment are usually associated to organic-rich fine-grained sediments (Förstner, 1989) related to the good complexation and peptidizing properties of organic matter (Wangersky, 1986) and the high specific surface and surficial charge of clay minerals (Horowitz & Elrick, 1987). The presence of coarse-grained particles in the sediments, that are mostly composed by inert substances (silicates, carbonates, feldspars), usually cause trace metal dilution (Förstner, 1989).

The grain-size effect can be observed in Ría de Vigo sediments, where elements associated with fine-grained fractions, such as Al, V or Ni, are correlated with the mud fraction of sediments (Fig. 2). In opposition, elements such as Si are more abundant in coarse-grained sediments (Fig. 2). Elements such as Ca and Sr, with a biogenic origin are mainly associated with the coarse-grained fractions, and cause a dilution of another elements contents (Fig. 2).

3.1 Normalization procedures

Several normalization methods are generally used in order to correct for grain-size effects (Fig. 3). They are based in different approaches: 1) Indirect approximations (Summers et al., 1996); 2) The physical separation of a specific grain-size fraction -usually that <63 µm

(Förstner, 1989); and/or 3) The normalization of the metal concentrations by the content of a conservative element associated to the fine-grained fraction. In the last case Al, Fe, Li and Rb are usually selected (Ackerman, 1980; Álvarez-Iglesias et al., 2003, 2006; Loring, 1990). Lithium is preferred in front of Al when analyzing sediments from high latitudes (Loring, 1990). Some workers (Prego et al., 2006, among others) have chosen Fe for normalizing because its high abundance in the Earth's crust and its similar behavior and geochemistry to those of many trace elements but this metal shows a high mobility by postdepositional diagenetical processes (Álvarez-Iglesias et al., 2003; Rey et al., 2005) and, furthermore, different coastal areas can show Fe pollution (Rubio et al., 2000a).

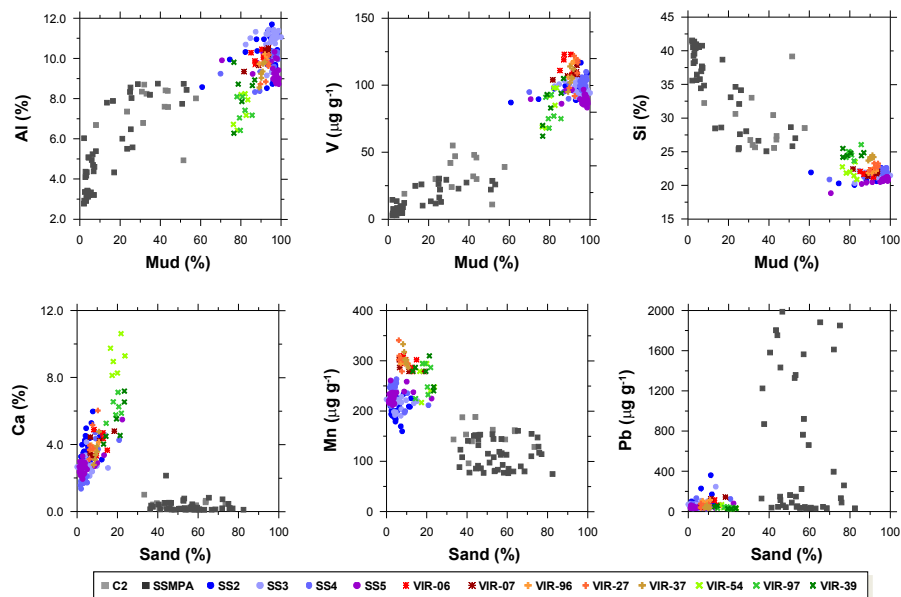


Fig. 2. Scatterplots of element concentrations vs mud (<63 μm) or sand contents in core samples ($N = 210$) from different sectors of the Ría de Vigo (core depths between 0.24 and 3.10 m): inner ría both intertidal (squares) and subtidal (circles) sediments, middle ría (doble crosses), middle-outer ría (crosses) and outer ría (vanes). Metal concentrations obtained from X-ray fluorescence (XRF) analyses. Note the positive correlation between Al or V vs mud and Ca vs sand, and the negative correlation between Si vs mud and Mn vs sand contents. Note also the extremely high values of Pb in the intertidal sediments. Sample location in Fig. 1.

The approaches 2 and 3 are generally combined (Álvarez-Iglesias et al., 2003) because, even in the grain-size fraction <63 μm , metal contents are not homogeneously distributed (Salomons et al., 1985). Nevertheless, in studies where fine-grained content is very high, normalization is usually accomplished by the use of a normalizer element on bulk sample results. These grain-size effects on metal concentrations can be clearly observed in the scatterplots of Fig. 3, where concentrations of Cr, Cu and Zn in Ría de Vigo sediments increased with the Al content. Note also in Fig. 3 that some samples show metal enrichments lying out of the general trend. This will be discussed in the following sections.

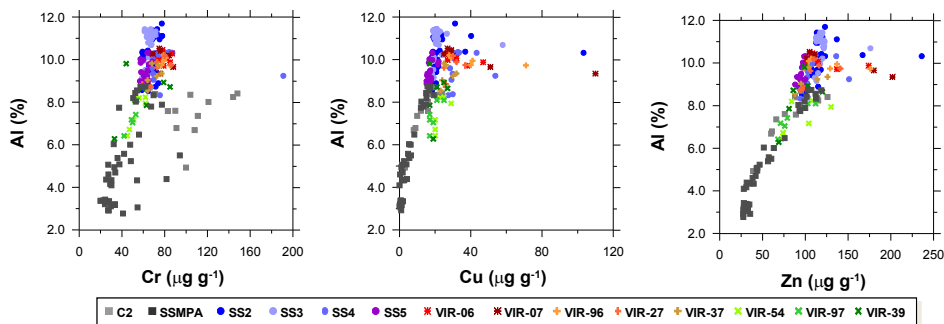


Fig. 3. Scatterplots of Al vs Cr, Al vs Cu and Al vs Zn in core samples (N=210) from different sectors of the Ría de Vigo (sample location in Fig. 1). Metal contents obtained from XRF analyses.

4. Determination of total metal concentration and speciation

The different anthropogenic inputs of metals to the marine environment will cause changes in sediment composition. A detailed study on the sedimentary record will allow evaluating environmental changes both spatially and temporally for a particular coastal area. It is important to consider also metal speciation, to evaluate potential mobility and bioavailability of the different trace metals (Bryan & Langston, 1992).

4.1 Total metal concentration

Total metal concentrations can be determined by XRF or by measuring metal contents, after acid digestion of the sediments, by different techniques such as Atomic Absorption Spectrometry (AAS) or Inductively Coupled Plasma-Mass Spectrometry (ICP-MS), among others.

Advantages of XRF are: 1) easy sample preparation, 2) quickness, 3) relatively low cost of the measurements, and 4) high analytical resolution (Boyle, 2000). Continuous high-resolution XRF core scanner devices allow making a qualitative exploratory analysis very quickly (1.0 m of a core in a few hours) analyzing directly fresh and undisturbed sediments (Rubio et al., 2011). This analysis can be refined by analyzing discrete samples by traditional XRF techniques (obtaining quantitative data).

Total metal concentrations can be also determined by digestion of the samples in open or closed systems with heating. The different workers usually utilize the following reactants, alone or in combination: HCl, HNO₃, H₂O₂, H₂SO₄, HClO₄ and HF (Álvarez-Iglesias et al., 2003; Belzunce-Segarra et al., 1997; Varekamp, 1991). Traditionally samples were acid digested applying dry (oven, hot plate) or humid (water bath) heat, but in the last decades the use of microwave ovens has been extended (Álvarez-Iglesias et al., 2003; Izquierdo et al., 1997; Rubio et al., 2001). The use of a closed system has several advantages: 1) the attack is effective, 2) the analytical results are similar to those traditional (Mahan et al., 1987), 3) the human errors are minimized, 4) the analytical contamination problems are reduced, 5) the losses by volatilization are minimal, 6) the efficiency of destruction under pressure is high (Uhrberg, 1982), and 7) the time for analysis is reduced.

If acids such as HCl, HNO₃ or HClO₄ are used alone or in combination but not HF, the obtained metal contents do not represent total metal but pseudo-total metal concentrations (Barreiro Lozano, 1991). Then, the selection of one or another analytical technique for determining metal concentration will depend on the objective of the study.

In order to check for accuracy and precision of the results of metal concentration it must be analyzed reference materials by the same techniques that those applied in the sediments under study (Table 1). Furthermore, the reference materials should have similar characteristics than those of the target sediments to avoid the matrix effect (Boyle, 2000). In the case of the Ría de Vigo the reference materials usually analyzed have been MESS-1, MESS-3 and PACS-1 (Álvarez-Iglesias et al., 2003, 2006; Prego et al., 2006; Vega et al., 2008).

	MESS-1			PACS-1	PACS-1	MESS-3	MESS-3
	CV	Measured ^{1a}	Measured ^{2b}	CV	Measured ³	CV	Measured ^{4d}
Al (%)	5.84±0.20	3.71±2.14	6.09	-	-	-	-
Fe (%)	3.05±0.17	2.47±0.12	2.99	4.87±0.08	5.11±0.09 ^a	-	-
Co (µg g ⁻¹)	10.8±1.9	-	9.4	-	-	-	-
Cr (µg g ⁻¹)	71±11	-	74.7	113±8	99±10 ^c	-	-
Cu (µg g ⁻¹)	25.1±3.8	23.84±2.17	24.9	452±16	424±37 ^c	33.9±1.6	31±5
Mn (µg g ⁻¹)	513±25	403.5±35.2	451	-	-	-	-
Ni (µg g ⁻¹)	29.5±2.7	-	29.2	-	-	-	-
Pb (µg g ⁻¹)	34.0±6.1	36.50±7.24	38	404±20	409±24 ^c	21.1±0.7	23.6±2.5
V (µg g ⁻¹)	72.4±17	-	101.3	-	-	-	-
Zn (µg g ⁻¹)	191.0±17.0	161.5±15.4	190.9	-	-	159±8	161±5

¹Álvarez-Iglesias et al. (2003); ²Álvarez-Iglesias et al. (2006); ³Prego et al., 2006; ⁴Vega et al. (2008)

^aAAS; ^bXRF; ^cET-AAS; ^dICP-OES.

Table 1. Comparison of certified values and measured values for several reference materials obtained in different studies. CV: Certified value. Measured values were obtained by different techniques: analysis of sediment extracts from total acid digestion in microwave oven by AAS, analysis of bulk sediments by XRF, Electrothermal atomic absorption spectrometry (ET-AAS) and Inductively coupled plasma-optical emission (ICP-OES). Note the differences in metal concentrations obtained by different techniques for the reference material MESS-1.

4.2 Speciation

The bioavailability, toxicity and mobility of a particular trace element depends on the sedimentary phase to which is bound to, that is, on metal speciation. It is necessary to distinguish and quantify the different metal species to study current and potential impacts of polluted sediments, to identify metal sources, and to understand the geochemical processes that take place in a particular environment. Metal association to the sediments can be diverse: adsorbed onto surfaces of clay-particles, Fe-Mn oxyhydroxides and organic matter; occluded in amorphous materials, such as Fe-Mn oxyhydroxides, Fe sulphides or remnants of biological organisms; or being part of the mineral structure. Direct determination of each single chemical form of a metal is not practical, and indirect methods are preferred such as: statistical correlations, thermodynamical calculations based on models of chemical equilibrium, computer simulations, and more commonly chemical extraction methods (Luoma & Bryan, 1981; Luoma, 1986; Tessier et al., 1979; Tessier & Campbell, 1988).

Chemical methods can be selective or non-selective. Non-selective methods extract operationally defined metal fractions that are not directly identifiable with an specific phase in the sediment (Loring, 1981). Although they do not correspond to one isolated chemical form, they suppose a better estimation of reactivity instead of total metal content. These methods can be one-single step or sequentials. The first ones can be grouped in three categories depending on the selected reactant: 1) diluted solutions from strong acids; 2) weak acids; and 3) solutions from strong reducing or complexing agents (Bryan & Langston, 1992; Imperato et al., 2003). Advantages of these methods are quickness, simplicity, cost-efficiency relationship, allowance of a better contrast between background values and anomalous values, and the non-utilization of dangerous acids such as HClO₄ or HF. The main inconvenient is the difficulty of finding a single reactant with the capacity of extracting the labile metal fraction (or any other target fraction) without attacking the residual fraction.

Operationally defined fractions					Reference		
A	B	C		D	E	Tessier et al., 1979	
A+B		C+D			E*	Salomons & Föstner, 1984	
A	B	C1	C2	D	E*	Salomons & Föstner, 1984	
A	B	C1	C2	D	-	Kersten & Föstner, 1987	
A+B+C				D1	D2	E*	Huerta-Díaz & Morse, 1990
A+B		C		D	-	Ure et al., 1993	
A	B	C1	C2	D	E*	Borovec, 1996	
A*	B+C*			D*	E	Dassenakis et al., 1996	
A	B	C1	C2	D	-	Howard & Shu, 1996	
A	B	C1	C2	D	E*	Izquierdo et al., 1997	
A*	B'	C1'	C2'	D	-	Flyhammar, 1998	
A+B		C		D	E	Gómez-Ariza et al., 2000	
A+B		C		D	E*	Stephens et al., 2001	

A: exchangeable

B: bound to carbonates

C: bound to Fe-Mn oxyhydroxides (reducible)

D: bound to organic matter-sulphides (oxidizable)

E: residual

oxyhydroxides

A*: easily interchangeable

B + C*: non-exchangeable inorganic fraction

D*: organic fraction

C1: Mn oxides(easily reducible)

C2: Fe oxides (moderately reducible)

B': metals non-extracted in A* and bound to carbonates

C1': Mn oxides and amorphous Fe oxides

C2': amorphous and poor-crystallized Fe

D1: bound to organic matter

D2: bound to sulphides

E*: bound to silicates (but without using HF)

Table 2. Comparison between the different metal fractions obtained with different sequential extraction methods.

Sequential methods consist of extracting the same sediment sample with a sequence of reactants, usually among 3 and 8, with increasing reactivity in the dissolution process or with different nature regarding the previous one. The application of these methods results in a series of operationally-defined phases. Reactants are diverse and can be grouped in: concentrated inert electrolytes, weak acids, reducing agents, complexing agents, oxidizing agents and strong mineral acids. There are different extraction techniques (Table 2). The lack of uniformity between the different sequential extraction methods prevents comparison of

the results among different techniques. The most applied sequential procedure is that of Tessier et al. (1979), directly applied, or with small modifications (Álvarez-Iglesias et al., 2003; Mahan et al., 1987).

The main inconvenients of sequential extraction methods are the non-specificity of the reactants, the redistribution of trace elements between phases and the overload of the chemical system if the metal content is too high. Furthermore, it has to be beard in mind that some speciation changes could occur because of sample preparation, and also, the lack of reference materials suitable for most of the utilized methods (Quevauviller et al., 1997).

Several complementary analysis can be performed to check for efficiency and selectivity of the extraction procedure: to analyze total organic and inorganic carbon and sulphide contents in the extracts or in the sediments that remains after the different extractions; to study the solids that remain after the different steps by XRF or Scanning Electron Microscopy (SEM); to extract pure samples of geochemically known phases; or to statistically analyze the metals extracted from the sediments and the main sedimentary components that can bind them (Luoma & Bryan, 1981; Rapin & Förstner, 1983).

Metal redistribution or readsorption between the remaining sedimentary phases during the sequential procedure is an inconvenient very difficult to avoid, this is due to the partial selectivity of the extractants (Tessier & Campbell, 1987). One example could be the existence of free sulphides that would cause precipitation of metals previously released from the sediments; another one would be sulphides oxidation (Ngiam & Lim, 2001). Several workers have shown that readsorption happens after the extraction (Guy et al., 1978; Rendell et al., 1980) but they have not agreed if this problem is significant or not.

The problems related to the overload of the chemical system can be solved repeating the same step several times. When metal content is high the quantity of reactant used can be insufficient to completely extract all the metal bound to a certain specific fraction, then, some of the metal would be still retained and would be extracted in the following step.

Regarding to the problems related to the possible changes in especiation because of sample preparation, several workers pointed out that this is more important in anoxic samples than in oxic samples, because most of the extraction procedures have been designed for oxic sediments (Tessier & Campbell, 1988). Techniques of sample preservation before analysis, frozen or keeping at low temperature are better preferred than drying.

In spite of the indicated inconvenients of sequential extraction procedures, these methods are useful to evaluate bioavailability and potential mobility, and to study early diagenetical processes. Among them, the usually applied methods are those proposed by Tessier et al. (1979), Ure et al. (1993) and Huerta-Díaz & Morse (1990). In the Tessier et al. (1979) method (called in the following Tessier's method) the parameters involved in the solubilization of the extracted metals are carefully controled, and five operationally-defined fractions are obtained (Table 2; Fig. 4). The Ure et al. (1993) method, usually known as the BCR method separates three fractions (Table 2), whereas the Huerta-Díaz & Morse (1990) method (called in the following H&M's method) separates four fractions (Table 2, Fig. 4). One important difference is that with the last method metals bound to organic matter are differentiated from those metals bound to sulphides. Nevertheless, the Tessier's method allows differentiating between interchangeable, bound to carbonates and bound to Fe-Mn

oxyhydroxides metal fractions, whereas all together represents one single fraction together with acid-volatile sulphides in the H&M's method and they are considered as two fractions in the BCR procedure (Table 2).

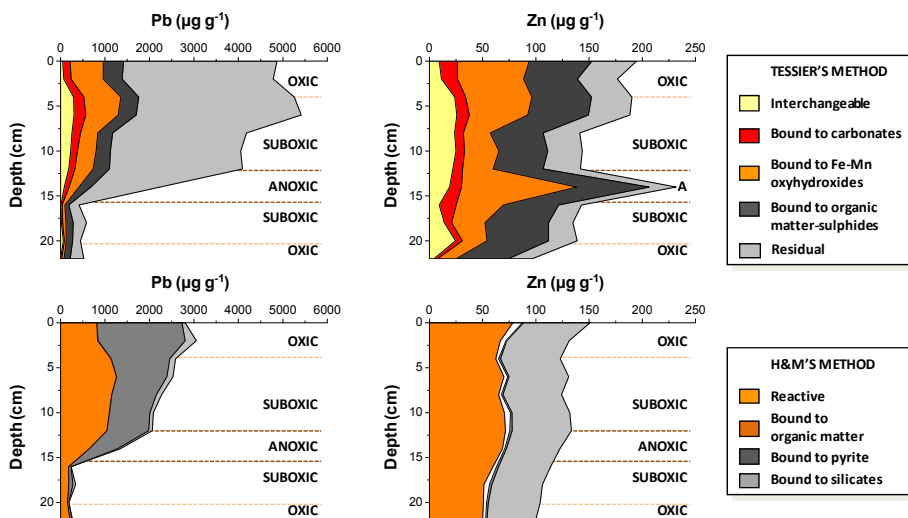


Fig. 4. Metal speciation distribution ($\mu\text{g g}^{-1}$) according to the sequential extraction methods of Tessier et al. (1979) and Huerta-Díaz & Morse (1990) for Pb and Zn in the fine-grained fraction of muddy sandy sediments (core C2) from inner Ría de Vigo. Note the different fraction recovery obtained for the same metal by the two procedures. Differences in the metal content in the silicate fraction or residual are due to the non-total leaching of silicates with the Huerta-Díaz & Morse method. Redox conditions (oxic, suboxic, anoxic-non sulphidic) in these sediments have been inferred according to DOP values (Álvarez-Iglesias et al., 2003).

The interchangeable fraction corresponds to those metals bound to low energy adsorption places and it is the most active fraction from a biological point of view (Campbell et al., 1988). In the fine-grained fraction of inner Ría de Vigo sediments it represents a relatively low content (average $\sim 50 \mu\text{g g}^{-1}$ for Pb and $\sim 10 \mu\text{g g}^{-1}$ for Zn, $N=34$), being more or less abundant depending on the grain-size distribution, the muddier the sediments, the higher the metal contents. The fraction bound to carbonates represents those metals bound or adsorbed into carbonates. In the fine-grained fraction of inner ría sediments it represents a relatively low content (average $\sim 77 \mu\text{g g}^{-1}$ for Pb and $\sim 12 \mu\text{g g}^{-1}$ for Zn, $N=34$). These two fractions together are more or less equivalent to the labile fraction of the BCR method. The labile fraction also represents a very low contribution in middle and outer ría sediments ($<1.1 \mu\text{g g}^{-1}$ for Cu, non-detected for Pb and $\sim 4.1 \mu\text{g g}^{-1}$ for Zn, $N=47$; Fig. 5).

The fraction bound to Fe-Mn oxyhydroxides corresponds to that metallic fraction bound to reducible Al, Fe and Mn oxides/hydroxides. They are unstable compounds under reducing conditions, which causes the release of associated metals. In the sediments of inner Ría de Vigo this fraction represents a significant percentage of the total concentration: around 20% of total Pb and 36% of total Zn (Fig. 4) decreasing to $\sim 6.9\%$ of total Pb and $\sim 14\%$ of total Zn in middle and outer ría sediments (Fig. 5).

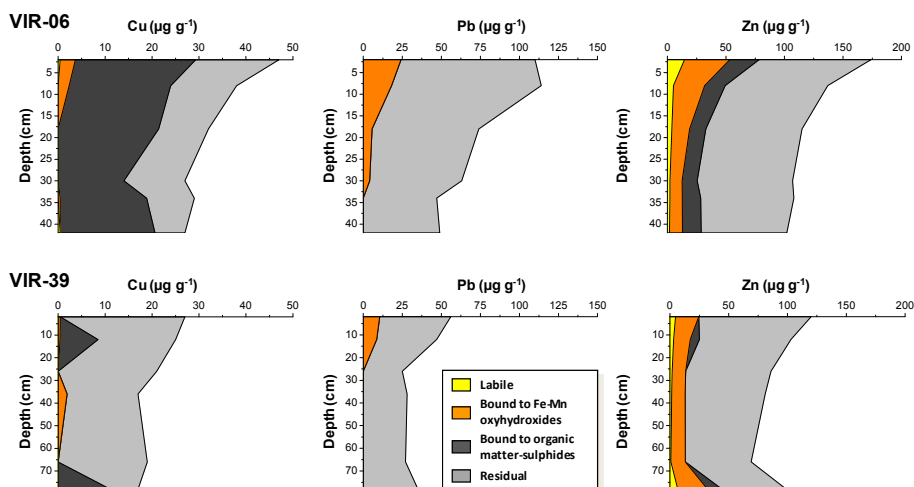


Fig. 5. Depthwise profiles of BCR fractions of Cu, Pb and Zn in cores from middle and outer ría (VIR-06 and VIR-39).

The metal fraction bound to carbonates, to amorphous and cristaline Fe-Mn oxyhydroxides (except goethite) and acid volatile sulphides (AVS) is extracted with the first step of the H&M's method, and then embracing the three fractions formerly discussed. It is called the reactive fraction. This fraction represents 43-75% of total Cu, 27-84% of total Pb and 33-57% of total Zn, in the fine-grained fraction of intertidal inner ría sediments (Fig. 4) and 0.1-51% of total Cu, 54-94% of total Pb and 11-53% of total Zn in subtidal inner ría sediments (Fig. 5).

The metal fraction bound to organic matter can be a significant sink for several metals depending on their relative abundance related to any other sedimentary phases. For example, this fraction represents 1.2-15% of total extracted Cu, 0.2-2.0% of total extracted Pb and 1.7-6.0% of total extracted Zn in intertidal and subtidal oxic sediments (N=20) of inner Ría de Vigo (Fig. 6), being their contribution lower in suboxic and anoxic sediments of the ría. Degradation of organic matter under oxidizing conditions will cause the release of metals bound to this phase.

The metal fraction bound to sulphides is significant in anoxic sediments, where metal sulphides, mainly pyrite, constitute a significant sink for several trace elements, as observed in the Ría de Vigo (Figs. 4, 6). This fraction can represent a high percentage of the total concentration of certain trace elements, such as Cu. For example, this fraction represents 26-94% of total extracted Cu, 5.0-47% of total extracted Pb and 1.2-9.4% of total extracted Zn in anoxic sediments (N=47) of inner Ría de Vigo, with a higher contribution for Cu and Zn in subtidal (Fig. 6) than in intertidal sediments.

These two fractions (bound to organic matter and to sulphides) are obtained as one single fraction, called oxidizable fraction, when applying the Tessier's and the BCR methods. The oxidizable fraction in the fine-grained fraction of intertidal sediments of inner Ría de Vigo according to the Tessier's method represents 7.4-31% of total extracted Pb and 6.1-51% of total extracted Zn (N=34, see examples for particular cores in Fig. 4), whereas this fraction in

middle and outer ría sediments represents, on average, 46% of total extracted Cu, ~1.0% of total extracted Pb and ~11% of total extracted Zn (N=47) in middle and outer ría sediments according to the BCR procedure (see examples for particular cores in Fig. 5).

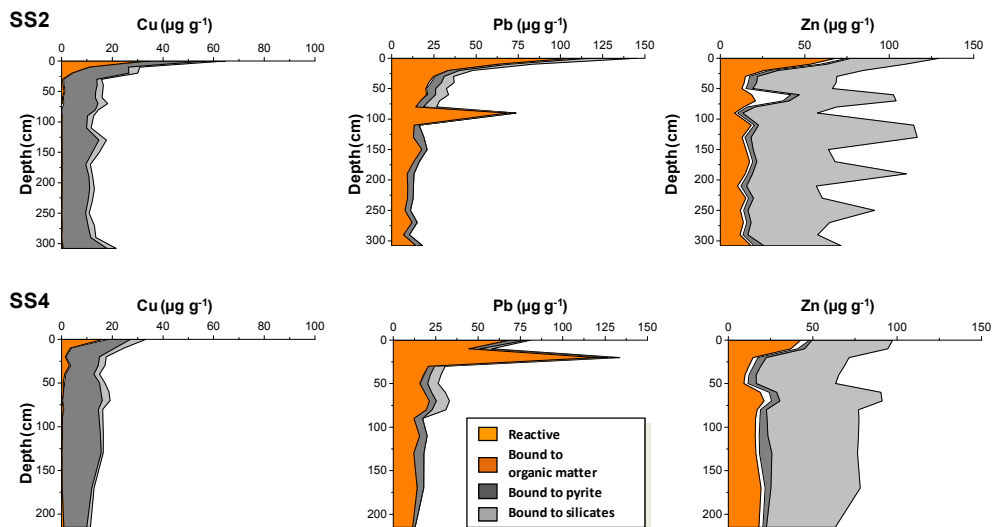


Fig. 6. Metal speciation distribution ($\mu\text{g g}^{-1}$) for Cu, Pb and Zn according to the Huerta-Díaz & Morse (1990) method for subtidal sediments of inner Ría de Vigo (cores SS2 and SS4).

The residual fraction is composed of primary and secondary detrital silicates that occur naturally and can hold trace elements into their crystal structure, resistant sulphides, and refractory organic matter (Tessier et al., 1979). Under natural conditions trace elements bound to this fraction are not expected to be released to the environment. Metal content in this fraction depends on mineral composition of the watershed, on physical properties that rules transport and deposit (grain-size, density, etc.) and on mineral stability and weathering intensity. This fraction is not obtained by some sequential procedures (Table 2) and then it can be obtained by subtraction. In other sequential methods, a silicate bound fraction is obtained but it does not represent the whole metal bound to this fraction. For example, in Fig. 4 the comparison of total concentrations obtained by the Tessier's and H&M's procedures showed clearly that the recovery for residual Pb was not complete with the second method. The comparison of total metal concentrations with the total recovery after applying these sequential extraction procedures showed differences depending on grain-size and mineralogy (Álvarez-Iglesias & Rubio, 2008, 2009): metal recovery was around 60-100% for Fe, 70-75% for Cu, 46-55% for Pb and 70-100% for Zn in inner ría sediments both subtidal and intertidal (fine-grained fraction). The residual fraction in intertidal sediments of inner Ría de Vigo according to the Tessier's method represents ~56% of total extracted Pb and ~18% of total extracted Zn (N=34, see examples in Fig. 4), whereas this fraction in middle and outer ría sediments represents on average ~52% of total extracted Cu, ~92% of total extracted Pb and ~71% of total extracted Zn (N=47) in middle and outer ría sediments according to the BCR procedure (see examples in Fig. 5).

5. Assessment of pollution in marine sediments

Establishing the degree of pollution by trace elements in marine sediments allows studying pollutants distribution for a particular area spatially and temporally and identifying pollutant sources (Dassenakis et al., 1996; Zwolsman et al., 1993). This is usually approached by determining several indexes and studying the relationships between metals and sediment characteristics. First, background levels (BLs) have to be considered, and second, the degree of pollution can be evaluated.

5.1 Background levels

Metal BLs correspond to the natural metal concentrations that exist or would exist in sediments without human influence. Several authors have proposed different BLs to global, regional and local scales, summarized in Tables 3 and 4, for major, minor and trace elements, respectively. Global or world-wide BLs correspond to average values calculated for the Earth crust (Taylor, 1964), granites, deep-sea clay sediments or lutites (Turekian & Wedepohl, 1961). Regional and local BLs take into account local geochemical variability (Rubio et al., 2000a). They can be determined in sediments from the target area or from adjacent areas by different methods such as 1) determination of pre-industrial metallic levels in dated cores; 2) application of regression techniques between a geochemically-stable element without human-influence and the rest of metals; 3) selection of pristine areas; 4) selection of the first-percentile in accumulated distributions of metal concentration; 5) determination of homogenous populations into the target data; 6) a combination of the previous procedure with modal analysis; 7) a direct comparison of polluted and non-polluted sediments from the same study area or an adjacent area; or 8) principal component analysis (Barreiro Lozano, 1991; Carral et al., 1995a, 1995b; Chester & Voutsinou, 1981; Hakanson, 1984; Rubio et al., 2000b; Summers et al., 1996).

The selection of the BL will conditionate the geochemical interpretation of a particular area (Rubio et al., 2000a). The use of local or regional BLs is recommended to take into account local geochemical variability. Even in a local study, BL should be selected considering the watershed composition. It is important to highlight that sediments can be enriched naturally in a particular trace element. For example, Álvarez-Iglesias et al. (2006) showed that sediments in inner Ría de Vigo from a schist-gneiss watershed were enriched in metals such as Fe, Cr and Ni when compared with sediments from a granitic watershed (Fig. 7). Circles in Fig. 7 correspond to a subtidal core of inner ría with relatively high Fe/Al ratios, pointing to a schist-gneiss source, in comparison to another subtidal core samples from inner ría. This can also be deduced for middle and outer Ría de Vigo sediments, with high Fe/Al ratios too. Grain-size and postdepositional physico-chemical processes can also affect to remobilization of some redox-sensitive elements. For example, it can be observed in Fig. 7 that some of the intertidal samples (light squares) showed higher Fe/Al ratios than others from the same area. This can be interpreted as Fe enrichments caused by diagenetic processes. Furthermore, it can be observed that intertidal samples of inner ría (Fig. 7, squares) showed higher coarse-grained particles content and lower concentrations of Fe and Ti than subtidal samples of the ría. Then, it is recommended the use of BLs with similar characteristics (grain size, composition, origin) to those of the sediments of the area under study to avoid misinterpretation of the data. It is also recommended the use of BLs obtained by similar analytical procedures than those applied on the target samples. This will avoid the possible differences in metal concentrations related

only to the efficiency of the followed protocol (Rubio et al., 2000a). For example, Rubio et al. (2000b) established a BL for Cr by XRF higher than that previously established for the same study area by triacid digestion (Rubio et al., 2000a) (Table 4).

Scale	Al	Ca	Fe	K	Mg	P	S	Si	Ti
Global ^{1,a}	8.00	2.21	4.72	2.66	1.50	0.07	0.24	7.30	0.46
Global ^{1,b}	8.40	2.90	6.50	2.50	2.10	0.15	0.13	25.00	0.46
Global ^{1,c}	7.20	0.51	1.42	4.2	0.16	0.06	0.03	34.7	0.12
Global ^{2,d}	8.89	1.64	4.83	2.82	1.57	-	-	27.11	0.43
Global ^{3,e}	8.23	4.15	5.63	2.09	2.33	0.105	0.026	28.15	0.57
Global ^{3,f}	7.70	1.58	2.70	3.34	0.16	0.070	0.027	32.3	0.23
Galicia ⁴	-	-	2.69	-	-	-	-	-	-
Galicia ⁵	-	-	2.6	-	-	-	-	-	-
Galicia ^{6,g}	-	-	2.9	-	-	-	-	-	-
Galicia ^{6,h}	-	-	3.3	-	-	-	-	-	-
RV ⁷	6.48	-	3.51	-	-	-	-	-	0.34
RV ⁸	6.48	-	3.51	-	-	-	-	-	0.34
SSB ⁹	9.82	3.16	3.53	2.59	1.05	0.10	1.06	21.49	0.36
SSB ^{10,i}	9.91	3.22	3.36	2.56	1.05	0.10	0.94	21.45	0.36
SSB ^{10,j}	9.36	2.81	4.44	2.75	1.05	0.08	1.69	21.70	0.37

¹Turekian & Wedepohl (1961); ²Wedepohl (1971, 1991); ³Taylor (1964); ⁴Barreiro Lozano (1991); ⁵Carral et al. (1995a); ⁶Carral et al. (1995b); ⁷Rubio et al. (2000a); ⁸Rubio et al. (2000b); ⁹Álvarez-Iglesias et al. (2006); ¹⁰This study.

^ashales, ^bdeep-sea clay sediments, ^clow Calcium granites, ^daverage shales, ^eEarth crust, ^fgranite average, ^gestuarine sediments from granitic watersheds, ^hestuarine sediments from schist-gneiss watersheds; ⁱría sediments with a granitic source; ^jría sediments with a schist-gneiss source. RV: Ría de Vigo, SSB: San Simón Bay (inner Ría de Vigo).

Table 3. Global, regional and local background levels for major elements (%).

Scale*	As	Cr	Cu	Mn	Ni	Pb	Rb	V	Zn
Global ^{1,a}	13	90	45	850	68	20	140	130	95
Global ^{1,b}	13	90	250	6700	225	80	110	120	165
Global ^{1,c}	1.5	4.1	10	390	4.5	19	170	44	39
Global ^{2,d}	-	90	-	-	68	-	-	130	95
Global ^{3,e}	1.8	100	55	950	75	12.5	90	135	70
Global ^{3,f}	1.5	4	10	400	0.5	20	150	20	40
Galicia ⁴	-	43	25	225	30	25	-	-	100
Galicia ⁵	-	32	28	275	32	53	-	-	122
Galicia ^{6,g}	-	30	20	248	31	78	-	-	136
Galicia ^{6,h}	-	54	35	395	38	50	-	-	120
RV ⁷	-	34	29	244	30	51	-	-	105
RV ⁸	-	55	20	244	30	25	-	-	105
SSB ⁹	16	65	21	216	33	51	198	94	110
SSB ^{10,i}	14	64	19	214	33	54	180	93	111
SSB ^{10,j}	19	70	30	229	35	34	298	99	104

*Uppercase notation similar to that of Table 3.

Table 4. Global, regional and local background levels for minor and trace elements ($\mu\text{g g}^{-1}$).

The first step for evaluating the degree of pollution of inner Ría de Vigo sediments would be to make the scatterplots of Al-Fe, Al-K, Al-S, Al-Si, Al-Ti and Al-Rb (Fig. 7) in order to decide which background value have to be selected for obtaining reliable data. Those samples out of the general trend in the scatter plots will be identified as enriched samples. In the samples under study, it is necessary to consider two different background values: one BL for the samples from middle and outer ría together with the samples of one subtidal core (SS4), and another BL for the rest of the subtidal core samples and the intertidal core samples from the inner ría.

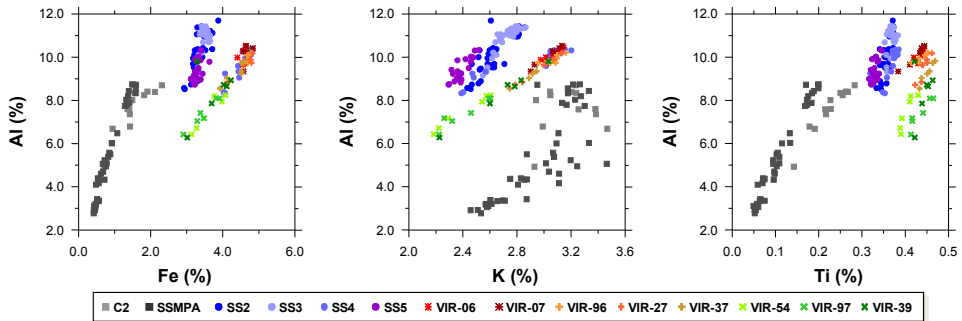


Fig. 7. Scatterplots of Al vs Fe, Al vs K and Al vs Ti in core samples (N=210) from different sectors of the Ría de Vigo (sample location in Fig. 1). Metal contents from XRF analyses. Note the marked differences between intertidal samples (with a higher coarse-grained particles content) and subtidal samples, and the striking differences within subtidal samples, where two populations can be observed, one, with higher Fe/Al ratios (those samples with a schist-gneiss source), the other, with lower Fe/Al ratios (most of the inner ría subtidal cores).

5.2 Degree of pollution

The indexes that are usually applied to evaluate the presence of metal pollution in sediments are the Contamination or Concentration Factor (CF) and the Enrichment Factor (EF) (Barreiro Lozano, 1991; Álvarez-Iglesias et al., 2003; Rubio et al., 2000a).

The CF (Hakanson, 1980) is based on the calculation of the relationship between the concentration of the potential pollutant element measured in the sample $[M]_i$ and the background level for that element $[M]_{BL}$. $CF = [M]_i / [M]_{BL}$. CF value would be close to 1 when there is no metallic enrichment. The degree of contamination can be classified as null or low ($CF < 1$), moderate ($CF: 1-3$), high ($CF: 3-6$) or very high ($CF > 6$).

The EF (Zoller et al., 1974) is based on the calculation of the relationship between the concentration of the potential pollutant element and a normalizer element measured in the sample ($[M]_i$ and $[N_e]_i$, respectively), divided by the same relationship considering the previously selected BL ($[M]_{BL}$ and $[N_e]_{BL}$, respectively): $EF = ([M]_i / [N_e]_i) / ([M]_{BL} / [N_e]_{BL})$. An $EF = 1$ indicates non-enrichment in comparison with the BL. Nevertheless, an EF lower/higher than 1 points to an impoverishment/enrichment, respectively, of the studied trace element. The degree of pollution can be classified in a similar way to that of CF.

Both CF and EF has been calculated for the different cores studied using the new BLs established (Fig. 8). The dispersion among cores considering the deepest samples is higher for CF than for EF depth-profiles, this is explained by the non-consideration of grain-size variability when calculating CF. Furthermore, the high grain-size variability of the intertidal cores, where coarse-grained sediments are very abundant at certain levels, explains the impoverishment observed for the considered trace metals at their bottom. Both CF and EF indexes show a moderate enrichment in Cu and Zn, in general, for the first 0.10-0.20 m of the sedimentary record, in general, for all the cores. Nevertheless, Pb pollution has been detected in the first 0.10-0.80 m, its degree varying from moderate to very high depending on core depth and position. Pollution was classified as high in the first decimeter of inner and middle subtidal cores, whereas the highest EF (up to 40-45) has been detected in the first 0.15-0.20 m of the intertidal core samples. These moderate or high contents of trace metals were explained as anthropogenic inputs, in particular for Cu and Zn from fertilizers and pesticides (Álvarez-Iglesias et al., 2006, 2007) and for Pb both from direct and indirect sources. The main Pb input since the 1970s to the inner ría has been a ceramic factory located at the head of the Ría but previously and nowadays diffuse sources, mainly coal and petrol combustion, have contributed and contribute to Pb inputs to the Ría de Vigo (Álvarez-Iglesias et al., 2003, 2007).

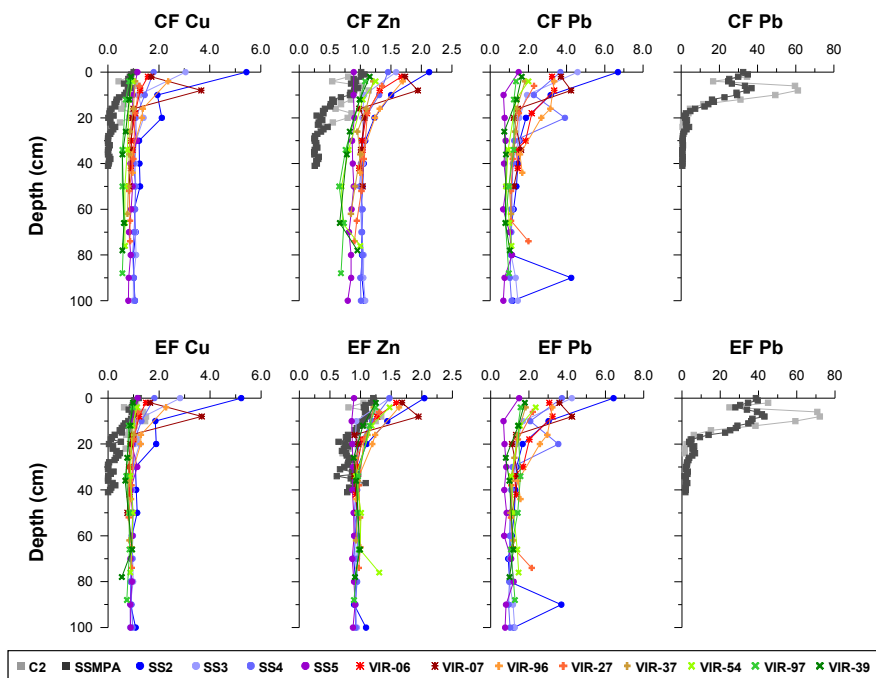


Fig. 8. Evaluation of the degree of pollution according to the CF and EF for Ría de Vigo core samples (sample location in Fig. 1). Note that for the particular case of the subtidal samples of the inner ría it has been only considered those from the first sampled meter in order to allow for a better comparison between cores. CF-Pb and EF-Pb for intertidal cores are showed in a separated graph because of their high pollution factors.

6. Early diagenesis of metals in marine sediments

Early diagenesis processes include all the post-depositional changes that happen in sediments in a short geological time-scale. After sediment deposition, its constituents can suffer chemical modifications, implying a new equilibrium between solid and dissolved species. Then, metal speciation can be modified, and thus, metal mobility and bioavailability too (Shaw et al., 1990). Organic matter degradation fuels early diagenesis processes. Their mineralization is mainly bacterially mediated following an ideal sequence of alternative electron acceptors (Froelich et al., 1979), where the most thermodynamically favoured reaction happens until exhaustion of the corresponding reactant, and then, the next favourable reaction starts. In this way, a diagenetic zonation can be described for the Ría de Vigo sediments.

6.1 Diagenetic zonation

Diagenetic zonation in marine sediments depends on the degree of oxygenation of the water column (Wignall, 1994). According to Berner (1981) different sedimentary environments can be differentiated considering redox potential, electron acceptors and typical mineral associations: oxic, suboxic, anoxic-sulphidic and anoxic-non sulphidic. These four diagenetic zones can be observed in sediments below oxic bottom waters and can be inferred by metal speciation procedures. Considering that sulphate reduction is a significant process in marine sediments, the protocols where the sulphide-bound fraction is independently obtained will be preferred (i.e., H&M's method). One index that is usually used is the degree of pyritization (DOP; Berner, 1970) where the relationship between the pyrite-bound and the reactive fractions is calculated. This index has recently been regarded as an indicator of interstitial water status in coastal sediments (Roychoudhury et al., 2003), with the limits for oxic with DOPs lesser than 42%, suboxic between 42 and 55%, anoxic between 55 and 75% and euxinic higher than 75% (León et al., 2004; Raiswell et al., 1988).

The oxic zone is characterized by the presence of oxygen, which is the first electron acceptor in the organic matter degradation process. Vertical diffusion of dissolved oxygen from the adjacent water column maintains oxygenated the interstitial water of freshly deposited sediments. Nevertheless, oxygen is rapidly consumed with depth because of the high metabolic rates of aerobic bacteria, avoiding vertical diffusion. Organic matter oxidation generates carbon dioxide, nitrate and phosphate (Froelich et al., 1979). CO₂ generation does not usually cause a pH diminution in the interstitial waters, but pH slightly diminishes because of an extensive oxidation of those sulphides migrating toward surface which also causes a carbonate subsaturation. Sediments contains oxides and oxyhydroxides of Fe (hematite, goethite) and Mn, and usually, a low content of organic matter, which is mostly degraded. The extension of the oxic zone is reduced, typically 0.10 m, but controlled by the rate of oxygen consumption which depends on organic matter abundance and sedimentation rate (Wignall, 1994). Bioturbation by organisms in this zone is significant. In inner Ría de Vigo sediments the oxic zone is extended, as a minimum, along the first 0.25 m of the sedimentary record in intertidal coarse-grained sediments (sediments with about 90% of sand and gravel; Álvarez-Iglesias & Rubio, 2009) but it is restricted to the first 0.06 m in sediment cores with a higher fine-grained particles content (around 37%, core C2). In subtidal inner and middle ría sediments oxic conditions hold only in the top few millimetres (Rubio et al., 2010; Álvarez-Iglesias & Rubio, 2012), whereas the oxic zone is restricted to the top decimetre of outer ría sediments (Rubio et al., 2010).

The suboxic zone is characterized by a very low concentrations of oxygen. Here nitrate reduction, Mn reduction and Fe reduction take place (Froelich et al., 1979). Once interstitial water O_2 is consumed, a narrow denitrification zone appears where nitrate is the oxidant. This process accounts for a small percent of the degradation of organic matter (Canfield & Raiswell, 1991). It is also observed an extensive oxidation of those sulphides migrating towards surface, generating elemental Sulphur and sulphate. Then, interstitial waters in the suboxic zone are slightly acidic, and dissolution of carbonated shells takes place. Sediments show glauconite and other Fe^{2+} - Fe^{+3} silicates, Mn carbonates (rhodocrosite), Fe carbonates (siderite), Fe phosphates (vivianite), non-sulphidic minerals and, usually, a low content of organic matter. In inner Ría de Vigo the suboxic zone is extended approximately from 0.06 to 0.22 m in intertidal sediment cores with a high fine-grained particles content (Álvarez-Iglesias & Rubio, 2009). In subtidal inner and middle ría sediments, the suboxic conditions extend down to 0.10-0.20 m, and in outer ría sediments, down to 0.40 m, excepting those areas of strong turbulent currents (core SS5), where suboxic conditions extend, as a minimum, down to a few meters (Rubio et al., 2010; Álvarez-Iglesias & Rubio, 2012).

Buried Mn oxides below surficial oxic layer are reductively dissolved in the suboxic layer and Mn^{+2} are released to the interstitial waters. These ions diffuse towards surface because of a concentration gradient, reprecipitating as a “second generation”, “third generation”, etc., of oxides in the bottom of the oxic layer. Then, it can be generated sedimentary layers highly enriched in Mn over the Mn-redox limit as a result of Mn oxidative reprecipitation in the oxic layer (called “Mn trap”). Similarly, Fe^{2+} diffusion towards surface will generate Fe oxyhydroxides reprecipitation. Then, Fe and Mn profiles can be highly affected by redox changes. This has clearly been observed in intertidal sand flat sediments of inner Ría de Vigo, where subsurficial maxima were detected for both elements related to Fe and Mn ions migration and reprecipitation (Álvarez-Iglesias et al., 2003). It has also been detected in middle and outer ría sediments, where it has been observed Mn reducible (BCR method) maxima in the metal content profiles (Rubio et al., 2010). Associated to those maxima it has also been observed Cu, Pb and Zn maxima in the reducible fraction of Ría de Vigo sediments, indicating trace metal coprecipitation with the authigenic oxyhydroxides.

The anoxic-sulphidic zone or sulphate-reduction zone (SRZ) is characterized by metal sulphide generation (Huerta-Díaz & Morse, 1992). Strict anaerobic bacteria run sulphate-reduction, which is a dominant process in marine sediments, in particular, this process accounts for about 50 % of organic matter degradation in coastal sediments (Jørgensen, 1982). When organic matter is degraded by sulphate reduction weak acids are generated (HCO_3^- , HS^- , HPO_4^{2-}), then carbonate subsaturation (coming from the previous zone) is maintained. Most of the generated sulphide ions are oxidized in the redox upper boundary but a significant proportion reacts with iron to form, in the last step, pyrite. The main Fe sources are detrital Fe minerals, in particular fine-grained Fe oxides. Sulphide ions can also react with organic matter and form organosulphur compounds, which represents usually a small fraction in coastal sediments (Berner, 1970, 1981; Fig. 9). While sulphide is removed from dissolution by sulphide generation, interstitial waters pH increase and then, carbonate saturation happens. Then, typical minerals in the SRZ are pyrite, marcasite, rhodocrosite, and alabandite. Different metal ions can coprecipitate with authigenic pyrite or form other sulphides, then, their bioavailability will be limited while environmental reducing conditions maintain. In anoxic sediments from the inner sector of Ría de Vigo it has been

observed that ~28% of Cu, ~34% of Pb and ~1.5% of Zn is retained in the pyrite-bound fraction in intertidal sediments, whereas ~82% of Cu, ~18% of Pb and ~5.1% of Zn in the same fraction of subtidal sediments (Álvarez-Iglesias & Rubio, 2008, 2009). In middle and outer ría sediments it has been observed, in general, an increase with depth in the contents of Cu and Zn in the oxidizable fraction (BCR method) that would probably be related to sulphide generation, taking into account that the organic fraction accounted for ~1.2% of Cu and ~5.2% of Zn in anoxic sediments and ~2.3% of Cu and ~5.1% of Zn in suboxic sediments from the subtidal inner ría sector.

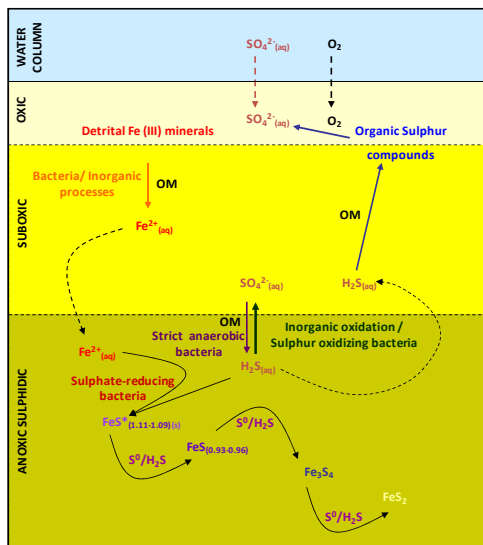


Fig. 9. Schematic representation of pyrite formation in marine sediments (modified from Berner (1970), Rickard et al. (1995) and Schoonen & Barnes (1991). OM= organic matter.

At low temperatures pyrite formation can be conceptually reduced to two steps: a) precipitation of an iron monosulphide precursor (FeS^*), and b) pyrite formation by S addition (Berner, 1970; Rickard et al., 1995; Schoonen & Barnes, 1991) (Fig. 9). Nevertheless, direct pyrite precipitation has been described in saltmarsh sediments without intermediate precursors (Giblin & Howard, 1984). The most common pyrite morphologies described in Galician rías sediments, are euhedral and single framboids or polyframboids (Rubio et al., 2001; Álvarez-Iglesias & Rubio, 2012).

In the SRZ it could be observed Mn peaks. Alkalinity genesis in this zone is avoided when organism galleries penetrate actively and regularly. This causes sulphide oxidation. Carbonate dissolution may happen too (Aller, 1982; Canfield & Raiswell, 1991). The limit between the suboxic zone and the SRZ is called redoxcline. It represents a barrier to element transport by diffusion because of the presence of amorphous Fe-Mn oxyhydroxides. It is a dynamic limit, changing its position temporally and spatially. It can be detected de visu in intertidal sediments, such as those of inner Ría de Vigo, by the colour change between the brown-reddish oxidized surficial sediments –which reflects Fe oxides precipitation- and the

dark grey-black reduced sediments-which reflects pyrite precipitation. The anoxic zone develops from 0.14 to 0.18 m in those intertidal sediment cores from the inner ría with a high fine-grained particles content (core C2; Álvarez-Iglesias & Rubio, 2009). In subtidal sediments from inner and middle ría the anoxic zone is extended down the first one-two decimetres of the sedimentary record (with the exception of turbulent areas), whereas in the outer zone, down the first 0.40 m (Rubio et al., 2010; Álvarez-Iglesias & Rubio, 2012). Then, the diagenetic zones all became thicker, as well as lying deeper, as the mouth of the ría was approached.

Finally, the anoxic-non sulphidic zone or methanogenic zone (MZ) is characterized by methane generation by bacterial fermentation (Froelich et al., 1979) which causes a slight pH diminution. Typical minerals in the MZ are siderite, vivianite, rhodocrosite and previously formed sulphides. The MZ only develops if high organic matter quantities have not been degraded in the SRZ. Then, its development is favoured in areas with a high organic carbon flux to the sediments and/or high sedimentation rates, where up to 10% of the sedimentary organic matter is consumed by methanogenesis. When methane solubility is exceeded, gas bubbles accumulate and methane gas will diffuse upwards. In subtidal sediments of the Ría de Vigo it has been described several shallow gas fields, where biogenic methane was detected (García-Gil et al., 2002; Iglesias & García-Gil, 2007) and gas bubbles have been observed in the sediments (Álvarez-Iglesias et al., 2006; García-Gil et al., 2002). The top of the gas fields was located at sediment depths ranging between 11 and 0 m, shallowing towards the ría head (García-Gil et al., 2002; Iglesias & García-Gil, 2007).

7. Conclusion

The study of the sedimentary record allows establishing metal pollution history spatially and temporally for a particular area and needs to be multidisciplinary. First, hydrological, hydrographical, geological and anthropological information (industrial and rural development) on the study area needs to be compiled. Second, adequate analytical techniques, reference materials and background levels have to be selected. Background levels and metal concentrations in target samples should be analyzed by the same analytical protocols.

It has to be considered the relationships between metal concentrations, mineralogy, grain-size and metal sources. Sediments from Ría de Vigo showed that lithogenic elements such as Al, V or Ni were more abundant in fine-grained sediments and elements such as Si, in coarse grained sediments, showing the typical association of trace metals to organic-rich fine-grained sediments. Furthermore, biogenic inputs caused a dilution of detrital metal inputs. For correction of this grain-size effect, the use of normalization techniques is highly recommended.

It is also recommended the use of local or regional background levels to take into account the geological variability of the study area. It is useful for its selection to analyze deep sediments with no-human influence and to use metal-Al scatter-plots to identify outliers (enriched samples). This procedure has shown that in the Ría de Vigo sediments two clear sediment populations can be differentiated influenced by the watersheds composition (metallic natural source) and two different BLs have been considered, depending on the population.

Metal pollution can be identified by the use of pollution indexes, such as the Contamination Factor and the Enrichment Factor. These indexes showed that sediments of Ría de Vigo are moderately polluted by Cu and Zn in the first one-two decimeters of the sedimentary record, whereas moderately to very highly polluted by Pb, specially in the inner ría sediments.

Metal concentration alone it is not enough to evaluate metal availability and mobility, then, metal speciation protocols have to be considered. The protocols usually followed are those non-selective. In Ría de Vigo sediments, in general, a significant percentage of Cu, Pb and Zn is hosted in the residual fraction, whereas a small content is retained in the interchangeable and bound to carbonates fraction. Metal fraction content bound to Fe-Mn oxyhydroxides is higher in intertidal than subtidal inner ría sediments. Nevertheless, the reactive fraction content contribution is higher in middle and outer ría sediments. Concentrations of Cu, Pb and Zn are very low in the labile fraction of middle and outer ría sediments, and also, the Zn contents in the interchangeable and bound to carbonates fractions. Nevertheless, Pb concentrations in these last two fractions-that are highly bioavailable- in intertidal sediments oversize the background levels established for total concentrations.

The modification of metal speciation patterns by diagenetical processes has been showed for Ría de Vigo sediments, where Mn enrichments were detected, clearly in sandy intertidal sediments. Different sedimentary environments -oxic, suboxic, anoxic-non sulphidic- and their extension has been detected in the studied ría sediments. The boundaries between these diagenetic zones became deeper towards the ría mouth.

8. Acknowledgment

This work was supported by the Spanish Ministry of Science and Technology through projects CTM2007-61227/MAR, GCL2010-16688 and IPT-310000-2010-17, by the IUGS-UNESCO through project IGCP-526 and by the Xunta de Galicia through projects 09MMA012312PR and 10MMA312022PR.

9. References

- Ackermann, F. (1980). A procedure for correcting the grain size effect in heavy metal analyses of estuarine and coastal sediments. *Environmental Technology Letters*, Vol. 1, pp. 518-527.
- Aller, R.C. (1982). Carbonate dissolution in nearshore terrigenous muds—the role of physical and biological reworking: *Journal of Geology*, Vol. 90, pp. 79-95.
- Álvarez-Iglesias, P.; Quintana, B., Rubio, B. & Pérez-Arlucea, M. (2007). Sedimentation rates and trace metal input history in intertidal sediments derived from ^{210}Pb and ^{137}Cs chronology. *Journal of Environmental Radioactivity*, Vol. 98, pp. 229-250.
- Álvarez-Iglesias, P. & Rubio, B. (2008). The degree of trace metal pyritization in subtidal sediments of a mariculture area: application to the assessment of toxic risk. *Marine Pollution Bulletin*, Vol. 56, pp. 973-983.
- Álvarez-Iglesias, P. & Rubio, B. (2009). Redox status and heavy metal risk in intertidal sediments in NW Spain as inferred from the degrees of pyritization of iron and trace elements. *Marine Pollution Bulletin*, Vol. 58, pp. 542-551.

- Álvarez-Iglesias, P. & Rubio, B. (2012). Early diagenesis of organic-matter-rich sediments in a ría environment: Organic matter sources, pyrites morphology and limitation of pyritization at depth. *Estuarine, Coastal and Shelf Science*, Vol. 100, pp. 113-123.
- Álvarez-Iglesias, P.; Rubio, B. & Pérez-Arlucea, M. (2006). Reliability of subtidal sediments as "geochemical recorders" of pollution input: San Simón Bay (Ría de Vigo, NW Spain). *Estuarine, Coastal and Shelf Science*, Vol. 70, pp. 507-521.
- Álvarez-Iglesias, P.; Rubio, B. & Vilas, F. (2003). Pollution in intertidal sediments of San Simón Bay (Inner Ría de Vigo, NW of Spain): total heavy metal concentrations and speciation. *Marine Pollution Bulletin*, Vol. 46, pp. 491-506.
- Álvarez-Salgado, X. A.; Gago, J.; Míguez, B. M.; Gilcoto, M. & Pérez, F. F. (2000). Surface waters of the NW Iberian Margin: upwelling on the shelf versus outwelling of upwelled waters from the Rías Baixas. *Estuarine, Coastal and Shelf Science*, Vol. 51, pp. 821-837.
- Barreiro Lozano, R. (1991): *Estudio de metales pesados en medio y organismos de un ecosistema de ría (Pontedeume, A Coruña)*. Ph.D. Thesis, Universidad de Santiago de Compostela, 227 p.
- Belzunce-Segarra, M.J.; Bacon, J.R.; Prego, R. & Wilson, M.J. (1997). Chemical forms of heavy metals in surface sediments of the San Simon inlet, Ria de Vigo, Galicia. *Journal of Environmental Science and Health*, Vol. A32, pp. 1271-1292.
- Berner, R.A. (1970). Sedimentary pyrite formation. *American Journal of Science*, Vol. 268, pp. 1-23.
- Berner, R.A. (1981). A new geochemical classification of sedimentary environments. *Journal of Sedimentary Petrology*, Vol. 51, No.2, pp. 359-365.
- Borovec, Z. (1996). Evaluation of the concentrations of trace elements in stream sediments by factor and cluster analysis and the sequential extraction procedure. *The Science of the Total Environment*, Vol. 177, pp. 237-250.
- Bryan, G.W. & Langston, W.J. (1992). Bioavailability, accumulation and effects of heavy metals in sediments with special reference to United Kingdom Estuaries: a review. *Environmental Pollution*, Vol. 76, pp. 89-131.
- Boyle, J.F. (2000). Rapid elemental analysis of sediment samples by isotope source XRF. *Journal of Paleolimnology*, Vol. 23, pp. 213-221.
- Campbell, P.G.C.; Lewis, A.G.; Chapman, P.M.; Crowder, A.A.; Fletcher, W.K.; Imber, B.; Luoma, S.N.; Stokes, P.M. & Winfrey, M. (1988). *Biologically available metals in sediments*. NRCC, Division of Chemistry Publication, Ottawa, 296 pp.
- Canfield, D.E. & Raiswell, R. (1991). Pyrite formation and fossil preservation, *Taphonomy: Releasing the Data Locked in the Fossil Record. Topics in Geobiology*. P.A. Allison & D.E.G. Briggs (Eds.), Vol. 9, 337-387.
- Carral, E.; Puente, X.; Villares, E. & Carballeira, A. (1995a). Background heavy metal levels in estuarine sediments and organism in Galicia (Northwest Spain) as determined by modal analysis. *Science of the Total Environment*, Vol. 172, pp. 175-188.
- Carral, E.; Villares, R.; Puente, X. & Carballeira, A. (1995b). Influence of watershed lithology on heavy metal levels in estuarine sediments and organisms in Galicia (North-west Spain). *Marine Pollution Bulletin*, Vol. 30, No.9, pp. 604-608.
- Chester, R. & Voutsinou, F. G. (1981). The initial assessment of trace metal pollution in coastal sediments. *Marine Pollution Bulletin*, Vol. 12, pp. 84-91.

- Dassenakis, M.I.; Kloukiniotou, M.A. & Pavlidou, A.S. (1996). The influence of long existing pollution on trace metal levels in a small tidal Mediterranean Bay. *Marine Pollution Bulletin*, Vol. 32, pp. 275-282.
- Duffus, J.H. (2002). "Heavy metals" – A meaningless term? *Pure Applied Chemistry*, Vol. 74, pp. 793-807.
- Fichet, D.; Radenac, G. & Miramand, P. (1998). Experimental studies of impacts of harbour sediments resuspension to marine invertebrates larvae: bioavailability of Cd, Cu, Pb and Zn and toxicity. *Marine Pollution Bulletin*, Vol. 36, pp. 509-518.
- Flyhammar, P. (1998). Use of sequential extraction on anaerobically degraded municipal solid waste. *The Science of the Total Environment*, Vol. 212, pp. 203-215.
- Förstner, U. (1989). *Contaminated Sediments. Lecture notes on Earth Science 21*. Springer-Verlag, London, 157 pp.
- Freire, J. & García-Allut, A. (2000). Socioeconomic and biological causes of management failures in European artisanal fisheries: the case of Galicia (NW Spain). *Marine Policy*, Vol. 24, pp. 375-384.
- Froelich, P.N.; Klinkhammer, G.P.; Bender, M.L.; Luedtke, N.A.; Heath, G.R.; Cullen, D.; Dauphin P.; Hammond, D. & Hartman, B. (1979). Early oxidation of organic matter in pelagic sediments of the eastern equatorial Atlantic: suboxic diagenesis. *Geochimica et Cosmochimica Acta*, Vol. 43, pp. 1075-1090.
- García-Gil, S.; Vilas, F. & García-García, A. (2002). Shallow gas features in incised-valley fills (Ria de Vigo, NW Spain): a case study. *Continental Shelf Research*, Vol. 22, pp. 2303-2315.
- Giblin, A.E. & Howarth, R.W. (1984). Porewater evidence for a dynamic sedimentary iron cycle in salt marshes. *Limnology and Oceanography*, Vol. 29, pp. 47-63.
- Gómez Ariza, J.L.; Giráldez, I.; Sánchez-Rodas, D. & Morales, E. (2000). Comparison of the feasibility of three extraction procedures for trace metal partitioning in sediments from South-West Spain. *The Science of the Total Environment*, Vol. 246, pp. 271-283.
- González-Pérez, J.M. & Pérez González, A. (2003). Demographic dynamics and urban planning in Vigo since 1960. The impact of industrialization. *Anales de Geografía de la Universidad Complutense*, Vol. 23, pp. 163-185.
- Guy, R.D.; Chakrabarti, C.L. & McBain, D.C. (1978). An evaluation of extraction techniques for the fractionation of Copper and Lead in model sediment systems. *Water Research*, Vol. 12, pp. 21-24.
- Hakanson, L. (1980). An ecological risk index for aquatic pollution control. A sedimentological approach. *Water Research*, Vol. 14, pp. 975-1001.
- Hakanson, L. (1984). Metals in fish and sediments from the River Kolbäcksan water system, Sweden. *Archiv für Hydrobiologie*, Vol. 101, No.3, pp. 373-400.
- Horowitz, A.J. & Elrick, K.A. (1987). The relation of stream sediment surface area, grain size, and composition of trace element chemistry. *Applied Geochemistry*, Vol. 2, pp. 437-451.
- Howard, J.L. & Shu, J. (1996). Sequential extraction analysis of heavy metals using a chelating agent (NTA) to counteract resorption. *Environmental Pollution*, Vol. 91, No. 1, pp. 89-96.
- Huerta-Díaz, M.A. & Morse, J.W. (1992). Pyritisation of trace metals in anoxic marine sediments. *Geochimica et Cosmochimica Acta*, Vol. 56, pp. 2681-2702.

- Huerta-Díaz, M.A. & Morse, J. (1990). A quantitative method for determination of trace metal concentrations in sedimentary pyrite. *Marine Chemistry*, Vol. 29, pp. 119-144.
- IGME (1981). *Mapa Geológico de España*, 1:50000, Servicio de Publicaciones Ministerio de Industria y Energía.
- Imperato, M.; Adamo, P.; Naimo, D.; Arienzo, M.; Stanzione, D. & Violante, P. (2003). Spatial distribution of heavy metals in urban soils of Naples city (Italy). *Environmental Pollution*, Vol. 124, pp. 247-256.
- Iglesias, J. & García-Gil, S., 2007. High-resolution mapping of shallow gas accumulations and gas seeps in San Simón Bay (Ría de Vigo, NW Spain). *Geo-Marine Letters*, Vol. 27, pp. 103-114.
- Izquierdo, C.; Usero, J. & Gracia, I. (1997). Speciation of heavy metals in sediments from salt marshes on the Southern Atlantic Coast of Spain. *Marine Pollution Bulletin*, Vol. 34, No. 2, pp. 123-128.
- Jørgensen, B.B. (1982). Mineralization of organic matter in the sea bed- the role of sulphate reduction. *Nature*, Vol. 296, pp. 643-645.
- Kersten, M. & Förstner, U. (1987). Effect of sample pretreatment on the reliability of solid speciation data of heavy metals -implications sesfor the study of early diagenetic processes. *Marine Chemistry*, Vol. 22, pp. 99-312.
- León, I.; Méndez, G. & Rubio, B. (2004). Geochemical phases of Fe and degree of pyritization in sediments from Ría de Pontevedra (NW Spain): Implications of mussel raft culture. *Ciencias Marinas*, Vol. 30, pp. 585-602.
- Loring, D.H. (1981). Potential bioavailability of trace metals in eastern Canadian estuarine sediments. *Rapports et Proces-Verbaux des Reunions, Conseil International pour l'Exploration de la Mer*, Vol. 181, pp. 93-101.
- Loring, D.H. (1990). Lithium-a new approach for the granulometric normalization of trace metal data. *Marine Chemistry*, Vol. 29, pp. 155-168.
- Luoma S.N. & Bryan, G.W. (1981). A statistical assessment of the form of trace metals in oxidized estuarine sediment employing chemical extractants. *The Science of the Total Environment*, Vol. 17, pp. 165-196.
- Luoma, S.N. (1986). A comparison of two methods for determining copper partitioning in oxidized sediments. *Marine Chemistry*, Vol. 20, pp. 45-49.
- Mahan, K. I.; Foderaro, T.A.; Garza, T.L.; Martínez, R.M.; Maroney, G.A.; Trivisonno, M.R. & Willging, E.M. (1987). Microwave digestion techniques in the sequential extraction of Calcium, Iron, Chromium, Manganese, Lead and Zinc in sediments. *Analytical Chemistry*, Vol. 59, pp. 938-945.
- Moore, H.W. (1991). *Inorganic Contaminants of Surface Water. Research and Monitoring priorities*. Springer-Verlag, New York, 334 pp.
- Ngiam, L.-S. & Lim, P.-E. (2001). Speciation patterns of heavy metals in tropical estuarine anoxic and oxidized sediments by different sequential extraction schemes. *The Science of the Total Environment*, Vol. 275, pp. 53-61.
- Pérez-Arlucea, M.; Méndez, G.; Clemente, F.; Nombela, M.; Rubio, B. & Filgueira, M. (2005). Hydrology, sediment yield, erosion and sedimentation rates in the estuarine environment of the Ría de Vigo, Galicia, Spain. *Journal of Marine Systems*, Vol. 54, pp. 206-226.

- Prego, R. & Cobelo-García, A. (2003). Twentieth century overview of heavy metals in the Galician Rias (NW Iberian Peninsula). *Environmental Pollution*, Vol. 121, pp. 425-452.
- Prego, R., Otxotorena, U. & Cobelo-García, A. (2006) Presence of Cr, Cu, Fe and Pb in sediments underlying mussel-culture rafts (Arosa and Vigo rias, NW Spain). Are they metal-contaminated areas? *Ciencias Marinas*, Vol. 32, No.2B, pp. 339-349.
- Quevauviller, Ph.; Rauret, G.; López-Sánchez, J-F.; Rubio, R.; Ure, A. & Muntau, H. (1997). Certification of trace metal extractable contents in a sediment reference material (CMR 601) following a three-step sequential extraction procedure. *The Science of the Total Environment*, Vol. 205, pp. 223-234.
- Raiswell, R.; Buckley, F.; Berner, R. & Anderson, T. (1988). Degree of pyritization of iron as a paleoenvironmental indicator of bottom-water oxygenation. *Journal of Sedimentary Petrology*, Vol. 58, pp. 812-819.
- Rapin, F. & Förstner, U. (1983). Sequential leaching techniques for particulate metal speciation: the selectivity of various extractants, In: *Proceedings of the 4th Conference on Heavy Metals and the Environment* (Heidelberg, Germany), 1074-1077.
- Rendell, P.S.; Bately, G.E. & Cameron, A.J. (1980). Adsorption as a control of metal concentrations in sediment extracts. *Environmental Technology Letters*, Vol. 14, pp. 314-318.
- Rey, D.; Mohamed, K.J.; Bernabeu, A.; Rubio, B. & Vilas, F. (2005). Early diagenesis of magnetic minerals in marine transitional environments: geochemical signatures of hydrodynamic forcing. *Marine Geology*, Vol. 215, pp. 215-236.
- Rickard, D.; Schoonen, M.A.A. & Luther III, G.W. (1995). Chemistry of iron sulfides in sedimentary environments, In: *Geochemical Transformations of Sedimentary Sulfur*, M.A. Vairavamurthy & M.A.A. Schoonen (Eds.), Vol. 612, 168-193. American Chemical Society Symposium Series.
- Roychoudhury, A.N.; Kostka, J.E. & Van Capellen, P. (2003). Pyritization: a palaeoenvironmental and redox proxy reevaluated. *Estuarine, Coastal and Shelf Science*, Vol. 57, pp. 1183-1193.
- Rubio, B.; Álvarez-Iglesias, P. & Vilas, F. (2010). Diagenesis and anthropogenesis of metals in the recent Holocene sedimentary record of the Ría de Vigo (NW Spain). *Marine Pollution Bulletin*, Vol. 60, pp. 1122-1129.
- Rubio, B.; Nombela M.A. & Vilas F. (2000a). Geochemistry of major and trace elements in sediments of the Ría de Vigo (NW Spain): An assessment of metal pollution. *Marine Pollution Bulletin*, Vol. 40, pp. 968-980.
- Rubio, B.; Nombela M.A. & Vilas F. (2000b): La contaminación por metales pesados en las Rías Baixas gallegas: nuevos valores de fondo para la Ría de Vigo (NO de España). *Journal of Iberian Geology*, Vol. 26, pp. 121-149.
- Rubio, B.; Pye, K.; Rae, J. & Rey, D. (2001). Sedimentological characteristics, heavy metal distribution and magnetic properties in subtidal sediments, Ría de Pontevedra, NW Spain. *Sedimentology*, Vol. 48 No.6, pp. 1277-1296.
- Rubio, B.; Rey, D.; Bernabeu, A.; Vilas, F. & Rodríguez-Germade, I. (2011). Nuevas técnicas de obtención de datos geoquímicos de alta resolución en testigos sedimentarios, el XRF core scanner, In: *Métodos y técnicas en investigación marina*. Editorial TECNOS, Madrid (Spain), 383-393.
- Salomons, W. & Förstner, U. (1984). *Metals in the hydrocycle*. Springer-Verlag, Berlin, 349 p.

- Salomons, W.; Kerdiijk, H.; Van Pagee, H. & Schreur, A. (1985). Behaviour and impact assessment of heavy metals in estuarine and coastal zones, In: *Metals in Coastal Environments of Latin America*. U. Seeliger; L.D. de Lacerda & S.R. Patchineelam (Eds.), 157-198.
- Schoonen, M.A.A. & Barnes, H.L. (1991). Reactions forming pyrite and marcasite from solution: II. Via FeS precursors below 100°C. *Geochimica et Cosmochimica Acta*, Vol. 55, pp. 1505-1514.
- Shaw, T.J.; Gieskes, J.M. & Jahnke, R.A. (1990). Early diagenesis in differing depositional environments: the response of transition metals in pore water. *Geochimica et Cosmochimica Acta*, Vol. 54, pp. 1233-1246.
- Stephens, S.R.; Alloway, B.J.; Parker, A.; Carter, J.E. & Hodson, M.E. (2001). Changes in the leachability of metals from dredged canal sediments during drying and oxidation. *Environmental Pollution*, Vol. 114, pp. 407-413.
- Summers, J.K.; Wade, T.L. & Engle, V.D. (1996). Normalization of metal concentrations in estuarine sediments from the Gulf of Mexico. *Estuaries*, Vol. 19, No.3, pp. 581-594.
- Taylor, S.R. (1964). Abundance of chemical elements in the continental crust: a new table. *Geochimica et Cosmochimica Acta*, Vol. 28, pp. 1273-1285.
- Tessier, A. & Campbell, P.G.C. (1987). Partitioning of trace metals in sediments: relationships with bioavailability. *Hydrobiologia*, Vol. 149, pp. 43-52.
- Tessier, A. & Campbell, P.G.C. (1988). Partitioning of trace metals in sediments, In: *Metal Speciation: Theory, Analysis and Application*, J.R. Kramer & H.E. Allen (Eds.), 183-199, Lewis Publishers, Inc.
- Tessier, A., Campbell P.G.C. & Bisson, M. (1979). Sequential extraction procedure for the speciation of particulate trace metals. *Analytical Chemistry*, Vol. 51, pp. 844-851.
- Turekian, K.K. & Wedepohl, K.H. (1961). Distribution of the elements in some major units of the Earth's Crust. *Geological Society of America Bulletin*, Vol. 72, pp. 175-192.
- Uhrberg, R. (1982). Acid digestion bomb for biological samples. *Analytical Chemistry*, Vol. 54, pp. 1906-1908.
- Ure, A.M.; Quevauviller, P.; Muntau, H. & Griepink, B. (1993). Speciation of heavy metals in soils and sediments: an account of the improvement and harmonization of extraction techniques undertaken under the auspices of the BCR of the Commission of the European Communities. *International Journal of Environmental Analytical Chemistry*, Vol. 51, pp. 135-151.
- Varekamp, J.C. (1991). Trace element geochemistry and pollution history of mud flats and marsh sediments from the Connecticut River estuary. *Journal of Coastal Research*, Vol. SI11, pp. 105-124.
- Vega, F.A.; Covelo, E.F & Andrade, M.L. (2008). Impact of industrial and urban waste on the heavy metal content of salt marsh soils in the southwest of the province of Pontevedra (Galicia, Spain). *Journal of Geochemical Exploration*, Vol. 96, pp. 148-160.
- Vilas, F.; Bernabeu, A. M. & Méndez, G. (2005). Sediment distribution pattern in the Rías Baixas (NW Spain): main facies and hydrodynamic dependence. *Journal of Marine Systems*, Vol. 54, pp. 261-276.
- Wangersky, P.J. (1986). Biological control of trace metal residence time and speciation: A review and synthesis. *Marine Chemistry*, Vol. 18, pp. 269-297.

- Wedepohl, K.H. (1971). Environmental influences on the chemical composition of shales and clays, In: *Physics and chemistry of the Earth*, L.H. Ahrens; F. Press; S.K. Runcorn & H.C. Urey, (Eds.), 307-331, Oxford, Pergamon.
- Wedepohl, K.H. (1991). The composition of the upper Earth's crust and the natural cycles of selected metals: metals in natural raw materials; natural resources, In: *Metals and Their Compounds in the Natural Environment*, E. Merian (Ed.), 3-17, Weinheim: VCH.
- Wignall, P.B. (1994). *Black shales and their controversies*, Oxford University Press, 124 p.
- Zoller, W.H.; Gladney, E.S.; Gordon, G.E. & Bors, J.J. (1974). Emissions of trace elements from coal fired power plants, In: *Trace Substances in Environmental Health*, D.D. Hemphill (Ed.), Vol. 8, 167-172, Rolla, University of Missouri, Columbia.
- Zwolsman, J.J.G; Berger, G.W. & Van Eck, G.T.M. (1993). Sediment accumulation rates, historical input, postdepositional mobility and retention of major elements and trace metals in salt marsh sediments of the Scheldt Estuary, SW Netherlands. *Marine Chemistry*, Vol. 44, pp. 73-94.

Organic Facies: Palynofacies and Organic Geochemistry Approaches

João Graciano Mendonça Filho¹, Taíssa Rêgo Menezes²,
Joalice de Oliveira Mendonça¹, Antonio Donizeti de Oliveira¹,
Tais Freitas da Silva¹, Noelia Franco Rondon¹
and Frederico Sobrinho da Silva¹

¹*Federal University of Rio de Janeiro, Palynofacies & Organic Facies Laboratory*

²*Geochemistry Section, PETROBRAS Research Center
Brazil*

1. Introduction

The concept of organic facies, as well as the definitions and means of the different facies became a very important tool to palaeoenvironmental characterization, basin analysis and fossil fuel exploration. The application of this concept is the best way to integrate microscopy and geochemical techniques to study kerogen contained in sedimentary rocks. Thus, palynofacies analysis and bulk geochemical methods (organic facies) are used to characterize the sedimentary organic matter (kerogen and bitumen). Palynofacies analysis involves the integrated study of all aspects of the kerogen assemblage: identification of the individual particulate components, assessment of their absolute and relative proportions and preservation states. The correlation between palynofacies and geochemical data provides the organic facies models that point out the depositional environmental conditions and hydrocarbon source rock potential.

2. Organic matter: Concepts and definitions

2.1 Origin and characterization of the sedimentary organic matter

Organic matter present in sedimentary rocks usually represents the lowest proportion of the sedimentary fraction. It is constituted by organic molecules (under the form of monomers and polymers) deriving directly or indirectly from the organic part of the organisms (composed by the elements C - carbon, H - hydrogen, O - oxygen, N - nitrogen, and S - sulfur). Skeletal parts, shells, bones, spines, and teeth are not included (Tissot & Welte, 1984; Tyson, 1995).

According to Tyson (1995), the study of the organic matter in sediments and sedimentary rocks focuses on the interaction between the biosphere and geosphere. A proper appreciation of the subject requires an understanding of the environmental controls which govern the production of organic matter in the biosphere, the ecological and sedimentological processes which control its deposition and distribution, the biogeochemical, and geomicrobiological factors which influence its preservation and

geochemical and physical processes which determine its modification during its incorporation in the geosphere. The characterization of the organic matter contained in sediments and sedimentary rocks is an important issue for many different types of biological, geological, and environmental scientists. The method used depend largely upon the age of the organic matter (or of the host sediment), the background of the investigators and the objectives of any given study. The integrated use of microscopy and geochemical techniques is particularly under-utilized.

2.2 Organic matter and biosphere evolution

From the Precambrian till the Devonian, the main producers of organic carbon were blue-green algae and photosynthetic bacteria. Since the Devonian an increasing amount of primary production has been contributed by higher terrestrial plants (Tissot & Welte, 1984). Throughout the Early Paleozoic (Cambrian, Ordovician, and Silurian), a variety of marine phytoplanktonic organisms, bacteria, and blue-green algae (Cyanophyta) were the dominant sources of organic carbon until land plants appeared on the continents and spread sufficiently by the Middle Devonian (Zimmermann, 1959). Vallentyne (1965) estimated that even today the marine phytoplankton and bacteria are responsible for 50 to 60% of the world organic carbon production.

The fossil records are inadequate to quantify the productivity of bacteria throughout the geological time. Because of microscopic size, and the lack of hard parts, the bacteria are rarely fossilized (Tissot & Welte, 1984). According to Moore (1967), fossilized bacteria are often associated with organic matter such as plant tissues, and animal and insect remains. Bacteria may be heterotrophic, autotrophic (photosynthesis without production of oxygen), or both.

Following phytoplankton and bacteria, higher plants are the third important contributor to organic matter in sediments. Quantitatively, the four most important contributors to organic matter in sediments are phytoplankton, zooplankton, higher plants and bacteria. Higher organized animals (e.g. fishes) contribute on the average so little to organic matter in sediments that they can practically be neglected (Tissot & Welte, 1984).

2.3 Biomass: Chemical composition

The sedimentary organic matter is derived from live organic matter and its metabolic products. The type of organic matter deposited and incorporated in sediments depends on biological productivity. The chemical composition of the biomass in a given area, and at a given time, is mainly dependent on the physical and chemical environment of the biological habitat and the evolutionary level of the organisms. Determining environmental factors include light, temperature, nutrients, and conditions of water (e.g. currents, temperature, etc.), besides the presence of groups of organisms (Tissot & Welte, 1984).

According Tissot & Welte (1984), basically all organisms are composed of the same chemical constituents e.g. proteins, carbohydrates, lipids, and lignins-tannins. However, differences exist between the chemical composition of marine planktonic algae and terrestrial higher plants. The organic matter of marine plankton is mainly composed of proteins (up to 50% and more), a variable amount of lipids (5 to 25%), and generally not more than 40% carbohydrates. Higher terrestrial plants are largely composed of cellulose (30 to 50%) and lignin (15 to 25%).

2.4 Organic matter accumulation

The accumulation of organic matter in sediments is controlled by a limited number of geological conditions (Tissot & Welte, 1984). The main factors that control the accumulation of organic matter include the production of the biomass and the degradation processes and transport of the organic matter. The quantity and quality of the organic matter accumulated in sediment are basically the result of the combined influence of the biomass productivity, biochemical degradation and of the organic matter depositional processes. The accumulation is practically restricted to sediment deposited in aquatic environments, which must receive a certain minimum amount of organic matter. In subaerial sediments, organic matter is easily destroyed by chemical or microbial oxidation. It is necessary balanced conditions between the energy level in a body of water and rate sedimentation to preserve and concentrate organic matter in sediments. This organic matter can be supplied on the form of particulate organic matter (in particles) or as dissolved organic matter (dissolved organic components).

2.5 Organic matter transformation

Among the liberation of biological products in the adjacent environment and its incorporation to the sediments, occurs the intervention of a number of physicochemical and biological factors, which will influence its chemical structure and will determine its space distribution in the deposits. Organic matter consists of a diverse variety of compounds, each differing in its inherent biochemical characteristics and susceptibility to microbial attack (Tyson, 1995).

Living tissues are composed of a biomolecules assembly which is thermodynamically unstable. When such molecules are secreted or excreted by the organisms, or even after the death of the organism, they tend to lose its integrity and they can be transformed in simple stable components such as CO_2 , CH_4 , NH_3 , H_2S , H_2O , etc. This process of degradation can be accomplished by the physicochemical processes (oxidation, photolysis, thermolysis, etc). Biological Molecules suffer modifications, of which the resulting products could be presented on the form of several components. The proportions and reactivity of these individual constituents determine the overall pattern of degradation, the most metabolizable compounds disappearing first and at faster rates (Tyson, 1995).

3. Thermal maturity

The physicochemical transformation of organic matter during the geological history of sedimentary basins cannot be considered as an isolated process. Such transformation is controlled by the same factors that also determine the variations of composition of the mineral fraction (solid inorganic phase) and of the interstitial water of the sediments: biological activity in an early stage, then temperature and pressure (Tissot & Welte, 1984). The chemistry of organic matter contained within a sedimentary rock changes over time, reflecting its temperature and burial history. This change or thermal maturity is measured and can be combined with quality of organic matter. The maturity level is the product of a number of variables, such as tectonic setting, burial history, and thermal history.

From the start of buried, organic matter in sedimentary rocks suffers numerous compositional changes, which are caused initially by the biological activity (microbial)

following for the action of the temperature and pressure. This continuous series of processes is denominated of thermal maturation and it is divided in consecutive stages of evolution: diagenesis, catagenesis, metagenesis and metamorphism. These consecutive stages of evolution act on the carbon cycle and cause, of irreversible way, progressive changes in the composition of sedimentary organic matter. Each stage is characterized by different types of chemical processes (Tissot & Welte, 1984). There is a correlation of various maturation indicators for organic matter in coal and kerogen and their relation to the organic maturation stages and the hydrocarbons generated based on Staplin, 1969, Teichmüller, 1974, Hunt, 1979, 1985, Mukhopadhyay, 1994, Pearson, 1990, Peters & Moldawan, 1993, etc.

3.1 Diagenesis

The physical, chemical, and microbiological changes, which occur during the deposition in the order of a few hundred meters of overburden, are called diagenesis. Diagenesis is a process through which the system tends to approach equilibrium under conditions of shallow burial, low temperature and pressure, and through which the sediment normally becomes consolidated. In the diagenetic interval, the increase of temperature and pressure is small, and transformations occur under mild conditions. During early diagenesis, one of the main agents of transformation is microbial activity, and a whole series of low-temperature reactions occur; such as decarboxylation, deamination, polymerization, and reduction. These contribute the kerogen of ancient rocks (Hunt, 1995). Within the sediment, organic material proceeds also towards equilibrium, previous biogenic polymers or "biopolymers" (proteins, carbohydrates) are destroyed by microbial activity during sedimentation and early diagenesis. Then their constituents become progressively engaged in new polycondensed structures ("geopolymers") precursing kerogen (Tissot & Welte, 1984).

3.2 Catagenesis

Catagenesis results from an increase in temperature during burial in sedimentary basins. Organic matter is subjected to increasingly higher temperatures with greater depth of burial. Consecutive deposition of sediments results in burial of previous beds to a depth that reaching several kilometers of overburden in subsiding basins. This means a considerable increase in temperature and pressure. Over time, these higher temperatures cause the thermal degradation of kerogen to yield petroleum-range hydrocarbons under reducing conditions (Hunt, 1995). Tectonics may also contribute to this increase. The temperature may range from about 50 to the 150°C and geostatic pressure due to overburden may vary from 300 to 1500 bars. Such increase again places the system out of equilibrium and results in new changes (Tissot & Welte, 1984). During the catagenesis organic matter experiences major changes and thermal degradation of kerogen is responsible for the generation of most hydrocarbons. Progressive evolution of the kerogen produces first liquid petroleum; then in a later stage "wet gas" and condensate; both liquid oil and condensate are accompanied by significant amounts of methane. This stage corresponds to the main stage of formation of oil and also wet gas.

3.3 Metagenesis

The final stage, after catagenesis and before metamorphism, is the metagenesis. Matagenesis is reached only at great depth and represents the last stage in the significant thermal

alteration of organic matter (Hunt, 1995). This stage of evolution of organic matter begins earlier than metamorphism of the mineral phase. At this stage the organic matter is composed only of methane and a carbon residue, where some crystalline ordering begins to develop. Methane generation diminishes and graphitic structures begin to form. Metagenesis is only concerned with the stage precursing metamorphism, which has been variously characterized and designated as early metamorphism, epimetamorphism, anchimetamorphism, etc. (Tissot & Welte, 1984).

3.4 Metamorphism

Metamorphism is the last stage of the evolution of sediments, where temperature and pressure reach high values in deep zones. In addition, rocks are exposed to the influence of magma and hydrothermal effects. True conditions of metamorphism result in greenschist, and amphibolites facies development. Constituents of the residual kerogen are converted to graphitic carbon (Tissot & Welte, 1984).

4. Kerogen: Composition and classification

The organic matter is composed by two fractions: kerogen (fraction of the organic matter insoluble in organic solvents), and bitumen (fraction of the organic matter soluble in organic solvents). The most common term used to describe the fossil organic matter in sedimentary rocks is kerogen. In the absence of migrant hydrocarbons, kerogen is usually 95% or more of total organic matter in sedimentary rocks (Tyson, 1995). Kerogen was originally named in 1912, but one of the first definitions was presented by Forsman and Hunt (1958) defining kerogen as the dispersed OM of ancient sediments insoluble in the usual organic solvents, in contrast to extractable OM (bitumen). Other definitions as those introduced by Durand (1980), Tissot & Welte (1984) and Vandenbroucke and Largeau (2007) or even those of the Organic Petrologists and Palynologists point out to the same concepts: insoluble fraction of the organic matter or residue isolated from a sedimentary rock after complete dissolution of the rock matrix by HCl and HF acids. The researchers that participants of Open Workshop on Organic Matter Classification (University of Amsterdam, June of 1991) decided to use the term *palynological organic matter* to describe the *kerogen* has been observed under transmitted white light.

Using a more simple and practical definition, kerogen is composed by particulate organic matter (organic constituent of the sedimentary rocks) and bitumen is composed by molecular organic matter (molecular organic compounds: saturated; aromatic and polar compounds - resins and asphaltenes). Owing to the characteristics of each fraction from the organic matter, they are studied using different techniques. For study of bitumen are used organic geochemical techniques; such as solvent extraction; liquid chromatography (LC); gas chromatography (GC); gas chromatography coupled to mass spectrometry (GC-MS), etc. Now, for the kerogen studies are used an association of microscopic and geochemical techniques. Techniques of microscopic examination (transmitted white light, reflected white light and fluorescence mode) can be applied to both kerogen-containing rock and previously isolated kerogen. There are many others techniques that can be used in the characterization of the kerogen, the appropriate technique will depend on the objective of the study.

About the kerogen composition and classification, different physical and chemical techniques of analysis are able to give valuable information on the structure and

composition of kerogen; such as: Elemental Analysis (C, H and O); Infra-Red Spectroscopy; Microscopic Examination; Degradative Oxidation; Various Experiments of Pyrolysis (Rock-Eval, Hydrous-pyrolysis, Laser Micro-pyrolysis, etc.).

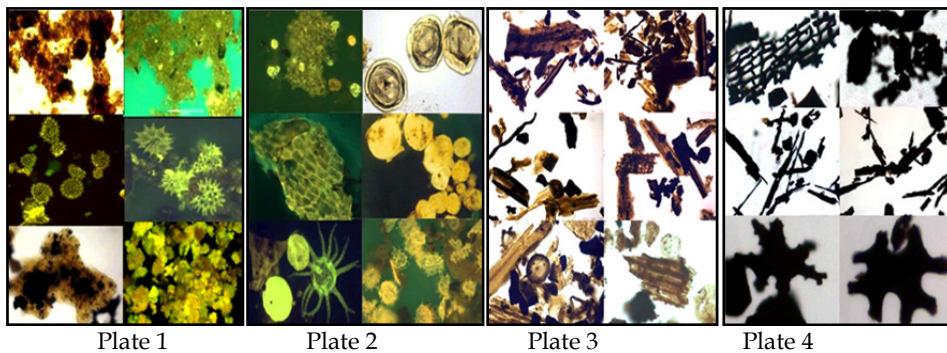
Through the elementary ratios it is possible to define the 3 types of kerogen using the global atomic composition of 3 major elements (C, H and O). This plot was first used by van Krevelen (1961) to characterize coals and their coalification path. Tissot & Welte (1984) proposed to call this diagram as “van Krevelen diagram” that can be represented the 3 principal types and evolution paths of kerogen using *Hydrogen Index (HI)* and *Oxygen Index (OI)* from Rock-Eval pyrolysis analysis.

Kerogen Type I (Plate 1) presents a high initial H/C atomic ratio and low initial O/C ratio; it comprises much lipidic material, particularly aliphatic chains; the content of polyaromatic nuclei and heteroatomic bonds is low; this type of kerogen is either mainly derived from algal lipids (fresh water algae) or from organic matter enriched in lipids by microbial activity (AOM); it presents a high potential to hydrocarbon generation;

Kerogen Type II (Plate 2) is particularly frequent in many petroleum source rocks with relatively high H/C and low O/C ratios; aliphatic chains of moderate length and naphthenic rings; the content of polyaromatic nuclei and heteroatomic ketone and carboxylic acid groups are more important than those are in type I, but less than in type III; it comprises pollen grains, spores, cuticles and marine organic matter deposited in a reducing environment, with medium to high Sulphur content; it presents a high potential to hydrocarbon generation;

Kerogen Type III (Plate 3) presents low H/C ratio, O/C ratio is comparatively higher than is the other 2 types of kerogen; it contains mostly condensed polyaromatic and oxygenated functional groups, with aliphatic chains; the organic matter is mostly derived from terrestrial higher plants; oil potential is moderate, although this kerogen may still generate abundant gas at greater depths;

Kerogens of intermediate composition can also occur, besides one type of Kerogen (type IV), which is a secondary type of kerogen.



- Plate 1:** Organic matter (AOM, *Pediatrum* and *Botryococcus* Algae) related to the Kerogen Type I
Plate 2: Organic matter (AOM, Pollen Grain, Cuticle, Prasinophyte Algae, Acritarchae and Dinocysts) related to the Kerogen Type II
Plate 3: Organic matter (wood tissues: non-opaque phytoclasts) related to the Kerogen Type III
Plate 4: Organic matter (carbonized wood tissues: opaque phytoclasts) related to the Kerogen Type IV

Kerogen Type IV (Plate 4) is a secondary type of kerogen; it contains practically only aromatic components; the organic matter is carbonized through the combustion/natural pyrolysis and /or oxidation (pre-depositional); it present no potential to hydrocarbon source rock.

4.1 Techniques used in the kerogen study

Techniques of microscopic examination (natural light reflectance and transmittance, or UV fluorescence) can be applied to both kerogen-containing rock and previously isolated kerogen. The evaluation of the kerogen in ancient sediments uses microscopy techniques that allow the analysis so much in samples that organic matter was isolated from the rock matrix.

4.2 Microscopy

Techniques of microscopic examination (natural light reflectance and transmittance, or UV fluorescence) can be applied to both kerogen-containing rock and previously isolated kerogen (Tissot & Welte, 1984). The evaluation of the kerogen in ancient sediments uses microscopy techniques that allow the analysis so much in samples that organic matter was isolated from the rock matrix, Palynofacies Analysis (e.g. Tyson, 1984, 1987; Oboh, 1992; Batten, 1996; Follows and Tyson, 1998; Mendonça Filho, 1999; Oliveira, 2003; Menezes & Mendonça Filho, 2004; Meyer *et al.*, 2005; Carvalho *et al.*, 2006; Mendonça Filho *et al.* 2010a) as in whole rock samples through the Organic Petrology (Chow *et al.*, 1995; Stasiuk, 1996, 1999; Stasiuk & Fowler, 2004).

According to Tyson (1995), the main advantages of the microscopy analysis of kerogen are: provides information on the relative abundance, as well as characteristics, of the different components of the organic matter assemblage; optical data is better correlated with the bulk geochemical composition than *vice versa*; solid insoluble organic matter represents 95% or more of the total organic matter in most sediment; the origin, preservation state, and degree of thermal alteration of the organic matter can often be determined by direct visual observation; the industry standard procedures for determining the level of organic maturation are optical (vitrinite reflectance and palynomorph color); microscopy can provide valuable information even when the techniques used are relatively "low tech" and inexpensive; and it can be done with only a few grams of sample.

The characterization of the origin of the organic matter (botanical precursors) and the all aspects of the palynological organic matter assemblage are achieved using a combination of the morphology and optical properties (reflectance, fluorescence, and translucency). Examination of kerogen concentrates isolated from the minerals shows that, except in certain types of sediments formed by massive accumulation of a single type of organism, heterogeneity of kerogen is common in sedimentary rocks; the size, shape, color and structure of the organic remnants vary (Tissot & Welte, 1984).

4.2.1 Transmitted light microscopy

For isolated kerogen examination (palynological organic matter assemblage), based on palynological type preparation, the microscopy analyses are performed on strewn slides of kerogen concentrate sample using transmitted white light and fluorescence mode.

According to Combaz (1964), the study of kerogen using transmitted light is derived from palynological examinations.

The type of organic matter is identified, using the translucency and shape of particles, and in some cases their fluorescence. The results of transmitted light studies mainly give information on the type of organic particles present and their thermal maturity. The characterization of the origin of the organic matter (botanical precursors) and the all aspects of the palynological organic matter assemblage, in transmitted white light microscopy and fluorescence mode, are achieved using a combination of the morphology and optical properties (qualitative fluorescence and translucency).

4.2.2 Fluorescence mode

Fluorescence microscopy is an important tool in the evaluation of thermal maturation and hydrocarbon generation potential of dispersed organic matter in sedimentary rocks. This is because organic components in coals and dispersed organic matter display fluorescence when illuminated with ultraviolet and/or blue light. This property is variable in intensity and color, and it depends on the composition and maturity level of the organic matter (see a summary in Taylor *et al.*, 1998).

The intensity of the fluorescence is influenced by the surrounding medium; less “quenching” occurs in oil-prone matrices. The most intense autofluorescence occurs in liptinitic oil-prone kerogen; vitrinite can also fluoresce, but much more weakly, such that it normally appears non-fluorescent to the eye (except in recent to sub-recent sediments) (Tyson, 1995).

The combination of transmittance and fluorescence microscopy makes possible the distinction of the different individual organic constituents from the kerogen assemblage. According to Tyson (1995), autofluorescence always reflects a combination of three factors: biological origin, preservation state, and level of maturation and is also good for a 3D morphology observation, recognition of palynomorphs masked by amorphous organic matter (AOM) matrix, and helping to distinguish sporomorphs (spores and pollen grains) and plankton. In this case, when immature, organic-walled microplankton often shows more intense and more greenish fluorescence color than sporomorphs and sporomorphs show more variable fluorescence colors. The fluorescent intensity of palynomorphs is usually greater than that of AOM, except in oil shale with very high hydrogen indices.

Fluorescence can be used in the study of organic matter for diagnosis of hydrogen-rich organic particles, mainly to identify AOM, particles of algal or bacterial origin. Fluorescence is also an important method in determining the level of maturity of kerogen by estimating the intensity and color of fluorescence (qualitative) or by quantitative measurement of the fluorescence spectrum (photometric microscope). Qualitative fluorescence is intense in immature samples and decreases during diagenesis and most of catagenesis, disappearing completely at the end of catagenesis. However the color of spectrum (quantitative fluorescence) is progressively changed, the wavelength range of the fluorescence light moves towards the red with increasing catagenesis.

5. Organic composition: Palynofacies analysis

Combaz (1964) introduced the term *palynofacies* in an important period for creation of Organic Petrology, because at beginning was Palynology and Coal Petrology. Following the

work of Combaz at *Compagnie française des pétroles*, the palynofacies means the total assemblage of microscopic organic constituents presents in a rock that remain after maceration in hydrochloric acid (HCl) for carbonates and by hydrofluoric acid - (HF) for silicates, concentration and mounting using normal palynological preparation procedures. This author used the microscope technique to observe, in organic debris isolated from sedimentary rocks after the destruction of their minerals regularities in proportions of the different components: spores, pollens, wood fragments, plant cells, amorphous organic matter. Combaz called palynofacies the diagram of the proportions of the different components (Durand, 2003).

Hughes & Moody-Stuart (1967) proposed the term palynological facies in the same general sense as "palynofacies" of Combaz (1964) to include all organic elements. These authors and Batten (1973) also applied the term in the concept of Combaz to refer to the general aspect of kerogen preparation. Quadros (1975) took the words *Organopalynology* and *Organopalynofacies* for the investigation of organic matter in sedimentary rocks using techniques of microscopy towards Organic Geochemistry in Petrobras Company. Batten (1982a, 1982b) applied this concept not only for palaeoenvironmental and biostratigraphic studies, as well as, for thermal maturity determination and source potential studies. Leopold *et al.* (1982) showed that a palynofacies does not necessarily reflect the biologic environment of the area near the basin of deposition but instead can be produced by a variety of geological and geochemical taphonomic processes associated with sedimentation. This sort of palynofacies is a product of the total sedimentary environment and is unlikely to be a *palynobiofacies*. Powell *et al.* (1990) defined palynofacies as a "distinctive assemblage of HCl- and HF-insoluble particulate organic matter (*palynoclasts*) whose composition reflects a particular sedimentary environment". Traverse (1988) defined a palynofacies as "the assemblage of palynomorphs *taxa* in a portion of a sediment, representing local environmental conditions and not typical of the regional palynoflora". Tyson in 1993 published a pioneering contribution in the area of palynofacies analysis. Traverse (1994) reported that since 1960 used the term palynofacies to refer to a more or less local concentration of particular palynomorphs, indicating a sort of *biofacies*. The author believes that the application of the word since then has been geologically oriented, and palynofacies is used primarily to indicate information about the enclosing *rock*, especially its environment of deposition should be called *palynolithofacies*. Beside this, the several papers edited by Alfred Traverse in 1994 (*Sedimentation of Organic Particles*) ranging from general overviews to detailed sequence-stratigraphic studies.

The book published by Tyson (1995) contains summation of the geochemical aspects of organic facies analysis. This work integrates the geological and biological aspects of palynofacies research. The modern palynofacies concept was introduced by Tyson (1995) and his definition of palynofacies is: "a body of sediment containing a distinctive assemblage of palynological organic matter thought to reflect a specific set of environmental conditions or to be associated with a characteristic range of hydrocarbon-generating potential" and the definition of palynofacies analysis is: "the palynological study of depositional environments and hydrocarbon source rock potential based upon the total assemblage of particulate organic matter". Furthermore, the third volume of Jansonius and McGregor's (1996) compendium of palynology include two chapters (Batten, 1996a, 1996b) with succinct and profusely illustrated summaries and exposition of the subject, including its application to petroleum exploration.

According to Mendonça Filho (1999) the palynofacies term refers to the study of the particulate organic matter presents in sediments and sedimentary rocks using the organic matter isolation methods for sample preparation (kerogen concentration) and applying microscopy techniques as principal tool for acquiring data and statistical methods for its interpretation.

According to Batten and Stead (2005), palynofacies are “associations of palynological matter (PM) in sediments, considered primarily in terms of the reasons for the association, which is usually geological, but may be connected to the biological origin of the particles”.

Palynofacies is a powerful analytical tool when used in conjunction with geological and geophysical information. It can be applied in the determination of kerogen types and their abundance, providing clues concerning depositional environment and hydrocarbon-generating potential. Palynofacies analysis involves the integrated study of all aspects of the palynological organic matter assemblage, which include the identification of the individual particulate components, assessment of their absolute and relative proportions, particle sizes, and their preservation states. It can be used in diverse studies, such as: geology (stratigraphy, sedimentology and palaeoenvironmental studies), paleontology (*biostratigraphic studies*), petroleum exploration, environmental studies, etc. (Tyson, 1995). According to Fleisher & Lane (1999), palynofacies data can be still combined with ancillary biostratigraphic information in a sequence-stratigraphic framework to help recognize reservoir-source rock geometry.

5.1 Kerogen groups

The classification of organic particles has always been rather subjective. Classifications often have a particular objective. Particles have been divided by their modification and thermal alteration, their depositional environments, botanical classification, degree of terrigenous supply and thereby distance from land, degree of degradation, and allochthonous and autochthonous fractions. It is essentially a morphological classification but it also incorporates the broad areas of provenance of particles (Tyson, 1993, 1995).

The classification of kerogen constituents is based primarily on their appearance and preservation state, using transmitted white light with ancillary observation employing fluorescence methods (UV mode). Many classification strategies have been proposed (Staplin, 1969; Correia, 1971; Burgess, 1974; Hart, 1979; Combaz, 1980; Masran & Pocock, 1981; Batten, 1981, 1982a; Batten & Morrison, 1983; Whitaker, 1984; Tyson, 1984; Boulter & Riddick, 1986; Hart, 1986; Traverse, 1988; Tyson, 1993; 1995, Mendonça Filho 1999, Mendonça Filho *et al.*, 2010b; 2011a) based on degradational state and biological derivation (i.e., plants debris, phytoplankton, etc.). However, the classification systems are still not standardized between studies.

There are many published kerogen classifications. According to Tyson (1993), a generally acceptable terminology for transmitted light work has proved elusive and they differ by the degree of emphasis placed on different aspects of kerogen assemblage providing more detailed subdivisions of the palynomorph, phytoclast and amorphous organic matter components by greater attention to botanical source, morphology, and/or preservation states. The much more standardized and systematic maceral terminology used by organic petrologists (in reflected light studies) should never be used in transmitted light work. Macerals can only be properly defined on reflected light characteristics; any other usage can

produce pseudo-accuracy, unnecessary confusion and futile controversy. However, regarding the kerogen groups and subgroups it is important to use a classification system which gives the maximum information about the variables involved. This means the classification system shall also emphasize the most relevant factors having in mind the objectives of the study. In that case, a rigorous subdivision of the categories should be present to identify any quantitative variation related to the main controls on the distribution of the organic matter and thus use those factors in the determination of the palaeoenvironmental meaning. According to Tyson (1995), in the case of palynofacies the main objectives of microscopy are to determine: the origin of the organic matter (in terms of its botanical precursors); the relative percentages of the different constituents; the preservation state of the different constituents; the hydrocarbon generating potential of the organic matter; the degree of thermal alteration (maturity) of the organic matter; the nature of the deposition palaeoenvironment (terrestrial inputs); the redox conditions (reducing versus oxidizing); and the palaeosalinity (to differentiate fresh water, brackish or marine environments).

In transmitted white light microscopy, the three main groups of morphologic constituents recognized within kerogen assemblage are: palynomorphs (organic walled constituents that remain after maceration using HCl and HF acids), phytoclasts (fragments of tissues derived from higher plants or fungi), and amorphous organic matter - AOM (structureless material derived from non-fossilizing algae, or advanced tissue biodegradation, phytoplankton or bacterially derived AOM, higher plants resins and amorphous products of the diagenesis of macrophyte tissues).

Tables 1, 2, and 3 show the detailed classification system of the individual palynological components based on Tyson (1995), Vincent (1995), Mendonça Filho (1999), and Mendonça Filho *et al.* (2002, 2010b), indicating the appropriate use of the nomenclature for the observation of kerogen under transmitted white light.

5.1.1 Phytoclast group

The phytoclast term was introduced by Bostick (1971) to describe all particles with size clay or fine-sand derived from higher plants or fungi. They are fragments of tissues derived from higher plants or fungi and its autofluorescence depends on derived tissue. Phytoclasts can be translucent (non-opaque) or opaque (black) and non-biostructured, biostructured, structured or "pseudoamorphous". Most are derived from the highly lignified mechanical support tissue of higher plants, i.e. wood (xylem), once lignin is highly resistant to decay and tends to become selectively preserved and therefore concentrated during decay. According to Tyson (1993, 1995), the original lignin content is 25-35% in softwood and 18-25% in hardwood, but up to 70% or more in subfossil (archaeological) wood. Lignin decay is mainly through "mouldering" by "white rot" fungi; this process requires oxygen. Wherever oxygen is in short supply, e.g. in water (26 times less O₂ than air), especially disoxic-anoxic water, lignin/wood preservation is enhanced. This is why coals are formed in wet swampy environments. Because it is mainly only the lignin-rich secondary cell walls that survives, even anaerobic degradation of wood produces a major weight loss (70-80%), due to degradation of the cellulosic tissues. Except in coals, it is mainly dispersed tracheid and other woody tissues which form the bulk of the phytoclast population. Other tissues may also be present, e.g. the thinner-walled material derived from "ray" tissues, but these

are produced in lower amounts, and are less well preserved (due to their lower lignin content). Gymnosperm (softwood/conifer) xylem is composed largely of tracheids-elongate cylindrical cells. These often show characteristic "bordered pits", pores in the cell wall by which adjacent cells communicate. Their pores have membranes, but these rarely survive, leaving only holes. Now, angiosperm (flowering plant) wood contains less tracheid, but has similar but larger structures called "vessels". Overall it has less lignin and is thus often less well preserved compared to gymnosperm wood.

GROUP	SUBGROUPS	DESCRIPTION			
PHYTOCLAST Fragments of Tissues Derived from Higher Plants or Fungi	Opaque	Equidimensional (Equant) length: width ratio < 2	Black or opaque in colour even at grain boundary. Sharp outline; mostly no internal structure.		
		Lath length: width ratio > 2	Black or opaque in colour even at grain boundary. Sharp outline; it may show pits.		
		Corroded	Black in colour. More diffuse outline; irregular.		
	Non-Opaque (Translucent)	<i>Undegraded</i> Sharp outline (may be slightly irregular). May be splintered. or <i>Degraded</i> Irregular and diffuse outline or <i>Pseudoamorphous/ "Amorphous"</i> Diffuse outline, it may be light brown, brown to dark brown in colour. Starting to show some features of AOM, but homogenous in appearance (<i>flat fluorescence</i>), not pyrite speckled, no inclusions. It may exhibit fluorescence. or <i>In decomposition "Highly preserved"</i> Irregular outline in transmitted white light, it exhibits coloration of fluorescence. The characteristics indicate a highly degree of chemistry preservation due to specific conditions.	Fungal Hyphae	Fragments of hyphae. Brown in colour. Individual filaments of the mycelium of the vegetative phase of eumycote (higher) fungi.	
			Non-biostructured	No botanical structure. Translucent, generally brown in colour. Lath or equant in shape.	
			Cuticle	Epidermal tissue of higher plants. Pale yellow-green, yellow, reddish-yellow in colour. Regular cell outlines; occur as sheet-like, in some cases with visible stomata. It may occur as thick translucent phytoclasts that present a yellow fluorescing cuticle coating. This particular feature (cuticular layer fragments associated with innermost part of epiderms) could be indicating that the land plant fragments derived from leaves.	
			Membrane	Pale yellow in colour; thin; sheet-like; irregular. Often fluorescent; highly translucent. Lack of diagnostic internal structure.	
			Biostructured	Generally brown in colour; lath to equant in shape; clearly visible internal structure. <i>Striate</i> : thin (regular fibrous lineation). <i>Striped</i> : Irregular or unequal stripes (may be thickenings). <i>Banded</i> : Regular and equal parallel sided thickenings. <i>Pitted</i> : Bordered or scalariform pits.	
	Sclereids	Generally opaque, but may be translucent (dark brown). Sclerenchymatic tissue cells, with thickened secondary wall and impregnated with lignin. Found in different parts of the plant (root, stem and leaf) with the sustentation function and mechanical resistance.			

Table 1. Detailed classification system of the individual palynological components from Phytoclast Group based on Tyson (1995), Vincent (1995), Mendonça Filho (1999), and Mendonça Filho *et al.* (2002, 2010b, 2011a).

5.1.2 Palynomorph group

Palynomorphs are organic-walled microfossils present in a rock that remain after maceration using HCl acid for carbonates and HF acid for silicates. Organic-walled

microfossils are composed of entirely unmineralized proteinaceous material, such as: chitinozoans, spores and pollen, prasinophytes, acritarchs, and dinoflagellates. The term of palynomorph was introduced by Tchudy (1961) to refer to all discrete HCl and HF-resistant, organic-walled (unicellular, multicellular, or colonial) microfossil that may be present in palynological preparations. They are discrete, coherent, individual or colonial entities and it can be subdivided into: terrestrial (sporomorphs) and aquatic (marine and fresh water) subgroups (Tyson, 1995).

Sporomorph Subgroup (terrestrial palynomorphs)

The term sporomorphs was originally defined as a useful collective term for all terrestrial spores and pollen grains. In this case, it would be all palynomorphs produced by land plants (although some would exclude fungal spores). This subgroup is composed by two components: spores and pollen grains (spores and pollen grains are not the same thing, they have a different position in the life cycle, but both are a means of indirect or direct dispersal of gametes), with variable fluorescence properties (Tyson, 1995).

Spores and pollen grains are parts of the reproductive cycle of plants and range in age from Late Ordovician and Carboniferous, respectively, to Holocene. Although land derived, the grains can be carried by wind and water currents into marine and nonmarine environments. The type and relative abundance of spores and pollen grains provide useful paleoenvironmental and paleoclimatic information, and they are widely used for basinal and regional stratigraphic correlation.

Spores are produced by Bryophyte, Pteridophyte (fern type) plants and their primitive ancestors. They first appear in the late Ordovician and continue to the present day. They are formed in tetrads. About the shape, spores are mostly triangular or circular; the most common type is the trilete spore, which has a Y-shaped mark. Monolete spores (oval and have an "I"-shaped mark) are less common. Different forms, sizes and ornamentation can occur and they may have a wide diversity of ornament on their outer ("distal") surface (spines, ridges, etc.).

Pollen Grain are produced by the seed-producing plants, such as Gymnosperms (e.g. Conifers), Carboniferous-Present; Angiosperms (flowering plants), Early Cretaceous-Present (dominate global flora from Late Cretaceous onwards). They are produced in dyad, tetrads and polyads, but only very rarely is a trilete mark visible. They are produced by the seed-producing plants. The presence of dyad, tetrads and polyads (pollen grain agglomerates) are an indication of proximity of a source area. Most pollen is circular or oval in outline.

Fungal Spore

According to Tyson (1995), the presence of fungal spores can indicate a close proximity to, or redeposition from, active fluvio-deltaic source areas (especially deltaic, estuarine, or lagoonal oxic facies). When these organic particles are associated with high numbers of dinocysts and foraminiferal linings, they can indicate upwelling areas.

Freshwater (Organic-Walled) Microplankton

Other subgroup from the palynomorph group is the fresh water microplankton. They belong to the aquatic constituents from this group. The main components from this group belong to the Chlorococcale Algae. There are 2 common forms, both colonial and exclusively freshwater: *Botryococcus* and *Pediastrum*.

***Botryococcus* (Carboniferous to Recent)**

Algae from *Botryococcus* genus are irregular globular colonies of variable size (30-2,000 μ m). The colonies often have several lobes (like miniature cauliflower heads) and they may show a vaguely radial texture. More structure, including circular pits on the surface (cell cups), may be visible under fluorescence. Usually a yellow glossy appearance in immature sediments and they can be orange-brown, presenting a typically strong fluorescence. The stratigraphic record of the colonial freshwater alga *Botryococcus* spans the Carboniferous to the present (about 360 Ma) and they occur widely in lagoonal and lacustrine facies (they occur in marine sediments only by redeposition or transportation, e.g. prodeltaic facies). They can tolerate elevated salinities, but only in lakes. Large modern blooms occur in temporary lakes in the Australian Coorong Region; drying out of the lakes deposits the buoyant algae, sometimes forming a rubbery mat-like deposit known as Coorongite. No equivalent ancient sediments are known. *Botryococcus*-rich oil shale is referred to as Torbanite (first described from carboniferous of the Edinburgh region); however, most of their kerogen is usually "AOM". Torbanites have type I kerogen (organic facies A or AB) and are excellent source rocks in some rift basins (Tyson, 1995). *Botryococcus* algae are very rich in lipids (hydrogen) and they can liberate hydrocarbons (oil) in life (Canter-Lund & Lund, 1998).

***Pediastrum* (Early Cretaceous-Recent)**

The other most common genus of fossilizing Chlorococcale algae is *Pediastrum*. Flat "cog-wheel"-shaped colonies (coenobia). According to Evitt (1963), the geological record of this genus extends back to the Early Cretaceous, and at least as early as the Late Barremian. The colonies of *Pediastrum* form characteristic non-mucilaginous, flat, discoidal units, which are one cell layer thick and have a "cog wheel shaped" outline. The flat "cog-wheel"-shaped colonies are called coenobia. The polygonal cells have a concentric arrangement and the outer cells have one or two triangular points each (giving the teeth of the "cogs"). Mostly 30-200 μ m in diameter and they are common in lacustrine facies, although rarely in the same samples as abundant *Botryococcus*, because they compete to the same environment. Most species prefer higher nutrient concentrations and reflect higher productivity settings. Nevertheless, they cannot tolerate elevated salinities, and thus tend to occur in lakes of wetter climates and can be redeposited into marine sediments. *Pediastrum*-rich sediments often have a type I or type II composition. They can represent important source rocks in Cretaceous and Cenozoic rift basins (e.g. W. Africa, China, Indonesia and Brazil). *Pediastrum*-rich oil shales do not have a specific name (Tyson, 1995).

Zygnemataceae Family (Carboniferous-Recent)

The Zygnemataceae are an extant Family of hydro-terrestrial, filamentous green algae which produce acid-resistant spores. Palynomorphs of probable zygnematacean affinity often referred to as "acritarchs", occur frequently in sediments of Late Palaeozoic to Holocene age. Only the filamentous algae spores are preserved. In Recent zygnematacean algae the form, size and markings of the spore wall are very important for species identification. The majority of species have spores of constant form, only a very few are polymorphic. The forms are of four primary types (globose, obovoid, ellipsoid and quadrangular) of which a number of variations are known (Grenfell, 1995). The filamentous Zygnemataceae algae inhabit a great variety of freshwater habitats including cold, swift flowing streams; warm,

stagnant pools and moist soils and peats. Most species prefer stagnant pools, ponds and ditches (Hoshaw and MacCourt, 1988).

Most Recent species of the Zygnemataceae form zygospores in clean, oxygen rich, stagnant and shallow freshwater. In the fossil record, the presence of a non-marine depositional environment may be inferred when the following are fairly abundant. Such non-marine environment would include fluvial and lacustrine facies where swamps, marsh and shallow, stagnant yet oxygenated water bodies persisted. Studies of extant Zygnemataceae indicate that they inhabit a wide range of hydro-terrestrial habitats but most species prefer fluvial and lacustrine facies. The presence and abundance of fossil zygnematacean spores are potential indicators of palaeoenvironment (Grenfell, 1995).

Marine (Organic-Walled) Microplankton

Other subgroup from the Palynomorph Group is the marine organic-walled microplankton. They belong to the aquatic constituents from this group as well as freshwater organic-walled microplankton (*Botryococcus* and *Pediastrum*).

The fossil record of the organic-walled microplankton (OWM) is very incomplete. Only a fraction of the original plankton biomass and taxa are preserved, generally only those parts of the life cycle that produce resistant “cysts” or similar structures, probably made of Algaenan- type substances (Tyson, 1995). Marine Microplankton includes dinocysts, acritarchs and prasinophytes. They exhibit variable fluorescence properties and some taxa may tolerate brackish conditions. Late Precambrian and Palaeozoic OWM are dominated by the Acritarchs and Prasinophytes. The period of low global sea levels in the carboniferous to E. Triassic resulted in elimination of most Acritarchs, and sediments of this age contain very little OWM. In the Mid-Late Triassic, as sea-level raised again, the cyst-forming dinoflagellate cysts (dinocysts) “evolved”, becoming common and diverse by the end of the M. Jurassic, dominating over the Acritarchs except in marginal marine environments. Dinocyst diversity is correlated with the global sea level and was highest during the Mid Late Cretaceous; they continue to the present day. Prasinophyte algae range in age from Precambrian to the present (Tyson, 1995; Mendonça Filho *et al.*, 2011a).

Prasinophyte algae

Prasinophyte algae are present an Age range from Precambrian to Recent. Fossilizing structures produced by small quadriflagellate phytoplankton which do not themselves fossilize. Modern flagellates occur in fresh to hypersaline waters, but fossil forms are exclusively marines. The fossilizing structures are referred to as phycmata (singular: phycma) to distinguish them from cysts; this is because they are not dormant, but the cell contents are actively dividing and growing during life. The phycmata are buoyant (due to internal lipid globule), float and thus have a pelagic distribution, occurring widely in shallow or deep waters. They are only sedimented when ingested or the living content has emerged. As the whole life cycle occurs in the surface water, it is described as “holoplanktic”. The mero/holo plankton (i.e. Dinocyst or Acritarch to Prasinophyte) ratio decreases offshore. Although occur a wide distribution, seldom these algae are common except in marine organic rich black shales (AOM-rich), where they may be the dominant OWM. Phycmata have a very oil prone composition; this may result in a rich organic facies (Tyson, 1995).

Acritarchs

Evitt (1963) introduced the name Acritarchs to describe a variety of diverse OWM which do not have characteristic dinocyst features (i.e. no paratabulation). They are marine microplankton of unknown biological affinity. Acritarchs are a polyphyletic group of palynomorphs whose name means “of uncertain origin” (*incertae sedis*) and may include cysts, egg cases, etc. They range from Precambrian to Holocene in age (Tyson, 1995).

They are excellent biostratigraphic indices for Proterozoic through Devonian strata but are less important in the Mesozoic and Cenozoic. They are most diverse during the Ordovician-Silurian. Distribution pattern indicates they were mostly marine phytoplankton. As they have no formal taxonomic status, and the organisms which produced these palynomorphs are either extinct or unknown, the acritarchs have been classified entirely on the basis of morphological characteristics. Post-Palaeozoic Acritarchs are less diverse, mostly simple, small (10-20µm), spiny forms with a central spherical body. Acritarchs occur abundantly in fine-grained rocks and are geographically widespread (Tyson, 1995).

Dinoflagellate Cysts (Dinocysts)

Dinoflagellates are the resting cysts of marine, unicellular red algae. Dinoflagellates present a cellulose composition and do not fossilize; only the resistant resting cyst produced during the sexual part of the life cycle survives. The life cycle alternates between active asexual planktic flagellate cells which live in the surface waters (using their flagellae to swim), and the dormant benthic resting cysts (zygotes) produced during the sexual phase of the life cycle. This part planktic and part benthic life cycle is described as “meroplanktic” (spending part of their life as a motile flagellate phase, and part as a benthic resting cyst). The fossil record of dinoflagellates is almost entirely confined to forms that have a meroplanktonic life; cysts are produced abundantly only by these forms. They occur abundantly in Upper Triassic to Holocene sediments and are excellent biostratigraphic indices because of their rapid evolution and widespread geographic distribution. Dinoflagellate cysts occur predominantly in marine rocks but also are present in Cretaceous and Cenozoic lacustrine facies. Cysts are produced abundantly only by those meroplanktic. Even those dinoflagellates that produce cysts do not do so to the same extent; in some species 50-85% of the motile individuals may produce cysts (e.g. *Operculodinium*), whereas in others (e.g. *Spiniferites*) the corresponding value may be only 0,2-3,0% (Dodge & Harland, 1991). Dinoflagellates live in unstable shallow shelf waters. Organic walled cysts are not produced in permanently stratified waters like the modern (oxic) ocean, nor apparently in some ancient deep shelf basins. Most dinocysts in ocean sediments have been redeposited from the shelf. The morphology and diversity of dinoflagellate assemblages can be used to differentiate marine environments (Tyson, 1995; Vincent, 1995).

Zoomorph Subgroup

Zoomorph subgroup is composed by animal-derived palynomorphs (discrete unitary animal-derived particles, whether whole or damaged, are classified as zoomorph palynomorphs) including foraminiferal linings, chitinozoa and scolecodonts (Müller, 1959; Tschudy, 1969). It is identifiable as fragment zoomorph palynomorphs (Tyson, 1989, 1995).

Zooclast Group

Zooclast Group is a different group from the organic matter comprising animal-derived organic particles (e.g. graptolites, crustacean eggs, tintinnids, insect cuticle fragments, and

other arthropod cuticle fragments). They are material of definite animal origin (has specific morphological characteristics). Zooclasts are unknown organic particle, structured, fragmentary particle (clast), angular broken outline, obviously not a whole discrete entity (spines, slits, hairs, joints, etc.) and those particles identifiable as fragmented zoomorph palynomorphs are not classified as zooclasts. The most common varieties of zooclasts include arthropod exoskeletal debris, organic linings from some bivalve shells and ostracod carapaces and graptolite fragments (Tyson, 1989, 1995).

GROUP	SUBGROUPS		DESCRIPTION	
PALYNOMORPH	Sporomorph	Spores	Terrestrial Palynomorph produced by Pteridophyte, Briophyte and Fungi. Triangular or circular form palynomorph, trilete mark ("Y") or monolete (scar). They can occur as massulae of the freshwater fern (<i>Azolla</i>), agglomerates and tetrad. "First spores" (Cambrian): Cryptospores (spore-like bodies) and Embryophyte Spores: Upper Ordovician-Recent.	
		Pollen Grain	Terrestrial Palynomorph produced by Gymnosperms and Angiosperms Palynomorph with varied ornamentation, most with circular or oval outline; could present opening or not. They can occur as agglomerates or tetrads. Devonian-Recent.	
	Freshwater Microplankton	<i>Botryococcus</i>	Chlorococcales Algae	Irregular globular colonies; size 30 to 2000 µm, sometimes with several lobes (like miniature cauliflower); Ordovician-Recent.
		<i>Pediastrum</i>		Colonial green algae (coenobia). Rounded colonies with 30-200 µm diameter. In polygonal form the cells have a concentric arrangement; cells present two horns in the side external. Jurassic (?) - Recent.
	Marine Microplankton	Dinoflagellate Cysts	Cell produced during the sexual phase of the dinoflagellate life cycle	The fossil record of dinocysts is almost entirely confined to forms that have a meroplanktonic life cycle. Major dinoflagellate cyst morphotypes: Proximate, Cavate and Chorate. Triassic-Recent.
		Prasinophyte	Fossilized structure produced by small quadri-flagellate motile phase.	Majority, like <i>Tasmanites</i> , are spherical; diameter 50 to 2000 µm. Modern species include freshwater. Precambrian-Recent.
		Acritarchs	Unicellular fossilized cysts with organic cell walls. They have no formal taxonomic status.	The acritarchs are a polyphyletic group of palynomorphs whose name means "of uncertain origin". <i>Acritarcha</i> (<i>akritos</i> = uncertain, mixed and <i>arche</i> = origin). Small dimension organism (5 a 150 µm). Symmetrically shaped with varied ornamentation. They first appeared in the late Precambrian, attained their acme during the Ordovician-Devonian.
	Zoomorph	Foraminiferal Test-Linings	Chitinous organic linings to calcareous shells of foraminifera.	The linings are typically dark brown colour, although their outer chambers are often more thin-walled and translucent. Good indicator of marine conditions.
		Scolecodonts	Elements of the jaw of benthic polychaete annelid worms.	They are the part-calcified and scleroproteinaceous ("chitinous") mouth parts ("pharyngeal jaws") of benthic polychaete annelid worms. Ordovician - Recent.
		Chitinozoa	Vesicles in format of flasks or small hollow bottles (30 to 2000 µm). Uncertain affinity.	They constitute an extinct group of organic-walled microfossils found in Palaeozoic marine sediments. Early Ordovician - Late Devonian.
	Others	Zooclasts (Graptolite, Crustacean eggs); <i>Spongiophyton</i>.		

Table 2. Detailed classification system of the individual palynological components from Palynomorph Group based on Tyson (1995), Vincent (1995), Mendonça Filho (1999) and Mendonça Filho *et al.* (2002, 2010a, 2011a).

5.1.3 Amorphous Group (Amorphous Organic Matter)

The Amorphous Group consists of all particulate organic components that appear structureless at the scale of light microscopy; including phytoplankton derived amorphous organic matter (traditionally referred to as "AOM"), bacterially derived amorphous organic matter (also traditionally referred to as "AOM"), higher plant resins, and amorphous products of the diagenesis of macrophyte tissues (Tyson, 1995).

Typical AOM (Amorphous Organic Matter) is directly or indirectly derived from phytoplankton (taxa or parts which do not fossilize as recognizable structures, i.e. not as palynomorphs) or bacteria (autotrophic or heterotrophic bacteria). They may be yellow, orange, brown or grey in color; irregular particles; rounded to angular; gradational margins; homogeneous or heterogeneous; varied common micro-inclusions; often strongly fluorescent, but can be variable. The amorphous material (especially "AOM") commonly acts as a matrix for a diversity of structured. AOM is the single most important source of hydrocarbons, and the main type of kerogen in source rocks. The main sources of AOM are the degradation of phytoplankton or bacteria; reworking of organic matter (phytoplankton) by heterotrophic bacteria and bacteria activity products (Tyson, 1995; Mendonça Filho *et al.*, 2010b).

GROUP	SUBGROUP	DESCRIPTION	
A M O R P H O U S O R G A N I C M A T T E R	"AOM" Phytoplankton or bacterially derived amorphous organic matter - derived from reworked microbiological matter.	Structureless material with no morphology or form; color: yellow-orange-red; orange-brown, ash; often has palynomorphs and pyrite inclusions, may sometimes exhibit fluorescence.	
	Resin Mostly produced by terrestrial higher plants in tropical climates.	Structureless particle (glassy shards), hyaline, usually round, homogeneous, strongly fluorescent.	
	Amorphous Products	Products of macrophyte tissues (<i>Pseudoamorphous/ "Amorphous"</i>)	Diffuse outline, light brown, brown and dark brown in colour. Starting to show some features of AOM, but homogenous in appearance (<i>flat fluorescence</i>), not pyrite specked, no inclusions. It may exhibit fluorescence.
		Microbial mats	They consist predominantly of the maceral lamalginite when examined in reflected white light. They form rather uniformly and strongly fluorescent cohesive particles which show relatively sharp and distinct (sometimes quite angular) outlines after maceration.
		Products from bacteria <i>Bacterial Extracellular Polymeric Substance (EPS)</i>	Mucilaginous sheet. Diffuse outline, thin, pale yellow, yellow, orange, ash in colour. Not pyrite specked, no inclusions. Exhibits intense fluorescence.

Table 3. Detailed classification system of the individual palynological components from AOM Group based on Tyson (1995), Vincent (1995), Mendonça Filho (1999), and Mendonça Filho *et al.* (2002, 2010b, 2011a).

The other component is amorphous organic matter terrestrially derived, which has been reworked to different extent exhibiting high content of carbohydrates. This AOM undergoes a microbiological reworked in reducing conditions (plant material reworked by heterotrophic

bacteria colony), where various amorphization stages can be distinguished ranging from subangular particles with neat boundaries to particles with diffuse limits and is associated predominantly to shales. In this case the derived amorphous organic matter is generally associated with the highest TOC content (Mendonça Filho *et al.*, 2010a, 2010b).

AOM can be derived by bacterial activity (autotrophic-photosynthetic bacteria) producing a bacterial mucilage and is associated with predominantly carbonate sediments. The mucilage, Extracellular Polymeric Substance (EPS), is rich in lipids and proteins and extremely resistant (higher preservation potential). Cyanobacterias (blue-green algae) and thiobacterias (sulphur bacteria) are the main responsible for the production of the EPS (Mendonça Filho *et al.*, 2010a). These organisms do not normally fossilize as recognizable entities, but the dominant forms have a filamentous growth habit (each filament consisting of a trichome – a chain of cells) surrounded by a mucilaginous sheath (cover), and under certain conditions, their constituent cyanobacteria and thiobacteria may be important sources of oil-prone amorphous organic matter and the microbial mats are among the most productive ecosystems in the world (Tyson, 1995). This type of material can appear in a pelicular AOM (*sensu* Combaz, 1980); imprinting the organic matter with a crater aspect, due to impression of the carbonate minerals following dissolution with HCl. The pelicular AOM is generally associated with low organic content (Mendonça Filho *et al.*, 2010a). The mucilaginous material also can suffer a microbiological reworking in reduction conditions (heterotrophic bacteria colonies reworking the EPS produced by the autotrophic bacteria) and appear as a dense, highly-fluorescent aspect, in a plate form, at times, with angular outlines. In this case the derived amorphous organic matter is usually associated with the highest organic content (Mendonça Filho *et al.*, 2010a).

Resin and Amber

Resins are natural products of higher plants which occur either as internal cell- or void-filling secretions, or as extracellular exudations on the plant (stem or leaf) surface and they are classified within the Amorphous Group because they are inherently structureless. They should not be referred to by the abbreviation “AOM”, which is traditionally reserved solely for material of a phytoplankton or bacterial origin. Higher plant resins (microscopic amber) can be intracellular or extracellular; resistant if not exposed to air; glassy (hyaline) shards easily rounded to beads; mostly produced by Angiosperm trees in tropical climates and very oil-prone, but usually minor component (Tyson, 1995).

Amorphous Terrestrial Humic Materials

The biodegradation of land plants (phytoclast degradation products, see pseudo-amorphous and amorphous phytoclasts) often results in the production of primary intra and extracellular amorphous material. They are rare even in coals, except when intracellular; they tend to be more homogeneous than “AOM” and present no organic inclusions (Tyson, 1995).

6. Organic composition: Geochemical analyses

6.1 Total Organic Carbon (TOC)

The abundance of organic matter in sediments is usually expressed as the relative percentage of organic carbon on a dry weight basis. The TOC is a measure of total organic

carbon in a sample (Jarvie, 1991; Bordenave *et al.*, 1993). The Total Organic Carbon (TOC) is determined on a device through the combustion of the organic carbon to CO₂ in an oxygen atmosphere using the decarbonated residue of powdered sample (after carbonate carbon has been removed by HCl acid treatment). The organic carbon analyses are performed on finely ground rock samples in a combustion apparatus utilizing an induction furnace and a thermal conductivity cell to measure the evolved CO₂. However, this procedure really determines only organic carbon content, and not the total organic matter or kerogen. In some cases, extractable organic matter (bitumen) is removed prior to determination of organic carbon. The percentage of organic carbon corresponding to bitumen is usually not more than 0.1% or 0.2% of the total (Tissot & Welte, 1984). Only part of the organic matter is carbon (the rest, in order of importance, is mostly O, H, N, and S). Even if there is 100% OM, there will not be 100% TOC. The carbon content of OM varies from 60-80% for kerogens and 30-75% for modern OM. It is high in both type I and type IV ancient kerogens (Tyson, 1989, 1995). The elemental composition of kerogen depends on type and level of evolution (thermal maturation). Thus, to compensate for other elements present in kerogen, the value found for organic carbon should be multiplied by a conversion factor (Tissot & Welte, 1984). The conversion factors can range from 1.07 (metamorphosed rocks) up to 1.40 for non-metamorphosed organic matter rich in oxygen (Forsman and Hunt, 1958).

The TOC determination technique provides a simple measure of organic matter content of sediments, however there are some problems with the interpretation of TOC data. According to Tyson (1995), the main problem is that of dilution; because TOC is expressed as a relative percentage, it depends not only on the supply and preservation of organic matter but also on the supply and preservation of siliciclastic and biogenic material. It is a purely relative concentration parameter, affected by the relative absolute accumulation of both organic matter and sediment. TOC is always controlled by a set of three master variables: the input of OM, the preservation of the supplied OM, and the dilution of this OM by mineral matter (Tyson, 1989, 1995). Besides, geochemically significant changes in the organic matter may not be represented by a change in the TOC. Despite these problems TOC% is widely used to express the quantity of organic matter and its analysis gives an excellent base for further other organic geochemical methods. The TOC analysis must be used in conjunction with other methods, e.g. Rock-Eval Pyrolysis or data from optical studies, in order to evaluate the nature of the organic matter present (Bustin, 1988; Tyson, 1989, 1995; Bordenave *et al.*, 1993), and TOC% can also provide an extra element of quantification to palynofacies studies when combined with percentage abundance data of the organic matter constituents.

6.2 Rock-eval pyrolysis and hidrous pyrolysis

Pyrolysis is defined as the thermal decomposition of organic matter through the application of heat in the absence of oxygen. This technique does allow the simulation of natural processes in laboratory under controlled experimental conditions; time, temperature, pressure and reaction system (Tissot & Welte, 1985).

In petroleum exploration, pyrolysis is a useful tool to study and understand petroleum system processes such as: hydrocarbon generation; cracking of oil to gas in reservoirs and

generation of carbon dioxide and organic acids. Experimental data can be used for basin modeling purposes, like kinetic of hydrocarbon generation or oil to gas cracking; vitrinite reflectance evolution or prediction of porosity and permeability.

Open-system and closed-system pyrolysis are the main pyrolysis methods which lend itself well to tasks in petroleum geochemistry. The open-system pyrolysis is an analytical technique which is conducted at high temperatures and over short heating times in a flowing stream of inert gas, is used to break down kerogen into volatile products. An example of analytical pyrolysis is the Rock-Eval Pyrolysis equipment. The closed-system or pyrolysis of simulation, differently of the open-system, is conducted at low temperatures and over longer heating times in a closed system. These conditions are used to gradually break down kerogen into volatile products. This process is considered to mimic natural petroleum formation. There are numerous closed-systems pyrolysis such as: hydrous pyrolysis confined (gold tube) pyrolysis and Micro Scale Sealed Vessel (MSSV).

Rock-Eval Pyrolysis

Espitalié *et al.* (1977) published the first paper on the development and application of the Rock-Eval Pyrolysis. This technique is considered a more cost-effective means of geochemical kerogen typing than elemental analysis because prior kerogen separation is not required. Rock-Eval pyrolysis is the one of the standard petroleum industry organic geochemical screening methods; when combined with TOC data it allows the identification of potential source rocks and gives an idea of their quality. The products from pyrolysis resulting in 3 different peaks: P₁, P₂, and P₃ and their correspondent areas S₁, S₂, and S₃, respectively and thus their mass (mg) can be determined:

Peak P₁ (S₁) represents any free hydrocarbons in the rock that either was present at time of deposition or was generated from the kerogen since deposition (S₁ is the amount of free hydrocarbons originally present in the rock - mg HC/g of rock).

Peak P₂ (S₂) represents the amount of milligrams of hydrocarbons per gram of rock that can be generated by pyrolytic degradation of the kerogen normalised to the weight of the samples; providing a reasonable evaluation of source rock potential.

Peak P₃ (S₃) represents the CO₂ yielded through the break of carboxyl groups from the kerogen the amount of CO₂ released from resistant components of the kerogen (mg CO₂/g of rock).

Normalization of the Rock-Eval Pyrolysis yields to the sample TOC permits the calculation of several parameters. According Espitalié *et al.* (1977), the ratio of mg HC in S₂/g TOC is called *Hydrogen Index (HI)*. The ratio of mg CO₂ in S₃/g TOC is called *Oxygen Index (OI)*.

Production index (PI) is defined as the ratio S₁/(S₁+S₂). This ratio is used as a maturity parameter when migration process did not occur.

The temperature corresponding to the maximum of hydrocarbon generation during the pyrolysis (maximum amount of hydrocarbons is generated - S₂) is considered a parameter for evaluation of the maturation stage. This parameter is called maximum temperature of pyrolysis (T_{max}).

T_{max} is the common parameter used to estimate the thermal evolution of the organic matter. Values increase with maturity. T_{max} values < 435°C represents immature organic matter; values between 435°C-470°C represents the oil window (mature organic matter) and T_{max} >470°C represents the overmature zone. However, T_{max} is partially dependent on other factors, such as type of organic matter (Tissot & Welte, 1984) and concentration of S2 peak (<0.2 mg HC/g rock, Peters, 1986).

Hydrous pyrolysis

Simulation pyrolysis is conducted at low temperatures and over longer heating times in a closed system to gradually break down kerogen into volatile products. This simulation can be performed in the presence (hydrous pyrolysis) or absence (anhydrous pyrolysis) of water. Hydrous pyrolysis experiments are conducted in autoclaves using water excess. The pressure of the system is equal of the water pressure. In a different way, anhydrous pyrolysis is performed in sealed gold tubes load in autoclaves without water (confined pyrolysis). In these experiments the pressure of the system is controlled and several samples can be heated at the same time. In this section only the hydrous pyrolysis technique will be discussed.

Hydrous pyrolysis technique can be defined as a hydrothermal experiment which allows the pyrolysis of potential petroleum-source rocks in the presence of water. Specific conditions of weight of sample and water, reactor volume and reaction temperature are necessary to ensure the liquid phase of water during heating (Lewan, 1993). The equipment is a simple system which basically consists in autoclaves with variable volumes and wall composition, an oven, manometer and a temperature controller.

For these experiments are necessary an immature sample with higher values of TOC and potential generation. This type of pyrolysis is normally undertaken over a period of 72 hours at one specific temperature.

A series of temperatures can be used to increase the thermal evolution of the organic matter in a source rock at different maturity levels. The amount and type of hydrocarbons produced can be measured and analyzed. Most immature source rocks will produce measurable amounts of oil and gas in such experiments. This analysis is probably the most useful for a complete evaluation of the amount and type of hydrocarbons that a source rock will produce at various maturity levels. Bitumens and expelled oils generated during hydrous pyrolysis experiments show the chemical composition trend similar to observed in natural samples. Bitumens are enriched in high-molecular-weight hydrocarbons and heteroatom compounds (resins and asphaltenes) while expelled oils are enriched in saturated hydrocarbons.

Hydrous pyrolysis products allow a better understanding of the petroleum systems. Comparative studies between the generated bitumen and its correspondent expelled oil are possible without interferences attributable to organic facies variations in the source rock or secondary process, such as biodegradation, water washing, migration or additional maturation, mixing with other oils or bitumens (Peters *et al.*, 1990).

Lewan (1993) determined through the monitoring of the hydrous pyrolysis products (expelled oil, heated sample or kerogen and retained bitumen) that petroleum generation involves two mainly reactions:



These reactions are also suggested in natural systems (Tissot & Welte, 1984). According to Lewan (1993) four stages can be described for petroleum formation:

1. Pre-oil generation: in this stage the organic matter occurs as an immature solid kerogen;
2. Incipient-oil generation: represents the beginning of thermal decomposition of the kerogen into a bitumen;
3. Primary-oil generation: this stage represents the thermal decomposition of bitumen into oil. During this decomposition the kerogen concentration remains constant;
4. Post-oil generation: in this stage bitumen and expelled oil are thermally decomposed into gas and pyrobitumen.

The role of the water during simulation of oil generation and expulsion was observed in the experiments reported by Comet *et al.* (1986), Tannenbaum *et al.* (1986), Lewan (1993) and Lewan & Roy (2011). These authors observed that the yields of products obtained by hydrous pyrolysis were higher than those obtained with the anhydrous pyrolysis. The presence of pyrobitumen was obtained when experiments were performed in the absence of water (anhydrous pyrolysis) and, no expelled oil was observed in these conditions. According to Lewan (1997), the presence of a pyrobitumen in anhydrous and an expelled oil in hydrous conditions suggests that two reactions pathways may occur during the experiments: cross-linking reactions (covalent bonds are made between carbon atoms intra- or inter-adjacent), and cracking reactions (bonds between carbon atoms are broken). These reactions are responsible for the products obtained in experiments under hydrous or anhydrous conditions. Cross-linking reactions promote the formation of insoluble products of high molecular weight (pyrobitumen or char) while cracking reactions promote the formation of soluble products with low molecular weight. Both reactions compete in conditions of heat stress and occur by free radical mechanisms (Lewan, 1997).

6.3 Organic matter extraction (bitumen)

Analysis of bitumen (e.g. sedimentary biomarkers) involves extracting the sediment with a suitable combination of organic solvents, usually followed by some separation procedure in order to aid component identification by proving less complex mixtures. Organic matter is extracted from rocks using Soxhlet apparatus and dichloromethane as solvent. Numerous solvent mixtures have been used by organic geochemists to extract bitumen from environmental and geological samples (e.g., benzene/MeOH, toluene/MeOH, chloroform/MeOH, dichloromethane and DCM/MeOH).

A crushed and dried rock sample is extracted by Soxhlet apparatus with an organic solvent such as dichloromethane. The sample is transferred to a cellulose extraction thimble, and covered with glass wool. The thimble is placed in the extraction tube, which itself sits on a flask containing an organic solvent (like dichloromethane). The solvent is boiled, and its

vapour travels upward through the extraction tube into the condenser tube. The cool water flowing around the outside of the condenser tube condenses the vapor, which then drips into the thimble, containing the sample. These samples are run in a Soxhlet extractor for 8 hours; reflux events occurred every 10-15 minutes. Removal of free sulphur is performed by simultaneous treatment with active copper filings. The Extractable Organic Matter (EOM) is weighed after removal of the solvent by evaporation. Although some light compounds are lost during evaporation step, steranes and triterpanes are unaffected by evaporative loss.

6.4 Liquid Chromatography (LC)

Biomarkers are commonly trace components in oils and bitumens and normally must be concentrated prior to analysis (Peters *et al.*, 2005; Bastow *et al.*, 2007). These types of separations are also useful when characterizing samples with large unresolved complex mixtures (UCMs) that are typical of biodegraded petroleum and can be difficult to characterize using a gas chromatograph-flame ionizing detector (GC-FID) or gas chromatograph-mass spectrometer (GC-MS) alone (Bastow *et al.*, 2007).

Some laboratories routinely use open-column chromatography with activated silica gel to separate saturated, aromatic and NSO compounds (Nitrogen, Sulphur and Oxygen containing non-hydrocarbons) from crude oils and rock extracts. The saturate fraction represents the non-aromatic compounds including normal, branched and cycloalkanes. The aromatic fraction contains organic compounds with one or more unsaturated rings such as monoaromatics and polycyclic aromatic hydrocarbons. In column chromatography, the bitumen sample is poured on to silica gel adsorbent in a glass column, and fractions are collected by successive elution of solvents with increasing polarity. Therefore, molecular separation in silica gel chromatography is based upon the polarity of a particular molecule.

In the procedure a 25 mm i.d. column is packed with pre-activated silica gel (28-200 mesh). Organic solvents such as *n*-Hexane, *n*-hexane / dichloromethane (8:2,v/v) and dichloromethane / methanol (1:1, v/v) are used to elute saturated, aromatic hydrocarbons and polar NSO fractions, respectively.

6.5 Gas Chromatography (GC)

Gas chromatography (GC) is the principal method of analysis for thermally stable volatile organic compounds present in mixtures that can span a wide range of complexity (Poole *et al.*, 1992).

The saturated fraction to be analyzed is injected into the gas chromatograph. Each injected sample is vaporized and mixed with an inert carrier gas (helium) and then moves through a capillary column. It is inside the column where the separation of the individual chemical components takes place.

The different compounds are separated during the movement down the column as they are repeatedly retained by stationary phase and release into the mobile phase depending on their volatility and affinity for each phase. Therefore, the separation of the hydrocarbons is

achieved primarily according to molecular weight and volatility. The separated compounds leave the gas chromatograph and achieve a flame ionization detector (FID) that responds any compound with C-H bond.

The whole extract analysis by GC is particularly useful for identifying the presence of polar contaminants which are removed by liquid chromatographic separation prior to saturate GC-MS analysis. This technique provides a fingerprint of all compounds which are solvent extractable from rocks.

6.6 Gas Chromatography coupled to Mass Spectrometry (GC-MS)

The separated compounds leave the gas chromatograph in sequence and enter the mass spectrometer's ion chamber, where they are analyzed in the same sequence. Each compound entering the mass spectrometer is bombarded with a high-energy electron beam that ionizes the molecules by knocking off one electron. The molecular ions formed in this manner are unstable, however; most break apart to give a variety of smaller fragment ions. The molecule and fragment ions produced in this manner differ in mass, but most bear a +1 charge. Because of the differences in their mass/charge caused by differences in mass, they can be separated by a magnetic field or quadrupole mass filters. The separated ions move sequentially to the detector where the relative abundances of each mass are recorded (Waples & Machihara, 1991).

The various classes of biomarkers fragment in characteristic ways in the mass spectrometer, depending upon their molecular structures (e.g. m/z 85, 191, 217 e 218 to *n*-alkanes, terpanes and steranes, respectively). The determination of biomarkers is generally accomplished using gas chromatography-mass spectrometry and techniques such as multiple-ion detection (selected-ion monitoring). High resolution mass spectrometry (HRMS) is often used to analyze biomarkers in petroleum, due to its ability to provide quantitative data for compounds present in complex mixtures. However, HRMS requires a significant financial investment as well as highly trained operators to assure valid results (Philp *et al.*, 1990).

6.7 Biomarkers

Biomarkers (chemical fossils) are sedimentary organic compounds whose basic skeletons suggest an unambiguous link with known contemporary natural products, and were synthesized by biota present at the time of the deposition of the sediment (Kohnen *et al.*, 1991). Lipids derived from organisms contributing organic matter to depositional environments can be preserve in the sedimentary record where they can act as biological markers (biomarkers) for both the organisms and the environmental conditions prevailing at the time of deposition (Farrimond *et al.*, 2003). As a result organic matter deposited in different environments is characterized by different molecular signals, depending upon both the assemblage of organisms contributing organic material to the sediment and the environmental conditions.

Therefore, organic geochemical study of organic matter preserved in sediments can provide valuable information which includes the biological source organisms that generated the organic matter, the environmental conditions that prevailed in the water column and

sediment at the time, the thermal history of both the rock and the oil, and the degree of microbial biodegradation.

Since biomarkers provide unique clues to the identity of source rocks from which petroleum samples are derived the fingerprints from migrated oil and source-rock extracts can be compared to infer genetic relationships, which represent an important tool in the search for petroleum, especially in areas with complex depositional and structural histories. In addition, when samples of proposed source rocks are unavailable, biomarkers in oils can still be used to constrain the identity of the source (Picha & Peters, 1998).

For these studies some biomarker parameters are arranged by groups of related compounds in order to identify characteristics of the source rocks (e.g. lithology, geologic age, type of organic matter, redox conditions). However these parameters are used in conjunction with other geochemical parameters to help solve oil exploration, development, and production problems (Peters *et al.*, 1986).

In studies of the effects of the diagenesis on biomarker composition initial variations due to depositional conditions have to be taken into account (Moldowan *et al.*, 1986). These studies have typically focused on transformations between individual precursors and products in the solvent-soluble organic matter (bitumen) of sediments and sedimentary rocks (Philp *et al.*, 1988).

During diagenesis biomarkers undergo the same main types of reactions as other biogenic organic compounds: defunctionalization, aromatization and isomerization. Oxygen-containing functional groups predominate among lipid components at the start of diagenesis and their loss involves reactions such as dehydration and decarboxylation. At the end of diagenesis, these defunctionalization process lead to the formation of hydrocarbons, either saturated or aromatic. However the reducing and oxidizing conditions, i.e. Eh and pH in the sediment, exert an influence on several biomarker precursor-product pathways.

6.8 Biogeochemistry

Bacteria are the oldest life form on the planet. They appeared 3.8 Gy, when the atmosphere of Earth was being reduced and gases like carbon dioxide, methane, nitrogen and ammonia were abundant (Crapez, 2009). Thanks to their activity throughout the course of evolution and geological time, microorganisms have been interacting with and modifying the physical environment ever since (Dilek *et al.*, 2008).

These organisms are considered geological agents and function as concentrators, dispersers and fractionators of mineral and organic matter. As *concentrating agents*, their activity results in a localized accumulation of mineral matter. As *dispersing agents*, they promote the dissolution of insoluble mineral matter. Finally, as *fractionizing agents*, they operate on several inorganic compounds promoting selective chemical changes involving one or more minerals (Ehrlich, 1996).

These matter-microbial life interactions are studied within the context of Geomicrobiology, defined as a scientific field concerned with the participation of microorganisms, both in the past and currently, in a wide variety of geological processes (Ehrlich, 1996). The main goals of studies in this new area of the Earth Sciences are identifying the role of microorganisms in

mineral formation and dissolution; in weathering and rock alteration; in the generation of sulfide minerals; in the fractioning of stable isotopes that facilitates mineral and rock diagenesis; the generation of porosity in deep sedimentary packages; in the formation of the aerobic biosphere; in the generation of fossils that record the evolution of microorganisms; in bioremediation process; in the cycling of biogeochemical elements; in the degradation of hydrocarbons and in the transformation of sedimentary organic carbon for the formation of fossil fuels (Dilek *et al.* 2008).

6.9 Bacterial activity in the degradation and cycling of organic carbon

Microorganisms are the main agents in the diagenesis of organic matter in soils, sediments (including the deepest layers of these), oceans and freshwater bodies. They take part in the recycling of inorganic elements that have limited availability in the environment, are nutritionally important and essential for life, like C, N, P and S (Ehrlich, 1996).

The composition of organic matter (OM) in sediments can be classified, regarding its solubility in organic solvents, in soluble (labile and refractory) and insoluble (labile and refractory) components, whose relative concentrations change according to origin, degradation, use, transformation, accumulation and exportation. It is comprised of an autotrophic fraction (primary organic matter), derived from photosynthesis, and a heterotrophic fraction (secondary organic matter) (Killops & Killops, 1993, Danovaro, 2000, Mendonça Filho *et al.*, 2010a, 2010b).

The labile fraction of the OM is organic carbon fraction most rapidly available to the organisms and is comprised of biopolymer molecules (lipids, proteins and carbohydrates (Dell'Anno, 2002). These three biochemical classes together make up the biopolymeric carbon (BPC) and respond for 10%-70% of all the organic carbon in the marine sediments (Danovaro, 2000). These fractions are more abundant in superficial sediments and in the early phases of diagenesis. Their concentration decreases as the burial and diagenesis processes advance (Tyson, 1995).

The remaining labile material, for geological and geochemical studies in older sediments, has been preserved due to special circumstances, such as dysoxic-anoxic sedimentary facies, and its quality and preservation has no direct bearing on its metabolization potential. This fraction of the metabolizable material can be adsorbed, chemically bonded or physically captured in protokerogen, kerogen or mineral constituents that restrain the action of microorganisms, protecting it from degradation and making it recalcitrant (Tyson, 1995; Danovaro *et al.*, 2001).

Biochemical analyses to verify the quality of the organic matter, i.e., the three main classes of biomolecules (lipids, proteins and carbohydrates), and enzymatic analyses to assess the acquisition and transformation of this energy are the procedures most widely employed (Tyson, 1995; Danovaro *et al.*, 2001).

7. Organic facies

The concept of "Organic Facies" was introduced during the increase of the integration between microscopy and organic geochemistry methods. The primary objective of organic

facies studies is the prediction of the likely occurrence (and lateral variability) of hydrocarbon source potential as a function of depositional environment (Tyson, 1995).

Depending on the objectives of the study and the parameters used for its definition, geoscientists observe the lateral variations of a certain organic facies both at the “basin scale” and at “slide scale”. Based on a paleoecological and paleoclimatic vision, an organic facies can identify both small and large cycles related to transgressive-regressive events. However, its characterization is also related with the depositional paleoenvironments and with the deposition of the stratigraphic units responsible for the generation of oil. In this manner, the application of this concept is wide and several authors consider the introduction of this term in the literature considering it is an indispensable exploration tool (Tyson, 1995).

According Peters & Cassa (1994), many authors use the term *organic facies* as a synonym of *kerogen facies*, based on chemical data, or *palynofacies* or *facies of the maceral association*, based on petrographic data.

The term organic facies was first used by Rogers (1980). Organic facies were defined by “the organic matter content (primarily type, less frequently amount), its source and depositional environment”. Cornford (1979) used the organic facies term, without questioning the concept, just for comparison the methods of studying organic matter and inter-related the interpretations. Cornford *et al.* (1980) summarized the group of organic parameters (organic petrography and geochemistry parameters) that characterize an association of sediments as “Organofacies”.

According to Peters *et al.* (1981), a sedimentary organic facies is determined in the type of the precursor organism, in the depositional paleoenvironments, and in the initial conditions of diagenesis of the organic matter.

Habib (1982) considered organic facies a particular aspect of the organic faciology (which can be determined by the palynological study of organic matter), and it can be considered as “palynologically defined organic facies”.

A formal definition was proposed by Jones & Damaison (1982), where an “organic facies is a detectable subdivision of a certain stratigraphic unit which can be discriminated by the characteristics of the organic constituents without considering the aspects of the inorganic fraction of the sediments”.

Powell (1987) presents the same concepts in his definition of organic facies, considering the effect of the depositional control on the composition of organic matter of potentially hydrocarbon source rocks. This effect regards to the nature of the primary biomass (algal, bacterial, or from land plants/higher plants), to the extent of bacterial degradation (reworking) during deposition and to the lithology of the source rock, and to the chemical composition of the waters present in the depositional paleoenvironment (salinity, pH, alkalinity and oxygenation).

Tuweni & Tyson (1994) consider that TOC and pyrolysis data combined with palynofacies analysis provides an excellent means of characterizing organic facies.

According to Tyson (1995), the concept of organic facies can be defined as a “group of sediments having a distinctive set of organic constituents that can be recognized by microscopy or be associated to a characteristic organochemical composition”.

7.1 Organic facies *sensu* Jones (1987)

Jones (1987) in a study developed the organic facies concept and defined seven organic facies using geochemical, and to a lesser extent optical data (microscopy). These organic facies have been assigned to either individual samples, groups of samples or whole stratigraphic units and the parameters used correspond to sedimentary intervals with low thermal maturity. This organic facies approach is probably more realistic than kerogen type in attempting to classify different kerogen assemblages as it takes into account the fact that the assemblages are controlled by preservational factors as well as their source, and that changes between assemblages are often gradational (Tyson, 1995).

According to Pasley (1991), the definition of organic facies presented by Jones is more appropriate due to the similarities of the organic facies with the detectable stratigraphic units discriminated by the composition of its organic matter. This author integrates the organic petrography and organic geochemistry data in the concept of sequence stratigraphy, not only to improve the better understanding of the occurrence of oil source rocks, but also to use as a prediction tool (Tyson, 1995).

The seven organic facies defined by Jones (1987) are: A, AB, B, BC, C, CD and D. According to Tyson (1995), the three main divisions are into anoxic-dysoxic (A, AB, B, BC), proximal fluvio-deltaic to prodeltaic-oxic shelf (C, CD), and distal deposited, oxic facies (D).

According to Tyson (1995) the major palaeoenvironmental controls on organic facies are:

1. Palaeoxygenation and redox conditions in the basin;
2. Relative proximity of the depositional site to active siliciclastic sediment (and terrestrial OM) sources;
3. Climatic controls on the production, preservation and export of terrestrial organic matter;

The main characteristics of each facies from Jones (1987) were discussed by Jacobson (1991) and Tyson (1995, 1996) and are presented below:

Organic Facies A: this organic facies presents $H/C \geq 1.45$ and $HI \geq 850$. The rocks are usually laminated and organic rich and are found in alkaline lakes and marine palaeoenvironment with persistent bottom water anoxia. The organic matter, often brightly fluorescent, is derived primarily from a single type of algae or bacteria. Organic facies A commonly occurs in carbonate settings. It is found in condensed sections of lakes and marine margins that are protected from oxygenated waters.

Organic Facies AB: this organic facies presents $H/C \sim 1.45-1.35$ and $HI \sim 850-650$. Rocks forming this facies are often laminated and organic rich. The organic matter is similar to that in organic facies A, except that it is diluted either with organic input of lesser quality or by partial degradation. It is volumetrically more important than Organic Facies A because its slightly lower H/C ratio can tolerate a small amount of terrestrial input and/or oxidization of the OM. Organic facies AB is found in both carbonates and shales deposited under a well-developed and persistent anoxic water column.

Organic Facies B: this organic facies presents $H/C \sim 1.35-1.15$ and $HI \sim 650-400$. This facies is the source of petroleum for the majority of the world's oil fields, although organic facies AB may have contributed more of the world's oil (Jones, 1987). It is often laminated

and may contain some terrestrial organic matter. It can be interbedded with less oil-prone facies, reflecting either fluctuations in bottom water anoxia or introduction of sediments with associated oxygen or poorer quality organic matter. Organic facies B and its systematic neighboring facies AB and BC can be mixtures representing biological source variation, some transported organic matter, or variations in preservation. Organic facies B encompasses most of the earth's best petroleum source rocks and is predominantly found in marine rocks, especially in deep water palaeoenvironment associated with upwelling.

Organic Facies BC: this organic facies presents $H/C \sim 1.15-0.95$ and $HI \sim 400-250$. This facies is found in both marine and lacustrine palaeoenvironment. It is often deposited in fine-grained siliciclastics where rapid deposition captures small oxygen volumes in the sediments. This "sedimentary oxygen" encourages biological activity in the sediments. Terrestrial organic matter can be a significant contributor, but bioturbation of bottom sediments may be sufficient to degrade marine organic matter to this quality.

Organic Facies C: this organic facies presents $H/C \sim 0.95-0.75$ and $HI \sim 250-125$. This facies is predominantly gas prone. The organic matter is primarily woody and terrestrial and makes up most coals. Organic facies C is found in marine environments on Tertiary and Mesozoic shelf margins where it includes mixtures of hydrogen-rich and hydrogen-poor macerals or degraded hydrogen rich macerals. Organic facies C and neighboring facies BC and CD are found in coal-forming swamp deposits, deltaic deposits, and bioturbated marine mudstones. The types of environments in which this facies occurs often correspond to the transgressive and early highstand systems tracts where some oxidation occurs and where different kerogen components can be deposited together.

Organic Facies CD: this organic facies presents $H/C \sim 0.75-0.60$ and $HI \sim 125-50$. It is heavily oxidized and frequently represents terrestrial organic matter that has been transported through oxidizing environments. This facies may represent recycled organic matter that has been eroded one or more times from sediments.

Organic Facies D: this organic facies presents $H/C \leq 0.60$ and $HI \leq 50$. This facies contains highly oxidized organic matter, which may represent burnt wood (charcoal), recycled terrestrial material, and thermally postmature constituents. It may include fragments of larger woody components recycled from porous sandy units where oxidation prevailed. This facies is usually encountered in small concentrations and has no hydrocarbon generative capacity. It occurs in prograding sediments associated with sea level highstands and redeposited sediments of lowstands. Organic facies D is the regionally distributed type IV kerogen. It is frequently found in fluvial palaeoenvironment, on offshore toes of deltas, and where organic carbon has been recycled. Sediments containing this kerogen can be found in all systems tracts, including the fine-grained parts of turbidites in lowstand systems tracts and the silts and muds of highstand prograding sediments. The oxidization can occur in innumerable depositional environments ranging from the deep ocean to terrestrial.

According to Jacobson (1991), organic facies are mappable units and their distribution reflects varying influences of biological productivity, preservation, and geological processes. Hydrogen-rich organic facies reflect hydrocarbon generative potential that helps exploration geologists map the distributions of possible petroleum source rock candidates. Petroleum

source rocks form where appropriate conditions for organic productivity and preservation of organic matter occur.

Tyson (1995) showed the relationship between some selected palynofacies kerogen parameters and organic facies *sensu* Jones (1987) in idealized marine siliciclastic facies. This relationship is represented in Table 4.

ORGANIC FACIES	A	AB	B	BC	C	CD	D
Palynofacies characteristics							
% 'AOM' of kerogen	dominant			mod	usually low/absent		
'AOM' matrix fluorescence	highest		mod-weak		weak	usually absent	
% prasinophytes of plankton	highest	mod	rare	usually very rare			
% phytoclasts of kerogen	low (dilution)			mod	usually dominant		
opaque:translucent phytoclasts	often high			usually low		increases	
Geochemical characteristics (for immature sediments)							
Hydrogen index	≥ 850	≥ 650	≥ 400	≥250	≥125	50-125	≤ 50
Kerogen type	I	I/II	II	II/III	III	III/IV	IV
TOC%	5-20+	3-10+		3-3+	≤ 3	< 0.5	
Environmental factors							
Proximal-distal trend	Distal			Proximal		Distal	
Oxygen regime	Anoxic	Anoxic-dysoxic			Oxic		V. Oxic
Sediment accumulation rate	Low	Varies		High		Mod	Low
ORGANIC FACIES	A	AB	B	BC	C	CD	D

Table 4. Relationship between some selected palynofacies kerogen parameters and organic facies *sensu* Jones (1987) in idealized marine siliciclastic facies (generalized relative trends only) (Tyson, 1995; 1996).

8. Summary and conclusions

Organic facies is a discipline of Geosciences that has been increasingly applied in studies devoted to the fossil fuels exploration and basin analysis. The present paper has intended to provide a general view of organic facies in relation to the techniques used for its applications in the field of geosciences, emphasizing its contribution to both fundamental and applied scientific knowledge. The scope of organic facies is broad, however encompasses some fundamental concepts, such as the organic content characterization, in terms of type and quality. Organic facies investigation uses techniques from microscopy (Palynofacies analysis) and organic geochemistry (TOC, Biomarkers, Biogeochemistry, etc.) and the application of these techniques mainly in the palaeoenvironmental characterization, basin analysis and fossil fuel exploration.

9. References

- Alef, R., Nannipieri, P. (1995). Enrichment isolation and counting of soil microorganisms. In: *Methods in applied soil microbiology and biochemistry*. Academic Press, London, pp.123-186.

- Arnosti, C. (2011). Microbial extracellular enzymes and the marine carbon cycle. *Annual Reviews of Marine Science*, 3, 401-425.
- Bastow, T.P., van Aarssen, B.G.K., Lang, D. (2007). Rapid small-scale separation of saturate, aromatic and polar components in petroleum. *Organic Geochemistry*, 38, 1235-1250.
- Batten, D. J. (1973). Use of palynologic assemblage-types in Wealden correlation. *Palaeont.* 16(1), 1-40.
- Batten, D.J. (1981). Palynofacies, organic maturation and source potential for petroleum. In: *Organic Maturation Studies and Fossil Fuel Exploration* Brooks, J. (Ed.), Academic Press, London, pp. 201-224.
- Batten, D.J. (1982a). Palynofacies, palaeoenvironments and petroleum. *Journal of Micropalaeontology*, 1, 107-114.
- Batten, D.J. (1982b). Palynofacies and salinity in the Purbeck and Wealden of southern England. In: *Aspects of Micropalaeontology*, Banner, F.T., Lord, A.R. (Eds.), pp. 278-308.
- Batten, D. J., Morrison, L. (1983). Methods of palynological preparation for palaeoenvironmental, source potential and organic maturation studies, Norwegian Petroleum Directorate Bull. 2, 35-53.
- Batten D.J. (1996a). Palynofacies and palaeoenvironmental interpretation. In: *Palynology: Principles and Application*, Jansonius J. and McGregor D.C. (Eds.), American Association of Stratigraphic Palynologists Foundation, 3, pp.1011-1064.
- Batten, D.J., Grenfell, H.R. (1996b). *Botryococcus*. In: *Palynology: Principles and Applications*, Jansonius J. and McGregor D.C. (Eds.), American Association of Stratigraphic Palynologists Foundation, 1, pp. 205-214.
- Batten, D. J., Stead, D. T. (2005). Palynofacies analysis and its stratigraphic application, In: *Applied Stratigraphy*, Koutsoukos, E. A. M. (Ed.), Springer Dordrecht, Netherlands, pp. 203-226.
- Bordenave, M.L., Espitalié, J., Laplat, P., Oudin, J. L., Vandenbrouke, M. (1993). Screening techniques for source rock evaluation, In: *Applied Petroleum Geochemistry*, Bordenave, M.L. (Ed.), Editions Technip, Paris, pp. 217-279.
- Bostick, N.H. (1971). Thermal alteration of clastic organic particles as an indicator of contact and burial metamorphism in sedimentary rocks. *Geoscience and Man, Baton Rouge*, 3, 83-92.
- Boulter, M.C., Riddick, A. (1986). Classification and analysis of palinodebris from the Palaeocene sediments of the Forties Field. *Sedimentology*, 33, 871-86.
- Burgess, J.D. (1974). Microscopic examination of kerogen (dispersed organic matter). In: *Petroleum Exploration*. Geological Society of American Special Paper, 153, 19-30.
- Bustin, R.M. (1988). Sedimentology and characteristics of dispersed organic matter in Tertiary Niger Delta: origin of source rocks in a deltaic environment. *American Association of Petroleum Geologists Bulletin*, 72, 277-298.
- Canter-Lund, H., Lund, J. W.G. (1995). *Freshwater Algae. Their microscopic world explored*. Bipress. England. 360 pp.
- Carvalho, M.A., Mendonça Filho, J.G., Menezes, T.R. (2006). Palaeoenvironmental reconstruction based on palynofacies analysis of the Aptian-Albian succession of the Sergipe Basin, Northeastern Brazil. *Marine Micropaleontology*, 59, 56-81.

- Chow N., Wendte J., Stasiuk L.D., 1995. Productivity versus preservation controls on two organic-rich carbonate facies in the Devonian of Alberta: sedimentological and organic petrological evidence. *Bulletin of Canadian Petroleum Geology*, 43, 433-460.
- Combaz, A. (1964). Les palynofaciès. *Revue de Micropaléontologie*, 7, 205-18.
- Combaz, A. (1980). Les kerogenes vus au microscope. In : Durand, B. (Ed.) *Kerogen - insoluble organic matter from sedimentary rocks*, Paris, Editions Technip, p. 55-111.
- Comet, P.A., McEvoy, J., Giger, W., Douglas, A.G. (1986). Hydrous and anhydrous pyrolysis of DSDP Leg 75 kerogens - A comparative study using a biological marker approach. *Organic Geochemistry*, 9, 171-182.
- Cornford C. (1979). Organic deposition at a Continental Rise: Organic geochemical interpretation and synthesis at DSDP Site 397, Eastern North Atlantic. In: *Initial Reports of the Deep Sea Drilling Project. Part. 1: Washington (U.S. Government Printing Office)*, von Rad, U., Ryan, W.B.F., Arthur, M.A., Cepek, P., Cita, M.B., Cornford, C., Garifal, L., Hamilton, N., Lopatin, B., Lutze, G.F., McCoy, F.W., Mountain, G., Sarnthein, M., Weser, O.E., Whelan, J.K., Wind F.H. (Eds.), v. 47, p. 503-510.
- Danovaro, R.; Armeni, M., Dell'Anno, A., Fabiano, M., Manini, E.; Marrale, D., Pusceddu, A., Vanucci, S. (2001). Small-Scale Distribution of Bacteria, Enzymatic Activities, and Organic Matter in Coastal Sediments. *Microbial Ecology*, 42, 177-185.
- Dell'Anno, A., Mei, M.L., Pusceddu, A., Danovaro, R., 2002. Assessing the trophic state and eutrophication of coastal biochemical composition of sediment organic matter. *Marine Pollution Bulletin*, 44, 611-622.
- Dilek, Y.; Furnes, H. and Muehlenbachs, K. (2008). Links between geological processes, microbial activities and evolution of life. *Modern approaches in solid Earth Sciences*, Springer, v.4, 348 p.
- Dodge, J.D., Harland, R. (1991). The distribution of planktonic dinoflagellates and their cysts in the eastern and north-eastern Atlantic Ocean. *New Phytologist* 118, 593-603.
- Durand, B. (1980). Sedimentary organic matter and kerogen. Definition and quantitative importance of kerogen. In: *Kerogen - Insoluble organic matter from sedimentary rocks*, Durand, B. (Ed.), Editions Technip, Paris, pp. 13-34.
- Durand B. (2003). A History of Organic Geochemistry. *Rev. IFP. Oil and Gas Science and Technology*, 58(2), 203-231.
- Ehrlich, H.L. (1996). How microbes influence mineral growth and dissolution. *Chemical Geology*, 132, 5-9.
- Espitalié J., Madec M., Tissot B., Mennig J.J., Leplat P. (1977). Source rock characterization method for petroleum exploration. In: *Annual Offshore Techn. Conference, 9th, Proceedings*, p. 439-444.
- Evitt, W. R. (1963). A discussion and proposals concerning fossil dinoflagellates, hystrichospheres, and acritarchs, *Proc. Nat. Acad. Sci.* 49(2-3), 158-164; 298-302.
- Farrimond, P., Love, G.D., Bishop, A.N., Innes, H.E., Watson, D.F., Snape, C.E. (2003). Evidence for the rapid incorporation of hopanoids into kerogen. *Geochimica et Cosmochimica Acta*, 67, 1383-1394.
- Fenchel, T., King, G. M., Blackburn, T. H. (1988). Bacterial biogeochemistry: the ecophysiology of mineral cycling. Edition, S.L., Academic Press, 307 pp.

- Fleisher, R. L., Lane, H.R. (1999). Applied Paleontology. In: *Volume Treatise of Petroleum Geology/Handbook of Petroleum Geology: Exploring for Oil and Gas Traps*, AAPG Special Volumes. pp. 17-1 - 17-65.
- Flemming, H.C., Wingender, J. (2010). The biofilm matrix. *Nature Reviews*, 8, 623-633.
- Follows, B., Tyson, R.V. (1998). Organic facies of the Asbian (early Carboniferous) Queensferry Beds, Lower Oil Shale Group, South Queensferry, Scotland, and a brief comparison with other Carboniferous North Atlantic oil shale deposits. *Organic Geochemistry*, 29(4), 821-844.
- Forsman, J.P., Hunt, J.M. (1958). Insoluble organic matter (kerogen) in sedimentary rocks. *Geochimica et Cosmochimica Acta*, 15, 170-182.
- Grenfell, H.R. (1995). Probable fossil zygnematacean algal spore genera. Review of Palaeobotany and Palynology, 84, 201-220.
- Habib D. (1982). Sedimentary supply origin of cretaceous black shales. In: *Nature and origin of Cretaceous Carbon-rich Facies*, Schlanger S.O., Cita M.B. (Eds.), Academic Press, London, pp.113-27.
- Hart, G.F. (1986). Origin and classification of organic matter in clastic systems. *Palynology*, 10, 1-23.
- Hart, G.F. (1979). Maceral analysis: Its use in petroleum exploration. Methods Paper 2. Baton Rouge, LA: Hartx Internacional Inc.
- Hoshaw, R.W., McCourt, R.M. (1988). The Zygnemataceae (Chlorophyta): a twenty-year update of research. *Phycologia*, 27, 511-548.
- Hughes, N.F. and Moody-Stuart, J.C. (1967). Palynological facies and correlation in the English Wealden. *Review of Palaeobotany and Palynology*, 1, 259-68.
- Hunt, J.M. (1995). *Petroleum geochemistry and geology*. W.H. Freeman and Company, New York, 743 pp.
- ICCP, 1971. *International Handbook of Coal Petrography, Supplement to the 2nd Edition*. Centre National de la Recherche Scientifique, Paris, France.
- Jacobson, S.R.(1991). Petroleum source rocks and organic facies. In: *Source and Migration Processes and Evaluation Techniques*, Merrill, R.K. (Ed.), Tulsa, Treatise of Petroleum Geology, American Association of Petroleum Geologists, p. 3-11.
- Jarvie, D.M. (1991). Total Organic Carbon (TOC) analysis. In: *Source and Migration Processes and Evaluation techniques*, Merrill, R.K. (Ed.), Tulsa, Treatise of Petroleum Geology. American Association of Petroleum Geologists, p. 113-118.
- Jones, R. W., Demaison, G. J. (1982). Organic Facies - stratigraphic concepts and exploration tool. In: *Proceedings of the Second ASCOPE Conference and Exhibition*, Saldivar-Sali, A. (Ed.), Manila, Asean Council on Petroleum, pp. 51-68.
- Jones, R.W. (1987). Organic Facies. In: *Advances in Petroleum Geochemistry*, Brooks, J. and Welte, D. (Eds.), Academic Press, London, 2, 1-90.
- Killops, S., Killops, V. (1993). *An introduction to organic geochemistry*. Blackwell Publishing, Oxford, UK, 408 pp.
- Killops, S., Killops, V. (2005). *Introduction to Organic Geochemistry*. Malden, MA: Blackwell. 393 p.
- Kohnen, M.E.L., Sinninghe Damste, J.S., De Leeuw, J.W. (1991). Biases from natural sulphurization in palaeoenvironmental reconstruction based on hydrocarbon biomarker distributions. *Nature*, 349, 775-778.

- Leopold, E. B, Nickmann, R., Hedges, J. I., and Ertel, J. R. (1982). Pollen and lignin records of Late Quaternary vegetation, Lake Washington, *Science* 218, 1305-1307.
- Lewan, M.D. (1993). Laboratory simulation of petroleum formation. Hydrous Pyrolysis. In: Engel, M.H., Macko, S.A. (Eds). *Organic Geochemistry*. Plenum Press, New York, 419-442.
- Lewan, M.D. (1997). Experiments on role of water in petroleum formation. *Geochimimica et Cosmochimica Acta*, 61(17), 3691-3723.
- Lewan, M.D. , Roy, S. (2011). Role of water in hydrocarbon generation from Type-I kerogen in Mahogany oil shale of the Green River Formation. *Organic Geochemistry*, 42(1), 31-41.
- Masran, T.C. & Pocock, S.A.J. (1981). The classification of plant-derived particulate organic matter in sedimentary rocks. In: Brooks, J. (ed.). *Organic Maturation Studies and Fossil Fuel Exploration*. Academic Press, London, p. 145-176.
- Mendonça Filho, J.G. (1999). Aplicação de estudos de palinofácies e fácies Orgânica em rochas do Paleozóico da Bacia do Paraná, Sul do Brasil. Universidade Federal do Rio Grande do Sul. PhD. Thesis, 338 pp.
- Mendonça Filho, J.G., Carvalho, M. A., Menezes, T.R. (2002). Palinofácies. In: *Técnicas e Procedimentos para o Trabalho com Fósseis e Formas Modernas Comparativas*, Dutra, T.L. (Ed.), Unisinos, São Leopoldo, pp. 20-24.
- Mendonça Filho, J.G., Chagas, R.B.A., Menezes, T.R., Mendonça, J.O., da Silva, F.S., Sabadini-Santos, E., (2010a). Organic facies of the Oligocene lacustrine system in the Cenozoic Taubaté basin, Southern Brazil. *International Journal of Coal Geology*, v. 84, 166 - 178.
- Mendonça Filho, J. G., Menezes, T. R., Mendonça, J. O., , Oliveira, A. D., Carvalho, M. A., Sant'Anna, A. J. , Souza, J. T. (2010b). Palinofácies. In: *Paleontologia*, Souza, C.I. (Ed.), Rio de Janeiro, Interciência, v. 2, pp. 379-413.
- Mendonça Filho, J.G., Menezes, T.R., Mendonça, J.O., 2011a. Organic Composition (Palynofacies Analysis). Chapter 5. In: *ICCP Training Course on Dispersed Organic Matter*, Porto, pp. 33-81.
- Mendonça Filho, J.G., Silva, T.F., Rondon, N.F., Kern, M.L., da Silva, F.S., Carvalho, S.B.V., Sabadini-Santos, E., 2011b. Organic Composition (Geochemical Analyses). Chapter 6. In: *ICCP Training Course on Dispersed Organic Matter*, Porto, pp. 83-98.
- Menezes, T.R., Mendonça Filho, J. G. (2004). Aplicação da faciologia orgânica na análise paleoceanográfica do talude continental superior recente da Bacia de Campos - RJ. *Revista Brasileira de Paleontologia*, 7(2), 177-188.
- Meyer, K.E.B., Mendonça Filho, J.G., Ashraf, A.R., Souza, P.A., Reichhart, K. (2005). Análise de palinofácies em sedimentos holocênicos da Lagoa dos Quadros, Planície Costeira do Rio Grande do Sul, Brasil. *Revista Brasileira de Paleontologia*, 8(1), 57-72.
- Moldowan, J.M., Sundararaman, P.; Schoell, M. (1986). Sensitivity of biomarker properties to depositional environment and/or source input in the Lower Toarcian of SW-Germany. *Organic Geochemistry*, 10, 915-926.
- Moore, L.R., (1967). Fossil bacteria. In: *The Fossil Record*, Eglinton, G., Murphy, M. T. J. (Eds.), Swansea Symposium, Geological Society of London, part II, 164-180.
- Mukhopadhyay, P.K. (1994). Vitrinite reflectance as maturity parameter: petrographic and molecular characterization and its applications to basin modeling. In: *Vitrinite*

- reflectance as a maturity parameter: applications and limitations*, Mukhopadhyay, P.K., Dow, W.G.(Eds.), American Chemical Society Symposium Series 570, p. 1-24.
- Müller, J. (1959). Palynology of Recent Orinoco Delta and shelf sediments: reports of the Orinoco Shelf expedition. *Micropaleontology*, 5, 1-2.
- Oboh, F.E. (1992). Middle Miocene palaeoenvironments of the Niger Delta. *Palaeogeography, Palaeoclimatology, Palaeoecology*, 92, 55-84.
- Oliveira, A.D. (2003). Reconstrução paleoambiental com base nas assembléias de dinoflagelados presentes nos sedimentos do Holoceno e Pleistoceno do Talude Continental Brasileiro da Bacia de Campos, RJ-Brasil. Universidade Federal do Rio de Janeiro, Dissertação de Mestrado, 198 pp.
- Pasley, M.A. (1991). Organic matter variation within depositional sequences stratigraphic significance of implication to petroleum source rock prediction. The Louisiana State, University and agricultural and Mechanical Col. Louisiana (USA). PhD. Thesis. 150 pp.
- Pearson, D. L. (1990). *Pollen / spore color "standard," version 2*. Phillips Petroleum Company Geology Branch, Bartlesville, Oklahoma.
- Peters, K.E., Cassa M.R. (1994). Applied source rock geochemistry. In: *The Petroleum System – from Source to Trap*, Magoon L.B. and Dow W.G. (Eds.), AAPG Memoir, 60, 93-120.
- Peters, K. E. (1986). Guidelines for evaluating petroleum source rocks using programmed pyrolysis. *AAPG Bulletin*, 70, 318-329.
- Peters, K.E., Moldowan, J.M., Sundararaman, P. (1990). Effects of hydrous pyrolysis on biomarker thermal maturity parameters: Monterey Phosphatic and Siliceous members. *Organic Geochemistry*, 15, 249-265.
- Peters, K. E., and Moldowan. J. M. (1993). *The Biomarker Guide, Interpreting molecular fossils in petroleum and ancient sediments*, Prentice Hall, 363 pp.
- Peters, K.E., Walters, C.C., Moldowan, J.M. (2005). *The Biomarker Guide*. Cambridge University, New York, 1132 pp.
- Philp, R.P., Oung, J.N., Yu, C.P., Lewis, S. (1990). The determination of biomarker distributions by tandem mass spectrometry. *Organic Geochemistry*, 16, 1211-1220.
- Picha, F.J., Peters, K.E. (1998). Biomarker oil-source rock correlation in the Western Carpathians and their foreland, Czech Republic. *Petroleum Geoscience*, 4, 289-302.
- Poole, C.F., Poole, S.K., Heftmann, E. (1992). Chapter 9 - Gas chromatography. *Journal of Chromatography Library*, 51, Part 1: A393-A447.
- Powell, A.J., Dodge, J.D., Lewis, J. (1990). Late Neogene to Plesitocene palynological facies of Peruvian continental margin upwelling, Leg 112. In: *Proceedings of the Ocean Drilling Project, Scientific Results*, Suess, E., Von Huene, R. (Eds.), College Station, Texas, 112, 297-321.
- Powell, T.G. (1987). Depositional controls on source rocks character and crude oil composition. In: *World Petroleum, 12, Congress, Proceedings*, Houston, 2, 31-42.
- Prescott, G.W. (1951). Algae of the Western Great Lakes area exclusive of Desmids and Diatoms. *Cranbrook Inst. Sci. Bull.*, 31.
- Quadros, L.P. (1975). Organopalinologia na prospecção de petróleo. Rio de Janeiro. *Boletim Técnico da Petrobras*, 18, 3-11.
- Rogers, M. A. (1980). Application of organic facies concepts to hydrocarbon source rocks evaluation. In: *Proceedings of the 10th World Petroleum Congress*, Bucharest 1979, Heyden, London, 2, 23-30.

- Staplin, F.L. (1969). Sedimentary organic matter, organic metamorphism and oil and gas occurrence. *Bulletin of Canadian Petroleum Geology*, 17: 47-66.
- Stasiuk, L.D. (1996). Organic facies in black shale of Devonian-Mississippian Bakken Formation, southeastern Saskatchewan. *Geological Survey of Canada. Current Research 1996-B*: 15-22.
- Stasiuk, L.D. (1999). Microscopic studies of sedimentary organic matter: key to understanding organic-rich strata, with Paleozoic examples from Western Canada. *Geoscience Canada*, 26, 149-172.
- Stasiuk, L.D., Fowler, M.G. (2004). Organic facies in Devonian and Mississippian strata of Western Canada Sedimentary Basin: relation to kerogen type, paleoenvironment, and paleogeography. *Bulletin of Canadian Petroleum Geology*, 52(3), 234-255.
- Tannenbaum, E., Huizinga, B.J., Kaplan, I.R. (1986). Role of minerals in thermal alteration of organic matter - II: A material balance. *AAPG Bulletin*, 70, 1156-1165.
- Taylor, G.H., Teichmüller, M., Davis, A., Diessel, C.F.K., Littke, R., Robert, P. (1998). *Organic Petrology*. Gebrüder Borntraeger, Berlin, 704 pp.
- Teichmüller, M. (1974). Generation of petroleum-like substances in coal seams as seen under the microscope. In: *Advances in Organic Geochemistry*, Tissot, B., Biennier (Eds.), Editions Technip, Paris, p. 321-349.
- Tissot, B.P., Welte, D.H. (1984). *Petroleum Formation and Occurrence*. Springer-Verlag, Berlin. 699 pp.
- Traverse, A. (1988). *Paleopalynology*. Unwin Hyman, London, 600 pp.
- Traverse, A. (1994). *Sedimentation of Organic Particles*. Cambridge University Press, New York, 647 pp.
- Tschudy, R.H. (1961). Palynomorphs as indicators of facies environments in Upper Cretaceous and Lower Tertiary strata, Colorado and Wyoming. In: *Wyoming Geological Society, 16th Annual Field Conference*, Guidebook, pp. 53-9.
- Tschudy, R.H. (1969). Relationship of palynomorphs to sedimentation. In: *Aspects of Palynology*, Tschudy, R.H., Scott, R.A. (Eds.), Wiley, New York, pp. 79-96.
- Tuweni A.O. and Tyson R.V. (1994). Organic facies variations in the Westbury Formation (Rhaetic, Bristol Channel, SW England). *Organic Geochemistry*, 21, 1001-1014.
- Tyson, R.V. (1984). Palynofacies investigation of Callovian (Middle Jurassic) sediments from DSDP Site 534, Blake-Bahama Basin, western Central Atlantic. *Marine and Petroleum Geology*, 1, 3-13.
- Tyson, R.V. (1987). The genesis and palynofacies characteristics of marine petroleum source rocks. In: *Marine Petroleum Source Rocks*, Brooks, J. and Fleet, A.J. (Eds.), Oxford, Geological Society Special Publication, Blackwell Scientific Publications, 26, pp. 47-67.
- Tyson, R.V. (1989). Late Jurassic palynofacies trends, Piper and Kimmmeridge Clay Formations, UK onshore and northern North Sea. In: *Northwest European Micropalaeontology and Palynology*, Batter, D.J., Keen, M.C. (Eds.), The British Micropalaeontological Society Series, Ellis Horwood, Chichester, pp. 135-172.
- Tyson, R.V. (1993). Palynofacies analysis. In: *Applied Micropalaeontology*, Jenkins, D.G. (Ed.), Kluwer Academic Publishers. The Netherlands, Amsterdam, pp. 153-191.
- Tyson, R.V. (1995). *Sedimentary Organic Matter. Organic facies and palynofacies*. Chapman and Hall, London, 615 pp.

- Tyson, R.V. (1996). Sequence-stratigraphical interpretation of organic facies variations in marine siliciclastic systems: General principles and application to the onshore Kimmeridge Clay Formation, UK. In: *Sequence Stratigraphy in British Geology*, Hesselbo, S.P. and Parkinson, D.N. (eds.), , Geol. Soc., Spec. Publ. No. 103, p75-96.
- Vallentyne (1965). Vallentyne, J. R.: *Net Primary Productivity in Aquatic Environments*, Goldman, C R. (Ed.), Berkeley California Univ. Press, 1965, p. 30
- Vicent, A.J. (1995). Palynofacies analysis of Middle Jurassic sediments from the Inner Hebrides. PhD Thesis, University of Newcastle upon Tyne. 475p.
- van Geel, B., Grenfell, H.R. (1996). Green and blue-green algae - Spores of Zygnemataceae. In: *Palynology: Principles and applications*, Jansonius, J., McGregor, D.C. (Eds.), Am. Assoc. Stratigr. Palynol. Found., v. 1, pp. 173-179.
- Vandenbroucke, M., Largeau, C. (2007). Kerogen origin, evolution and structure. *Organic Geochemistry*, 38, 719-833.
- Waples, D.W., Machihara, T. (1991). Biomarkers for Geologists-A Practical Guide to the Application of Steranes and Triterpanes in Petroleum Geology. *Methods in Exploration Series*, American Association of Petroleum Geologists, 9, 91 p.
- Weiss, M. S, Abele, U, Weckesser, J, Welte, W, Schiltz, E., Schulz, G. E. (1991). Molecular architecture and electrostatic properties of a bacterial porin. *Science*, 254, 1627-1630.
- Whitaker, M.F. (1984). The usage of palynology in definition of Troll Field geology, reduction of uncertainties. In: *Innovative reservoir geomodelling, 6th Offshore Northern Seas Conference and Exhibition*, Stavanger, Norsk Petroleums-forening, Paper G6, 44p.
- Zimmermann, W. (1959). *Die Phylogenie der Pflanzen*. Gustav Fisher, Stuttgart, 777 pp.

The Genesis of the Mississippi Valley-Type Fluorite Ore at Jebel Stah (Zaghouan District, North-Eastern Tunisia) Constrained by Thermal and Chemical Properties of Fluids and REE and Sr Isotope Geochemistry

Fouad Souissi^{1,2}, Radhia Souissi² and Jean-Louis Dandurand³

¹*Département of Geology, Faculty of Sciences, University El Manar*

²*Institut National d'Analyses Physico-chimiques (INRAP), Sidi Thabet*

³*University of Toulouse, UPS (OMP), LMTG, Toulouse*

^{1,2}*Tunisia*

³*France*

1. Introduction

The fluorite district of Zaghouan, North-eastern Tunisia (Fig. 1), is characterized by occurrences of F-(Ba-Pb-Zn) mineralization associated with uplifted blocks of Jurassic reef limestone. The host rocks belong to the Hettangian-Lower Sinemurian Oust Formation and the Kimmeridgian-Tithonian-Berriasian Ressas Formation, capped by emergence surfaces and layers of condensed phosphate-bearing rocks. The uplifted blocks belong to the Jurassic mountain area; most of which run along the Zaghouan Fault (Turki, 1988), which extends over 80 km along the NE-SW Atlas fold trend with a vertical throw of 4,000 to 5,000 m. The Zaghouan Fault is considered to be a major lineament of the African block (Richert, 1971), behaving as a reverse fault crosscutting both the basement and the sedimentary cover (Castany, 1954). Local brecciated and chaotic masses of evaporates, claystones and black dolostones of Triassic age outcrop along the fault. No post-Triassic magmatic or metamorphic events have been reported in the region.

The F-(Ba,Pb,Zn) deposits of the Zaghouan district (Fig. 1) consist of stratabound and/or stratiform bodies, either within or immediately above, the Jurassic reef limestones, along unconformity surfaces (shoals, condensed layers, stratigraphic gaps, karst or paleosoil features) which separate the Oust Formation (Stah, Kohol), or the Ressas Formation (Zriba-Guebli, Mecella), from the overlying series. Mineralization may also occur within fractures crosscutting the limestone uplifted blocks and their overburden (Hammam Jedidi, Oust, Sidi Taya). Despite the gross similarity of the Liassic series throughout the major part of the district (Stah, Kohol, Oust, Zaress, Bent Saidane, Fkirine; Fig. 1), stratabound fluorite deposits featuring a strong epigenetic dolomitization of the country rocks, are known only from the locality of Jebel Stah and in the neighbouring area of Jebel Kohol.

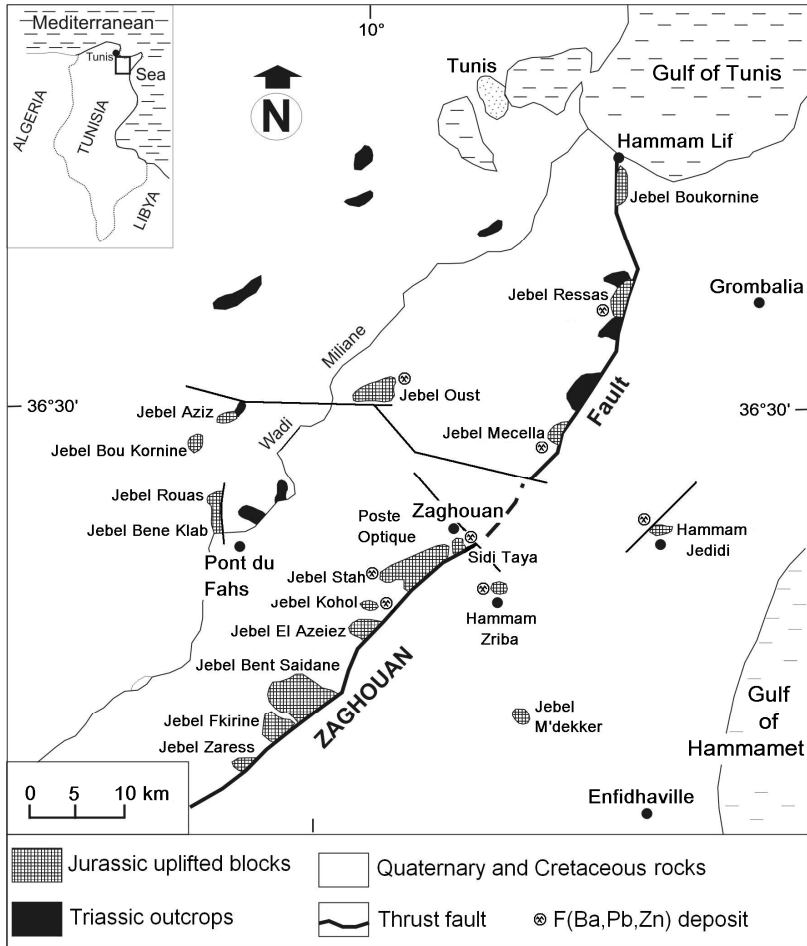


Fig. 1. Location map showing the Jurassic uplifted blocks and Triassic outcrops, along with F-(Ba,Pb,Zn) deposits, in North-eastern Tunisia.

Using detailed petrographic description of the fluorite ore bearing rocks, fluid inclusion (FI) microthermometry, metallic trace element (MTE), rare earth element (REE) and Sr isotope geochemistry, the authors reconstruct the geological history of the mineralization and propose a genetic model for the fluorite deposit of Jebel Stah.

2. Geological setting

Field observations show that the lithostratigraphic successions associated with ore-bearing series and barren equivalents are significantly different. The lithostratigraphic column at Jebel Stah (Figs. 2 and 3) consists of the complete stratigraphic sequence between the Lower Liassic and the Lower Cretaceous. Mineralization occurs both in the upper part of the Oust Formation (grey Hettangian-Lower Sinemurian limestones) which forms an uplifted block,

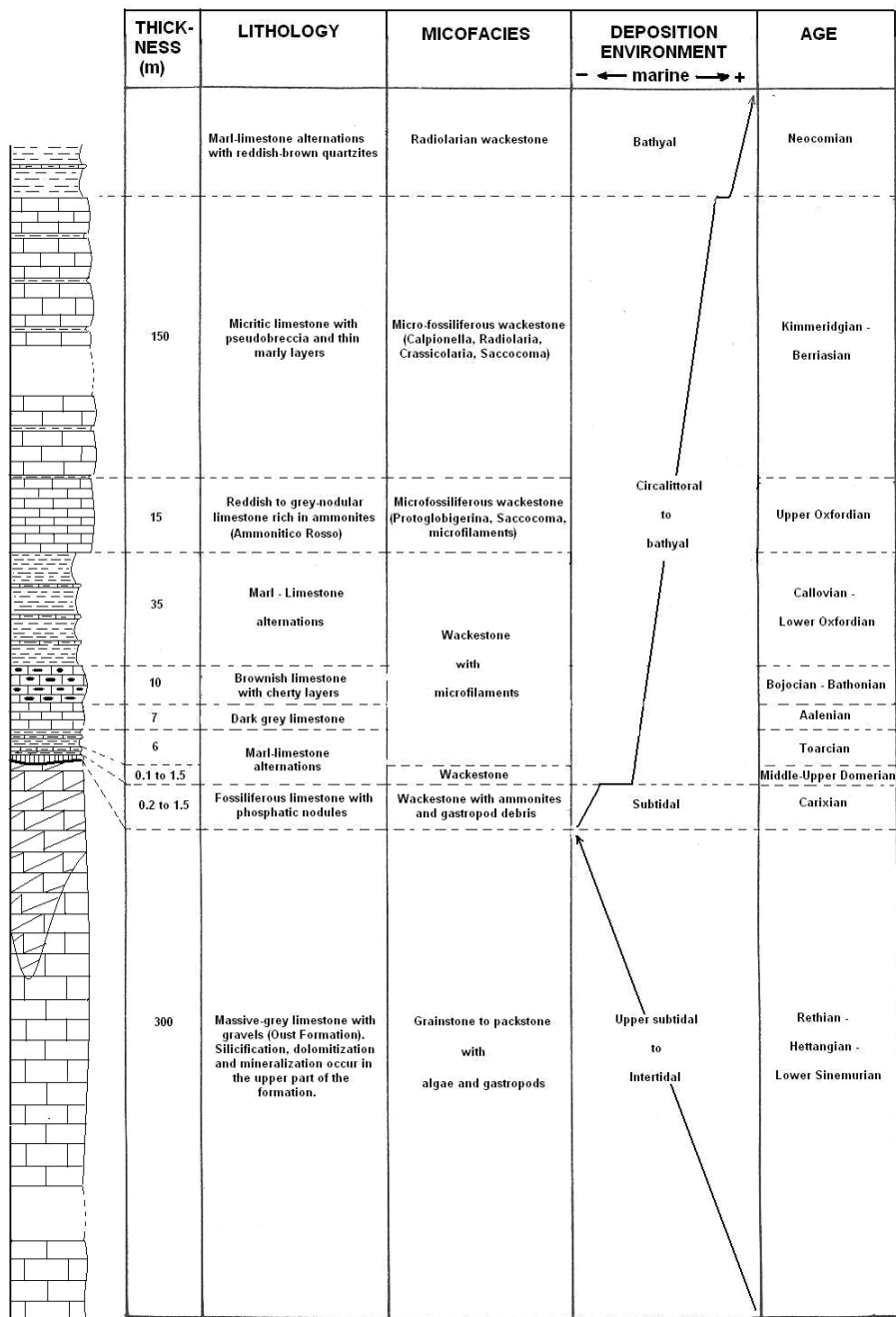


Fig. 2. Lithostratigraphic column of Jebel Stah and its petrographic, paleoenvironmental and chronological characteristics.

as well as within the overlying Carixian layer. The upper part of the Oust Formation limestones underwent diagenetic silicification and a subsequent strong dolomitization. The Oust Formation is overlain by an emergence surface evidenced by a hard ground and small karstic cavities. The Middle-Upper Carixian condensed layer (0.2 to 1.2 m thick) overlies the Oust Formation and consists of lenticular limestones rich in phosphatic nodules, ammonites and gastropods, and in grains of glauconite and authigenic quartz. The limestone beds are covered by a pyritic crust a few mm in thickness. Detrital silico-carbonate deposits, accumulated in karstic cavities at the top of the Oust Formation, provide evidence for a second emergence phase during the Lower Domerian period (Rakus and Biely, 1970). The overlying Middle-Upper Domerian to Neocomian series is represented by an alternation of marls and limestones.

At Jebel Stah and Jebel Kohol, ore mainly consists of fluorite and calcite. Other minerals are also present (sphalerite, galena, barite, celestite, malachite, azurite, siderite, ankerite, quartz), albeit sporadically.

At Jebel Stah, fluorite used to be extracted in open pits (Fig. 3), from 1937 to 1942 (6,500 tons; Sainfeld, 1952). The same pattern emerged again from 1969 to 1974 (60,000 tons; ONM, 1990), to provide ore grading 70% CaF₂ that could be marketed for metallurgical use. It is, however, interesting to note that exploration programs, conducted by ONM (1990), have shown that the adjacent Jebel Kohol deposit contains in excess of 230,000 tons of certified ore reserves and 76,000 tons of probable reserves, grading 29% CaF₂, 2% Pb and 2% Zn.

At Jebel Oust (Figs. 1 and 4), like at Jebel Stah, the Oust limestones are overlain by the Carixian condensed phosphatic limestone unit showing a ferruginous crust and a slight karstification at the top. Authigenic quartz is scarce and no dolomitization occurs in the upper part of the Oust Formation. The Carixian layer is overlain by the Upper Jurassic (Callovian to Tithonian) marl-limestone sequence. Mineralization mainly consists of fluorite with accessory Cu-bearing sulphosalts occurring within a vertical to sub-vertical extensive fault system induced by a NW-SE strain (σ_1) and related to the Late-Miocene compressive phase. The N160°-180°E direction fits with the extensive faults s.s., while those trending N010°-030°E and N090-110°E behave as sinistral and dextral strike-slip faults, respectively. The fractures cut through the Lower-Middle Liassic, the overlying Upper Jurassic series, and extend to the Lower Cretaceous units (Souissi et al., 1996).

In contrast to the above, the Lower-Middle Liassic units at the Poste Optique (at the ENE limit of Zaghouan Mountain, almost 5 km from Jebel Stah; Fig. 1) consist of a thick, complete and non-fossiliferous sequence (Fig. 4). Ore occurrences are totally absent in this area (Souissi, 1987).

3. Host rocks and ore petrography

The mineralization of Jebel Stah runs along the Middle-Liassic unconformity. Several distinct types of orebodies are recognized (Fig. 5): (i) stratabound ores constitute the economic volume of the deposit and run along the unconformity surface, occurring as replacement clusters or open space fillings in the Carixian layer, but also in the upper part of the Lower Liassic and at the bottom of the Middle-Upper Domerian rocks in the hanging wall as small lenses (20 to 40 cm long and a few mm thick) replacing thin carbonate layers; (ii) fracture-controlled mineralization within vertical extensional veins which cut the entire

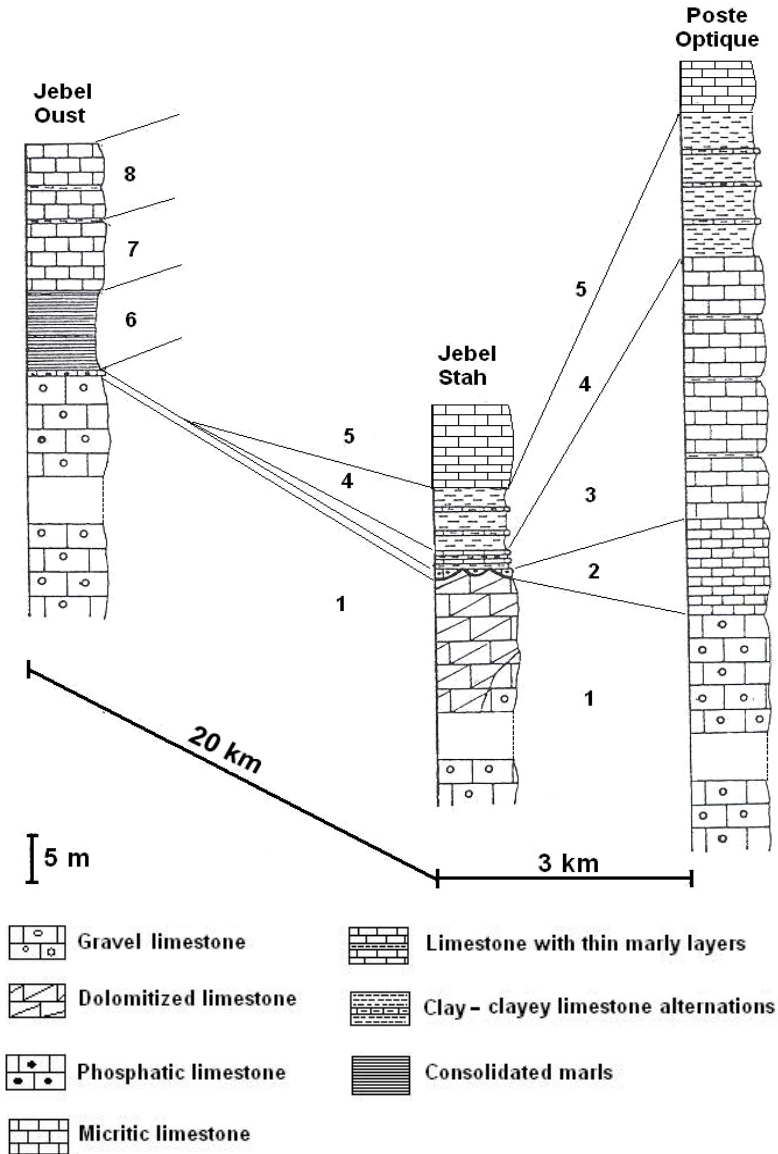
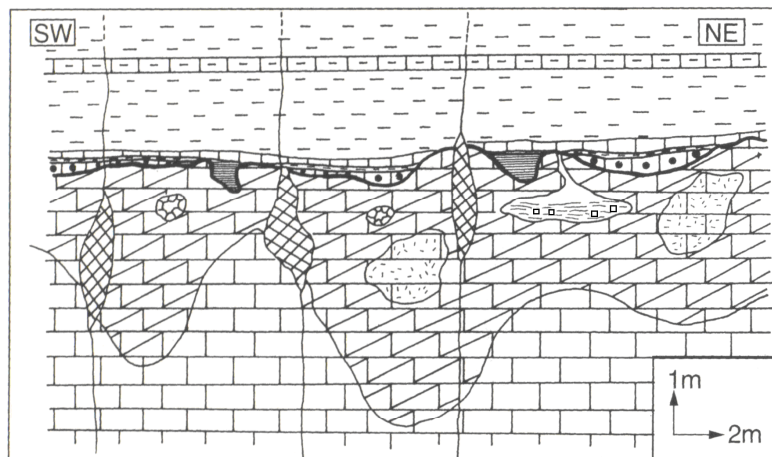


Fig. 4. Correlation between the Liassic series of Jebel Stah and Poste Optique (Zaghouan) and Jebel Oust (1: Hettangian-Lower Sinemurian, 2: Carixian (Upper Sinemurian-Carixian at Poste Optique), 3: Domerian (Middle-Upper at Jebel Stah), 4: Toarcian, 5: Aalenian, 6: Callovian-Lower Oxfordian, 7: Upper Oxfordian, 9: Kimmeridgian-Lower Tithonian).









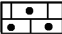


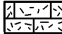
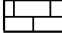
-  Fluorite in geode (F3)
-  Intradolomitic solution void with pelites and cubic fluorite (F3)
-  Breccia fillings with calcite and fluorite within vertical lodes (F2)
-  **Toarcian**: Clays and marly limestones
-  **Domerian**: clays and marly limestones (dolomitized and mineralized in their lower part)
- Carixian**
-  Karstic cavities with dolomitized sediments replaced by fluorite (F1a, b)
-  Phosphatic limestones (partially dolomitized and mineralized) (F1a, b)
- Hettangian-Lower Sinemurian**
-  Hard ground
-  Reddish dolostone (mineralized in its upper part) (F1a, b)
-  Grey limestone with authigenic quartz
-  Grey limestone

Fig. 5. Schematic cross-section of the Lower-Middle Liassic sequence at Jebel Stah showing the location and the morphology of the fluorite orebodies. F1a, F1b, F2 and F3 are petrographic types of fluorite (after Souissi et al., 1997, 1998).

Liassic series, where large openings are created and filled with fluorite and sparry calcite; (iii) fluorite within cavities; and (iv) accessory fluorite and massive smoky quartz within fractures.

The country limestones of the Oust Formation are characterized by grainstone to packstone microfacies rich in green and incrusting algal debris (*Paleaodasycladus* and *Thaumatoporella*, respectively), oncolites and skeletons of foraminifera (Fig. 6A, B). This facies indicates sedimentation under strong hydrodynamic conditions. The abundance of the green algae indicates a shallow water environment, probably in a back reef zone. Near the top of the formation, the presence of fibrous calcite, surrounding the framework grains, indicates a deposition in a vadose environment; while the abundance of dissolved gypsum crystals molds and authigenic quartz crystals (Fig. 6C) provide evidence that pre-evaporitic conditions prevailed. The product of dolomitization consists of a reddish, homogeneous dolosparite extending beyond the emergence surface, and partially affecting the Carixian and Domerian units. The crystallization of dolomite after quartz (Fig. 7A) and the emergence phases (Fig. 8A) testify to its late diagenetic to epigenetic origin. The top of the dolomitic horizon consists of an anisotropic facies occurring as banded (Fig. 7B) or solution-breccia (Fig. 7C) structures, and consisting of a dark-coloured dolosparite, similar to the one described above, and associated with a light-coloured (yellow to white) dolomacrosparite of antipolar growth.

All dolomite types show a sweeping extinction between crossed polars. This petrographic type of dolomite is known as “ferroan dolomite” (Choquette, 1971); “baroque dolomite” (Folk and Assereto, 1974); “sparry dolomite” (Beales and Hardy, 1980), “saddle dolomite” (Radke and Mathis, 1980), or “xenotopic dolomite” (Gregg and Sibley, 1984). Radke and Mathis (1980) and Gregg and Sibley (1984) considered that this type of dolomite crystallizes after burial, at temperatures ranging from 50–60 °C to 100–150 °C. According to Beales (1971) and Choquette (1971) these dolomites crystallize in the same conditions as the associated ore minerals.

The banded dolomites are known in the literature as “franciscaine” (Jacquin, 1970; Trona, 1973), “banded spar” (Martini, 1976), “Zebra texture” (Beales and Hardy, 1980), “diagenetic crystallization rhythmites or DCRS” (Fontboté, 1981; Fontboté and Amstutz, 1983), “Zebra rock” (Spangenberg et al., 1993; Spangenberg et al., 1995). This petrographic type of dolomite is similar to those present within the gangue of several Pb-Zn-Ba-F Mississippi Valley type (MVT) deposits, where they always accompany the ore minerals (Beales and Hardy, 1980; Ohle, 1985; Fontboté and Gorawski, 1990; Fontboté, 1993). According to Fontboté and Gorawski (1990) the DCRs result from the interaction of hot brines within the host rocks in an open system, long after the lithification; these brines are similar to those giving rise to the Mississippi Valley ore deposits.

The mineralization consists mainly of four distinct petrographic types (Table 1). Ore types F11a and F11b occur within the stratabound ore bodies, type F12 corresponds to the fluorite in the sub-vertical lodes (Fig. 5) and type F13 corresponds to fluorite occurring in cavities.

F11a. Replacement clusters which may be considered as the early fluorite generation. They are closely connected in space to the epigenetic dolomitization of the host rocks (Souissi et al., 1998). This facies consists of a microgranular (sub-mm- to mm-sized) fluorite and occurs

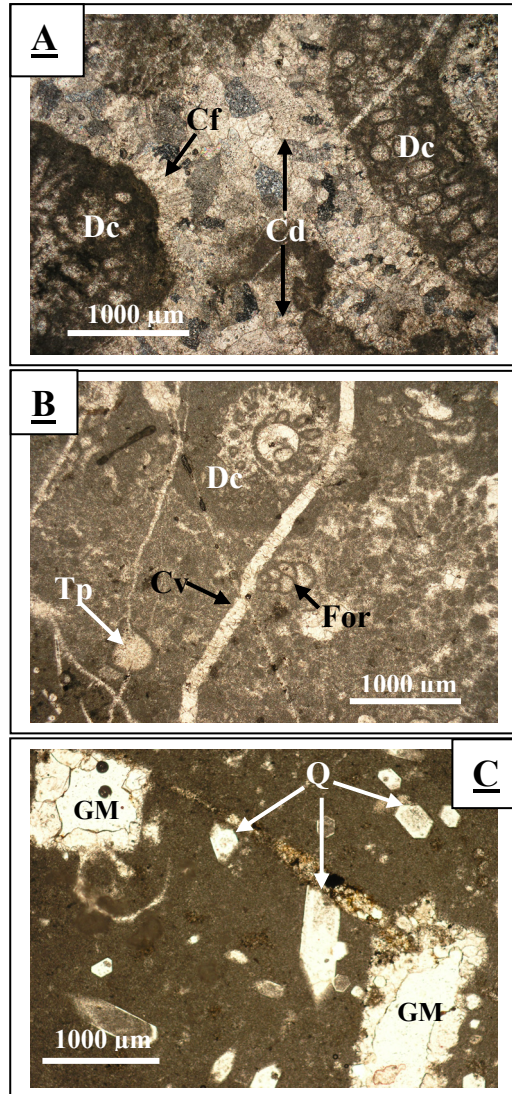


Fig. 6. Petrography of the grey limestone country rocks of the Hettangian-Lower Sinemurian, in thin sections. (A) Grainstone rich in green algal (Dasycladals: Dc) debris (sample L5-8, crossed polars). Note that the grains are surrounded by fibrous calcite (Cf). Voids are cemented by a drusy calcite (Cd). (B) Grainstone to packstone including green algal (Dasycladals "Dc") and red algal (Thaumatoporels "Tp") debris and foraminifera tests (For), crosscut by a calcite vein (Cv), (sample JSII-14; polarized light). (C) Carbonate matrix (M) including authigenic quartz (Q) and gypsum molds (GM) (sample JS3-8, polarized light).

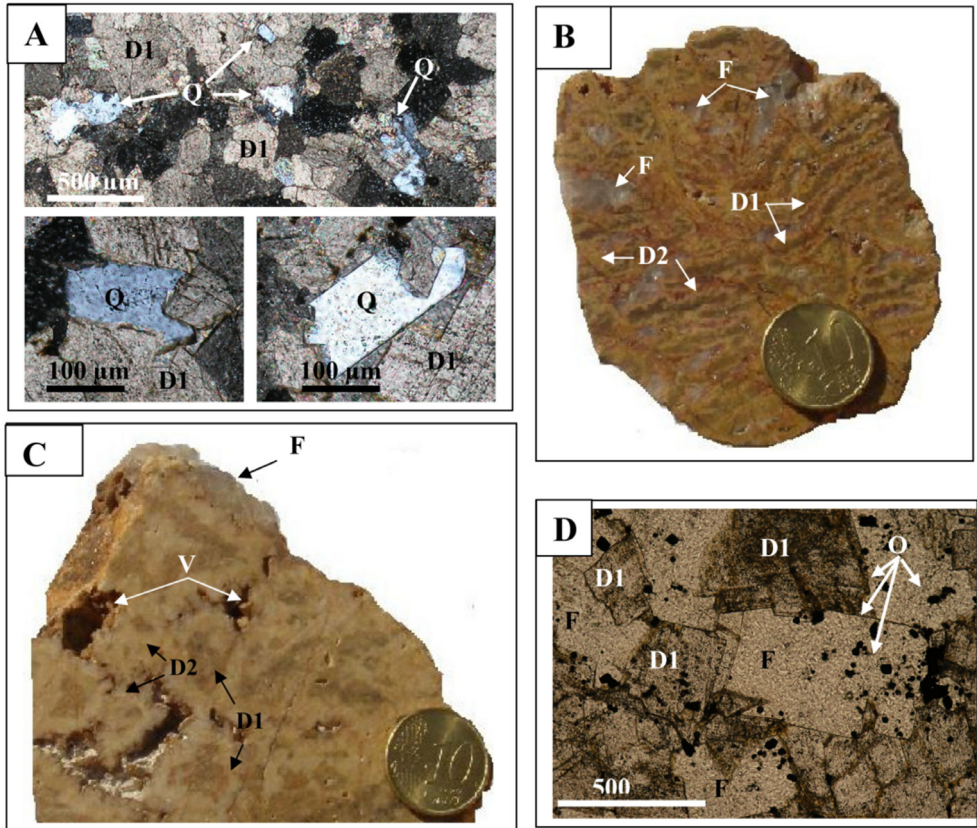


Fig. 7. Petrography of the dolomitized country rocks of the Hettangian-Lower Sinemurian. (A) Equigranular dolosparite (D1) with authigenic quartz (Q) remains (thin section, sample L6-31, crossed polars). (B) Banded dolosparite showing an alternation of dark dolosparite layers (D1) and recrystallized light-coloured dolomacrosparite (D2). Open spaces are filled with colourless fluorite (F), (sample C5-Dr), (C) Dolomitic breccia showing dark elements made of dolosparite (D1) cemented by a light-coloured dolomacrosparite (D2). Note the presence of open spaces (V), some of which are filled with colourless fluorite (F), (sample C5-Db), (D) Microfacies of the massive, mineralized dolostone; the matrix consists of a homogeneous dolosparite (D1) replaced by fluorite (F), (thin section, sample L3-22, polarized light).

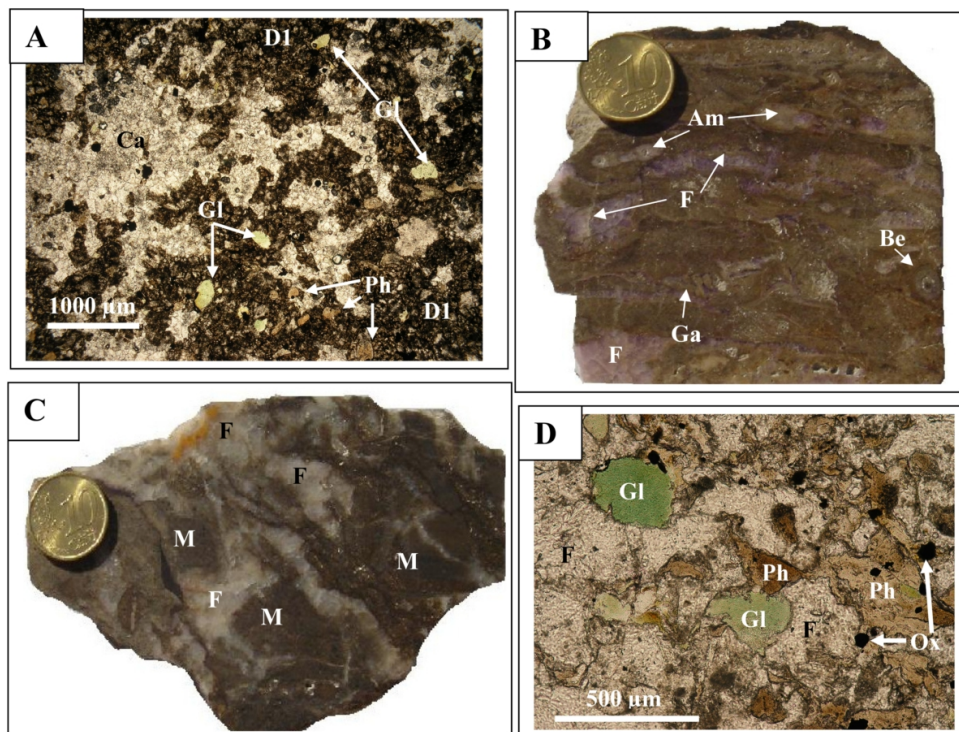


Fig. 8. Petrography of the Carixian facies. (A) Carixian phosphatic limestone affected by epigenetic dolomitization. Ferruginous dolosparite (D1) includes remains of glaucinite (Gl) and phosphate (Ph) grains and is invaded by a late calcitization (Ca), (thin section, sample CC6-90, polarized light); (B) Fossiliferous limestone, rich in ammonites (Am), gastropods (Ga) and belemnite rostra (Be) filled with internal phosphatic cement. Macrogranular purple fluorite (F) has replaced part of the phosphate-carbonate matrix, epigenized fossil shells (Ga, Be) and filled the interiors of others (Am), (C) Brecciated facies of the phosphatic limestone showing elements of the matrix (M) cemented by a white macrogranular fluorite (F); (D) Detail from (C) showing the matrix (M) strongly replaced by fluorite (F). Only remains of phosphate (Ph), glaucinite (Gl) grains and oxides (Ox) are preserved (thin section, sample JS1-6, slightly-crossed polars).

Petrographic group	Lithology / Ore facies / orebody	Age of layer/ore-bearing layer(s)	Sample	Petrographic description [Number of the old extraction open pit, as indicated in Fig. 3]	Petrographic type of fluorite	Mineralogy
I: Limestone and authigenic quartz	Backreef limestones		L6-5	Grey limestones [6]	-	Calcite
			L6-30	Grey limestones with authigenic quartz [6]	-	Calcite, quartz
			L6-30Q	Authigenic quartz [6]	-	Quartz
			L5-3	Massive yellow dolosparite [5]	-	
II: Dolostones and associated fluorite	Dolostones (Upper part of the Oust Formation)	Lower Sinemurian	DZ6-G	Grey dolosparite of the pseudo-brecciated facies (Fig. 7c) [6]	-	Dolomite
			DZ6-J	White sparry dolosparite of antipolar growth of the pseudo-brecciated facies (Fig. 7c) [6]	-	
			DZ6-F	Colourless fluorite filling voids in the pseudo-brecciated dolostone facies (Fig. 7c) [6]	Fl3	Fluorite
III: Phosphatic limestone and associated fluorite	Phosphatic limestone Macrocrystalline fluorite associated with the phosphatic limestone		JS1-6P	Nodular grey phosphate [1]	-	Apatite, calcite
			CC3-3 CC3-2	Macrogranular purple fluorite (Fig. 8b) [3]		
			JS1-6F	Macrogranular white fluorite (Fig. 8c) [1]	Fl1b	Fluorite
IV: Finely-laminated dolostones and associated fluorite	Finely laminated karst deposits	Carixian	L3-21D	Dolomicrite (Fig. 9a,c) [3]	-	Dolomite, quartz ^s
			L3-21F	Microgranular fluorite replacing the carbonated matrix (Fig. 9a,c) [3]		Fluorite, dolomite ^s
			L5-16	Microgranular black fluorite with remains of matrix (Fig. 10a,b) [5]	Fl1a	quartz ^m
			L5-15F	Microgranular fluorite rich in matrix remains (Fig. 10c) [5]		Fluorite, quartz ^s , dolomite ^s , calcite ^s , apatite ^m
			L5-15G	Mesogranular-purple fluorite layers alternating with sample L5-15F [5]	Fl1b	
V: Banded ore			FZ-5N	Microgranular fluorite with matrix remains (Fig. 11a,b) [5]	Fl1a	
			FZ-5B	Macrogranular-white fluorite (Fig. 11a,c) [5]	Fl1b	Fluorite, quartz ^s
VI: Megacrystalline fluorite and calcite in lodes		Sinemurian to Lower Toarcian	JS5-F	Cm-sized fluorite crystals [5, 6]	Fl2	Fluorite
			JS6-F			
			JS5-C	Cm- to dm-sized rhombohedral calcite crystals [5, 6]	-	Calcite
			JS6-C			
VII: Fluorite in cavities	Intradolomitic pockets filled with residual clays Geode	Lower Sinemurian Carixian	L4-2	Cm- to dm-sized, cubic blue and purple fluorite [4]	Fl3	Fluorite
			JS3-5	Cm-sized cubic fluorite [3]		

Table 1. Samples selected for the MTE, REE and isotopic Sr geochemistry in the different petrographic facies of the wallrocks and the fluorite ore of Jebel Stah (^s: secondary mineral phase, ^m: minor mineral phase).

as diffused clusters or lenticular bodies, resulting from the replacement of the carbonated matrix in the dolomitized horizon at the top of the Oust Formation (Fig. 7D), in the Carixian phosphatic layer (Fig. 8B-D) and in the intrakarst, finely-laminated deposits (Fig. 9). They contain relict dolomite, calcite, together with, apatite, glauconite and authigenic quartz, with rare sphalerite, galena and pyrite.

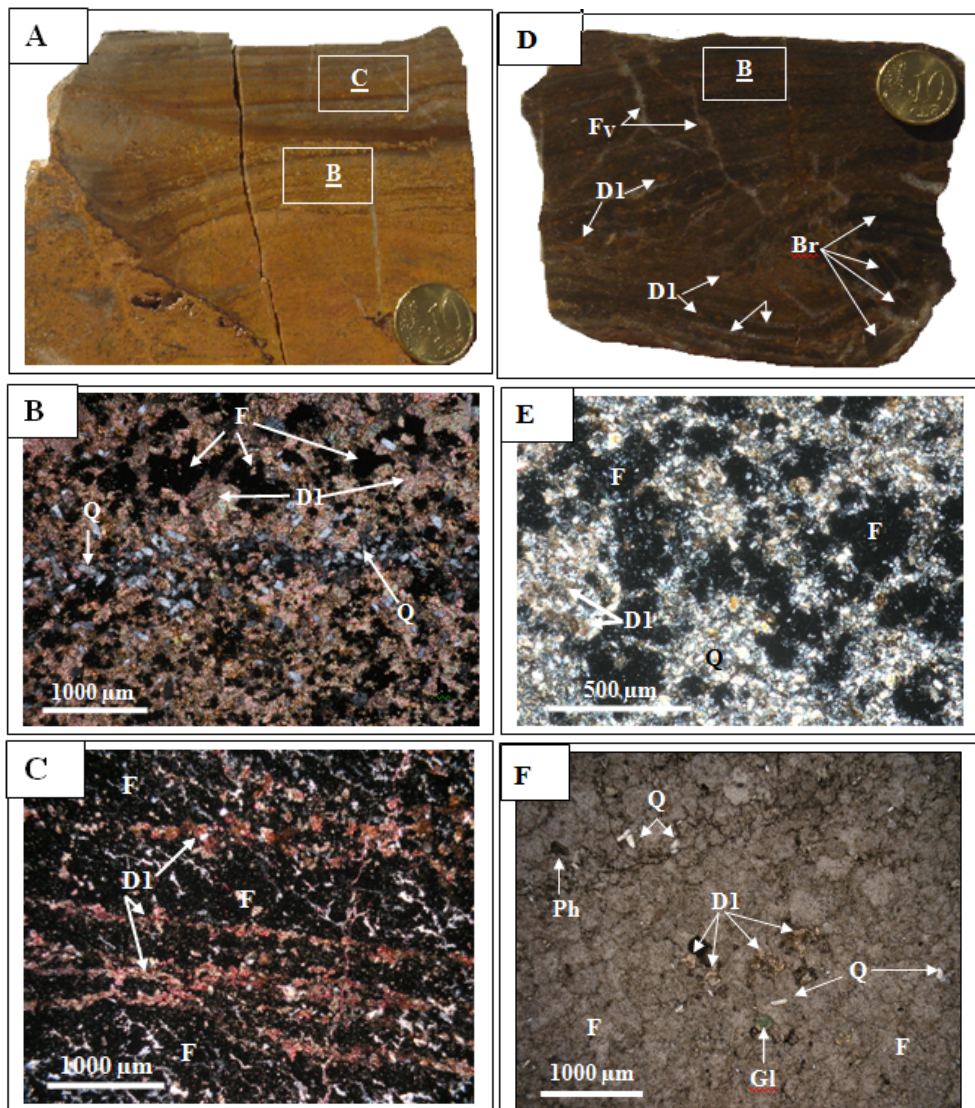


Fig. 9. Petrography of the fluorite-bearing Carixian facies. (A) Finely-laminated sediment filling a karst cavity at the top of the Hettangian-Lower Sinemurian, affected by epigenetic dolomitization (light grey laminae) and subsequent fluoritization (dark grey laminae), (Sample

L3-21, see B and C). (B) Strong dolomitization (D1) has affected the sediment in the lower part of the karst, only authigenic quartz (Q) in thin layers remains as a former sediment. Part of the dolomitic matrix has been replaced by fluorite (F), (thin section, crossed polars). (C) Dolomitic matrix (D1) at the top of the cavity, including remaining quartz crystals is replaced by a microgranular fluorite (F) rich in interstitial silica (thin section, crossed polars). (D) Finely-laminated dark sediment filling a karst cavity at the top of the Hettangian-Lower Sinemurian, including a sedimentary breccia (Br) wholly replaced by fluorite. The latter is evidenced macroscopically by light-coloured fluorite occurring as veinlets (F_v) and thin layers (F_L). Remains of the former matrix consist of only small yellow patches of dolomite (D1), (sample L5-16); (E) Details of the area delineated in A: the replacement of the former matrix by fluorite is almost total. Only small dolomitic patches (D1), quartz crystals (Q), phosphate (Ph) and glauconite (Gl) grains are preserved (thin section, sample L5-16, slightly crossed polars). (F) Details of a finely-laminated sediment filling a karst cavity at the top of the Hettangian-Lower Sinemurian, showing small patches of fluorite (F) replacing part of the matrix. This one is made of abundant authigenic quartz microcrystals (Q) with some dolomitic (D1) remains (thin section, sample L5-15, polarized light).

Fl1b. White-to-purple macrogranular fluorite, resulting from the recrystallization of the early fluorite generation (Fl1a) along the Carixian layer (Fig. 8B, C). Sometimes, the recrystallization gives rise to stratabound-banded structures which consist of an alternation of mm- to cm-scale dark layers of early fluorite and white layers consisting of a macrocrystalline fluorite of antipolar growth. Interstitial silica may be observed in either the microgranular (Fig. 9C) or the macrogranular fluorite-bearing layers.

Fl2. Large open-space fillings within vertical to sub-vertical extensional faults trending N030°-060°E and N090-130°E, and crosscutting the entire Liassic series, including the hanging wall Toarcian marls (Fig. 5). Fluorite consists of cm-sized colourless or white-to-yellowish crystals accompanied by calcite occurring as cm- to dm-sized white-to-pink rhombohedra.

Fl3. Colourless, white or purple fluorite occurring as small open space fillings (Fig. 7B, C) or as cm-to-dm-scale cubic crystals within large solution cavities either at the top of the Lower Liassic formation or within the Carixian layer.

4. Sampling and analytical methods

The microthermometric analyses were conducted with a "Chaixmeca" heating-freezing stage microscope which allows temperature measurements within the range -196 to +600 °C (Poty et al., 1976). Pure CO₂ and pure water specimens were used for calibration. The precision of temperature measurements is of the order of ±1 °C for the final melting temperatures (T_m) and the homogenization temperatures (T_h) in the -100 °C to +250 °C interval.

The crush-leach method (Roedder 1984) was used to collect the fluids contained in the inclusions (cf. Ames 1955; Hall and Friedman 1963; Roedder 1963, 1967, 1979; Sawkins 1968; Grappin et al. 1979; Deloule 1982). Fluorite samples were crushed in distilled water to extract the fluid trapped in the inclusions. The solids were then washed with distilled water. In order to separate the fluids contained in the inclusions of different generations, a large number of chips containing mainly primary, pseudosecondary, or secondary inclusions, are

selected by microscopic observations. The recovered solutions are analyzed for Na⁺, K⁺ by flame photometry (iso Bio type PHF 90D), Ca²⁺, Mg²⁺ by atomic absorption (Perkin Elmer Zeeman 5000) and F⁻, Cl⁻ and SO₄²⁻ by ionic chromatography (Dionex 2000i). There was a mean analytical error of 5% for all methods.

The geochemical characterization of fluorite was based on analysis for metallic trace elements (MTE), REE and Sr isotopes. Limestone (2 samples), authigenic quartz (1 sample), dolostone (4 samples) and phosphates (1 sample) from the wallrocks, along with samples representing the different petrographic facies and bodies of the fluorite ore at Jebel Stah (14 samples) have been collected from geological outcrop in the different open pits (Fig. 3; Table 1). Each has been described in the field, in hand specimen and in thin section. Prior to crushing, the broken samples were investigated and sub-divided under a binocular microscope to separate the different petrographic phases: carbonates, phosphates, microgranular "impure" fluorite including matrix remains (dolomite, silica, phosphate, clayey fraction) and macrogranular "pure" fluorite.

For the MTE and the REE determinations, 0.1 g of each powdered sample was dissolved in 0.5/0.6 ml HF/HNO₃ within a sealed teflon backer (savillex). After evaporation at 50 °C on a heating plate for 12 hours, the sample is redissolved in twice-distilled HNO₃ (2.8 ml) on the heating plate (sealed backer) for 24 hours. After dilution in 100 g of twice-distilled water (solution 1), 250 µl of ultrapure H₂O₂ (for the complexation of the Ta, to prevent its complexation by the REE) and 100 mg of powdered boric acid (to keep fluoride in solution by complexation), are added to the solution. The fluorite is completely dissolved by heating for 24 hours at 60 °C (solution 1). MTE and REE analysis was undertaken with an ICP-MS (type Elan 5000-Perkin Elmer). The standard limestone "CAL-S" (CRPG standard limestone; Potts et al., 2000) was used for calibration. Measurement reproducibility was better than 5 % relative for all elements.

For the Sr isotopic determinations, 1 ml of solution 1, was evaporated overnight at 50 °C. The residue was re-dissolved in 1 ml 6N HCl. A blank was prepared at the same conditions. Strontium was separated from the solutions using ion exchange columns. The ⁸⁷Sr/⁸⁶Sr ratio was measured on a 7-collector Finnigan MAT 262 thermal ionization mass spectrometer. Reproducibility of this ratio among replicate samples was always to an uncertainty below 0.000005 (2σ). Measured blanks for the procedure are negligible, yielding uncertainties significantly lower than reproducibility. The average value for the NBS 987 standard was ⁸⁷Sr/⁸⁶Sr = 0.710242 ± 0.000005 (2σ).

5. Fluid inclusions

5.1 Description of fluid inclusions

The studied fluid inclusions occurred in fluorites and in the massive quartz from Jebel Stah. Primary, pseudosecondary and secondary inclusions were recognized by microscopic observations of thin cleavage splinters.

5.1.1 The primary and pseudosecondary inclusions

These are up to 500 µm in size and often take the shape of negative crystals. Two types are observed:

- *Two-phase liquid-vapor aqueous (L+V type) inclusions* at room temperature, visible within the fluorite crystals of Jebel Stah. Some of these samples show trapped dolomite crystals. The liquid phase accounts for 95% of the inclusion volume. The initial melting temperature is about -50 °C, which is clearly lower than the eutectic temperature of the NaCl-H₂O system (-20.8 °C). This indicates the presence of bivalent cations such as Mg²⁺ and Ca²⁺ (Crawford 1981; Roedder 1984).

The salinity (S) of the fluids was obtained from the final melting temperatures of ice (T_m). The homogenization temperatures (Th) are measured during heating runs; all of the inclusions homogenize in the liquid state. The mean salinity ranges between 18 and 22.5 wt % NaCl equivalents for the early fluorites (F11b and F12). The homogenization temperatures range from 120 to 160 °C. Type 3 fluorite (F13) is characterized by medium salinity (10 wt % NaCl equivalents) and a higher mean Th range (175-180 °C). The inclusions contained in the quartz samples are characterized by low salinities of 5.5 wt% NaCl equivalents and homogenize in the range of 205-215 °C.

- *Two-phase gaseous CO₂-rich inclusions (L+V+CO₂G type)* within the massive quartz of Jebel Stah with variable phase ratios (50-95% liquid content). These inclusions freeze between -90 and -100 °C. Melting of solid CO₂ starts between -92 and -95 °C; mean final melting temperature (T_mCO₂) is -57.1 °C, which is lower than the eutectic temperature of pure CO₂ (-56.6 °C). The homogenization occurs in the gaseous state at a mean temperature (ThCO₂) of 19 °C. The density of CO₂ (0.19) was deduced from the relationship between the temperature of homogenization (ThCO₂) and the density of the CO₂ phase (Valakovich and Altunin, 1968, in: Shepherd et al., 1985).

5.1.2 Secondary inclusions

Two types of secondary inclusions were observed:

- Two-phase (L + V) aqueous fluid inclusions. The liquid phase fills up to 95% of the inclusion volume. The homogenization temperatures range between 140 and 200 °C. The salinities are low (3-6 wt% NaCl equivalents).
- Three-phase (L + P + V type) aqueous inclusions containing a droplet of petroleum (P) and visible in the large cubic fluorite crystals of Jebel Stah (F13).

5.2 The microthermometric results

The results of the microthermometric analyses are summarized in Table 2, where the final melting temperature of ice (T_m) and the homogenization temperature (Th) are given by their mean values. These are deduced by statistical analysis from histograms (symmetric distribution in most cases) constructed with a 10 °C interval for Th and T_mNaCl and 0.5 °C interval for T_m. More than 75 % of the temperature values lie in the modal value ±15 °C interval for Th and in the modal value ±0.75 °C interval for T_m. Finally, mean T_m and Th values are accepted with an error equivalent to the standard deviation interval, e.g. ±1 °C for T_m and ±5 °C for Th. The mean homogenization temperatures and salinities are translated in a Th Vs S plot (Fig. 10).

The fluorites F11 and F12 from Jebel Stah are characterized by similar mean homogenization temperatures and salinities that are, for the most part, clustered around 130 ± 5 °C and 19.5 ±

Sample	Sample description (Petrographic type)	Generation and composition of inclusions	Size (μm)	N	Salinity ± 1		
					T _m ± 1 ($^{\circ}\text{C}$)	(wt% NaCl equivalent s)	T _h ± 5 ($^{\circ}\text{C}$)
JSF-D	Fluorite in fine aggregates replacing dolomite (F11a)	Primary L+V	10-50	26	-20	22.5	120
L6-1	Fluorite filling voids in the dolomite (F11b)	Primary L+V	20-200	16	-14	18	125
CC5	Fluorite in fine aggregates			24			
CC5-51	replacing carbonates of the CC4-41 karstic deposits (F11a)	Primary L+V	20-100	7	-16	19.5	145
JS1-6	Massive fluorite filling voids in the phosphatic carbonates (F11b)	Primary L+V	10-100	23	-17	21	130
L3	Massive fluorite of the banded ore (F11b)	Primary L+V	10-100	25	-16	19.5	150
JS3-8	White sparitic fluorite of the intradolomitic karstic druses (F12)	Primary L+V	50-300	25	-15	19	125
		Pseudosecondary L+V	10-50	32	-15	19	120
JS3-5	White fluorite of the intradolomitic geodes (F12)	Primary L+V	50-500	25	-16	19.5	160
		Pseudosecondary L+V	50-200	35	-16	19.5	125
		Primary L+V	50-500	26	-6.5	10	180
JS1-5	White fluorite of the intradolomitic geodes (F13)	Pseudosecondary L+V	10-50	32	-6	9.5	140
		Secondary L+V+P	50-500	21	-	-	115
L4-2	Macrocrystalline fluorite associated with marly intradolomitic dissolution druses (F13)	Primary L+V	100- 700	32	-6.5	10	175
CC1-3	Purple sparitic fluorite of the intradolomitic karstic druses (F13)	Primary L+V	100- 500	24	-6.5	10	175
		Secondary L+V+P	10-50	28	-2	4	200
		Primary L+V					
JS1-14	Massive quartz from the intradolomitic fractures	Pseudosecondary L+V	50-400	42	-3	5.5	215
		Primary and	10-100	25	-3	5.5	205
		pseudosecondary CO ₂ gas	20-200	20	-57.1	-	19*

Table 2. Sample description, generation and composition of inclusions and microthermometric results of the fluid inclusions in the fluorites and the quartz of Jebel Stah. N number of inclusions, T_m ice melting temperature, T_h homogenization temperature, L aqueous liquid, V aqueous vapor.

1 wt% NaCl equivalents, respectively (Fig. 10, Table 2). The deposition of the fluorite F13, followed by the massive quartz, is accompanied by an increase in temperature (mean T_h = 175 \pm 5 $^{\circ}\text{C}$ and 207 \pm 5 $^{\circ}\text{C}$) and a decrease in the mean salinity (10 \pm 1 wt % NaCl equivalents and 5.5 \pm 1 wt % NaCl equivalents; Fig. 10, Table 2). These figures, show that the fluorites F11 and F12 (types 1 and 2) belong to the first generation. Field observations alone did not allow this distinction. Consequently, the vertical faults (Fig. 3) should be the drain that channelled the ascending hydrothermal ore fluids that deposited the fluorite F12 within the large dissolution cavities superimposed to the faults near the unconformity surface. The fluids infiltrated horizontally through the porous rocks of the Lower-Middle Liassic allowing the replacement of the carbonate substratum and giving rise to fluorite F11. The

fluorite F13 corresponds to a second generation, which crystallized later in large, well-shaped cubic crystals within geodes.

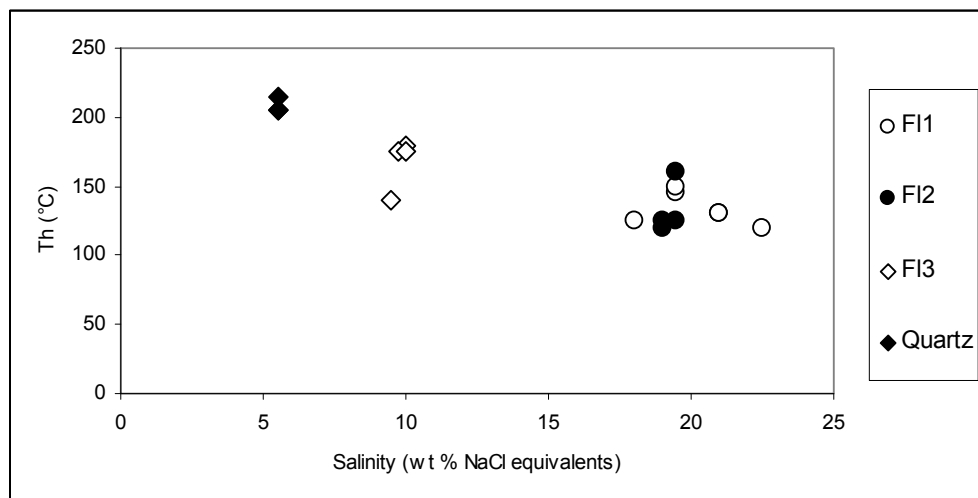


Fig. 10. Mean homogenization temperature versus mean salinity of primary and pseudosecondary aqueous fluid inclusions in fluorite and massive quartz from Jebel Stah.

The fluids trapped either within the secondary inclusions of fluorite or within the primary and pseudosecondary inclusions of the massive quartz of Jebel Stah are characterized by the lowest salinities ($3-6 \pm 1$ wt % NaCl equivalents), and mean homogenization temperatures ranging from 140 ± 10 °C to 200 ± 10 °C as well as the presence of gaseous CO₂. These observations strongly suggest the presence of fluids rich in gaseous CO₂ which permeate at a late stage the Jebel Stah and give rise to the massive quartz. Perthuisot (1978) and Perthuisot et al. (1978) also documented the presence of CO₂-rich fluids associated with diapirism in northern Tunisia. At Hammam Zriba, earlier microthermometric studies of the inclusions occurring in the fluorite (Bouhlef 1982; Bouhlef et al. 1988) also indicated a homogenization temperature increase from 100 to 185 °C from the first to the third fluorite generation.

5.3 Temperatures of formation (T_f) of host minerals

The formation temperature (T_f) of a mineral is equal to, or higher than, the homogenization temperature (T_h) of its primary or pseudosecondary inclusions. It may be given by: $T_f = T_h + \Delta T$, where ΔT is the pressure correction (Roedder 1979, 1984). Bouhlef et al. (1988) suggested a $\Delta T \leq 20$ °C for the aqueous inclusions of the fluorite from Hammam Zriba hosted at the top of the Jurassic series, and proposed $T_f = (T_h + 10 \text{ °C}) \pm 10 \text{ °C}$ as a relation including all the possible temperature correction values in the 0-20 °C interval. The geologic setting allows us to work with $\Delta T \leq 30$ °C (Potter and Calif 1977) for the mineralizations of Jebel Stah, hosted in the Lower Jurassic series.

Stretching has to be considered for the fluorite samples formed under the lower temperature conditions, e.g. the fluorites F11 and F12 (Fig. 10, Table 2). The consequent overheating is

estimated to be caused by temperatures approaching the crystallization temperature of the Jebel Stah massive quartz. In such conditions, the fluorites F11 and F12 have undergone an overheating of 80 ± 10 °C, while the fluorite F13 has undergone a lower overheating of 35 ± 10 °C. The mean Th values ($Th \pm 5$ °C) should be lowered by a ΔTh (amount of stretching, Bodnar and Bethke, 1984) of about -10 °C for the fluorites F11 and F12 and -5 °C for the fluorite F13. The fluid inclusions of the massive quartz as well as the secondary inclusions are supposed not to be subjected to significant overheating, to stretch.

Taking into account the errors on Th rising from both of the statistical analysis (± 5 °C), and the stretching ($-\Delta Th$), the relation given by Bouhlef et al. (1988) becomes: $T_f = \{(Th - \Delta Th + \Delta T/2) \pm (5 + \Delta T/2)\}$ °C. It follows that the mean formation temperatures will be (Table 3): 135 ± 20 °C for the fluorites F11 and F12, 185 ± 20 °C for the fluorite F13 and 225 ± 20 °C for the massive quartz.

Mineral	Petrographic type	$T_m \pm 1$ (°C)	Salinity ± 1 (wt % NaCl equivalents)	$Th \pm 5$ (°C)	Generation	Overheating ± 10 (°C)	ΔTh (°C)	$T_f \pm 20$ (°C)
Fluorite	F11a, b	-16.5	20	130	I	80	-10	135
	F12	-15.5	19	130				
	F13	-6.5	10	175	II	35	-5	185
Quartz	-	-3	5.5	210	-	-	0	225

Table 3. Average final melting temperatures (T_m), salinities, and homogenization temperatures (Th) deduced from microthermometric analyses, fluorite generations, and formation temperatures (T_f) of primary and pseudosecondary fluid inclusions in fluorite and massive quartz of Jebel Stah.

6. Composition of the ore fluid

The analytical results are reported in Table 4. The measured concentration values depend on the dilution factors related to the washing process and cannot be compared from one sample to another. The dilution factors are estimated by comparing the salinity values deduced from the microthermometric measurements (Table 2) and chemical analysis (Weisbrod and Poty 1975). They range between 6.10^3 and 10^5 . The calcium concentration in the inclusions (Ca^*) was calculated by subtracting from the measured value the quantity of Ca resulting from fluorite dissolution during the aqueous crushing and rinsing. Fluorite dissolution was estimated from fluoride concentration in the leachates. Fluorite solubility is about $0.3 \cdot 10^{-3}$ mol/kgH₂O in a 2-4 M NaCl solution at 25°C (Strubel 1965). Taking into account the dilution, fluorite concentrations in the leachates should not exceed 10^{-7} mol/l, if fluorite dissolution did not occur during the aqueous crushing and rinsing, but the observed values were higher than 0.17 mol/l. Therefore, the fluoride concentration in the leachates can be attributed essentially to fluorite dissolution during the extraction run (within an error lower than 0.1%).

The molar ratios Cl/Na, Mg/Na, Ca/Na and SO₄/Cl, calculated from the ionic concentrations (Table 4), show that the ore-forming fluids are sodium-calcium-chloride brines. Fig. 11 shows the variations of these molar ratios versus the salinity of the solutions. The inclusions in the fluorites of the first generation (F11 and F12) result from highly saline (20 ± 1 wt % NaCl equivalents) and Na-rich fluids. They exhibit comparable molar ratios for all the major elements.

Fluorite type	Sample (Inclusion generation)	Salinity (wt% NaCl equiv.)	Concentrations in leachates mol/l X10 ⁵								Charge balance Δ epm%	Molarity				Temperature ($\pm 25^\circ\text{C}$)	
			Na ⁺	K ⁺	Mg ⁺⁺	Ca ⁺⁺	Cl ⁻	SO ₄ ⁻⁻	F ⁻	Na		K	Ca*	Mg	Na-K	Na-K-Ca	
1	JS1-6 (P)	21	20	2.6	0.5	22.7	19.3	0.9	46.75	1	3.1	0.4	-	0.08	310	-	
3	JS1-5 (P)	10	3.6	0.7	0.28	19.7	5	0.3	36	3.2	0.95	0.2	0.45	0.06	380	300	
3	CC1-3 (P)	10	2.2	0.4	-	-	2.6	-	-	0.2	-	-	-	-	270	-	
3	L4-2 (P)	10	4.6	1	0.4	19.3	5.8	0.6	35.7	2.8	1	0.22	0.34	0.09	390	310	
2	JS3-8 (PS)	19	5.4	0.75	0.2	15.7	5.5	0.3	29.3	3.7	3	0.43	0.6	0.1	300	300	
3	JS1-5 (PS)	9.5	2.5	0.25	0.2	9.6	3.6	0.4	17	2.2	0.95	0.09	0.42	0.07	260	240	
3	CC1-3 (S)	4	4.6	0.5	0.25	17.4	10.6	0.5	31.9	-3.6	0.45	0.04	0.14	0.02	270	240	

Table 4. Chemical composition and molar ratios in the inclusion fluids recovered after the washing in the inclusions; calculated Na, K, Ca and Mg molar concentrations and estimated reservoir temperatures from the Na, K, Ca concentrations in the fluorite fluid inclusions. (Ca* = Ca total - Ca associated to fluoride, see text).

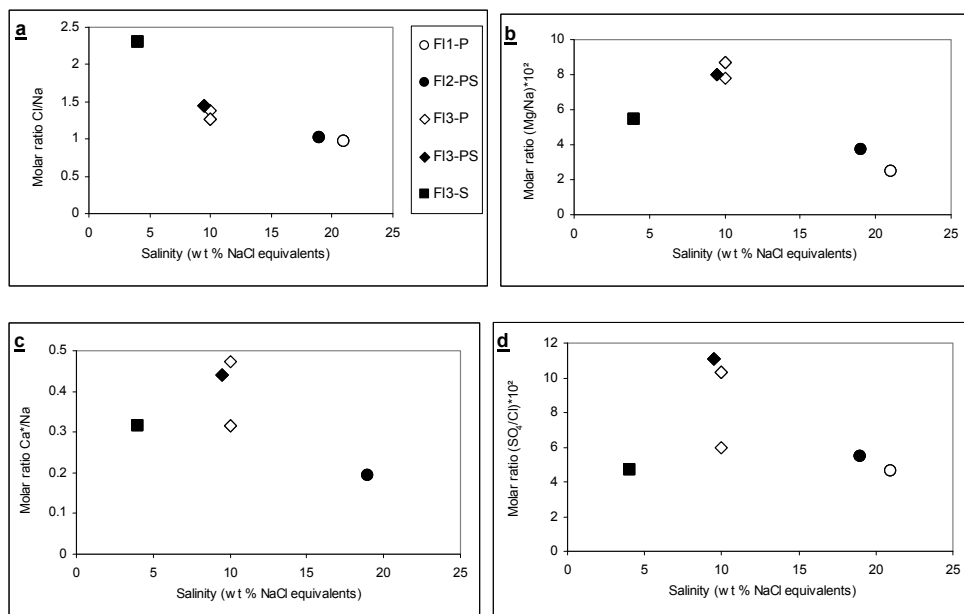


Fig. 11. a-d) Plot of the molar ratios Cl/Na, Mg/Na, Ca*/Na and SO₄/Cl versus the salinity in the extracted inclusion fluids from the fluorites of Jebel Stah (Ca* = Ca total - Ca associated to fluoride, see text and table 4).

The inclusion fluid of the second fluorite generation (FI3) is clearly distinct from that of the first generation: the Cl/Na molar ratio increases from 1 to 1.5 (Fig. 11a), Mg/Na increases

from 3.10^{-2} to 8.10^{-2} (Fig. 11b), Ca/Na increases from 0.25 to 0.45 (Fig. 11c) and SO_4/Cl increases from 5.10^{-2} to 11.10^{-2} (Fig. 11d). NaCl represents more than 90 mol% of the fluid salt content for the fluorites Fl1 and Fl2 and only 70 mol% for the Fluorite Fl3. Thus, the lowering of the salinity (10 ± 1 wt% NaCl equivalents) is accompanied by a relative increase in the concentration of the dissolved species other than NaCl (e.g. $CaCl_2$, $MgCl_2$). This confirms the generation of the Jebel Stah fluorite from two chemically distinct fluids and during two successive phases, as previously deduced from the microthermometric results (Fig. 10).

The calculated molarities of Na, K, Ca and Mg, taking account of the dilution, are reported in Table 4. Their variations are plotted in Fig. 12 as a function of the salinity of the fluids. The molarities exhibit linear correlation with salinity for all the cations. However, the molarity decrease observed for the late fluorite Fl3, is due to dilution of the highly saline and Na-rich fluid by mixing with warmer, less saline and Na-poor fluid in addition to its high Ca and Mg content. The latter fluid should be the one trapped in the secondary inclusions of the fluorite Fl3 (4 ± 1 wt% NaCl equivalents).

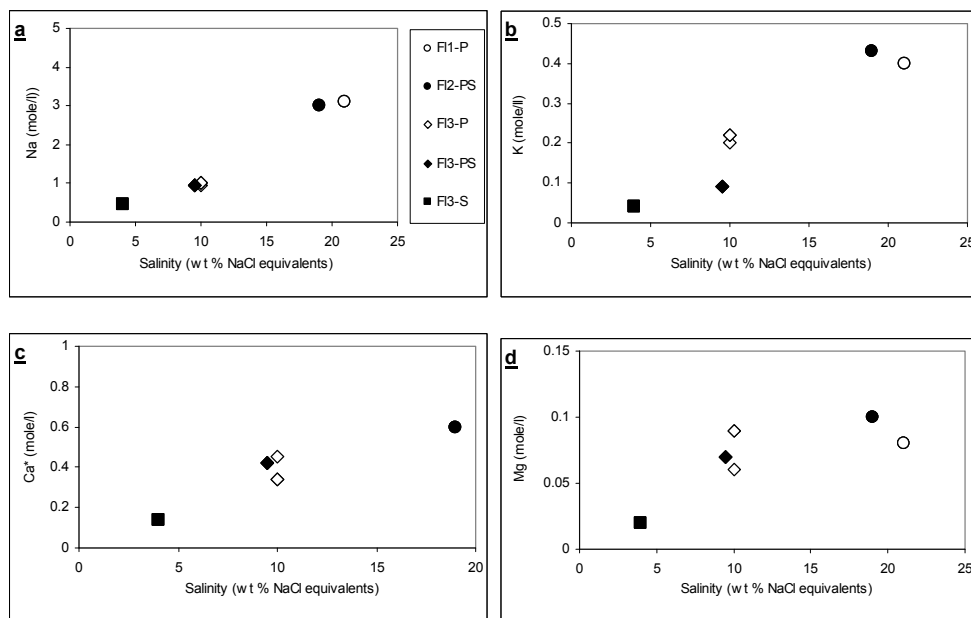


Fig. 12. a-d: Plot of the Na, K, Ca and Mg concentrations versus salinity in the extracted inclusion fluids from the fluorites of Jebel Stah ($Ca^* = Ca$ total - Ca associated to fluoride, see text and table 4).

7. Estimation of the reservoir temperature

Relations between the reservoir temperature and the chemical composition of hydrothermal fluids have been established from studies dealing with present geothermal sources (Ellis

1970; Fournier and Trusdell 1973). Fournier and Trusdell (1973) have shown that the results can be extended to the fluids contained in fluid inclusions.

The “Na-K” geothermometer presupposes the equilibrium between the fluid and Na-K feldspars. The temperature of the fluid is related to the Na/K ratio by: $T = [908/\log(\text{Na}/\text{K}) + 0.7] - 273.15$; where T is expressed in °C and the concentrations in mol/l. This relation can be used for the Ca-poor alkaline solutions close to neutrality (Ellis 1970). The temperatures calculated from this equation are listed in Table 4. They are generally close to 275 ± 25 °C; the uncertainty, due to the analytical errors on Na, K and Ca, averages 10% and is nearly equal to the mean deviation from the mean temperature value.

The “Na-K-Ca” geothermometer (Fournier and Trusdell 1973) can be applied to Ca-rich solutions. The temperature of the fluid is expressed by: $T = [1647((\log \text{Na}/\text{K} + 1/3 \log(\text{Ca}/\text{Na})) + 2.24)] - 273.15$; (T in °C and concentration in mol/l). The temperatures calculated from this equation are listed in Table 4. They are consistent with the Na-K temperatures, with the exception of two samples (JS1-5 and L4-2), for which the $T_{\text{Na-K}}$ are anomalous and higher than the corresponding $T_{\text{Na-K-Ca}}$ values. These samples are characterized by the lowest Na/K ratios. On the other hand, post-Jurassic [Lower Cretaceous (Neocomian and Barremo-albian), Upper Cretaceous-Paleocene, Oligocene and Miocene] extensional phases are well documented in Tunisia (Turki 1988, Bagdasarian et al., 1972; Bouaziz et al., 2002). These phases induced the recurrent movement of the major faults (Zaghouan and associated faults) and thus hydraulic fracturing which favored the circulation of basinal fluids initially in contact with ante-Jurassic sediments.

8. Fluorite characterization

The selected host rock and fluorite ore samples (Table 1) were the objects of a geochemical study consisting of MTE, REE and Sr isotope analysis.

8.1 MTE geochemistry

In comparison to average concentrations of MTE in carbonates (Mason, 1966) and limestones (Rose et al., 1979), our results (Table 5, Fig. 13) show that no MTE anomalies are associated with the Lower Liassic wallrock limestones. In fact, they are even depleted in Mn, Ni, Ga, Rb, Th and U with respect to average concentrations in carbonates. The Carixian phosphatic limestones are depleted in Mn, but rich in Zn and Cd. Compared to Lower Liassic limestones, the dolomitic facies [massive (Fig. 7a), banded (Fig. 7b) or pseudo-brecciated (Fig. 7c)] are characterized by a distinct Zn anomaly and are rich in Mn.

Among the ore samples, only the microgranular fluorite of the finely-laminated karst deposits and the dark layers of the banded ore (early fluorite generation: F11a, Table 1) are anomalous in terms of Zn (101 to 409 ppm), Cd (0.7 to 13.5 ppm) and Pb (49 to 150 ppm). Indeed, all these sediments contain high proportions of phosphatic remains, as attested by the petrographic observations. However, obvious concentrations of U (29.7 ppm) and Rb (25.2 ppm) are observed only in sample L5-15F. The former should be justified by the

presence of phosphate remains (Prévôt et al., 1979), while the latter is due to the presence of a significant clay mineral fraction (Rose et al., 1979), as demonstrated by chemical analysis (3.4 wt.% Al₂O₃).

Fluorites of all other petrographic types (F11b, F12, F13; Table 1) are strongly depleted in all MTE, and particularly in Mn (≤ 0.1 ppm), and except for the high content in Co (13.4 to 40.5 ppm), and with respect to either the carbonate host-rocks (limestone, dolostone, phosphatic limestone) or the early fluorite facies (F11a). It is noteworthy, however, that in the subvertical lodes, a chemical fractionation of Mn and Co is observed between the megacrystalline fluorite (F12) and the coeval calcite: Mn permeating preferentially the lattice of calcite and Co that of fluorite.

	I			II				III			
	L6-5	L6-30	L6-30Q	L5-3	DZ6-G	DZ6-J	DZ6-F	JS1-6P	CC3-3	CC3-2	JS1-6F
Mn	61.5	58	11	158	534.4	572.5	0.43	1.6	0.12	0	0
Co	2	2	0.25	< d.l.	6.16	7.32	7.33	5.5	7.34	17	7.4
Ni	3	1.25	2	< d.l.	3.300	1.830	0.33	6.5	0.85	4.5	8
Cu	2	1.5	0.7	1	1.43	0.65	0.5	9	0.54	3	3
Zn	34	9	20.5	36	205	159.9	3.46	467	3.82	5.5	2
Ga	0.03	0.02	0.021	< dl	0.14	0.08	0	4.56	0.01	0.019	0.07
Rb	0.08	0.03	0.038	0.04	0.21	0.1	0.01	7.82	0.09	0.039	0.036
Mo	0	0.06	0.46	0.16	2.89	1.19	0.08	0.35	0.04	0.035	0
Cd	0.2	0.13	0.02	0.036	0.04	0.05	0	5.78	0.02	0.031	0.02
Ba	9	9	9.5	0.12	5.14	3.35	0.59	6	3.28	0.6	0.02
Pb	10.2	2.25	3	0.6	2.69	1.49	0.12	9.75	0.36	3.25	0.5
Th	0.009	0.02	0.049	0.007	0.05	0.02	0.01	1.32	0.13	0.118	0.033
U	0.459	0.27	0.08	0.326	0.21	0.1	0.004	4.98	0.11	0.028	0.012
La	0.384	0.35	0.068	0.17	0.56	0.21	0.01	4.354	0.12	0.068	0.076
Ce	0.47	0.42	0.109	0.24	0.73	0.3	0.01	4.717	0.2	0.122	0.144
Pr	0.09	0.08	0.019	0.034	0.11	0.06	0.0027	1.313	0.05	0.036	0.04
Nd	0.444	0.39	0.075	0.146	0.38	0.28	0.02	6.618	0.31	0.224	0.237
Sm	0.107	0.1	0.019	0.024	0.037	0.061	0.011	1.506	0.104	0.088	0.08
Eu	0.05	0.05	0.006	0.011	0.007	0.015	0.003	0.609	0.03	0.051	0.042
Gd	0.129	0.13	0.019	0.025	0.034	0.075	0.023	1.752	0.229	0.232	0.197
Tb	0.016	0.02	0.002	0.003	0.006	0.011	0.003	0.23	0.038	0.037	0.03
Dy	0.094	0.11	0.013	0.018	0.034	0.066	0.022	1.394	0.253	0.244	0.197
Ho	0.018	0.02	0.003	0.004	0.009	0.015	0.005	0.284	0.056	0.054	0.043
Er	0.054	0.06	0.007	0.013	0.031	0.047	0.01	0.744	0.154	0.146	0.114
Tm	0.007	0.01	0.001	0.001	0.005	0.007	0.001	0.085	0.017	0.016	0.012
Yb	0.037	0.05	0.006	0	0.04	0.055	0.002	0.262	0.091	0	0
Lu	0.006	0.01	0.001	0.001	0.007	0.01	2 ^E -04	0.064	0.012	0.012	0.009
ΣREE	1.91	1.8	0.35	0.69	1.99	1.212	0.12	23.9	1.66	1.33	1.221
⁸⁷ Sr/ ⁸⁶ Sr						0.708180				0.708613	0.708154
±2σ						± 7				± 12	± 8

	IV					V		VI				VII	
	L3-21D	L3-21F	L5-16	L5-15F	L5-15G	FZ-5N	FZ-5B	JS5-F	JS6-HF	JS5-C	JS6-HC	L4-2	JS3-5
Mn	184.9	15.96	50	19.9	227.9	19.6	0.75	0.09	0.103	152.1	156.1	0.029	0.04
Co	2.53	5.15	6	10	5.85	5.09	13.4	14.56	40.49	2.88	11.9	7.723	30
Ni	5.23	1.37	8.65	15.13	15.65	1.34	1.68	0.95	5.64	0.56	1.25	1.31	2.16
Cu	5.09	5.27	6	13	4	10.23	0.65	0.463	1.16	0.248	0.56	0.701	1.16
Zn	401	169	105	180	138	409	46.3	2.93	1.38	4.28	1.55	1.628	2.4
Ga	0.05	0.048	1.173	6.16	1.71	1.52	0	0.005	0.003	0.006	0.03	0.006	0.005
Rb	0.16	0.259	5.091	25.2	6.81	3.48	0.04	0.024	0.023	0.034	0.03	0.017	0.01
Mo	1.16	0.347	0.39	1.82	0.9	0.86	0.05	0.085	0.058	0.118	0.11	0.169	0.22
Cd	2.15	1.59	0.7	0.09	1.2	13.5	0.28	0.004	0.013	0.046	0.01	0.004	0.01
Ba	12.08	2.71	7.5	33.9	29.8	248.4	1.48	1.73	1.35	1.26	0.57	2.298	5.17
Pb	58.6	20.81	90	48.7	87.8	149.7	3.48	0.16	1.08	0.92	0.26	0.15	0.13
Th	0.06	0.06	0.251	3.04	0.78	0.32	0.12	0.007	0.005	0.04	0.19	0.014	0.01
U	0.21	0.19	1.12	29.7	5.71	0.64	0.06	0.001	0.001	0.05	0.09	0.001	0.002
La	0.15	0.149	1.792	11.5	3.36	1.41	0.03	0.007	0.004	0.154	0.458	0.008	0.01
Ce	0.22	0.256	2.32	14.8	4.23	1.95	0.07	0.02	0.012	0.73	1.83	0.017	0.01
Pr	0.03	0.048	0.372	3.32	0.856	0.27	0.02	0.004	0.004	0.218	0.61	0.003	0.0032
Nd	0.13	0.237	1.562	16.9	3.89	0.95	0.13	0.022	0.023	1.37	4.06	0.024	0.02
Sm	0.028	0.057	0.249	4.79	0.946	0.15	0.051	0.014	0.012	0.54	2.14	0.01	0.015
Eu	0.008	0.016	0.099	1.06	0.217	0.043	0.017	0.006	0.004	0.138	0.64	0.005	0.005
Gd	0.044	0.106	0.302	5.18	1.09	0.202	0.129	0.029	0.032	0.62	2.92	0.021	0.035
Tb	0.007	0.015	0.043	0.67	0.146	0.032	0.022	0.004	0.004	0.091	0.486	0.003	0.004
Dy	0.045	0.1	0.272	3.47	0.766	0.218	0.153	0.024	0.019	0.491	2.59	0.014	0.024
Ho	0.011	0.022	0.059	0.643	0.145	0.049	0.032	0.005	0.004	0.09	0.46	0.003	0.005
Er	0.033	0.06	0.157	1.629	0.377	0.134	0.091	0.01	0.008	0.23	1.13	0.006	0.01
Tm	0.004	0.006	0.018	0.19	0.043	0.016	0.009	0.001	0.001	0.028	0.129	4 ^E -04	0.001
Yb	0.022	0.031	0	1.08	0.251	0.093	0.05	0.004	0.006	0.17	0.789	0.003	0.006
Lu	0.003	0.004	0.015	0.163	0.035	0.013	0.006	0.001	0.001	0.022	0.109	5 ^E -04	0.001
ΣREE	0.74	1.107	7.26	65.4	16.4	5.53	0.81	0.151	0.13	4.892	18.4	0.12	0.15
⁸⁷ Sr/ ⁸⁶ Sr ±2σ	0.708212 ±8					0.7083330.708154 ±9 ±8		0.708280 ±10		0.708309 ±12			

Table 5. Results of the MTE, REE (ppm) and ⁸⁷Sr/⁸⁶Sr ratios analysis conducted on the country rocks and the different petrographic types of the fluorite ore of Jebel Stah. [Samples and petrographic groups (I to VII) are the same as in Table 1; <d.l.: values below the minimum detection limit (0.0075 ppm for Co and 0.366 ppm for Ni, NA: not analyzed)]

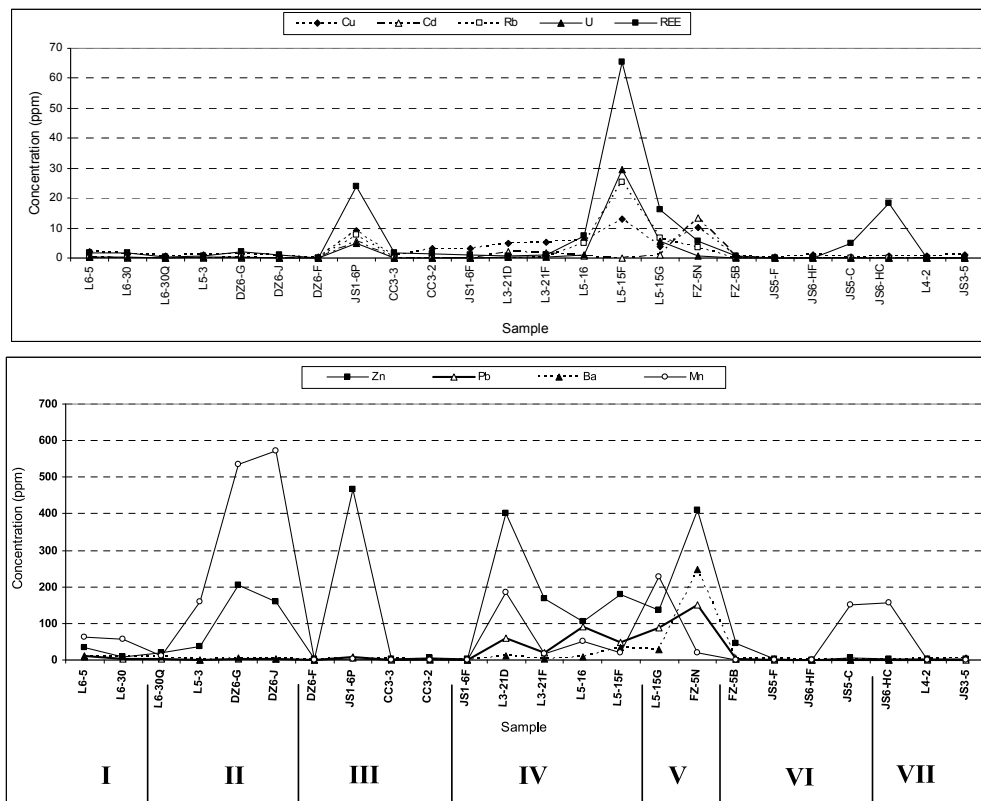


Fig. 13. Total rare earth element (REE) and MTE concentrations in the wallrocks and the different petrographic types of fluorite ore. Samples and petrographic groups I to VII are as in Table 1.

8.2 REE geochemistry

Due to its physico-chemical behaviour during the genesis of hydrothermal deposits, fluorite is one of the most important indicators of ore-forming processes in carbonate sediments (Schneider et al., 1975, 1977; Bau et al., 2003; Sallet et al., 2005). Fluorite is capable of fossilizing, with almost no deformation, thus preserving the lanthanide signature of the ore-forming solutions (Möller et al., 1984; Sallet et al., 2000; Schwinn and Markl, 2005). The results of REE analysis conducted on the wallrocks and the different fluorite-bearing facies are summarized in Table 5. The interpretation is based on the total REE content (Σ REE) and on the ratios between the different REE. REE patterns are normalized to chondrites according to Taylor and McLennan (1985).

The Σ REE values show differences according to the petrography and the mineralogy of the samples (Fig. 13). Among the wallrocks, carbonates (limestones and dolostones) are characterized by low Σ REE (0.35 to 2 ppm). Among the fluorite-bearing samples, those associated with the karst deposits (early fluorite ore; type F11a), are rich in REE (Σ REE = 7.25

to 65.4 ppm). The macrogranular fluorites, associated with Carixian deposits of type F12 (JS1-6F, CC3-2, CC3-3, FZ-5B) are characterized by $\sum\text{REE}$ values that are much lower (0.8 to 1.6 ppm) than those in the phosphatic limestones. The lowest $\sum\text{REE}$ values (0.12 to 0.15 ppm) are recorded in type F12 fluorites occurring within the vertical lodes (samples JS5-F, JS6-F), or in type F13 samples occurring within cavities (samples JS3-5, L4-2). The megacrystalline calcites in the vertical lodes (samples JS5-C, JS6-C), are characterized by $\sum\text{REE}$ values (5 to 18.35 ppm) higher than those in coeval fluorite.

Figure 14 shows that the chondrite-normalised REE patterns may be split into three groups:

- Wallrock limestones and phosphatic limestones (Fig. 14a) are characterized by “normal marine” patterns (gradual decrease from La to Lu), being slightly enriched in light REE (LREE) relative to heavy REE (HREE), along with a negative Ce anomaly. In addition, these signatures assume a specific shape due to a weak positive Eu anomaly superimposed onto all the REE patterns.
- Epigenetic dolomites (Fig. 14b) and microgranular fluorites of the type F11a (Fig. 14c) are characterized by REE patterns sloping to the right of the diagram. Such patterns are reminiscent of shales onto which small Ce and Eu anomalies are superimposed.
- Macrogranular fluorites belonging to the petrographic types F11b, F12 and F13 (Table 1). All the REE patterns display LREE depletion [$(\text{Tb}/\text{La})_N > 1$], in comparison with the other rock types above. The patterns also display weak Ce and Eu anomalies. The peak is centred on Sm-Gd for calcites and on Gd for fluorites.

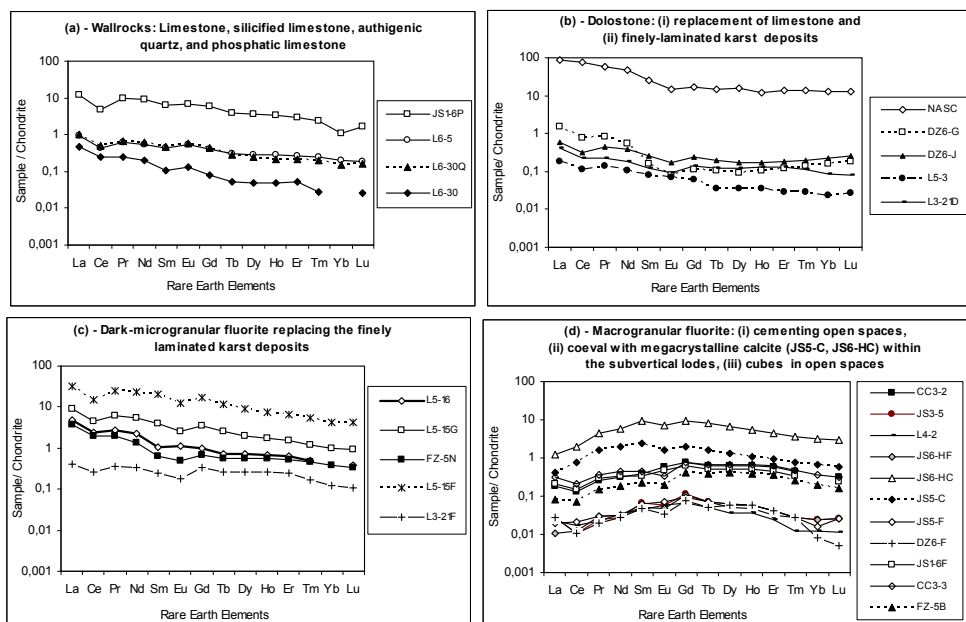


Fig. 14. REE spectra of the wallrocks (a, b) and the different petrographic types of fluorite (c, d). [REE abundances in chondrites and in the North American Shale Composite (NASC) are from Taylor and McLennan, 1985].

Figure 15 depicts relationships between the normalized ratios Tb/Lu, La/Sm and Eu/Eu*. It can be seen that:

- i. as far as the La/Sm ratio is concerned (Fig. 15a, b), samples split into two clusters: the first one, characterized by $La/Sm > 1$, contains all the wallrock (limestone, phosphatic limestone, dolostone) and fluorite type F11a samples; the second (characterized by $La/Sm < 1$), contains all the samples belonging to types F11b, F12 and F13.
- ii. the Tb/Lu ratio remains almost constant for all samples (Fig. 15a).
- iii. Eu/Eu* ratios of the fluorite-bearing samples range from 0.57 to 1.1; 70% of values falling between 0.6 and 0.8. This suggests that the ratio has remained almost constant during the crystallization processes.

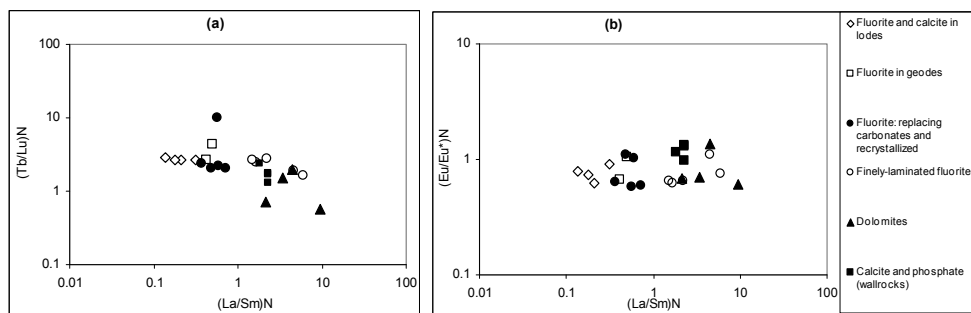


Fig. 15. Relations between chondrite normalized REE ratios of the wallrock minerals and the different petrographic types of fluorite. (a): $(Tb/Lu)_N$ vs. $(La/Sm)_N$; (b): $(Eu/Eu^*)_N$ vs. $(La/Sm)_N$.

8.3 Strontium isotopes

It is well known that strontium (as Sr^{2+}) enters the lattice of gangue minerals such as calcite, dolomite, fluorite and barite. On the other hand, these minerals typically contain negligible concentrations of rubidium. Their $^{87}Sr/^{86}Sr$ ratios thus represent a measure of the isotopic composition of Sr in the mineralizing fluids and do not need to be corrected (Barbieri et al., 1987; Ruiz et al., 1988; Valenza et al., 2000; Sallet et al., 2005). These ratios can therefore be used to identify the reservoirs from which ore fluids have derived their strontium (Kessen et al., 1981).

Strontium isotope analysis has been conducted on six fluorite and two carbonate (dolomite, calcite) samples. The fluorite samples belong to different ore facies: (i) microcrystalline fluorite (L3-21F), associated with finely-laminated karst deposits (type F11a); (ii) dark microcrystalline fluorite (FZ-5N) of the banded ore (type F11a); (iii) white (JS1-6F), and purple (CC3-2)-macrocrystalline fluorites, associated with Carixian phosphatic limestone (type F11b); (iv) megacrystalline fluorite (JS5-F), occurring in a subvertical lode (type F12). The sampled carbonates consist of: (v) white sparry dolomite (DZ-6J) cementing the dolomitic dissolution breccia at the top of the Oust Formation; and (vi) megacrystalline calcite (JS5-C) associated with fluorite JS5-F in the subvertical lode. The samples are described in Table 1. Results (Table 5, Fig. 16) show that, apart from the fluorite sample CC3-2 ($^{87}Sr/^{86}Sr = 0.708613 \pm 12$), which is associated with the Carixian phosphatic

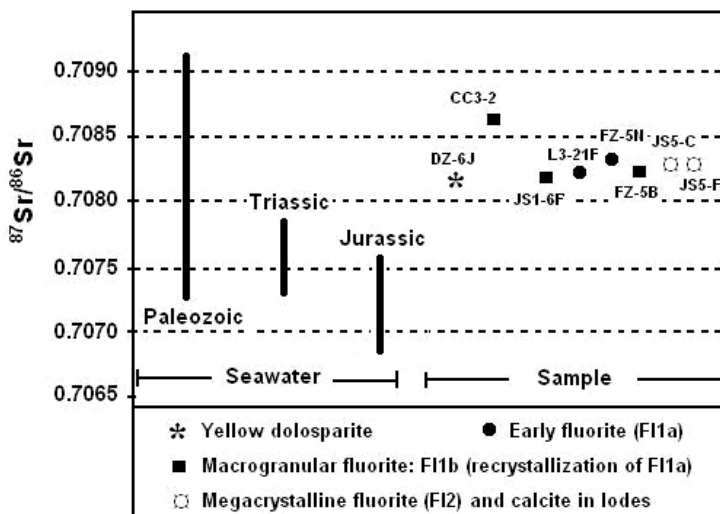


Fig. 16. $^{87}\text{Sr}/^{86}\text{Sr}$ ratios of the wallrocks (DZ-6J), the fluorite ore samples and the associated calcite (JS5-C). Isotopic strontium intervals of the Jurassic and Triassic sea water are from Burke et al. (1982) and Koepnick et al. (1990); those of the Paleozoic are from Burke et al. (1982).

limestone layer, all the Sr isotope ratios fall into a narrow range between 0.708154 ± 8 and 0.708333 ± 8 . The high value of sample CC3-2 could be attributed to enrichment in radiogenic Sr due to the presence of a Rb-bearing phase in the detrital fraction of the karst deposits (e.g., sample L5-15, Table 5). However, these ratios are higher than both Jurassic and Triassic seawater (0.70677 to 0.70778 and 0.70690 to 0.70794 , respectively; Burke et al., 1982; Koepnick et al., 1990). Consequently, the mineralizing fluid at Jebel Stah is related to more radiogenic basinal brines derived from even more-deeply buried sedimentary strata.

9. Discussion

The deposition temperature ($135 \pm 20^\circ\text{C}$) of the early fluorite (F11a, F11b) suggests a burial depth of 3500 m to 5000 m in the case of a normal geothermal gradient (25 to $30^\circ\text{C}/\text{km}$). So, as proposed previously for the whole of northern part of Tunisia (Perthuisot et al., 1978; Ben Dhia, 1987a, b), an abnormally regional geothermal gradient prevailed during the deposition of fluorite. The multitude of the depositional phases (generations I and II of fluorite, succeeded by massive quartz) shows that this gradient prevailed over a long period of time. The presence of many geothermal sources in the region (Oust, 58°C ; Zriba, 45°C ; Jedidi, 60°C); (Jellouli, 1973) gives another evidence about the presence of the high regional gradient, and its continuity until today.

The circulation of the highly saline mineralizing fluids was induced by a major post-Jurassic extensional phase. Massive quartz generated subsequently to fluorite from a weakly saline and gaseous CO_2 -rich fluid. The late heating observed during the depositional history at Jebel Stah should be related to the opening of fractures within a such geothermal context. The deposition of fluorite could have resulted from the interference between many

parameters: pressure decrease due to tectonic relaxation during extensional phases; temperature decrease during the ascent of hydrothermal fluids, as well as increase in the dissolved Ca^{2+} activity caused by the dissolving of the carbonate host rocks. The occurrence of the mineralization along the unconformity surface at the top of a carbonated paleorelief which has undergone a strong epigenetic dolomitization, the temperature ($135 \pm 20^\circ\text{C}$) and the salinity (20 ± 1 wt % NaCl eq.) of the fluids which deposited the main body of fluorite, as well as the presence of a minor liquid hydrocarbon phase in late fluorite and massive quartz, allow to compare the fluorite deposit of Jebel Stah to the Mississippi Valley-type group (Roedder, 1984; Anderson and McQueen, 1988; Sangster et al., 1994), especially to those dominated by fluorite in the USA, such as those of Southern Illinois (Grogan and Shrode, 1952; Hall and Friedman, 1963) or Sweetwater-Tennessee (Grogan and Bradburry, 1967; Zimmerman and Kesler, 1981; Vietz and Leach, 1990).

The geochemical results presented in this work are innovative since they deal with a Jurassic mountain district. To our knowledge, only two ore deposits, both located in the domes area of Tunisia, have, until now, been investigated with respect to their REE and Sr-isotope geochemistry. These are the Bougrine Zn-Pb deposit (Sr isotope ratios; Orgeval, 1994) and the Jebel Doghra Sr deposit (REE geochemistry; Souissi et al., 2007). In addition to that, this work provides the first geochemical results relative to the microgranular fluorite associated to the finely laminated karst deposits, and considered as the most early phase of the ore of Jebel Stah (type FI1a). Note that, previous studies based on FI microthermometry and geochemistry (Souissi et al., 1997, 1998) have not allowed the characterization of this fluorite type.

The MTE geochemical data allow us to point out that the dolomitization and mineralization processes were accompanied by geochemical exchange between host rocks and fluids. Indeed, the Lower Liassic limestones are not anomalous in MTE, whereas the Carixian phosphatic limestones are highly anomalous with respect to Zn and Cd. The dolomitized horizons are enriched in Mn and Zn in comparison with the wallrock limestones. This suggests that high contents of these elements have been transported in a dissolved state by the dolomitizing fluid. Nevertheless, part of the Zn should have been derived from dissolution of the Carixian phosphates.

The early ore facies (FI1a) consisting of the mineralized-finely-laminated karst deposits of the Carixian layer is anomalous in Zn, Cd and Pb, but it is admitted that these elements are contained in the reworked micro-phosphatic debris accumulated in the karsts rather than in the epigenetic fluorite portion of the ore. The recrystallization of the aforementioned fluorite facies and the subsequent remobilization of fluorite in open spaces, (giving rise to FI1b, FI2 and FI3, respectively), took place in the presence of an evolved fluid which was depleted in Mn and enriched in Co. Most of the Mn load was taken up by carbonates during the dolomitizing process, while Co has been concentrated in the residual fraction of the fluid.

The REE geochemistry results allowed differences between the wallrock limestones and the fluorite-bearing samples to be identified. Indeed, the $\sum\text{REE}$ values are low in the aforementioned limestones (0.35 to 2 ppm), in accordance with the rather low REE concentrations (<10 ppm) reported for sedimentary carbonate rocks (Taylor and McLennan, 1985; Chetty and Frimmel, 2000). Although higher values are recorded in the phosphatic limestones (≈ 24 ppm), $\sum\text{REE}$ values are, however, significantly below their analogues in

Eocene formations of the phosphate basins of Central and Southern Tunisia (100 to 2,140 ppm and 50 to 1,950 ppm, respectively; Sassi, 1999).

Among the fluorite-bearing samples, the results have shown that the highest Σ REE values (7.25 to 65.4 ppm), are recorded for early F11a fluorite associated with finely-laminated karst deposits. These values are due to the presence of remnant phosphate, as well as to clay minerals in the matrix. Clay minerals typically have much higher Σ REE compared to the other fractions in sediments (Bellanca et al., 1981; McLennan, 1989). The recrystallization of F11a facies gives rise to the white-to-purple macrogranular fluorites of type F11b, characterized by Σ REE values (0.8 to 1.6 ppm) which are too low with respect to the inferred parent material. Megacrystalline fluorites F12 and F13, occurring within open spaces (lodes and cavities, respectively), bear the lowest Σ REE values. The decrease in REE contents in the later fluorites indicates that, during crystallization, the ore fluid becomes depleted in these elements (Schönenberger et al., 2008). However, the megacrystalline calcite in the vertical lodes is characterized by Σ REE values (5 to 18.35 ppm), higher than those in the coeval fluorite. Such values show that in open spaces, REE are fractionated between the two minerals, permeating more easily into the carbonate phase.

Σ REE values of the fluorites under consideration are, on the whole, low in comparison with fluorites from other hydrothermal deposits, such as those of the d'El Hammam district, Morocco (Jebrak et al., 1984), the main fluorite occurrences in Brazil (Dardenne and Touray, 1988; Ronchi et al., 1993), the North Pennines of England (Shepherd et al., 1982) or the Marche occidentale, France (Grappin et al., 1979). They are, however, similar to those recorded for fluorites from the Asturian Province, Spain (Ferrand et al., 1978), the Tarn in France (Hubert et al., 1982) and the Eastern-Alpine area in Germany (Schneider et al., 1975).

The chondrite-normalized REE patterns allow differences between the wallrocks unaltered by hydrothermal circulation (limestone, phosphatic limestone) and the dolostones and different ore facies to be identified. Calcite and apatite of the wallrock layers have acquired their REE imprint during diagenesis of Lower-Middle Liassic sediments in equilibrium with seawater trapped in the interstitial porosity. The REE patterns of the dolomites plot within the field of their hydrothermal homologues (Henderson, 1984). The hydrothermal origin of the epigenetic dolomites was demonstrated earlier by Souissi et al. (1998), on the basis of petrographic analysis and fluid inclusion microthermometry. The latter authors pointed out that the dolomitization and deposition of the exploitable ore (fluorites F11a, F11b and F12) took place under the same conditions. Therefore, and by taking into account that both the epigenetic dolomites and the microgranular-early fluorite (F11a) are characterized by similar REE patterns, reproducing that of the NASC (Taylor and McLennan, 1985), it is believed that this geochemical imprint was inherited from a fluid that had remained in equilibrium with deep shales. Such a statement leads to the conclusion that all the samples of this group may be considered as coeval (Dardenne and Touray, 1988). The preferential concentration of LREE [(Tb/La)_N < 1] indicates that fluorite F11a belongs to the early stage of crystallization (Ekambaram et al., 1986; Subias and Fernandez-Nieto, 1993; Schönenberger et al., 2008). LREE depletion, for both the macrocrystalline fluorites (F11b) resulting from recrystallization of type F11a, or the megacrystalline fluorites F12 and F13, occurring in open spaces, provide evidence for REE fractionation during the later stages of mineralization (Ekambaram et al., 1986) in a closed system. Similar REE patterns are reported by Subias and Fernandez-Nieto (1993) for late hydrothermal fluorites from the Valle de Tena, Spanish Central Pyrenees, hosted in

Paleozoic pelitic, psamitic and carbonatic rocks. According to Richardson and Holland (1979) and Tropper and Manning (2007), the solubility of fluorite strongly increases in chloride-rich solutions (≈ 20 wt % NaCl equivalent at Jebel Stah). Strong et al. (1984) state, however, that REE are dominantly present as fluorocomplexes in such solutions. The observed LREE depletion and relative HREE enrichment are justified by a dissolution-reprecipitation process with a decrease of fluorine activity in the fluids. This process causes the changing of REE from difluoro- to monofluoro-complexes, and thus, a decreasing ability of the hydrothermal solutions to transport LREE with respect to HREE (higher stability of HREE monofluorocomplexes; Henderson, 1984; Strong et al., 1984; Ronchi et al., 1993).

The weak negative Ce and Eu anomalies seen in all REE patterns for fluorites and other fluorite-bearing samples (dolostones and finely laminated karst deposits) are assumed to record the signature of the hydrothermal fluoride-bearing solution. Regarding the Ce anomaly, Bellanca et al. (1981) defend the hypothesis that this anomaly occurs when fluorite crystallizes from solutions which are derived from sediments with high oxygen fugacities. In such environments, Ce becomes oxidized prior to mobilization, resulting in a lower migration coefficient for Ce^{4+} than would be the case for the trivalent ions of the other REE. The REE patterns of all fluorite-bearing samples and the associated calcites are slightly depleted in Eu. Such a depletion characterizes all post-Archean sedimentary rocks (Taylor and McLennan, 1985; McLennan, 1989).

In addition, all fluorites - regardless to their petrographic types - are characterized by Sm/Yb ratios of 1.02 to 5.5, close to values commonly measured in shales (about 2.0). This is consistent with REE derived from siliciclastic sources, or even from the dissolution of LREE-enriched evaporates (Cai et al., 2008).

Taking the ratios La/Sm, Tb/Lu and Eu/Eu* into consideration, information has been gathered about the fluid properties, along with REE behaviour during all the epigenetic processes (dolomitization, deposition of early-stage fluorite and its further recrystallization or remobilization to be redeposited in open spaces). From the La/Sm ratios, it has been deduced that the dolomites and early fluorite (F11a) have been generated from a fluid which is geochemically different from the one that gave rise to the late fluorites (F11b, F12 and F13). Being depleted in LREE, the second fluid is generated from the residual fraction of the above-mentioned one. Therefore, the uniformity of the Tb/Lu ratios, allowed us to deduce that, unlike the LREE, the HREE did not undergo fractionation during the crystallization process. On the other hand, it is well established that the oxidation state of Eu incorporated in hydrothermal minerals provides an additional tool to constrain the chemistry of ancient fluids and the mechanisms responsible for mineral precipitation (Brugger et al., 2008). In this respect, the uniformity of the Eu/Eu* ratios provides evidence that the fluorites contain Eu predominantly as Eu^{3+} and might have crystallized from relatively oxidized fluids that bear very small inherited Eu anomalies (Ghaderi et al., 1999; Schönerberger et al., 2008). Therefore, and according to Sverjensky (1984) and Bau and Möller (1992), temperature is the most important parameter controlling the Eu^{3+}/Eu^{2+} redox potential in hydrothermal environments. At temperatures exceeding 250 °C, Eu^{2+} dominates over Eu^{3+} and may substitute for Ca^{2+} preferentially over trivalent REE, leading to positive Eu anomalies in mineral precipitates. The lack of any positive Eu_{CN} anomaly, for either the epigenetic dolomites or the fluorites considered in this study thus indicates that the fluid from which they were precipitated never reached such high temperatures (Schönerberger et al., 2008; Uysal et al., 2008).

The determination of the $^{87}\text{Sr}/^{86}\text{Sr}$ ratios for the epigenetic carbonates (dolomite, calcite) and fluorite showed a uniformity of this ratio throughout the deposit, providing evidence for isotopic homogeneity (Ayuso et al., 2004) and, consequently, the identity of the source of the mineralizing fluid. As deduced from the aforementioned petrographic analysis, fluid inclusion microthermometry and REE geochemistry, these observations strongly support the idea that dolomitization and mineralization were produced by the same hydrothermal system (Savard et al., 2000). Since they are higher than those of both the Jurassic or the Triassic seawater, these ratios might, however, be interpreted in terms of basinal brines, trapped within the Paleozoic sedimentary column, which should be characterized by even higher Sr isotopic ratios (0.7067 to 0.7091; Burke et al., 1982; Fig. 16). The measured ratios fall within the range of all Pennsylvanian, Late Devonian, Lower Silurian and Middle Ordovician $^{87}\text{Sr}/^{86}\text{Sr}$ intervals. In Tunisia, apart from the marine-Permian outcrop of Jebel Tebaga, the Paleozoic series is known in Southern Tunisia only at subsurface thanks to oil-field drilling programs (Memmi et al., 1986). The sedimentary series (sandstones, siltstones, shale, carbonates) are related to the well-oxygenated-shallow environments of the continental shelf (Chauvel and Massa, 1981). They are represented by megasequences (>10 km-thick), rich in detrital fraction and separated by major discontinuities (Burolet and Busson, 1983). The Precambrian basement is made of phyllites along with granodiorites and granites cut by acid and basic volcanic rocks (Bajanik, 1972). The present authors support the idea that the radiogenic Sr measured in the fluorite ore deposit of Jebel Stah could have been sourced in the connate waters trapped in the Paleozoic sedimentary column. Thus, the mineralizing fluids relate to deep thermally-driven basinal fluid circulations (Souissi et al., 1997, 1998, 2010). In another respect, the same authors have pointed out that deposition of the ore at Jebel Stah, hosted in the Lower-Middle Liassic layers, took place at $135 \pm 20^\circ\text{C}$, from a fluid derived from a reservoir where temperature was $275 \pm 25^\circ\text{C}$ on average. The difference in temperature is in the order of 140°C . Assuming a mean geothermal gradient of $50^\circ\text{C}/\text{km}$, according to the estimations of Perthuisot (1978), Perthuisot et al. (1978) and Ben Dhia (1987a, b), the reservoir should be 2.5 to 3 km below the deposition level. This interval should include the Lower Liassic (≤ 700 m), the Triassic (> 1000 m; Bonnefous, 1972) and the upper part of the Paleozoic series.

Remobilization of deep-seated primary deposits, hosted in the Paleozoic sequence, seems to be a very plausible hypothesis, especially as Zn-Pb-Ba veins are hosted in the "Upper Dolostones" of Late Permian age at Jebel Tebaga in Southern Tunisia (Sainfeld, 1952). The same hypothesis is also strongly supported by the presence of several intra-Paleozoic fluorite ores hosted in a sedimentary series to which magmatic events may be associated and that are documented all around the Mediterranean basin. These include: (i) in France, the Tarn department (Couturier, 1980; Béziat et al., 1982; Deloule, 1982), the Pyrénées-Atlantiques (Martin, 1979; Thibieroz, 1982) and the Cordes (Marchand et al., 1976); (ii) in Spain, the Asturian province (Garcia-Iglesias and Loredo, 1982; Ferrand et al., 1978) and the Valle De Tena in the Huesca Province (Subias and Fernandez-Nieto (1993); (iii) In Italy, the Sarrabus area of Sardinia (Harvey et al., 1984).

The hypothesis of a deeply-seated origin for the metal-bearing fluids in northern Tunisia is now largely accepted (Perthuisot et Saliot, 1979; Rouvier et al., 1985; Orgeval, 1994; Sheppard et al., 1996; Souissi et al., 1997, 1998, 2007, 2010; Decrée et al., 2008; Jemmali et al., 2011). Fluid circulation is triggered in response to hydraulic fracturing in high geothermal gradient settings, especially along the major structural trends (Ben Dhia, 1987a, b). Such

geothermal-gradients prevailed for a long time and are evidenced either by SHMS-Sedex ore deposits in the Bougrine area within the Dome Zone related to the Cenomano-Turonian period (Orgeval, 1994), to the Upper Miocene in the area of Sidi Driss-Dhouahria farther North, within the Nappe Zone (Décrée et al., 2008), or to Miocene magmatic activity (rhyodacites, granodiorites), with which Fe-, Mn-, Pb-, Zn-, Cu-, Ag- and F-bearing mineralization is associated in the latter zone (Bellon, 1976; Laridhi-Ouazaa, 1994).

10. Conclusions

The F-(Ba, Pb, Zn) deposits of northern Tunisia have been previously considered as the result of continental alteration and sedimentation (Florida, 1973; Fuchs, 1973; Thibieroz, 1974 and 1976; Touhami, 1979). This study gives evidence that the fluorite deposit of Jebel Stah resulted from the replacement of carbonate rocks after they underwent an epigenetic dolomitization along the intra-Liassic unconformity, located at the top of a paleorelief. The economic ore (fluorite I: F11a, F11b, F12) as well as the dolomitic DCRs structures resulted from highly saline (20 ± 1 wt % NaCl eq.) Na-Ca-Cl hydrothermal (135 ± 20 °C) brines. Later on, a less saline (10 ± 1 wt % NaCl eq.) and warmer (185 ± 20 °C) fluids deposited fluorite within geodes (fluorite II). In the last stage, silica and minor fluorite deposited within fractures owing to the circulation of a low salinity (5.5 ± 1 wt % NaCl eq.) but yet warmer (225 ± 20 °C) and CO₂-rich fluid. These fluids probably arose from the reservoir where the temperature was on average 275 ± 25 °C. This study confirmed the existence of a high regional geothermal gradient, which prevailed over a long period of time extending probably since the Upper Miocene until today. So, the late heating observed during the depositional history of fluorite and quartz at Jebel Stah, should be related to the opening of fractures during extensional phases within a such geothermal context. Deposition of the workable fluorite ore has at Jebel Stah resulted from the decrease in temperature and the increase of the calcium activity due to dissolution of carbonate rocks. Taking the geological framework, the epigenetic character of the ore deposit, the mineralogical association and the temperature and composition of the fluids into consideration, the fluorite ore deposit of Jebel Stah is considered to represent a fluorite-dominant MVT-type deposit.

The MTE, REE and Sr isotope geochemistry gives new arguments to support the genetic model for fluorite ore at Jebel Stah. Both petrography and REE geochemistry show a close spatial and temporal association between the epigenetic dolomitization that affected the Lower-Middle Liassic host carbonates and the subsequent fluorite ore deposition. This association, along with the REE and Sr isotope geochemistry of epigenetic carbonates (dolomite, calcite) and fluorite, shows that dolomitization and mineralization were produced by the same hydrothermal system and indicate that at least part of the fluoride has been transported in solution as MgF⁺ complexes by an oxidized fluid derived from a sedimentary basin. The source of this fluoride is suggested to be the geological sequence underlying the Lower-Middle Liassic horizons that host the fluorite ore. These results are in accordance with those of Souissi et al. (1997, 1998) who supposed, on the basis of microthermometric and geochemical analysis of fluid inclusions, that the mineralizing fluids giving rise to F-(Ba,Pb,Zn) deposits in the Zaghouan district, may be assimilated to basinal brines (connate waters) released by hydraulic fracturing during a major post-Jurassic and most probably an Upper Miocene extensional phase. Recently, a similar age is accepted for several mineralizations occurring in northern Tunisia (Décrée et al., 2008; Souissi et al., 2010;

Jemmali et al., 2011). The Triassic units are the least probable source for the fluoride, especially if one takes into consideration the results of the Sr isotope study, as well as the scarcity of this element in the remaining geological zones of northern Tunisia (Trough zone, Dome area, Nappe zone). The Paleozoic series is the preferred source of the mineralizing fluids and remobilization of primary fluorite ores, hosted in this series, seems to be a plausible hypothesis. If true, the large distribution of the deposits in space and time, throughout the district of Zaghouan, indicates that the buried stocks should be of paramount importance.

It is suggested that the Paleozoic series, cropping out nowhere in the Jurassic mountains area of North-Eastern Tunisia, may potentially bear significant primary F-(Pb, Zn, Ba, Sr) reserves. Taking into account both the geological and geothermal settings, such deposits should lay between the reservoir of the fluids (Upper part of the Paleozoic series) and the Paleozoic-Triassic contact (1500 to 2000 m beneath the Lower-Middle Liassic contact at the locality of Jebel Stah and in the neighbouring area of Jebel Kohol).

11. References

- Ames L. (1955). Chemical analysis of the fluid inclusions in a group of New Mexico minerals. *Econ. Geol.*, 53, pp. 473-480.
- Anderson G.M & McQueen R.W. (1988). Mississippi Valley-type lead-zinc deposits. In: *Ore deposit models*, Roberts R.G. and Seahan P.A., pp. (79-90). Geoscience, Geological Association of Canada publications, Ottawa, Reprint 3.
- Ayuso R.A., Kelley, K.D., Leach, D.L. & Young, L.E. (2004). Origin of the Red Dog Zn-Pb-Ag deposits, Brooks Range, Alaska: Evidence from regional Pb and Sr isotope sources. *Economic Geology*, 99, pp. 1533-1553.
- Badgasarian G.P., Bajanik S. & Vass D. (1972). Age radiométrique du volcanisme néogène du Nord de la Tunisie. *Notes Serv. Géol. Tunisie*, 40, pp. 79-85.
- Bajanik S. (1972). Précambrien en Tunisie (Plateforme saharienne). *Notes du Service Géologique de Tunisie*, 40, pp. 5-17.
- Barbieri M., Bellanca A., Neri R. & Tolomeo L. (1987). Use of strontium isotopes to determine the sources of hydrothermal fluorite and barite from Northwestern Sicily (Italy). *Chemical Geology*, 66, pp. 273-278.
- Bau M. & Möller P. (1992). Rare-earth element fractionation in metamorphogenic hydrothermal calcite, magnesite and siderite. *Mineralogy and Petrology*, 45, pp. 231-246.
- Bau M., Romer R.L., Lüders V., Dulski P. (2003). Tracing element sources of hydrothermal mineral deposits: REE and Y distribution and Sr-Nd-Pb isotopes in fluorite from MVT deposits in the Pennine Orefield, England. *Mineralium Deposita*, 38, pp. 992-1008.
- Beales F.W. (1971). Cementation by white sparry dolomite. In: *Carbonate cements*, Bricker O.P., pp. 330-338, Johns Hopkins Univ Press, Baltimore.
- Beales F.W. & Hardy J.L. (1980). Criteria for the recognition of diverse dolomite types with an emphasis on studies on host rock for Mississippi Valley-type ore deposits. In: *Concepts and models of dolomitization*, Zenger D.J., Dunham J.B. & Etlington R.L., pp. 197-213, SEPM Spec Nr 28.

- Bellanca A., Di Salvo P., Möller P., Neri R. & Schley F. (1981). Rare earth and minor element distribution and petrographic features of fluorites and associated Mesozoic limestones of Northwestern Sicily. *Chemical Geology*, 32, 255-269.
- Bellon H. (1976). Séries magmatiques néogènes et quaternaires du pourtour de la Méditerranée occidentale comparées dans leur cadre géochronologique. Implications géodynamiques. *Thèse Doct. ès Sciences*, Université d'Orsay.
- Ben Dhia H. (1987a). The geothermal gradient map of central Tunisia: Comparison with structural, gravimetric and petroleum data. *Tectonophysics*, 142, pp. 99-109.
- Ben Dhia H. (1987b). La carte du gradient géothermique de Tunisie- Etablissement à partir de données de températures particulières. *Bulletin Centre Recherche Exploration Production Elf Aquitaine*, II (2), pp. 221-231.
- Beziat P., Bles J.L., Fortuné J.P. & Lhegu J. (1982). Les filons à fluorine de l'Albigeois; présentation générale, guide de prospection. *Bulletin du BRGM*, section II (4), pp. 417-426.
- Bodnar R.J. & Bethke P.R. (1984). Systematics of stretching of fluid inclusions, I: fluorite and sphalerite at 1 atmosphere confining pressure. *Economic Geology*, 79, pp. 141-146.
- Bouaziz, S., Barrier, E., Soussi, M., Turki, M. & Zouari H. (2002). Tectonic evolution of the northern African margin in Tunisia from paleostress data and sedimentary record. *Tectonophysics*, 357, pp. 227-253.
- Bouhlef S. (1982). Distribution du baryum et du strontium dans la province fluorée tunisienne; application aux gîtes de Hammam Zriba-Jebel Guebli. *Thèse 3ème Cycle*, Université Toulouse.
- Bouhlef S., Fortuné J.P., Guilhaumou N. & Touray J.C. (1988). Les minéralisations stratiformes à F-Ba de Hammam Zriba-Jebel Guebli (Tunisie nord-orientale): l'apport des études d'inclusions fluides à la modélisation génétique. *Mineralium Deposita*, 23, pp. 166-173.
- Bonnefous J. (1972). Contribution à l'étude stratigraphique et micropaléontologique du Jurassique de Tunisie. *Thèse doctorat ès Sciences Naturelles*, Université de Paris VI.
- Brugger J., Etschmann B., Pownceby M., Liu W., Grundler P. & Brewe D. (2008). Oxidation state of europium in scheelite: Tracking fluid-rock interaction in gold deposits. *Chemical Geology*, 257, pp. 26-33.
- Burke W.H., Denison R.E., Hetherington E.A., Koepnick R.B., Nelson H.F. & Otto J.B. (1982). Variation of sea water $^{87}\text{Sr}/^{86}\text{Sr}$ throughout Phanerozoic time. *Geology*, 10, pp. 516-519.
- Burollet P.F. & Busson G. (1983). Plateformes et bassins. Danger d'un actualisme exagéré. *Notes et Mémoires de la Compagnie Française des Pétroles*, Paris 18, pp. 9-16.
- Cai C., Li K., Li H. & Zhang B. (2008). Evidence for cross formational hot brine flow from integrated $^{87}\text{Sr}/^{86}\text{Sr}$, REE and fluid inclusions of the Ordovician veins in Central Tarim, China. *Applied Geochemistry*, 23, pp. 2226-2235.
- Castany G. (1954). Les grands traits structuraux de la Tunisie. *Bull. Soc. Géol. France*, section IV (6), pp. 151-173.
- Chauvel J.C. & Massa D. (1981). Paléozoïque de Libye occidentale. Constantes géologiques et pétrographiques. Signification des niveaux ferrugineux oolithiques. *Notes et Mémoires de la Compagnie Française des Pétroles*, Paris, 16, pp. 25-66.
- Chetty D. & Frimmel H.E. (2000). The role of evaporates in the genesis of base metal sulfide mineralisation in the northern platform of the Pan-African Damara belt, Namibia:

- geochemical and fluid inclusion evidence from carbonate wall rock alteration. *Mineralium Deposita*, 35, pp. 364-376.
- Choquette RW (1971) Late ferroan dolomite cement, Mississippian carbonates, Illinois Basin USA. In: *Carbonate cements*, Briker O.P., pp. (339-346), Johns Hopkins Univ Press, Baltimore.
- Couturier P. (1980). Contribution à l'étude géologique et gîtologique du district à fluorine de l'Albigeois cristallin. *Thèse de 3^{ème} cycle*, Université de Toulouse.
- Crawford M.L. (1981). Fluid inclusions in metamorphic rocks. Low and medium grade. In: *Short course on fluid inclusions: application to ore petrology*, Hollister L.S. & Crawford M.L., pp. (157-181), Mineralogical Association of Canada, Calgary.
- Dardenne M.A. & Touray J.C. (1988). La fluorine du Brésil. Gisements filoniens traditionnels et nouveaux types de minéralisations. *Chronique de la Recherche Minière*, 490, pp. 5-46.
- Decrée S., Marignac C., De Putter T., Deloule E., Liegeois J.P. & Demaiffe D. (2008). Pb-Zn mineralisation in a Miocene regional extensional context: the case of the Sidi Driss and the Dhouahria ore deposits (Nefza mining district, Northern Tunisia). *Ore Geology Reviews*, 34, pp. 285-303.
- Deloule E. (1982). The genesis of fluor spar hydrothermal deposits at Montroc and Le Burc, The Tarn as deduced from fluid inclusion analysis. *Economic Geology*, 77, pp. 1867-1874.
- Ekambaran V., Brookins D.G., Rosenberg P.E. & Emanuel K.M. (1986). Rare earth element geochemistry of fluorite-carbonate deposits in Western Montana, U.S.A. *Chemical Geology*, 54, pp. 319-331.
- Ellis A.J. (1970). Quantitative interpretation of chemical characteristics of hydrothermal systems. *Geothermics*, Spec Iss 2, pp. 516-528.
- Ferrand A., Grappin C., Garcia-Iglesias J. & Touray J.C. (1978). Nouvelles données sur le gîte de fluorine de Villabona (Asturies-Espagne) et ses conditions de genèse. *Bulletin du BRGM*, section II (4), pp. 357-369.
- Floridia S. (1973). La province fluorée tunisienne. Aperçu géologique et métallogénique. In: *Livre jubilaire M. Solignac*, Ann. Mines Géol. Tunis, 26, pp. 459-477.
- Folk R.L. and Assereto R. (1974). Giant aragonite rays and baroque white dolomite in tepee-fillings. Triassic of Lombardy, Italy (abst.). AAPG, Abst., Ann. Meet., San Antonio, pp. 34-35.
- Fontboté L. (1981). Stratabound Zn-Pb-F-Ba deposits in carbonate rocks: new aspects of paleogeographic location, facies factors and diagenetic evolution (with a comparison of occurrences from the Triassic of Southern Spain, the Triassic-Liassic of Central Peru and other localities). *PhD thesis*, Heidelberg University.
- Fontboté L. (1993). Self-organization fabrics in carbonate-hosted ore deposits: the example of diagenetic crystallization rhythmites (DCRs). In: *Current Research in Geology applied to ore deposits*, Fenoll Hach-Ali P., Torres-Ruiz J., Gervilla F., pp. 11-14, Proceedings of the second biennial SGA Meeting, 84-338-1772-8, Granada,
- Fontboté L. & Amstutz G.C. (1983). Facies and sequence analysis of diagenetic crystallization rhythmites in stratabound Pb-Zn-(Ba-F) deposits in the Triassic of Central and Southern Europe. In: *Mineral deposits of the Alps and of the Alpine Epoch in Europe*, Schneider H.G., pp. 347-358, Springer, Berlin-Heidelberg-New York.

- Fontboté L. & Gorawski H. (1990). Genesis of the Mississippi Valley-type Zn-Pb deposit of San Vicente Central Peru: geological and isotopic (Sr, O, C, S) evidences. *Economic Geology*, 85, pp. 1402-1437.
- Fournier R.O. & Trusdell A.M. (1973). An empirical Na-K-Ca geothermometer for natural waters. *Geochim Cosmochim Acta*, 37, pp. 1255-1275.
- Fuchs Y. (1973). Sur les relations entre émigration et concentrations métallifères, quelques exemples tunisiens. In : *Livre jubilaire M. Solignac*, Ann. Min. Géol. Tunis, 26, pp. 480-509.
- Garcia-Iglesias J. & Loredó-Pérez J. (1982). Conditions physico-chimiques de formation des minéralisations à fluorine de la province des Asturias (Espagne): corrélation et synthèse. *Bulletin du BRGM*, section II (4), pp. 353-357.
- Ghaderi M., Palin J.M., Campbell I.H. & Sylvester P.J. (1999). Rare earth element systematics in scheelite from hydrothermal gold deposits in the Kalgoorlie-Norseman Region, Western Australia. *Economic Geology*, 94, pp. 423-438.
- Grappin C., Treuil M., Yaman S. & Touray J.C. (1979). Le spectre des terres rares de la fluorine en tant que marqueur des propriétés du milieu de dépôt et des interactions entre solutions minéralisantes et roches sources. Exemple pris dans le district de la Marche occidentale (France). *Mineralium Deposita*, 14, pp. 297-309.
- Gregg J.M. & Sibley D.F. (1984). Epigenetic dolomitization and the origin of xenotopic dolomite texture. *J. Sediment. Petrol.*, 54, pp. 908-931.
- Grogan R.M. & Bradburry J.C. (1967). Origin of the stratiform fluorite deposits of Southern Illinois. In: J.S. Brown Ed., Genesis of stratiform lead-zinc-barite-fluorite deposits (Mississippi Valley-type deposits). *Economic Geology*, Monogr. 3, pp. 40-51.
- Grogan R.M. & Shrode R.S. (1952). Formation temperatures of Southern Illinois bedded fluorite as determined from fluid inclusions. *Amer. Mineral.*, 37, pp. 555-566.
- Hall W.E. & Friedman I. (1963) Composition of fluid inclusions, Cave-in-Rock fluorite district, Illinois and Upper Mississippi Valley zinc-lead district. *Economic Geology*, 58, pp. 886-911.
- Harvey E.B., De Vivo B. & Valera R. (1984). Fluid inclusion study of some Surrabus fluorite deposits, Sardinia, Italy. *Economic Geology*, 79, pp. 409-414.
- Henderson P. (1984). Rare earth elements geochemistry. In: *Developments in Geochemistry*, Vol. 2, Henderson P., Elsevier, Amsterdam.
- Hubert P., Joron J.L., Touray J.C. & Treuil M. (1982). Le spectre des lanthanides de la fluorite, indicateur possible de l'origine et de l'histoire des solutions hydrothermales. Application au district du Tarn (France). *Bulletin du BRGM*, section II (4), pp. 365-369.
- Jacquín J.P. (1970). Contribution à l'étude géologique et minière de la Sierra de Gador (Almería, Espagne), Tome II, Géologie Minière. *Thèse 3^{ème} cycle*, Université de Nantes.
- Jebrak M., Debbah B. & Touray J.C. (1984). Saumures associées aux fluorines filoniennes du Maroc central dans le district d'El Hammam. *Bulletin de Minéralogie*, 107, pp. 233-240.
- Jellouli A. (1973). Géochimie de quelques sources thermo-minérales de Tunisie. In : *Livre jubilaire M. Solignac*, Ann. Min. Géol. Tunis, 26, pp. 571-579.

- Jemmali N., Souissi F., Villa I.M. & Vennemann T.W. (2011). Ore genesis of Pb–Zn deposits in the Nappe zone of Northern Tunisia: Constraints from Pb–S–C–O isotopic systems. *Ore Geology Reviews*, 40, pp. 41–53.
- Kessen K.M., Woodruff M.S. & Grant N.K. (1981). Gangue mineral $^{87}\text{Sr}/^{86}\text{Sr}$ ratios and the origin of Mississippi Valley-type Mineralization. *Economic Geology*, 76, pp. 913–920.
- Koepnick R.B., Denison R.E., Burke W.H., Hetherington E.A. & Dahl D.A. (1990). Construction of the Triassic and Jurassic portion of the Phanerozoic curve of sea water $^{87}\text{Sr}/^{86}\text{Sr}$. *Chemical Geology (Isotope Geoscience Section)*, 80, pp. 327–349.
- Laridhi-Ouazaa N. (1994). Etude minéralogique et géochimique des épisodes magmatiques mésozoïques et miocènes de la Tunisie. *Thèse Doctorat ès Sciences*, Université de Tunis.
- Marchand L., Joseph D., Touray J.C. & Treuil M. (1976). Critères d'analyse géochimique des gisements de fluorine bases sur l'étude de la distribution des lanthanides. Application au gîte du Maine (71 – Cordesse, France). *Mineralium Deposita*, 11, pp. 357–379.
- Martin F. (1979). Les gisements de fluorine post-hercyniens (karstiques et filoniens) dans le Paléozoïque de la région du Pourtalet (Pyrénées atlantiques – Province de Huesca). *Thèse 3ème cycle*, Université de Paris VI.
- Martini J.E.J. (1976). The fluorite deposits in the dolomite series of the Marico District, Transvaal, South Africa. *Economic Geology*, 71, pp. 625–635.
- Mason B. (1966). *Principles of Geochemistry* (3rd edition). John Wiley and Sons, ISBN 0-471-57526-7, New York.
- McLennan S.M. (1989). Rare earth elements in sedimentary rocks: influence of provenance and sedimentary processes. In: *Geochemistry and mineralogy of rare earth elements*, Ribbe P., pp. (169–200), Reviews in Mineralogy 21: Geochemistry and mineralogy of rare earth elements, ISBN 0-939950-25-1, Chelsea-Michigan.
- Memmi L., Burolet P.F. & Viterbo I. (1986). Lexique stratigraphique de la Tunisie. Première partie : Précambrien et Paléozoïque. *Notes du Service Géologique de Tunisie*, 53, pp. 1–66.
- Möller P., Morteani G. & Dulski P. (1984). The origin of calcites from Pb–Zn veins in the Hartz mountains, Federal Republic of Germany. *Chemical Geology*, 45, pp. 91–112.
- Office National des Mines (ONM) (1968). Projet des travaux géologiques de recherche pour le gisement de Djilet Staa Tunisie. Unpublished internal report.
- Office National des Mines (ONM) (1990). Zone fluorée de Zaghouan. Projet de réouverture des mines de Mecella, Jebilet el Kohol, Sidi Taya et Stah. Unpublished internal report.
- Ohle E.L. (1985). Breccias in Mississippi Valley-type deposits. *Economic Geology*, 80, pp. 1736–1752.
- Orgeval J.J., 1994. Peridiapiric metal concentration: example of the Bougrine deposit (Tunisian Atlas). In: *Sediment-hosted Zn-Pb ores*. Society for Geology Applied to Mineral Deposits, Fontboté & Boni, pp. 354–389, Special Publication No 10, , Soc. Geol. Applied to Mineral Deposits, Sediment-Hosted Zn-Pb Ores, Springer, Verlag Berlin Heidelberg.
- Perthuisot, V., 1978. Dynamique et pétrogenèse des extrusions triasiques en Tunisie septentrionale. *Thèse doctorat ès Sciences*, Ecole normale supérieure de Paris.

- Perthuisot V., Guilhaumou N. & Touray J.C. (1978). Les inclusions fluides hypersalines et gazeuses de quartz et de dolomites du Trias évaporitique nord-tunisien. Essai d'interprétation géodynamique. *Bulletin de la Société géologique de France*, XX, 2, pp. 145-155.
- Perthuisot V. & Saliot P. (1979). Néofonnations silicatées dans le Trias des diapirs tunisiens. Rôle des solutions hydrothermales. *Sciences de la Terre*, XXIII, 2, pp. 75-83.
- Potter R.W. II & Calif M.P. (1977). Pressure corrections for fluid inclusion homogenization temperatures based on the volumetric properties of the system NaCl-H₂O. *J Res US Geol Surv*, 5, pp. 603-607.
- Poty B., Leroy J. & Jachimowicz L. (1976). Un nouvel appareil pour la mesure des températures sous le microscope: l'installation de microthermométrie chaixmecc. *Bull Soc Fr Mineral Cristallogr*, 99, pp. 182-186.
- Potts, P.J., Thompson M., Kane J.S., Webb P.C. and Carignan J. (2000). GeoPT6 - An international proficiency test for analytical geochemistry laboratories - Report on round 6 (OU-3: Nanhoron microgranite) and 6A (CAL-S: CRPG limestone). Unpublished Report, (Report.pdf).
- Prévôt L., Lucas J., Nathan Y. & Shiloni Y. (1979). Répartition des éléments traces dans les phosphorites marines. In: *Origin and distribution of the elements. Second symposium, Physics and chemistry of the Earth volume 11.*, Ahrens, pp. 293-304, ISBN 0-08-022947-6, Oxford.
- Radke B.M. & Mathis M.L. (1980). On the formation and occurrence of Saddle dolomite. *J. Sediment Petrol*, 50, pp. 1149-1168.
- Rakus M. & Biely A. (1970). Stratigraphie du Lias dans la dorsale tunisienne. *Notes du Service Géologique*, 32, pp. 46-63.
- Richardson C.K. & Holland H.D. (1979). The solubility of fluorite in hydrothermal solutions, an experimental study. *Geochimica et Cosmochimica Acta*, 43, pp. 1313-1325.
- Richert J.P. (1971). Mise en évidence de quatre phases tectoniques successives en Tunisie. *Notes du Service Géologique de Tunisie*, 34, pp. 115-125.
- Roedder E. (1963). Studies of fluid inclusions, II: freezing data and their interpretation. *Econ. Geol.*, 58, pp. 167-211.
- Roedder E. (1967). Environment of deposition of stratiform (Mississippi Valley-Type) ore deposits, from studies of fluid inclusions. In: *Genesis of stratiform lead-zinc-barite-fluorite (Mississippi Valley-type deposits)*, pp. 349-362, Econ. Geol., Monogr 3.
- Roedder E (1979) Fluid inclusions as samples of ore fluids. In: *Geochemistry of hydrothermal ore deposits*, 2nd ed., Barnes H.L., pp. 684-737, Wiley, New York.
- Roedder E (1984) Fluid inclusions. In: *Reviews in Mineralogy*, Vol. 12, Ribbe P.H., Mineralogical Society of America, 0-939950-16-2, Chelsea-Michigan.
- Ronchi L.H., Touray J.C., Michard A. & Dardenne M.A. (1993). The Riberia fluorite district, Southern Brazil. Geological and geochemical (REE, Sm-Nd isotopes) characteristics. *Mineralium Deposita*, 28, pp. 40-252.
- Rose A.W., Hawkes H.E. & Webb J.S. (1979). *Geochemistry in mineral exploration*. Academic Press, ISBN 0-12-596252-5, London.
- Rouvier H., Perthuisot V. & Mansouri A. (1985). Deposits and salt bearing diapirs in Southern Europe and North Africa. *Economic Geology*, 80, pp. 666-687.

- Ruiz J., Richardson C.K. & Patchett P.J. (1988). Strontium isotope geochemistry of fluorite, calcite, and barite of the Cave-in-rock Fluorite District, Illinois. *Economic Geology*, 83, pp. 203-210.
- Sainfeld P. (1952). *Les gîtes plombo-zincifères de la Tunisie*. Annales des Mines et de la Géologie, n° 9, Société Française d'Éditions en Afrique du Nord, Tunis.
- Sallet R., Moritz R. & Fontignie D. (2000). Fluorite $^{87}\text{Sr}/^{86}\text{Sr}$ and REE constraints on fluid-melt relations, crystallization time span and bulk D^{Sr} of evolved high-silica granites. Tabuleiro granites, Santa Catarina, Brazil. *Chemical Geology*, 164, pp. 81-92.
- Sallet R., Moritz R. & Fontignie D. (2005). The use of vein fluorite as probe for paleofluid REE and Sr-Nd isotope geochemistry: The Santa Catarina Fluorite District, Southern Brazil. *Chemical Geology*, 223, pp. (27-248).
- Sangster D.F., Nowlan G.S. & McCracken A.D. (1994). Thermal comparison of Mississippi Valley-type lead-zinc deposits and their host rocks using fluid inclusion and Conodont colour alteration index data. *Economic Geology*, 59, pp. 493-544.
- Sassi A. (1999). Les phosphates dans les bassins paléogènes de la partie méridionale de l'Axe Nord-Sud (Tunisie). *Thèse doctorat ès Sciences*, Université de Tunis El Manar.
- Savard M.M., Chi G., Sami T., Williams-Jones A.E. & Leigh K. (2000). Fluid inclusion and carbon, oxygen and strontium isotope study of the Polaris Mississippi Valley-type Zn-Pb deposit, Canadian Arctic Archipelago: implications for ore genesis. *Mineralium Deposita*, 35, pp. 495-510.
- Sawkins F.J. (1968). The significance of Na/K and Cl/SO₄ ratios in fluid inclusions and surface waters, with respect to the genesis of Mississippi Valley-type deposits. *Econ Geol*, 63, pp. 935-942.
- Schneider H.J., Möller P. & Parekh P.P. (1975). Rare earth elements distribution in fluorites and carbonate sediments of the East-Alpine Mid-Triassic sequences in the Nordliche Kalkalpen. *Mineralium Deposita*, 10, pp. 330-344.
- Schneider H.J., Möller P., Parekh P.P. & Zimmer E. (1977). Fluorine contents in carbonate sequences and rare earths distribution in fluorites of Pb-Zn deposits in East-Alpine Mid-Triassic. *Mineralium Deposita*, 12, pp. 22-36.
- Schönenberger J., Köhler J. & Markl G. (2008). REE systematics of fluorides, calcite and siderite in peralkaline plutonic rocks from the Gradar Province, South Greenland. *Chemical Geology*, 247, pp. 16-35.
- Schwinn G. & Markl G. (2005). REE systematics in hydrothermal fluorite. *Chemical Geology*, 216, pp. 225-248.
- Shepherd T.J., Darbyshire D.P.F., Moore G.R. & Greenwood D.A. (1982). Rare earth element and isotopic geochemistry of the North Pennine ore deposits. *Bulletin du BRGM*, section II (4), pp. 371-377.
- Shepherd T.J., Rankin A.H., Alderton D.H.M. (1985). A practical guide to fluid inclusion studies. Blackie and Sons, pp. 229. ISBN 0-216-91646-1, Glasgow.
- Sheppard, S.M.F., Charef, A. & Bouhlef S. (1996). Diapirs and Zn-Pb mineralization: a general model based on Tunisian (N. Africa) and Gulf Coast (U.S.A) deposits. In: Carbonate-hosted lead-zinc deposits, Sangster D.F., pp. 230-243, Society of Economic Geologists Special Publication 4, ISBN 1-887483-95-0, Michigan.
- Souissi F. (1987). Etude géologique et conditions de formation des gisements de fluorine (Pb-Zn-Ba) du Jebel Zaghouan (J. Stah et Sidi Taya) et du Jebel Oust, Tunisie nord-orientale. *PhD thesis*, University of Toulouse III.

- Souissi F., Fortuné J.P., Sassi R. & Bouhleb S. (1996). L'association fluorine-cuivre gris du J. Oust (Tunisie nord-orientale). Géologie, minéralogie et inclusions fluides. *Notes du Service Géologique de Tunisie*, 62, pp. 89-104.
- Souissi F., Dandurand J.L. & Fortuné J.P. (1997). Thermal and chemical evolution of fluids during fluorite deposition in the Zaghouan province (north-eastern Tunisia). *Mineralium Deposita*, 32, pp. 257-270.
- Souissi F., Fortuné J.P. & Sassi R. (1998). La minéralisation fluorée de type Mississippi Valley du Jebel Stah (Tunisie nord-orientale). *Bulletin de la Société Géologique de France*, 169 (2), pp. 163-175.
- Souissi F., Sassi R., Bouhleb S., Dandurand J.L. & Ben Hamda S. (2007). Fluid inclusion microthermometry and rare earth element distribution in the celestite of the Jebel Doghra ore deposit (Dome zone, Northern Tunisia): towards a new genetic model. *Bulletin de la Société Géologique de France*, 178, pp. 459-471.
- Souissi F., Souissi R. & Dandurand J. (2010). The Mississippi Valley-type fluorite ore at Jebel Stah (Zaghouan district, north-eastern Tunisia): contribution of REE and Sr isotope geochemistries to the genetic model. *Ore Geology Reviews*, 37, pp. 15-30.
- Spangenberg J., Sharp Z.D & Fontboté L. (1993). Apparent stable isotope heterogeneities in carbonates due to the effect of organic matter and sulphides: Case study on the San Vicente MVT zinc-lead deposit, Peru. In: *Current Research in Geology Applied to Ore Deposits*, Fenoll Hach-Ali P., Torres-Ruiz F. & Gervilla F., pp. 241-244, Proceedings of the second biennial SGA Meeting, 84-338-1772-8, Granada.
- Spangenberg J., Sharp Z.D & Fontboté L. (1995). Apparent stable isotope heterogeneities in gangue carbonates of the Mississippi Valley-type Zn-Pb deposit of San Vicente, Central Peru. *Mineralium Deposita*, 30, pp. 67-74.
- Strong D.F., Fryer B.J. & Kerrich R. (1984). Genesis of the St Lawrence fluorspar deposit as indicated by fluid inclusion, rare earth element, and isotopic data. *Economic Geology*, 79, pp. 1142-1158.
- Strubel G. (1965). Quantitative Untersuchungen über die hydrothermale Löslichkeit von Fluospat (CaF₂). *Neues Jahrb Min*, 3, pp. 83-95.
- Subias I. & Fernandez-Nieto C. (1993). REE fractionation and fluid inclusion studies in fluorites from the Valle de Tena (Spanish Central Pyrenees). In: *Current Research in Geology Applied to Ore Deposits*, Fenoll Hach-Ali P., Torres-Ruiz F. & Gervilla F., pp. (249-252), Proceedings of the 2nd biennial SGA Meeting, ISBN 84-338-1772-8, Granada.
- Sverjensky D.A. (1984). Europium redox equilibria in aqueous solution. *Earth and Planetary Science Letters*, 67, pp. 70-78.
- Taylor S.R. & McLennan S.M. (1985). *The continental crust: its composition and evolution. An examination of the geochemical record preserved in sedimentary rocks*. Blackwell, ISBN 0-632-01148-3, Oxford.
- Thibieroz J. (1974). Hammam Jedidi et Hammam Zriba: étude géologique et minière de deux gisements stratiformes dans le cadre de la province fluorée tunisienne; l'association des concentrations fluorée aux surfaces d'émergence. *Thèse 3ème cycle*, Université de Paris VI.
- Thibieroz J. (1976). Reconstitution chronologique du rôle des surface d'émergence dans l'histoire du gisement de fluorine de Hammam Zriba (région de Zaghouan-Tunisie). *Mém. H. s. Soc. géol. Fr.*, 7, pp. 33-37.

- Thibieroz J. (1982). Typologie des gîtes de fluorine. Répartition des gisements en France et dans les régions voisines. *Bulletin du BRGM*, section II (4), pp. 437-449.
- Touhami A. (1979). Contribution à l'étude géologique et métallogénique de la province fluorée tunisienne; rôle de l'altération superficielle dans la formation des concentrations fluorées. *Thèse 3ème Cycle*, Université de Tunis.
- Trona F. (1973). Position des horizons dolomitiques minéralisés en fluorine et galène au sein des sédiments triasiques de la Sierra de Lujar (Grenade. Evolution et géochimie. *Thèse Doctorat ès Sciences*, Paris.
- Tropper P. & Manning C.E. (2007). The solubility of fluorite in H₂O and H₂O-NaCl at high pressure and temperature. *Chemical Geology*, 242, pp. 299-306.
- Turki M.M. (1988). Polycinématique et contrôle sédimentaire associé sur la cicatrice Zaghouan-Nebhana. *Thèse Doctorat ès Sciences*, Université de Tunis.
- Uysal I.T., Zhao J.X., Golding S.D., Lawrence M.G., Glikson M. & Collerson K.D. (2008). Sm-Nd dating and rare-earth element tracing of calcite: Implications for fluid-flow events in the Bowen Basin, Australia. *Chemical Geology*, 238, pp. 63-71.
- Valenza K., Moritz R., Mouttaqi A., Fontignie D. & Sharp Z. (2000). Vein and Karst Barite Deposits in the Western Jebilet of Morocco: Fluid Inclusion and Isotope (S, O, Sr) Evidence for Regional Fluid Mixing Related to Central Atlantic Rifting. *Economic Geology*, 95, pp. 587-606.
- Vietz J.C. & Leach D.L. (1990). Genetic implications of regional and temporal trends in ore fluid geochemistry of Mississippi Valley-type deposits in the Ozark region. *Economic Geology*, 85, pp. 842-861.
- Weisbrod A. & Poty B. (1975). Thermodynamics and geochemistry of the hydrothermal evolution of the Mayres pegmatite, Southeastern Massif Central (France). *Pétrologie*, Part 11, pp. 1-16.
- Zimmerman R.K. & Kesler S.E. (1981). Fluid inclusions evidence for solution mixing. Sweetwater (Mississippi Valley) district, Tennessee. *Economic Geology*, 76, pp. 134-142.

Potential and Geochemical Characteristics of Geothermal Resources in Eastern Macedonia

Orce Spasovski
*University "Goce Delcevo" Stip, Faculty of Natural and Technical Sciences
Macedonia*

1. Introduction

Geothermal explorations in the Republic of Macedonia were intensified in the 70's, during the first effects from the energetic crisis. As a result of those explorations, there were established over 50 springs with mineral and thermo-mineral water, with maximum potential of over 1400 l/s and evidenced reserves as deposit for exploitation of around 1000 l/s, with temperature higher than the mean season swings for this part of the Earth in the range 20-79 °C, accumulated quantities of geothermal power. Geologically and hydro-geologically spoken, these geothermal resources are mainly located in eastern and southeastern Macedonia, in the Bregalnica-Strumica region composed by 23 municipalities. This region, in its geological past has undergone many big tectonic changes and its composition is formed by almost every type of stones, including the youngest and oldest formations, forming hydro geothermal systems, that currently are the only ones worthwhile to be explored and exploited. The most important hydro geothermal systems in this area are the tertiary basins of Kochani valley, Kezhovica Spa near Shtip, and the Kratovo-Zletovo volcano region, exactly the micro regions included in the REDEM region as the territory from the project target group. In order to valorize this geothermal potential in eastern and southeastern Macedonia certain pre-conditions should be created for using these resources in Bregalnica-Strumica region. This means that serious project documentation should be prepared followed by the targets that should be accomplished and tasks for faster development in order to use this important geothermal potential in this region, but at the same time following the positive legislation for issuing a concession for carrying out Detailed Geological Explorations (DGEs) and exploitation of the geothermal energy in the Republic of Macedonia (RM), according to the Law on mineral raw materials (Official Gazette of the RM, no. 18/99 and 29/02). With the project "Creation of pre-conditions for utilization of the geothermal potential in the eastern and south-eastern region", the basic information about the geothermal resources in the RM will be presented in brief. In addition, the project will present details of the potentials of this region showing the energetic value of the geothermal resources in this region, currently available capacities, technical capabilities and deposit characteristics.

Simple definition of the geothermal energy is that it is a quantum of calories (the thermal energy in warm water) that the Earth holds in its inside part. According to the location

where the geothermal energy is accumulated, in which stratum of the Earth's surface, it can be divided into: hydro geothermal, litho geothermal, magma geothermal and pneumatic geothermal energy. The geothermal energy can be accumulated in the fluids, in the solid rocks, in magma and in gases. Definition of geothermal resource is that it is a part from the Earth's inside heat (higher than the mean annual temperature) that can be exploited, using its economic effect but following the legislation, nowadays or in the near future. Hydro geothermal resources are part of the geothermal resources and presents the part of the Earth's stratum in which apart from the conductive way of transfer of the geothermal energy through rocks as isolators, is also transferred by a convective way among the rocks and their joints that serve as reservoirs, which calories can be rationally used as energy, i.e. exploited. According to the way this geothermal energy is being transferred near the Earth's surface, the hydro geothermal resources are divided in conductive and convective systems.

The group of conductive systems gathers the systems with dominant conductive way of transfer of the geothermal energy. In this group we find the tertiary basins of Ovce Pole, Tikvesh, Delchevo-Pehchevo region, Skopje valley, Strumica valley, Gevgelija valley, Polog and Pelagonija valley (Arsovski and Stojanov, 1995). The group of convective systems is developed in crags, capillary crags and with capillary porosity. Major characteristics of all convective systems are: high hydraulic gradients and high pressures due to the big difference in the heights levels of zones of influx (where the underground water enters the reservoir) and the zones of outflow, where the underground water leaves the pool (Serafimovski, 2001). Before we analyze the geo-thermal potentials of eastern and southeastern Macedonia, we will present the main characteristics of the hydro geothermal resources in the RM.

2. Research methodology

Since the study subject have been terrains with complex geological evolution, an application of complex methodology of field and modern analytical methods, was required which should provide more exact data for realistic interpretation of established goals.

Efforts were made for the first time in this researched area and one large set of geological and non geological data were collected during a longer period of time and studies were conducted along different criteria, their analysis and synthesis by same criteria.

During these studies geological and non-geological methods were used. In regards of geological methods were applied: analysis and synthesis of previous geological studies with special review of tectonic studies, geotectonic concepts and distribution of formations of carbonaceous composition.

These non-geological methods were applied: analysis and synthesis of data from chemical analyses of thermal waters with special attention given to sampling of specimens and applied analytical methods, analysis and synthesis of chemical studies and temperature measurements in realized drill holes.

3. Geothermal resources in Macedonia

Geothermal energy is the warmth that the Earth holds in its inside part. This energy comes from the inner nature of our planet, the physical processes that occur underground. Getting

to and using this warmth is conditioned by a certain carrier - that transports the energy like warmth near the Earth's surface, at considerable depth. This carrier usually is some fluid.

Hydro geothermal energy and resources nowadays are the only ones of the commercially approved sources of energy kept in hot/warm water or steam, accumulated in rock's joints or in porous sedimentary structures at depths going from few hundreds to 4000 m underground. Depending on the temperature and the dominant phase of the fluid, the hydro geothermal resources generally are categorized in 3 groups: low temperature water, mainly used for central heating in homes, apartments, offices, supporting agricultural production in greenhouses (hothouses), and few industrial processes; medium temperature water (<140°C), used in some industrial processes and production of electric energy (using binary cycles-plants that use Freon, known as ORC turbines); and high temperature water or steam (140-350°C) is used for electric energy production in turbine plants (of which 2/3 work in the moderate area 150-200°C).

3.1 Geological characteristics and tectonic placement of the RM

Macedonia is situated in the middle of the Balkans peninsula and has 25.713 km². The geotectonic position is determined by its location. It belongs to the Alps - Caucasus - Himalaya geosyncline belt, and the history in creating of the terrain is tightly connected with the former geosynclinals Tetis and the Alpine orogeny, also with the primordial position of the lithosphere. Generally spoken, over the components of the Alps orogen, the territory of RM belongs on two tectonic systems: the western part including the Vardar valley belongs to the Dinarides (Helenides) whereas the eastern Macedonian mountainous terrain and valley's depressions are segment of the Serbian-Macedonian massif. Additionally, along the Macedonian-Bulgarian borderline, a small separated zone belongs to the Carpatian-Balkanides, the Kraishtide zone (Dimitrievic, 1974).

According to this geotectonic reorganization, the main part of the Macedonian territory that spreads west from the Dojran-Strumica-Zletovo-Kumanovo line is divided in four (4) geotectonic units: Vardar zone, Pelagonian horst-anticlinorium, western Macedonian zone, and the Korab zone better known as Cukali-Krasta zone Fig. 1.

To the East from the mentioned line lies the Macedonian massif of mountains which is connected with the Rodopi Mountains in Bulgaria through the Ograzhden Mountain. In the borderline zone with Bulgaria, to the north of Berovo-Delchevo, as a wedge in the old Rodopi Mountains there are elements from the Carpatian-Balkanides massif separated in the Struma zone (better known as Kraishtide zone, after I. Bonchev). Every separate unit is one structural entity, characterized with its separate geological development including the specific processes of tectonic deformations and manifestation of magma differentiation.

The terrain that forms the territory of the RM in its geological past has undergone big tectonic changes and it is represented by almost every type of rocks, from the oldest to the youngest, starting with Precambrian metamorphosis rocks, with high cristalinity and than the youngest neogenesis and quarter sedimentary complexes. Also, there are found vast surfaces with eruptive rocky masses, from ultra basal to extremely acid and alkaline magma rocks. As a result of all above mentioned, we have found forms with highly specific geological, hydro geological and geomorphologic characteristics. Because of the heterogeneous geologic-lithologic composition and the tectonic past of the terrain as well as

from the different geomorphologic and climate characteristics, there are found different types of underground water. In the mountainous part of the terrain there are more dispersed springs usually found, as opposed to the numerous valleys, there are also springs that are more compactly settled, some with free surface and other under pressure (artesian wells-springs), while in the seismic active zones we find the thermal and mineral waters, i.e. the hydro geothermal resources.

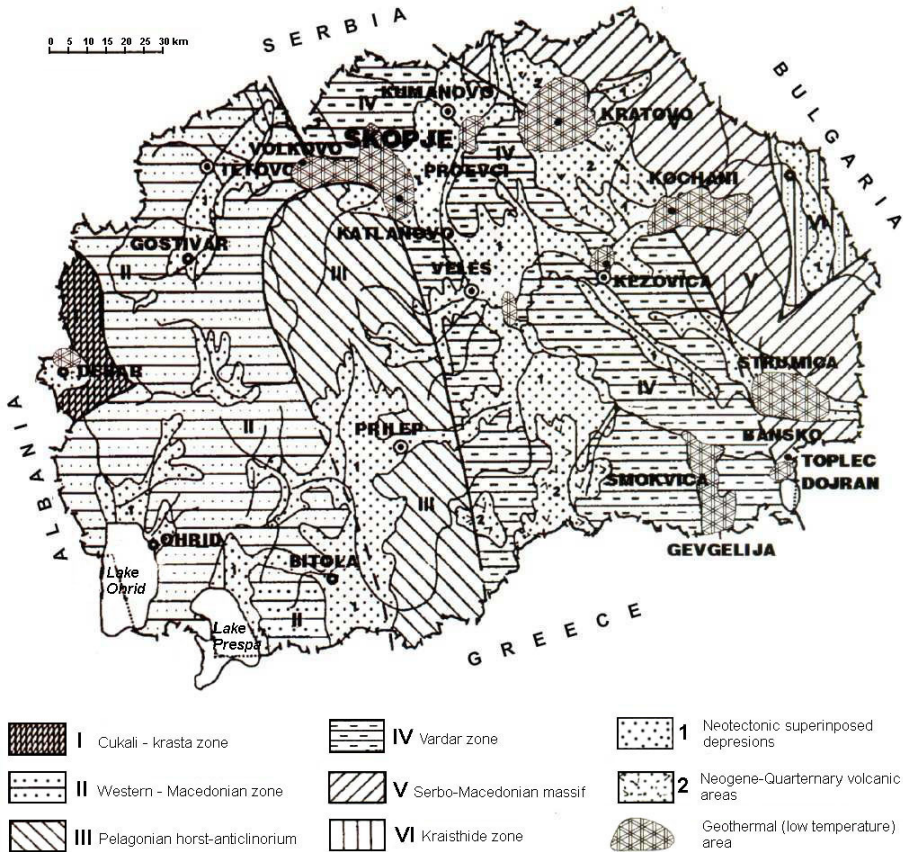


Fig. 1. Main geothermal areas in the Republic of Macedonia and regional tectonic setting (Arsovski, 1997)

3.2 Geothermal characteristics

According to the way of transmission of the geo-thermal energy, hydro-geo-thermal resources are divided in two groups: convective and conductive hydro-geo-thermal systems. The group of conductive systems gathers the systems with dominant conductive way of transfer of the geothermal energy. In this group in the RM we find the tertiary basins of Ovce Pole, Tikvesh, Delchevo-Pehchevo basin and the basins of Skopje valley, Strumica valley, Gevgelija valley, Polog and Pelagonija valley. In the group of convective hydro

geothermal systems a convective way of transfer of the geothermal energy dominates. The most important convective hydro geothermal systems in the territory of the RM are: Skopje valley, Kocani valley, Strumica valley, Gevgelija valley, Kezhovica near Shtip, Toplic-Topli dol on the Kozuf Mountain, Toplec near Dojran, Proevci near Kumanovo, Strnovec, Zdravevci at the river Povishnica near Kratovo, Sabotna voda near Veles, as well as the systems in the western Macedonia - Kosovrasti and Debar spa, and Banice at the river Pena near Tetovo.

In the following text we will present the data and the parameters on the most important hydro geothermal systems in the eastern and south-eastern part of Macedonia. Location of the main geothermal fields and their systems are shown on Fig. 2.

On the Macedonian territory there are rocks from different ages, starting from Precambrian to Quarter, presented by almost all litho logic types. The oldest, Precambrian rocks are composed of gneiss, micaschists, marlstone and orthometamorphides, the Paleozoic rocks are mostly green schists and Mesozoic are presented by marlstone, limestone, acid-, alkali- and ultra alkali magma stones. Tertiary sediments are composed of flysch and lake sediments, sandstones, limestones, claystones and sands. What stands to the structural relations the territory can be divided in six geotectonic units: Chukali-Krasta zone, west Macedonian zone, Pelagonian horst anticlinorium, Vardar zone, Serbian-Macedonian massif and Kraishtida zone. The tectonic position is based upon the terrain itself and the geological data without using geo-thermal hypothesis (Arsovski, 1997). The first four tectonic units are part of the Dinarids, the Serbian-Macedonian massif is part of Rodopi and Kraishtida zone is part of Carpatian-Balkanidi zone.

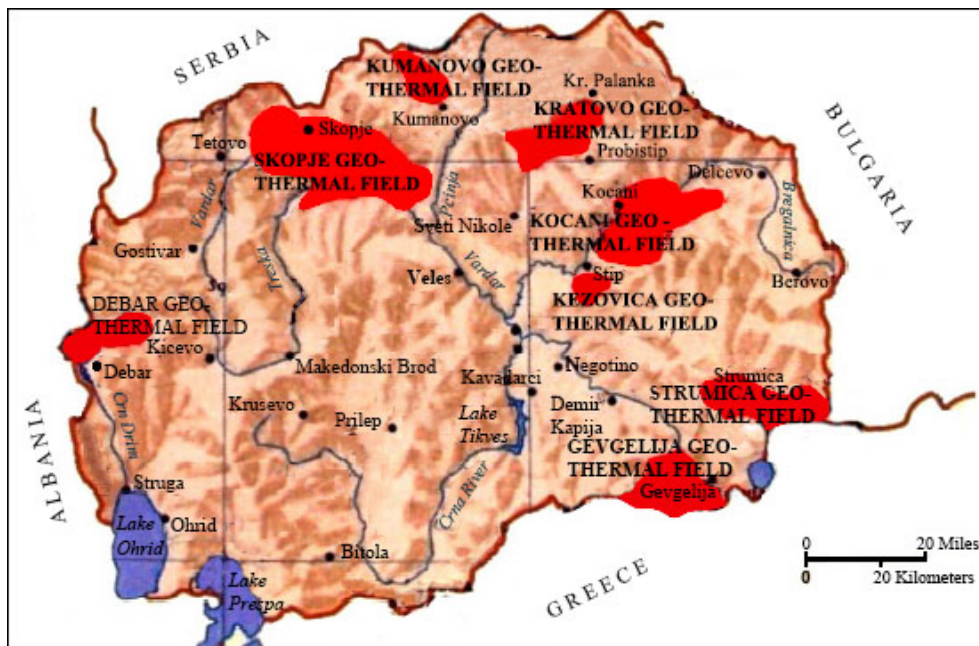


Fig. 2. Main geothermal fields in Macedonia (Popovski & Micevski, 2005)

The territory of the RM as a whole is part of the Alps-Himalayan zone, the Alps sub zone that is still volcanic active. This chain starts in Hungary, runs across Serbia, Macedonia and Northern Greece and all the way to Turkey. Few geothermal regions, including the Macedonian region that is connected with Vardar tectonic unit are set aside. This region shows positive geothermal anomalies. The hydro geothermal systems currently are the only one worthy to be explored and they are exploited. There are 18 geothermal fields known in the country, with over 50 thermal springs, boreholes and hot water wells. The maximal capacity is 1000 l/sec water flow with temperatures from 20-79°C. Thermal water is mostly hydrocarbon according to the dominant anion and equally mixed with Na, Ca and Mg. The concentration of the dissolved minerals stands from 0, 5-3, 7 g/l. All thermal waters in Macedonia are with meteoric origin. The thermal spring is a part from the regional thermal flow, which in the Vardar zone 100-120 mW/m², while in other part of the country is 60-80 mW/m², with 32-35 km thick stratum. The following text will present the details on the data and the parameters for the most important convective hydro geothermal systems in eastern and south-eastern Macedonia, a territory composed of 23 municipalities from Bregalnica-Strumica region.

4. Main geothermal fields in eastern Macedonia that are currently exploited

This presentation will show basic data about the energetic resources in eastern and southeastern Macedonia, current capacities in Macedonia, the technical capability and perspective locations in this part of the country, as well as the methodologies for their valorization from the geothermal aspect.

4.1 Hydro geothermal system of Kochani valley

The geothermal locality "Podlog"-Banja-Kochani is not only important deposit of geo-thermal water in Macedonia, but also in the world (verified with the studies of the American enterprise GeothermaEx and the Austrian consortium ARGE GTM), having in mind the balanced reserves from 157x106 m³ GTW, with exclusively good chemical characteristic, and mean temperature of 75°C. This great potential of the deposit from the aspect of energy, especially the characteristic restorable reserves, has offered the main prerequisite for preparation of the concept, project and implementation of the exploitation system GTW "Geoterma".

The geothermal system "Geoterma" with its installed capacity 300 l/sec exploits and distributes geothermal water to the end users:

1. Heating the Agro-complex - production in greenhouses
2. Low-temperature procedures
3. Central heating of public and administrative buildings
4. Recreation centers and balneology

Basic data for the geothermal deposit Podlog-Banja (geography, morphology, geology, petrology, hydro-geology and chemistry).

Kochani geothermal region i.e. deposit Podlog-Banja is situated in the north-eastern part of Macedonia between the 41° 40' and 42° 00' NGW and 22° 00' and 22° 30' EGL.

Kochani valley with its surroundings is generally spread in East/ West direction and has about 400 km², medium altitude of 330 m. By its morphology the valley is an elongated field

in the medial part of the Bregalnica river basin. The economic, cultural and political center is the city of Kochani (30.000 inhabitants).

The deposit itself in regional-geological sense belongs to the zone of higher thermal flow that stretches from Turkey, across northern Greece, eastern Macedonia all the way to the Panonian basin. In a tectonic sense the region is a complicated orogene area that belongs to the two tectonic units: Serbian-Macedonian basin and the Vardar zone with highly expressed volcanic activity of the Kratovo-Zletovo volcanic area Fig. 3.

The deposit from the point of view of supplementation is an infiltration type.

Based upon the completely done interdisciplinary researches, it is verified as maybe one of the world largest non-magma deposit of geothermal water, with overall balanced static reserves of approximately 150.000.000 m³ over 70°C. The chemistry of the water is Na-bicarbonate water with pH=7, none corrosive enclosed systems, that gives its possibility for various applications. The presence of some elements (Se, F and etc.) in controlled referent limits, gives the water special quality and it can be used as a bottled drinking water (Table 1).

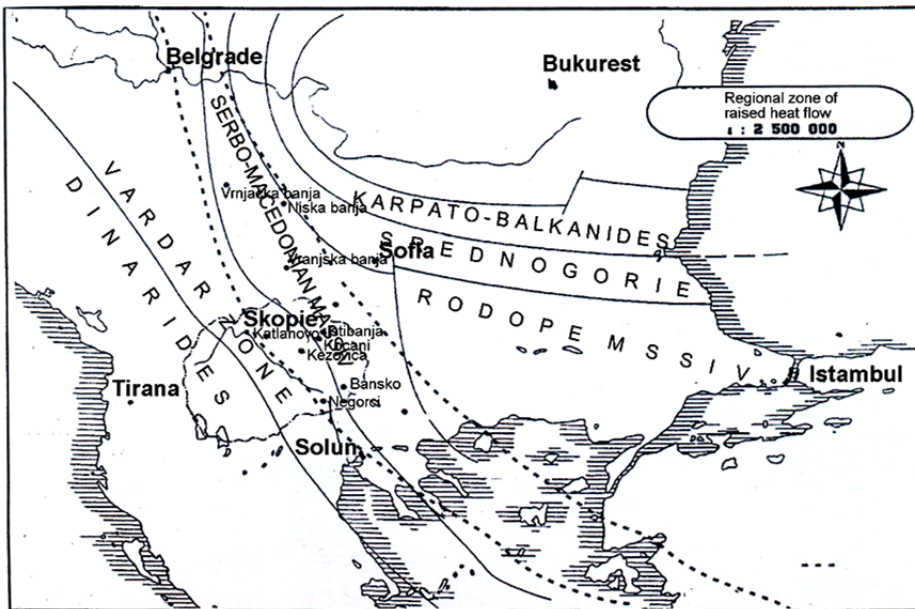


Fig. 3. Regional zone with increased thermal flow (Bonchev, 1974)

In order to take a look on the activities that practically have verified the deposit of geothermal water in "Podlog-Banja" and established the "Geoterma" system, we will present a review, chronology and results organized in three temporal stages (Naunov, 2003).

4.1.1 First stage

The first stage is typically explorative and is located at the very beginning, in the year 1973 and all the way to the year 1984. This period, organized by the Council of the Municipality

	Name of the chemical substance	Average value mg/l	MDK, for drinking water mg/l
1	Color, Co/Pt	< 5	100
2	starring, NTU	0.7	< 0.6
3	dry remrant on - 105 o S, mg/l	599.6	-
4	dry remrant on - 180 o S, mg/l	620.0	-
5	dry remrant on	493.5	< 500
6	pH - value	6.99	6.8 - 8.5
7	p - value, ml 0.1 N HCl/l	0	-
8	m - value, ml 0.1 N HCl/l	86.4	-
9	Bicarbonate ions, [HCO ₃], mg/l	527.4	-
10	total solidity, [VT], o D	9.27	-
11	Carbonate solidity, [KT], o D	23.02	-
12	Calcium solidity, [Ca T], o D	6.08	-
13	Magnesium solidity, [Mg T], o D	2.90	-
14	Chlorides, [Cl], mg/l	17.9	25.0
15	Sulphates, [SO ₄], mg/l	50.38	25.0
16	Calcium, [Ca ²⁺], mg/l	48.32	100.0
17	Magnesium, [Mg ²⁺], mg/l	11.71	30.0
18	Total Fe, [Fevk], mg/l	0.14	0.05
19	Manganese, [Mn ²⁺], mg/l	0.019	0.02
20	Sodium, [Na ⁺], mg/l	142.4	20.0
21	Potassium, [K ⁺], mg/l	18	10.0
22	Silicon Dioxide, [SiO ₂], mg/l	44.2	-
23	Free CO ₂ , mg/l	109.8	-
24	Aggressive CO ₂ , mg/l	20.7	-
25	Conductivity	775	to 300
26	Nitrites, [NO ₂], mg/l	0.0034	-
27	Nitrates, [NO ₃], mg/l	0.29	5.0
28	Ammonium, [NH ₄ ⁺], mg/l	0.305	0.01
29	Phosphate, [P ₂ O ₅], mg/l	2.29	0.03
30	Solubler oxygen, [O ₂], mg/l	5.16	-
31	Cyanides, [CN], mg/l	0.0	-
32	Sulphides, [S], mg/l	0.0	-
33	Lead, [Pbvk], mg/l	< 0.01	0.05
34	Cadmium, [Cd ²⁺], mg/l	< 0.002	0.005
35	Chromium, [Crvk], mg/l	< 0.005	0.05
36	Copper, [Cu ²⁺], mg/l	< 0.005	0.1
37	Zinc, [Zn ²⁺], mg/l	0.14	0.1
38	Nickel, [Ni ³⁺], mg/l	< 0.005	0.01
39	Consumption of KMnO ₄	2.13	to 5

Table 1. Summary values of the results from the chemical analyses of the geothermal waters on the locality Podlog - Banja, Kocani (Naunov, 2003)

of Kochani - Study and research office and the Institute on explorative works in mines of RM (Republic of Macedonia), realized by the Geologic institute Skopje and Ljubljana (Slovenia) and GeothermEx (USA), the following researches have been done:

Detailed geologic and hydro-geologic explorations

Detailed structural-petrologic works

Geophysical works (deep geophysics, gravimetric, seismic and shallow geo-thermometric)

Micro location of the exploration boreholes; Based upon the synthesis of all gathered information from the exploration, officially elaborated the following results: the geothermal area in the Kochani valley is being fully characterized in all segments (geologic, petrologic, geophysical, structural and hydro-geological characteristics).

4.1.2 Second stage

Activities in the second stage were mainly organized around promotion of the results and the detailed explorative works from the first stage at the location Podlog-Banja, all with a role of creating an objective ground for establishing a re-injection system. The period of these activities is after 1984 and is characterized with organizing new personnel, at the beginning like an investment group within PCE "Vodovod"-Kochani, and later transformed in an independent experts group of the geothermal system "Geoterma". Since 1984 till present it is the main initiator and animator of the activities concerning the system.

During this period a lot of domestic and foreign experts, also exploration institutions took part and successfully finished the following tasks:

- located and drilled exploiting wells EW MP-1, EW2, EW3 as well as re-injecting borehole P-10, and then in 1999, well EW-4;
- for utilization of the capacities of the deposit 'Podlog-Banja', the concept was prepared, feasibility study elaborated and the project prepared of the exploitation system GTW "Geoterma" (Fig. 4.)
- The system "Geoterma" was built and activated as an exploitation-distribution system; the basic "Geoterma" technical-technological parts are:
- Exploitation wells for geothermal water (GTW)
- Pipeline
- Pumping and distributing unit
- Distribution pipeline for GTW

At this phase of development, the system has installed capacity of 300 l/sec, and practically an annual average of 1.400.000 m³ GTW pumped and distributed with mean temperature of 75°C.

The main usage of the geothermal water is for the needs of:

- agricultural production in greenhouses, around 18 ha
- low-temperature technological processes
- Central heating of public and administrative buildings in the downtown Kochani

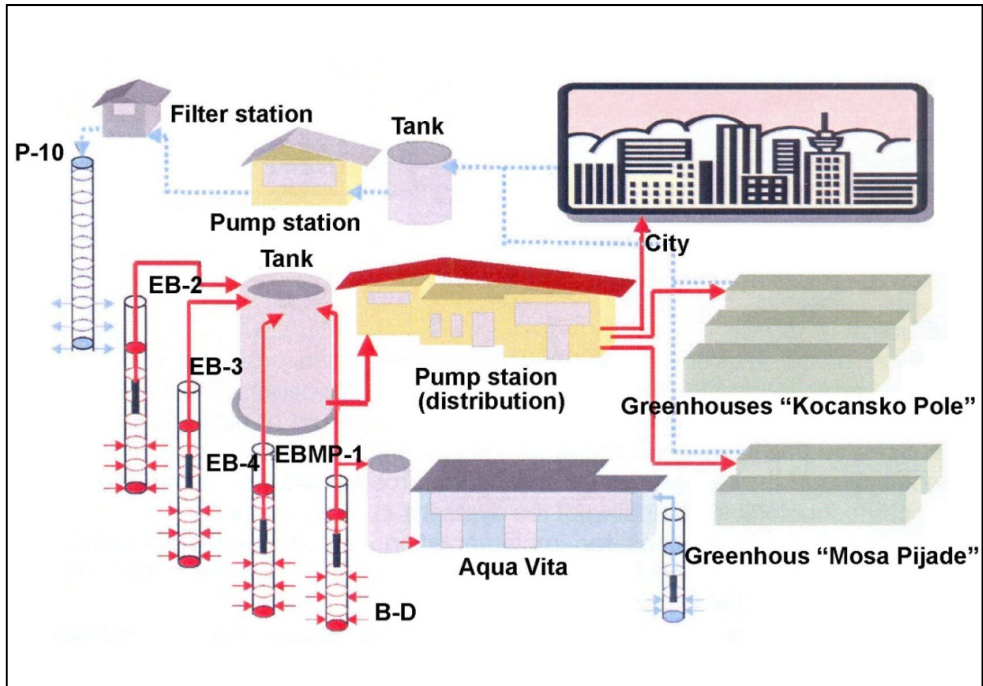


Fig. 4. General scheme of the System for exploitation, distribution and reinjection "Geoterma" – Kochani (Naunov, 2003)

Partial realization of the investment-technical conception of the "Geoterma" system as well as the findings and the results gained during the exploitation phase in the period of 1985-89 with registration of the piezometric level of the basin, clearly and without doubts has shown an urgent need of building of the re-injecting phase of the system (Fig. 5).

For this purpose a ^3H -tritium traced detailed explorative researches have been done and at the same time the unlimited possibility of applying of the re-injection was proven. Afterwards, upon these results and the created project solutions, the basic part of the re-injecting system was realized as an inseparable i.e. complementary part of the whole exploitation system and practically encircled the system "Geoterma".

The re-injection system in this stage of equipment has the main role to cap the used quantities of GTW from the agro complexes (at this stage only from AC "Mosa Pijade"-Podlog) and through the re-injection pump system to inject it back in the re-injection borehole P-10 in the village of Banja. But, besides the big expectations from this re-injecting system, from well known reasons-transformation of 2-valence Fe in to 3-valence Fe in the GTW and creation of voluminous sediment threatening to close the re-injecting borehole-it didn't work well with full capacity.

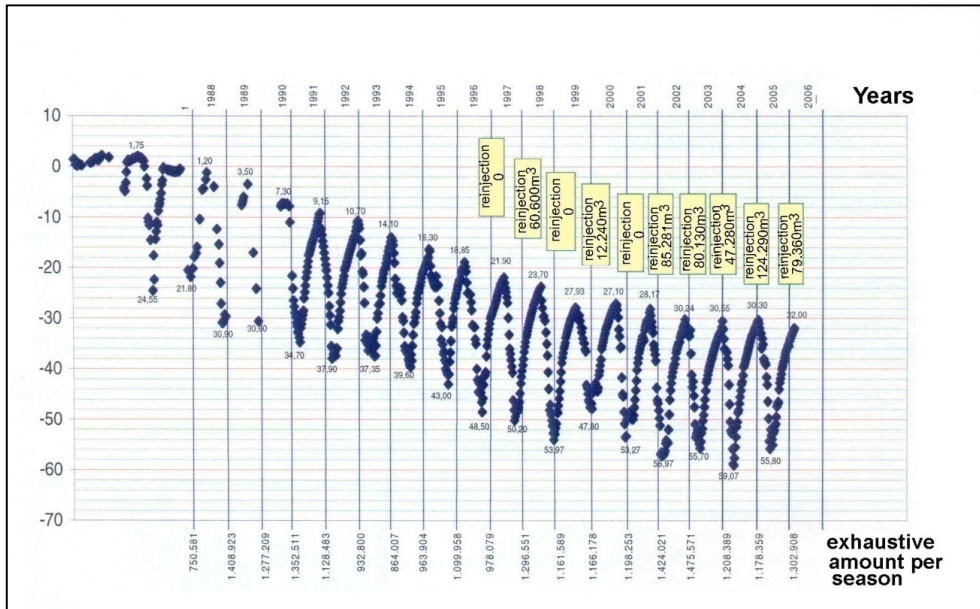


Fig. 5. Chart of the piezometric level of the basin in the period from 01.01.1987 -19.10.2006

4.1.3 Third stage

This stage of the activities: 1995-2003, treats mainly the problems that originated from our experience in exploitation of GTW, as well as problems with development program for the system "Geoterma". Organized as it is with very few innovations and participation of renowned experts and institutions on this field, in this stage we should emphasize the following activities:

- intensification of the researches for solving the problem with the re-injecting system;
- technical-technological equipping of the system;
- researches and preparations for implementation, and the implementation of the project-bottling of GTW;
- encircling of the central heating system for the town of Kochani
- continuity in the research activities for defining the mechanisms of supplementation of the deposit, and completely defining of the one (shown at the prognostic pattern, (Fig. 6);

The other effects are clearly expressed in few segments, above all in using the GTW for bottling, with accent on its outstanding quality and the special wellness characteristics positive for the health of the consumers, as well as for balneology-recreation purposes;

In the scientific-research segment it is a special contribution as applied explorative model and its results;

In the administrative-legislative segment - also as an avant-garde object-project, that helped the development of geothermal science and utilization of geothermal waters in Macedonia.

4.2 Hydro geothermal system Istibanja-Vinica

The hydro geothermal system Istibanja-Vinica, with its thermo-mineral springs is directly settled in the immediate surroundings of the village Istibanja (Vinica), along the flow of river Bregalnica (Fig. 7).

The geothermal field Istibanja - Vinica from geological point of view lies on the contact between two tectonic units (the Serbian-Macedonian massif on the East and the Vardar zone on the West) at the eastern periphery of the Kochani valley, very close to Istibanja and Vinica. The microlocation of the exploitation wells 1-3,1-4 and 1-5 is between the regional motorway Kochani-Istibanja-Delchevo and the river Bregalnica, drilled in the river terrace along the river bed.

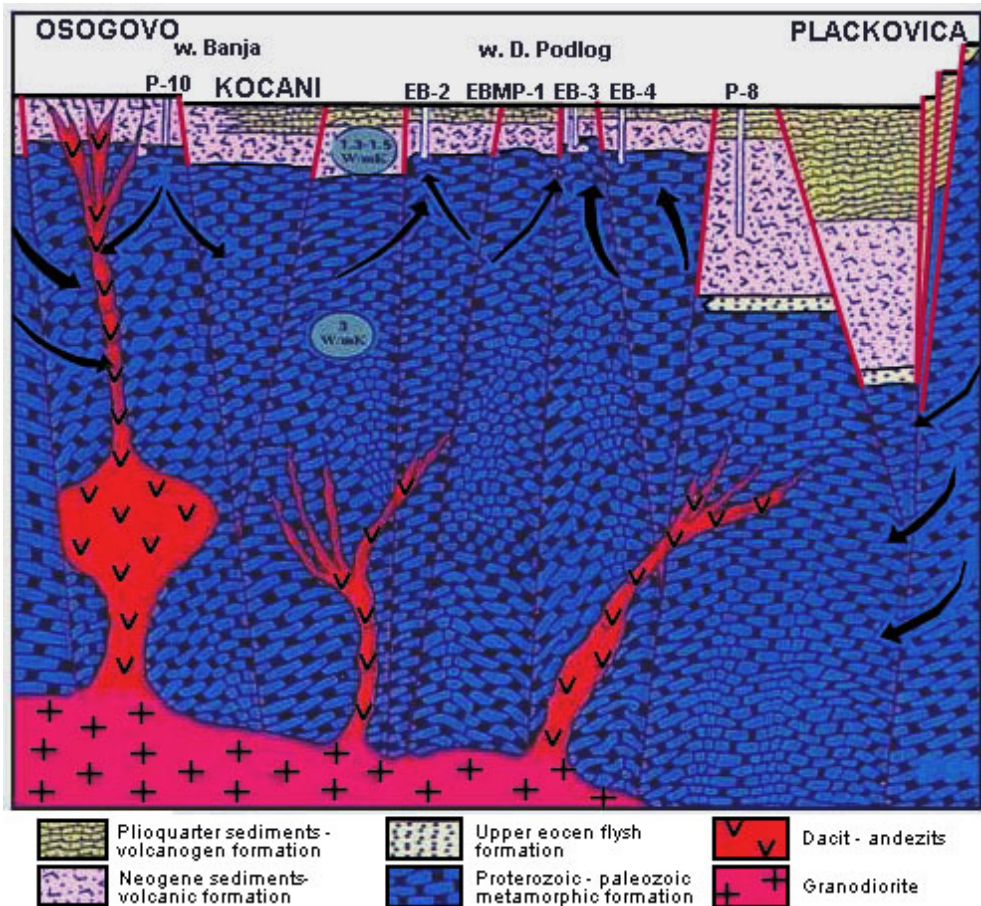


Fig. 6. Forecasted geological model of the geothermal system of the Kochani valley (Naunov, 2003)



Fig. 7. Geothermal field Istibanja-Vinica

As separated hydro geothermal system from the Kochani geothermal field (Podlog-Banja system) is micro-located on a terrain with rocky masses as part of the Serbian-Macedonian geotectonic unit.

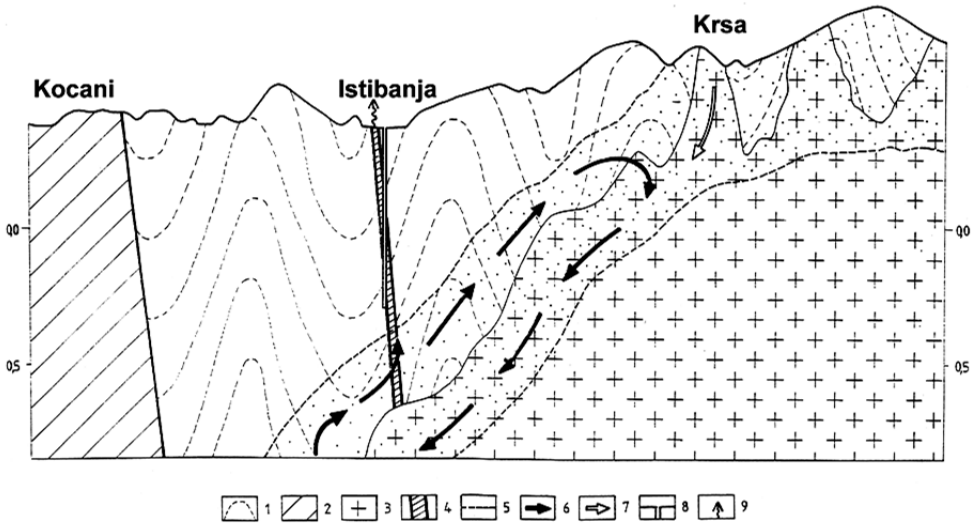
The Serbian-Macedonian massif in the area of Istibanja and Vinica is built up of old Precambrian and Riphean - Cambrian rocks. The former, Precambrian rocks are presented by double-mica striped gneisses (Gmb), a variant of micaschists and amphibolites (Kovacevic et al 1973; .Rakicevik et al, 1973).

While analyzing the neotectonic fault zone (shear) structures, gathered as information from the satellite recordings and the geotectonic map of the RM (Arsovski , 1987) in proportional ratio 1:200.000, we can clearly match the difference between the Vardar zone on one side (western part) and the Serbian-Macedonian massif on the other (eastern part). Many ring like structures with different dimensions are typical for both systems in this region (Podlog, Banja and Istibanja). The neotectonic structural forms in the Serbian-Macedonian massif, where the Istibanja hydro geothermal system belongs are different than the tectonic structures in the Vardar zone. Also, it should be mentioned that the Vardar zone belt has deep shear structures with pretty much expressed seismic activity, contrary to the relatively stable Serbian-Macedonian massif.

The deposit-reservoir of the hydro geothermal system in the geothermal field of Istibanja-Vinica is composed of ruptured Paleozoic gneisses and granites, as shown at the prognostic model on the figure. The supplementation zone for this system is formed by the gneisses,

micaschists and schist's from the Golak downhill- Krshla in the eastern part of the valley as well as from the north-eastern parts of Osogovo Mountains (Fig. 8).

The outflow zone of the system is presented with contemporary geo-thermal occurrences as natural springs in the very surrounding of Istibanja and the exploitation wells I-3, I-4 and I-5 in the very surrounding of the river Bregalnica, to the south of the village Istibanja, Vinica. According to the type of hydro-geo-thermal system, it is found in the group of semi-closed systems in ruptured (jointed) gneisses and granites from the Paleozoic age where the outflow zones are located in the shears.



1.Pt-gneisses, 2. Pz-shall, 3. granite, 4. fault zone, 5. boundary of the reservoir hydrogeothermal, 6. superior direction of movement of thermal water, 7. superior direction of movement of cold water, 8. constructed boreholes, 9. thermal source.

Fig. 8. Forecast model of the geo-thermal field Istibanja – Vinica

The GTW from this hydro geothermal system is used in the greenhouse complex (6 ha), that is warmed using combination of geothermal water and crude oil. Supported by the grants from the Austrian government in the period after the year 2000, the system was reconstructed and prepared for production and export. The geothermal system Istibanja is using geothermal water from three exploitation wells with total capacity of 56 l/sec and water temperature of 67°C, connected with pipelines long 3,25 km. The actual available capacity that reaches the greenhouses (agricultural complex) is 50 l/sec with water temperatures of 61 °C.

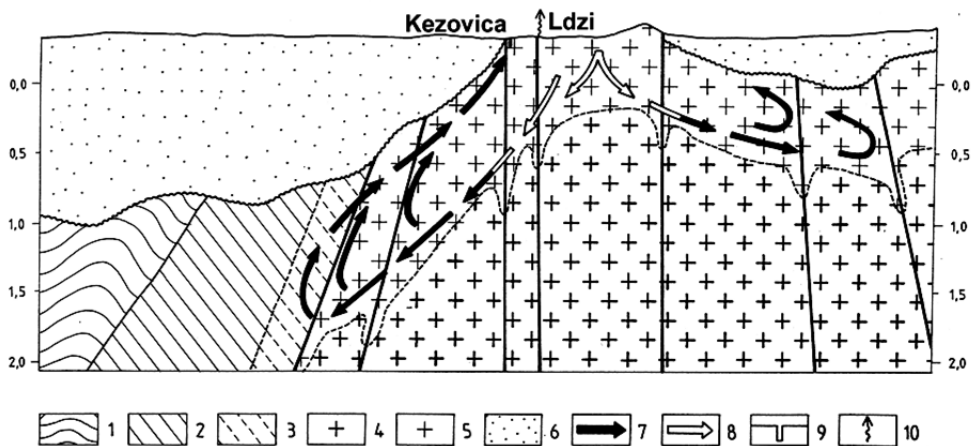
4.3 Hydro geothermal system Kezhovica - Shtip

On the right shore of river Bregalnica, approximately 2 km to the southwest from the center of Shtip, on the exit of Novo Selo, lays the geothermal system Kezhovica - Ldzhi (Fig. 9).



Fig. 9. Geothermal spring Ldži, near Shtip

Hydro geothermal system Kezhovica - Ldži is near of Kezhovica spa at Novo Selo - Shtip. The reservoir of this hydro-geo-thermal system is built on Jurassic joint granites (Fig. 10). Big part of these granites is covered with tertiary sediments of Ovchepole and Lakavichki basin (Fig. 11).



1. shall, 2. gneisses, 3. reservoir of gneisses, 4. massive granite, 5. cracked granite, 6. tertiary sediments, 7. superior direction of movement of thermal water, 8. superior direction of movement of cold water, 9. constructed boreholes, 10. thermal source.

Fig. 10. Forecasted model of the Kezhovica - Ldži geothermal system

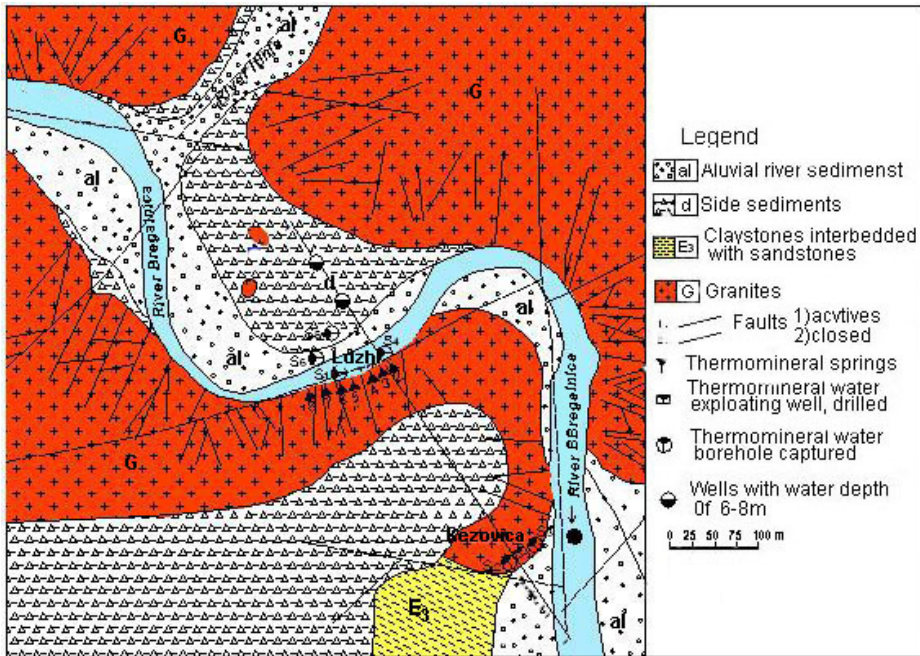


Fig. 11. Geological map of the hydro geothermal system of Kezovica Spa

Kezhovica spa today uses water from two shallow wells with capacity of 4,5 l/sec with temperature of 63°C. The supplementation of the system comes from the granite, south from Shtip. The chemic ingredient of the water shows supplementation also from the filch sediments Ovche Pole. According to the type, this system belongs to the half opened hydro geothermal systems. With chemical analysis of the water in this system is from Na-Cl type (Alekin,1953), and the calculate geothermometers are applying that the forecasted temperature of the tank is 100 - 115 °C.

The site of these geothermal waters is located between the hills Isar and Kumlako from the left and Marite from the right side of the river Bregalnica. In Kezovica, 30 years ago there w only one drilled well which was used as capping in the old Shtip spa, and by the Ldzhi, as nc capped thermo mineral water leaking in few places directly on the surface. With the research made in 1953 and with information gained, on the location of the old spa in the next few years new spa has been built, with modern areas and pools and also modern rehabilitation center has been built. Kezhovica as a spa is known since the Ottoman's Empire in Macedonia, when it was used as healing thermal water, too.

Contrary to Kezhovica, the locality Ldzhi, except the relatively shallow researched drills E the formed pipelines around these drills, until these days nothing more has been done researching of this hydro geothermal system (Kekic and Mitev, 1976).

Kezhovica Spa and the thermo-mineral system Ldzhi, although are well known as import hydro geothermal phenomena especially with their great radioactivity and healing characteristic for their exploration and valorization of their geothermal fluid, nothing particular

has been do Thermo-mineral waters in Kezhovica Spa are not overflowing, but today they are used by shallow wells with capacity of 4,5 l/s and water temperature of 57 - 63°C.

In Ldzhi locality there are more thermo-mineral waters in form of springs. Their maxi capacity is minimal and around 0,03-1,0 l/s. Captivated spring that exists today is with capacity 0,5-1,0 l/s. All these springs are with the same origin and are hydraulically connected, and t temperature varies from 28 - 59°C. The water in Ldzhi Spa has variable maximal capacity depends on the water in the river Bregalnica. It has the characteristic that with the raising of level of the water in the river Bregalnica, beside the capacity of the thermo-mineral water in L springs, there is uprising of the temperature of this water. That is explained with deep infiltrate of the river flow underground this terrain, through existing joints where the same has capability, besides the emerging of the capacity of the thermo-mineral water, to heat to a hi | temperature.

According to the results from ht chemical analysis of the thermo-mineral water in Kezhovica Spa and Ldzhi springs, it can be said that they are CI - Na waters. Total mineralization of the water in the capping of Kezhovica Spa is 1450 mg/l, and at Ldzhi springs varies from 1310,4 -1507,9 mg/l. Kezhovica Spa by its radioactivity belongs to one of the most radioactive thermo-mineral waters not only in Macedonia, but also in the wider region. The radioactivity in the capping Kezhovica is 42,82 Mach units, and the water in Ldzhi springs is 11,57 Mach units. This bigger radioactivity of the water in Kezhovica Spa related to the radioactivity of the water from Ldzhi springs, should be taken in consideration of the tectonic or seismic-tectonic activity of the main stratum that passes near Kezhovica, which is the main seismic dislocation that spreads from Strumica on the South through Kezhovica and Sveti Nikole all the way to Kumanovo (Kotevski, 1977).

During the years 1953 and 1964, there were six shallow explorative holes drilled (C-1 to C-6), and a large one (D-7). Their maximal capacity in terms of exploitation done in that period was 20 l/s. During the year 1983, nearby Ldzhi springs, on the right side of river Bregalnica, there was another research hole drilled, B-4 with maximum capacity of 30 l/s and with the temperature of the water 32°C. The temperature now is lowered because the water is a mixture of the surface Bregalnica water and hot water from the deep springs of cracked granites which are the tank (reservoirs) of this geothermal system, nearby Shtip.

The healing power of the water from Kezhovica Spa is in its high temperature, radioactivity and the chemical structure.

Total amount of the balanced reserves of the hydro geothermal system Kezhovica-Ldzhi are shown on Table 2.

Well number	Location	Capacity Q (l/s)	Water temperature t(°C)
S - 53 g.	Kezhovica Spa	2,7	62
B - 1/76	Kezhovica Spa	1,3	58
Total (1)	Kezhovica Spa	4,0	58 - 62°C
Well B - 2/97	Ldzhi	11,5	53
Well B - 3/97	Ldzhi	6,5	60
Total (2)	Ldzhi	17,5	53 - 60°C
Total (1) + (2)	Kezhovica Spa + Ldzhi	21,5	53 - 62°C

Table 2. Balance reserves of the Kozovica-Ldzhi systems

5. Utilization of the geothermal energy in the spa complexes

Macedonia although a small country is very rich in thermal and thermo-mineral water, that are currently used in the thermal spas and medical recreation centers. The geothermal energy of these geothermal and thermo-mineral waters is used in eight thermal spas, and four are located in the eastern and southeastern part of Macedonia. The thermo-mineral water in these complexes has various physical-chemical characteristics and temperatures, depending on the site and localization of the geothermal field where the spa complex is located. The water temperatures in the spas in Macedonia, starting with the highest are: Spa Bansko - 73°C, Kezhovica Spa - 54°C, Spa Negorci 38°C etc. With regards to the quantities of available flow of geothermal water in the spas in eastern and southeastern Macedonia: in Spa Bansko - 35 l/s, Kezhovica Spa - 5,4 l/s, Spa Negorci 1,8 l/s, etc. The utilization of the geothermal energy in the spa complexes in eastern and southeastern Macedonia and their thermal power are presented in Table 3.

Nr.	Location	Flow Q (kg/s)	Temp. (°C)	Thermal power for this temp. ¹ 15°C (MW _t)	Annual usage ² (TJ/year)
1	Spa Bansko	35	70	8,05	253,9
2	Kezhovica Spa	5,4	54	0,88	27,7
3	Negorci Spa	1,8	38	0,17	5,46
4	Kocani Spa	30	63	6,02	189,9
I	TOTAL	72,2		15,12	476,96

¹) Thermal power (MW_t) = Max flow Q (kg/s) h inflow T(°C) - outflow T(°C) × 0,004184 (MW=10⁶W)

²) Annual usage (TJ/year) = Average spend Q (kg/I) × inflow T(°C) - outflow T(°C) × 0,1319 (TJ/year)

Table 3. The utilization of the geothermal energy in the spa complexes in eastern and southeastern Macedonia and their thermal power

The planned reconstructions of the heating installations that use the geothermal water in the spa and recreational complexes in eastern and south-eastern Macedonia are still not implemented because of unsolved property issues. However, one can't expect positive developments unless the ownership over the public spa complexes is defined.

6. Comparison of the geothermal potential resources with the other sources of energy and the geothermal

In order to analyze the economic aspects of the exploitation of the geothermal energy as a power source, a unique and adequate access towards forming of the prices of every separate kind of energy source is needed, which are produced and distributed from the energetic systems, as well as for the market price of the oil at the moment when the analysis are being done. Macedonia is a part of the group of developing countries. After the independence in 1991, it entered the period of "transition" and change of the capital from public into private that also influenced the sector of industrial production and energy.

Macedonia as main power source is using domestic coal and hydro energy from power plants and imported oil. The utilization of the solar energy is insignificantly small related to the needs and the possibilities, and the utilization of the natural gas is still in a phase of preparation, but also it's imported. The energy from the biomasses is still in experimental phase.

The coal is the best researched power source in Macedonia. Total deposits of coal are 906.247×10^3 t.

The hydro power of the rivers in Macedonia is still not used enough and currently it's exploited in a thermal equivalent of 411 MW. The needs and the participation of every single power source in the energy balance of Macedonia is presented in Table 4.

Type of power sources	Annual consumption (TJ)	Part in the whole consumption (%)
Coal	59.700	56,13
Woods	10.097	9,49
Liquids	33.044	31,07
Renewable	500	0,47
Hydropower	2.498	2,35
<i>Geothermal</i>	510	0,48
Total	106.347	100

Table 4. The needs and the participation of every single power source in the energy balance of Macedonia

7. Hydrochemical analysis of tested water

In the recent period, from geochemical point of view, the best studied are thermo - mineral waters from the springs Ldзи and Kezovica. Further will be presented the hydrochemical characteristics of mentioned system.

Analyses of the chemical composition of the thermo - mineral waters, done on the samples from the exploited well in the spa and the springs Ldзи, showed that in both cases waters are of chloride - sodium, for the springs Ldзи of first type, and for the spa Kezovica of second type.

Total mineralization of the water from the spa Kezovica is 1450.0 mg/l, and from the springs Ldзи varies within 1310.4 to 1507.9 mg/l in the main spring, where in 1953 was drilled the borehole C-4. pH value of this spring and the spa Kezovica is 7.2, based on the examinations of "Industroproject" Zagreb this value is 7.6 for Kezovica and 7.8 for Ldзи Table 5. It is obvious that these waters are on the border between the neutral and alkaline.

About the hardness of the waters from these localities, the general hardness for the gathering on Kezovica is 8.5 dH^o, and the carbonate is 9.0 dH^o. For the springs Ldзи, the general hardness is 5.9 dH^o, and the carbonate is within 7.7 to 9.6 dH^o. The largest hardness in the springs Ldзи is in the spring No. 7 where the total mineralization is the smallest. Also, this spring has the lowest temperature (30^o C). Probably, it is because of mixing of the thermo - mineral waters with the water from the river Bregalnica, which could be seen on the terrain.

Analyses made from "Industroproject" Zagreb showed increased general hardness - For Kezovica 10 dH^o, and for the springs Ldзи 14 dH^o.

It should be said that there is no magnesium in the springs Ldзи, and in the gathered waters of the spa Kezovica, the amount of magnesium is 33.0 mg/l and according "Industroproject" Zagreb is 35 mg/l. the question arises why this is present when both waters appeared in the

ANIONS mg/l										CATIONS mg/l											
SO ₄ ²⁻	Cl ⁻	HCO ₃ ⁻	NO ₃ ⁻	NO ₂ ⁻	CO ₃ ²⁻	HBO ₃ ⁻	H ₂ AsO ₄ ⁻	SUM	Ca ⁺⁺	Mg ⁺⁺	Na ⁺	K ⁺	Fe ⁺⁺	SUM							
145.0	492.0	166.0	-	-	14.0	120.0	1.0	938.0	10.0	35.0	448.0	12.5	1.0	506.5							
COLOIDAL SOLVED OXIDES mg/l										SOLVED GASES mg/l						ELEMENTS IN					
Fe ₂ O ₃	MnO ₂	SiO ₂	Al ₂ O ₃	SUM	CO ₂	H ₂ S	NH ₄	SO ₂	Cl ₂	O ₂	SUM	Li	Cs	Br	As	Hg					
-	0.20	3.0	0.04	3.24	-	-	0.04	-	-	4.0	4.04	0.20	0.12	-	-	-					
TRACES mg/l										Radio-activity (Mah)						Curl's formula					
Rb	F	J	Sb	Pb	Total mineral (mg/l)	Dry residue (mg/l)	Lost of ignition (mg/l)	Total hardness (dH)	pH	Eh	t (°C)	Cl ₅₈ HbO _{3,7} SO _{4,13} HCO _{3,11} Ml.4-----t57 ⁰ Na ₈₄ Mg ₁₂									
0.15	2.5	-	0.002	0.001	1445.0	1400.0	1350.0	10.0	7.6	+210	57	11.57									

Table 5. Chemical analysis of thermo - mineral waters from spa Kezovica ("Industroproject" - Zagreb)

granites on the fault lines. It should be bearing in mind that thermo- mineral waters Kezovica are on the fault line between granites and Upper Eocene sediments and the springs Ldzi occurred in granites. Magnesium is always present in the sediments which is concluded and from the chemical analyses of the springs with cold water Ribnik (79.2 mg/l magnesium) and Krstot (28.8 mg/l magnesium) Table 6. Also, chemical analyses from Novo Selo showed presence of this element in range of 15.1 - 40.3 mg/l, which means that underground waters from the sediments contain magnesium unlike the waters from the granites.

7.1 Radioactivity

Based on the radioactivity, thermo - mineral waters in the vicinity of Shtip are different, although they are placed in the same rock masses and on the fault lines which through the transverse faults and the tectonic cracks communicate with each other. Based on the analyses of S. Miholik, radioactivity of the waters from the gathering of the waters in Kezovica is 42.82 Mache units (ME), and from Ldzi is 11.57 ME. Based on this, the spa Kezovica is one of the most radioactive spas in Europe.

The increased radioactivity of the water in Kezovica related to that from the spring Ldzi is because of the tectonic, i. e. seismo - tectonic activity of the main fault passing by the Kezovica. This fault is principal seismic dislocation that extends from Strumica, through Kezovica and Sveti Nikole to Kumanovo.

From this arises that with analysis of the radioactivity of dipper underground waters that followed the fault lines could help in exploration of contemporary seismic activity of this terrain.

8. Geological exploration and exploitation of mineral raw materials

Thermal mineral waters by their nature are classified in the group of energy mineral raw materials and are goods of common interest for Macedonia.

According to the Law on Mineral Raw Materials (OGORM no.18/99 and 29/02), a DGE aimed at finding, identifying deposits of thermal mineral water, as well as evaluating their economic effects is conducted by means of a concession.

The Law on Mineral Raw Materials regulates the conditions and the manner of conducting geological explorations, as well as the conditions for exploitation of mineral raw materials situated in the ground or on its surface, concessions for geological research and concessions for exploitation of mineral raw materials, the realization, the maintenance and the utilization of geothermal waters, work safety measures, environmental protection during the exploration and the exploitation of the given area and the geological measurements and plans.

The concession for conducting DGE is issued by the Government of the Republic of Macedonia. The Ministry of Economy, as the competent body responsible for coordination of the procedures for conducting DGE, undertakes inter-sectoral consultations with the state administration bodies with regards to the application for the concession, and primarily with the body responsible for environmental protection and water protection.

Mutual rights and obligations of the Government of the Republic of Macedonia and the concessionaire are regulated with a Concession Contract.

No.	Cadastral num.	Type and location of the object	Water temp. (°C)	pH	CATIONS (mg/l)							ANIONS (mg/l)					Dry residue on 110°C (mg/l)	General hardness (°dH)	Carbonate hardness (°dH)	Class, Group and type of water according Alskin			
					Ca ⁺⁺	Mg ⁺⁺	Na+K+Fe ⁺⁺	Σk (mg/l)	SO ₄ ⁻	Cl ⁻	HCO ₃ ⁻	CO ₃ ⁻	NO ₃ ⁻	NO ₂ ⁻	SiO ₂	Al ₂ O ₃					ΣA (mg/l)		
1	1	Drilled well spa "Kezovica"	58	7.2	15.1	33.0	483.3	0.15	467.5	162.4	511.2	195.2	15.5	-	-	75.0	1.2	886.3	1450.0	1419.2	8.5	9.0	Chloride, sodium, second type
2	2	Thermal well Novo Selo - Ldži	55	7.2	18.2	-	483.3	0.02	571.5	164.4	538.0	169.0	12.0	Trace	-	62.0	1.0	883.4	1507.9	1480.8	2.5	8.4	Chloride, sodium, first type
3	3	- II -	48	7.0	18.2	-	475.3	0.06	563.5	130.3	545.8	195.2	3.0	-	-	-	-	874.3	1437.8	-	2.6	9.0	Chloride, sodium, first type
4	4	- II -	41	7.0	15.1	-	481.7	0.02	496.8	164.8	539.6	164.8	6.0	-	-	-	-	875.2	1372.0	-	2.2	8.1	Chloride, sodium, first type
5	5	- II -	47	7.0	18.1	-	467.8	0.06	532.9	158.2	525.4	172.0	4.5	-	-	-	-	860.1	1400.0	-	2.6	8.1	Chloride, sodium, first type
6	6	- II -	43	7.0	18.1	-	482.9	0.26	501.2	179.5	543.2	156.7	6.2	-	-	-	-	885.6	1386.8	-	2.6	7.7	Chloride, sodium, first type
7	7	- II -	30	7.0	28.4	3.6	455.9	0.06	487.9	165.5	546.4	206.4	4.2	-	-	-	-	822.5	1310.4	-	5.9	9.6	Chloride, sodium, first type
8	12	Digged well Novo Selo	13	7.2	102.8	40.3	46.7	0.02	189.8	70.5	67.4	414.8	-	-	-	-	-	552.7	742.5	-	23.8	19.0	Hydrocarbonate, calcium, third type
9	9	- II -	15	7.2	21.1	15.1	56.5	0.02	92.7	42.6	33.7	335.5	-	-	-	-	-	411.8	504.5	-	15.1	15.4	Hydrocarbonate, calcium, first type
10	10	- II -	14	7.2	84.8	32.4	77.7	0.02	194.9	73.8	61.1	384.3	-	-	-	-	-	518.2	713.1	-	19.6	17.6	Hydrocarbonate, calcium, third type
11	13	Spring Ribnik	14	7.0	64.0	79.2	59.1	0.02	202.3	106.6	19.9	579.5	-	-	-	-	-	705.0	907.3	-	27.5	26.6	Hydrocarbonate, magnesium, second type
12	15	Spring Krstot	18	7.4	32.4	28.8	105.7	0.13	167.0	47.5	21.3	427.0	-	-	-	-	-	495.8	662.8	-	11.2	19.6	Hydrocarbonate, calcium, first type

Table 6. Chemical analysis of the underground waters – spa "Kezovica" and the wider vicinity

Concession for DGE is issued by the Government of the Republic of Macedonia based on a public tender and based on the application/offer submitted by an interested legal entity or natural person. In instances when there are no interested subjects for the public tender, the concession may also be granted based on an offer, which is submitted to the Ministry of Economy.

The applications for issuing a concession is accompanied by a topographic map with a scale of 1:25.000 or 1:50.000 with drawn boundaries of the area where DGE will be conducted or where the exploitation of mineral raw materials will be carried out, as well as a proof of the right to use the results of the DGE, if there have been other prior DGE conducted in the same area

The application for issuing a concession for DGE includes in particular:

- data of the applicant
- type of mineral raw material
- location where that particular mineral raw material is found, in this case geothermal water
- technical and technological explanation for the need to conduct DGE
- Certificate from the Ministry of Finance - Public Revenue Office stating that the applicant has paid all its taxes
- Certificate from the competent Court stating that applicant is not subject to a bankruptcy procedure.

If the area for which a concession for DGE or exploitation of mineral raw materials is being issued, is partially or completely state owned, the Government of the Republic of Macedonia at the request of the concessionaire will grant the use of that land.

A concession for DGE and for exploitation of mineral raw materials can be issued to a domestic or foreign legal entity or natural person (concessionaire) under the conditions stipulated by this Law and the Law on Concessions.

Before the approval of the concession for DGE, the Ministry of Economy will request an opinion from the competent body for environmental protection and protection of nature, the competent body for water protection, as well as other competent bodies.

The legal entity or natural person which has acquired the concession for conducting DGE automatically gains the right to receive a concession for exploitation of mineral raw materials, if the conditions for exploitation of mineral raw materials provided by this Law are fulfilled.

This right is acquired by submitting an application for receiving a concession for exploitation of mineral raw materials at least 6 months prior to the expiration of the concession for DGE.

The concession for DGE is granted for a particular location and for maximum period of 8 years, without a possibility for extension. The location for DGE or exploitation of underground waters or thermal mineral waters can not exceed 2,0 km².

The results obtained from the DGE under the terms of a concession are property of the concessionaire and can be sold for an adequate compensation.

Concessions for exploitation of mineral raw materials can be granted for a period of maximum 30 years with a possibility for extension of another 30 years, by signing a new Concession Contract. The application for extension of the concession is submitted at least 3 months prior the expiration of the period for which the concession is granted.

The concession for DGE and exploitation of mineral raw materials can be transferred to another party with the consent from the Government of the Republic of Macedonia. The amount for the concession is determined with the Concession Contract, which is adopted by the Government of the Republic of Macedonia based on a proposal from the Ministry of Economy.

9. Conditions for conducting DGE

Detailed geological explorations (DGE) can be conducted by a domestic or foreign legal entity or natural person, registered for performing the given activity, which fulfils the conditions prescribed by the Law on Mineral Raw Materials and other related laws. During the DGE, all measures for occupational safety and environmental protection must be provided and undertaken. Eventual damages made during the DGE are compensated according to indemnity regulations. DGE and exploitation of mineral raw materials can be conducted on a land or facilities which are public property, and in other areas which are protected by the Law only with a prior approval from a competent body.

DGE is initiated on a defined location based on a previously granted concession and approval for DGE.

The location for the DGE is a part of a terrain circumfered by dots, connected with straight lines and is spreading out to unlimited depth underground between the virtual planes which pass through those lines or natural boundaries which are recorded on the topographic maps, in an appropriate scale.

DGE of mineral raw materials are explorations which provide: detailed information for the hydrogeology of the terrain, the location, the capacity and genesis of the deposit of raw materials, the available deposits of raw materials and the exploitation possibilities accompanied by an assessment of the economic benefit.

The concessionaire has to obtain an Approval for conducting DGE from a competent body in order to start with the on-site works.

10. Approval for conducting detailed geological explorations (DGE)

Approval for conducting DGE is issued on the base of the application submitted by the legal entity or natural person. With the application for issuing of an Approval for DGE the following documents are submitted: Concession contract, Program for DGE, topographic map with the actual border lines of the research area in adequate scale.

The Approval for DGE contains:

- Information about the legal entity or natural person to whom the approval is issued.
- Mineral raw materials which are subject of the DGE
- The area of the DGE with specific coordinates
- The type and scope of the activities that should be performed
- The deadline to start with the exploratory work and
- The duration of the DGE and the deadline for the submission of a performance report on the DGE.
- The holder of the Approval can not start with the DGE, unless he has resolved all property and legal issues for the area defined in the Approval for DGE.
- Approval for DGE is issued within 60 days from the day when the application was submitted.

Against the decision with which the application for the approval is rejected, a complaint can be submitted within 15 days from the day of its receipt, to the Committee for resolving administrative procedures of the second instance in the area of economy of the Government of the RM.

The Ministry of Economy can revoke the Approval from Article 33 of this Law, if the legal entity or natural person which is conducting the DGE doesn't start within the determined deadline or if the explorations have been stopped for more than 3 years, unless the reasons for this stoppage were of technical or economic nature, or if the holder of the Approval is not responsible for the reasons for stopping (*vis major*).

After the stopping or completion of the DGE it's obligatory to file a report to the Ministry of Economy, i.e. an Elaborate for the conducted explorations is being prepared, with complete documentation of the results. The results obtained with the DGE are property of the concessionaire and can be alienated for an appropriate compensation.

11. Exploration of geothermal waters

According to the Law on Mineral Raw Materials which also includes geothermal waters, exploitation of mineral raw materials is an act of obtaining, or releasing mineral raw materials from their natural state (*in situ*), including the preparatory, accompanying and consequent activities related to the exploitation of mineral raw materials. Exploitation of geothermal waters is carried out in a specifically defined space, determined in accordance with the DGE report. The area for the DGE or exploitation of underground waters or geothermal water is maximum 2 km².

The right of exploitation of mineral raw materials, which include geothermal waters, is obtained through the granting of a concession for exploitation of geothermal waters.

Before the concession for exploiting is issued, the Ministry of Economy, as a the body responsible for coordination of procedures for exploitation of mineral raw materials, conducts inter-sectoral consultations with other state administration bodies regarding the application for the issuance of a concession, and primarily with the competent body for protection of the environment, waters, forests and cultural heritage, as well as the competent body for transport infrastructure.

The concession for conducting exploitation is granted by the Government of the Republic of Macedonia. The period for which the concession is granted is limited by law to 30 years. The mutual rights and obligations of the Government of the Republic of Macedonia and the concessionaire are regulated with the concession contract.

The issuance of concessions for exploitation of geothermal waters, as well as for other mineral raw materials in accordance with the Law on Mineral Raw Materials (OGORM no. 19/99 and 29/02) is performed by the Government of R.M based on a public competition or on application/offer of an interested legal entity or natural person.

The application for granting a concession for exploitation of geothermal waters as well as for other mineral raw materials should contain:

- data of the applicant
- proof of the right to use the results of the conducted DGE
- type of mineral raw materials
- location where the mineral raw material is identified, or in this case the geothermal water
- topographic map on a scale of 1:25.000 or 1:50.000 with coordinates of the border lines of the location
- technical and technological explanation of the exploitation of geothermal waters
- Certificate from the Ministry of Finance - Public Revenue Office of paid public taxes by the applicant
- Certificate from the competent Court certificate stating that the applicant is not subject to a bankruptcy procedure and
- Certificate form the competent Court that no bans for performing activities has been issued against the applicant

The exploitation of the geothermal waters can start after the approval for exploration is given to the applicant.

This approval is issued by the Ministry of Economy. For the purpose of granting of the approval for exploitation, the applicant should submit the following:

- Concession contract for exploitation of mineral raw materials.
- Main project for exploitation of mineral raw materials and the deposit, with an expert assessment (review).
- *Elaborate on the environmental impact assessment.*
- Decision for utilization of constructed facilities foreseen in the main project, successively after their construction.
- Proof of resolved property legal relations (this refers to resolved property legal relations with regards to the micro-location of geothermal exploitation)
- Situational plan with defined borderlines of the area where exploitation of the mineral raw materials will be conducted, to the extent it allows defining the boundaries of the area, as well as defining public and other facilities.
- Transfer of concession for carrying out the exploitation of mineral raw materials (geothermal waters) can be carried out in accordance with the Government of the Republic of Macedonia.

The Ministry of Economy can revoke the Approval for exploitation from Article 63 of the Law on Mineral Raw Materials (according to the Law on Changes and Amendments to the Law on Mineral Raw Materials, OGoRM no. 29/02) if the performer of exploitation of mineral raw materials doesn't start within 3 years of the day of the issuance of the Approval, or if regular exploitation was stopped for more than 3 years, unless the reasons for the stoppage were of technical or economic nature, or if the holder of the Approval was not responsible for the reasons for the stoppage (*vis major*).

Supervision over implementation of the Concession Contract is carried out by the Concedent, i.e. the Ministry of Economy and the State Inspectorate for Technical Inspection through mining and geological inspectors.

The amount of the concession fees is determined with a special Decision for determining the criteria for the amount of the concession fee for conducting DGE and exploitation of mineral raw materials, adopted by the Government of the Republic of Macedonia.

It's important to note that the calculation of the concession fee is done per production unit of produced mineral raw material.

For a complete overview of the administrative procedure for concessions for geological explorations and exploitation of mineral raw materials, including geothermal water, a brief presentation of the required documents and the procedure is provided below.

12. Commentary instead of conclusion about the legislation for issuing concessions for exploiting the geothermal energy in the Republic of Macedonia

Geothermal resources (geothermal waters and their geothermal energy) by their nature are classified in the group of energy mineral raw materials and are goods of common interest of the country, according the Law on Mineral Raw Materials (OGoRM no. 18/99 and 29/02). Detailed geological explorations (DGE) aimed at finding; identifying deposits with thermal mineral water, as well as evaluating their economic effects are conducted through concession. Concession as an institute in legislation entails obtaining a certain right, with or without certain conditions, for a limited or unlimited time. A Concession for DGE, as well as Concession for exploitation of mineral raw materials, can be issued to a domestic and foreign legal entity and natural person (concessionaire) under the conditions defined by the Law on Mineral Raw Materials and Law on Concession. With regards to geothermal energy, the experiences in this area show that two types of concession are characteristic: the right to perform geological explorations in order to identify the energy resource and right to use the resource under specific conditions. Unfortunately, this is where all similarities with mineral raw materials end, because the concessions mostly apply to using hot water or steam, which automatically includes the application of the Law on Waters. Because of the potential negative environmental impact caused by the use of hot water and water with high mineral content, the legal provisions related to environmental protection are applied in conjunction with the Law on Ecology.

This immediately poses the question whether is it possible to harmonize three different legal areas in order to ensure more efficient resolution of the problem, and if this is not possible,

is it necessary to create a special legislation for utilization of geothermal energy, which will define all aspects involved in geological exploration and exploitation of this specific energy resources. Concessions are granted by the Government of the Republic of Macedonia, based on a submitted application.

There is a clear difference in the legislations of European countries regulating the obtaining of licenses for exploration and exploitation of the geothermal resources, as a consequence of the specific development of the legislations in general and the specificities of the geothermal resource themselves. However, the application in practice of certain provisions is common for all European countries, and the Republic of Macedonia should strive and move in this direction, as described below:

Ownership of the energy resource

Geothermal energy resources are owned by the state and can not be alienated. The ownership of the energy resource is in no form related to the ownership of the land under which the resource is located. The former means that the owner of the land has no right to obstruct any investigations or exploitation of the energy resource, regardless of the use of the land, but in the same time means fair compensation for possible damages made in the course of exploration, building the infrastructure or exploitation. The owner of the land is given priority in applying for concession for DGE or exploitation if he offers the same or approximately the same conditions as the most favourable offer, because the concessions are issued through a public tender.

Conducting of exploratory work for identification of the energy resource

The state issues Approval for DGE under strictly defined procedures and conditions only to qualified companies and institutions which have to provide technical documentation and bank guarantees, ensuring its implementation. The role of the state is to control and provide full protection of the energy resource and the environment where the exploration is carried out or to prevent speculations aimed at stopping the activities for activating the energy resource.

Exploitation of the geothermal resource

The state grants the rights for exploitation of the geothermal resource under strictly defined procedures and conditions. The license for exploitation of the energy resource entails full protection of the energy resource from excessive or improper usage. The right to control also means accepting direct responsibility to the holder of the concession i.e. the state can not issue concession for geothermal fields for which it has already issued concessions to specific users.

In the procedure for issuing concessions for exploration and exploitation, it is important to emphasize the system of dual responsibilities i.e. full protection of the rights of the state, but also the rights of the holders of the license for exploration and exploitation of the energy resource. The more they are defined by law in a clear and directly applicable manner, the more their practical application will be efficient.

All these aspects in the development of the legislation regulating the issuance of concessions for exploration and exploitation, and consequently the utilization of the geothermal energy, are mostly applied in various European countries that have a tradition in the utilization of

this specific resource and can provide useful insights for the development of a concrete legislation in the Republic of Macedonia.

The implementation of the current Law on Mineral Raw Materials in practice, as well as the taking of responsibilities as a result of the need for approximation of Macedonian with European legislations, lead to the need to draft a new Law on Mineral Raw Materials. The law proposal was drafted by the Ministry of Economy in collaboration with the German Technical Cooperation (GTZ).

The main characteristic of the new law proposal is that a much clearer systematization of the provisions is applied as compared to the existing one. Also, the proposal for adoption of the Law incorporates Directives which are indirectly transposed in this Law through the Law on Environment.

Other specific new feature of the text of the law proposal is the introduction of the National program for development and planning in the field of mineral raw materials. This National program defines the scope, goals and guidelines for the geological exploration, as well as the sustainable utilization of mineral raw materials, while respecting the specificities of different areas, the features and distribution of mineral raw materials, and the need for exploitation of mineral raw materials which are crucial for the development of the economy of the Republic of Macedonia.

The new text of the law also proposes that the rights for DGE is to be obtained through an approval that will be issued by the competent body for management of mineral raw materials (until now the right to conduct DGE was obtained through the granting of a concession for DGE). Another novelty in the law proposal is the possibility for transfer of the license for DGE another person, but under the same conditions. Also, the rights from the finished DGE can be transferred to a third person, which is in accordance with the principles of market economy. The right to exploit mineral raw materials will be obtained through the granting of a concession for exploitation of mineral raw materials. There are two ways for the granting of a concession for exploitation of mineral materials which are foreseen. The first one is through a public tender in cases which are stipulated in the National Program for Development and planning in the area of mineral raw materials, as well as when the Republic of Macedonia possess revised elaborates of conducted individual DGE. In accordance with market economy principles, the text provides full or partial transfer of the concession for exploitation of mineral raw materials under strictly defined conditions. The criteria, amount and the method of payment of the concession fees will be determined by the Government of the Republic of Macedonia, in accordance with the principles of market and open economy.

Another important new feature is the allocation of funds received from concession fees.. This law proposal stipulates that half of the funds from concession fees for exploitation of mineral raw materials (which includes thermal mineral waters) are to be transferred to the Budget of the Republic of Macedonia, and the other half to the budget of the Municipality where the exploitation takes place (50%-50%). It also introduces the obligation for rehabilitation of damages caused by the operations of the entity in the course of exploitation of mineral raw materials. The main intention of the new law is to emphasis

the commitment to protecting the environment. Consequently, it imposes an obligation on the performers of the DGE and exploitation of mineral raw materials to comply with the requirements of this law and the Law on Environment and it reinforces the penal policy in the area of exploitation of mineral raw materials and geothermal waters as a mineral raw material.

13. Conclusions

1. Geothermal energy is not a "new" and unknown source of energy in our country. The same is proven in the past with its economic benefit and it is competitive to any other kind of energy source in Macedonia.
2. In eastern and eastern Macedonia, at the moment are registered over 30 springs and occurrences of mineral and thermo-mineral waters with maximum capacity of more than 1.400 l/s and evidenced deposits for exploitation of around 1.000 l/s with water temperatures from 20-79°C, with significant quantities of geothermal energy.
3. The calculation of the valorization of the total balance of the geothermal exploitation reserves in eastern and south-eastern Macedonia (standing 2006) shows: maximum available power is equal to 173 MW or capacity for annual production of 1.515.480 MWh/ year as heat equivalent.
4. Eastern Macedonia has numerous occurrences of thermal and thermo-mineral water that are used in spas and recreational medical centers in the balneology sphere. The geothermal energy from this thermo-mineral water is used in four existing thermal spas with total yield of 250 l/s, total caloric power (heating power) of 35 MW and annual exploitation of 112.5TJ.
5. Taking in consideration that the existing production capacities are based either upon natural springs or shallow boreholes, the maximal current capacity can not give the actual picture for the real capacity of this energetic resource. Based on the existing data it is evident that if supported with relatively small investments in the already started exploration works of these potentials during the 80's of the past century, the capacity could be easily doubled. By providing bigger support it could help to increase and multiply the current capacities over 4-5 times in the next few years. Anyway, the amount of the investments needed for exploration and exploitation of geothermal water wells, points out that without direct support from the state it is not possible to enjoy the benefits of this energy. That is why the Government should treat the geothermal resources as energy of special importance.
6. Further explorations of the geothermal energy above all requires changes in the attitude toward this kind of energy and the dealing with the legislation in this area, which will help to reach a higher level in the utilization of the geothermal waters. This is especially applicable for the hydro geothermal waters with temperatures lower than 40°C that still are not used as energy source. A question which could be imposed here: Is it necessary to adopt special legislation for utilization of the geothermal energy which will define all the aspects in the field of geological explorations and the utilization of this specific energetic resource.
7. Future exploration works in eastern and south-eastern Macedonia should be focused in the already registered areas where there is an indications for increased terrestrial

thermal flow (yield), and registered superficial manifestations from the previous geothermal explorations like in the Delchevo region, broadening of Vinica and Kochani geothermal field, Probishtip region, Radovish region, Dojran - Valandovo-Gevgelija region, in the Vardar zone and the contact-part with the Serbian-Macedonian massif in Bregalnica-Strumica region.

14. References

- Alekin, O. A., 1953: Basics of Hydrochemistry, Leningrad
- Arsovski, M., 1997: The tectonics of Macedonia. Faculty of Mining and Geology - Stip. Page 300.
- Arsovski, M., Stojanov, R., (1995): Geothermal phenomenon related to the Neotectonics and the magmatism in the area of R. Macedonia. Special edition, MANU, Skopje.
- Bonchev, E., 1974: Kraistides. Tectonics of the Carpathian ' Balkan Regions, Bratislava.
- Dimitrievic, M., (1974): The Serbo-Macedonian Massif. The tectonics of the Carpathian-Balkan Regions. p.p. 291-296, Bratislava.
- Georgieva, M., 1995: Geothermal resources in the area of Vardar and the Serbian - Macedonian mass in the territory of Macedonia (Doctoral dissertation) Faculty of Mining and Geology - Stip page 190.
- Kekic, A., Mitev, Z., 1976: A report on the thermo-mineral waters of the bath Kezovica and Ldзи with a special review on the drilling process in the bath in 1975-1976. Professional fund of the Institution of Geology - Skopje.
- Kotevski, G., 1977: Hydrogeological research on minerals and thermal waters on the territory of S.R. of Macedonia (Final analysis). Professional fund of the Institution of Geology - Skopje.
- Kovacevic, M., Petkovski, P., Temkova, V., 1973: Explanation for sheet Delcevo, BGM SFRY, M 1:100 000, Geological Institute, Skopje.
- Miholic S. 1953 - Previous report on the research on the thermo-mineral waters of the Stip spa and the acid waters in Bogoslovec. Professional archives of spa Kezovica - Stip
- Miholic S. 1953 - A report on the research on the thermo-mineral waters in the spa Stip (spring Ldзи). Professional archives of spa Kezovica - Stip
- Naunov, J., 2003: Geothermal system Geoterma. Second conference for geothermal energy in Macedonia (Proceedings). Bansko. Pages 5-15.
- Popovski K., Micevski E., Popovska-Vasilevska S., 2005 Macedonia - Country Update 2004, Proceedings, World Geothermal Congress, Antalya, Turkey, 24-27.
- Rakicevic, T., Kovacevic, M., 1973: Basic geological map of SFRJ, sheet Delcevo, M 1:100 000, Geological Institute, Skopje.
- Serafimovski, T. 2001: The relationship between geothermal systems and hydrothermal mineralization systems. First Counseling on geothermal energy in Macedonia., Bansko, Proceedings.
- Vidanovic M. 1955 - Proposal for central therapeutic facility in the bath Kezovica. Professional archives of spa Kezovica - Stip.

Vidanovic M. 1955 - Anticipating indications for treatment and the use of thermo-mineral waters in the bath Kezovica. (A foundation for building bath facilities). Professional archives of spa Kezovica - Stip.

Using a Multi-Scale Geostatistical Method for the Source Identification of Heavy Metals in Soils

Nikos Nanos¹ and José Antonio Rodríguez Martín²

*¹School of Forest Engineering - Madrid Technical University
Ciudad Universitaria s/n, Madrid*

*²I.N.I.A. Department of the Environment, Madrid
Spain*

1. Introduction

For quite a long time, soil has been considered a means with a practically unlimited capacity to accumulate pollutants without immediately producing harmful effects for the environment or for human health. Presently, however, we know that this is not true. Public awareness has been raised on the harmful potential of some soil trace elements –commonly known as heavy metals- that can accumulate in crops and may end up in human diet through the food chain. Many studies have confirmed that heavy metals may accumulate and damage crops or even mankind (Otte et al., 1993; Dudka et al., 1994; Söderström, 1998). Along these lines, the most dangerous metals owing to their toxicity for human beings are Cd, Hg and Pb (Chojnacka et al., 2005).

Natural concentration of heavy metals in soil is generally very low and tends to remain within very narrow limits to ensure an optimum ecological equilibrium. Nonetheless, human activities that involve emitting large quantities of heavy metals into the environment have dramatically increased natural concentrations in the last century. Although soils are quite capable of cushioning anthropogenic inputs of toxic substances, there are times when this capacity is exceeded, which is when a pollution problem arises.

The natural concentration of heavy metals in soils depends primarily on geological parent material composition (Tiller, 1989; Ross, 1994; Alloway, 1995; De Temmerman et al., 2003; Rodríguez Martín et al., 2006). The chemical composition of parent material and weathering processes naturally conditions the concentration of different heavy metals in soils (Tiller, 1989; Ross, 1994). In principle, these heavy metals constitute the trace elements found in the minerals of igneous rocks at the time they crystallize. In sedimentary rocks, formed by the compactation and compression of rocky fragments, primary or secondary minerals like clays or chemical precipitates like CaCO₃, the quantity of these trace elements depends on the properties of the sedimented material, the matrix and the concentrations of metals in water when sediments were deposited. In general, concentrations of heavy metals are much higher in igneous rocks (Alloway, 1995; Ross, 1994). Nonetheless, these ranges vary widely, which implies that the natural concentration of heavy metals in soil will also vary widely.

Variability of heavy metals in soil is also associated with the variability of the physico-chemical properties of soil. pH, organic matter, clay minerals, metal oxides, oxidation-reduction reactions, ionic exchange processes, or adsorption, desorption and complexation phenomena, are the main edaphic characteristics relating to retention of metals in soil. Nonetheless, some metals show a strong affinity to organic matter, while others have a strong affinity to clays, and to Fe and Mn oxides; yet they are elements which tend to precipitate in a carbonate form. Most of these soil properties will depend on the geological parent material. However, they will also be subject to not only the electric charge of metals in relation to the former saturation of other ions, but to all the interactions taking place naturally among the various edaphic parameters.

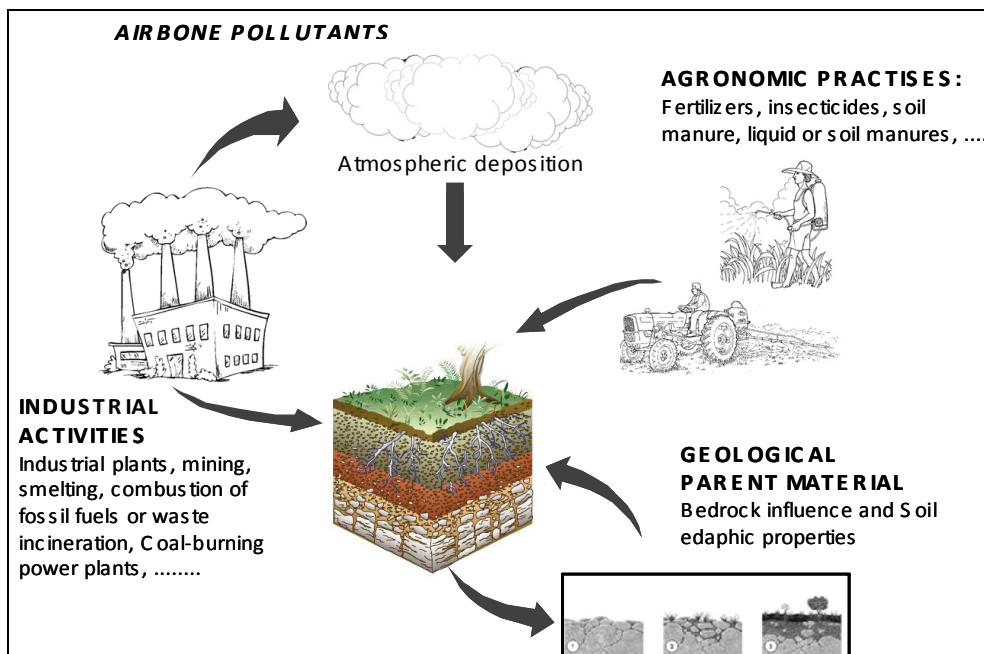


Fig. 1. Heavy metal input in soil

1.1 Anthropogenic influence on the content and distribution of heavy metals in soil

Many productive activities like mining, smelting, industrial activity, power production, pesticides production or waste treatment and spillage, represent sources of metals in the environment (Gzyl, 1999; Weber & Karczewska, 2004). The concentration of metals in soil can increase directly, or be due to the impact of atmospheric deposition (Figure 1) caused by proximity to industrial plants (Colgan et al., 2003) or through fossil fuel combustion (Sanchidrian & Mariño, 1980; Martin & Kaplan, 1998). Thus the atmosphere, which is an important means of transport for heavy metals originating from various emission sources, is the first factor that enriches soil in heavy metals. Although the natural entrance of metals to the atmosphere derives from volcanoes and the evaporation of the earth's crust and oceans, the main current input is of an anthropic origin. Airborne pollutants produced by mining, combustion of fossil fuels or waste incineration have significantly increased the emission of

heavy metals into the atmosphere, which are subsequently deposited on the soil surface by deposition (Figure 2). The effects of this pollution can become evident in soil at a distance of hundreds of kilometers from the emission source (Hutton, 1982; Nriagu, 1990; Alloway & Jackson, 1991; Navarro et al., 1993; Engle et al., 2005).

In addition, normal agricultural practices may cause enrichment of heavy metals (Errecalde et al., 1991; Kashem & Singh, 2001; Mantovi et al., 2003). These practices are an important source of Zn, Cu, and Cd (Nicholson et al., 2003) due to the application of either liquid and soil manure (or their derivatives, compost or sludge) or inorganic fertilizers. Finally, there is also the pollution resulting from spillages, which are normally isolated and easy to identify, generally because they lead to very high values which multiply the expected soil content by several units. These sporadic sources of pollution are not usually observed in areas employed for growing crops.

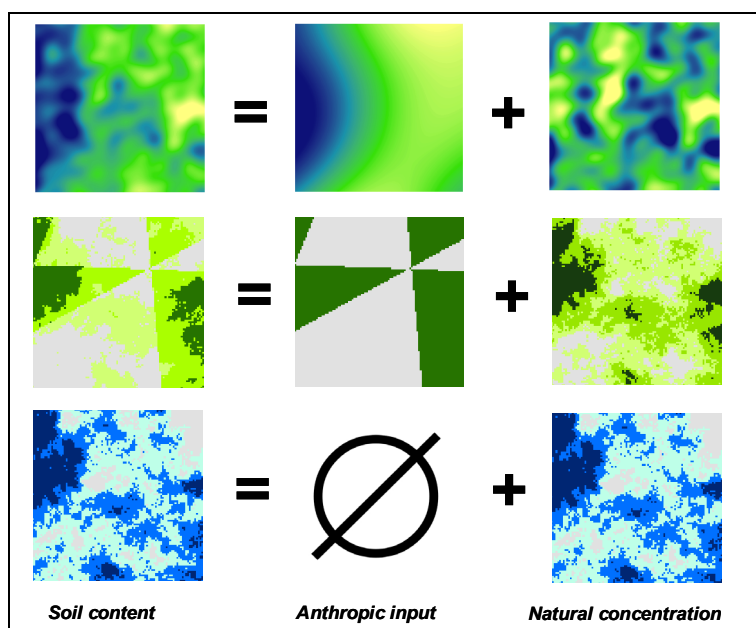


Fig. 2. Schematic representation of multiple sources of heavy metals in soil. In the upper panels, we present the spatial distribution of a heavy metal enriched by airborne pollution – and subsequent deposition-. In the middle panels, we provide a hypothetical example of a heavy metal enriched by agricultural practices such as fertilization (green indicates input of heavy metals). In the lower panels, natural soil content is assumed to not be enriched by any human activity. Note that in real case studies we may only observe the sum of two inputs.

1.2 Identification of sources of soil heavy metals

Source identification and apportionment of metal elements in soil are not straightforward. Quantities of metals introduced into soil through industrial activities, or any other human activity, do not provide any trace of their anthropogenic origin and, once inside soil, they behave like any other similar natural analogue which is already in soil. Likewise metal like

copper, which forms part of soil after fertilizing farmland, shows no distinguishing element of its origin. This makes us wrongly think that human input does not exist if the total concentration in soil does not reach levels considered to be polluting. Consequently, what we observe in the analysis of these elements in soil tends to result from summing the two inputs (Figure 2).

Despite the difficulty of separating human input from natural input, the separation task is greatly needed for correct edaphic resource management and to prevent its pollution. In this chapter, we present a multiscale geostatistical method known as a factorial kriging analysis which -under certain circumstances- can provide a mathematical framework to distinguish natural soil enrichment from that of an anthropogenic kind in heavy metals. The method was initially presented by Matheron (1982) and has been used repeatedly in soil science (Goovaerts, 1992, Castrignano, 2000, Rodriguez et al., 2008).

1.3 Description of the study areas used in the analysis

The information used in this chapter originates from the sampling and the analysis of the two most important hydrographic basins in Spain (Figure 3) in a study conducted to obtain reference values in Spanish soils (Rodríguez et al., 2009). They all present different lithologies and geologies, as well as common edaphic processes. Likewise, they also reflect possible inputs from both farming treatments and industrial activities which modify the contents and distribution of these elements in each valley.



Fig. 3. Localization of the Duero and Ebro basins. Soil samples are plotted over the two river basins

1.3.1 The Duero basin

The Duero river basin is the largest of its kind in the Iberian Peninsula, with a total surface of 97,290 km², of which 78,954 km² are found in Spanish territory (Confederación Hidrográfica del Duero, www.chduero.es). From a geological point of view, the hydrographic Duero basin consists of a well-defined geological unit, the Duero depression and its borders. The Duero Basin is an intraplate continental basin which developed from the Late Cretaceous to the Late Cenozoic. Over this time span, the basin acted as a foreland basin of the surrounding Cantabrian Zone and the Basque-Cantabrian Range in the north, the Iberian Range in the east and the Central System in the south, which constitute complex fold and thrust belts. These Alpine compressional ranges, constituted by Palaeozoic and Mesozoic rocks, are thrusting, in many cases, the Cenozoic deposits of the Duero Basin, which are virtually undeformed (Gomez et al., 2006). The basin is filled mainly with siliciclastic sediments on the margins and evaporites in central areas, showing an endorrheic arrangement (Tejero et al., 2006). The basin's general facies distribution corresponds to a continental foreland basin model with alluvial fan deposits grading into alluvial plains, and evaporitic and carbonated lacustrine environments toward the centre of the basin (Gomez et al., 2006).

The total population in the basin is around 2,210,541 inhabitants (Municipal Register, 2006), which has barely varied in the last hundred years. The Spanish Autonomous Community of Castilla y León is one of the main cereal-growing areas in Spain. Apart from pulses, such as carob and chickpea, the practice of growing sunflowers has extended in the southern countryside. However, the number of cultivated vineyard hectares (56,337 ha) lowered considerably in the last three decades of the past century.

1.3.2 The Ebro basin

The Ebro Valley, in the northeast region of the Iberian Peninsula, is framed by three mountain ranges: the Pyrenees to the north, the Iberian Chain to the southwest, and the Catalonian Coastal Ranges to the southeast. The structural development of these ranges controlled the evolution of this basin in tectonic and structural terms, and as regards stratigraphic and sedimentologic aspects. The Pyrenean range is a fold and thrust belt that developed during the Tertiary (the following 60 million years) as the Iberian block converged toward the European Plate. Its metamorphic core marks the border between France and Spain, with foreland structures verging into both countries. The tertiary stratigraphic units also increase in thickness northwardly. The tectonic load of the allochthonous units and the formation of a cold lithospheric root during Pyrenean shortening induced the deflection of the Ebro basin (Brunet, 1986; Roure et al., 1989). The depth of the Tertiary basin increases northwardly, reaching values of 4000 m beneath the sea level below the Pyrenees (Riba et al., 1983). The most exposed rocks within the basin area are of the Oligocene-Miocene age (including clastic, evaporite and carbonate facies) and of an alluvial and lacustrine origin (Riba et al., 1983; Simon-Gomez, 1989). During the Quaternary, incision of the drainage system caused the isolation of structural platforms, the tops of which are composed of near-horizontal Neogene limestones. Contemporaneously, several nested levels of alluvial terraces and sediments developed (Simón and Soriano, 1986). The Quaternary levels comprise mainly gravels, sand and slits.

The Ebro river region, with a population of around 3.25 million, is intensively industrialized. The Ebro river region is also an important agricultural area in Spain, with 4.2 million ha (Fig. 1) of agricultural topsoil (the total basin area is 9.5 million ha).

1.3.3 Soil samples and chemical analysis

The sampling scheme was based on an 8x8 km grid. Samples were located using GPS and topographic maps on a scale of 1:25,000. Each sample was defined as a composite made up of 21 subsamples collected with the Eijkelkamp soil sampling kit from the upper 25 cm of soil in a cross pattern. Further details can be found in Rodríguez et al. (2009).

Soil samples were air-dried and sieved with a 2 mm grid sieve. Soil texture was determined for each sample. After shaking with a dispersing agent, sand (2 mm–63 μ m) was separated from clay and silt with a 63 μ m sieve (wet sieving). A standard soil analysis was carried out to determine the soil reaction (pH) in a 1:2.5 soil-water suspension (measured by a glass electrode CRISON model Microph 2002) and organic matter (%) by dry combustion (LECO mod. HCN-600) after ignition at 1050°C and discounting the carbon contained in carbonates. Carbonate concentration was analyzed by a manometric measurement of the CO₂ released following acid (HCl) dissolution (Houba et al., 1995).

Metal contents (Cr, Ni, Pb, Cu, Zn, Hg and Cd) were extracted by aqua regia digestion of the soil fraction in a microwave (ISO 11466, 1995). Heavy metals in soil extracts were determined by optical emission spectrometry (IPC) with a plasma spectrometer ICAP-AES. Mercury in soil extracts was determined by cold vapor atomic absorption spectrometry (CVAAS) in a flow-injection system. The summary statistics of soil parameters and heavy metal contents are listed in Table 1.

	Duero basin 721 soil samples					Ebro basin 624 soil samples				
	Mean	Median	S.D.	1st Qu	3rd Qu	Mean	Median	S.D.	1st Qu	3rd Qu
<i>S.O.M</i>	1.74	1.3	1.494	0.88	2.08	2.24	2	1.41	1.4	2.6
<i>Soil pH</i>	7.19	7.7	1.234	6	8.3	8.04	8	0.59	8	8.4
<i>E.C</i>	0.18	0.15	0.16	0.1	0.21	0.59	0.27	0.85	0.21	0.45
<i>CaCO₃</i>	9.41	3	14.45	1	10.1	29.68	31	16.08	20	40
<i>Sand</i>	59.2	61	19	46	75	38.67	38	17.09	26	50
<i>Silt</i>	20.9	19	12.7	10	31	22.05	21	8.7	16	27
<i>Clay</i>	19.9	19	10.6	12	26	39.41	39.4	13.08	30	48
<i>Cr</i>	20.53	18	14.9	10	27	19.82	18	11.18	13	24
<i>Ni</i>	15.08	13	9.99	8	20	19.26	18	8.64	13	23
<i>Pb</i>	14.06	13	6.79	9	17	16.98	15	7.63	12	20
<i>Cu</i>	11.01	10	7.84	6	15	16.68	13	11.89	10	21
<i>Zn</i>	42.42	38	23.01	27	53	57.4	55	24.27	41	69
<i>Hg</i>	42.05	30	58.43	18	50	33.83	27	38.66	16	44
<i>Cd</i>	0.159	0.1	0.14	0.07	0.2	0.413	0.4	0.159	0.3	0.5

1st Qu, 3rd Qu, first and third quartile; SD, standard deviation ; SOM, soil organic matter (%); CaCO₃, carbonates (%); EC, Soil electrical conductivity (dS m⁻¹)

Table 1. Statistical summary of metal concentrations of soil (in mg/kg for Zn, Fe, Cu, Cd and μ /kg for Hg) and some soil properties.

2. Factorial kriging analysis

2.1 Univariate analysis

Usually physical and chemical soil variables are intrinsically structured around more than one scale of variation, and it is up to the researcher to identify the most important one(s) for his/her study. In factorial kriging -and in geostatistics in general- identification of the scale (or scales) of variation of a variable is done via the variable's sample (or experimental) variogram.

Let us consider a regionalized variable sampled at N points $\{ x_a : a=1, \dots, N \}$ such as the Cd concentration in Ebro basin top soil. The sample variogram for Cd is then computed according to the formula:

$$\hat{\gamma}(h) = \frac{1}{2N(h)} \sum_{x_\beta - x_\alpha \approx h} [z(x_\beta) - z(x_\alpha)]^2 \quad (1)$$

where $N(h)$ is the number of pairs of data locations separated by, approximately, distance h and $\hat{\gamma}(h)$ the semivariance for lag h . In fact, the sample variogram is constructed by grouping pairs of observations into several discrete distance classes or lags. The average separation distance of all the pairwise points falling within lag h is plotted against half the average semivariance for each lag computed with formula 1, giving raise to a scatter plot similar to that depicted in Figure 4. Typically, semivariance exhibits an ascending behavior near the origin ($h=0$), whereas at longer separation distances, it levels off at a maximum value called the variogram sill. The distance at which the sill is reached is called the variogram range, while the term nugget is used for the semivariance value at a distance of $h=0$.

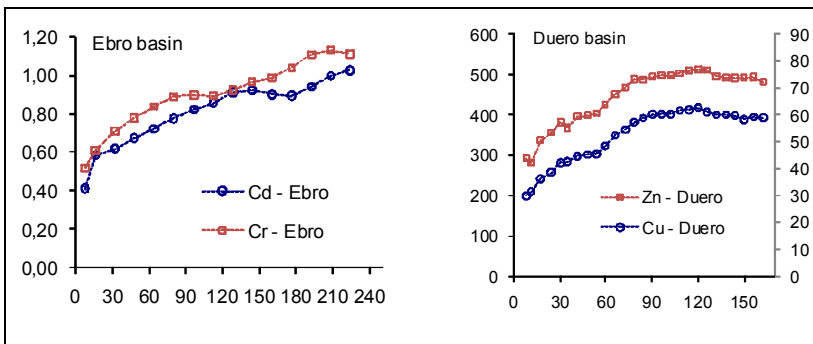


Fig. 4. The sample variograms for Cd and Cr (Ebro river basin) and for Zn and Cu (Duero basin). Horizontal distance is measured in km; vertical axes project the semivariance for a certain distance lag. Note also that the semivariance values for the Ebro have been standardized to unit variance (this is not the case for Duero basin). Note too how the slope of the sample variograms changes before reaching the sill, indicating possible variation on several spatial scales.

Sample variograms, like those shown in Figure 4, indicate that the variable is not distributed randomly in space, rather it is spatially correlated -with an extended spatial correlation

equal to the range of the variogram- so that the pairs of observations separated by a distance shorter than the range of the variogram are more similar on average than usual. When sample variograms also show two or more distinct slopes while ascending toward the sill, the variable can be considered a multi-scale distributed variable. In the Ebro case study, for instance, the sample variograms for Cd and Cr exhibit two different slopes before the sill. More specifically, Cd presents a steep slope in the first distance lag (20 km), a second one up to approximately 100 km, and a last slope change until ca. 220 km. Cr, on the other hand, exhibits two slopes at approximately 90 km and 200 km. Conversely, the sample variograms for Zn and Cu in the Duero basin seem to reach the variogram sill at distance of 100 km. Zinc presents a considerable step ascension in its semivariance at short distances of less than 20 km.

2.1.1 Variogram modeling in the univariate case

After the sample variogram has been calculated, it is modeled using either a unique variogram model or a combination of more than one variogram models (also called structures). The variables presenting spatial variation on a unique spatial scale are conveniently modeled using a combination of two variogram models: a nugget model and a structure with a range of spatial correlation equal to the range of the sample variogram. However, whenever multiscale variation is present in the sample variogram, models with more structures should be adopted for modeling. Several variogram models can be used at this stage (a detailed list of variogram models and their characteristics can be found in Chilés and Delfiner (1999)). However, for multiscale variation, modeling practice has shown that spherical models are the most convenient. If we consider that $k=1, \dots, q$ denotes the number of structures used to model the experimental variogram, so the variogram model (also called the linear model of regionalization) can be written as:

$$\gamma(\mathbf{h}) = \sum_{k=1}^q \gamma_k(\mathbf{h}) = \sum_{k=1}^q b_k g_k(\mathbf{h}) \quad (2)$$

where b_k is the partial sill and $g_k(\mathbf{h})$ is the variogram model of the k th structure.

A very important property of the linear model of regionalization is that it can be used to decompose the original random function $Z(x)$ into q independent random functions (called spatial components) corresponding to spatial scale k . Decomposition is based on the following model:

$$Z(x) = \sum_{k=1}^q a_k Y_k(x) + m \quad (3)$$

where a_k are known coefficients and $Y_k(x)$ are the orthogonal spatial components with spatial covariance $c_k(\mathbf{h})$:

$$E\{Z(x)\} = m$$

$$E\{Y_k(x)\} = 0$$

$$\text{Cov} \{Y_k(x), Y_{k'}(x+\mathbf{h})\} = \begin{cases} c_k(\mathbf{h}) & \text{if } k = k' \\ 0 & \text{otherwise} \end{cases}$$

This decomposition is of important practical interest: it makes the distinction of the original random function $Z(x)$ into q uncorrelated random functions possible, which represent different scales of variation. Additionally, the estimated spatial components can be mapped using a modified kriging system of equations, which may assist in their interpretation (see also the example in the next Chapter). Mapping spatial components is done with a modified kriging system of equations. Given a set of n observations, the optimal weights (λ_β) for the estimation of spatial component k are given by the solution of the following system of equations (ISATIS, 2008):

$$\begin{cases} \sum_{\beta=1}^n \lambda_\beta \gamma_{\alpha\beta} + \mu = \gamma_{\alpha 0}^k \\ \sum_{\beta=1}^n \lambda_\beta = 0 \end{cases} \quad a = 1, \dots, n \quad (4)$$

where $\gamma_{\alpha\beta}$ is the semivariance between data locations a and β , and $\gamma_{\alpha 0}^k$ is the semivariance between location a and the point where an estimation is required. System [4] is identical to a usual kriging system of equations, save the term $\gamma_{\alpha 0}^k$, which is the semivariance computed using only the variogram model corresponding to the k th structure. Another difference is that kriging weights λ_β must sum to zero (unlike ordinary kriging where weights sum to unity). This difference is due to the fact that the mean of the random function $Z(x)$ is considered a part of the spatial component with the largest range [$\max(k)$]. In this case (i.e., when estimating the largest range component) the system [4] should be rewritten in order to account for the varying spatial mean of the function (Isatis, 2008):

$$\begin{cases} \sum_{\beta=1}^n \lambda_\beta \gamma_{\alpha\beta} + \mu = \gamma_{\alpha 0}^{\max(k)} \\ \sum_{\beta=1}^n \lambda_\beta = 1 \end{cases} \quad a = 1, \dots, n \quad (5)$$

2.1.2 Example: A model of regionalization for zinc in the Duero basin

The sample variogram for Zn concentration in Duero basin soil samples presents two different slopes before reaching the sill at a distance of approximately 120 km (Figure 5). Apparently, the total spatial variability of this variable is structured around two spatial scales at 20 km (local) and at 120 km (regional). The model of regionalization adjusted to the sample variograms of Zn in the Duero Basin is composed of three structures, namely a nugget effect model and two spherical models, with 20 km and 120 km ranges of spatial correlation. The spatial components corresponding to this model may now be used to decompose the original variable into two components by separating the variation observed on a small spatial scale from the one on a larger scale (see the maps in Figure 5).

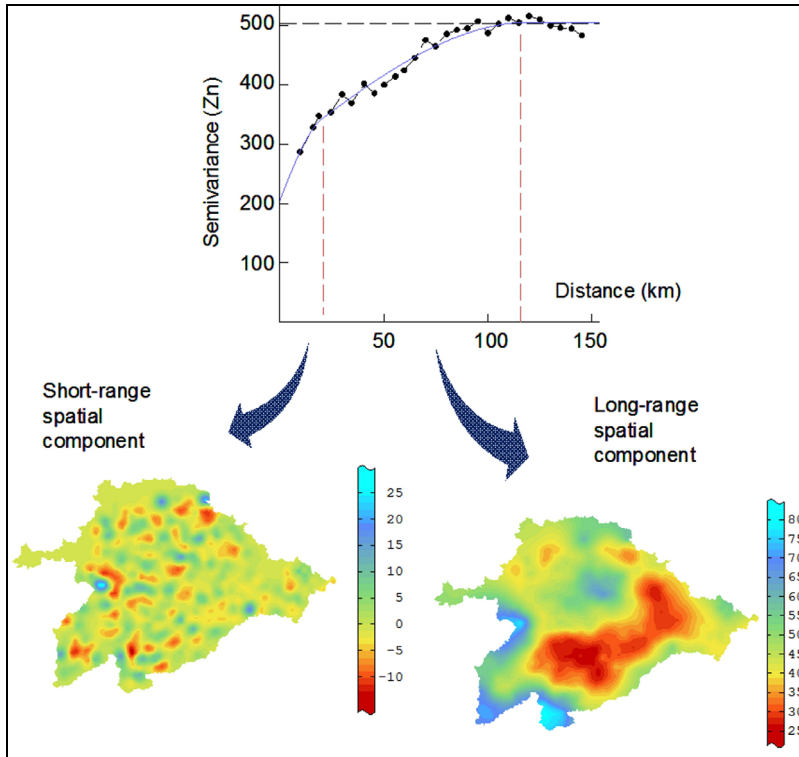


Fig. 5. Mapping two spatial components for Zn concentration in Duero basin soils. The upper panel shows the linear model of regionalization adjusted to the experimental variogram. The lower panels present the estimated spatial components with short- (left panel) and long- (right panel) range variation.

The variation of the component with the longest range (120 km in this case) in the distribution of heavy metals in soils tends to attribute to geological-type factors of a natural origin. Rock decomposition and its input of elements to soil formation (Alloway, 1995) are two main factors that influence on this scale. Hence, large lithological units determine zinc distribution on this scale in the Duero valley. On the other hand, zinc is not a metal related with atmospheric deposition processes over long distances, and is not associated with an industrial activity that might influence the Duero valley on such a large scale. An alternative interpretation of the influence of farming treatments on zinc content in soil is limited to the extension of plots used for crop-growing. The spatial extent of the spatial component in Figure 5 is much greater than the extended land use polygons in the study area.

Unlike the long-range component, its counterpart has a range of spatial correlation of just 20 km, which may be attributable to both antropogenic and natural factors. To a minor spatial extent, zinc in soil would be related with edaphic parameters, such as organic matter, clays, cationic exchange capacity, or presence of oxides of other metals like Fe or Al, which favor its metals retention and whose variation in soil may correspond to the ranges of this scale. On the

other hand, the variability on this small-range scale (20 km) may also reflect anthropogenic activities in either agriculture or small industrial plants. With this kind of statistical analysis, it is impossible to distinguish the repercussion or influence of both factors (human input from natural input) beyond assumptions. However, and in relation to some low Zn contents (save the odd exception), it would be possible to rule out that inputs originating from generic industrial activities, spillages or sporadic pollution sources would be of much influence on this scale. Nonetheless, it would be necessary to know the relationship with other edaphic parameters, specifically with those metals that might relate more with farming activities.

2.2 Multivariate analysis

The natural extension of the variogram to include two random functions (i and j) is called the cross-variogram between Z_i and Z_j , which is estimated as:

$$\hat{\gamma}_{ij}(h) = \frac{1}{2N(h)} \sum_{x_\beta - x_\alpha \approx h} [Z_i(x_\beta) - Z_i(x_\alpha)][Z_j(x_\beta) - Z_j(x_\alpha)] \quad (6)$$

where all the symbols are as in (1) but using the subscript i or j to distinguish between the two variables.

Variogram modeling is more complicated in the multivariate case since one needs to model a total of $p(p+1)/2$ direct and cross-variograms (where p is the number of variables). Multivariate variogram fitting is usually accomplished with the use of multiple nested structures where each one corresponds to a different scale of variation. The model –called the linear model of coregionalization, LMC– can be written as:

$$\gamma_{ij}(\mathbf{h}) = b_{ij}^{(1)}g^{(1)} + b_{ij}^{(k)}g^{(k)}(\mathbf{h}) + \dots + b_{ij}^{(q)}g^{(q)}(\mathbf{h}) \quad \forall i, j \quad (7)$$

where $\gamma_{ij}(\mathbf{h})$ is the variogram model for variables i and j (for $i=j$ the auto-variogram is obtained), $b_{ij}^{(k)}$ is the partial sill for the ij th variogram for structure k , while $g^{(k)}(\mathbf{h})$ represents the type of variogram model (i.e., exponential, spherical, etc.) for structure k . The first structure $g^{(1)}$ represents the nugget effect model.

The flexibility of a specific LMC (that is, its ability to model a set of experimental variograms) is based on the total number of basic structures (q) and their corresponding range of spatial correlation, as well as the partial sill $b_{ij}^{(k)}$ for each variogram model and structure. Partial sills $b_{ij}^{(k)}$ may vary across variograms (under some restrictions; see Wackernagel (1998)), but the range of spatial correlation of each structure $g^{(k)}(\mathbf{h})$ should be the same for the set of $p(p+1)/2$ variogram models. If we arrange the partial sills $b_{ij}^{(k)}$ of the LMC in a matrix form, we obtain the so-called co-regionalization matrices. The coregionalization matrix for structure k is a positive semi-definite symmetric ($p \times p$) matrix with diagonal and off-diagonal elements of the partial sill of the auto- and cross-variogram models, respectively, obtained from the LMC:

$$\mathbf{B}_k = \begin{bmatrix} b_{11}^{(k)} & \dots & b_{1p}^{(k)} \\ \dots & \dots & \dots \\ b_{p1}^{(k)} & \dots & b_{pp}^{(k)} \end{bmatrix} \quad (8)$$

Note that the LMC is a permissible model, but only when all the co-regionalization matrices \mathbf{B}_k are positive definite. This constraint makes multivariate variogram fitting a difficult task. Should only two variables be implicated ($p=2$), the linear model of coregionalization can be fitted manually. However for $p>2$, a weighted least squares approximation is needed which offers the best LMC fit under the constraint of positive semi-definiteness of \mathbf{B}_k (Goulard and Voltz 1992). However, the use of the LMC facilitates multivariate variogram modeling since it reduces the problem of fitting a total of $p(p-1)/2$ variogram models to their experimental counterparts to the problem of deciding the total number (q) of structures to use, as well as the type (i.e., spherical, exponential, etc.) of each structure. This is a central decision in the MFK framework. There are no general rules to guide this decision; however, some recommendations may prove useful (see also Goulard and Voltz (1992)):

- Experimental variograms are the basis for deciding the number and range of elementary structures to be used for modeling. One usually tries to find subsets of variables that have similar variogram characteristics (equal range of spatial correlation).
- In practice, it is difficult to distinguish more than three structures (a nugget plus two other structures) in a set of experimental variograms. Practical experience has shown that three basic structures are sufficient for modeling a large number of variables.
- Usually some of the original variables in the dataset should share the same structures.
- Specifically for heavy metal distribution in soils, geological maps can prove most helpful for deciding the number and ranges of the spatial correlation of individual model structures. The spatial distribution of heavy metals in soil has been observed to be in close relationship with the basic geological features –and their spatial extent– of the study area.

2.2.1 Example: Fitting the linear model of coregionalization in the Ebro river basin

Let us now describe the procedure for fitting a linear model of coregionalization for the spatial distribution of heavy metals in the Ebro basin (Rodriguez et al., 2008). By looking at the direct experimental variograms (Figure 6), we note a change in their slope at a distance of approximately 20 km, which is more prominent for some metals (Hg and Cd) than for others (Zn). This common feature in all the sample variogram indicates that the linear model of coregionalization should include a short-range structure. Note also that all the sample variograms seem to reach the sill value at a distance of approximately 200 km, a fact which also makes necessary the inclusion of a long-range component in the model of coregionalization to be built. Finally, we note that the ascension in the semivariance observed between the shortest range (20 km) and the longest one (200 km) is not linear; instead we observe a stabilization at distances of approximately 100 km.

The features observed in the sample variograms act as a basis for deciding that the linear model of coregionalization to be postulated –and fitted afterward to the sample variograms–

should be composed of at least three structures with ranges of approximately 20 km, 100 km and 200 km (plus a nugget effect model which is present in all the sample variograms). Cross variograms - not presented here - were also taken into account when building the model. However, the postulated model should be chiefly designed to fit the direct rather than the cross-variograms as precisely as possible.

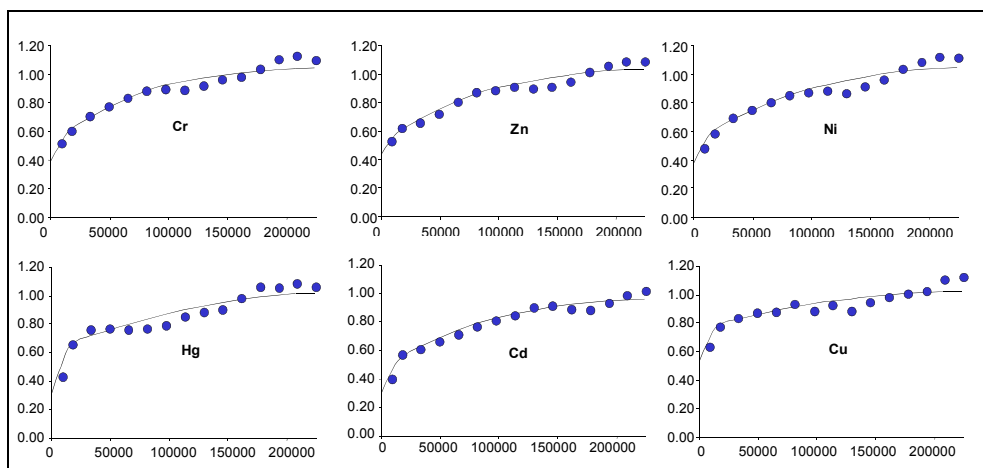


Fig. 6. Six of the seven variogram models of the linear model of coregionalization for the concentration of heavy metals in Ebro basin soils. Horizontal axes units are provided in meters, while vertical axes represent the standardized -to unit sill- semivariance of the corresponding element.

In Figure 6, we graphically present the linear model of coregionalization fit after an iterative procedure included in the Isatis software (Isatis, 2008). The fit is not actually perfect, especially for some elements such as Hg. Yet when considering a multiple variogram model, a compromise between model simplicity and accuracy of fit should be reached.

The number and range of the structures adopted in this model are coherent from a practical viewpoint. Note that within the study area, we have reported the presence of several industrial activities that may potentially enrich the basin soil through airborne pollution and subsequent deposition. We expect that this activity may have altered the spatial distribution at intermediate distances from the point source. Mercury emitted from industrial plants, for instance, has been reported to travel tens of thousands of kilometers before being deposited in soil. On the other hand, large geological features within the study area make us think that natural geological variation could be responsible for the spatial distribution of some heavy metals on a large spatial scale (that with the longest range). Finally, differences in land use and short-range scale natural processes affecting pedogenesis are believed to act on short spatial scales, and are presumably responsible for the short-range scale effects in the distribution of soil heavy metals.

In a very similar way, we built the linear model of coregionalization for heavy metals concentration in Duero basin soils. The sample variograms features in this basin are similar: variograms present a short-range structure at a distance of 20 km and a medium-range

structure at 100 km – 120 km. A substantial difference, however, between the two basins is noted in the absence of long-range variation in the Duero basin. Therefore, the long-range structure (220 km) found in the Ebro region is absent in this model (see also Figure 7).

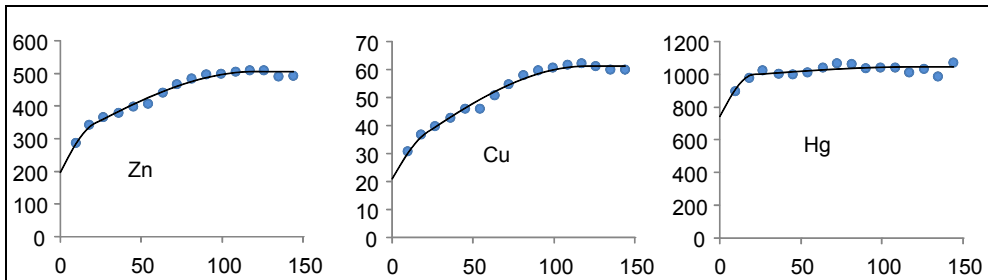


Fig. 7. Three of the seven variogram models of the linear model of coregionalization for the heavy metals concentration in Duero basin soils. Horizontal axes units are provided in kilometers, while vertical axes represent the semivariance of the corresponding element.

2.2.2 Extracting spatial components

Analogically to the univariate case, the LMC permits the decomposition of the original random functions $Z_i(x)$ into a linear combination of the q mutually uncorrelated random functions Y_{lk} , called regionalized factors (RFs):

$$Z_i(x) = m_i(x) + \sum_{k=1}^q \sum_{l=1}^p a_{il}^k Y_{lk}(x) \quad i = 1, \dots, p$$

or in matrix form:

$$\mathbf{Z} = \mathbf{m} + \sum_{k=1}^q \mathbf{A}_k \mathbf{Y}_k \quad (9)$$

where $m_i(x)$ is the varying mean of the function and \mathbf{A}_k is a matrix of unknown coefficients. In fact, only the coregionalization matrix for the k th structure:

$$\mathbf{B}_k = \mathbf{A}_k \mathbf{A}_k' \quad (10)$$

can be estimated. Matrix \mathbf{A}_k is not uniquely defined since there is an infinite number of \mathbf{A}_k which satisfies Equation (10). However, a principal components analysis (PCA) can provide a natural determination of matrix \mathbf{A}_k (Chilés and Delfiner 1999). More specifically, a PCA is applied to each coregionalization matrix \mathbf{B}_k separately, to provide a set of p eigenvalues and their corresponding eigenvectors (\mathbf{u}_l):

$$\mathbf{B}_k = \mathbf{Q}_k \mathbf{\Lambda}_k \mathbf{Q}_k' \quad (11)$$

where \mathbf{Q}_k is the orthogonal matrix of eigenvectors and $\mathbf{\Lambda}_k$ is the diagonal matrix of eigenvalues for spatial scale k .

Matrix \mathbf{A}_k can then be estimated since:

$$\mathbf{A}_k = \mathbf{Q}_k \mathbf{\Lambda}_k^{1/2} \quad (12)$$

Using decomposition (9) and the estimation of matrix \mathbf{A}_k from (12), one can decompose the p original variables into a set of uncorrelated RFs. Note that these factors have some remarkable properties:

- They are linear combinations of the p original variables.
- The first factors, corresponding to the largest eigenvalues, account for most of the variability observed in the dataset. Therefore, it is possible to reduce the dimensionality of the data and to visualize the phenomenon.
- It is possible that the resulting RFs represent some common mechanisms underlying the spatial distribution of the original variables. Hopefully, RFs can have meaningful interpretations (analogically to a classical PCA).
- RFs remain uncorrelated at any separation distance \mathbf{h} and not just at the same location (Chilés and Delfiner 1999). A classical PCA provides uncorrelated factors, but only for the separation distance $\mathbf{h}=0$.
- Perhaps the most remarkable property is that RFs can be constructed for each spatial scale separately. Therefore, by incorporating the spatial correlations revealed by the variograms, they can reveal mechanisms that act on different scales and that control the spatial distribution of the studied attributes.

2.2.3 Interpreting the regionalized factors: The circle of correlation

Interpretation of an RF is not always feasible given that RFs are determined using statistical and not ecological/physical criteria (maximize variance under the constraint of orthogonality). Nevertheless, the interpretation of RFs is of crucial importance for the analysis since it will be the basic tool for determining the exact physical mechanisms acting on different spatial scales and for controlling the spatial distribution of the studied variables.

The interpretation of the meaning of an RF can be assisted by all the well-known tools of a classical PCA, such as “scree” plots, loadings, and especially by the correlation between the regionalized factors and the regionalized variables, which is computed by:

$$\rho_{il} = q_{il} \sqrt{\frac{\lambda_l}{\sigma_i^2}} \quad (13)$$

where q_{il} is the loading of the i th variable for the l th principal component, λ_l is the variance of the l th RF and σ_i^2 the variance of the i th regionalized variable.

The pair of correlations of a regionalized variable with two RFs (usually the first two, which account for most of the variability) is plotted on a graph, called the circle of correlation (Saporta, 1990). When a variable is located near one of the two axes of the graph and away from the origin, it is well correlated with that specific RF and much of its variance is explained by the RF.

2.2.4 Example: Multiscale correlations among heavy metals in the Ebro river basin

In this Chapter, we use the linear model of corregionalization to decompose the initial multivariate set of heavy metal concentrations. Then we derive a new set of composite regionalized factors for several scales of variation. Finally, we employ a factorial kriging analysis results in an attempt to decompose the original dataset into a few regionalized factors.

For the Ebro river, three spherical models with ranges of 20 km, 100 km and 220 km were used. The three circles of correlation shown in Figure 8 represent heavy metal associations for the three scales of variation used in the linear model of corregionalization for soil samples. The association of different metals substantially differs if we compare the three circles of correlation. This indicates that, indeed, the correlation among soil elements depends on the spatial scale considered and that, conclusively, multiscale correlation is present in the study area. Grouping metals in the circle of each scale tends to reflect the influence phenomena that are common for all grouped elements. Changes made to the grouping of these metals when amending the observation scale also implies a change in the dominant factor which influences these elements. Note that in the absence of multiscale correlation, we expect the elemental associations to remain unchanged when moving from one spatial scale to another.

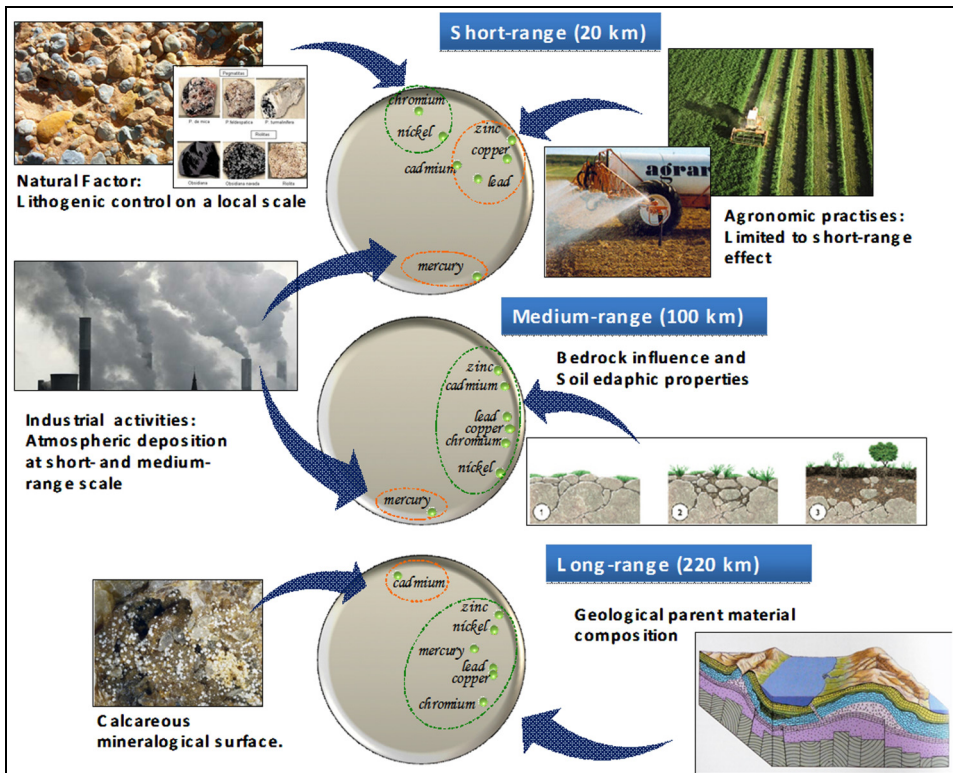


Fig. 8. Correlation circles for the concentration of seven heavy metals in the Ebro river basin. Correlation circles correspond to the three structures used to build the linear model of corregionalization.

The association between Hg and other elements is the most representative example of a correlation dependent on scale. Note that Hg seems to be an isolated element in the correlation circles for the short- and medium-range correlation circles, but seems to be associated with other elements when looking at the long-range correlation circles. Obviously, there should be a factor that acts on the smallest scale of variation, but not on the largest one, which makes mercury distribution different from that of the other elements. In general, mercury accumulations in soils are associated with atmospheric deposition (Engle et al., 2005). Anthropogenic emission of Hg represents about 60–80% of global Hg emissions. Mercury is an extremely volatile metal which can be transported over long distances (Navarro et al., 1993). In the Ebro valley, soil enrichment by atmospheric mercury covers small (20km) to medium (100km) scales. Not surprisingly, soil enrichment in mercury is not observed on the largest (among those studied) spatial scales, so man-made alteration of soil Hg has not become evident –at least not yet- on this scale.

Cd is another interesting element which shows correlations with other elements that change across scales. In the largest scale of variation (220 km), we may denote Cd as an isolated element in the circle of correlation which is, however, not observable on smaller spatial scales. Unlike Hg, however, this change can be attributed to natural factors. More specifically, Cd is the only element that tends to accumulate in calcareous soils (Boluda et al., 1988). Cadmium is adsorbed specifically by crystalline and amorphous oxides of Al, Fe and Mn. Metallic (copper, lead and zinc); alkaline earth cations (calcium and magnesium) particularly reduce Cd adsorption by competing for available specific adsorption and cation-exchange sites (Martin and Kaplan, 1998). Therefore, the isolated occurrence of Cd in the long-range correlation circle is due to the spatial distribution of the calcareous mineralogical surface generating major Cd accumulation.

On the local spatial scale (20km), association of Zn, Cu, Pb and Cd results concentrations after fertilization of arable soils, or pesticides and fungicides use related to crop protection. The association of four elements is caused by common agricultural practices, which may also prove evident on a small scale. Copper and zinc (Mantovi et al., 2003) increase through such practices especially copper which has been used as a pesticide form (copper sulfate) in viticulture. Zinc and cadmium concentrations increase through use of fertilizers. It is estimated that phosphated fertilizers make up more than 50% of total cadmium input in soils (de Meeûs et al., 2002). On the other hand, natural phenomena act in a short range, and variability of Cr and Ni is associated with the mineralogical structure of the study area (basic and ultramafic rock). Generally, anthropic inputs of Cr and Ni in fertilizers, limestone and manure are lower than the concentrations already present in soil (Facchinelli et al., 2001).

2.2.5 Example 2: Multiscale correlations among soil heavy metals in the Duero river basin

The linear model of co-regionalization in the Duero basin is developed from two structures, with scale ranges between 20 km and 120 km. Unlike the Ebro valley, no higher scale of variation is noted, which is around 200 km, despite having a similar surface. The Duero valley can be considered more homogeneous in terms of all the aspects that can influence the distribution of heavy metals in soils, and reducing spatial variation structures may well reflect this. Moreover, the Duero depression is shaped as a basin with tertiary and

quaternary sediments of a continental origin. However, Paleogene materials of variable extensions outcrop from among the tertiary sediments, although they mainly limit the depression on the basin's edges. Variability from a geological viewpoint is inferior to variability in the Ebro. Yet from the farming perspective, crops do not present much diversity as dominant crops are cereals and vineyards. As mentioned in Section 1.4.4, the Duero valley is one of the main cereal-growing areas in Spain.

On the short-range scale (20km), only two groups of metals are seen, which are expressed as mercury isolation and a large series with the remaining elements (Figure 9). The main difference found with the Ebro valley lies in chrome and nickel grouping with metals like copper or zinc, which relate to farming practices. Although natural and inorganic fertilizers contain small amounts of both chrome and nickel, they do not significantly increase the soil natural content. The geological influence of nickel and chrome content has been clearly demonstrated (Alloway, 1995). The highest nickel concentrations are found in ultrabasic igneous rocks (peridotites, dunites and pyroxenites), followed by basic rocks (gabbro and basalt). Acid igneous rocks present lower chrome or nickel contents. Sedimentary rocks are especially poor in Cr or Ni. On the other hand, the edaphic parameters that influence heavy metals content in soil (texture, organic matter, etc.) evidence their influence on this scale. Soils with a thick and sandy texture contain less Cr or Ni than clayey soils, which is also a common process for the remaining metals (Cu, Pb, Cd and Zn). As expected, low heavy metal contents are also associated with low organic matter contents.

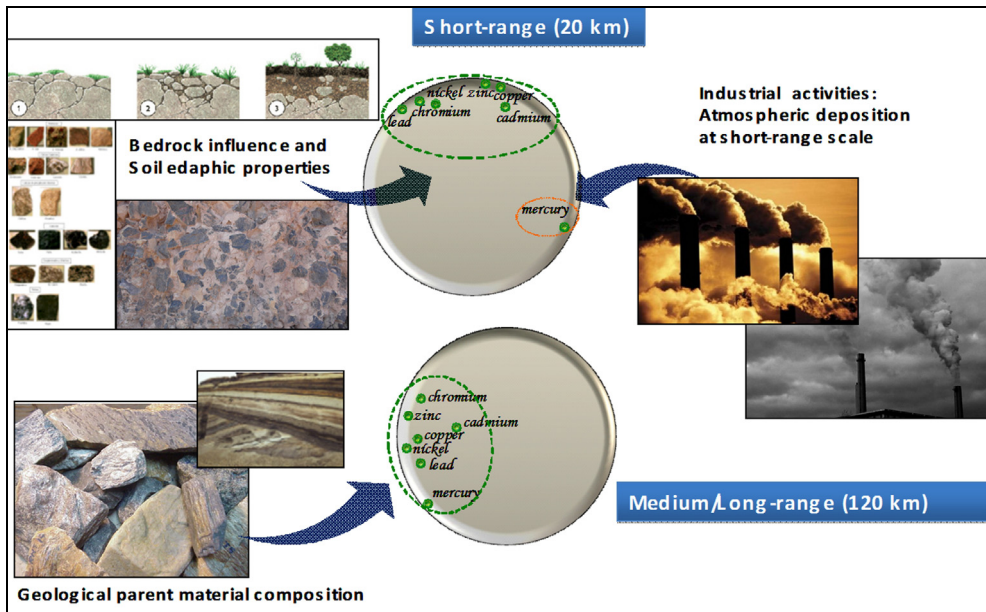


Fig. 9. Correlation circles for the concentration of seven heavy metals in the Duero basin. Correlation circles correspond to the two structures used to build the linear model of corregionalization.

On the medium-/long-range scales (120km), all heavy metals are grouped in the circle of correlation (Figure 9), which is the result of a common source of variability. On this scale, only large lithologies can influence the distribution of heavy metals in soils which, for the River Duero basin, derive mainly from the sedimentary materials deposited in its interior. However, the coordinated distribution of all metals, including Hg, on this scale evidences an edaphogenic process.

In conclusion, human activity is only shown on a small scale (20km) and is motivated by mercury inputs. As mentioned earlier, atmospheric deposition is the main way that mercury enters soil. Besides, on this small scale, it is probably a case of mercury being associated with ash and soot particles, which are deposited near pollution sources, such as those originating from coal power stations, or from heating systems to a lesser extent. Basically, no influence of farming treatments is observed. This aspect is linked to some relatively low levels of metals in soil, such as Cu, Cd or Zn. The dominant factor in the content and distribution of heavy metals in the Duero is natural, and is influenced by soil’s physico-chemical properties in a short range and, to a greater extent, by geological parent material composition.

2.2.6 Spatial estimation of regionalized factors

The final step in factorial kriging analysis consists in mapping composite regionalized factors. Estimation is done with a modified cokriging step technique. Note that ordinary cokriging provides a spatial estimation of the primary variable using data for the primary variable and for one or more secondary variables. Typically, the primary variable is sampled over a limited number of points, while secondary data are more densely sampled (Wackernagel 1998). Estimation of regionalized factors is done by means of a modified cokriging system of equations, where measurements of the primary data are not available, and the cross covariance between the regionalized factor and the regionalized variables cannot be inferred directly. However, the spatial estimation of regionalized factors is possible thanks to the model of coregionalization’s properties. More specifically, to account for decomposition [8], the cross covariance between the random variable $Z_i(x)$ and the l th RF of the k th spatial structure (Y_{lk}) is determined as (Goovaerts 1997):

$$Cov\{Z_i, Y_{lk}\} = a_{il}^k c_{a_i 0}^k \tag{14}$$

where $c_{a_i 0}^k$ is the covariance (for the k th structure) between point a_i (where the i th variable has been measured) and the location where the prediction is required, while a_{il}^k is the element of the i th row of the l th column of matrix A_k determined by (12). The optimal cokriging weights $\lambda_{\beta_j l}^k$ assigned to each data location for each regionalized factor are provided by the solution of the following cokriging system of equations:

$$\begin{cases} \sum_{j=1}^p \sum_{\beta_j=1}^{n_j} \lambda_{\beta_j l}^k C_{ij}(\mathbf{u}_{\alpha_i} - \mathbf{u}_{\beta_j}) + \mu_{il}^k = a_{il}^k c^k(\mathbf{u}_{\alpha_i} - \mathbf{u}) & \alpha_i = 1, \dots, n_i \quad i = 1, \dots, p \\ \sum_{\beta_i=1}^{n_i} \lambda_{\beta_i l}^k = 0 & i = 1, \dots, p \end{cases} \tag{15}$$

where n_i and n_j are the number of sample locations for the original variable i and j , respectively, while c_{ij} is the auto- (or cross-) covariance for variables i and j between locations. Finally, λ_i is the Lagrange multiplier for the i th variable and the l th regionalized factor.

The cokriging system in (15) differs from the classical cokriging system as far as the way to compute the cross covariance between primary and secondary data and in the unbiasedness constraints is concerned. More specifically, since the regionalized factors have (by definition) a zero mean, the cokriging weights have to sum to zero for the system to be overall unbiased.

2.2.7 Example: Spatial estimation of regionalized factors in the Duero

The first regionalized factor of the long-range scale of variation presents an area of high positive values in the southern part of the Duero basin. This area is characterized by a higher metal concentration for all the analyzed elements. According to the results presented in Section 2.2.3, the basin's great lithological features are responsible for enriching this area with heavy metals. Conclusively, the variability depicted in this map, representing a juxtaposition between metal-rich areas and poorer ones, is caused by the chemical composition of the geological substrate; human sources of heavy metals are not obvious in this map.

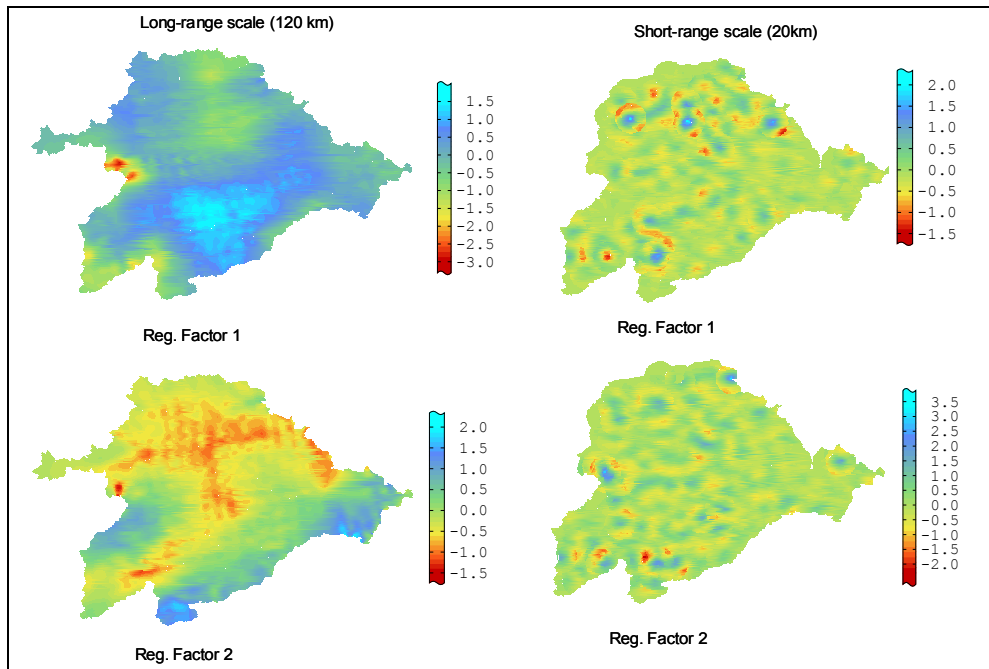


Fig. 10. Spatial estimation of regionalized factors for the Duero case study. Note that several grid points in the short-range spatial components cannot be estimated due to the limited number of data points. Thus, the study areas seem smaller in the maps of the short-range structure.

In contrast, variability in the first regionalized factor of the 20 km range scale is, according to the previous results, due to man-made enrichment of soil with Hg. Therefore, areas with higher regionalized factor values for this map depict those areas where mercury enrichment by human activities has been observed. The second regionalized factor for the same scale of variation depicts small-scale variability in all elements –except the previously reported Hg– which is due to the natural edaphic properties of soil (texture, soil organic matter, etc.) observed on small spatial scales..

3. Conclusion

Several human activities, such as agriculture, mining or industry, have dramatically increased the concentration of some heavy metals in soil causing, in some cases, severe soil pollution. Source identification of heavy metals can prove to be a great step forward in the prevention of soil pollution and rationalization of soil management practices. However, when multiple sources of heavy metals contribute to total concentration and are mixed with natural metals in soil, then the task of identifying and assigning pollutant sources remains an unresolved problem.

Fortunately, some human heavy metal sources enrich soil on different spatial scales. For instance, the impact of fertilization of crops in arable soil is on a rather local range. This is the case of Zn, Cu, Pb and Cd on the local scale of variation in the Ebro basin. Conversely, contaminant sources, such as industrial plants, disperse large quantities of heavy metals over long dispersal distances. The most obvious case was detected in both the Ebro and Duero basins for the spatial distribution of Hg. Finally lithological features, which also control the –natural– spatial distribution of heavy metals, may have a much broader range of spatial distribution than human enrichment factors. This was the case in the Ebro basin where Cd distribution on the longest-range spatial scale was found to be controlled by lithology.

A factorial kriging analysis was presented as a tool to provide some evidence about the source identification of soil heavy metals. From a statistical viewpoint, the method relies heavily on a scale-dependent decomposition of the original variables (the heavy metal concentration) in a new set of composite functions (regionalized factors). These new unobservable functions may be interpreted using the correlation circle and spatial distribution maps. Regionalized factors have the remarkable property of being scale-specific. Regionalized factors are constructed based only on the scale-specific correlations among the original variables. Thus they can be used to filter out variability on unwanted spatial scales and to reveal scale-specific common sources of heavy metals in soil.

4. Acknowledgment

We appreciate the financial assistance provided by the Spanish Ministry of Innovation through project JC2010-0109. We are also grateful to Ministerio de Ciencia e Innovacion, proyect: CGL2009-14686-C02-02 and to CAM project: P2009/AMB-1648 CARESOIL.

5. References

Alloway, B.J. (1995). Heavy metals in soils. Chapman & Hall, (Ed.). Glasgow, UK.

- Alloway, B.J. & Jackson, A.P. (1991). The behaviour of heavy metals in sewage sludge-amended soils. *The Science of the Total Environment*, Vol. 100, pp. 151-176.
- Boluda, R. ; Andreu, V. ; Pons, V. & Sánchez, J. (1988). Contenido de metales pesados (Cd, Co, Cr, Cu, Ni, Pb y Zn) en suelos de la comarca La Plana de Requena-Utiel (Valencia). *Anales de Edafología y Agrobiología*, Vol. 47, No. 11-12, pp. 1485-1502.
- Brunet, M. F. (1986). The influence of evolution of the Pyrenees on adjacent basins. *Tectonophysics*, Vol. 129, pp. 343-354.
- Castrignanò, A. ; Giugliarini L. ; Risaliti R. & Martinelli, N. (2000). Study of spatial relationships among some soil physico-chemical properties of a field in central Italy using multivariate geostatistics. *Geoderma*, Vol. 97, No 1-2, pp. 39-60
- Chilés, J.P. & Delfiner, P. (1999). Geostatistics: modeling spatial uncertainty. John Wiley & Sons (Ed.), New York, 695 pp.
- Chojnacka, K.; Chojnacki, A.; Górecka, H. & Górecki, H. (2005). Bioavailability of heavy metals from polluted soils to plants. *The Science of the Total Environment*, Vol. 337, pp. 175-182.
- Colgan, A.; Hankard, P.K.; Spurgeon, D.J.; Svendsen, C.; Wadsworth, R.A. & Weeks, J.M. (2003). Closing the loop: A spatial analysis to link observed environmental damage to predicted heavy metal emissions. *Environmental Toxicology and Chemistry*, Vol. 22, pp. 970-976.
- De Meeùs, C.; Eduljee, G. & Hutton, M. (2002). Assessment and management of risks arising from exposure to cadmium in fertilizers. *The Science of the Total Environment*, Vol. 291, pp 167-187.
- De Temmerman, L.; Vanongeval, L.; Boon, W.; Hoenig, M. & Geypens, M. (2003). Heavy metal content of arable soils in northern Belgium. *Water, Air and Soil Pollution*, Vol. 148, pp. 61-76.
- Dudka, S.; Piotrowska, M. & Chlopecka, A. (1994). Effect of elevated concentrations of Cd and Zn in soil on spring wheat yield and the metal contents of the plants. *Water, Air, and Soil Pollution*, Vol. 76, pp. 333-341.
- Engle, M.A.; Gustin, M.S.; Lindberg, A.W. & Ariya, P.A. (2005). The influence of ozone on atmospheric emissions of gaseous elemental mercury and relative gaseous mercury from substrates. *Atmospheric Environment*, Vol. 39, pp. 7506-7517.
- Errecalde, M.F.; Boluda, R.; Lagarda, M.J. & Farre, R. (1991). Indices de contaminación por metales pesados en suelos de cultivo intensivo: aplicación en la comarca de L'Horca (Valencia). *Suelo y Planta*, Vol.1, pp. 483-494.
- Facchinelli, A. ; Sacchi, E. & Mallen, L. (2001). Multivariate statistical and GIS-based approach to identify heavy metal sources in soil. *Environmental Pollution*, Vol. 114, pp. 313-324.
- Gómez, J.J.; Lillo, J. & Sahún, B. (2006). Naturally occurring arsenic in groundwater and identification of the geochemical sources in the Duero Cenozoic Basin, Spain. *Environmental Geology*, Vol. 50, pp. 1151-1170.
- Goovaerts, P. (1992). Factorial kriging analysis: A useful tool for exploring the structure of multivariate spatial information. *Journal of Soil Science*, Vol. 43, pp. 597-619.
- Goovaerts, P. (1997). Geostatistics for natural resources evaluation. Applied geostatistics series. Oxford University Press (Ed.), New York.
- Goulard, M. & Voltz, M. (1992). Linear coregionalization model: tools for estimation and choice of cross variogram matrix. *Mathematical Geology*, Vol. 24, No 3, pp. 269-286.

- Gzyl, J. (1999). Soil protection in Central and Eastern Europe. *Journal of Geochemical Exploration*, Vol. 66, pp. 333-337.
- Houba, V.J.G.; Van Der Lee, J.J. & Novozamsky, I. (1995). Soil and plant analysis, a series of syllabi. Part 5B: In: *Soil analysis procedures, other procedures*. Dept. of Soil Science and Plant Nutrition, Agricultural Univ (Ed.), Wageningen.
- Hutton, M. (1982). Cadmium in European Community, In: *MARC Report N° 2*, MARC (Ed.), London.
- Isatis (2008). Isatis software manual. Geovariances & Ecole des Mines de Paris, 579 pp.
- ISO 11466. 1995. Soil quality: Extraction of trace elements soluble in aqua regia, Genova, ISO.
- Kashem, M.A. & Singh, B.R. (2001). Metal availability in contaminated soils: Effects of flooding and organic matter on changes in Eh, pH and solubility of Cd, Ni and Zn. *Nutrient Cycling in Agroecosystems*, Vol. 61, pp. 247-255.
- Mantovi, P.; Bonazzi, G.; Maestri, E. & Marmiroli, N. (2003). Accumulation of copper and zinc from liquid manure in agricultural soils and crop plants. *Plant and Soil*, Vol. 250, pp. 249-257.
- Matheron, G. (1982). Pour une analyse krigéante de données régionalisées, Centre de Géostatistique, Fontainebleau.
- Martin, H.W. & Kaplan, D.I. (1998). Temporal changes in cadmium, thallium, and vanadium mobility in soil and phytoavailability under field conditions. *Water, air and soil pollution*, Vol. 101, pp. 399-410.
- Navarro, M.; López, H.; Sánchez, M. & López, M. (1993). The effect of industrial pollution on mercury levels in water, soil, and sludge in the coastal area of Motril, Southeast Spain. *Archives of Environmental Contamination and Toxicology*, Vol. 24, pp. 11-15.
- Nicholson, F.A.; Smith, S.R.; Alloway, B.J.; Carlton-Smith, C. & Chambers, B.J. (2003). An inventory of heavy metal input to agricultural soil in England and Wales. *The Science of the Total Environment*, Vol. 311, pp. 205-219.
- Nriagu, J.O. (1990). Global metal pollution. Poisoning the biosphere?. *Environment*, Vol. 32, pp. 28-33.
- Otte, M.L.; Haarsma, M.S.; Broekman, R.A. & Rozema, J. (1993). Relation between heavy metal concentrations and salt marsh plants and soil. *Environmental Pollution*, Vol. 82, pp. 13-22.
- Riba, O.; Reguant, S. & Villena, J. (1983). Ensayo de síntesis estratigráfica y evolutiva de la cuenca terciaria del Ebro. In: *Geología de España*, pp. 41-50, IGME Jubilar J. M. Ríos.(Ed.), Madrid, Spain.
- Ross, S.M. (1994). Toxic metals in Soil-Plant Systems. John Wiley and Sons Ltd. (ed SM Ross). Chichester.
- Rodríguez Martín, J.A.; López Arias, M. & Grau Corbí, J.M. (2006). Heavy metal contents in agricultural topsoils in the Ebro basin (Spain). Application of multivariate geostatistical methods to study spatial variations. *Environmental Pollution*, Vol. 144, pp. 1001-1012.
- Rodríguez Martín, J.A.; López Arias, M. & Grau Corbí, J.M. (2009). Metales pesados, materia orgánica y otros parámetros de los suelos agrícolas y de pastos de España. MARM-INIA (Ed.). ISBN 978-84-491-0980-5. Madrid. Spain.

- Rodríguez, J.A.; Nanos, N.; Grau, J.M.; Gil, L. & López-Arias, M. (2008). Multiscale analysis of heavy metal contents in Spanish agricultural topsoils. *Chemosphere*, Vol. 70, pp. 1085-1096.
- Roure, F.; Chokroune, P. & Deramond, J. (1989). ECORS deep seismic data and balanced cross-sections, geometric constraints to trace the evolution of the Pyrenees. *Tectonics*, No 8, pp. 41-50.
- Sanchidrian, J.R. & Mariño, M., (1980). Estudio de la contaminación de suelos y plantas por metales pesados en los entornos de las autopistas que confluyen en Madrid. II contaminación de suelos. *Anales de Edafología y Agrobiología*, Vol. 39, pp. 2101-2115.
- Saporta, A. (1990). Probabilités, analyse des données et statistique. Technip, Paris.
- Simón, J. L. & Soriano, M. A. (1986). Diapiric deformations in the Quaternary deposits of the central Ebro basin, Spain. *Geological Magazine*, Vol. 123, pp. 45-57.
- Simon-Gomez, J. L. (1989). Late Cenozoic stress field and fracturing in the Iberian Chain and Ebro Basin (Spain). *Journal of Structural Geology*, Vol. 11, No3. pp. 285-294.
- Söderström, M. (1998). Modelling local heavy metal distribution: a study of chromium in soil and wheat at ferrochrome smelter in south-western Sweden. *Acta Agriculture Scandinavica*, Vol. 48, pp. 2-10.
- Tejero, R.; González-Casado, J.J.; Gómez-Ortiz, D. & Sánchez-Serrano, F. (2006). Insights into the "tectonic topography" of the present-day landscape of the central Iberian Peninsula (Spain). *Geomorphology*, Vol. 76, pp. 280- 294.
- Tiller, K.G. (1989). Heavy metals in soils and their environmental significance. *Advances in soil science*, Vol. 9, pp. 113-142.
- Wackernagel, H. (1998). Multivariate geostatistics: an introduction with applications. Springer, 285 pp.
- Weber, J. & Karczewska, A. (2004). Biogeochemical processes and the role of heavy metals in the soil environment. *Geoderma*, Vol. 122, pp. 105-107.

Environmental Impact and Drainage Geochemistry of the Abandoned Keban Ag, Pb, Zn Deposit, Working Maden Cu Deposit and Alpine Type Cr Deposit in the Eastern Anatolia, Turkey

Leyla Kalender

*Firat University, Department of Geological Engineering, Elazig
Turkey*

1. Introduction

This study includes the effect on the environment of abandoned and working mine deposits which are lead, zinc, silver and copper deposit in Keban, working copper deposits in Maden and chromite deposit in Alacakaya. These are the largest metallogenic province of Turkey (Figure 1).

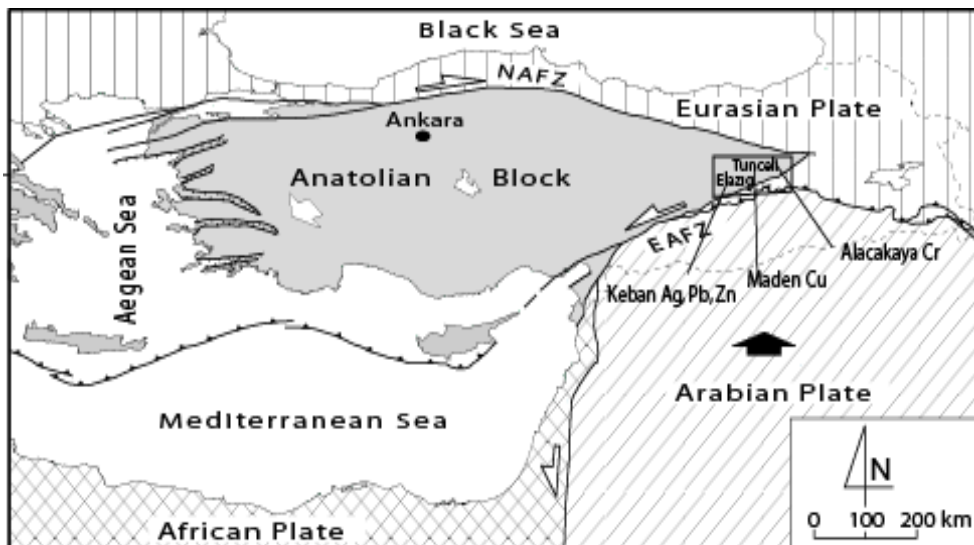


Fig. 1. Location map of the study area.

The Keban region was one of the most important base metal areas of eastern Turkey. The Keban area has been an important mining area since B.C. Archaeological studies revealed that ancient miners have mined the Keban area for gold, copper, lead, silver and iron. During twentieth century, the mining activity was restricted to iron, lead, zinc, silver and fluorite. The Keban mine was operated for Pb and Zn production at various times between the 1940s and the late 1980s. There were several prospect pits and mining tunnels in the area. However, mining ceased in 1988 and the site was abandoned. The west and east Euphrates slag sites account for on average 2.16 ppm Au, 66.41 ppm Ag, 2.38 % Pb, and 0.52 % Zn (Kalender & Hanelçi, 2001). The Euphrates River and its tributaries, in particular, Karamağara Stream, drain the former metal-mining areas, which have been contaminated by the release of heavy metals from old mining operations within the Keban mining district. Many geological studies have been conducted around the Euphrates River (Kalender & Hanelçi, 2001; Kumbasar, 1964; Kineş, 1969; Zisserman, 1969; Köksoy, 1975; Kipman, 1976; Akıncı et al., 1977; Balçık, 1979; Yılmaz et al. 1992; Çelebi & Hanelçi, 1998; Çalık, 1998; Kalender, 2000; Kalender & Hanelçi, 2001; 2002, Bölücek, 2002). However, none of these studies have addressed the issue of environmental contamination in the area. In this study will be presented geochemical results from several sampling media (sediments, mine-drainage waters, spring waters, river waters, moss, and algae) from the Keban mining district.

Maden copper deposit was important ore deposit of Turkey. Mining activity had been operated from 4000 B.C. up to the recent (Seeliger ve diğ., 1985, Tızlak, 1991). The mine was run by Rome, Seljuk and Ottoman Empires (1860-1915) and the Republic of Turkey. Maden copper mining operations have been transferred with the establishment of Etibank in 1935. Due to exhaustion of economic reserves were decided to close the facilities in 1995. However, Ber-Oner Mining has operated of the waste from 1995 to 2005. Since 2007, Maden copper mining waste has been operated by Eti Holding and SS Yıldızlar Holding and produced 20 000 tons of copper a year. Many geological studies have been conducted around the Maden copper deposit area (Erdoğan, 1977; Özkaya, 1978; Özdemir & Sağıroğlu, 1998; Özdemir & Sağıroğlu, 2000; Kirat et al, 2008).

In this study will be stressed dissolution methods and metal dispersion patterns were determined suitable for such an area by stream sediment survey. The physical and chemical feature of the area indicate that the metallic contents of the stream sediments originate from physical events rather than chemical events. In this case, 180-106 μm sediment fraction were analysed. In addition to surface and seepage water samples were collected from the area and several elements were analyzed and data were evaluated in term of pollution. After study was conducted to evaluate the influence of anion (sulfate) and metals (copper, iron, manganese, zinc and nickel) on the reduction by these bacteria. Furthermore, the sulphate reducing bacterium methods were evaluated to selectively precipitate metals and reduction sulphate from Maden (Elazığ) copper Deposits AMD seepage waters in two samples locations. Initial and final metals and sulphate concentration before and after experiments, were measured and finally evaluated influence of bacteria.

Guleman ophiolite made up of tectonites which comprises dunite and chromite bearing hazburgites and cumulates which contain dunites, wehrlite, clinopyroxenite, gabbros,

diabase dykes, sheetdyke complex and basic volcanites are other constituents of the ophiolite. This area has been studied by Erdoğan, 1977; Erdoğan, 1982; Başpınar, 2006. There are thirty rock samples of Guleman Ophiolite were analyzed by Başpınar in 2006 and ten groundwater samples were analyzed by Kalender in 2010. This study includes correlation of both analysis results of data.

This study mainly focus on the concentrations and distributions of heavy metals and potentially toxic elements in the various sampling media impacts on environment pollution in the three different ore deposit

2. Keban Ag-Pb-Zn deposit

2.1 Sampling and analytical methods

Water, stream-sediment, algae samples were collected from the study area. Water samples were taken from natural springs (LK 1, LK 2, LK 3, LK 4, LK 6, LK 7, LK 8, LK 9, LK 10), mine-drainage waters (LK 5: fluorite production gallery; LK 8: Pb-Zn underground-mine production workings) and the Euphrates River (LK 11). Algae samples were collected from the bed of the Euphrates River (AK 13, AK 14, AK 18) and only one moss sample. Sediment samples were collected from the Euphrates River bed (LZ 120, LZ 150, LZ 160, LZ 170), from Karamağara Stream (LZ 270, LZ 310, LZ 330, LZ 340, and LZ 350) and from precipitates at the gallery mouth (LZ 370) (Figure 2). All of the sampling work was done in June 2002 (Kalender & Bölücek, 2004; Bölücek, 2007).

Water samples were collected into 250-ml polyethylene containers and filtered through 0.5 µm membrane filter paper (4.5 cm diameter). Temperature and pH measurements were conducted at the sampling sites. 5 ml concentrated HNO₃ (MerckTM ultra pure) was added to the samples for metal analyses. Samples were stored in the laboratory at +4°C until they were analyzed. For each sediment sample, 2 kg of sediment was sampled from a depth of about 10 cm by sieving to 2 mm mesh size. For analyses, samples dried in the laboratory were sifted using stainless steel sieves to mesh sizes between -80 and +140. The samples were subjected to partial-digestion involving the use of a cold solution of 0.3 % NaCN and 0.1 NaOH to extract weakly-bound elements from clay, organic matter, and amorphous Mn and Fe hydroxides (Kelly et al., 2003). Green algae *Cladophora glomerata* in sample AK 14 is a typical species in rivers; it is found together with macroalgae (Entwistle, 1989; Power, 1992). *Cladophora glomerata* is found mainly in volcanic areas (Whitton et al. 1998). The presence of *Cladophora glomerata* is used as an indicator of good-quality water. Aksın et al. (1999) examined the Keban stream algae and determined 70 taxa from the *Chlorophyta*, *Cyanophyta*, *Bacillariophyta*, and *Dinophyta*. These workers reported that diatoms are the dominant group of organisms among the pelagic and benthic algae population because of the rapid water flow of Keban Stream. Algae species living in the Euphrates River differ from those in Keban Stream due to the temperature and low current velocity in the former. They are quite common in the river beds having low current velocity, that receive little light, and that have temperatures above 10°C (Schönborn, 1996). The temperature of the Euphrates (12.4–12.7°C) is suitable for the growth of this type of algae. Investigations indicate that the amount of this organism will increase with increasing temperature. The size of *Didymodon tophaceus* is around 0.5–5 cm. It is composed of circular cells that widen toward the base, and is mainly

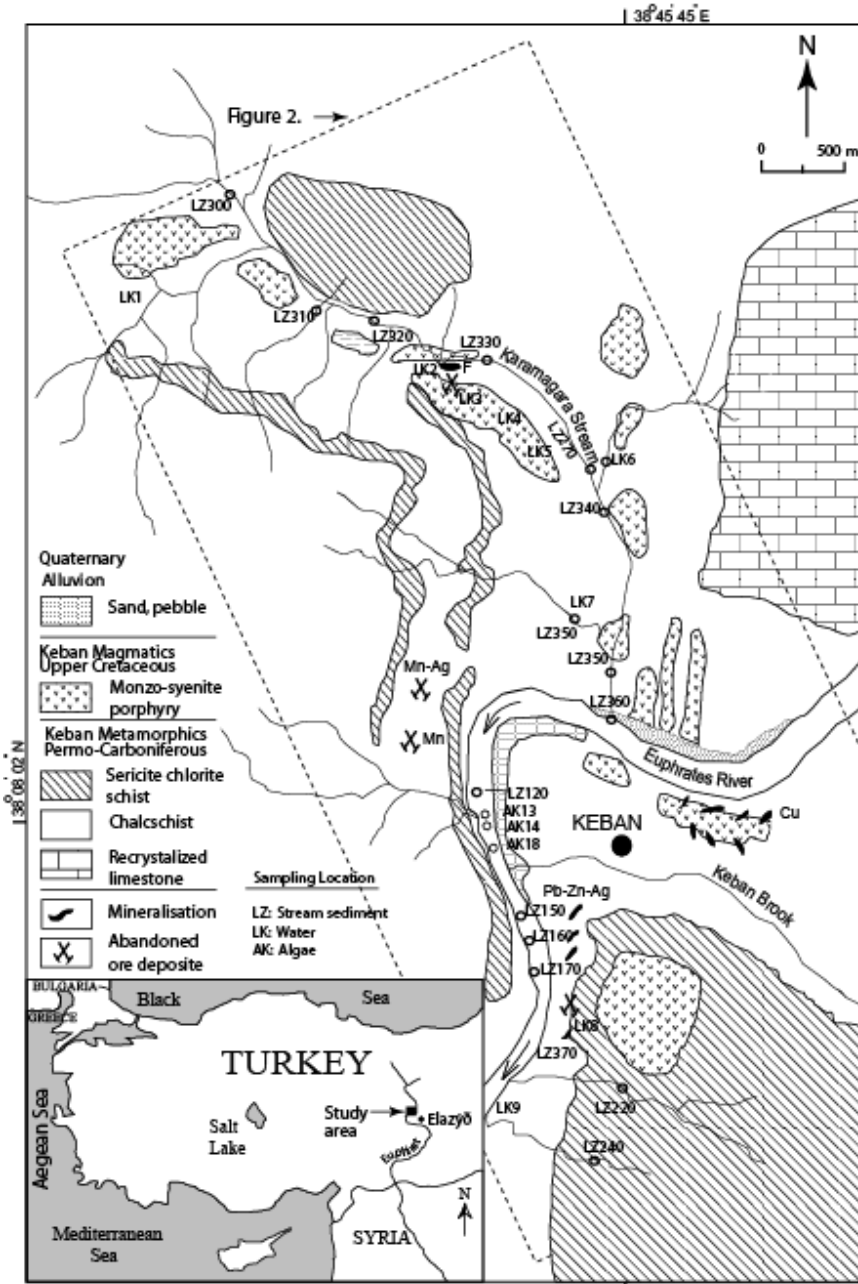


Fig. 2. Simplified geological map of the study area Kalender & Hanelçi, (2001; 2002) and locations of sampling sites (natural spring waters: LK 1-LK 4, LK 6, LK 7, LK 9, LK 10; mine-drainage waters: LK 5, LK 8; Euphrates River water: LK 11).

olive green but turns brown in its lower parts. Moss and algae samples were washed using distilled water and dried in air in the laboratory. 0.5 gr sample batches were digested to dryness at a temperature of 95°C for one hour after adding 2 ml of HNO₃ and then 3 ml of a 2:2:2 HCl:HNO₃:H₂O mixture. A total of 38 elements in the water samples were analyzed by ICP/MS (inductively coupled plasma/mass spectrometry); F in water was analyzed by ion electrode. Sediment samples were analyzed by ICP/MS, except for Au and Hg which were determined by atomic absorption (AA) after MIBK extraction and flameless AA, respectively. The algae and moss samples were analyzed by the ICP/ES (inductively coupled plasma emission spectrometry) and ICP/MS methods.

2.2 Results and discussion

It was determined that Mg, Ca, S, Fe, F, Mn, Zn, Mo, Ba, Pb, U, Ni, Cd, Co, Ag, Cu, Sb and Se contents of groundwater are above the standards of drinking water and it is also enriched in some toxic elements such as Al, Cd, Cr, Fe, K, Mg, Mn, Na, Pb, Sb, SiO₂, Tl and Zn. The springs particularly issuing from the mine galleries are probably the main source of pollution parameters. Analyses of weak leaching elements of -80 +140 mesh size sands collected from some main river and creeks indicate high As, Cu, Zn, Mo and Ag contents, various algae samples are characterized with high Cu, Pb, Zn, Ag, Cd and Cr concentrations. In this study will be determined the source and impact on environment of pollution in water, stream sediment and plants.

Element concentrations in different water samples are variable, with the Ba, Ca, Cd, Ce, Co, Cr, Cs, Mg, Mo, Pb, Rb, S, Se, U, Zn contents of most of these samples being above the world averages encountered in ground water (Table 1). The high metal concentrations in the samples originated from waters moving through the old mine adits or unexploited mineralized areas. This conclusion is supported by the compositions of waters collected from the adits (LK 5, LK 8).

In Table 2, the results of chemical analyses are compared to various standards in order to evaluate the drinking quality of waters. The concentrations of Cd, Pb, Tl, Cr, and Sb measured in these samples were higher than 0.005 mg/l⁻, 0.015 mg/l⁻, 0.002 mg/l⁻, 0.05 mg/l⁻, 0.006 mg/l⁻, respectively, which exceed the limits allowed for drinking waters (USEPA, 2002; WHO, 1993; Canada MAC, 2001; EEC, 1992). According to international standards, the concentrations of some other elements (Al, Fe, K, Mg, Mn, Na, SiO₂, Zn, and F) are significantly higher than the maximum permissible levels and, therefore, these waters should not be used for drinking. In light of these data, it is concluded that contamination of these waters by heavy metals and other toxic elements through mining, production galleries, and slag sites also causes environmental contamination.

Spearman correlation coefficients were calculated and their values at a significance level of $\alpha=0.05$ are summarized in Table 3. Spearman correlation coefficients given in brackets for the element pairs are: As-Cs (0.68), As-Re (0.65), Cd-Co (0.75), Cd-Cu (0.64), Cd-Fe (0.66), Cd-Mn (0.89), Cd-Zn (0.88), Se-S (0.85), Se-Re (0.86). Se, a chalcophile element found in appreciable amounts in polymetallic sulfide ores, easily dissolves in water by oxidation of sulfides and shows significant correlation with S and Re.

Elements	Median	Mean	Detection Limits	St. Dev.	Maximum	Groundwater World Average
As	2.5	3.3	0.5	2.91	11	2
B	20	27.4	5	13.23	58	10
Ba	43.345	44199	0.05	24.21	76.82	20
Br	46	124	5	195	654	20
Ca	89825	163275	0.05	154884	455325	50000
Cd	0.115	2.475	0.05	5.17	14.82	0.03
Ce	0.115	0.504	0.01	1.2	3.9	-
Cl	4000	10800	1	14413	49000	20000
Co	0.11	2.219	0.02	4.89	14.82	0.1
Cr	12.75	53.96	0.5	127.79	416.3	1
Cs	0.43	0.71	0.01	0.82	2.48	0.02
Cu	2.55	3.64	0.1	3.03	10.2	3
Fe	31	166	10	356.36	1171	100
In	47.5	45.3	0.01	7.85	57	7
K	2745.5	6410	0.05	8189	27565	3000
La	0.065	0.74	0.01	2.09	6.69	0.2
Li	6.5	13	0.1	14.32	41	3
Mg	27742	73133	0.05	94490	307178	7000
Mn	4.64	4421	0.05	13559	43000	15
Mo	15.9	34.38	0.1	39.96	109	1.5
Na	4228.5	15716	0.05	26916	90025	30000
Nd	0.055	0.18	0.01	0.38	1.25	-
P	22	24.7	20	5.4	33	20
Pb	10.75	15.86	0.1	14.58	47	3
Rb	14.54	21.94	0.01	24.89	82.28	1
Re	0.04	0.46	0.01	1.19	3.84	-
S	36000	138700	1	176251	399000	30000
Sb	0.575	1.49	0.05	2.24	7.26	2
Sc	5.135	5.38	1	1.49	8.29	-
Se	1.15	2.05	0.5	2.07	7.5	0.4
Si	19	18.5	40	5.43	29.6	16
Sn	0.425	0.992	0.05	1.26	4.3	0.1
Sr	1082.63	2008	0.01	2125	5668	400
Tl	1.31	4.36	10	8.51	27.75	0.002
U	17.58	17.71	0.02	14.08	32.02	0.5
Y	0.04	0.15	0.01	0.33	1.09	-
Zn	101.55	2466	0.5	5881	18573	20
F*	-	-	-	-	2200	100

Table 1. Statistical parameters for chemical composition of water samples ($n=10$, $\mu\text{g l}^{-1}$, * mg l^{-1}). Elemental contents in groundwater are from Rose et al., 1979; Concentrations higher than the normal values for water are shown in bold.

sensitive to dissolution. However, their enrichment in the waters is attributed to formation of complex Pb–Mn and Pb–Cr oxides (oxyhydroxide complexes). Negative correlation between Al and pH (Table 3) indicates that the amount of aluminum dissolved in water increases with increasing acidity. As seen in the underground spring, the presence of CaF_2 in the water affects Al solubility by forming AlF_6^{-3} type complexes.

The elemental contents of water, syenite porphyry, fluorite, molybdenite, silver-manganite and stream sediments are given in Table 4. To date, no analyses have been done for As, B,

Elements	**Fluorite molibdenite	**Silver manganite	***Syenite porphyry	Detection Limits	Stream Max.	Sediment Min.	Mean	Detection Limits
Al	47900	2700	46300	100	<10	<10	<10	%0.01
As	168	328	-	1	99999	0.245	13.712	0.1
Ba	10600	774000	2516	5	1.57	0.01	0.67	0.5
Br	11.64	21	-	0.1	<5	<5	<5	5
Ca	250000	148400	26200	100	20	5	12	5
Cd	16.75	3	-	0.1	-	-	-	-
Cl	-	126	-	0.1	85	10	29	10
Co	7.35	6	9.86	0.2	0.061	0.002	0.021	0.1
Cr	33.05	34	-	0.5	0.12	0.05	0.08	0.5
Cu	163	82	173	0.1	13.57	0.3	6.1	0.01
Fe	22800	84800	5200	100	12	5	5.86	0.01
K	4900	950	73400	100	172	19	59	0.01
Mg	18900	76600	5800	100	<5	<5	<5	0.01
Mn	3200	51900	3300	100	0.5	0.1	0.33	1
Mo	2500	-	-	0.1	12.75	13	2.94	0.01
Na	1500	270	15500	100	-	-	-	0.001%
P	200	43600	20	10	3	1	1.44	0.0001%
Pb	5500	6100	98.18	0.1	0.12	0.01	0.03	0.01
Rb	89	15	181	0.1	-	-	-	-
S	2500	3700	-	5	-	-	-	-
Sb	89	61	-	0.1	0.04	0.005	0.014	0.02
Se	25.84	7	-	0.5	1.34	0.07	0.41	0.01
Si	181200	35800	617800	100	-	-	-	-
Sn	45.55	65	-	1	-	-	-	-
Sr	700	-	673	0.5	2.47	0.02	1.4	0.5
Tl	4.08	10	-	0.1	-	-	-	0.02
Zn	872	456	163	1	14303	0.38	1665	0.1
U	49.71	6	-	0.1	-	-	-	0.05
F(n=4)	183000	571	-	100	6120	460	2542	100

Table 4. Content of elements in mineralizations and syenite porphyry and stream sediments in ppm (**= Çelebi ve Hanelçi, 1998, n=21, ppm; *** Kalender, 2000, n=22, ppm).

Br, Cd, Ce, Cl, Cs, La, Li, Mo, Nd, S, Sb, Sc, Se, Sn, Tl, U, and F in the syenite porphyries. The F, Mo, Mn, and Ag in the water samples were derived from fluorite (CaF_2), molybdenite (MoS_2), pyrolusite (MnO_2) and Ag-sulfosalts while their Cd, Co, Cr, Cu, Fe, Sb, Se, Sn, and Z contents originated from dissolution of chalcopyrite (CuFeS_2), arsenopyrite (FeAsS), enargite ($\text{Cu}_3\text{AsSbS}_4$), and loellingite (FeAs_2). The Na, Al, Ca, K, and SiO_2 concentrations of the waters resulted from the dissolution of the syenite porphyries themselves (Bölücek & Kalender, 2009).

Bioaccumulation values were calculated from two algae and one moss species. Bioaccumulation is a parameter that describes bioconcentration as the ratio of the concentration of a chemical species an organism to the concentration in the surrounding environment. Bioaccumulation factor (BAF) is calculated as follows:

$$\text{BAF} = (\text{whole body concentration of X}) / (\text{exposure media concentration of X})$$
The element contents and BAF values of the species are given in Table 5. *Bangia atropurpurea* (red algae) in the samples (AK 13 and AK 18) from the Euphrates river bed ($T=13^\circ\text{C}$, $\text{pH}=8$) was first described by Kishler & Taft (1970), in Lake Erie. This species is generally common in marine environments, gulfs and bays (estuarine). However, it is also found in continental waters where climatic conditions are suitable. *Bangia atropurpurea* is commonly found in iron-rich alkaline ($\text{pH}=8-8.7$) fresh waters. When compared to *Cladophora glomerata*, it has a higher capacity for absorption of Cu, Pb, Ni, Mn, Au, Cr, Mg and S. *Bangia atropurpurea* contains 6 fold Cu, 26 fold Ni, 2.7 fold Mn, 11.5 fold Au, 20.5 fold V, and 77 fold Cr compared to *Cladophora glomerata*. As is well-known, bioaccumulation is the net accumulation of a chemical by an aquatic organism as a result of uptake from all environmental sources. Thus, BAF values in this study were calculated for green and red algae samples according to the elemental contents of river water and, for moss samples, according to the elemental contents of spring and mine-drainage waters collected from the same locations (Table 5). The chemical concentrations in tissues of aquatic organisms and water can be defined in terms of chemical partitioning between different biological or chemical phases. BAF values in *Bangia atropurpurea* for Mo, Cu, Ag, Sb, P, Mg, Ba, and SO_4 are higher than those *Cladophora glomerata*, whereas BAF values for Zn, Co, V, Ca, La, B, Al, Hg, and Se are higher in *Cladophora glomerata* than those in *Bangia atropurpurea*. Total BAF (total concentration of the chemical in tissue / total concentration of chemical in water) values for *Bangia atropurpurea* are higher than those for *Cladophora glomerata* (Table 5). In sample AK-14 in comparison to *Bangia atropurpurea*, *Cladophora glomerata* has higher capacity of absorption for Cd, Bi, B, Hg, Se, Fe, Co, Ag, and Zn (Table 5). Particularly, the Hg (13 fold) and Cd (3.8 fold) contents of *Cladophora glomerata* may indicate that these algae may have a direct effect on the ecosystem. The moss, *Didymodon tophaceus* (Brid.) Lisa generally grows on Paleozoic limestones and dolomites, and is generally observed along banks and hilly areas close to river bed with gentle slopes. The highest BAF values in this study were observed in moss (*Didymodon tophaceus*) sample MK 20, indicating that the moss tissues have an ability to absorb heavy and toxic metals from mine-drainage waters. In this study, it was observed that there is considerable pollution of the waters and stream sediments in the Euphrates River. However, the presence of water plants have a positive effect on the aquatic ecosystem by absorbing the heavy metals and toxic elements (Pb, Hg, Cd, Cr, and As). Therefore, algae and moss can be used to remove some of the heavy metals and toxic elements from mining-waste water.

Elements	Detection Limits	LK13	LK 14	LK 18	LK 20	LK 8	LK 11
		<i>Bangia atropurpurea</i>	<i>Cladophora glomerata</i>	<i>Bangia purpurea</i>	<i>D. Tophaceus (Brid.) Lisa</i>	<i>Derebaca Gallery</i>	<i>Eupharate River</i>
Mo	0.01	0.38	0.26	0.33	0.36	0.001	0.003
Cu	0.01	13.15	1.54	9.26	68.61	0.002	0.003
Pb	0.01	1.75	<0.01	1.85	269.76	0.004	0.0002
Zn	0.1	155.4	267	117.9	3051.3	5.19	0.003
Ag*	2	11	70	8	1575	-	<0.05
Ni	0.1	6.3	0.1	2.6	25.1	-	<0.0002
Co	0.01	0.49	0.65	0.28	6.96	0.007	0.000008
Mn	1	22	15	41	1034	1.076	<0.00005
Fe	0.001%	730	930	390	3450	1.171	<0.01
As	0.1	6.3	13.9	13.3	123.5	0.011	0.003
U	0.01	0.27	0.39	0.15	6.86	0.04	0.0074
Au*	0.2	3.3	<0.2	2.3	17.3	<0.05	<0.05
Th	0.01	0.1	0.11	0.04	0.03	-	<0.00005
Sr	0.5	41.4	53.3	56.6	307.8	2.181	0.842
Cd	0.01	0.21	0.57	0.15	12.22	0.009	<0.00005
Sb	0.02	0.03	<0.02	0.19	0.98	0.007	0.001
Bi	0.02	0.05	145	0.02	0.09	-	<0.00005
V	2	11	226	11	12	-	0.001
Ca	0.01%	10400	13800	9800	46900	436.67	55.37
Pb	0.01	3020	840	4210	2060	0.02	0.023
La	0.01	0.29	2.21	0.12	1.02	0.0003	0.00001
Cr	0.1	4.98	0.05	3.87	3.87	0.011	<0.0016
Mg	0.0001%	2130	1830	2080	2091	163.11	18.56
Ba	0.1	8.2	22.3	12.6	30.3	0.016	0.026
Ti	1	14	13	14	7	-	<0.01
B	1	12	347	9	336	0.034	0.1
Al	0.001%	300	400	200	300	0.013	0.01
Na	0.001%	840	830	460	420	24.36	21.06
K	0.001%	300	300	1200	10600	10.047	1.82

Table 5. Content of elements in moss, algae and water in the Euphrate River,* = ppb; the other elements are given ppm.

2.3 Conclusions

The present study focused on the environmental geochemistry samples of water, stream sediment, algae and moss from the Keban mine district. The average concentrations of Mo, Cu, U, Sb, Mg, Hg, Se ve SO₄, Sr, V, Ca, P, Ba, B, Na, and Sc in Euphrates River water collected from near the former mining district were found to be elevated relative to average element concentrations reported for river waters. The concentrations of Al, Cd, Cr, F, Fe, Mg, Mn, Na, Pb, Sb, SiO₂, Tl, and Zn in water samples collected near the mineralized locations were higher than the maximum permissible standards for drinking water and, thus, it was determined that these waters are not drinkable. Consequently, these waters, which are used for drinking and agricultural purposes in rural areas, may pose a serious risk to public health. The high concentrations of As, Mo, Se, Cu, Zn, and Pb in the Karamağara Stream and Euphrates River sediments and waters suggest that both mechanical and chemical dispersions are dominant in the area. The element concentrations

in tissues of green and red algae collected from the Euphrates River bed were compared with those in moss collected from the mouth of the mine adit. The concentrations of Cu, Pb, Ni, Mn, Au, V, and Cr in *Bangia atropurpurea* were found to be higher than those in *Cladophora glomerata*, but Zn, Co, Fe, Cd, Hg, Se, Ga levels in *Cladophora glomerata* are much higher than those in *Bangia atropurpurea*. The Cu, Pb, Zn, Mn, Ag, Ni, Co, Fe, As, U, Sr, Cd, Ca, K, Mg, Ba, and Au contents of *Didymodon tophaceus* (Brid.) Lisa are higher than those of the algae. Total BAF values for *Bangia atropurpurea* are higher than for *Cladophora glomerata*, while the total BAF values of the moss are highest.

These geochemical results suggest that chemical leaching–precipitation reactions are taking place near the Keban mine slags. The spatial distributions of metals in the sampling media of the Keban mining district suggest that the causes of the contamination are primarily the previous mining activities and to a lesser extent natural weathering products of the various types of mineralized zones in the area.

3. Maden copper deposit

3.1 Sampling and analytical methods

The second study area is Maden Copper deposit in which the water and stream sediment geochemistry were studied (Figure 3; Figure 4). The water samples were collected from

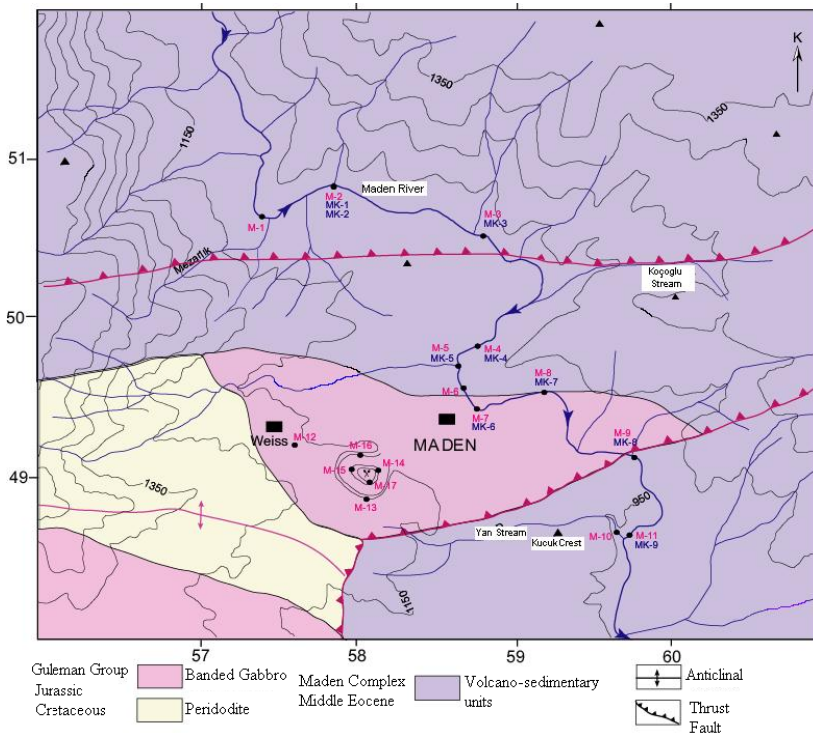


Fig. 3. Geology map of the Maden copper deposit and sediment samples location (MK: stream sediment samples, M: water samples; modified Kırat et al.2008; Kalender et. al. 2010).



Fig. 4. AMD waters in the Maden copper deposit.

M1- M11 (spring water samples; M12-M17 seepage water samples; M18-M24 waste water samples from copper flotation) and sediment samples from Maden Stream sediment then sediment samples were sieved in different size sediment fractions (range 850 to -500μ ; 500 to -180μ ; 180 to -106μ ; 106 to -75μ ; $<75 \mu$) analyzed by ICP-OES and IC (for SO_4).

3.2 Results and discussion

The water samples taken from the vicinity of copper deposits within the scope of this study were determined for the metal content.

The waste waters from copper flotation (M18-M24) has increased over the metal content than the other samples. However, the mean values of analysis of water for all the sample points are given in Table 6 and these values are compared with drinking water standards. According to Table 6 Al, Ca, Fe, Mg, Mn and Zn values are higher than drinking water contents. Kalender & Bölücek (2007) indicated that metal contents are higher than maximum contaminat levels for drinking water and quite high enough to be dangerous to agriculture and stock raising and, thus to human health.

Elements	Max.Conta- minant Level (mg ^l ⁻¹)	Water samples	
		Mean (mg ^l ⁻¹)	Max. (mg ^l ⁻¹)
Al*	0.20	20.90	53.125
Ca	10-100	125.26	478.832
Cd	0.003	0.042	0.156
Co	1	10.42	21.546
Cu	1	107	314.962
Fe	0.2	9.65	22.106
Mg	125	486.47	491.564
Mn**	0.05	7.72	27.253
Ni	0.02	0.90	3.513
Pb	0.0015	0.0092	0.0388
Se	0.01	0.058	0.075
Zn	5	51.02	43.304
SO ₄ ***	400	162	13224

Table 6. Drinking water maximum contamination level, (*: EEC, **: USEPA, ***: EQS fresh water, the others from WHO, standard values taken from Pais & Jones, 2000; Siegel, 2002). n=24.

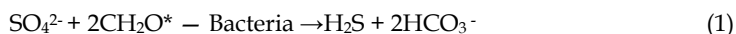
Within the scope of this study, Cu, Fe, Mn, Zn, Ni and SO₄ values of two seepage water in location no M15-M16 which had the highest metal concentration were analyzed before and after sulfate-reducing bacteria experiment (Figure 3 and 4; Kalender et.al. 2010).

Table 7 presents Cu, Fe, Mn, Zn, Ni and SO₄ values analyzed before and after adding bacteria to AMD water samples (M15, M16). It was found that in M15 and M16 locations, Cu values decreased from 151 µg^l⁻¹ to average 5.82 µg^l⁻¹, from 1447 µg^l⁻¹ to average 29.1 µg^l⁻¹; Fe values decreased from 132.2 µg^l⁻¹ to average 2.43 µg^l⁻¹, from 517 µg^l⁻¹ to average 9.92 µg^l⁻¹; Mn values decreased from 75.7 µg^l⁻¹ to average 19.33 µg^l⁻¹, from 1695 µg^l⁻¹ to average 449.46 µg^l⁻¹; Zn values decreased from 34.4 µg^l⁻¹ to average 0.45 µg^l⁻¹, from 3212 µg^l⁻¹ to average 40.22; Ni values decreased from 4.3 µg^l⁻¹ to average <0.1, from 70.4 µg^l⁻¹ to average 4.49 µg^l⁻¹; SO₄ values decreased from 1417.8 µg^l⁻¹ to average 788.38 µg^l⁻¹ and from 1719.2 to average 925.22 respectively.

Before Experiment						
Sample code	Cu	Fe	Mn	Zn	Ni	SO ₄
M15	151.1	132.2	75.7	34.4	4.3	1417.8
M16	1447	517	1695	3212	70.4	1719.2
Detection Limits	0.1	10	0.05	0.5	0.2	0.1mgL ⁻¹
After Experiment						
	Cu	Fe	Mn	Zn	Ni	SO ₄
M15-1-0.2	1.81	2.30	18.92	0.34	0.55	784.2
M15-2-0.2	1.70	2.40	19.23	0.37	<0.1	794.7
M15-1-2	2.63	2.60	19.45	0.42	<0.1	778.4
M15-2-2	2.7	2.72	19.98	0.48	<0.1	786.2
M15-1-20	13.51	2.25	18.9	0.52	<0.1	785.3
M15-2-20	12.6	2.28	19.5	0.56	<0.1	798.5
M16-1-0.2	36.18	9.07	423.5	30.2	3.6	924.4
M16-2-0.2	35.20	10.6	426.2	36.5	4.7	919.3
M16-1-2	23.12	10.7	452.5	40.5	4.5	920.5
M16-2-2	25.6	10.96	460.2	43.80	5.6	925.6
M16-1-20	26.7	8.87	462.2	44.66	4.33	932.5
M16-2-20	27.9	9.32	472.2	45.67	4.2	929.3

Table 7. pH values and metal contents ($\mu\text{g l}^{-1}$) of acidic seepage waters in two different sample collection locations before and after bacteria experiment M1.; 1: G20, 0.2 ml; M1.; 2: NO132, 0.2 ml; M1, 1: G20, 2ml; M1; 2: NO132, 2ml; : M1; 1: G20; 20 ml; M1, 2: NO132, 20ml; M2.; 1: G20, 0.2 ml; M2.; 2: NO132, 0.2 ml; :M2, 1: G20, 2ml; M2; 2: NO132, 2ml; M2; 1: G20; 20 ml; M2, 2: NO132, 20ml.

According to Table 8, alkalinity values of M15 and M16 locations were found to be 164 and 143 ppm before bacteria cultivation. EC (electrical conductivity) value of the mentioned acidic seepage waters was found to be 2056-2200 $\mu\text{S/cm}$. These values must have resulted from high metal content in the solution. *Desulphovibrio desulfurican* (G 20 - NO 132) sulfate-reducing bacteria used in the tests in the present study can convert the sulfate produced from the Maden main deposit (SO_4^{2-}) in the water which is rich in SO_4 into sulfur (S^2). The bacteria can form bicarbonate (HCO_3) in the presence of an organic carbon source using sulfate as an electron donor under anoxic and reducing conditions (Bechard et al.,1995; Dalsgaard & Bak, 1994; Fyson et al.,1995).



$\text{CH}_2\text{O}^* =$ Ordinary organic molecule (lactate or acetate)

During the process of sulfate-reducing, firstly HS^- is formed. HS^- forms hydrogen sulfur (H_2S) by reacting with free hydrogen ion (1). Then, hydrogen sulfur reacts with metals and form insoluble metal complexes and thus metals removal occurs. Produced bicarbonate provides higher alkalinity and pH in the medium when compared to the initial values. Electrical conductivity (EC, $\mu\text{S/cm}$) which is lower than the initial value, suggests decreased metal concentration in the solution (Table 8). Sulfate-reducing *Desulphovibrio desulfurican* is not active in conditions with a pH lower than 5 (Egiebor & Oni, 2007). For this reason,

Sample code	Sulphate reducing bacteria	ml	pH	EC $\mu\text{S/cm}$	Alk ppm
Before experiment					
M15			5.1	2056	164
M16			2.5	2200	143
After experiment					
	G20	0.2	8.7		
	G20	2	7.8	2000	250
	G20	20	6.2		
M15	NO-132	0.2	8.2		
	NO-132	2	7.8	2009	238
	NO-132	20	7.2		
	G20	0.2	8.6		
	G20	2	8.5	2083	279
M16	G20	20	8.2		
	NO-132	0.2	7.8		
	NO-132	0.1	7.6	2030	252
	NO-132	1	7.2		

Table 8. The effects of two types of bacteria cultivated to different media on pH, EC and alkalinity values.

reaction was realized in newly created neutralization conditions. Since suitable pH value for the survival of the bacteria was 7.8, a pH value of the solution was set to 7.8. After the incubation of the bacterium, pH values increased from 5.1 to 8.7 in M15 location and from 2.5 to 8.6 in M16 locations (Table 7; 8). It was found that the bacterium 0.8 increased pH value.

Reduction of manganese and iron can make significant contributions to neutralization process.

It was observed that Fe value increased approximately 57 times while Mn values decreased 4 times. Heterotrophic bacteria like *Desulfovibrio* analyzed in the study can directly reduce iron and manganese by using iron as the last electron acceptor in anaerobic conditions. When Fe^{3+} is reduced to Fe^{2+} , removal of iron from AMD becomes easier. Fe^{2+} reacts with the sulfide formed after sulfate reduction and as a result, contributes to removal of iron and increase of alkalinity (Akçıl & Koldaş, 2006). The fact that Zn value decreased approximately 100 times suggests that like Fe, Zn also reacted with sulfate. When hydrogen sulfur gas (H_2S) which is removed from Maden waste sites during sulfate reduction, permanent alkalinity values can be determined. Ni values in sulfate containing solution varied from 5.6 $\mu\text{g/l}$ to below detection limit.

Element distributions in different sediment size fractions are presented in Table 9. The fact that the elements in the study area were in the form of primary sulfides indicates that chemical degradation is low. Aqua regia is a quite good solvent for these types of samples (Allcott & Latin, 1978; Rubeska et al. 1987). This mixture can also dissolve colloidal metals, oxide sediments and minerals and many elements can be analyzed by dissolving of only one sample. As the metal distribution dissolved with this method decrease in current flow

Elements	Detection Limits	-20+35	Size fractions -35+80	-80+140	-140+200	-200
As	0.1	31.52	47.84	73.28	63.1	59.64
B	1	6	6	6.6	6.6	5.4
Ba	0.5	55.26	69.86	82.9	93.08	110.36
Bi	0.02	0.428	0.638	1.146	1.142	1.324
Cd	0.01	0.376	0.494	0.988	1.054	1.134
Co	0.1	292.28	302.08	310.8	253.8	297.42
Cu	0.01	1419.35	2153.28	3877.24	4261.61	5198.03
Cr	0.5	227.48	237.38	216.54	198.82	179.98
Ga	0.1	6.42	6.44	6.22	6.24	6
La	0.5	6.44	6.56	6.48	6.54	7.3
Mn	1	1068	1170	1266.2	1292.4	1642.8
Mo	0.01	7.34	8.352	8.878	7.864	7.664
Ni	0.1	151.46	164.54	198.64	205.16	195.26
Pb	0.01	82.04	126.28	270.37	284.16	318.98
Sb	0.02	1.87	3.13	7.064	7.306	6.878
Sc	0.1	8.3	8.54	8.5	8.56	8.2
Se	0.1	2.06	2.9	6.86	7.48	8.08
Sr	0.5	40.94	41.4	47.06	54.9	68.66
Te	0.02	0.21	0.31	0.65	0.72	0.75
Th	0.1	0.92	0.92	0.98	1	1.04
Tl	0.02	0.19	0.25	0.43	0.45	0.51
U	0.05	0.32	0.36	0.68	0.74	0.62
V	2	105.2	120	111.2	99	92.6
Zn	0.1	832.64	760.98	533.4	472.74	485.44
ppb						
Ag	2	301.4	477	1071.2	1133	1441.8
Au	0.2	27.56	64	960.3	124.22	283.3
Hg	0.1	40	64	170.2	198.4	280
%						
Al	0.01	2.06	2.14	2.29	2.39	2.33
Ca	0.01	1.56	1.52	2.03	2.65	3.68
Fe	0.01	8.76	9.37	9.15	7.52	6.96
K	0.01	0.08	0.08	0.10	0.11	0.11
Mg	0.01	2.19	2.28	2.74	2.71	2.35
Na	0.001	0.01	0.01	0.02	0.02	0.02
P	0.001	0.04	0.04	0.04	0.05	0.05
S	0.02	0.32	0.55	2.18	1.28	1.15
Ti	0.01	0.12	0.13	0.12	0.12	0.11

Table 9. Stream sediment element concentrations in different size fractions along the Maden River sediment size fraction=mesh; by Aqua regia (3HCl+HNO₃) digestion method.

direction, according to Rose et al. (1979) it suggests that mechanical distribution is effective in the region. For this reason, it can be stated that physical processes are more effective than

chemical processes in distribution of element in stream sand. Higher enrichment of As, Co, Cr, Mo, Ni, Sb, Zn and particularly Au values in -80 mesh sediment grain size when compared to -200 mesh grain size suggest that these elements were enriched by attaching on silica, that this dissolution method is not effective in dissolving silica and particularly in releasing Au.

3.3 Conclusion

Metal concentration is high in the vicinity of Maden copper deposit both in surface and ground waters and in stream sand samples. For this reason, two locations which particularly have high metal contents were determined and the change in sulfate was tried to be observed through anaerobic purification method. However, the decrease in Cu, Fe, Ni, Mn and Zn values along with sulfate after anaerobic purification experiments indicated that bacteria can decrease the concentrations in water by precipitation of metals.

As a result of analysis indicate that water samples are above the standards of fresh water and it is also enriched in some toxic cations and anion such as Cu, Fe, Mn, Zn, Ni and SO₄. Cu 151.1-1447 mg l⁻¹ (EQS fresh water max contamination level (mcl) 0,16 mg l⁻¹), Fe 132.2-517 mg l⁻¹ (mcl 1 mg l⁻¹), Mn 75.7-1695 mg l⁻¹ (mcl 0.30), Zn 34.4-3212 mg l⁻¹ (mcl 0,125), Ni 4.3-1447 mg l⁻¹ (mcl 0.20 mg l⁻¹). SO₄ values reach to 1417.8 mg l⁻¹ and 1719.2 mg l⁻¹ (mcl 400 mg l⁻¹) in different location in acide mine drainage waters. That is why the sulphate reducing bacteria experience was done in these water samples *Desulfovibrio desulfuricans* can initiate some metal precipitation in the parallel to indirect sulfide-mediated precipitation. Initial and final metals and sulphate concentration before and after experiments, were measured and finally evaluated influence of bacteria in different ratio (0.2; 2; 20 ml) in AMD waters at two different sample locations (M15 and M16) . The experimental results show that, Cu, Fe, Mn, Zn, Ni and SO₄ values have been decreased by using sulphate reducing bacteria, Cu values, range of 96 to 98 % ; Fe values, 98 %; Mn values, range of 73 to 74%; Zn values, 98 %; Ni values, range of 93.62 to 97.67% ratio and SO₄ values, range of 44.36 to 46.18% ratio, respectively.

Initial, metals are dissolved due to <pH in AMD waters, but after bacteria experiments metals are precipitated as complex compound due to >pH (>7 at the neutralize pH condition) and high alkalinity. Consequently, in this study bacteria experiments observed that SRB (sulphate reducing bacteria) affected on both precipitation of the metals and the sulphate reducing in the AMD waters from the Maden copper deposit. These data will be evaluated including in literature and investigated impact on environment pollution.

In stream sediment samples reach to high concentrations Zn values -500 μ, Fe values -180 μ, As values -106 μ; Cu, Pb and Cd values <75 μ in size fraction. These values were correlated with average of diabase according to NIST and observed to high concentration of the Cu, Pb, Zn, As, Cd and Fe values. It was found that metal concentrations in stream sand samples increased mostly by mechanical transportation, however metal content in various water samples increased chemically in high reducing conditions.

4. Alacakaya chromite deposit

Thirth study area is Alacakaya alpine type chromite deposit in which the water geochemistry was studied (Figure1).

4.1 Sampling and material method

The water samples were collected from natural springs and ground water in the chromitite deposit area. The samples were taken using a hand pump and water sampler and filtered using 0.5 μm membrane filter paper (4.5 cm diameter); subsequently, 5 ml of prepared 65% concentrated HNO_3 solution were added to 250 ml of each water sample and the samples were stored in the laboratory at 4°C until analysed. Analysis were done in Kanada ACME Labs. by ICP-OES method. Detection limits and the results of the water samples analyses are given in Table 10.

4.2 Result and discussion

There are many waste place in chromite mining area (Fig. 5). The waste is an important factor on ground water contamination by leaching. The second effect is surface waters seepage to the deep and after mixing to ground waters (Fig. 6A). Figure 6B shows serpentine formation in the study area. The spring and ground water element contents in the Alacakaya chromite mining area are showed in Table 10. When element contents are correlated to natural ground water chemical composition, Al, Fe and Mn values are high. Maximum Mg, Al and Mn values are 1912.706 mg l^{-1} , 672.72 mg l^{-1} and 125.56 mg l^{-1} in groundwater samples in the Guleman Ophiolites, Upper Cretaceous. According to Rose et al. (1979) natural groundwater element contents were pointed out as Mg 7000 mg l^{-1} , Al 10 mg l^{-1} and Mn 15 mg l^{-1} . However, the same element contents are correlated to drinking water maximum contamination levels that all metal contents are above drinking water maximum contamination levels (Table 10). The average concentration of Cr in the basaltic and ultramafic rocks the average concentration is 200 ppm. The average concentration of Mg in basaltic rocks the average concentration is 45000 ppm. The average concentration of Ni in the basaltic rocks is 150 ppm (Krouskopf, 1979). The results of rock samples analysis are given in Table 11.



Fig. 5. Waste in the Alacakaya Cr deposit.



Fig. 6. Seepage waters from surface to deep (A) in the gallery; serpentinite and chromitite (B).

Element	Mean	Max	Min	Dedection Limits	Ground-water	Max. allowed values	Drinking water (MCL)
Al	75.576	672.72	0.005	1	10	50a	0.20
As	0.003	0.002	0.001	0.5	2	50a	-
B	0.1	0.31	0.03	20	10	-	-
Ba	0.01	0.018	0.003	0.05	20	50b	-
Ca	139.14	463.78	13.47	50	5000	-	10-100
Cd	0.03	0.16	0.0005	0.05	0.03	5b	0.005
Co	5.6	39.35	0.001	0.02	0.1	-	1
Cu	74	447.75	0.002	0.1	3	1000a.b	1
Cr	0.05	0.23	0.001	0.5	1	50a	0.1
Dy	0.02	0.18	0.001	<0.01	-	-	-
Fe	31.83	302.03	0.1	10	100	300a.b	0.3
Mg	252.88	1912.71	2.88	50	7000	50000b	50**
Mn	14.8	125.56	0.003	0.05	15	50b	0.05
Na	7.4	21.26	1.7	50	30000	20000b	20
Nd	0.07	0.65	0.0005	<0.01	0.08*	-	-
Ni	0.95	6.3	0.002	0.50	-	-	0.02
P	1.2	11.12	0.02	20	20	-	-
Pb	0.01	0.06	0.001	10	3	15b	0.015
Rb	0.002	0.013	0.003	0.01	1	-	-
S	0.6	4408	11	1000	30000	-	-
Y	0.09	0.85	0.004	<0.01	0.06*	-	-
Zn	10.18	60.48	0.03	0.50	20	5000a.b	5

Table 10. Element concentrations of the spring and ground water samples (in mgL⁻¹); element contents of natural ground water (in mgL⁻¹) from Rose et al. (1979); *= Jenssen & Verweij 2003; **= EEC; a- Ley 18284 (1969) Codigo Alimentario Argentino; Modificaciones (1988) and (1994); b- USEPA 1980, 2000. MCL= maximum contamination level; n= 10.

Major oxide (%) and minor element (ppm)	Harzburgite	Dunite	Pyroxenite	Detection Limits
SiO ₂	44.56	43.3	49.56	0.01
Al ₂ O ₃	0.63	0.46	6.33	0.01
Fe ₂ O ₃	9.35	9.1	5.4	0.04
MgO	42.85	43.4	17.46	0.01
CaO	0.69	0.59	18.28	0.01
Na ₂ O	0.04	0.02	0.17	0.01
K ₂ O	<0.04	<0.04	<0.04	0.01
TiO ₂	<0.01	<0.01	<0.01	0.01
P ₂ O ₅	<0.01	<0.01	<0.01	0.01
MnO	0.12	0.11	0.12	0.01
Cr ₂ O ₃	1.14	0.51	0.41	0.002
Co	110.9	11.5	46.2	0.001
Ni	2634	2682	231	20*
Cu	14.5	25.4	32.7	0.0001
Zn	36	58	42	0.0001
Rb	0.6	<0.5	<0.5	0.5*
Nd	<0.4	<0.4	0.7	0.4*
Dy	<0.05	<0.05	0.65	0.005*
Y	0.2	0.3	6.6	0.01*

Table 11. Major oxide and minor element concentrations of harzburgite, dunite and pyroxenite from the Alacakaya chromitite deposit area from Başpınar (2006), Detection limits in %; * = ppm.

The high metal concentration in both spring and ground water samples indicated that source of contamination is lithological units (harzburgite, dunite, pyroxenite and alteration produce serpentinite) due to surface erosion, leaching and tectonism.

Talc is an alteration mineral. Altering serpentine ($3\text{MgO} \cdot 2\text{SiO}_2 \cdot 2\text{H}_2\text{O}$) can also form talc. Serpentine commonly contains chrysotile asbestos, a carcinogen listed by the EPA. That is why; groundwater geochemistry was investigated in the Alacakaya chromite deposit area (Kalender, 2009).

4.3 Conclusion

These studies show that the major and minor elements may be useful geochemical tracers but they have dramatically effect on environmental pollution especially in mining area. The present studies have demonstrated that the distribution and behavior of toxic and non toxic element content in the different media (water, sediment, and plants) may be bonded to high concentrations in geological units.

This study focuses on environmental effect of the metal pollution in the different origin ore deposits.

5. Acknowledgement

Keban Ag-Pb and Zn and Maden Cu deposit studies were financially supported by Firat University, Grant Number 628 and 1506, respectively.

6. References

- Akcıl, A. & Koldaş, S. (2006). Acid Mine Drainage (AMD): Causes, treatment and case studies. *Journal of Cleaner Production*, Vol.14, pp. 1139-1145, ISSN 0959-6526
- Akıncı, O., Acar, E. & Tüfekçi, S. (1977). A study of Plan Keban Pb-Zn ore, *General Directorate of Mineral Research and Exploration: Report*, pp. 68-76, ISSN 0026-4563
- Aksın, M., Çetin, A. K. & Yıldırım, V. (1999). The Algae of Keban Stream (Elazığ, Turkey), *Firat University, Journal of Science*, Vol. 11, pp.59-65, ISSN 1308-9072 (in Turkish).
- Allcott, G.H. & Latin, H.W. (1978). Tabulation of Geochemical Data Furnished by 109 Laboratories for Six Explorations Reference Samples. *U.S. Geological Survey, Open File Report*, pp. 78-163, ISSN 0196-1497
- Balçık, A. (1979). Mineralizations of Keban Nalliziyaret and Karamağara Dere (Bamas), *General Directorate of Mineral Research and Exploration: Report*, pp. 23, ISSN 0026-4563
- Başpınar, G., (2006). Geochemistry and Contents of Platinum Group Elements of Guleman Chromite Deposit, Elazig, Turkey. *Firat University, Science Institute, Master Thesis*, pp. 125. Elazig, Turkey (Unpublished).
- Béchar, G., Mc Cready, R. G. L., Koren, D.W. & Rajan, S. (1995). Microbial Treatment of Acid Mine Drainage at Halifax International Airport Sudbury, Ontario. Canada, In: *Proceedings of Sudbury'95: Mining and the Environment Conference Proceedings*, Sudbury, Ontario. 28 May - 1 June, Vol. 2, pp. 545-554. ISSN 1319-8025
- Bölücek, C. (2002). A Stream Sediment Geochemical Orientation Study in Derince (Keban-Elazığ) Vicinity, *Bulletin of Earth Sciences, Application and Research Centre of Hacettepe University*, Vol. 25, pp. 51-63, ISSN 1301-2894 (in Turkish).
- Bölücek, C., (2007). Environmental Contamination in The Keban Mining District, Eastern Turkey, *AJSE*, Vol.32/1A, pp.3-18, ISSN 1319-8025
- Bölücek, C. & Kalender, L, (2009). Drainage Sediment Geochemical Orientation Study Under Semi-Arid Conditions, Keban, Eastern, Turkey. *AJSE*, Vol. 34, 1A, pp. 91-102, ISSN 1319-8025
- Çalık, A. (1998). Keban Plutonits; its Relation to Mineralogy, Petrogenesis and Wall Rocks, *Ph. D. Thesis, University of Istanbul*, pp. 18, 1 Istanbul, Turkey, (unpublished).
- Çelebi, H. & Hanelçi, Ş. (1998). Geochemische und Geostatistische Untersuchungen an Mn-Erzen des Lagerstaettdistriktes Keban, Elazığ/Osttürkei, *Geologisches Jahrbuch, Hannover*, Vol.108, pp. 3-33, ISSN0016-7851
- Canada MAC, *Guidelines for Canadian Drinking Water Quality*, 2001.
- Dalsgaard, T. & Bak, F. (1994). Nitrate Reduction in a Sulfate-Reducing Bacterium, *Desulfovibrio desulfuricans*, Isolated from Rice Paddy Soil. Sulfide Inhibition, Kinetics, and Regulation. *Applied and Environmental Microbiology*, Vol. 60 (1), pp.291-297, ISSN00992240
- Egiebor, N.O. & Oni, B. (2007). Acid Rock Drainage Formation and Treatment: A Review. *Asia-Pacific Journal of Chemical Engineering*, Vol. 2, pp. 47-62, ISSN 1932-2135

- Entwisle, T. J. (1989). Phenology of the Cladophora-Stigeoclonium Community in to Urban Creeks of Melbourne, *Australian Journal of Marine and Freshwater Research*, Vol. 40, pp. 471–489, ISSN 0067-1940
- Environmental Quality Standards (EQS) are Annual Average Concentrations with Maximum Allowable Concentrations in brackets. Esdat Environmental Database Management Software, www.esdat.net
- Erdoğan, B. (1977). Geology, Geochemistry and Genesis of the Sulphide Deposits of the Ergani-Maden Region, SE Turkey. Ph.D. Thesis, The University of New Burnswick, p. 289 (unpublished).
- Erdoğan B. (1982). Geology and volcanic rocks of the ophiolitic zone in the Maden area. *Geological Bulletin of Turkey*, Vol. 25, pp.49-60, ISSN 1016-9164 (in Turkish).
- Europium Economy Community (EEC), (1992). Standard Statistical Classification of Surface Freshwater Quality for the Maintenance of Aquatic Life. CES/733, 13 April 1992. United Nations, Economic and Social Council.
- Fyson, A. Kalin. M. & Smith, M.P. (1995). Nickel and Arsenic Removal from Mine Wastewater by Muskeg sediments. *Proceedings of the 11th Annual General BIOMINET Meeting, Ottawa, Ontario*, January 16, pp. 103-118.
- Janssen R.P.T. & Verweij, W. (2003). Geochemistry of some rare earth elements in groundwater, Vierlingsbeek, The Netherlands. *Water Research*, Vol. 37, pp. 1320–1350, ISSN: 0043-1354
- Kalender, L. (2000). Geology, Origin and Economic Importance of the Copper Mineralization of Keban (Elazığ), East Euphrates Kemandere Area, Ph.D. Thesis, *Firat University*, pp. 110, Elazığ, Turkey. (in Turkish).
- Kalender L. & Hanelçi, Ş. (2001). Mineralogical and Petrographical Features of Nallıziyaret Tepe (Keban-Elazığ) Copper Mineralization, *Istanbul University Earth Sciences*, Vol.14, pp. 51–60, ISSN 1016-9806 (in Turkish).
- Kalender L. & Hanelçi, Ş. (2001). Mineralogical and Geochemical Features of Au, Ag, Pb and Zn Mineralization in Keban (Elazığ) Wastes, *Geological Bulletin of Turkey*, Vol. 44, pp.91-104, ISSN 1016-9164 (in Turkish).
- Kalender L. & Hanelçi, Ş. (2002). General Features of Copper Mineralization Nallıziyaret Tepe (Keban-Elazığ): An Approach to its Genesis, *Geosound*, Vol. 40/41, pp.133–149, ISSN 1019-1003 (in Turkish).
- Kalender, L. & Bölücek, C. (2004). Major And Trace Element Contamination of Groundwaters, Stream Sediments and Plants of the Abandoned Mines in Keban District (Elazığ) of Eastern Anatolia, Turkey. 57. *Geological Congress of Turkey*. 08-12 March, pp.187-188.
- Kalender, L. & Bölücek, C., (2007). Environmental Impact and Drainage Geochemistry in the Vicinity of the Harput Pb-Zn-Cu Veins, Elazığ, SE Turkey, *Turkish Journal of Earth Sciences*, Vol.16, pp. 241-255, ISSN 1300-0985
- Kalender, L. (2009). Impacts on Environmental of Ore Deposits in Elazığ Area. Ministry of Environment and Forest, Environmental Legislation Remediation and Applied Conference, (oral presentation), TAIEX, 25 March 2009, Elazığ, Turkey.
- Kalender, L., Kırbağ, S., Kırat, C. & Bölücek, C., (2010). The Sulfate Reducing Bacterium Experiments In AMD Waters of The Maden (Elazığ) Copper Deposit, *Firat University, Journal of Engineering*, Vol. 22/2, pp. 197-204, ISSN 1308-9072
- Kalender, L., Kırbağ, S., Kırat, C. & Bölücek, C., (2010). The Sulfate Reducing Bacterium Experiments in AMD Waters of the Maden (Elazığ) Copper Deposit, Seventh

- International Symposium On Eastern Mediterranean Geology, 18-22 October 2010, pp. 130, Adana / Turkey.
- Kelley, D.L., Hall, G.E.M., Closs, L.G., Hamilton, I.C. & Mc Ewen, R.M. (2003). The Use of Partial Extraction Geochemistry for Copper Exploration in Northern Chile. *Geochemistry: Exploration, Environment, Analysis*, Vol. 3, pp. 85-104, ISSN 1467-7873
- Kineş, T. (1969). The Geology and Ore Mineralization of the Keban Area, Eastern Turkey, *Ph.D. Thesis, Istanbul University*, pp.213, Istanbul, Turkey, (unpublished).
- Kipman, E. (1976). Geology and Petrology of Keban, *Ph.D. Thesis, Istanbul University*, pp.189, Istanbul, Turkey, (unpublished).
- Kırat, G., Bölücek, C., Kalender, L., (2008). Distribution of Cu, Pb, Zn, As Cd and Fe in stream sediments around of Maden copper deposit. *Geosound/Yerbilimleri*, Vol.53, pp. 203-217, ISSN 1019-1003.
- Kishler J. & Taft, C.E. (1970). *Bangia atropurpurea* (Roth) in Western Lake Erie, *Ohio Journal of Science*, Vol. 70, pp. 56-57, ISSN 0050-0950
- Köksoy, M. (1975). Geochemical Leakage Anomalies in the Vicinity of Keban Mine, *Bulletin of Geological Society of Turkey*, Vol. 18, pp. 131-138, ISSN 1016-9164 (in Turkish).
- Krauskopf, K. B. (1979). Introduction to Geochemistry. Tokyo: McGraw-Hill Kogakusha, Ltd., ISBN 0070358206
- Kumbasar, I., (1964). Petrographic and Metallogenic Features Mineralisations in Keban Vicinity, *Ph. D. Thesis, Istanbul Technical University*, pp. 157, Turkey, (unpublished).
- Ley 18284. Código Alimentario Argentino (1969). Sancionada y promulgada el 18/7/69. B.O. 28/7/69. Modificación 1988 y Modificación 1994, Buenos Aires, Argentina.
- Özdemir, Z. & Sağıroğlu, A. (1998). The Study of Biogeochemical Anomalies for Fe along the Maden River (Maden-Elazığ). *Geological Bulletin of Turkey*, Vol. 41/1, pp. 49-54, ISSN 1016-9164
- Özdemir, Z. & Sağıroğlu, A. (2000). The Study of Biogeochemical Anomalies for Zn along the Maden River (Maden-Elazığ). *Mersin University, Series of Essay*, Vol. 4, pp. 93-100, 0002-6417
- Özkaya, İ. (1978). Stratigraphy of Ergani-Maden vicinity. *Geological Bulletin of Turkey*, Vol. 21, pp. 129-139, ISSN 1016-9164
- Pais, I. & Jones J. B. Jr. (2000). *The Handbook of Trace Elements*, St. Lucie Press, Boca Raton, ISBN 0849314585, Florida,
- Power, M. E. (1992). Benthic Turfs vs. Floating Mats of Algae in River Food Webs, *Oikos*, Vol.58, pp. 67-79, ISSN 0030-1299
- Rose, A. W., Hawkens, H.E. & Webb, J.S. (1979). *Geochemistry in mineral exploration*. (2nd edition). Academic Press, ISBN 0-7718-8893-7, London.
- Rubeska, I., Ebarvia, B., Macalalad, E., Ravis, D.& Roque, N. (1987). Multi Element Preconcentration by Solvent Extraction Compatible with an Aquaregia Digestion for Geochemical Exploration Samples. *Analyst*, Vol. 112, pp. 27-29, ISSN 0003-2654
- Schönborn, W. (1996). Algal Aufwuchs on Stones, with Particular Reference to the Cladophora-Dynamics in a Small Stream in Thuringia. (Germany): Production, Decomposition and Ecosystem Reorganizer, *Limnologica*, Vol. 26, pp. 375-383, ISSN 0075-9511
- Seeliger, T.C., Pernicka, E., Wagner, G.A., Begeman, F., Schmitt-Strecker, S., Eibner, C., Öztunalı, Ö. & Baranyı, I., (1985). *Archo-metalurgische untersue-hungen ni Nord und*

- Ostanatolien*. 32. Jahrbuch des Römisch. Germanischen Zentralmuseums, p.597-659, Mainz, Germany.
- Siegel, F. R. (2002). *Environmental Geochemistry of Potentially Toxic Metals*, Springer-Verlag GmbH, pp. 218, ISBN 3 540 42030 4, Berlin and Heidelberg, Germany
- Tızlak, E, (1991). Mining in the Keban - Ergani area (1780- 1850). *Ph.D. Thesis, Firat University, pp. 402, Elazığ, Turkey.* (in Turkish).
- United State Environmental Protection Agency, (2002). *List of Drinking Water Contaminants and MCL*.
- Whitton, B.A., John, D. M., Johnson, L. R. , Boulton, P. N. G. , Kelly, M. G. & Haworth, E.Y. (1998). Perspective on the Coded List of the Freshwater Algae of the British Isles. *The Science of the Total Environment*, Vol. 210/211, pp. 283-288, ISSN 0048-9697
- World Health Organization, (1993). *Guidelines for Drinking-Water Quality*, Geneva: WHO.
- Yılmaz, A., Ünlü, T. & Sayılı, S. (1992). An Approach to Mineralization of Pb-Zn in Keban (Elazığ), *Mineral Research and Exploration Geology Review*, Vol. 114, pp. 47-70 (in Turkish). ISSN 0026-4563
- Zisserman, A. (1969). Geological and Mining Study of Keban Madeni, Elazığ (Turkey), *Ph.D. Thesis, BRGM France*.

Application of Nondestructive X-Ray Fluorescence Method (XRF) in Soils, Friable and Marine Sediments and Ecological Materials

Tatyana Gunicheva

*A. P. Vinogradov Institute of Geochemistry
Russia*

1. Introduction

X-ray fluorescence (XRF) analysis is accepted as the most suitable physical method for the exploration of the elemental composition of rocks and minerals. This is due to fusing the sample with appropriate flux. The desired result is achieved because rocks and minerals are oxidic systems relative to major components. Soils, friable and marine sediments, silt and ecological materials differ from the above in the presence of an organic constituent (Corg), the weight fraction of which may vary considerably. The bioorganic diversity of Corg is the main source of errors, arising from sampling and analyzing procedure (Bock, 1972). Therefore, the possibility to analyze samples without having them destructed (nondestructive), preserving the study material after the results have been obtained, remains the unique advantage of XRF. This chapter reports information on nondestructive XRF procedures to determine the contents of rock-forming and some minor elements in powder of the materials listed. A satisfactory quality of XRF results, their validity and prospective viability for multi-purpose interpretations and environment monitoring have been discussed.

2. Nondestructive X-ray fluorescence (XRF) analysis of soils, friable and marine sediments

Their organic constituents consist of a mixture of plant and animal products, decomposed to different extents, and compounds which are chemically and biologically synthesized in soil. The resultant products of these processes are humic matter, low and high molecular weight organic acids, carbohydrates, proteins, peptides, amino acids, lipids, waxes, polycyclic aromatic hydrocarbons and lignin fragments. In addition, the secretions of root systems, consisting of a wide range of simple organic acids, are also present in the soils. The humic matter has the structure of a twisted polymer chain and consists of a relatively large number of functional groups (CO₂, OH, C=C, COOH, SH, CO₂H). Owing to a specific combination of various groups (particularly OH and SH), the humic matter is capable of producing complex compounds with some cations (Kabata-Pendias & Pendias 1986; Bolt & Bruggenwert 1976; Greenland & Hayes 1978; Lindsay 1979). The composition and properties of the organic constituents of soil depend on climatic conditions, the type of soil and agrotechnical techniques. Their interactions with soil metals may be described with the help of such

phenomena as ion-exchange reaction, surface sorption, chelate formation, coagulation and peptization. Biochemical complexity of the organic constituent of the materials considered radically alters melting with the flux. The formation of metal carbides, conversion of organic carbon into its modifications, the combustion point of which is very high (is not below 1600°C) and other phenomena arising in this situation inhibit homogenization. Therefore, the formal utilization of XRF analysis of rocks for soils and sediments seems to be possible only when their Corg. content does not exceed 1.5-2% (Kabata-Pendias & Pendias 1986). In all other instances fusing leads to the isolation of carbon at the glass disc surface. Concerning the materials ashed, because of the large number of non-investigated effects taking place under the recommended ashing at temperature $525 \pm 25^\circ \text{C}$ conversion from the ashed to the initial system is so uncertain that its analysis becomes meaningless.

This part of paper reports information on the nondestructive XRF determination of Na, Mg, Al, Si, P, K, Ca, Ti, Mn, Fe, S, Ba, Sr and Zr in secondary natural matters. Except for drying at 105°C and pressing, it does not require any preliminary treatment of the sample. The necessity for additional drying is connected with the fact that the certified estimates of composition for standard materials used for calibration are given for those dried and sterilized at 105°C .

2.1 Radiator preparation

Tablets from the powder samples were pressed on a boric acid backing under constant pressure. The amount of material required to produce a specimen for XRF analysis is different because of the varying organic content. Thus, if for soil and loam 6 g are sufficient, then for deposits the amount should not be less than 8 g. For humus and forest litter, its total trace element content does not exceed 5-6%, so that an 'infinitely thick' layer is ensured by about 12-14 g.

2.2 XRF equipment

The intensities of analytical lines were measured with a CPM-25 x-ray spectrometer with 16 fixed channels. The rhodium target x-ray tube was operated at 40 kV. The scattered Rh $K\alpha$ - line intensity measured with the 16th channel was used as an internal standard for some elements. It should be kept in mind that the wavelength of this line is the shortest among those measured.

2.3 Standard set for calibration

For calibration and assessment of the accuracy of analysis we used sets of Russia national certified standards of soils, marine sediments and friable deposits (Arnautov 1987). With the help of Chinese reference standards of soils and river sediments the possibility of the joint use of the Russia and Chinese national collections was also estimated.

In Table 1 for standard materials of various types of soil, sediment and friable deposits, the results obtained by the proposed XRF procedure (XRF) are compared with the certified values. For Al and Si, the XRF values were calculated using the set of calibration standards restricted to standards of the same type. The agreement between the XRF and certified values is satisfactory (Ostroumov 1979). With the exception of Si and partly for Al, for all elements the

differences among them are not significant and do not exceed the permissible standard deviations for all types of the above materials. The discrepancies observed for Al and Si are not surprising. In our opinion, the reason is that these elements are major and present in distinct mineral phases. However, our aim was to show the accuracy of the analytical results which the proposed method will provide for samples prepared in the required way. If the analytical data user is to obtain such results, real-world samples must be treated in the same manner, otherwise the quality of the final results will be significantly worse than the above.

Component	SP-1 black earth soil		SP-2 podzol soil		SKR red earth soil		SSK grey earth carbonate soil	
	Certified	XRF	Certified	XRF	Certified	XRF	Certified	XRF
Na ₂ O	0.80±0.03	0.81±0.02	1.15±0.05	1.09±0.02	0.15±0.03	<0.2	1.64±0.05	1.76±0.03
MgO	1.02±0.03	1.10±0.02	0.77±0.01	0.64±0.02	0.92±0.05	0.79±0.03	2.99±0.09	3.17±0.06
Al ₂ O ₃	10.37±0.08	10.56±0.09	9.57±0.06	9.43±0.07	17.01±0.26	17.02±0.14	11.48±0.14	11.51±0.10
SiO ₂	69.53±0.21	70.40±0.26	78.33±0.12	78.68±0.27	59.18±0.30	58.93±0.24	52.65±0.17	53.28±0.21
P ₂ O ₅	0.170±0.010	0.180±0.010	0.075±0.006	0.067±0.008	0.100±0.010	0.110±0.020	0.170±0.010	0.170±0.010
K ₂ O	2.29±0.06	2.28±0.02	2.47±0.05	2.50±0.03	0.98±0.03	1.08±0.02	2.09±0.04	2.07±0.02
CaO	1.63±0.05	1.73±0.03	0.81±0.04	0.74±0.03	0.17±0.04	0.17±0.01	11.47±0.10	11.48±0.06
TiO ₂	0.75±0.02	0.75±0.01	0.84±0.03	0.83±0.01	1.56±0.04	1.61±0.04	0.64±0.02	0.63±0.01
MnO	0.077±0.002	0.079±0.002	0.070±0.002	0.069±0.002	0.051±0.002	0.052±0.001	0.089±0.003	0.085±0.002
Fe ₂ O ₃	3.81±0.05	3.87±0.04	2.98±0.05	3.01±0.03	7.86±0.08	7.97±0.05	4.60±0.05	4.73±0.05
S	0.069±0.015	0.63±0.005			0.040±0.010	0.040±0.005	0.040±0.010	0.040±0.005

Component	SDPS podzol sandy loam		SDO-2 marine sediment		SGH-1 carbonate background silt		SCHM-3 friable aluminosilicate deposit	
	Certified	XRF	Certified	XRF	Certified	XRF	Certified	XRF
Na ₂ O	0.51±0.03	0.53±0.01	4.03±0.04	4.03±0.03	0.53±0.02	0.56±0.02	0.61±0.04	0.65±0.04
MgO	0.13±0.05	0.11±0.01	4.67±0.08	4.34±0.09	6.06 ± 0.11	6.01±0.16	11.70±0.14	11.80±0.20
Al ₂ O ₃	3.36±0.11	3.23±0.14	14.33±0.17	14.29±0.12	9.48 ± 0.14	9.32±0.07	5.03±0.10	5.06±0.04
SiO ₂	91.24±0.23	90.86±0.65	43.61±0.12	44.43±0.27	47.00 ± 0.20	46.68±0.29	25.07±0.29	25.24±0.21
P ₂ O ₅	0.036±0.006	0.037±0.002	0.280±0.020	0.290±0.010	0.13±0.01	0.150±0.005	1.820±0.050	1.830±0.020
K ₂ O	1.23±0.03	1.31±0.02	1.36±0.02	1.37±0.03	2.26 ± 0.07	2.26±0.02	1.13±0.04	1.11±0.02
CaO	0.27±0.03	0.25±0.02	7.81±0.12	7.93±0.08	7.76 ± 0.10	7.77±0.08	17.76±0.22	17.99±0.31
TiO ₂	0.29±0.01	0.25±0.01	2.32±0.06	2.30±0.03	0.50 ± 0.02	0.55±0.01	0.27±0.01	0.27±0.01
MnO	0.011±0.001	0.011±0.001	0.270±0.010	0.270±0.005	0.30 ± 0.01	0.300±0.005	0.500±0.030	0.500±0.010
Fe ₂ O ₃	0.99±0.05	0.95±0.04	11.91±0.09	11.99±0.20	5.92 ± 0.04	5.94±0.04	10.59±0.20	10.92±0.20
S			(0.04; 0.16)		(0.037)		0.050±0.010	0.050±0.005

Component	SGH-3 terrigenous background silt		SGH-5 anomalous silt		SGHM-1 friable carbonate-silicate deposit		SCHT typical black earth soil	
	Certified	XRF	Certified	XRF	Certified	XRF	Certified	XRF
Na ₂ O	1.61±0.05	1.48±0.03	2.33±0.06	2.36±0.02	0.87±0.05	0.91±0.02	0.81±0.02	0.76±0.02
MgO	1.60±0.05	1.59±0.03	2.54±0.06	2.34±0.05	5.82±0.10	5.70±0.10	0.95±0.03	1.01±0.03
Al ₂ O ₃	16.46±0.19	15.73±0.20	14.40±0.11	13.69±0.12	11.60±0.13	10.77±0.10	9.81±0.14	10.07±0.07
SiO ₂	60.54±0.20	59.42±0.22	60.85±0.14	60.95±0.23	45.59±0.29	46.90±0.60	71.49±0.27	72.35±0.25
P ₂ O ₅	0.190±0.010	0.180±0.010	0.180±0.10	0.110±0.010	0.150±0.010	0.130±0.005	0.180±0.020	0.180±0.010
K ₂ O	2.43±0.08	2.45±0.03	3.56±0.09	3.39±0.03	2.96±0.07	2.90±0.03	2.42±0.04	2.49±0.02
CaO	0.41±0.03	0.48±0.03	2.95±0.05	2.87±0.04	7.05±0.20	6.81±0.07	1.60±0.05	1.79±0.20
TiO ₂	0.98±0.03	0.96±0.01	0.62±0.01	0.58±0.01	0.63±0.04	0.68±0.01	0.74±0.03	0.73±0.01
MnO	0.130±0.010	0.140±0.005	0.087±0.003	0.086±0.002	0.073±0.004	0.082±0.002	0.079±0.002	0.081±0.002
Fe ₂ O ₃	8.76±0.08	8.77±0.06	5.45±0.10	5.28±0.04	4.62±0.06	4.75±0.05	3.48±0.06	3.45±0.04
S	(0.027)		(0.10)		0.050±0.010	0.050±0.005	0.050±0.010	0.068±0.005

Component	GSS-4, limy-red soil		GSS-2, chestnut soil		GSS-5, yellow-red soil		GSD-10, stream sediment	
	Certified	XRF	Certified	XRF	Certified	XRF	Certified	XRF
Na ₂ O	0.11±0.01	0.12	1.62±0.02	1.65	0.122±0.009	<0.1	(0.04)	<0.1
MgO	0.49±0.02	0.60	1.04±0.02	1.05	0.61±0.02	0.67	0.12±0.02	0.20
Al ₂ O ₃	23.45±0.11	25.92	10.31±0.05	10.17	21.68±0.09	24.46	2.84±0.04	3.35
SiO ₂	50.95±0.08	57.31	73.35±0.11	74.56	52.57±0.25	50.85	88.89±0.12	89.42
P ₂ O ₅	0.159±0.003	0.218	0.102±0.002	0.085	0.089±0.004	0.102	0.062±0.002	0.054
K ₂ O	1.03±0.03	1.17	2.54±0.02	2.39	1.50±0.02	1.57	0.125±0.007	0.27
CaO	0.26±0.02	0.36	2.36±0.02	2.37	(0.095)	0.01	0.70±0.02	0.71
TiO ₂	1.801±0.027	1.969	0.452±0.005	0.415	1.049±0.015	1.121	0.212±0.005	0.18
MnO	0.183±0.004	0.202	0.066±0.001	0.061	0.176±0.004	0.175	0.130±0.002	0.12
Fe ₂ O ₃	10.30±0.05	11.16	3.52±0.03	3.33	12.62±0.08	13.34	3.86±0.04	3.38
S	0.018±0.003	<0.02	0.021±0.003	<0.02	0.041±0.004	0.038	0.009±0.00	<0.02

Table 1. Comparison of XRF results and certified and recommend values for Russia national certified and Chinese reference standards (%), respectively

3. A case study of the XRF determination of Na, Mg, Al, Si, P, S, Cl, K, Ca, Mn, Fe, Ni, Cu, Zn, Rb, Sr and Zr in dry powder of fish muscle tissue

The study of fundamental relations between natural constituents of aquatic ecosystems, as well as multi-purpose ecological investigations, focused on assessment of environment state and its protection from man-made impact, necessitates development of targeted analytical methods. Notice that when investigating aquatic ecosystems in the context of indicative ecology attention was so given to Hg, and to a lesser extent to Cd and Pb behavior (Nemova, 2005). The list of other elements to be examined was very constrained (Moiseenko, 2009) because multielement instrumental techniques became available only in the late the 20th century (Vetrov & Kuznetsova, 1997). At the moment diverse instrumental techniques, e.g. AAA, XRF, AES, NAA, AES ICP and MS ICP, are widely applied in the investigations of living matter of aquatic ecosystems (Moiseenko, 2009; Tolgyessy & Klehr, 1987), each method having specific limitations in terms of detection limit, selectivity and expressness (Vetrov & Kuznetsova, 1997; Kuznetsova et al., 2002).

The living matter of aquatic ecosystems is the medium uncommon for XRF, because of specific bioorganic composition; high and low contents of water and total mineral components, correspondingly, and in addition, lack of proper multicomponent certified standard materials (CRM) of both of national and international production. Utilization of artificial mixtures for calibrating and evaluating the accuracy by the «introduced-defined» method is restrained by the lack of inert material of required purity, as well uncertainty of modeling mixtures compositions. This part of paper reports information on nondestructive XRF procedure to determine the contents of elements Na, Mg, Al, Si, P, S, Cl, K, Ca, Mn, Fe, Ni, Cu, Zn, Rb, Sr and Zr in dry powder of fish muscle tissue.

3.1 Samples and their preparation

A series of 60 emitters were produced from certified reference material of composition of Baikal perch muscle tissues BOK-2 (CRM No.9055-2008 (BOK-2)) (CATALOGUE, 2009) to be employed in the experiment. Three emitters were made of the materials of twenty sealed and labeled polyethylene jars. Besides, our objective was muscle tissue powders of omul, golyan and river perch (group I), the same as perch and plotva (group II). Fishes of group I were collected in the Chivyrkuy Bay of Baikal Lake, while those of group II were caught in various parts of the Baikal and Bratsk man-made water reservoir. The sampling sites differed in the rate of technogenic pollution.

The muscle tissues of group II fishes were lyophilized to a steady weight using a Labconco lyophilizer (method 1). The muscle tissue of omul, river perch and golyan (fishes of group I) were slowly dried to a steady weight on the water bath at $T=60\pm 3^{\circ}\text{C}$ (method 2). The emitters weighing 4 g were pressed under 4 tons pressure in the mold heated to $T=38\pm 0.1^{\circ}\text{C}$ (Gunicheva et al., 2005). The temperature was regulated by TRM-101 thermostat manufactured by TERMIK Co. in Moscow. The emitting layer for the analytical lines of elements Na, Mg, Al, Si, P, S, Cl, K, Ca, Mn, Fe, Ni, Cu and Zn is thick, whereas for the lines of elements Rb, Sr, Zr and Rh it is intermediate. The uncertainty of the thickness of emitting layer is assigned to weighing mass 4 g on weights BP 61S Sartorius, Max 61, $d=0.1$ mg.

3.2 XRF equipment

The intensities of analytical lines and background were measured in vacuum by the X-ray spectrometer with wave dispersion S4 Pioneer (Bruker Firm, Germany). Temperature in a vacuum cell is equal to 38° C. The conditions for excitation and registration of x-ray fluorescence and background are listed in Table 2.

Ana-lyte	2θ, °		Crystal	Detec-tor	Time, s		Voltage, kV	Current, mA	Collimator, °
	Kα ₁ -	Back-ground							
Na	24.90	23.87	OVO-55	PC	100	50	30	40	0.46
		25.89				50			
Mg	20.58	21.96	OVO-55	PC	30	30	30	40	0.46
Al	144.61	145.82	PET	PC	60	60	30	40	0.23
Si	108.99	109.78	PET	PC	30	30	30	40	0.23
P	89.43	91.40	PET	PC	10	10	30	40	0.46
S	75.75	74.77	PET	PC	10	10	30	40	0.46
Cl	65.41	66.87	PET	PC	10	10	30	40	0.46
K	136.67	139.54	LiF(200)	PC	10	10	30	40	0.46
Ca	113.11	115.17	LiF(200)	PC	10	10	30	40	0.46
Mn	62.97	62.26	LiF(200)	PC	30	15	50	40	0.23
		63.72				15			
Fe	57.52	58.28	LiF(200)	PC	30	30	50	40	0.23
Ni	48.66	48.17	LiF(200)	CC	30	15	50	40	0.23
		49.08				15			
Cu	45.04	44.40	LiF(200)	CC	30	15	50	40	0.23
		45.71				15			
Zn	41.75	40.98	LiF(200)	CC	30	15	50	40	0.23
		42.53				15			
Rb	26.61	26.08	LiF(200)	CC	30	15	50	40	0.23
		27.23				15			
Sr	25.14	24.61	LiF(200)	CC	30	15	50	40	0.23
		25.62				15			
Zr	22.51	21.74	LiF(200)	CC	30	15	50	40	0.23
		23.21				15			
Rh	18.47	-	LiF(200)	CC	10	10	50	40	0.23

Table 2. Conditions of excitation and registration of XRF by S4 Pioneer spectrometer.

The emitter was being measured for no more than 19 minutes. After measuring 9 emitters (in ~6 hours) "the reference emitter" made from certified reference material of Tr-1 (see

Table 3) was measured in order to control the equipment drift. It permitted to use both absolute and relative intensities. For estimating the long-time stability of emitter from dry powder of fish muscle tissue all measurements were carried out during a year. The measurements for every emitter were executed $6 < n < 12$ times, in total 480.

Sample No	Reference Material	Producers
1	Tea (GSV-4)	Institute of Geophysics. & Geochem. Exploration (IGGE), Heibei, China
2	Leaf of birch (Lb-1)	Siberian Branch of Russian Academy of Sciences, Institute of Geochemistry, Irkutsk, Russia.
3	Mixture of meadow herbs (Tr-1)	Siberian Branch of Russian Academy of Sciences, Institute of Geochemistry, Irkutsk, Russia.
4	Canadian pondweed (Ek-1)	Siberian Branch of Russian Academy of Sciences, Institute of Geochemistry, Irkutsk, Russia.
5	Baikal perch tissue (BOK-2)	Siberian Branch of Russian Academy of Sciences, Institute of Geochemistry, Irkutsk, Russia.
6	Potatoes tuber (SBMK-02)	Central Institute of Agrochemical Service of Agriculture and Sverdlovsk Branch VNIIM
7	Wheat grain (SBMP-02)	Central Institute of Agrochemical Service of Agriculture and Sverdlovsk Branch VNIIM
8	Cereal herb mix (SBMT-02)	Central Institute of Agrochemical Service of Agriculture and Sverdlovsk Branch VNIIM
9	Milk Powder IAEA - 153	Report: IAEA/AL/010 Australia
10	Milk Powder IAEA A11	Report: IAEA/AL/010 Australia
11	Microcrystal cellulose	Sigmacell Cellulose, Type 50, S5504-1KG
12	Aminoethanole acid	analyzed by ICP-OES using certified technique
13	L-asparagine	analyzed by ICP-OES using certified technique
14-16	Milk-based infant formulas	International Nutrition Co, Denmark

Table 3. Specifications of certified reference materials and samples

3.3 Content computation

The key points of procedure: generation of calibrating samples set, taking into account their physical and chemical properties; optimization of approximation capacity of calibration functions due to a proper selection of regression equation and regression approach to determine the parameters of calibration function. The certified reference materials and samples are tabulated in Table 3. Characteristics of calibration collection are given in Table 4. The influence of inadequacy of composition of organic matrix of the certified reference materials set and bioorganic matrix of fish muscle tissue on the XRF results of fish tissues was not studied yet. Only the principal XRF fitness was estimated. Admitting a rough similarity of bioorganic compositions of dry residue of cow milk and fish muscle tissue, it is believed that the systematic error due to this effect will not be over 8 %

(Gunicheva, 2010). The calibration functions have been selected out of the calibrations implemented by the software of X-ray spectrometer S4 («SPECTRAPLUS», 2002). The approach of alpha coefficients was applied for correcting the matrix effects when measuring elements Na, Mg, Al, Si, P, S, Cl, K and Ca:

$$C_i = m_i I_i * (1 + \sum \alpha_{ij} I_j), \quad (1)$$

where: (a) C_i is the concentration of analyte i ; (b) I_i is intensity of its analytical line corrected for the background; (c) m_i is slope of calibration plot; (d) I_j is intensity of matrix element analytical lines corrected for the background; (e) α_{ij} is the value of the corresponding alpha coefficient calculated by the linear regression equation. The contents of Mn, Fe, Ni, Cu, Zn, Rb, Sr and Zr were analyzed by the background standard method. A characteristic line of the x-ray tube anode (see Table 2), incoherently scattered from sample, was the standard. The concentration of analyte i was calculated by the equation:

$$C_i = m_i * (I_i + K_i) / I_j, \quad (2)$$

where: (a) I_j is pure intensity of comparison line; (b) K_i is expression of intensity correction, (c) m_i is slope of calibration plot. Intensity I_j is proportional to $1 / (1+M)$, where M is the coefficient for correcting matrix effects. The parameters of calibration functions (1-2) were optimized by regression approach («SPECTRAPLUS», 2002).

Analyte	Interval, ng/g	RM quantity
Na	40 - 6900	9
Mg	40- 4400	10
Al	20 - 3000	8
Si	2- 5450	9
P	80 - 3600	11
S	1000 - 3600	11
Cl	200 - 8400	8
K	20 - 23900	11
Ca	10 - 16200	11
Mn	0.2 - 1240	10
Fe	2.5 - 990	8
Ni	0.7 - 5.8	8
Cu	0.4 - 17.3	10
Zn	2 - 94	9
Rb	3.5 - 74	10
Sr	2.2 - 72	10
Zr	0.2 - 5.5	8

Table 4. Characteristics of calibration collection

3.4 The temporal trends of X-ray fluorescence intensities

The regression equations of temporal trends for x-ray fluorescence intensities, both absolute and relative ones, for the elements to be determined are provided in Table 5.

Parameters of equations are presented as the range of their magnitudes, obtained for the entire series of emitters. Both absolute and relative intensities of all elements are expressed as $R^2_{exp} < r_{xy}$. It is proposed to accept: (a) absence of paired correlation and (b) contribution of temporal change is small in comparison with the discrepancy in values of a_0 and a_1 for the emitters pressed from various polyethylene jar materials. This fact is no surprise, since material of CRM BOK-2, as any biological medium, is *a priori* natural non-equilibrium system (Vernadsky 1978; Marchenko, 2003). The data in Table 5 disclose stress of processes proceeding within substance when converted in powder state, x-ray irradiation and effects of increased temperature and vacuum, set by instrument parameters of S4 Pioneer («SPECTRAPLUS», 2002). The influences of the specified processes on the accuracy of XRF data on fish tissue are still to be properly considered. The further study would require a thorough planning and implementing with fish tissue material of a set mass and fresh sample preparation.

	Absolute intensities	R^2_{exp}	Relative intensities	R^2_{exp}
Na	$y = -0.001x + (28 \div 45)$	0.3 ÷ 0.5	$y = -(0.001 \div 0.002)x + (25 \div 63)$	0.0 ÷ 0.2
Mg	$y = -(0.001 \div 0.003)x + (43 \div 82)$	0.3 ÷ 0.6	$y = -(0.001 \div 0.002)x + (40 \div 72)$	0.1 ÷ 0.6
Al	$y = -(0.000 \div 0.001)x + (12 \div 45)$	0.3 ÷ 0.5	$y = -(0.000 \div 0.001)x + (14 \div 36)$	0.0 ÷ 0.1
Si	$y = 0.001x + (28 \div 45)$	0.3 ÷ 0.5	$y = -(0.000 \div 0.001)x + (12 \div 46)$	0.0 ÷ 0.2
P	$y = -(0.01 \div 0.03)x + (463 \div 980)$	0.2 ÷ 0.5	$y = -(0.000 \div 0.001)x + (15 \div 40)$	0.0 ÷ 0.1
S	$y = -(0.03 \div 0.07)x + (1087 \div 2155)$	0.2 ÷ 0.6	$y = -(0.000 \div 0.001)x + (14 \div 33)$	0.1 ÷ 0.3
Cl	$y = -(0.004 \div 0.010)x + (183 \div 348)$	0.1 ÷ 0.5	$y = -(0.000 \div 0.001)x + (17 \div 28)$	0.1 ÷ 0.3
K	$y = -(0.05 \div 0.11)x + (0.11 \div 0.43)$	0.1 ÷ 0.4	$y = -(0.000 \div 0.001)x + (18 \div 32)$	0.1 ÷ 0.2
Ca	$y = -(0.004 \div 0.007)x + (169 \div 288)$	0.3 ÷ 0.5	$y = -(0.00 \div 0.01)x + (13 \div 25)$	0.1
Mn	$y = -(3E-06 \div 7E-05)x + (1.1 \div 1.9)$	0.2 ÷ 0.5	$y = (0.6 \div 0.7)x + (0.24 \div 0.38)$	0.5 ÷ 0.6
Fe	$y = -0.001x + (47 \div 551)$	0.5	$y = -0.001x + (21 \div 58)$	0.5
Ni	$y = -9E-05x + (3.6 \div 4.8)$	0.2 ÷ 0.3	$y = -(0.000 \div 0.001)x + (16 \div 37)$	0.0 ÷ 0.1
Cu	$y = -0.001x + (30 \div 53)$	0.3 ÷ 0.2	$y = 1.0x + (0.01 \div 0.03)$	0.4
Zr	$y = -1E-05x + (0.1 \div 2.8)$	0.0 ÷ 0.3	$y = -(0.000 \div 0.001)x + (15 \div 40)$	0.2 ÷ 0.5
Sr	$y = -1E-05x + (2 \div 10)$	0.02	$y = -(0.000 \div 0.001)x + (14 \div 24)$	0.2 ÷ 0.5
Rh	$y = -(0.000 \div 0.001)x + (2.6 \div 2.8)$	0.0 ÷ 0.4	$y = -(0.000 \div 0.001)x + (5 \div 9)$	0.3 ÷ 0.5

Table 5. Regression equations of temporal trends; * $r_{xy} = 0,537$ for $p < 0.01$

3.5 Selection of intensities for concentration computation

The series of absolute and relative intensities for the emitters were compared by two-factor analysis of variance with different dispersions. The results are given in Table 6.

Analyte	Trend	Average	Dispersion	n	t_{exp}	Resume
Na	abs.	0.4413	0.0325	20	1.75	By absolute intensities
	rel.	0.3229	0.0577	20		
Mg	abs.	0.4905	0.0171	20	2.08	By absolute intensities
	rel.	0.3760	0.0424	20		
Al	abs.	0.2177	0.022	20	1.70	By absolute intensities
	rel.	0.1400	0.0187	20		
Si	abs.	0.3236	0.0212	20	1.03	Both schemes are comparable
	rel.	0.2679	0.0354	20		
P	abs.	0.3874	0.0180	19	1.45	Both schemes are comparable
	rel.	0.3064	0.0423	20		
S	abs.	0.4072	0.0177	19	1.56	Both schemes are comparable
	rel.	0.3214	0.0404	20		
Cl	abs.	0.3003	0.0161	20	2.13	By absolute intensities
	rel.	0.1941	0.0328	20		
K	abs.	0.2822	0.0104	19	2.19	By absolute intensities
	rel.	0.1871	0.0259	20		
Ca	abs.	0.2270	0.0159	20	0.74	Both schemes are comparable
	rel.	0.1921	0.0267	20		
Mn	abs.	0.2776	0.0622	20	-0.18	Both schemes are comparable
	rel.	0.2922	0.0701	20		
Fe	abs.	0.5318	0.0427	20	-0.24	Both schemes are comparable
	rel.	0.5456	0.0282	20		
Ni	abs.	0.2250	0.0152	20	1.45	Both schemes are comparable
	rel.	0.1635	0.0207	20		
Cu	abs.	0.3976	0.0726	20	0.34	Both schemes are comparable
	rel.	0.3574	0.0849	20		
Zn	abs.	0.2205	0.0198	20	-0.36	Both schemes are comparable
	rel.	0.2400	0.0452	20		
Rb	abs.	0.0215	0.0014	18	-3.21	By relative intensities
	rel.	0.1001	0.0104	20		
Zr	abs.	0.1272	0.0368	20	-1.73	By relative intensities
	rel.	0.2324	0.0374	20		
Sr	abs.	0.0653	0.0058	20	-1.82	By relative intensities
	rel.	0.1534	0.0407	20		
Rh	abs.	0.1577	0.06786	20	0.03	Both schemes are comparable
	rel.	0.1554	0.0377	20		
$t_{critical}$ one-way $p=0.01$				1.69	abs. -absolute intensities	
$t_{critical}$ two-way $p=0.01$				2.03	rel. -relative intensities	

Table 6. Comparison of absolute and relative intensities.

The empirical values of t - Student coefficients t_{exp} are more tabular t_{tab} for elements Na, Mg, Al, Cl, K (set 1) and less for Rb, Zr and Sr (set 2). Therefore to compute concentration for elements

of set 1 the absolute intensities were used and for set 2 elements these were relative ones. For elements Si, P, S, Ca, Mn, Fe, Cu и Zn selection of the intensities for concentration computation is non-critical and XRF analysis results are comparable when using both intensity sires.

3.6 The metrological characteristics of the XRF procedure

Constituents of random error were assessed by three-factor analysis of variance. The values characterizing convergence error of intensity measurement $S_{r,c}$, the error of emitter preparation and its setting up in the holder S_{rp} and total intralaboratory XRF accuracy error $S_{r,tot}$ are summarized in Table 7. It also provides the ranges $N_{min} - N_{max}$ and the maximum values of count statistics error $1/\sqrt{N}$ (N denotes the number of counts) to ease understanding. N_{max}/N_{min} ratios are changed from 2.5 for Zr to ~1.1 for elements Mg, Al, Si, P, K, Cu, Zn and Rb. In column of $S_{r,tot}$ values the brackets enclose the estimations computed for relative intensities. It is evident that for only Ca and S statistics errors are the dominant contributions into evaluation of total intralaboratory XRF random error. For the rest of analytes the effects are not so simple. For elements Si, Cl, Mn, Ni, Cu, Zn, Rb, Sr and Zr values of $S_{r,tot}$ are mainly caused by error of intensity measurement. For analytes Na, Mg, Al, P, K, Fe and Rh the errors of emitter preparation and its setting up in the holder are maximal signified, i.e. behavior of each analyte is unique and requires careful consideration.

Analyte	$N_{min}-N_{max}$, counts	$1/\sqrt{N}$	$S_{r,c}$	S_{rp}	$S_{r,tot}$	$t_{2,1\text{ exp}}$	$t_{3,2\text{ exp}}$	C_{min} , ppm
Na	83.6÷184.8	0.11	2.26	10.14	9.23 (13.61)	47.90	2.00	*
Mg	0.76÷0.82	1.15	0.45	1.36	1.19 (1.21)	19.25	2.32	*
Al	0.854÷0.885	1.08	0.34	0.81	0.74 (0.93)	12.32	1.99	*
Si	0.233÷0.242	2.07	8.92	n.s.	8.45 (7.60)	1.17	0.08	*
P	1.482÷1.567	0.82	0.31	0.93	0.81 (0.97)	19.19	1.45	*
S	0.13÷0.15	2.77	0.48	1.97	1.67 (2.36)	34.03	2.77	*
Cl	0.0291÷0.0448	5.86	12.60	n.s.	10.34 (9.04)	0.50	1.22	3.2
K	1.119÷1.142	0.95	1.06	2.24	2.08 (2.77)	10.00	2.37	5.0
Ca	0.0134÷0.0216	8.64	4.61	9.06	8.55 (10.47)	8.71	1.64	4.3
Mn	0.0315÷0.0448	5.63	12.60	n.s.	10.34 (8.42)	0.50	1.22	0.9 (2.8)
Fe	0.922÷1.170	1.04	4.50	4.81	5.71 (6.13)	3.29	0.94	1.3 (2.6)
Ni	0.173÷0.218	2.40	7.67	n.s.	7.01 (6.98)	0.98	0.05	0.4 (0.8)
Cu	1.144÷1.257	0.94	2.03	n.s.	1.67 (1.76)	0.53	1.92	1.4 (1.4)
Zn	2.566÷2.775	0.62	1.32	n.s.	1.16 (1.20)	0.8	1.25	0.4 (1.1)
Rb	4.79÷5.11	0.46	1.24	n.s.	1.15 (1.32)	1.06	2.50	0.5 (1.6)
Sr	0.435÷0.590	1.52	8.71	n.s.	7.15 (7.25)	0.51	1.65	0.3 (1.8)
Zr	0.095÷0.238	3.24	21.74	n.s.	20.79 (19.93)	1.22	0.64	0.3
Rh	1.667÷1.988	0.77	1.97	2.68	2.85 (3.12)	4.72	1.09	
$t_{2,1}(0,01,40,60)_{tab.}=3.99$		n.s.- insignificant; * stands for the elements with limits of contents being essentially beyond 10σ .						
$t_{3,2}(0,01,19,40)_{tab.}=2.03$								

Table 7. Estimates, % of random error components

Column of C_{\min} presents detection limits, calculated with 3σ -criterion using the results of 20 measurements of emitters produced from powder of L- asparagine, aminoethanol acid, cellulose and reference samples OM-1 and OK-1 (muscle tissues of the Baikal omul and perch). They vary from $(3\div 9) \times 10^{-6}$ for elements of Mn, Ni, Zr, Rb, Sr and Zn to $(2\div 5) \times 10^{-5}$ for Cl, K, Ca, Fe and Cu, which is to say that XRF data are acceptable to investigate the living matter of aquatic ecosystems.

The detection limits were not given for elements of Na, Mg, Al, Si, P and S, because their contents in fish tissues exceed substantially the limits of quantitative determination (10σ). The brackets enclose detection limits from reference (Gunicheva et al., 2005). The larger magnitudes for the latter are due to the difference in bioorganic and organic compositions of dry powder of fish muscle tissues and plant materials.

3.7 The accuracy of XRF data

The classical assessment of accuracy of XRF data on the fish tissues would be impossible because of unavailability of proper certified reference materials and reference samples (ISO, 1994). Therefore, the XRF results for muscle tissues of various fishes have been compared with similar literature data. These data (Vetrov & Kuznetsova, 1997; Leonova, 2004; Moore & Ramamurti, 1987; Grosheva et al., 2000) are given for the fishes, collected in the southern and middle Baikal, Selenga River estuary, Angara River in the environments of Bratsk and Ust'-Ilimsk man-made water reservoirs (i.e. for the sites of CRM BOK-2 sampling), and were acquired by the authors through span 1987-2005 by different instrumental techniques.

Table 8 presents their types and sample preparation described in the references. It indicates that digestion is prevailing in sample preparation, when investigating the living matter of aquatic ecosystems.

Reference	Type of benefic organism	Sampling site	Instrumental technique	Sample preparation
Leonova, 2004	Golyan, perch, plotva, omul	Chivyrkuy Bay of Baikal Lake	Atomic emission spectrometry (AES)	Digestion
Leonova & Bychinskiy, 1998	Perch	Bratsk man-made water reservoir, Lake Baikal	AES with evaporating sample powders in canal of arc graphite electrode	Digestion
Grosheva et al., 2000	Perch, plotva	Lake Baikal	Substoichiometric isotope dilution	Lyophilization
Moore & Ramamurti., 1987	Perch	The upper stream of river Ob' in site of town Barnaul water intake	Atomic absorption spectrometry (AAS)	Solubilizing
Vetrov & Kuznetsova, 1997	Omul, plotva, perch	Lake Baikal	AES	Digestion

Table 8. Details of instrumental techniques and sample preparation used in references

Comparison is presented in Tables 9-10. At Table 9 the column of analytes shows the elements certified for reference material BOK-2 by bold print; italics type designate for recommended

Ana-lyte	CRM BOK-2	Bratsk man-made water reservoir		Southern and Middle parts of the Baikal						
		XRF*	Leonova & Bychinskiy, 1998; Moore & Ramamurti, 1987	XRF*	XRF*	XRF ⁺	Grosheva et al., 2000	Vetrov & Kuznetsova, 1997	Leonova, 2004; Ciesielski et al., 2000	Ciesielski et al., 2005
Al	28±18	10.3±2.6		8.6±1.6		31±3		17±8	3.8±0.9	
Fe	53±11	25.9±7.2	10.0	10.97±3.83		33.4±2.4	61.87 ± 7.17	41±21	57.2±3.9	672
K	15900±700	14002±589		15476±307		15653±88				
Mn	1.66±0.24	0.60±0.35	10.0	1.11±0.35		1.09±0.18	2.24 ± 0.22	0.64±0.06	3.2±0.6	
Ni	0.42±0.27	1.09±0.05	0.2	1.07±0.06		0.54±0.16		0.26±0.13	2.24±0.18	
Rb	21.9±4.3	19.3±2.4		33.9±1.2		21.9±0.4				2.0
S	11000 ± 2000	9304 ± 259		8723 ± 226		10412±54				
Sr	2.8 ± 0.3	3.5 ± 0.8		2.4 ± 0.3		2.7 ± 0.3			194±31.1	
Zn	23.0±1.2	32.4±2.6	18.2÷37.2	27.3±1.4		27.5±4.7	9.29 ± 1.25	24±6	113.4±17.1	80
Ca	1720±250	1125±174		859±114		1452±34			4911±119	
Mg	1040±110	1066±66		1325±54		1261±29			1484±103	
Na	2770±90	4836±648		3438±258		2778±42			5444±495	
P	9500±500	7946±293		9329±211		9289±63			9977±12.37	
Cl	2800 ± 200	2499±404		2074 ± 157		2494± 24				
Si		35.9±6.7		33.7 ± 15.3		106±8			6.3±0.1	
Br	49 ± 5	23.3 ± 5.7		99±6		55±0.2				

Table 9. Contents of analytes in perch muscle tissues (dry weight, ng/g)

Ana-lyte	Golyan		Omul		Perch		Plotva	
	XRF*	Leonova, 2004	XRF*	Leonova, 2004	XRF*	Leonova, 2004	XRF+	Leonova, 2004
Na	6184±182		4840±118	3166±171	4229±163	2600±204	3000±500	5750±531
Mg	820±21	32,70	1108±23	2700±307	1454±50	1933±1160	1250±80	2750
Al	43±3	2,43	41±3	105±51	26±4	0,9±0,3	11±4	46
Si	145±4		159±4	968±354	82±10	7,5±1,8	33±9	550±437
P	11328±317		8732±168	6333±341	8618±278	3500±341	8710±390	2500±625
S	6762±110		6182±73		9176±270		8310±340	
Cl	3032±94		3492±125		2289±96		1660±370	
K	8730±150		14052±210		13620±336		14800±400	
Ca	13100±210		740±10	6333±341	1268±30	1000±546	830±80	2500
Mn	3,65±0,67	0,22	1,34±0,42	3,3±1,8	0,66±0,22	2,4±1,0	1,03±0,08	
Fe	68±1	3,14	35±8	146±20,5	62±1	55,0±13,6	26±6	34,5
Ni	0,80±0,02		1,05±0,07	0,39±0,08	0,92±0,04	0,3±0,1	1,08±0,11	1,7
Zn	22,30±0,71	0,72	24,4±0,8	12,6±0,7	13,16±0,05	27,3±9,5	39,7±6,6	47,5
Rb	1,6±0,1		26,1±1,4		2,4±0,2		9,1±1,1	
Sr	11,7±0,1		3,2±0,2	52±2,7	0,5±0,1		3,1±1,1	
Br	11,4±0,2		55,1±1,5		8,9±0,2		29,3±12,1	

Table 10. Contents of analytes in muscle tissues of different fish kinds, (dry weight, ng/g)
The sampling site is the Chivyrkuy Bay of Baikal Lake

value; * denotes for the median of sampling and empty cell shows data absence. The data of the XRF columns have been gained by statistic treatment of no less than ten samples (free emitters for each). It is safe to say that the XRF information bulk for fish tissues is more excessive in comparison with the referenced information. It should be noted that information on content of Br, Cl, S, K, Cs, Sr and Sc in fishes of Baikal region is entirely absent in the references. Contents for the other elements belong in concentration intervals given by the other authors.

Microelement contents in perch tissues from Novosibirsk man-made reservoir (river Ob') (Leonova, 2004) are also comparable with the data for BOK-2. Notice that among the references, the only the data of (Leonova, 2004) is close to XRF results being conformable. Considering features of used analytical techniques some discrepancy being visible to the human eye is existent. Nevertheless the observed ranges of element contents are beyond methodical errors. They are indicative of fish tissue composition dependence on situation of aquatic ecosystems. We emphasize that irrespective of the difference in analytical techniques, the levels of concentrations and a series of decreasing element contents $P > Na > Ca > Mg > Zn > Mn$ are fairly similar in all data.

As to Table 10 for all fish kinds in general consistency of data is enough apparent regardless of the fact that instrumental techniques and sample preparations are not identical.

Table 11 gives some relationships between the XRF concentrations of some elements for muscle tissues of plotva and perch fish, collected in the southern and middle Baikal and Bratsk man-made water reservoir, as well as omul. Statistically significant interrelationships are given by bold print. These correlations are conformable to those, represented in the liver

of Baikal seal (Ciesielski et al., 2006). They reflect not only techniques used when preparing samples and conditions of ecosystem in the sampling sites, but also fish trivial heredity. They can give usable information to interpret environment impact and element interactions with numerous factors, both biotic and abiotic. These correlations also demonstrate that the XRF data may be utilized as the efficient and sensitive indicator of changing element constituents of geochemical background.

Analyte pair	Bratsk man-made water reservoir		Various parts of the Baikal		the Chivyrkuy Bay
	perch	plotva	perch	plotva	omul
Mn-Br	0.05	-0.28	-0.46	-0.91	-0.13
Fe-Br	-0.43	-0.54	-0.80	-0.93	0.13
Zn-Br	-0.76	-0.65	-0.94	-0.99	-0.58
Rb-Br	0.97	0.99	0.92	1.00	0.16
Sr-Br	-0.47	0.92	-0.38	-0.62	-0.15
Zn - Rb	-0.62	-0.57	-0.65	-0.97	0.47
Zn - Sr	0.84	-0.40	-0.09	0.36	-0.34
Rb - Sr	-0.31	0.77	0.41	-0.49	-0.24
Fe - Zn	0.12	0.84	0.73	0.66	0.39
Zn - Al	0.36	0.28	0.91	-0.31	-0.11
Mn - Fe	-0.32	0.25	0.09	0.26	-0.41
Fe - Ni	-0.56	-0.18	-0.09	0.46	0.20
Na - Cl	0.97	0.98	0.95	0.62	0.95
Na - K	-0.91	0.48	0.53	-0.06	0.96
Mg - Ca	0.35	0.91	0.93	-0.57	0.90
S - P	-0.06	0.93	0.90	0.22	-0.05
S - Cl	0.60	0.74	0.82	0.33	-0.19
Cl - P	-0.67	0.86	0.00	0.89	0.99
Ca - P	0.34	0.77	-0.49	0.74	0.93
Al - Ca	-0.53	0.06	0.04	-0.61	0.48
Al - Na	-0.90	-0.12	-0.10	-0.82	0.53
Al - Si	0.77	0.49	-0.17	-0.54	0.41
Al - Sr	-0.20	0.10	-0.17	-0.48	-0.27
Ca - Na	0.48	0.87	0.02	0.89	0.81
Ca - Si	-0.58	0.56	-0.09	0.96	0.80
Ca - Sr	0.94	0.95	-0.09	0.90	0.02
Fe - K	0.70	-0.73	0.18	-0.30	0.32
Fe - Mg	-0.62	0.05	-0.12	-0.87	0.24
Fe - P	0.08	-0.51	-0.28	-0.73	0.30

Table 11. Some element correlations

4. Conclusion

Environmental problems and the modelling cycle of major and minor elements in soil-plant systems under natural conditions and in response to man's activities require the extensive analyses. Most of the analytical problems that occur are simple to solve by XRF spectrometry. This technique provides accurate analyses of rocks and materials which may be homogenized by fusion with an appropriate flux. Such an approach as a rule is impossible for XRF analysis of materials which are abundantly supplied with organic constituents. Its biochemical complexity inhibits homogenization and, as a result, does not allow the extension of this procedure.

We have demonstrated that the use of nondestructive XRF method ideally suits the quantitative determination of Na, Mg, Al, Si, P, S, Cl, K, Ca, Mn, Fe, Ni, Cu, Zn, Rb, Sr and Zr contents in dry powders of muscle fish tissues. The regression equations of temporal trends for x-ray fluorescence intensities, both absolute and relative ones, for the elements were determined and shown that contribution of temporal change is small in comparison with the discrepancy in values of a_0 and a_1 for the emitters pressed from various polyethylene jar materials. This fact is not subitaneous because of material of CRM BOK-2, as any biological medium, is *a priori* natural non-equilibrium system. This imposes the strict initial conditions of the similarity: means of sampling and treatment.

Constituents of random error were assessed by three-factor analysis of variance. It is evident that behavior of each analyte is unique and requires careful consideration and tracing.

The quantitative analyses indicate that in various environmental situations the samples of all kinds of fish contain enumerated elements in different amounts and, therefore, they confirm validity of using fishes as indicating metal contamination. The metrological parameters of the technique allowed the sources of the errors to be identified, and the issues of further investigations to be projected.

The tendencies identified with the XRF results on the dry powders of fish muscle tissues do not contradict the features recognized in toxicology of aquatic ecosystems and environmental biogeochemistry. They disclose the potential of their utilization for multi-purpose interpretations in environmental monitoring of freshwater ecosystems.

5. References

- Arnautov N. V. (1987). *Reference Samples of Natural Media Composition*. Procedure Recommendations. Novosibirsk. 99 p.
- Bock R. (1972) *Digestion methods in analytical chemistry*. Verlag Chemie GmbH, Weinheim/Bergstr. 432p.
- Bolt G. H. and Bruggenwert M. G. M. (1976). *Soil Chemistry. A. Basic Elements*, 281 p. Elsevier, Amsterdam
- CATALOGUE of reference materials of composition of natural and technogenic media. Irkutsk, (2009). <http://www.igc.irk.ru>
- Ciesielski T., Pastukhov M. V., Fodor P., Bertenyi Z., Namiesnik J., Szefer P. (2006). Relationship and bioaccumulation of chemical elements in the Baikal seal (*Phoca sibirica*) *Environmental Pollution*, V. 139, no 2, 372-384.

- Greenland D. J. and Hayes M. H. B. (1978). (Eds). *The Chemistry of Soil Constituents*, p. 469. Wiley, New York.
- Grosheva E.L., Voronskaay G.N., Pastukhov M.V. (2000), Trace element bioavailability in Lake Baikal. *Aquatic Ecosystem Health and Management*, 3, 229-234.
- Gunicheva T.N., Pashkova G.V., Chuparina E.V. (2005), Results on hot pressing applicability for non-destructive XRF of plants. *Analytics and Control*, 9, 273-279.
- Gunicheva T.N. (2010). Advisability of X-ray fluorescence analysis of dry residue of cow milk applied to monitor environment. *X-Ray Spectrometry*, 39, 22-27
- INTERNATIONAL REFERENCE MATERIALS A Compilation of Currently Certified or Accepted Concentrations LOS ALAMOS NATIONAL LABORATORY Operated by the University of California for the US Department of Energy Copyright © UC 2000 - Disclaimer <http://www.geostandards.lanl.gov/MaterialsByNumber/htm>
- ISO 5725 -1 – 1994. Accuracy (trueness and precision) of measurement methods and results. Part 1. General principles and definitions.
- ISO 5725 -2 – 1994. Accuracy (trueness and precision) of measurement methods and results. Part 2. Basic method for the determination of repeatability and reproducibility of a standard measurement method.
- ISO 5725 -3 – 1994. Accuracy (trueness and precision) of measurement methods and results. Part 3. Intermediate measures of the precision of a standard measurement method.
- ISO 5725 -4 – 1994. Accuracy (trueness and precision) of measurement methods and results. Part 4. Basic methods for the determination of the trueness of a standard measurement method.
- ISO 5725 - 5 – 1998. Accuracy (trueness and precision) of measurement methods and results. Part 5. Alternative methods for the determination of the precision of a standard measurement method.
- Kabata-Pendias A. and Pendias H. (1986). *Trace Elements in Soils and Plants*, CRC Press, Boca Raton, FL. 439 p.
- Kuznetsova A.I., Zarubina O.V. and Leonova G.A. (2002), Comparison of Zn, Cu, Pb, Ni, Cr, Sn, Mo concentrations in tissues of fish (roach and perch) from Lake Baikal and Bratsk Reservoir. *Environmental Geochemistry and Health*, 24, 205-212.
- Lindsay W. L. (1979). *Chemical Equilibria in Soils*, p. 449. Wiley-Interscience, New York.
- Ostroumov G. V (1979). The Metrological Basics of Exploration of Rock, Ore and Mineral Chemical Composition. The Bowels of the Earth. Moscow (Ed.). 400 p.
- Leonova G.A., Bychinskiy V.A. (1998). Hydrobionts of the Bratsk water reservoir as the sites of heavy metal monitoring. *Water resources*, 25, 603.
- Leonova G.A. (2004). Biogeochemical indication of natural and technogenic concentrations of chemical elements in components of aqua systems, exemplified by Siberian water reservoirs. *Electronic Journal «Explored in Russia»*, 197, 2196 <http://zhurnal.ape.replarn.ru/articles/2004/197.pdf>.
- Marchenko E.D. (2003). *Memory of globe experience*. St. Petersburg, Author Center "RADATS", 376 p
- Moiseenko T.I. (2009). *Aqua toxicology: Theoretical and applied aspects*. Moscow, Nauka, 400p. ISBN 978-5-02-036166-9
- Moore D.S., Ramamurti S. (1987). *Heavy metals in natural waters. Control and assessment of effect*. Moscow, Mir, 285 p.
- Nemova N.N. (2005). *Biochemical effects of mercury accumulation in fish*. Moscow, Nauka. 200 p

- Rudneva N.A. (2001), *Heavy metals and microelements in hydrobionts of the Baikal region*. Inst. Exper. Biology, SB RAS, Ulan-Ude. Publ. H. B.S.C. SB RAS, 134 p.
- Schnitzer M. and Khan S. U. (1978). *Soil Organic Matter*, 319 p .. Elsevier, Amsterdam.
- «SPECTRAPLUS» for users of spectrometer S4 EXPLORER. Karlsruhe: Bruker AXS Center. 2002.
- Tolgyessy J. and Klehr E.H. (1987). *Nuclear methods of chemical analysis of environment*. Ellis Horwood Limited. 192 p.
- Vernadsky V.I. (1978). *Living matter*. M.: Science. 358p.
- Vetrov V.A., Kuznetsova A.I. (1997). *Microelements in natural media of Lake Baikal region*. RAS, Inst. Geochem. SB RAS Novosibirsk: 234 p.

Lanthanides in Soils: X-Ray Determination, Spread in Background and Contaminated Soils in Russia

Yu. N. Vodyanitskii and A. T. Savichev

*Department of Soil Science, Moscow State University; Geological Institute, RAS
Russia*

1. Introduction

Rare elements in soils are poorly studied because of the problems in their determination (Perelomov, 2007). The rare earth elements include lanthanum (La) and its group of 14 elements. They are subdivided into two subgroups: the light cerium group of elements with atomic masses lower than 153 (La, Ce, Pr, Nd, Sm, and Eu) and the heavy yttrium group of elements with atomic masses higher than 153 (Y, Gd, Tb, Dy, Ho, Er, Tm, Yb, and Lu, with an exception for Y) (Tyler, 2004a).

The interest in rare earth elements in soils increased in the 1990s, when they found wide use as microfertilizers for some crops in China, which increased the yield and quality of grain (Evans, 1990; Wu, Guo, 1995; Zhu et al., 1995). Rare earth elements are accumulated in soils due to fertilization. Groundwater and plants can be contaminated in the regions enriched with soluble rare earth metals and in the soils fertilized with sewage sludge for long time (Zhu et al., 1995). Data are available on the strong contamination of coastal sediments with lanthanidecontaining industrial waste (Savichev, Vodyanitskii, 2009). Neither positive nor negative geochemical anomalies of natural or technogenic rare earth metals have been revealed in Russia until now. The contribution of rare earth metals to the main soilforming processes is not clear.

The content of lanthanides was compared to their soil clarkes. Questions arise in this connection. The yttrium clark value is 40 mg/kg (Bowen, 1979). We shall take this value, although we consider it to be too high.

We analyzed the clarkes of the rare earth elements (La and Ce) according to the book by Kabata-Pendias and Pendias (1985), in which they were borrowed from three sources. Let us judge the validity of the published La and Ce clarkes according to the Ce : La ratio in the world soils. The clarkes proposed by Lawl et al. (according to Kabata-Pendias and Pendias, 1985) are the least probable of all, as they give a too low ratio of Ce : La = 29.5 : 29.5 = 1. On average, the Ce : La ratio = 2.2 for the soils in Japan; it is equal to 2.0, for the soils in China; and to 1.8, for the soils in Bryansk oblast of Russia. According to our data, this ratio is equal on average to 1.5 in the soils of the Kolyma depression, as well as in the alluvial fine earth of the small rivers and the Kama River in Perm (Savichev, Vodaynitskii, 2009). Bowen (1979)

also suggests too low a ratio ($Ce : La = 50 : 60 = 1.2$). This ratio reaches a probable value only for the clarkes proposed by Yuri and Baikon: $Ce : La = 49 : 34 = 1.4$. These values of the lanthanum (34 mg/kg) and cerium (49 mg/kg) clarkes we shall use further. In sedimentary rocks, the clarkes of La and other lanthanides depend on the particle size distribution, because these elements are accumulated in the clay fraction $<2 \mu m$. As a result, their content is higher in argillites and clays (56 mg/kg) and lower in sandstones and carbonates (19 and 8 mg/kg, respectively) (Ivanov, 1997).

The clarkes of other studied lanthanides in the earth's crust are as follows (mg/kg): Pr, 9; Nd, 40; and Sm, 7 (Greenwood, Ernshaw, 1997). In soils, they are lower (mg/kg): Pr, 7.6; Nd, 19; and Sm, 4.5 (Dyatlova et al., 1988). The values of the soil clarkes are used to detect positive and negative geochemical anomalies. Unfortunately, there are no clear criterions for such identification. As a first approximation, we use the condition that a soil belongs to the territory of a strong positive anomaly at the double excess of the clarke ($X_s : X_{cl} > 2$).

2. Methods

The recent progress in the study of rare earth elements was related to the use of the expensive method of inductively coupled plasma mass spectroscopy (ICP MS) (Kashulina et al., 2007; Perelomov, 2007).

The expensive method of neutron-activation analysis using a nuclear reactor with the use of a gamma spectrometer allows determining the different dispersed elements in soils – Hf, La, Ce, Sm, Eu, Yb, Lu, Th, and U – even at low concentrations (Inisheva et al., 2007; Nikonov et al., 1999). However, the identification of Pr and Nd by this method is complicated because of the short lifetime of these elements (Ivanov et al., 1986).

X-ray fluorescence is the simplest and least expensive method for studying the heavy metals in soils (Savichev, Sorokin, 2000). The contents of rare (Zr and Nb) and rare earth (Y) elements are determined by this method. However, when a Mo, Rh, or Ag anode of the X-ray tube and a common voltage of 35–40 kV are used, other rare earth elements can be identified only from the *L*-lines. Their intensities are lower than those of the *K*-lines by several times, and the weak *L*-lines are overlapped by the strong *K*-lines of macroelements. Niobium with $Z = 41$ is the last element reliably identified by conventional X-ray fluorescence analysis, because the scattered lines of the anode material are located father in the energy spectrum, and the elements with atomic numbers higher than that of the anode material are not excited.

A radically different situation is observed when the X-ray radiometric modification of the energy dispersive X-ray fluorescence method is used, in which the sample is excited by a highenergy radioisotope source ^{241}Am rather than by the X-ray tube radiation. This source is the most suitable for this purpose. An advantage of this method is that the *K*-lines of the heavy metals are actively excited in this case and are not overlapped by the lines of macroelements. Other advantages are the low background radiation compared to X-ray tubes, the high stability, and the small size.

The aim of this part of work is to elaborate methods of X-ray radiometric determination of the first lanthanides (lanthanum and cerium) and barium and to determine the content of these elements in some soils.

Calibration diagrams were compiled with the use of standard samples of rocks and soils. There were 18 samples of magmatic rocks, including ultramafic (UMR), mafic (MR), acidic (AR), and alkaline (ALR) series (Khitrov, 1984). Thus, standard samples of gabbro (SGD-1A), granites (SG-1A and SG-2), trappan rock (ST-1), siltstone (SA-1), and others were analyzed. Standard soil samples included Kursk chernozem (SP-1), Moscow soddy-podzolic soil (SP-2), Caspian light chestnut soil (SP-3), krasnozem (SKR), and calcareous serozem (SSK). Detailed data on these standard samples are given in (Arnautov, 1987). It is important that the intensities of characteristic lines of studied elements do not depend on the mineralogical and textural specificity of the samples.

Conventional X-ray fluorescence and X-ray radiometric approaches were compared with the use of two energy dispersive X-ray fluorescence analyzers EX-6500 (Baird) and Tefa-6111 (Ortec). An EX-6500 analyzer had the following parameters: voltage 35 kV, current 400 μA , Rh-anode, Rh-filter, and storage time 400 s. The regime of a Tefa-6111 (Ortec) analyzer was as follows: voltage 30 kV, current 200 μA , Mo-anode, Mo-filter, and storage time 400 s. Samples were prepared for traditional working regimes via tableting. The main requirement for tablets was that they should produce saturated emission spectra, which was achieved upon their mass of about 3 g.

Instead of the traditional sample excitation by emanation from an X-ray tube, excitation by isotope source ^{241}Am with energy of 59 keV and activity of $3.7 \cdot 10^{10} \text{ s}^{-1}$ was used for a Tefa-6111 analyzer. Preparation of the samples for the X-ray radiometric method was simple: powdered samples were placed in polyethylene dishes with 5- μm -thick Mylar bottoms. The mass of the powdered samples was about 8 g (exact weight of the sample is not required for this analysis). For an EX-6500 analyzer, the radioisotopic excitation was not efficient, because hard quanta of *K*-lines of the investigated elements penetrated through the detector and were only slightly slowed down by it.

Spectra of microelements in a standard sample of granite (SG-1A) obtained on an EX-6500 analyzer are given in Fig. 1. Upon a traditional X-ray fluorescence analysis, niobium is the last determined element. Elements with greater numbers are not excited, and scattered lines of the anode material are only situated farther on the energy spectrum.

The spectra from granite (SG-1A) and chernozem (SP-1) upon their excitation by the radioisotope source are shown in Fig. 2. The needed *K*-lines of Cs, Ba, La, Ce, and Nd are clearly seen. A comparison of the spectra shown in Figs. 1 and 2 indicated that the X-ray radiometric approach is useful for determining Cs–Nd series. Cesium is reliably determined, when its content exceeds 10 mg/kg, which is typical of the soils enriched by natural or anthropogenic Cs. Upon the X-ray radiometric excitement, *K*-lines of neodymium are overlapped by *K*-line (β components) of barium and are well seen in the samples with the low Ba content (in particular, in granites). In the soils with the Ba content above 400 mg/kg, the determination of neodymium is difficult. Thus, only Ba, La, and Ce are reliably determined in the soils.

We studied metrological characteristics of the new approach using a set of 30 standard samples of soils and rocks. The limit of element determination was 4 mg/kg at storage time of 800 s.

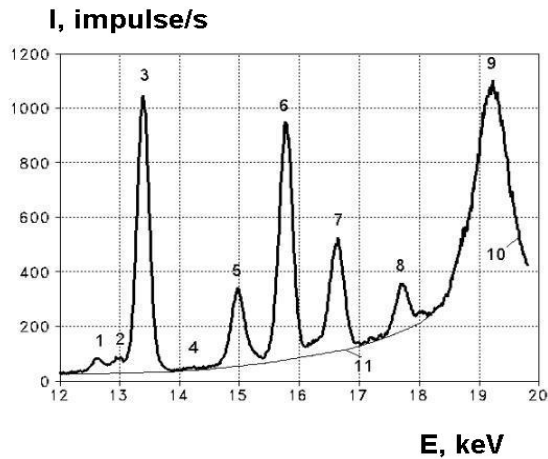


Fig. 1. Part of the SSC SG-1A spectrum from Pb L_{β} to Zr K_{β} (EX-6500 analyzer, X-ray fluorescence method). Position of characteristic lines on the curve: (1) Pb L_{β} , (2) Th $L_{\alpha'}$ (3) Rb $K_{\alpha'}$, (4) Sr $K_{\alpha'}$ (5) Y K_{α} + Rb $K_{\beta'}$ (6) Zr $K_{\alpha'}$ (7) Nb K_{α} + Y $K_{\beta'}$ (8) Zr $K_{\beta'}$ (9) incoherent scattering Rh K_{α} (material of anode), (10) distribution given by multichannel analyzer, (11) approximation of background radiation.

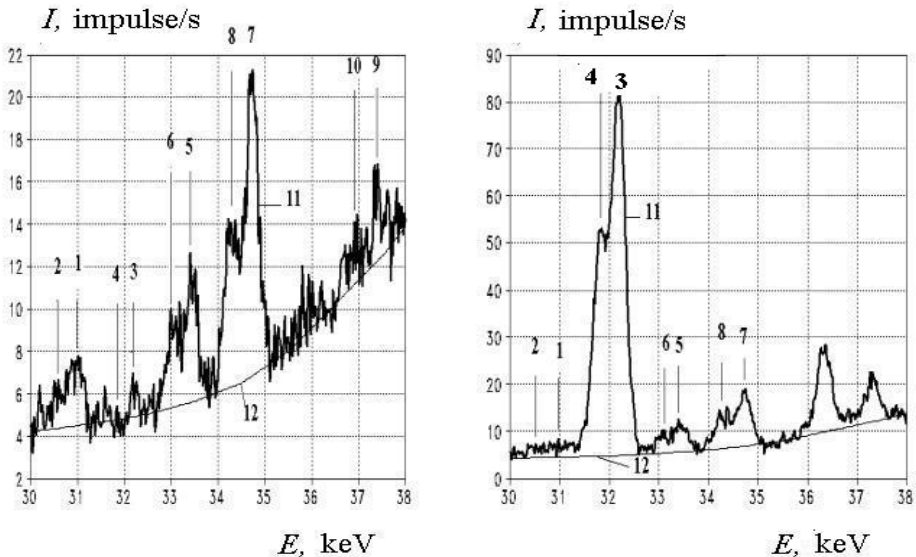


Fig. 2. Parts of the SSC SG-1A spectrum of granite (left) and SSC SP-1 spectrum of chernozem (right) from Cs K_{α} to Nd K_{α} (TEFA-6111 analyzer; X-ray radiometric method). Position of characteristic lines: (1) Cs $K_{\alpha 1'}$, (2) Cs $K_{\alpha 2'}$ (3) Ba $K_{\alpha 1'}$, (4) Ba $K_{\alpha 2'}$ (5) La $K_{\alpha 1'}$, (6) La $K_{\alpha 2'}$ (7) Ce $K_{\alpha 1'}$ (8) Ce $K_{\alpha 2'}$ (9) Nd $K_{\alpha 1'}$ (10) Nd $K_{\alpha 2'}$ (11) distribution given by multichannel analyzer, and (12) approximation of background radiation.

The error of the new analytic approach should be known. Absolute ΔC or relative $\Delta C/C$ deviation from the mean is usually used for error assessments. The advantage of the relative deviation is that it gives different estimates of the error upon high and low concentrations of determined elements. A multiplier $1/C$ is a statistical weight of an absolute error. However, relative deviation also depends on element concentrations changing within a wide range of values. The requirements of the Scientific Council on analytic methods (Berenshtein et al., 1979) are met upon the specification of element concentrations into small ranges and with the determination of the relative deviation in each range. The lower an element concentration, the higher the relative deviation. In order to obtain a more consistent estimate of the error working in a wide range of element concentrations, a different statistical weight should be chosen. Multiplier $1/C^{1/2}$ is the best statistical weight. The error measure equal to $\Delta C/C^{1/2}$ (K -factor) should be used (Savichev, Fogel'son, 1987). The K -factor makes it possible to describe the error within a wide range of concentrations without its subdivision into smaller ranges. In addition, the structure of K -factor agrees with the fact that the detection of X-ray roentgen spectra is based on the counting of impulses, which is a Poisson process, for which the variance correlates with the square root of the mean.

The accuracy of determination corresponds to the third category (according to the requirements of the Scientific Council on analytic methods) at the lower limit of determinable concentrations (8 mg/kg), to the second category at concentrations about 100 mg/kg, and to the first category at the concentrations about 500 mg/kg. Metrological data on the Ba, La and Ce elements are given in Table 1.

Element	Range of measured concentrations, mg/kg	K -factor
Ba	10-2000	1.28
La	10-150	1.02
Ce	10-250	1.07

Table 1. Metrological data on the X-ray radiometric analysis of microelements in soils.

The detection of Pr, Nd, and Sm faces some problems. Their determination is complicated by the fact that the $K_{\alpha 1,2}$ lines of Pr and Nd are overlapped by the Ba $K_{\beta 1,2}$ and La $K_{\beta 1}$ lines. The determination of Pr is also complicated by its low content in soils. The problems of the Sm identification are the same as for Pr and Nd.

The general view of the spectra for the region of elements from Ba to Sm is shown in Fig. 3A for the SGD-1A gabbro-essexite reference standard. An especially strong overlapping is observed in the energy region of 35-38 keV, which appreciably deforms the true intensities of the Pr and Nd spectral lines. A detailed view of this spectral region is shown in Fig. 3B.

The main objective in the determination of the true line intensities of Pr and Nd is to correctly simulate the disturbing Ba $K_{\beta 1,2}$ and La $K_{\beta 1}$ lines. For this purpose, an adequate model should be selected for the spectral line contour. There are two main approaches. The first is an experimental approach in which the line contours of pure elements are used as model spectral lines. The second is an analytical approach in which the model line contour is specified by a mathematical function (in our case, a Gaussian curve). However, both approaches presume the intensity ratio of the α and β components to be stable. The

experimental ratio between the Ba $K_{\alpha 1}$ and Ba $K_{\beta 1}$ line intensities is 5:1. However, in the spectra of real samples, this ratio was found to be slightly lower (by 20%) and varied (by about 10%) among the samples; i.e., this ratio is subjected to matrix effects, which should be taken into consideration in the determination of the true intensities of the Pr and Nd lines. Therefore, the Gaussian model was used as a model of the spectral line contours, and the ratio between the α and β components was selected for each sample on the basis of the best agreement between the top segment of the Ba $K_{\beta 1}$ line and the experimental spectrum, as is shown in Fig. 3B. An adjustment of the model contour on the energy scale was also performed: a parallel shift within an arbitrary number of the analyzer channels (for the energy resolution, 10 eV/channel).

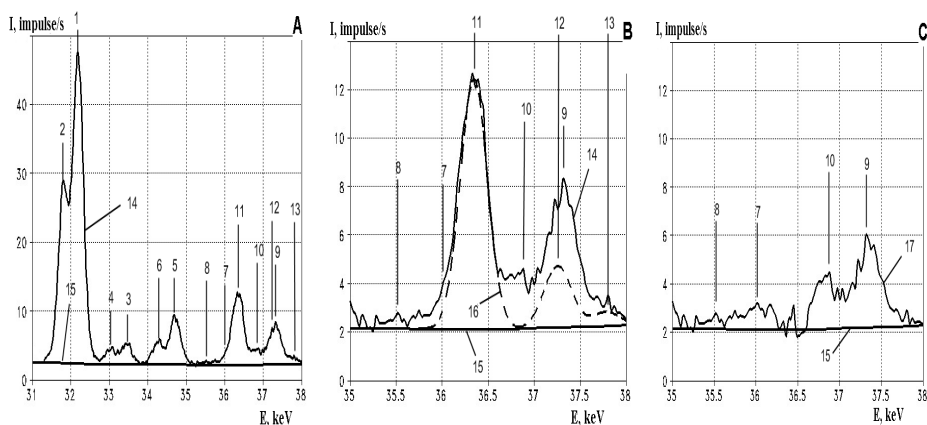


Fig. 3. Spectral segment corresponding to the K -lines of Ba, La, Ce, Pr, and Nd for the SGD-1A (gabbro-essexite) reference standard: (A) general spectrum view; (B) detailed interpretation of the spectrum for Pr and Nd with the simulation of the K_{β} components of the Ba and La lines; (C) the spectrum after the subtraction of the K_{β} components. The spectral lines: (1) Ba $K_{\alpha 1}$; (2) Ba $K_{\alpha 2}$; (3) La $K_{\alpha 1}$; (4) La $K_{\alpha 2}$; (5) Ce $K_{\alpha 1}$; (6) Ce $K_{\alpha 2}$; (7) Pr $K_{\alpha 1}$; (8) Pr $K_{\alpha 2}$; (9) Nd $K_{\alpha 1}$; (10) Nd $K_{\alpha 2}$; (11) Ba $K_{\beta 1}$; (12) Ba $K_{\beta 2}$; (13) La $K_{\beta 1}$. (14) the original spectrum obtained by the energy dispersive analyzer; (15) approximation of the background radiation; (16) simulation of the K_{β} components of the Ba and La lines; (17) true spectrum after the subtraction of the K_{β} components.

After the optimum selection of the K_{β} components for Ba and La, their lines were subtracted from the original spectrum by the least squares method. The difference represents the true intensity spectrum of the Pr and Nd K_{α} lines (Fig. 3C). An analogous procedure for the determination of the true spectrum in the region of the Sm lines is shown in Fig. 4.

None of the soil reference standards was certified for Pr, Nd, and Sm; only three rock standards were certified for Nd; and one rock standard was certified for Pr and Sm. Therefore, the correlation between the intensities of the spectral lines and the concentrations of the elements cannot be found by conventional methods.

We proposed a generalized calibration curve to be used. The values of the analytical parameter (the ratio between the spectral line intensity and the incoherently scattered exiting radiation intensity) determined by the standard background method as functions of the La, Ce, Pr, Nd, and Sm concentrations for the set of reference standards are shown in Fig. 5. It can be seen that the points for La and Ce (elements sufficiently certified in the reference standards) lie on the generalized curve with good accuracy. All the known points for Pr and Nd also lie on the generalized curve. It can be concluded that the relationship between the analytical parameter and the element concentration will be the same for five lanthanides: La, Ce, Pr, Nd, and Sm. This conclusion is well founded if the closeness of the lines of these elements in the energy spectrum and the remoteness of the exiting radiation are taken into consideration.

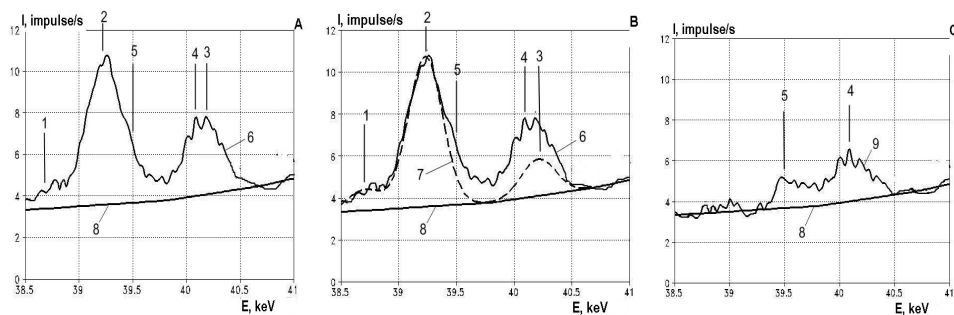


Fig. 4. Spectral segment for the Sm identification (the same sample as in Fig. 3): (A) general spectrum view; (B) detailed interpretation of the spectrum with the simulation of the K_{β} components of the La and Ce lines; (C) the spectrum after the subtraction of the K_{β} components. The spectral lines: (1) La $K_{\beta 2}$; (2) Ce $K_{\beta 1}$; (3) Ce $K_{\beta 2}$; (4) Sm $K_{\alpha 1}$; (5) Sm $K_{\alpha 2}$; (6) the original spectrum obtained by the energy dispersive analyzer; (7) simulation of the K_{β} components of the La and Ce lines; (8) approximation of the background radiation; (9) true spectrum after the subtraction of the K_{β} components.

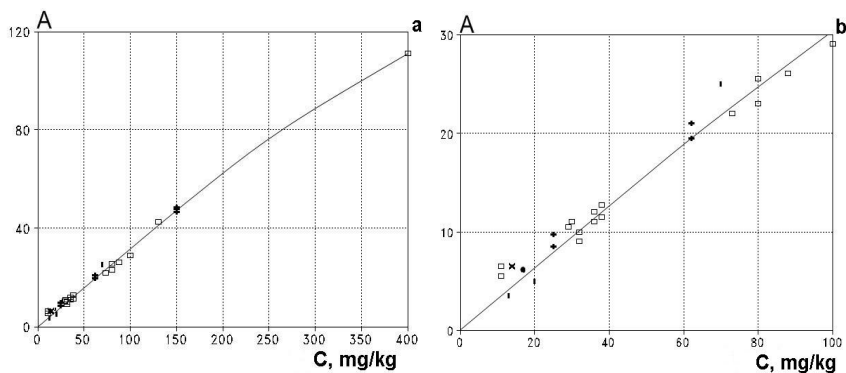


Fig. 5. The analytical parameter (the ratio between the spectral line intensity and the incoherently scattered exiting radiation intensity) as a function of the element concentration: (\square) La; (+) Ce; (\times) Pr; (l) Nd; (\cdot) Sm. (a) general view for the set of reference standards; (b) detailed view of the initial part of the curve.

The error of determining Pr, Nd, and Sm cannot be estimated by the conventional method because of the insufficient certification of the reference standards for Pr, Nd, and Sm. The estimation can be based only on indirect considerations. The previously determined values of the *K*-factors are 1.02 for La and 1.07 for Ce. This implies that, first, the determination the error of these elements almost completely consists of the determination of the error of the spectral line intensity; i.e., the relationship between the analytical parameter and the element concentration (generalized calibration curve) is selected adequately. Second, the values of the *K*-factors show that an almost ultimate accuracy was reached in the measurements of the line intensities. For the Poisson process of the pulse counting in an energy dispersive analyzer, the absolute error of the intensity measurement is equal to the square root of the intensity. The accuracy of the intensity measurements for Pr, Nd, and Sm will obviously be worse than those for La and Ce, because the intensity of the latter elements is measured after the subtraction of the superimposed lines; the value of the *K*-factor for them can be estimated as 2.

The metrological parameters were then improved by increasing the time of the spectrum accumulation. The improvement of the parameters was proportional to the square root of the accumulation time. For the samples with low contents of the elements determined, the time of the spectrum accumulation in the ReSPEKT analyzer was increased to 1.5 h.

3. Key results

3.1 Background soils

Podzolization is one of the leading elementary soil forming processes in the forest zone. It is considered to develop due to metal complexing with organic ligands. At present, the following main properties of the podzolic horizon are distinguished: (1) the light gray and whitish color of the horizon (instead of a red or yellowbrown one) due to Fe and Mn removal and the residual accumulation of silica; (2) the acid soil reaction of this horizon and the substantial base unsaturation; and (3) the depletion in nutrients, sesquioxides, and clay particles (Kaurichev, 1989). Fe and Al migrate with the organic complexes from the eluvial to the illuvial horizon. This is also true for K, Na, Ca, and Mg. The podzol formation is assessed according to the degree of the profile differentiation of the iron and aluminum. Special attention is historically paid to Fe, Al, K, Na, and Mg, because the investigation of the soil chemical composition started with measurements of the total content of macroelements.

Later, the development of the cheap express method of X-ray fluorescence analysis permitted obtaining reliable data on the content of heavy metals in podzolic soils. However, the study with this method was somehow misbalanced, as not all heavy metals were involved in investigation in podzolic soils, and an important group of rare earth metals (yttrium and lanthanides) was omitted (Perel'man, 1975). The situation somewhat improved after researchers began to study lanthanides (La and Ce) using X-ray radiometric analysis.

The analysis of the redistribution of specific heavy metals (including the rare earth elements) upon podzolization will facilitate the better understanding of the complex soilformation process and revealing its additional identification criteria.

We studied the taiga soils with eluvial-illuvial profile differentiation in two regions of the European part of Russia, i.e., Arkhangel'sk oblast (the northern taiga) and the Perm region (the southern taiga).

Two soils were investigated in the Pinega district of Arkhangel'sk oblast: an ironilluvial podzol formed on alluvial sandy deposits of a river terrace (further referred to as the *podzol*) under a 40-yearold pine forest that was transformed by numerous fires. A podzolic contact bleached soil with a podzol microprofile (further called the *podzolic soil*) formed on twolayer moraine (loamy sand / sandy heavy loam) under a spruce forest. The E_{pyr} horizon in the podzol contains many charcoal inclusions, and different horizons (BHF_n and BF) are identified at a depth of 5–15 cm at different profile walls. The podzol formed on sand is characterized by an acid and weakly acid (in the BC horizon) soil reaction. In the podzolic soil on the two member deposits, the soil reaction varies from acid (to a depth of 16 cm) to neutral (deeper than 30 cm). Some properties of these soils are described in detail in (Goryachkin, Pfeifer, 2005).

The soddypodzolic loamy soil was studied in the town of Chusovoi in the Perm region in the woodland park on the left bank of the Chusovaya River. The soil is acidic to a depth of 85 cm, and deeper the soil reaction is neutral.

Podzol, Pinega. This soil is specified by a low content of heavy metals, which is below their clarkes. Even the illuvial horizons are depleted in Ni, Cu, Ga, Zr, Pb, Fe, Al, Sr, Ba, Y, La, and Ce. The low content of heavy metals is controlled by the light texture of the podzol.

Podzolic soil, Pinega. The content of heavy metals is higher in this soil than in the sandy podzol. The list of metals whose content is below the clarke is much shorter: Ni, Zr, Pb, Sr, Y, and La (Table 2). This is related to the heavy soil texture and, consequently, the lower initial sorting of the moraine substratum.

The soddypodzolic soil in the town of Chusovoi. The content of heavy metals is the highest in this soil. The list of metals whose content is below their clarke values is very short—Zr, Sr, Y, and Ba (Table 2)—which is explained by the heavy texture of the soil.

The average content of these metals in the podzolic soils is below their clarke values. The content of Ce is the highest (29 mg/kg), La ranks second (18 mg/kg), and Y ranks third (16 mg/kg). The higher content of La than Y in the soils is worth noting, although the clarke of Y equal to 40 mg/kg (we consider it to be overestimated) exceeds the clarke of La (34 mg/kg). In this connection, let us point out that the clarke of Y is only 25 mg/kg in the soils of the USA (Ivanov, 1997). The geochemical closeness of Y and La mentioned in publications is proved by the high correlation coefficient between them in the podzolic soils ($r = 0.90$).

We may state that the podzolic soils are depleted in the rareearth metals. In spite of this, the rareearth metals respond readily to the soil podzolization.

As seen in Table 2, the metals differ significantly by their participation in the podzolization process. Let us divide them into three groups according to the illuviation index value. $K_{\text{III}} > 5$ for the metals participating actively in podzolization; $5 > K_{\text{III}} > 1.5$ for the metals that are moderately active, and $K_{\text{III}} < 1.5$ for the metals virtually not participating in this process.

Let us list the data about the illuviation coefficients of the metals into a summary table (Table 3) in which the metals are divided into three groups according to the degree of their participation in the eluvial-illuvial profile differentiation. This table also manifests the variation coefficients of the illuviation index K_{III} . They show the variation degree of the

eluvial-illuvial distribution of the same metals in different soils. This is evidently related to the different share of reactive metal particles in the different soils.

Horyzon	Depth, cm	Y	La	Ce
Podzol, Pinega				
E _{pyr}	0-2	10	7	10
E	2-5	5	5	6
BHF _n	5-13	9	11	12
BF	6-10	10	13	17
BC	13-36	7	7	9
Bce	36-49	8	12	20
D	49-110	11	15	24
Clarke		40	34	43
C _{BF} :C _{el}		2.0	2.6	2.8
Podzolic soil, Pinega				
Ele	0-6	14	13	18
ELf	6-16	17	14	19
2EL	16-20	16	21	37
2ELBT	20-30	20	24	44
2BT1	30-65	22	29	53
2BT2	65-90	24	33	54
2BC	90-130	20	31	47
Clarke		40	34	49
C _{ELBT} :C _{el}		1.4	1.8	2.4
Soddypodzolic soil, Chusovoi				
AY	3-12	18	15	23
EL	12-27	18	21	30
BEL	27-59	22	21	36
BT1	59-85	36	38	53
BT2	85-104		30	40
C	104-150	23	20	32
Clarke		40	34	43
K _{ill}		2.0	2.5	2.3

Table 2. Content of lanthanides (mg/kg) in the studied soil (podzol, Pinega; podzolic soil, Pinega and soddypodzolic soil, Chusovoi).

Factors influencing the profile redistribution of heavy metals. We studied the influence of the following factors: the pH, the content of clay particles, the organic carbon, and the iron (both total and oxalatesoluble). We calculated the pair correlation coefficients between these soil parameters and the content of lanthanides (using Excel-2007-software). To rule out the impact of the lithogenic factor, the statistical bonds were considered only for the upper horizons. The reliability level was taken for probability of $P = 0.95$ (Table 4).

Metal	Values	Mean	Variation coefficient, %
Highly active metals			
Mn	33; 4.5; 1.3	12.9	135
Fe	4.7; 4.2; 18	9.0	87
Cr	12; 5.9; 1.4	6.4	83
Zn	14; 3.7; 1.3	6.3	106
Moderately active metals			
Cu	4.3; 4.5; 2.1	3.6	37
Ni	4.0; 2.3; 2.8	3.0	29
Ce	2.8; 2.4; 2.3	2.5	11
La	2.6; 1.8; 2.5	2.3	19
Y	2.0; 2.0; 2.0	2.0	0
Pb	2.5; 1.8; 1.5	1.9	27
Al	2.5; 1.4; 1.5	1.8	34
Zr	3.3; 1.2; 1.0	1.8	70
Ga	1.4; 1.0; 2.3	1.6	41
Inert metals			
Sr	1.4; 1.1; 1.0	1.2	17
Ba	1.3; 1.1; 1.0	1.1	14

Table 3. Values of the illuviation coefficient K_{III} of the metals in the soils of the podzolic group (podzol, Pinega; podzolic soil, Pinega and soddypodzolic soil, Chusovoi).

In the sandy podzol lanthanum is accumulated in the fine silt. In the texturally differentiated podzolic soils the content of lanthanides depends on the pH of the soil solution. The contents La and Ce (which respond to the acidification of soil in the podzolic horizon) depend reliably on the pH value. These metals are cationogenic, with their mobility growing upon the soil's acidification. The content Y is also reliably connected to the amount of clay particles. In soddypodzolic soil, the content of lanthanides Y, La and Ce depends on the soil ferrugination; these metals act as siderophores.

The classic definition of podzolization as a process of iron and aluminum oxides destruction and removal of the decay products should be supplemented by the phenomena of leaching of a number of heavy metals. In addition to Fe and Al, many heavy metals manifest well pronounced eluvial-illuvial redistribution in podzolic soils (Mn, Cr, Zn, Cu, Ni, Ce, La, and Y). The dimensions of these heavy metals' redistribution exceed that of Al. The inactive participation of Al in the redistribution is explained by the insignificant share of its reactive fraction. Although the soils of the podzolic group are depleted in the rare earth metals, the latter readily respond to soil podzolization. In a sandy podzol, the degree of leaching of such heavy metals as Mn, Cr, Zn, Ni, and Zr is markedly higher than in loamy podzolic soil. The leaching of heavy metals from the podzolic horizons has a diagnostic significance, whereas the depletion of metals participating in plant nutrition and biota development is of ecological importance.

Factor	Y	La	Ce
Podzol, Pinega			
pH _{water}	-0.08	0.40	0.33
C _{org}	0.64	0.04	0.10
Fe _{tot}	0.52	0.77	0.59
Clay	0.49	0.42	0.29
Fine silt	0.55	0.94*	0.83
Medium silt	0.52	0.85	0.86
Coarse silt	0.44	0.53	0.55
Fine sand	0.48	0.67	0.75
Medium and coarse sand	-0.55	-0.72	-0.78
Podzolic soil, Pinega			
pH _{water}	0.82	0.98*	0.98*
C _{org}	-0.56	-0.87	-0.90
Fe _{tot}	0.74	0.48	0.45
Clay	0.95*	0.78	0.74
Fine silt	0.64	0.36	0.33
Medium silt	-0.75	-0.84	-0.81
Coarse silt	-0.42	-0.23	-0.16
Fine sand	-0.96	-0.76	-0.74
Medium and coarse sand	-0.91	-0.70	-0.65
Soddypodzolic soil, Chusovoi			
pH _{water}	-0.18	-0.36	-0.37
C _{org}	-0.43	-0.52	-0.61
Fe _{tot}	0.94*	0.89*	0.96*
Clay	0.85	0.86	0.93*
Fine silt	-0.60	-0.40	-0.49
Medium silt	-0.81	-0.64	-0.76
Coarse silt	-0.46	-0.59	-0.61
Fine sand	-0.52	-0.69	-0.68
Medium and coarse sand	-0.56	-0.57	-0.69

*reliable for $P = 95\%$.

Table 4. Pair correlation coefficients between the content of lanthanides and the pH_{water}, the content of clay particles, and the organic carbon in the soils' studied (podzol, Pinega; podzolic soil, Pinega and soddypodzolic soil, Chusovoi).

Leaching of heavy metals is most closely related to the destruction of clay particles (in heavy textured podzolic soils in particular); the soil's acidity's influence is less noticeable.

3.2 Soils from natural positive geochemical anomalies

3.2.1 Tundra soils of the Kolyma Lowland

Gley and peat gley cryozems were sampled in tundra of the Kolyma Lowland. Nineteen samples of the fine earth were studied. The soils were described in detail in (Vodyanitskii, Mergelov et al., 2008).

Data on the concentrations of La and Ce in these soils are given in Table 5, and their statistical characteristics are presented in Table 6. The mean element concentrations are high. The accumulation of lanthanides is even more pronounced. Thus, the average concentrations of La and Ce in cryozems reach 46 and 79 mg/kg, which is considerably higher than the Clarke values of these elements in the pedosphere (26 and 49 mg/kg) and in the lithosphere (35 and 66 mg/kg, respectively). Hence, the tundra zone of the Kolyma lowland is an example of a positive geochemical anomaly of lanthanides.

Horizon	Depth, cm	La	Ce
Gleyed cryozem, pit T6P2			
Gox	40-50	49	79
Cr(Cg)	50-70	49	75
Gleyed cryozem, pit T8P1			
Gox	3-10	47	74
CR	10-16	48	72
	16-33	46	71
Gox	33-42	51	71
Cr(Cg)	42-52	44	66
Gleyed cryozem, pit T9P3			
CR	0.5-3	43	66
CR _{g''}	3-10	45	66
CR	10-35	42	64
CR _{g''}	35-54	46	71
Cr(Cg)	54-59	49	71
Gleyed cryozem, pit T10P3			
CR _{g''}	8-18	44	69
	18-35	50	74
Cr(Cg)	58-60	46	70
Peat gleyed cryozem, pit T9P5			
CR _{g''}	12-23	48	69
Cr(Cg)	23-35	46	67
Peat gley soil, pit T9P7			
Gox	10-17	42	59
	17-45	46	71

Table 5. The contents of La and Ce in cryozems of the Kolyma Lowland, mg/kg.

The loss of lanthanides from the soil profile is favored by peat formation and gleyzation. For Ce, the mean concentrations in the cryozems and in the gley horizons of peat gley soils are equal to 71 and 66 mg/kg; and for La - 47 and 45 mg/kg, respectively. However, these differences are statistically unreliable and may be considered a weakly pronounced tendency.

It should be noted that the concentrations of La and Ce in the studied tundra soils are low variable (Table 6): the variation coefficients are equal to 5–6%, which points to the weak differentiation of these elements in the soil profiles.

Element	Mean	Range	Variation coefficient, %
mg/kg			
Gleyed cryozems			
Lanthanum	47	43-51	5.7
Cerium	71	64-75	5.6
Peat gley soils			
Lanthanum	45	42-48	5.6
Cerium	66	59-71	8.0

Table 6. Statistical characteristics of the La and Ce contents in cryozems of the Kolyma Lowland.

3.2.2 The Kola Peninsula soils

The contents of lanthanides in the soils were determined in northern taiga region: the Khibiny–Lovozero province (Kola Peninsula), where the soils of the background area were studied. On the eastern bank of Lake Umbozero, peatpodzolic soils were sampled (profiles 10 and 11); in the region of a geochemical anomaly due to the closeness to a deposit of loparite ores, samples were taken in three places: a soddy podbur was sampled on the western bank of Lake Lovozero (profile 2); a peaty podzolic soil was sampled on the northern bank of Lake Seidozero (profile 5), and a podzol was sampled on the bank of the Elmoraikok River (profile 9). All the soils were acid (pH_{water} 3.6–5.6) with light sandy and loamy sandy textures. Only the mineral horizons of the soils were analyzed (Table 7).

The background soils and those of the geochemical anomaly formed under the effect of the Lovozero deposit of loparite ores were studied. The content of rare earth metals in loparite is very high (up to 35% in terms of the element oxides). The average chemical composition of loparite with the conventional formula $\text{NaCeTi}_2\text{O}_6$ (Ivanov, 1997) is as follows (in terms of oxides, %): rare earth metals - 30; Ti - 40; Nb - 12; Na - 8; Sr - 3; Ca - 5; and Ta - 0.8. Among the rare earth elements, Ce is predominant (rel. %): Ce - 49.6; La - 28.4; Pr - 3.4; Nd - 15.5; and Sm - 2.4.

Because of the enrichment of loparite with rare earth metals, their contents exceed the Clarke values for the earth's crust by many times: Ce - $133900 : 66 = 2030$; La - $76\,700 : 35 = 2190$; Pr - $9180 : 9 = 1020$; Nd - $41850 : 40 = 1050$; and Sm - $6480 : 7 = 926$. Thus, the loparite containing parent rocks can be significantly enriched with lanthanides, especially the lightest ones (Ce and La). The enrichment of loparite with Pr, Nd, and Sm is twice lower, although it reaches 1000 times. The geochemical anomaly can be heterogeneous because of the different occurrence depths of loparites.

Table 7 shows that the content of Pr in the upper horizons of the soils in the background area is lower than the Clarke value by 2 times, and that of Nd by 3 times; the content of Sm is below the detection limit (lower than 1 mg/kg). An eluvial distribution of lanthanides was observed in some of the profiles studied. A similar situation was previously observed in

podzolic soils of Sweden and the Kola Peninsula (Nikonov et al., 1999; Tyler, 2004b). Based on the hypothesis about the original layer structure, Sweden soil scientists estimated the losses of lanthanides. A podzol lost 40–50% of the initial contents of Y, La, Ce, Nd, Pr, and Sm over 14000 years (Tyler, 2004a). An analogous calculation shows that 36–47% of the Nd and 0–54% of the Pr were leached from the E horizon of peatpodzolic soils in the Khibiny–Lovozero province; 53% of the Nd, 60% of the Pr, and 50% of the Sm were leached from the E horizon of a podzol. The instability of lanthanides in the acid soils of the taiga zone was confirmed.

Horizon	Depth, cm	Pr	Pr _s : Pr _c	Nd	Nd _s : Nd _c	Sm	Sm _s :Sm _c	Pr : Nd	Pr :Sm
Background Profile 10. Umbozero bank. Peatpodzolic soil									
E	12-18	4	0.53	8	0.42	-	-	0.50	-
BT	18-28	2	0.26	7	0.37	-	-	0.29	-
C	28-47	4	0.53	15	0.79	-	-	0.27	-
Profile 11. Umbozero bank. Peatpodzolic soil									
E	8-10	3	0.42	7	0.37	-	-	0.43	-
BT	10-29	3	0.42	6	0.32	-	-	0.50	-
C	29-49	3	0.42	11	0.58	-	-	0.27	-
Geochemical anomaly Profile 2. Lovozero bank. Soddy podbur									
AY	5-12	14	1.8	44	2.3	11	2.4	0.32	1.27
BF	12-40	13	1.7	57	3.0	10	2.2	0.23	1.30
BC	40-50	12	1.6	59	3.1	10	2.2	0.20	1.20
Profile 5. Seidozero bank. Peatpodzolic soil									
E	13-24	21	2.7	104	5.5	18	4.0	0.20	1.17
BT	24-40	30	3.9	142	7.5	23	5.1	0.21	1.30
C	40-62	46	6.0	198	10.4	35	7.8	0.23	1.31
Profile 9. Elmoraik River bank. Podzol									
E	5-15	22	2.9	106	5.6	16	3.5	0.21	1.37
BT	15-30	36	4.7	156	8.2	26	5.8	0.23	1.38
C	30-52	55	7.2	224	11.8	32	7.1	0.24	1.72
Clarke (c)		9		40		7.0		0.22	1.29
Clarke (s)		7.6		19		4.5		0.40	1.69

Table 7. Pr, Nd, and Sm in the mineral horizons of soils in the Khibiny–Lovozero province, mg/kg.

In the Lovozero geochemical anomaly, the contents of Pr, Nd, and Sm in the mineral horizons exceed the clark values. In the soddy podbur on the Lovozero bank, their contents are higher than the clarkes by 1.6–1.8 times for Pr, 2.2–2.4 times for Sm, and by 2.3–3.1 times for Nd. The concentrations of lanthanides in the peatpodzolic soil on the bank of Lake Seidozero and in the podzol on the bank of the Elmoraik River are even higher. Here, the clark values are exceed by 2.7–7.2 times for Pr, by 4–7.8 times for Sm, and even by 5.5–11.8 times for Nd. Thus, the soils are strongly enriched with these lanthanides, especially Nd.

The statistical relationships with a wide range of lanthanides studied previously were considered. In the background area, Y was related to La and Ce, and La was related to Ce with high reliability ($r = 0.83-0.96$). The content of Pr, on the contrary, was not related to any lanthanide. The peculiar behavior of Pr in the soil can be related to its increased biophilicity.

Let us discuss the reason for the difference in the distributions of Pr and Nd, although their contents in loparite, the main rare earth mineral of the province, are similar with consideration for their clarkes. The difference in the biophilic properties of the lanthanides is a probable reason. No reliable data are available on the biophilic properties of lanthanides. The coefficients of the biological absorption of lanthanides are absent in the review of Perel'man (1975). This group of elements was called biotrophic (biophilic). Phosphorus is a known biophil with a high coefficient of biological absorption (~100) (Perel'man, 1975); therefore, it can be taken that lanthanides are also biophils for some plants. This is also true for mosses and peatforming plants in the Khibiny-Lovozero province. According to Dyatlova et al. (1988), the content of Sm in the moss and lichen ash is 2–40 mg/kg (its clark is only 7 mg/kg), and the content of Nd is 8–150 mg/kg (its clark is 19 mg/kg). This confirms the biophilic character of lanthanides.

The degrees of biophilicity of lanthanides can be different. The comparison of the Pr and Nd clarkes in the soil and the earth's crust indicates the different degrees of their global persistence in soils. The index of accumulation/dispersion in the soil, $IA = \text{Clarke (soil)} : \text{Clarke (earth crust)}$, is $19 : 40 = 0.47$ for Nd and $7.6 : 9 = 0.84$ for Pr. Our data confirm the thesis about the higher biophilicity of Pr compared to Nd. The analysis of the ash of lowash peats from the surface of peatpodzolic soils showed a difference in the biological absorption coefficients A_x (against the earth's crust clark) of these two lanthanides: $A_{Pr} = 1.1$ and $A_{Nd} = 0.5$ on the average for the background area; $A_{Pr} = 3.3$ and $A_{Nd} = 2.7$ for the anomaly area. There is no reliable correlation between the contents of Pr and Nd: $r = 0.47$.

In the profile of the peatpodzolic soils in the background area and the soddy podbur in the anomaly, the distribution of Pr is uniform, and that of Nd is eluvial, which explains the abovenoted absence of a statistical correlation between the contents of Pr and other lanthanides in the mineral layers. This can be due to the relative (biogenic?) accumulation of Pr in the upper layer of soils with relatively homogeneous textures: sandy soils in the background area and loamy sandy soils in the anomaly.

3.3 Contaminated soils

3.3.1 Urbanozems and soddy-podzolic soils of Perm

Urban soils (urbanozems) and soddy-podzolic soils from the city of Perm were studied. Samples from surface (0–20 cm) layers of soddy-podzolic soils were taken in parks in the central part of the city. Samples of urbanozems from the same depth were also taken on the lawns along roadways polluted by heavy metals in the central part of the city. To compare distribution patterns of the studied elements with those of well-known air pollutants, the contents of lead and nickel were determined in these soils by the routine X-ray fluorescence analysis. In total, twenty soil samples were studied.

In addition to La and Ce, the concentrations of Ba, Ni and Pb in the surface layers of these soils were determined, and their distribution patterns were compared. They differed for the two groups of metals (Table 8). The concentrations of Ni and Pb in these soils vary considerably, which is typical of urban soils, including soils of Perm (Eremchenko, Moskvina, 2005). The variation coefficients are 53% for Ni and 126% for Pb. This is explained by the fact that the samples were taken not only in parks with soddy-podzolic soils but also from

urbanozems near roads with intensive traffic. Variations in the contents of Ba, La, and Ce are considerably lower ($V = 21\text{--}33\%$). Thus, the portion of metals of technogenic origin for these three elements is much lower than that for Ni and Pb.

Element	Mean	Range	Variation coefficient, %
	mg/kg		
Nickel	145	31–268	53
Lead	113	24–630	126
Barium	382	301–627	21
Lanthanum	19	12–31	28
Cerium	26	18–44	33

Table 8. Statistical characteristics of the Ni, Pb, Ba, La and Ce contents in urbanozems and soddy-podzolic soils in Perm.

Despite the presence of technogenic elements, average concentrations of Ba, La, and Ce are low and remain below the clark values, which attests to the removal of lanthanides and Ba from the soil profiles. This regularity is especially pronounced in comparison with the soils of the Kolyma lowland. In the automorphic soils of Perm, the mean Ba and lanthanides' contents are by 1.6 and 2.4–2.7 times lower than those in the tundra soils of the Kolyma Lowland. Thus, active weathering and the removal of Ba, La, and Ce under conditions of humid climate are typical of these automorphic soils.

3.3.2 Alluvial soils of Perm

Meadow-bog alluvial soils were studied on floodplains of small rivers and the Kama River in Perm. Overall, 16 samples of the fine earth and nodules and rhyzoconcretions from these soils were examined. To judge about the accumulation or depletion of Ba, La, and Ce in the nodules and rhyzoconcretions, the coefficient of element accumulation (C_{ac}) in them was calculated: $C_{ac} = C_{concr} : C_{fine}$ earth, where C_{concr} and C_{fine} earth are the contents of particular elements in the concretions and fine earth, respectively. The studied soils were described in (Vodaynitskii, Vasil'ev et al., 2007).

We studied fine earth and iron-manganic concretions (nodules and rhyzoconcretions) (Table 9). The content of Ba in the fine earth of soils varies from 406 to 527 mg/kg, while its content in the concretions varies greatly (from 588 to 2848 mg/kg). The coefficient of Ba accumulation in the concretions also varies considerably: from 1.2 to 6.0 barium fixation in them. Light-colored formations with a size of about 20 μm were identified on their internal surface. The microanalyzer showed that these formations of composed of barite (BaSO_4). Neoformations of barite were earlier determined by Bronnikova and Targulian (2005) on the surface of cutans in podzolic soils. Barium is not typical of the soils of forest landscapes, so its accumulation in the cutans is related to the soil pollution. In the nodules from the alluvial soils, Ba is mainly accumulated as barite particles precipitated on the active matric of the nodules.

In the gleyed alluvial agrozem on the floodplain of the Mulyanka River polluted by wastewater, Ba redistribution in the soil profile takes place. In the fine earth, the Ba content

is relatively stable (421–474 mg/kg). In the nodules, the concentration of Ba varies considerably and reaches its maximum (2840 mg/kg) in the C4g,t horizon at a depth of 107–137 cm. In this coarse-textured alluvial soil, Ba migrates easily to a considerable depth and is concentrated in the nodules.

Horizon; depth, cm	Substrate	Ba	C _{ac} (Ba)	La	C _{ac} (La)	Ce	C _{ac} (Ce)	Ce/ La
Typical humus-gley soil on the Obva River floodplain, pit 51								
C2g, 37-75	Fine earth	527		37		58		1.6
	Rhyzoconcretions	623	1.2	25	0.7	38	0.6	1.5
G~, 75-90	Fine earth	523		41		60		1.5
	Rhyzoconcretions	673	1.3	14	0.3	16	0.3	1.1
Stratified typical alluvial soil on the Obva River floodplain, pit 53								
C2~, 20-27	Fine earth	410		28		41		1.5
C6~, 71-78	Fine earth	406		26		38		1.5
Mineralized humus-gley soil on the Kama River floodplain, pit 41								
G~, 31-55	Fine earth	452		38		57		1.5
	Nodules	715	1.6	56	1.5	191	3.3	3.4
Gleyed agrozem on the Mulyanka River floodplain, pit 33								
C2~, 49-75	Fine earth	430		31		47		1.5
	Nodules	1957	4.5	104	3.3	324	6.9	3.1
C3~, 75-107	Fine earth	421		31		46		1.5
	Nodules	2120	5.0	108	3.5	302	6.6	2.8
C4g,t~, 107-137	Fine earth	474		34		45		1.3
	Nodules	2840	6.0	100	2.9	243	5.4	2.4
C5g~, >137	Fine earth	441		30		48		1.6
	Nodules	588	1.3	86	2.9	150	3.1	1.7
Average			3.0		2.2		3.7	

Table 9. The contents of Ba, La, and Ce (mg/kg) in the fine earth and nodules of alluvial soils in the Cis-Ural region, coefficients of metal accumulation in the nodules (C_{ac}), and the Ce-to-La ratios (Savichev, Vodyanitskii, 2009).

The La content in the fine earth varies from 28 to 41 mg/kg. In the nodules, it varies from 14 to 108 mg/kg, and the coefficient of La accumulation in the nodules varies from 0.3 to 3.5. In the gleyed alluvial agrozem studied on the floodplain of the Mulyanka River polluted by wastewaters, including those from the petroleum refinery, the content of La in the fine earth remains practically stable (30–34 mg/kg). Its content in the nodules changes from 86 mg/kg in the deepest C5g horizon to 108 mg/kg in the C3 horizon at a depth of 75–107 cm. The technogenic lanthanum migrates to a considerable depth in this coarse-textured soil.

The Ce content in fine earth varies from 38 to 60 mg/kg. In the nodules, it varies from 16 to 324 mg/kg. The corresponding coefficients of Ce accumulation in the nodules vary

from 0.3 to 6.9. In the gleyed alluvial agrozem on the floodplain of the Mulyanka River, the Ce content in the fine earth remains almost stable throughout the soil profile (45–48 mg/kg). In the nodules, it changes from 150 mg/kg in the deepest C5g horizon to 324 mg/kg in the C2 horizon at a depth of 49–75 cm. Being most active among lanthanides, the technogenic Ce migrates down the soil profile to a relatively shallow depth and is fixed in the nodules. This is also confirmed by other data. Thus, in the tropical laterites of Cameron, lanthanides are removed from the top iron-enriched horizons and are accumulated in the deeper layers. Cerium is deposited just below the eluvial horizon, and other lanthanides are accumulated in the deeper horizons (Braun, Viers et al., 2005). Similar differentiation of lanthanides is seen in the soil profiles on granodiorites in the New Southern Wales (Australia).

It should be noted that the contents of La and Ce in the studied soils of Perm region remain below the clarke values for the pedosphere despite the soil pollution (Taunton, Welch et al., 2000).

Different mechanisms of the formation of rhyzoconcretions and iron nodules are responsible for the difference in the accumulation coefficients of the three elements. Rhyzoconcretions formed with participation of organic root exudates on the floodplain of the unpolluted Obva River are characterized by the weak Ba accumulation ($C_{ac} = 1.2-1.3$) and the depletion of La and Ce ($C_{ac} = 0.3-0.7$). Organic ligands in the rhyzoconcretions are mainly spent for iron fixation. This is reflected in the wide Fe-to-Mn ratio in them (25–100). Iron-manganic nodules are formed under conditions of alternating redox regime and are enriched in all the three elements. They are characterized by a more even accumulation of elements and a lower Fe-to-Mn ratio (1.4–12).

The degree of pollution of the river is also important. In the floodplain soil of the strongly polluted Mulyanka River, the accumulation coefficient of Ba in concretions varies from 1.3 to 6.0, the accumulation coefficient of La reaches 2.9–3.5, and the accumulation coefficient of Ce is as high as 3.1–6.9. Polluted waters of the Mulyanka River enter the deep Kama River and are diluted. As a result, nodules in the soils on the Kama River floodplain have lower concentrations of the studied elements; the coefficients of their accumulation are equal to 1.6 for Ba, 1.5 for La, and 3.3 for Ce.

According to the average coefficients of element accumulation in the concretions, the studied elements form the following sequence: Ce(3.7) > Ba(3.0) > La(2.2). The degree of an element accumulation in the concretion depends on its sensitivity to changes in the redox regime, sorption capacity, and the capacity of the element to form stable complexes with organic ligands. The most pronounced accumulation of Ce in the concretions is explained by its sensitivity for changes in the redox regime. Intermediate position of barium is explained by the precipitation of barite crystals on the active matrix of the concretions; Ba is a manganophilic element. A relatively low accumulation of La in the concretions is explained by its physicochemical inactivity.

Let us compare the Ce-to-La ratios in the fine earth and concretions. In the fine earth, this ratio is practically constant and averages to 1.5, which is close to the clarke value (1.9). In the concretions, it varies from 1.1 to 3.4 and averages to 2.3. A wider Ce-to-La ratio in the concretions signifies that Ce accumulation in them is more active as compared with La.

3.3.3 The soils contaminated with the emissions from the Noril'sk metallurgical enterprise

Noril'sk is the center of the industrial region in the south of the Taimyr Peninsula. Three metallurgical plants are located in the immediate vicinity of the town producing a high technogenic load and a high level of soil contamination. In the town, the lawn soils are formed by mixing metallurgical and coal slags with soil or peat. Lawns are situated above the heating mains laid at the surface. The gas and dust emissions of the metallurgical enterprise affect the soils outside the town.

The soils were sampled in June of 2004. We analyzed the contaminated soils of Noril'sk and its suburbs located at a different distance from the town to the northeast. Mixed samples of the surface soil horizon (0–5 cm) were taken, as well as samples from the genetic horizons of the gley cryozem profile formed on heavy and medium marine loams. The soils develop under the conditions of permafrost occurring close to the surface, which results in the weak evaporation of moisture and the development of gley.

The investigated region is subdivided into two zones according to their contamination, i.e., (1) the urban territory, where the soil contamination is controlled by the slags to a great extent; (2) the suburb area at a distance of 4–15 km, where the soil contamination is controlled by aerosols. The soils in Noril'sk are maximally contaminated. The clarkes of the Cu, Ni, Cr, Zn, Fe, and S are exceeded by 287, 78, 4.7, 3.8, 4.1, and 3.5 times, respectively. In the suburbs, the main pollutants remain the same; however, the pollution's degree is lower; the clarkes excess is equal to 65 for Cu, 35 for Ni, and 2.4 for Fe. The town and its suburbs form a technogenic copper–nickel anomaly. The contamination decreases unevenly. As compared to the town, the nickel's contamination decrease is less pronounced in the suburbs than the copper contamination. The slags in the town apparently contain more copper than nickel.

The average content of lanthanides is far below their clarkes values in the suburban soils: clarkes of concentration for La and Ce being equal to 0.4. The territory in the town's vicinity represents a negative technogenic geochemical anomaly according to the content of these metals (Table 10).

Distance from Noril'sk, km	Horizon	Depth, cm	Y	La	Ce
Noril'sk city					
0	A	0-10	34-23	21-15	30-19
Noril'sk suburb					
4	B	3-70	24	17	28
	G	70-90	33	19	29
6	Mixed	0-10	18	9	13
8	Mixed	0-10	30	14	19
9	Mixed	0-10	19	13	17
10	A	2-4	16	10	15
	B1	4-45	34	19	34
12	Mixed	0-10	18	15	22
14	Mixed	0-10	25	13	20
15	Mixed	0-10	16	12	19
Clarke			40	34	49

Table 10. Content of lanthanides (mg/kg) in the soils of the Noril'sk technogeochemical anomaly.

We may judge about the bearing phases of the pollutants from Table 11, which manifests the correlation coefficients between the content of the heavy metals and the iron and sulfur. Chromium and zinc operate as siderophilic elements in the urban soils, which is explained by the soil's contamination with slags containing magnetite. The high magnetic susceptibility of the soils ($840 \times 10^{-8} \text{ m}^3/\text{kg}$) points to the presence of magnetite. The content of the principal pollutants (nickel and copper) correlates with that of sulfur proving the sulfidic nature of the technogenic Ni and Cu. It is no surprise because the copper-nickel deposits in Noril'sk and Talnakh are of the sulfide type (Ivanov, 1997).

Correlation	Y	La	Ce
Noril'sk city			
Fe - Ln	-0.27	-0.06	-0.43
S - Ln	-0.63	-0.22	-0.73
Noril'sk suburb			
Fe - Ln	0.76*	0.82*	0.87*
S - Ln	-0.67*	-0.66*	-0.65*

*Reliable at $P = 0.95$.

Table 11. Correlation coefficients between the content of sulfur and iron and the content of lanthanides (Ln) in the soils of Noril'sk ($n = 14$) and its suburbs ($n = 10$)

The situation is more difficult for the suburban soils. Two opposite processes are effective there: the siderophilic properties are intensified for some elements, and the chalcophilic properties for others. Lanthanides manifest siderophilic properties. This phenomenon is controlled by the increasing influence of the background conditions, under which the content of lanthanides depends on the iron (hydr)oxides. The comparison of the correlation coefficients between lanthanides and Fe in the town (where they are negative) and in the suburbs (where they are positive and high) leads us to the conclusion that the lanthanides enter the soil from the slags rather than from natural bodies in the town. We may speak about the technogenic origin of the lanthanides, although this conclusion cannot be drawn from other more rough indices.

4. Conclusion

1. X-ray fluorescence method is the simplest and cost-effective method for studying heavy metals in soils. However, under normal working conditions, niobium with $Z = 41$ is the last element that may be identified by this method. The use of X-ray radiometric method makes it possible to determine more elements. In this method, a sample is excited not by emission of the X-ray tube, but by the radioisotope source with a great radiant energy. We have developed the methods for determining Ba, La, and Ce contents with the use of ^{241}Am isotope source. The new method has made it possible to obtain data on geochemistry of Ba, La and Ce in soils of humid landscapes.
2. We developed a procedure for the identification of Pr, Nd and Sm using a ^{241}Am isotope source. The procedure is based on the exclusion of the disturbing effect of Ba and La on the lines of Pr and Nd, as well as the effect of La and Ce on the lines of Sm. On the basis of the new method, data were obtained on the geochemistry of three lanthanides in the northern taiga soils.

3. The classic definition of podzolization as a process of iron and aluminum oxides destruction and removal of the decay products should be supplemented by the phenomena of leaching of a number of heavy metals. In addition to Fe and Al, many heavy metals manifest well pronounced eluvial-illuvial redistribution in podzolic soils (Mn, Cr, Zn, Cu, Ni, Ce, La and Y). The dimensions of these heavy metals' redistribution exceed that of Al. The inactive participation of Al in the redistribution is explained by the insignificant share of its reactive fraction. Although the soils of the podzolic group are depleted in the rare earth metals, the latter readily respond to soil podzolization. In a sandy podzol, the degree of leaching of such heavy metals as Mn, Cr, Zn, Ni and Zr is markedly higher than in loamy podzolic soil. The leaching of heavy metals from the podzolic horizons has a diagnostic significance, whereas the depletion of metals participating in plant nutrition and biota development is of ecological importance.

Leaching of heavy metals is most closely related to the destruction of clay particles (in heavytextured podzolic soils in particular); the soil's acidity's influence is less noticeable.

The heavy alkalineearth metals (Sr and Ba) do not participate in podzolization.

4. In the cryozems of the Kolyma Lowland, the high content of La and Ce has been determined. Weathering processes in these cold soils are retarded, which is confirmed by the low role of iron oxidogenesis. This results in preservation of lanthanides and barium in the cryozems.
5. In the Khibiny-Lovozero province of the Kola Peninsula, the area is divided into two parts. In the soils near Lake Umbozero, the contents of Pr and Nd are lower than their clarkes, and the content of Sm is below the detection limit. In the background area, the lanthanides are strongly leached from the podzolic soils with Nd being leached more strongly than Pr.

In the region of the geochemical anomaly (near Lake Lovozero), the contents of Pr, Nd, and Sm are significantly higher than their clarkes due to the effect of the adjacent deposit of loparites. In the background area, Y is related to La and Ce, and La is related to Ce with high reliability, while the content of Pr is not related to any lanthanide. This is explained by the uniform profile distribution of Nd, in distinction from the eluvial distributions of Y, La and Ce.

Positive rare earth anomalies can be expected in soils located not far from the deposits of apatitenephelines, loparites and phosphorites and in the soils developed on alkaline granites and carbonate weathering crusts.

6. In the soddy-podzolic soils and urbanozems of Perm, the variability in the contents of Ba, La, and Ce is considerably lower than that of Ni and Pb. The first three elements are characterized by a smaller portion of technogenic elements as compared with Ni and Pb. The mean contents of Ba, La, and Ce are low despite the possible contribution of technogenic sources. Soil weathering accompanied by the removal of these elements under conditions of humid climate, which is responsible for their low content in the soil profiles.
7. In the alluvial soils of Perm, Ba is fixed in rhyzoconcretions as barite (BaSO_4) of, probably, technogenic nature. In the gleyed alluvial agrozem on the Mulyanka River

floodplain, Ba migrates intensively in the soil profile and is fixed in iron-manganic nodules. The contents of La and Ce in the fine earth of polluted soils remain practically stable, and lanthanides are accumulated in the concretions: the accumulation coefficient reaches 3.5 for La and 6.9 for Ce.

8. The soil cover in the area influenced by the Noril'sk metallurgical enterprise may be subdivided in terms of the soil contamination into two territories: Noril'sk proper and its suburb at a distance of 4–15 km. The urban soils are maximally polluted with their clark excesses being equal to 287, 78, 4.7, 4.1, and 3.5 for copper, nickel, chromium, iron, and sulfur, respectively. In the Noril'sk suburbs, the principal pollutants are the same; however, the clark excess is lower: 65 for Cu, 35 for Ni, and 2.4 for Fe. The urban and suburban territory represents a technogenic copper-nickel-chromium anomaly. By the content of a number of superheavy metals (Ba, La and Ce), the territory near the town forms a negative geochemical anomaly. The situation is different in the suburban soils. The rare earth elements (Y, La and Ce) have pronounced siderophilic properties due to the natural factors' influence.

5. References

- Arnautov N.S. (ed.) (1987). *Standard Samples of the Chemical Composition of Natural Mineral Substances. Methodological Guidelines*, Novosibirsk. [in Russian].
- Berenshtein L.E., Masolovich N.S., Sochevanov V.G. & Ostroumov G.V. (1979). *Metrological Basis of Quality Control of Analytical Works*, In: *Methodological Basis of Studying the Chemical Composition of Rocks, Ores and Minerals*, pp. 23–118, Nedra, Moscow. [in Russian].
- Bowen H.J.M. (1979). *Environmental Chemistry of Elements*, Academic, New York.
- Braun J.J., Viers J. & Dupre B. (2005). Solid/Liquid REE Fractionation in the Lateritic System of Goyoum, East Cameroon: The Implication For the Present Dynamics of Soil Covers of the Humid Tropical Regions. *Ceochim. Cosmochim. Acta*, Vol. 62, pp. 273–299.
- Bronnikova M.A. & Targul'yan V.O. (2005). *The Cutan Assemblage in Texture-Differentiated Soils*, Akademkniga, Moscow. [in Russian].
- Dyatlova N.M., Temkina V.Ya. & K. I. Popov K.I. (1988). *Complexones and Complexonates of Metals*, Khimiya, Moscow. [in Russian].
- Eremchenko O.Z. & Moskvina N.V. (2005). The Properties of Soils and Technogenic Surface Formations in the Multistory Districts of Perm City. *Pochvovedenie*, No. 7, pp. 782–789. [*Eur. Soil Sci.* 38 (7) (2005)], ISSN 1064-2293.
- Evans C.H. (1990). *Biochemistry of the Lanthanides*, Plenum, New York.
- Goryachkin S.V. & Pfeifer E.M. (ed.) (2005). *Soils and Perennial Underground Ice of Glaciated and Karst Landscapes in Northern European Russia*, Inst. Geogr., Moscow.
- Greenwood N.N. & Earnshaw A. (1997). *Chemistry of Elements*, 2nd ed., Elsevier.
- Inisheva L.I. & Ezupenok E.E. (2007). Contents of Chemical Elements in Highmoor Peats, In: *Current Problems of Soil Pollution: II International Scientific Conference, Moscow, Russia (Moscow, 2007)*, Vol. 2, pp. 63–67. [in Russian].
- Ivanov I.N. & Burmistenko Yu.N. (1986). *Neutron-activation Analysis and the Use of Short Living Radionuclide*, Energoizdat, Moscow. [in Russian].
- Ivanov V.V. (1997). *Ecological Geochemistry of Elements*, Ekologiya, Moscow. [in Russian], ISBN 5-247-03178-4.
- Kabata-Pendias A. & Pendias H. (1985). *Trace Elements in Soils and Plants*, CRC, Boca Raton.

- Kashulina G.M., Chekushin V.A. & Bogatyrev I.V. (2007). Physical Degradation and Chemical Contamination of Soils in Northwestern Europe, In: *Current Problems of Soil Pollution: II International Scientific Conference, Moscow, Russia* (Moscow, 2007), Vol. 2, pp. 74–78. [in Russian].
- Kaurichev I.S. (ed.) (1989). *Soil Science*, Agropromizdat, Moscow. [in Russian].
- Khitrov V.G. (1985). The Results of Attestation of the System of Standards of the Chemical Composition of Magmatic Rocks. *Izv. Akad. Nauk SSSR, Ser. Geol.*, No. 11, pp. 37–52.
- Nikonov V.V., Lukina N.V. & Frontas'eva M.V. (1999). Trace Elements in Al-Fe-Humus Podzolic Soils Subjected to Aerial Pollution from the Copper-Nickel Production Industry in Conditions of Varying Lithogenic Background. *Pochvovedenie*, No. 3, pp. 370–382. [*Eur. Soil Sci.* 32 (3), 338–349 (1999)], ISSN 1064-2293.
- Perel'man A.I. (1975). *Geochemistry of Landscape*, Vysshaya shkola, Moscow. [in Russian].
- Perelomov L.V. (2007). Interactions of Rare Earth Elements with Biotic and Abiotic Soil Components. *Agrokimiya*, No. 11, pp. 85–96, ISSN 0002-1881.
- Savichev A.T. & Fogel'son M.S. (1987). X-ray Fluorescent Analysis of Silicate Rocks on a Spectrometer. *Izv. Akad. Nauk SSSR, Ser. Geol.*, No. 8, pp. 103–108.
- Savichev A.T. & Sorokin S.E. (2000). X-Ray Fluorescence Analysis of Microelements and Heavy Metals in Soils. *Agrokimiya*, No. 12, pp. 71–74, ISSN 0002-1881.
- Savichev A.T. & Vodyanitskii Yu.N. (2009). Determination of Barium, Lanthanum, and Cerium Contents in Soils by the X-Ray Radiometric Method. *Eur. Soil Sci.*, Vol. 42, No 13, pp. 1461–1469, ISSN 1064-2293.
- Taunton A.E., Welch S.A. & Banfield J.F. (2000). Microbial Control on Phosphate and Lanthanide Distributions during Granite Weathering and Soil Formation. *Chem. Geol.*, Vol. 169, pp. 371–382.
- Tyler G. (2004a). Rare Earth Elements in Soil and Plant Systems: A Review. *Plant Soil*, Vol. 267, pp. 191–206, ISSN 0032-079X.
- Tyler G. (2004b). Vertical Distribution of Major, Minor, and Rare Elements in Haplic Podzol. *Geoderma*, Vol. 119, pp. 277–290, ISSN 0016-7061.
- Vodyanitskii Yu.N., Mergelov N.S. & Goryachkin S.V. (2008). Diagnostics of Gleyzation upon a Low Content of Iron Oxides (Using the Example of Tundra Soils in the Kolyma Lowland). *Pochvovedenie*, No. 3, pp. 261–279. [*Eur. Soil Sci.* 41 (3), 231–248], ISSN 1064-2293.
- Vodyanitskii Yu.N., Vasil'ev A.A. & Kozheva A.V. (2007). Influence of Iron-Containing Pigments on the Color of Soils on Alluvium of the Middle Kama Plain. *Pochvovedenie*, No. 3, pp. 318–330. [*Eur. Soil Sci.* 40 (3), 289–301], ISSN 1064-2293.
- Wu Z.M. & Guo B.S. (1995). *Bioinorganic Chemistry of Rare Earth Elements*, J. Z. Ni (ed.), Science Press, Beijing, pp. 13–55.
- Zhu W.F., Xu S. & Zhang H. (1995). Biological Effect of Rare Earth Elements in Rare Earth Mineral Zone in the South of China. *Chin Sci. Bull.*, pp. 914–916.

Cu, Pb and Zn Fractionation in a Savannah Type Grassland Soil

B. Anjan Kumar Prusty*, Rachna Chandra and P. A. Azeez
*Environmental Impact Assessment Division
Sálim Ali Centre for Ornithology and Natural History (SACON)
Anaikatty (PO), Coimbatore
India*

1. Introduction

Heavy metal contamination in soil has received much attention and extensive research has been conducted on estimation of metals in soils. Several heavy metals are known to accumulate in water, soil, sediments and tissues of organisms (Chaphekar, 1991; Lambou & Williams, 1980; Ramadan, 2003) and cause chronic to acute toxicity in due course of time. For evaluation of the heavy metal burden in the environment, it is not sufficient to measure only total metal concentrations, it is also very important to establish the proportions of heavy metals present in various soil solid phase forms their bioavailability and toxicity. Quantifying the geochemical phases of metals associated with soil is an important step in predicting the ultimate fate, bioavailability, and toxicity of metals (Azeez et al., 2006; Lu et al., 2005; Prusty et al., 1994). Easily soluble fractions that are bioavailable and most mobile in the environment are commonly investigated by single extraction procedures such as that of Deely et al. (1992), while the partitioning of heavy metals between easily and sparingly soluble fractions in soils and sediments is investigated by sequential extraction procedures.

Sequential extractions, although operationally defined, give information about the association of heavy metals with geochemical phases of soil, and hence helps to reveal the distribution of heavy metals in fractions and to assess the mobility and toxicity of metals in soils (Ahnstrom & Parker, 1999; Quevauiller et al., 1993). Several sequential chemical extraction procedures are in practice in speciation studies to assess metals in different environmental matrices (Badri & Aston, 1983; Kersten & Förstner, 1986; Pickering, 1981; Tessier et al., 1979; Young et al., 1992). Element specific methods have also been developed as that of Poulton & Canfield (2005) for iron partitioning. Of these, the five step extraction method by Tessier et al. (1979) is a widely used one, although the disadvantages of this extraction scheme, e.g., non-specificity of extraction (Nirel & Morel, 1990; Reuther, 1999) and re-sorption (Howard & Shu, 1996; Howard & Vandenbrink, 1999) have been well recognized. According to this protocol, metals in soil are fractionated into five geochemical pools, *viz.*, exchangeable (EXC), carbonate- (CA), multiple hydroxide (Fe-Mn oxide), organic matter and sulphide (oxidizable, OM-S), and lithogenic or residual

* Corresponding Author

(RES). The mobility and bioavailability of metals decrease approximately in the order of extraction sequence (Prusty et al., 1994) and hence the strength of the chemical reagents used in extraction increases with the sequence. Generally, exchangeable form is considered readily mobile and easily bioavailable, while lithogenic or residual form is considered as incorporated into crystalline lattice of soil minerals and the most inactive. The carbonate, Fe-Mn oxide and organic matter-bound fractions could be relatively active depending on the physical and chemical properties of the medium. Metals bound to sulphides and organic matter are more stable and hard to take part in the geochemical cycle and generally act as a sink and reservoir for pollutants (Prusty et al., 1994; Yuan et al., 2004).

Heavy metal partitioning in soil has become imperative as this acts as a potential environmental indicator and soils enriched in metals may eventually become sources of metal contamination during oxidative weathering and be available for plant uptake. Metal speciation studies have been extensively undertaken in aquatic systems (Fan et al., 2002; Jagadeesh et al., 2006; Li et al., 2000, 2001; Mathew et al., 2003; Prusty et al., 2007a; Shanthi et al., 2003) for assessment of metal mobility and bioavailability. However, less progress has been made in terrestrial environments, mainly owing 1) to the difficulties in measuring metal activities in soil systems, and 2) to the heterogeneous nature of the soil environment, where exposure of organisms to metals occurs through solid, liquid, and gaseous pathways (Nolan et al., 2003). The Keoladeo National Park (KNP), India in spite of being one of the early Ramsar sites in the country is lacking studies on soil characterization and assessment of metal distribution in the soil. The impetus behind the research presented here was to investigate the chemical partitioning of Cu, Pb and Zn in the soil profile of the grassland system in the park. The particular objectives were to 1) examine the distribution of the metals amongst different operationally defined geochemical pools, and 2) assess the variation of metal distribution among years and soil layers.

2. Study area

Field investigations were carried out in the Keoladeo National Park (KNP, Figure 1), Bharatpur, India in summer of 2003, 2004 and 2005. It was declared as a protected area and bird sanctuary in 1956 and later upgraded to a National Park in 1981 (Sharma & Praveen, 2002). This 29 Km² park (27°7.6' to 27°12.2'N and 77°29.5' to 77°33.9'E, almost equidistant about 180 km from Delhi and Jaipur), existing for more than 250 years (Azeez et al., 1992) is one of the early Ramsar sites (Mathur et al., 2005). The park is segmented into 15 blocks or compartments, named alphabetically from A to O, separated by earthen dykes or mud trails, for the ease of management and tourism. The large number of migratory water fowls, the range of habitats (Prusty et al., 2006) clearly distinguished by vegetation types (Davis & van der Valk, 1988) and hydrological parameters (Azeez et al., 2007) available in the area are the distinctive features of the park. About 8.5 km² large central depression of the park is (Figure 1) wetland, while the rest is covered by grassland and woodland (Azeez et al., 2000). The grassland is comprised of *Vetiveria zizanioides*, *Desmostachya bipinnata* and *Cynodon dactylon* as characteristic vegetation (Sharma & Praveen, 2002). While the study was conducted in all the habitats, for the scope of this chapter only the results from the grassland habitat were synthesized and presented here.

The area is a part of the Aravalli Supergroup and falls under semi-arid hot dry zone of India (Pal et al., 2000) and experiences four distinct seasons; summer / pre-monsoon (April to June), rainy / monsoon (July to Mid-September), post monsoon (mid-September to mid-November) and winter (mid-November to March, Prusty & Azeez, 2004). Usually the temperature in the Park varies from 1°C to 49°C, showing strong diurnal and seasonal fluctuations. The soil type of the park is clay loam (terrestrial areas) to clayey (aquatic areas) with scattered saline patches in the terrestrial areas.

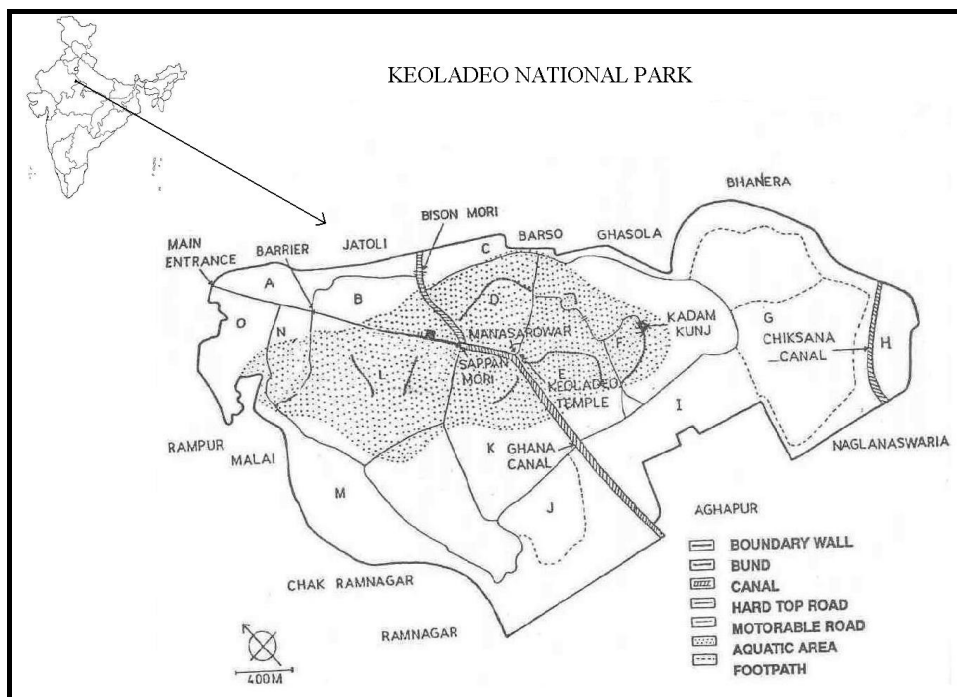


Fig. 1. Study Area Map

3. Methods

3.1 Soil sampling, processing and analyses

Of the total grassland area, three blocks were considered for the present study and the samples were collected in mid June of the year. A trench of 1 m³ was dug up in three locations in each block and the uppermost litter layer was removed by scrapping with a plastic scrapper. Subsequent soil layers from 0, 25, 50, 75 and 100 cm depths were removed using a plastic scoop. The soil samples were packed in pre-cleaned, acid treated and airtight plastic bags and transferred to the laboratory for further processing and analyses. In the laboratory, the soil samples were air-dried at room temperature (Jackson, 1958), homogenized / gently crushed using an agate mortar and pestle and sieved through a standard sieve of 2 mm mesh size (Tandon, 2001). The soil samples with particle size of <2 mm were stored in acid washed plastic containers. Equal proportion of samples from all the

three points from each block were thoroughly mixed to get a representative sample per block.

Total Organic Carbon (TOC, %) in soil was estimated following the wet digestion method of Walkley & Black (1934) and the values were converted to the Total Organic Matter (TOM) empirically assuming that TOC comprises 58% of TOM. The Carbonate Carbon (CO₃-C, %) content in soil was estimated following the rapid titration method of Allen (1989). The chemical fractionation of metals was assessed following Sequential Extraction Procedure based on Tessier et al. (1979). It was carried out progressively on an initial weight of 1.0 g of homogenized material using the following extractions:

Step 1. 0.5 M Magnesium chloride adjusted to pH 7.0 with 10% ammonia solution.

Step 2. 1 M Sodium acetate adjusted to pH 5.0 with Acetic acid.

Step 3. 0.04 M Hydroxylamine hydrochloride in 25% Acetic acid.

Step 4. 30% Hydrogen peroxide in 0.02 M Nitric acid.

Step 5. Aquaregia digestion.

Of the five steps mentioned above, step 1 to step 4 were performed following Tessier et al. (1979) and step 5 was performed following Ure (1990). The method is intended to distinguish five fractions representing the following phases; Exchangeable (EXC - step 1), Carbonate and specifically adsorbed (CA - step 2), Fe-Mn oxide (Fe-Mn - step 3), Organic matter and sulphide (OM-S - step 4) and Residual / lithogenic (Res - step 5). Aquaregia digestion was performed to estimate the total metal (pseudototal level) content which was compared with the sum of all the five fractions. The geochemical phases at each extraction step are largely operationally defined and indicate relative rather than absolute chemical speciation. The main interpretations are based on the solubility of metals.

Simultaneously blanks and internal standards were also run to verify the precision of the method and accuracy. The precision and bias was generally <10%. The estimated detection limits of the metals in the soil (µg/g) and the recovery rate for all the metals are given in Table 1. Analysis of standardised soil samples showed an average recovery rate of 94.6 ± 1.9%. Values for constituents lower than the method detection limits (< DL) were substituted with DL/2 prior to statistical analysis (Farnham et al., 1998; Ryu et al., 2006). For quality assurance throughout the experiments and analyses, all extracting reagents were prepared using metal free, AnalaR grade chemicals procured from Qualigens Fine Chemicals Division of GlaxoSmithKline Pharmaceuticals Limited, Mumbai and double distilled water prepared using quartz double distillation assembly was used for the reagent preparations. Room temperature was 30°C, while extractions were carried out. Polypropylene centrifuge tubes and bottles were subjected to cleaning procedures prescribed by Laxen & Harrison (1981). The metals in the extracts were analyzed using an AAS (Perkin Elmer AAnalyst 800).

Metal	Cu	Pb	Zn
Detection level in soil (µg/g)	0.01	0.01	0.1
Recovery rate (%)	94.3	92.9	96.7

Table 1. Detection limits for metals

3.2 Statistical analyses

Basic descriptive statistics and two-tail Correlation matrix were performed on the analytical data using "MEGASTAT" to infer the range, distribution and association of different metal fractions among themselves and with TOM and CO₃-C. Univariate tests were performed following the General Linear Model (GLM) to assess variations of the distribution of the metals among fractions, soil layers and years. Post-hoc analysis, i.e. One Way Analysis of Variance (ANOVA) was performed coupled with a test of Least Significant Difference (LSD), only in the cases with significant differences. The statistical tests were performed using SPSS 11.0 (Norusis, 1986).

4. Results and discussions

4.1 Distribution of heavy metals in soil profile

Of the metals studied, Zn was seen highest in soil while Pb was seen the least. The total concentration of Cu in soil ranged from 23.6mg/Kg to 46.4 mg/Kg. The range for Zn was 35.9 mg/Kg to 63.2 mg/Kg and Pb was 8.7 mg/Kg to 13.1 mg/Kg. Cu was seen least at a depth of 25 cm during 2003 and was seen highest in the surface layer during 2004. Pb was found minimum at the depth of 100 cm during 2005, while maximum was seen at a depth of 50 cm during 2005. The lowest concentration of Zn was at a depth of 25 cm during 2003 and the highest at the bottom of the profile. Two-Way ANOVA test results show that the variation of Cu and Zn was highly significant among the years (Table 2). Of the three metals studied, Cu and Zn had an increasing pattern along the soil profile during all the years (Figure 2). However, a sustained pattern of increase throughout the depth profile was observed during 2005 only. Irrespective of the year and metal, the metal level decreased from surface layer to the immediate next layer, i.e. to a depth of 25 cm and then gradually increased till the bottom of the soil profile. The depthwise trend of increase in metals concentration could be associated with their lithogenic nature. The extent of their lithogenic nature is discussed in the subsequent paragraphs. The higher metal levels in the surface layers compared to the subsequent layer might be because of the two reasons, of which the first being the contribution from the plant litters during the process of decomposition. The results of the earlier works by the authors in the KNP reports several species of plants showing notable uptake rates for elements such as Cu, Pb and Zn from the soil (Azeez et al., 2007; Prusty et al., 2007b). The second reason may be the automobile exhausts, they being one of the substantial sources for metals such as Pb (Baker, 1990). KNP has one of the major and busy National High-way (Delhi-Jaipur) traversing beside its immediate boundary. Moreover, its proximity to Bharatpur city might add substantially to the cause.

Metal	Source of variation	F actual	F critical	P value
Cu	Years	6.169	4.459	*0.024
	Soil Layers	0.228	3.838	0.915
Pb	Years	0.666	4.459	0.54
	Soil Layers	2.139	3.838	0.167
Zn	Years	20.432	4.459	*7.18-04
	Soil Layers	1.253	3.838	0.363

* Significant at p<0.05

Table 2. ANOVA of total metal content in soil

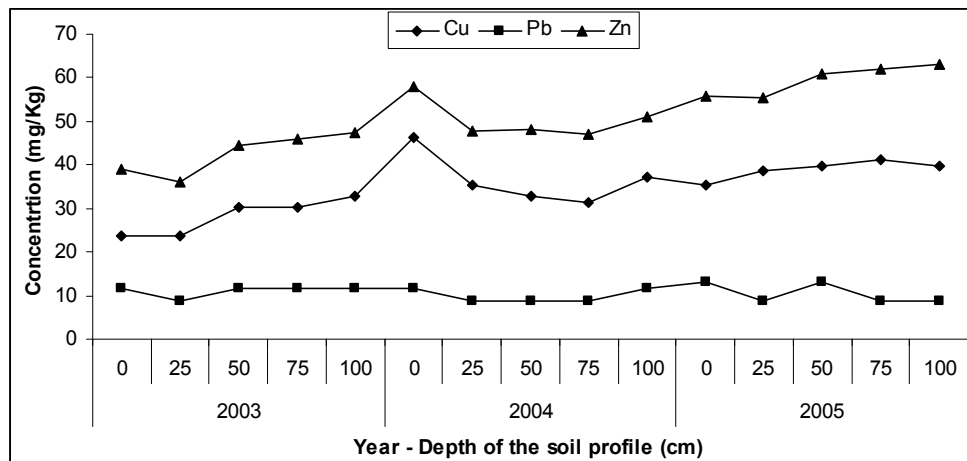


Fig. 2. Variation of total metal content in the soil profile

4.2 Fractionation of heavy metals in soil profile

The association of the three metals to various geochemical phases is presented in Figure 3 to Figure 5. Of the three metals studied, Cu was mainly associated with RES phase while it showed least preferences to the EXC phase (Figure 3). Cu was seen in the range of 30.4% to 76.2% in the residual phase and 0.01% to 0.7% in the EXC phase and the order of the fractions in terms of Cu concentration was Res > Fe-Mn > OM-S > CA > EXC. In contrast, Pb was mostly contained in the multiple hydroxides fraction and least attached with the EXC phase (Figure 4). Pb was seen in the range of 36.6% to 74.0% in the Fe-Mn oxide phase and 0.02% to 7.5% in the EXC phase and the order of fraction in terms of Pb concentration was Fe-Mn > Res > OM-S > CA > EXC. Zn, similar to Cu, had preference towards RES phase and least preference towards EXC phase (Figure 5). Zn was seen in the range of 60.7% to 88.9% in the RES phase, while 0.1% to 1.6% was seen in the EXC phase. The fractions in terms of Zn levels was in the order Res > Fe-Mn > OM-S > CA > EXC. The results indicate two major points: (1) RES phase is the major binding site for Cu and Zn, indicating that the major proportion of the metal is incorporated in the silicate mineral matrix. This may indicate that this element was derived from natural geological sources. (2) Fe-Mn phase is the important binding site for Pb and the reducible Fe and Mn plays a major role in binding these metals. Fe-Mn phase represents the second most significant sink for Cu and Zn after RES phase. It has been shown that in Saline - alkaline soils, as in the case of KNP, the second extraction step (CA phase) may not be effective in removing all the carbonate minerals into solution. Metals extracted in step 3 (Fe-Mn phase) therefore may contain a proportion of the carbonate forms in addition to those bound to Fe-Mn oxides (Maskall & Thornton 1998). The observed higher attachment of Cu and Zn to the RES phase is consistent with observations of Li et al. (2001). The highest affinity of Zn towards RES phase was also reported by Svetec et al. (2001) in a study on the chemical partitioning of Zn from a mine area.

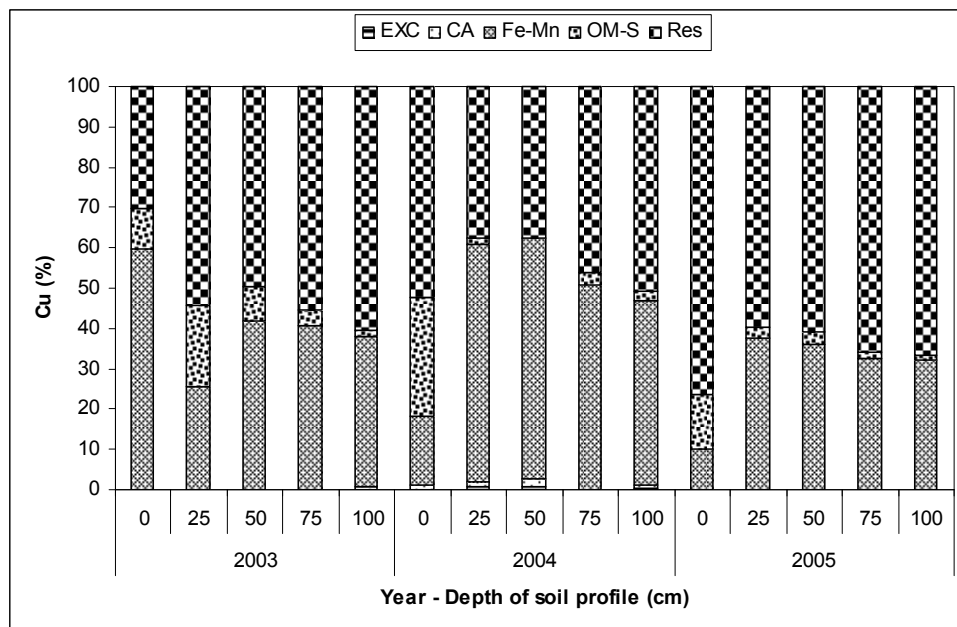


Fig. 3. Cu fractionation in grassland

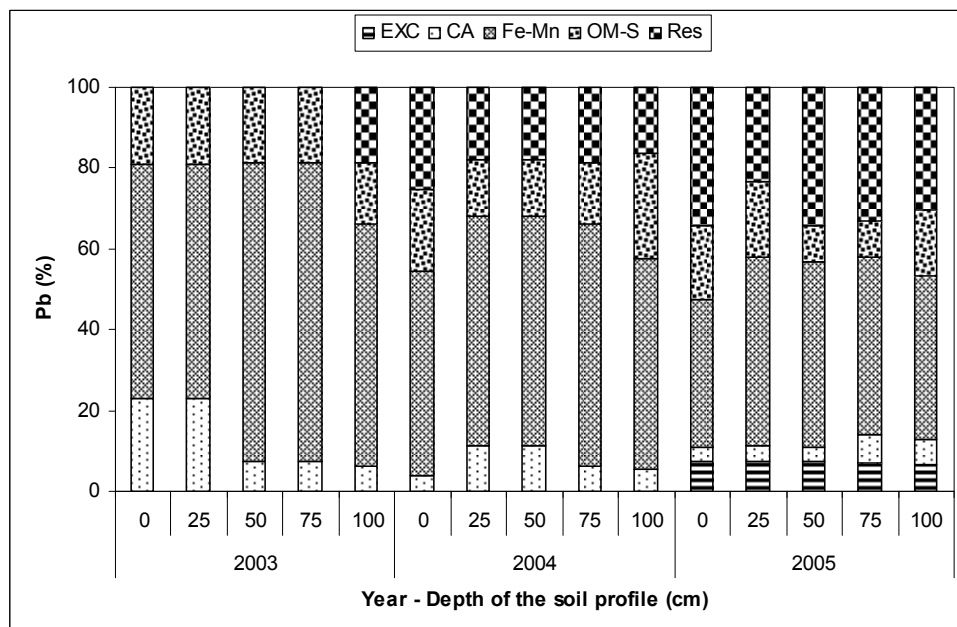


Fig. 4. Pb fractionation in grassland

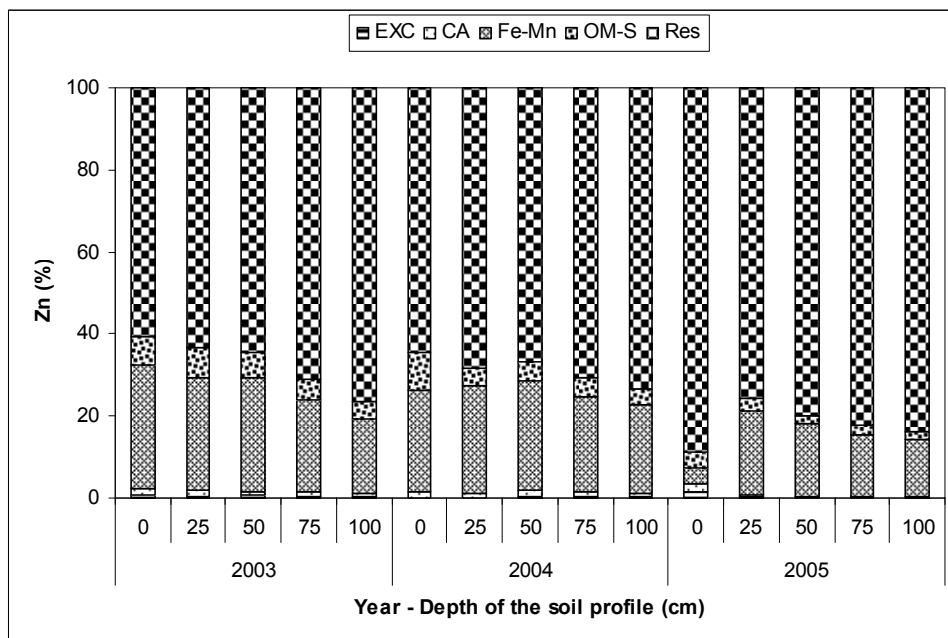


Fig. 5. Zn fractionation in grassland

Although all the metals showed least preference to the exchangeable pool, the order of the metals with average percentage bound to the EXC pool in parenthesis was Cu ($0.1 \pm 0.2\%$) < Zn ($0.4 \pm 0.3\%$) < Pb ($2.4 \pm 3.4\%$). This indicates that the anthropogenic input of Pb is comparatively higher than those of Cu and Zn. As the sampling was done in summer months that have less organic matter in soil as evidenced by our earlier reports, the metals mostly remain attached either with the RES phase and/or with the Fe-Mn oxides phase, and the attachment to organic matter (OM-S) phase is comparatively less. Fan et al. (2002) & Li et al. (2000) also reported similar findings. The apparently greater contribution made by the hydroxylamine hydrochloride-extractable (Fe-Mn) fraction to the Pb compared to Cu and Zn was also reported from other environments (Jones, 1987).

The extent of association among different fractions, and with TOM (%) and $\text{CO}_3\text{-C}$ (%) is shown in Table 3. Among the non residual fractions only Fe-Mn was negatively correlated with the RES fraction in the case of all the metals. However, in specific cases such as Zn, OM-S was also negatively correlated with RES fraction. The OM-S was positively correlated with the TOM (%) only in the case of Cu ($r = 0.673$, $P < 0.05$). Similar results were also reported by the authors in their study on heavy metal fractionation in woodland soil (Prusty et al., 2009). However, the negative correlation of CA with $\text{CO}_3\text{-C}$ (%) needs further investigation. The contribution of RES fraction to the total metal content in soil was supported by their positive correlation, which was significant only in the case of Zn ($r = 0.743$, $P < 0.05$) indicating the contribution of the lithogenic fraction to the total concentration. The proportion of the metals in the RES phase increased and that in the Fe-Mn oxide fraction decreased along the soil profile in case of all the metals.

Cu								
	EXC	CA	Fe-Mn	OM-S	Res	SP-PT	TOM (%)	CO ₃ -C (%)
EXC	1.000							
CA	.787*	1.000						
Fe-Mn	.570*	.366	1.000					
OM-S	-.344	-.055	-.592*	1.000				
Res	-.509	-.466	-.826*	.038	1.000			
Total metal	.021	.166	-.396	.018	.455	1.000		
TOM (%)	-.275	-.069	-.617*	.673*	.289	.176	1.000	
CO ₃ -C (%)	-.393	-.110	-.107	-.250	.312	.157	-.070	1.000
Pb								
	EXC	CA	Fe-Mn	OM-S	Res	SP - PT	TOM (%)	CO ₃ -C (%)
EXC	1.000							
CA	-.435	1.000						
Fe-Mn	-.773*	.281	1.000					
OM-S	-.423	.126	.204	1.000				
Res	.744*	-.659*	-.847*	-.461	1.000			
Total metal	.017	-.247	.037	.218	.012	1.000		
TOM (%)	.228	-.070	-.445	.219	.276	.490	1.000	
CO ₃ -C (%)	.446	-.160	-.203	-.780*	.396	-.359	-.070	1.000
Zn								
	EXC	CA	Fe-Mn	OM-S	Res	SP - PT	TOM (%)	CO ₃ -C (%)
EXC	1.000							
CA	.593*	1.000						
Fe-Mn	-.395	.238	1.000					
OM-S	.098	.650*	.612*	1.000				
Res	.218	-.441	-.964*	-.791*	1.000			
Total metal	-.216	-.538*	-.683*	-.583*	.743*	1.000		
TOM (%)	.664*	.594*	-.408	.352	.180	.160	1.000	
CO ₃ -C (%)	-.129	-.250	-.326	-.382	.381	.362	-.070	1.000

45 Sample size, $\pm .514$ critical value, $P < 0.05$ (two-tail), * Significant

EXC = Exchangeable metal, CA = Carbonate bound metal, Fe-Mn = Iron - Manganese bound metal, OM-S = Bound to organic matter and sulphur, Total metal = Pseudototal metal, TOM = Total Organic Matter, CaCO₃ = Carbonate carbon

Table 3. Correlation matrix of metal fractions in the soil

The Univariate test performed following the GLM showed that the distribution of metals was significant only among fractions ($P < 0.05$) and hence the Post-hoc analysis (One-Way ANOVA - LSD) was performed on the fractions and the results are shown in Table 4 to Table 6. Fe-Mn phase was found to contribute significantly to the reported variability in the case of all the metals studied. However, there are other additional phases in case of specific metals, for e.g., in the case of Cu, RES was also a significant contributor to the cause (Table 4). In the case of Pb, it was EXC and CA (Table 5), and in the case of Zn, the significant contributor was OM-S and RES (Table 6). As indicated earlier, the findings in the case of Cu and Zn indicate the lithogenic nature of the metals, while in the case of Pb it indicates to the anthropogenic influences. The significant contribution of CA in the case of Pb may be due to the relatively high pH values in soil at the study site, which have been elevated due to the release of Ca and Carbonate compounds from the soil. Previous study undertaken by the authors report saline and alkaline patches throughout the terrestrial area in the park wherein, the $\text{CO}_3\text{-C}$ content in grassland soil in KNP ranged from 5.4% to 27.5%. The highest pH in the grassland system in KNP was reported to be 9.97. Maskall & Thornton (1998) reported similar observations and ascribe these to the release of Ca from soil. It can be explained by specific adsorption, which is more important for Pb than other two metals (Borůvka et al., 1997).

Multiple Comparisons

Dependent Variable: CU
LSD

(I) FRACTION	(J) FRACTION	Mean Difference (I-J)	Std. Error	Sig.	95% Confidence Interval	
					Lower Bound	Upper Bound
EXC	CA	-.2417	3.42211	.944	-7.0669	6.5835
	Fe-Mn	-38.8850*	3.42211	.000	-45.7102	-32.0598
	OM-S	-6.7867	3.42211	.051	-13.6119	.0385
	RES	-53.4141*	3.42211	.000	-60.2393	-46.5889
CA	EXC	.2417	3.42211	.944	-6.5835	7.0669
	Fe-Mn	-38.6433*	3.42211	.000	-45.4685	-31.8181
	OM-S	-6.5450	3.42211	.060	-13.3702	.2802
	RES	-53.1724*	3.42211	.000	-59.9976	-46.3472
Fe-Mn	EXC	38.8850*	3.42211	.000	32.0598	45.7102
	CA	38.6433*	3.42211	.000	31.8181	45.4685
	OM-S	32.0983*	3.42211	.000	25.2731	38.9235
	RES	-14.5291*	3.42211	.000	-21.3543	-7.7039
OM-S	EXC	6.7867	3.42211	.051	-.0385	13.6119
	CA	6.5450	3.42211	.060	-.2802	13.3702
	Fe-Mn	-32.0983*	3.42211	.000	-38.9235	-25.2731
	RES	-46.6274*	3.42211	.000	-53.4526	-39.8022
RES	EXC	53.4141*	3.42211	.000	46.5889	60.2393
	CA	53.1724*	3.42211	.000	46.3472	59.9976
	Fe-Mn	14.5291*	3.42211	.000	7.7039	21.3543
	OM-S	46.6274*	3.42211	.000	39.8022	53.4526

*. The mean difference is significant at the .05 level.

Table 4. LSD of Cu – fractions

Multiple Comparisons

Dependent Variable: PB
LSD

(I) FRACTION	(J) FRACTION	Mean Difference (I-J)	Std. Error	Sig.	95% Confidence Interval	
					Lower Bound	Upper Bound
EXC	CA	-6.2347*	3.06070	.045	-12.3390	-.1303
	Fe-Mn	-51.8199*	3.06070	.000	-57.9242	-45.7155
	OM-S	-14.3561*	3.06070	.000	-20.4604	-8.2517
	RES	-15.6058*	3.06070	.000	-21.7102	-9.5014
CA	EXC	6.2347*	3.06070	.045	.1303	12.3390
	Fe-Mn	-45.5852*	3.06070	.000	-51.6896	-39.4808
	OM-S	-8.1214*	3.06070	.010	-14.2258	-2.0170
	RES	-9.3711*	3.06070	.003	-15.4755	-3.2668
Fe-Mn	EXC	51.8199*	3.06070	.000	45.7155	57.9242
	CA	45.5852*	3.06070	.000	39.4808	51.6896
	OM-S	37.4638*	3.06070	.000	31.3594	43.5682
	RES	36.2141*	3.06070	.000	30.1097	42.3184
OM-S	EXC	14.3561*	3.06070	.000	8.2517	20.4604
	CA	8.1214*	3.06070	.010	2.0170	14.2258
	Fe-Mn	-37.4638*	3.06070	.000	-43.5682	-31.3594
	RES	-1.2497	3.06070	.684	-7.3541	4.8546
RES	EXC	15.6058*	3.06070	.000	9.5014	21.7102
	CA	9.3711*	3.06070	.003	3.2668	15.4755
	Fe-Mn	-36.2141*	3.06070	.000	-42.3184	-30.1097
	OM-S	1.2497	3.06070	.684	-4.8546	7.3541

*. The mean difference is significant at the .05 level.

Table 5. LSD of Pb – Fractions

Multiple Comparisons

Dependent Variable: ZN
LSD

(I) FRACTION	(J) FRACTION	Mean Difference (I-J)	Std. Error	Sig.	95% Confidence Interval	
					Lower Bound	Upper Bound
EXC	CA	-.5969	1.80145	.741	-4.1898	2.9959
	Fe-Mn	-20.8475*	1.80145	.000	-24.4403	-17.2546
	OM-S	-4.2336*	1.80145	.022	-7.8265	-.6407
	RES	-72.2304*	1.80145	.000	-75.8233	-68.6375
CA	EXC	.5969	1.80145	.741	-2.9959	4.1898
	Fe-Mn	-20.2505*	1.80145	.000	-23.8434	-16.6577
	OM-S	-3.6367*	1.80145	.047	-7.2295	-.0438
	RES	-71.6335*	1.80145	.000	-75.2263	-68.0406
Fe-Mn	EXC	20.8475*	1.80145	.000	17.2546	24.4403
	CA	20.2505*	1.80145	.000	16.6577	23.8434
	OM-S	16.6139*	1.80145	.000	13.0210	20.2067
	RES	-51.3829*	1.80145	.000	-54.9758	-47.7901
OM-S	EXC	4.2336*	1.80145	.022	.6407	7.8265
	CA	3.6367*	1.80145	.047	.0438	7.2295
	Fe-Mn	-16.6139*	1.80145	.000	-20.2067	-13.0210
	RES	-67.9968*	1.80145	.000	-71.5897	-64.4039
RES	EXC	72.2304*	1.80145	.000	68.6375	75.8233
	CA	71.6335*	1.80145	.000	68.0406	75.2263
	Fe-Mn	51.3829*	1.80145	.000	47.7901	54.9758
	OM-S	67.9968*	1.80145	.000	64.4039	71.5897

*. The mean difference is significant at the .05 level.

Table 6. LSD of Zn – Fractions

The heavy metal partitioning in soil could be used to determine its mobility and possible sources. Fractionation of total metal contents might give indications about the origin of the metals. The levels in the EXC, CA and Fe-Mn fraction may indicate pollution from anthropogenic origin, and those in OM-S and RES fraction are relatively immobile. Hence, the Fe-Mn phase being the common factor in all the metals, needs further attention from the point of view of metal mobility and bioavailability. Due to their high scavenging capacity, Fe and Mn oxides has been recorded as significant heavy metal sink in soil. Although the dynamics of metal scavenging by Fe and Mn oxides is still poorly understood, assuming that the extraction using Hydroxylamine hydrochloride with acetic acid is an appropriate indicator of metals associated with amorphous iron and manganese oxides, this process seems to exert a significant control on the metals studied in this grassland system. Although the attachment of metals to Fe-Mn oxides indicates that metals are relatively immobilized, slight chemical changes in the ambient conditions could result in their likely mobility and easy absorption by plants. pH and redox changes are the two crucial factors in this regard.

5. Conclusions

The analysis of the extracts produced by a sequential extraction procedure allowed the determination of metals in different fractions of the soil samples. Of all the metals studied the proportion of Pb was maximum in EXC phase and the order of metals in this fraction was $Cu < Zn < Pb$ indicating their relative anthropogenic input. Fe-Mn oxide phase was found to be the common sink for all the metals under study and a significant contributor to the reported variability of each of these metals. However, to confirm this more detailed investigations of the mechanisms controlling the distribution and mobility of different metal species are required.

6. Acknowledgements

We acknowledge the Council of Scientific and Industrial Research (CSIR), India for the financial support as Senior Research Fellowship (Grant No.- 9/845 (4)/06 - EMR-I) to the first author. M/s Brijendra Singh, Randhir Singh and Rajesh Singh assisted during the trench (soil) sampling. Ms. Jayalakshmi was helpful during the sequential chemical extraction of the soil samples.

7. References

- Ahnstrom, Z. S., & Parker, D. R. (1999). Development and assessment of a sequential extraction procedure for the fractionation of soil cadmium. *Soil Science Society of America Journal*, Vol. 63, pp. 1650-1658.
- Allen, S. E. (1989). *Chemical Analysis of Ecological Materials* (2nd Edition), Blackwell Scientific Publications, London, pp. 368.
- Azeez, P. A., Nadarajan, N. R., & Mittal, D. D. (2000). The impact of a monsoonal wetland on ground water chemistry. *Pollution Research*, Vol. 19, No. 2, pp. 249-255.
- Azeez, P. A., Nadarajan, N. R., & Prusty, B. A. K. (2007). Macrophyte decomposition and changes in water quality. In: *Environmental Degradation and Protection*,

- Eds: K. K. Singh, A. Juwarkar, A. K. Singh, pp. 115-156, MD Publications, New Delhi.
- Azeez, P. A., Prusty, B. A. K., & Jagadeesh, E. P. (2006). Chemical speciation of metals in environment, its relevancy to ecotoxicological studies and the need for biosensor development. *Journal of Food, Agriculture and Environment*, Vol. 4, No. 3 & 4, pp. 235-239.
- Azeez, P. A., Ramachandran, N. K., & Vijayan, V. S. (1992). The socioeconomics of the villagers around Keoladeo National Park, Bharatpur, Rajasthan. *International Journal of Ecology and Environmental Sciences*, Vol. 18, pp. 169-179.
- Badri, M. A., & Aston, S.R. (1983). Observations on heavy metal geochemical associations in polluted and non-polluted estuarine sediments. *Environmental Pollution (Series. B)*, Vol. 6, pp. 181-193.
- Baker, D. E. (1990). Copper. In: *Heavy metals in soils*, Ed. B. J. Alloway, pp. 151-176, Blackie & Sons, London.
- Borůvka, L., Křišťoufká, S., Kozák, J., & Huan-Wei, Ch. (1997). Speciation of Cadmium, lead and zinc in heavily polluted soils. *Rostlina Vyroba*, Vol. 43, No. 4, pp. 187-192.
- Chaphekar, S. B. (1991). An overview on bioindicators. *Journal of Environmental Biology*, Vol. 12, pp. 163-168.
- Davis, C. B., & van der Valk, A. (1988). *Ecology of a semitropical monsoonal wetland in India: The Keoladeo National Park, Bharatpur, Rajasthan*. Final Report, September 1988, Ohio State University, 104 pp.
- Deely, J. M., Tunnicliss, J. C., Orange, C. J., & Edgerley, W. H. L. (1992). Heavy metals in surface sediments of Waiwhetu stream, Lower Hutt, New Zealand. *New Zealand Journal of Marine and Freshwater Research*, Vol. 26, pp. 417-427.
- Fan, W., Wang, W. X., Chen, J., Li, X. D., & Yen, Y. F. (2002). Cu, Ni and Pb speciation in surface sediments from a contaminated bay of northern China. *Baseline Marine Pollution Bulletin*, Vol. 44, pp. 816-826.
- Farnham, I., Smiecinski, A., & Singh, A. K. (1998). Handling chemical data below detection limits for multivariate analysis of groundwater. *First International Conference on Remediation of Chlorinated and Recalcitrant Compounds*. Monterey, CA, pp. 99-104.
- Howard, J. L., & Shu, J. (1996). Sequential extraction analysis of heavy metals using a chelating agent (NTA) to counteract resorption. *Environmental Pollution*, Vol. 91, No. 1, pp. 89-96.
- Howard, J. L., & Vandenbrink, W. J. (1999). Sequential extraction analysis of heavy metals in sediments of variable composition using nitrilotriacetic acid to counteract resorption. *Environmental Pollution*, Vol. 106, pp. 285-292.
- Jackson, M. L. (1958). *Soil Chemical Analysis*. Constable & Co Ltd, London, pp. 498.
- Jagadeesh, E. P., Azeez, P. A., & Banerjee, D. K. (2006). Modeling chemical speciation of copper in River Yamuna at Delhi, India. *Chemical Speciation and Bioavailability*, Vol. 18, No. 2, pp. 61-69.
- Jones, J. M. (1987). Chemical fractionation of Copper, Lead and Zinc in ombrotrophic peat. *Environmental Pollution*, Vol. 48, pp. 131-144.
- Kersten, M., & Förstner, U. (1986). Chemical fractionation of heavy metals in anoxic estuarine and coastal sediments. *Water Science Technology*, Vol. 18, pp. 121-130.

- Lambou, V. W., & Williams, L. R. (1980). Biological monitoring of hazardous wastes in aquatic systems. *Second Interagency Workshop on in-situ Water Sensing: Biological Sensors*, Pensacola Beach, Florida, pp. 11-18.
- Laxen, D. P. H., & Harrison, R. M. (1981). Cleaning methods for Polythene containers prior to the determination of trace metals in fresh water samples. *Analytical Chemistry*, Vol. 53, pp. 345-350.
- Li, X. D., Shen, Z., Wai, O. W. H., & Li, Y-S. (2000). Chemical partitioning of heavy metal contaminants in sediments of the Pearl River estuary. *Chemical Speciation and Bioavailability*, Vol. 12, No. 1, pp. 17-25.
- Li, X. D., Shen, Z., Wai, O. W. H., & Li, Y-S. (2001). Chemical forms of Pb, Zn and Cu in the sediment profiles of the Pearl River estuary. *Marine Pollution Bulletin*, Vol. 42, No. 3, pp. 215-223.
- Lu, A., Zhang, S., & Shan, X. (2005). Time effect on the fractionation of heavy metals in soils. *Geoderma*, Vol. 125, pp. 225-234.
- Maskall, J. E., & Thornton, I. (1998). Chemical partitioning of heavy metals in soils, clays and rocks at historical lead smelting sites. *Water, Air and Soil Pollution*, Vol. 108, pp. 391-409.
- Mathew, M., Mohanraj, R., Azeez, P. A., & Pattabhi, S. (2003). Speciation of heavy metals in bed sediments of wetlands in urban Coimbatore, India. *Bulletin of Environmental Contamination and Toxicology*, Vol. 70, pp. 800-808.
- Mathur, V. B., Sinha, P. R., & Mishra, M. (2005). *Keoladeo National Park World Heritage Site*. Technical Report No. 5, UNESCO-IUCN-Wild Life Institute of India, Dehradun, India.
- Nirel, P. M. V., & Morel, F. M. M. (1990). Pitfalls of sequential extractions. *Water Research*, Vol. 24, pp. 1055-1056.
- Nolan, A. L., Lombi, E., & McLaughlin, M. J. (2003). Metal bioaccumulation and toxicity in soils – why bother with speciation? *Australian Journal of Chemistry*, Vol. 56, pp. 77-91.
- Norušis, M.J. (1986). *SPSS/PC+4.0 Base Manual – Statistical Data Analysis*. SPSS Inc.
- Pal, D. K., Bhattacharyya, T., Deshpande, S. B., Sarma, V. A. K., & Velayutham, M. (2000). *Significance of minerals in soil environment of India*, NBSS Review Series 1. National Bureau of Soil Survey & Land Use Planning, Nagpur, India, pp. 68.
- Pickering, W. F. (1981). Selective chemical extraction of soil components and bound metal species. *CRC Critical Reviews in Analytical Chemistry*, Vol. 12, pp. 233.
- Poulton, S. W., & Canfield, D. E. (2005). Development of a sequential extraction procedure for iron: implications for iron partitioning in continentally derived particulates. *Chemical Geology*, Vol. 214, pp. 209-221.
- Prusty, B. A. K., & Azeez, P.A. (2004). Seasonal variation in water chemistry of a monsoonal wetland. *Souvenir of the National Conference on Water Vision-2004*, PSGR Krishnamal College for Women, Coimbatore, 06-08 October, pp. 47
- Prusty, B. A. K., Azeez, P. A., & Jagadeesh, E. P. (2007b). Alkali and Transition Metals in Macrophytes of a Wetland System. *Bulletin of Environmental Contamination and Toxicology*, Vol. 78, No. 5, pp. 405-410 (May 2007).
- Prusty, B. A. K., Azeez, P. A., Vasanthakumar, R., & Jayalakshmi, V. (2006). Carbon and nitrogen dynamics in the soil system of a wetland-terrestrial ecosystem complex.

- Proceedings of National Conference on Environment and Sustainable Development* (Ed: R. Mohanraj), Bharathidasan University, Trichirappalli, India, 19-17 February, pp. 12.
- Prusty, B. A. K., Jagadeesh, E. P., Azeez, P. A., & Banerjee, D. K. (2007a). Distribution and chemical speciation of select transition metals in the waters of River Yamuna, New Delhi. *Environmental Science: An Indian Journal*, Vol. 2, No. 3, pp. 139-144 (September 2007).
- Prusty, B. A. K., Chandra R., & Azeez, P. A. (2009). Distribution and chemical partitioning of Cu, Pb and Zn in the soil profile of a semi arid dry woodland. *Chemical Speciation and Bioavailability*, Vol. 21, No. 3, pp. 141-151 (September 2009).
- Prusty, B. G., Sahu, K. C., & Godgul, G. (1994). Metal contamination due to mining and milling activities at the Zawar zinc mine, Rajasthan, India. 1. Contamination of stream sediments. *Chemical Geology*, Vol. 112, pp. 275-291.
- Quevauiller, P. H., Rauret, G., & Griepink, B. (1993). Conclusions of the workshop: single and sequential extraction in sediments and soils. *International Journal of Environmental and Analytical Chemistry*, Vol. 57, pp. 135-150.
- Ramadan, A. A. (2003). Heavy metal pollution and biomonitoring plants in lake Manzala, Egypt. *Pakistan Journal of Biological Sciences*, Vol. 6, pp. 1108-1117.
- Reuther, R. (1999). Trace metal speciation in aquatic sediment: methods, benefits and limitations. In: *Manual of Bioassessment of Aquatic Sediment Quality*, Eds: A. Mudroch, J. M. Azcue and P. Mudroch, Lewis, Boca Raton, pp. 1-54.
- Ryu, J. S., Lee, K. S., Kim, J. H., Ahn, K. G., & Chang, H. W. (2006). Geostatistical analysis for hydrochemical characterization of the Han River, Korea: Identification of major factors governing water chemistry. *Bulletin of Environmental Contamination and Toxicology*, Vol. 76, No. 1, pp. 01-07.
- Shanthi, K., Ramasamy, K., & Lakshmanaperumalsamy, P. (2003). Sediment quality of Singanallur wetland in Coimbatore, Tamil Nadu, India. *Bulletin of Environmental Contamination and Toxicology*, Vol. 70, pp. 372-378.
- Sharma, S., & Praveen, B. (2002). *Management Plan: Keoladeo National Park, Bharatpur*, Plan Period 2002-2006, Department of Forests and Wildlife, Rajasthan, pp. 182.
- Svete, P., Milacic, R., & Pihlar, B. (2001). Partitioning of Zn, Pb and Cd in river sediments from a lead and zinc mining area using the BCR three-step sequential extraction procedure. *Journal of Environmental Monitoring*, Vol. 3, pp. 586-590.
- Tandon, H. L. S. (2001). *Methods of analysis of soils, plants, waters and fertilizers*, Fertilizer Development and Consultation Organization (FDCO), New Delhi, pp. 143.
- Tessier, A., Campbell, P. G. C., & Bisson, M. (1979). Sequential extraction procedure for the speciation of particulate trace metals. *Analytical Chemistry*, Vol. 51, pp. 844-851.
- Ure, A. M. (1990). Methods of analysis for heavy metals in soils. In: *Heavy Metals in Soils*, Ed: B. J. Alloway, Blackie and John Wiley & Sons, New York, pp. 39-80.
- Walkley, A., & Black, I.A. (1934). An examination of the Degljareff method for determining soil organic matter and a proposed modification of the chromic acid titration method. *Soil Sci*, Vol. 37, pp. 29-38.
- Young, L. B., Dutton, M., & Pick, F. R. (1992). Contrasting two methods for determining trace metal partitioning in oxidized lake sediments. *Biogeochemistry*, Vol. 17, pp. 205-219.

Yuan, C., Jiang, G., Liang, L., Jin, X. and Shi, J. (2004). Sequential extraction of some heavy metals in Haihe river sediments, People's' Republic of China. *Bulletin of Environmental Contamination and Toxicology*, Vol. 73, pp. 59-66.

Characteristics of Baseline and Analysis of Pollution on the Heavy Metals in Surficial Soil of Guiyang

Ji Wang^{1,2} and Yixiu Zhang^{1,2}

*¹School of Geographical and Environment Sciences
Guizhou Normal University, Guiyang, Guizhou*

*²Key Laboratory of Remote Sensing Applications in Resources and Environments, Guizhou
China*

1. Introduction

The term “Environmental Geochemical Baseline (EGB)” first appeared in the International Geochemical Mapping Program (IGCP259) and the International Geochemical Baseline Program (IGCP360) of International Geo-graph Contrast Program. The definition of EGB refers to natural changes in the concentrations of chemical materials (chemical elements) in the Earth’s surface material (Salminen & Tarvainen, 1997). But the definition is becoming clearer with deepening research on EGB. The geochemical baseline reflects the natural concentration of one element in a particular material (e.g. soil, sediment, and rock). At the same time, it can be described as the unitary limit to distinguish the geochemistry backgrounds and anomalies (Salminen & Gregorauskiene, 2000).

As for the EGB, it is required to establish the archives of the current Earth’s surface environment and provide the database to monitor environmental variation. The aim of EGB is to reveal natural changes in mineral and chemical elements so as to make comparisons with anthropogenic influences. The EGB provides the definition of geochemical variation in natural space. It can not only guide policy-makers to make policies toward environmental problems, but also can educate the public who are interested in environmental problems (Darnley, 1997).

All countries attach great importance to the study of EGB, e.g. Mapping of EGB in Europe (Darnley, 1997). For coping with the world EGB studies, China kicked off the program of “Chinese Environment Geochemistry Supervision and Control Network, and the National Dynamic Mapping of Geochemistry Items” in 1992 (Chen Hangxin et al., 1998). Use of the EGB to study the environment impact of mining and smelting activities was carried out in the region of Panzhihua, Sichuan Province, Southwest China (Teng Yanguo et al., 2002, 2003).

In this chapter there has been established the surficial soil EGB of heavy metals (Hg, Cd, As, Pb, Cr, Cu, Ni and Zn) in Guiyang City (covering an area of 8046 km²), Guizhou Province. With soil environmental geochemistry research as the main line the spatial distribution of the heavy metals in surficial soil is combined with research on environmentally geochemical mechanism. An appropriate guideline is chosen to distinguish the influence of natural processes from that of anthropogenic processes on soil environment.

2. Materials and methods

2.1 Study area

Guiyang City was selected as the study area which is the capital of Guizhou Province in South-west China. Guiyang City, situated between east longitude $106^{\circ}07'$ to $107^{\circ}17'$, north latitude $26^{\circ}11'$ to $27^{\circ}22'$, lies in the middle of Guizhou Province and on the eastern slope of Yunnan-Guizhou Plateau (Fig.1). Guiyang, with abundant natural resources, ample energy resources and good natural environment, has a mild-moist subtropical climate because of diversity in geographical and topomorph features, high elevation and low latitude. The total area of Guiyang was 8046 km², including farmland (35.91%), woodland (33.09%), grassland (3.59%), water area (1.89%), construction land (e.g. residential area, industry, mining, transportation, et al.) (6.00%), garden area (0.70%) and no-use land (18.82%)(e.g. wilderness, ribbing, lake-beach, et al.) according to the land use. Soils in the study area mainly include yellow soil (3.335×10^5 hm², 41.53%), umber soil (1.49%), limestone soil (2.021×10^5 hm², 25.17%), rocky soil (2.17%), coarse-bone soil (12.64%), purple soil (1.93%), marsh soil (0.11%), paddy soil (1.156×10^5 hm², 14.39%), and mountainous meadow soil (0.5%) (Fig.2).



Fig. 1. Map showing the study site in Guizhou.

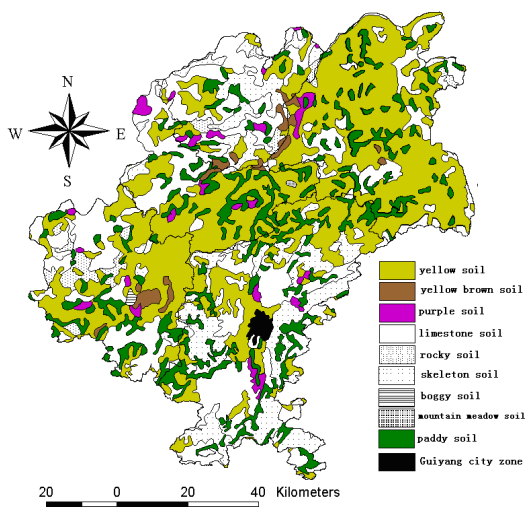


Fig. 2. The distribution of surficial soil of Guiyang, Guizhou.

2.2 Sampling

The snake-form distribution sampling method was adopted because of the bigger sampling area, relief topography and un-uniform soil. The topsoil layer (5~15 cm) was sampled after cover rock and remained roots were removed(HJ/T 166-2004). Guiyang has 1286 villages 83 towns and the sample of Hg, Cd, Pb, Cr and As localities were distributed in 487villages and 75 towns of Guiyang. So the samples account for 37.87% and 90.36%, respectively. The sample of Cu, Ni and Zn localities were distributed in 332 villages and 50 towns, and the samples account for 25.82% and 60.24%. Hg, Cd, Pb, Cr and As localities are shown in Fig. 3. Cu, Ni and Zn localities are shown in Fig. 4.

The soil samples were collected 67 at January19 to March 4, and 420 at July 11 to October 11.

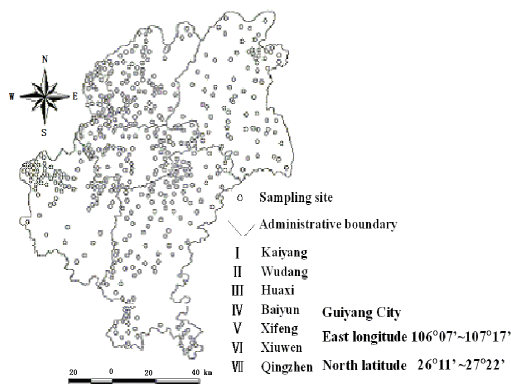


Fig. 3. The distribution on of Cd, Hg, Cr, Pb, As sites in Guiyang, Guizhou.

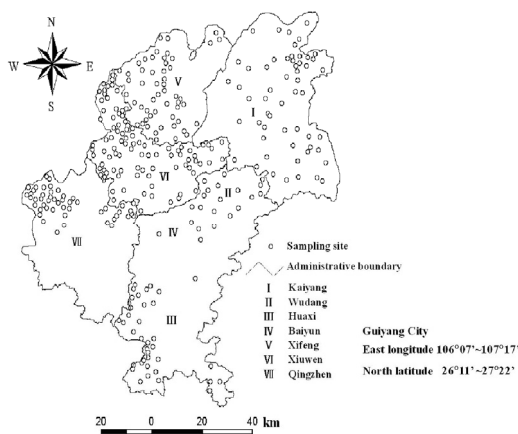


Fig. 4. The distribution on of Cu, Zn, Ni sites in Guiyang, Guizhou.

2.3 Analytical techniques

The content of As was digested with a mixture acids: H_2SO_4 - HNO_3 - $HClO_4$ ($H_2SO_4 / HNO_3 / HClO_4$, 1:1:3) and using diethyl disulfide generation amino acid silver spectrophotometric

method to determine the contents of As in the samples(GB/T17134-1997). The limits of determination were 0.5 mg/kg (As) according to 0.5g sample which was dispelled in 50ml. The content of Pb and Cd were digested with mixture acids: HCl-HNO₃- HF- HClO₄, and using graphite furnace atomic absorption spectrometry to determine the contents of Pb and Cd, the limits of determination were 0.1mg/kg (Pb), 0.01mg/kg (Cd) according to 0.5g samples which were dispelled in 50ml(GB/T17141—1997). The total content of Cr were determined by diethyl carbon phenol by two spectrophotometric method after the samples were digested with a mixture acids: HCl-HNO₃-HF, and the limits of determination was 1.0mg/kg(Cr) according to 0.5g samples which was dispelled in 50ml (GB/T17137—1997). Using flame-atomic absorption spectrophotometry to determine the contents of Cu, Zn and Ni in the samples(Cu and Zn: GB/T17138—1997; Ni: GB/T17139—1997). The limits of determination were 1.0 mg/kg (Cu), 5.0 mg/kg (Ni), 0.5 mg/kg (Zn) according to 0.5g sample which was dispelled in 50ml. The samples of Cu, Ni and Zn were digested with HCl-HNO₃- HF- HClO₄. The total content of Hg was digested with a mixture of ultrapure acids: H₂SO₄-HNO₃-KMnO₄(H₂SO₄/HNO₃,1:1) and analyzed by cold atomic absorbent spectrophotometry, the limits of determination was 0.005mg/kg(Hg) according to 2g samples which was dispelled in 50ml(GB/T17136—1997). The concentrations of Hg, Pb, Cd, Cr, Cu, As, Ni and Zn in the solution were measured under the optimum condition. For quality assurance and quality control, reagent blanks, 20% duplicated samples and sol standard reference materials GSS-1, GSS-3, GSS-4 obtained from Center of National Standard Reference Material of China were prepared and analyzed with the same procedure and reagents.

The table 1 showed that the accuracy and precision of testing of the above.

The available data sets were analyzed using the SPSS 16.0, ArcGIS, and ArcView.

Elements	SU	SS	GV(mg/kg)	ORM(mg/kg)	IRSD (%)	RSDBR(%)	RE(%)
As	14	GSS-1	10.7±0.8	10.7	2.0	5.6	0.0
	15	GSS-3	15.9±1.3	17.1	1.3	4.3	7.5
	12	GSS-4	11.4±0.7	11.4	3.8	4.8	0.0
Cd	25	GSS-1	0.083±0.011	0.080	3.6	6.2	-3.6
	28	GSS-3	0.044±0.014	0.045	4.1	8.4	2.3
Cr	16	GSS-1	57.2±4.2	56.1	2.0	9.8	-1.9
	18	GSS-3	98.0±7.1	93.2	2.3	8.3	-4.9
	35	GSS-1	20.9±0.8	20.7	2.3	6.8	-0.96
Cu	34	GSS-3	29.4±1.6	29.2	2.0	4.8	-0.68
	30	GSS-4	26.3±1.7	25.6	2.3	3.9	-2.7
	25	GSS-1	0.016±0.003	0.016	6.2	32.5	0.0
Hg	26	GSS-3	0.112±0.012	0.100	3.4	20.0	-10.7
	24	GSS-4	0.021±0.004	0.019	8.4	20.5	-9.5
	29	GSS-1	29.6±1.8	29.1	2.5	8.4	-1.7
Ni	32	GSS-3	33.7±2.1	34.0	2.6	6.0	0.89
	33	GSS-4	32.8±1.7	34.1	2.9	9.1	4.0
Pb	19	GSS-1	23.6±1.2	23.7	4.2	7.3	0.42
	21	GSS-3	33.3±1.3	33.7	3.9	8.6	1.2
Zn	32	GSS-1	55.2±3.4	56.2	2.8	7.3	1.8
	31	GSS-3	89.3±4.0	88.4	1.6	5.0	1.0
	31	GSS-4	69.1±3.5	68.1	3.2	4.1	-1.4

SU: sample numbers; SS: standard samples; GV: guaranteed value; ORM: overall mean
IRSD: indoor relative standard deviation; RSDBR: relative standard between room; RE: relative error

Table 1. The accuracy and precision of contents of heavy metals in soil.

3. Experimental results

Table 2 indicated that the statistical analysis results of soil heavy metals concentrations in Guiyang city. The mean value, standard deviation and maximum of As separately are 18.09 mg/kg, 11.57 mg/kg and 79.30 mg/kg in the surficial soil in Guiyang. The content of As in 95.9 per cent sample are smaller than 40 mg/kg., of Cd separately are 0.302mg/kg, 0.363mg/kg, 2.620mg/kg and 95.7 percent smaller than 1.000mg/kg., of Cr 75.3 mg/kg, 37.3 mg/kg, 271.0 mg/kg and 95.9 percent smaller than 150.0 mg/kg, of Cu separately are 43.1mg/kg, 30.3mg/kg, 213.0mg/kg and 94.6 percent smaller than 100.0mg/kg, of Pb are 43.2mg/kg, 31.3mg/kg, 318.9mg/kg and 95.5 per cent smaller than 100.0mg/kg, of Hg are 0.222mg/kg, 0.531mg/kg, 7.030mg/kg and 98.2 smaller than 1.000mg/kg, of Ni are 38.3mg/kg, 14.9mg/kg, 102.5mg/kg and 95.8 percent smaller than 70.0mg/kg, of Zn are 84.7mg/kg, 49.8mg/kg, 385.0mg/kg and 94.3 percent smaller than 150.0mg/kg.

Elements	SN	Min(10 ⁻⁶)	Max(10 ⁻⁶)	Mean(10 ⁻⁶)	SD	CV
As	486	2.70	79.00	18.09	11.57	0.64
Cd	487	0.001	2.620	0.302	0.363	1.20
Cr	487	6.9	271.0	75.3	37.3	0.50
Cu	333	2.1	213.0	43.1	30.3	0.70
Pb	487	0.9	318.9	43.2	31.3	0.7
Hg	487	0.010	7.030	0.222	0.531	2.39
Ni	333	9.2	102.5	38.3	14.9	0.39
Zn	333	0.1	385.0	84.7	49.8	0.59

SN: sample numbers; SD: standard deviation; CV: coefficient of variation

Table 2. The statistical analysis results of heavy metals concentration in soil, Guiyang city.

4. Analysis and discussions

4.1 Results analysis

4.1.1 Establishment of the baselines of heavy metals in surficial soil

4.1.1.1 Establishment of the baselines of As in surficial soil

4.1.1.1.1 Relatively accumulative total amount analysis

Assuming the concentrations of chemical elements in natural surficial soil are of logarithmic normal distribution, the inflexion in the figure of relatively accumulative density to the concentration of chemical element represents the boundary line between the background value and the abnormal value. The range of baseline values of chemical elements is the average value plus double standard deviation of less than the boundary value (Lepeltier, 1969).

The double logarithmic figure of relatively accumulative density (RAD) to the concentration of the chemical element As in topsoil of Guiyang was shown in Fig.5. The inflexion (black points in the figure) is 17.2 mg/kg. So the range of baseline values of As in topsoil of Guiyang is 7.75~15.15 mg/kg, i.e., the average value of 11.45mg/kg plus a double standard deviation of 3.70 mg/kg less than 17.2 mg/kg.

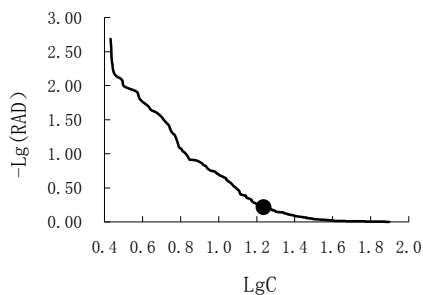


Fig. 5. The logarithm of the concentrations on As and the logarithmic curve of relatively accumulative density in surficial soil.

4.1.1.1.2 Relatively accumulative frequency

The normal decimal coordinates are adopted. There are two inflexions in the figures of relatively accumulative frequency to the concentration of chemical element. The lower one may represent the upper limit of the baseline of chemical elements and the upper one may represent the lower limit of abnormality, i.e., the influence of human activity on the two inflexions. The average or median that is less than the lower inflexion can be regarded as the baseline of chemical elements. The metrical values between the two inflexions may have something with the influence of human activities, or have nothing to do. If the distribution curve looks like a straight line, the measured values may represent the baseline range (Bauer & Bor, 1993, 1995); Bauer et al. 1992; Matschullat et al., 2000)

The figure of relatively accumulative frequency to the concentration of As in topsoil of Guiyang is shown in Fig. 6. There are two inflexions: one is 13.0 mg/kg and the other is 29.0 mg/kg. So the first inflexion (13.0 mg/kg) represents the upper limit of baseline values of As in topsoil of Guiyang. The average of 9.20 mg/kg or the median of 9.04 mg/kg less than the first inflexion can be regarded as the baseline of As in topsoil of Guiyang. The second inflexion (29.0 mg/kg) may represent abnormality, i.e., the influence of human activity.

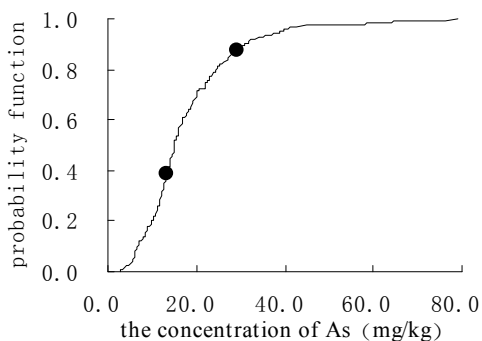


Fig. 6. The probability functions of As in surficial soil.

Comprehensively considering the results of calculation using the two kinds of methods, we respectively take 9.04mg/kg as the baseline values of As in topsoil of Guiyang.

4.1.1.2 Establishment of the baselines of Cd in surficial soil

4.1.1.2.1 Relatively accumulative total amount analysis

The double logarithmic figure of RAD to the concentration of the chemical element Cd in topsoil of Guiyang was shown in Fig.7. The inflexion (black points in the figure) is 0.189 mg/kg. So the range of baseline values of Cd in topsoil of Guiyang is 0.029~0.123 mg/kg, i.e. the average value of 0.076mg/kg plus double standard deviation of 0.047 mg/kg less than 0.189mg/kg.

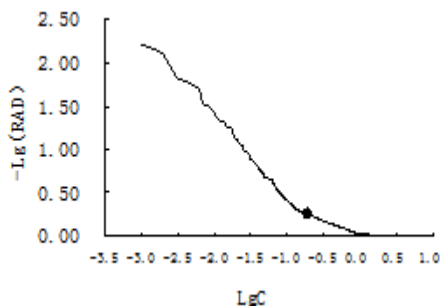


Fig. 7. The logarithm of the concentration on Cd and the logarithmic curve of relatively accumulative density in surficial soil.

4.1.1.2.2 Relatively accumulative frequency

The figure of relatively accumulative frequency to the concentration of Cd is shown in Fig.8. One inflexion is 0.149 mg/kg and the other is 1.010 mg/kg. So the first inflexion (0.149 mg/kg) represents the upper limit of baseline values of Cd in topsoil of Guiyang. The average of 0.068 mg/kg or the median of 0.068 mg/kg less-than the first inflexion can be regarded as the baseline of Cd in topsoil of Guiyang. The second inflexion (1.010mg/kg) may regard as represent abnormality, i.e., the influence of human activities.

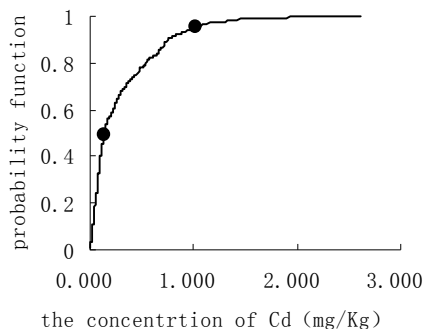


Fig. 8. The probability functions of Cd in surficial soil of Guiyang.

Comprehensively considering the results of calculation using the two kinds of methods, we respectively take 0.068 mg/kg as the baseline values of Cd in topsoil of Guiyang.

4.1.1.3 Establishment of the baselines of Cu in surficial soil

4.1.1.3.1 Relatively accumulative total amount analysis

The double logarithmic figure of RAD to the concentration of the chemical element Cu in topsoil of Guiyang is shown in Fig.9. The inflexion (black points in the figure) is 32.6 mg/kg. So the range of baseline values of Cu in topsoil of Guiyang is 14.2~28.4 mg/kg, i.e., the average value of 21.3mg/kg plus a double standard deviation of 7.1 mg/kg less than 32.6 mg/kg.

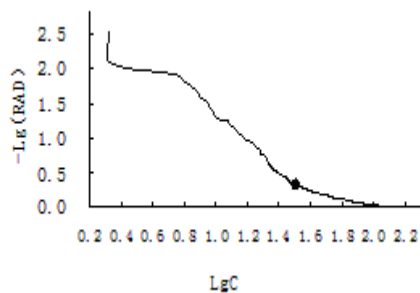


Fig. 9. The logarithm of the concentrations on Cu and the logarithmic curve of relatively accumulative density in surficial soil.

4.1.1.3.2 Relatively accumulative frequency

The figure of relatively accumulative frequency to the concentration of Cu in topsoil of Guiyang is shown in Fig.10. There are two inflexions: one is 28.1 mg/kg and the other is 68.4 mg/kg. So the first inflexion (28.1 mg/kg) represents the upper limit of baseline values of Cu in topsoil of Guiyang. The average of 18.8 mg/kg or the median of 21.9 mg/kg less than the first-inflexion can be regarded as the baseline of Cu in topsoil of Guiyang. The second inflexion (68.4 mg/kg) may represent abnormality, i.e., the influence of human activity.

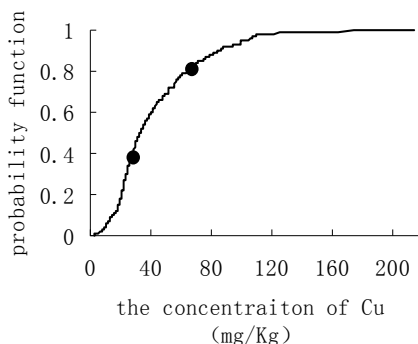


Fig. 10. The probability functions of Cu in surficial soil.

Comprehensively considering the results of calculation using the two kinds of methods, we respectively take 18.8 mg/kg as the baseline values of Cu in topsoil of Guiyang.

4.1.1.4 Establishment of the baselines of Zn in surficial soil

4.1.1.4.1 Relatively accumulative total amount analysis

The double logarithmic figure of RAD to the concentration of the chemical element Zn in topsoil of Guiyang is shown in Fig.11. The inflexion is 114.0 mg/kg. So the range of baseline values of Zn in topsoil of Guiyang is 46.5~91.3 mg/kg, i.e., the average value of 68.9mg/kg pluses double standard deviation of 22.4 mg/kg less than 114.0mg/kg.

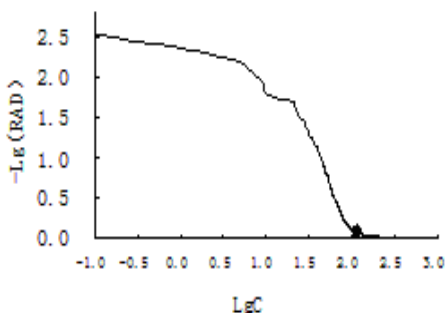


Fig. 11. The logarithm of the concentrations on Zn and the logarithmic curve of relatively accumulative density in surficial soil.

4.1.1.4.2 Relatively accumulative frequency

The figure of relatively accumulative frequency to the concentration of Zn in topsoil of Guiyang is shown in Fig.12. There are two inflexions. One inflexion is 56.5 mg/kg and the other is 112.0 mg/kg. So the first inflexion (56.5 mg/kg) represents the upper limit of baseline values of Zn in topsoil of Guiyang. The average of 41.6 mg/kg or the median of 46.3 mg/kg less-than the first inflexion can be regarded as the baseline of Zn in topsoil of Guiyang. The second inflexion (112.0 mg/kg) may regard as represent abnormality, i.e., the influence of human activities.

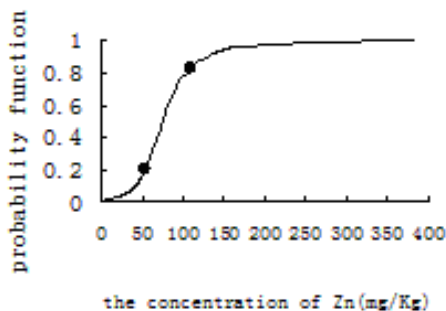


Fig. 12. The probability functions of Zn in surficial soil.

Comprehensively considering the results of calculation using the two kinds of methods, we respectively take 46.3 mg/kg as the baseline values of Zn in topsoil of Guiyang.

4.1.1.5 Establishment of the baselines of Pb in surficial soil

4.1.1.5.1 Relatively accumulative total amount analysis

The double logarithmic figure of RAD to the concentration of the chemical element Pb in topsoil of Guiyang is shown in Fig.13. The inflexion (black points in the figure) is 26.8 mg/kg. So the range of baseline values of Pb in topsoil of Guiyang is 14.0~25.4 mg/kg, i.e., the average value of 19.7mg/kg plus a double standard deviation of 5.7 mg/kg less than 26.8 mg/kg.

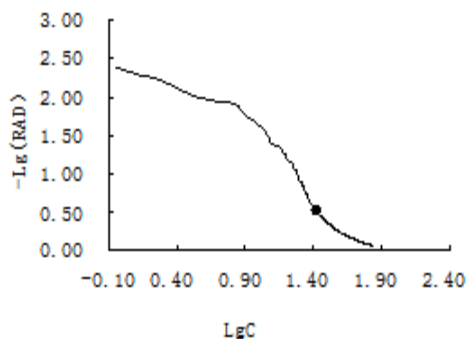


Fig. 13. The logarithm of the concentrations on Pb and the logarithmic curve of relatively accumulative density in surficial soil.

4.1.1.5.2 Relatively accumulative frequency

The figure of relatively accumulative frequency to the concentration of Pb in topsoil of Guiyang is shown in Fig.14. There are two inflexions: one is 20.4 mg/kg and the other is 70.1mg/kg. So the first inflexion (20.4 mg/kg) represents the upper limit of baseline values of Pb in topsoil of Guiyang. The average of 16.0 mg/kg or the median of 14.8 mg/kg less than the first-inflexion can be regarded as the baseline of Pb in topsoil of Guiyang. The second inflexion (70.1mg/kg) may represent abnormality, i.e., the influence of human activity.

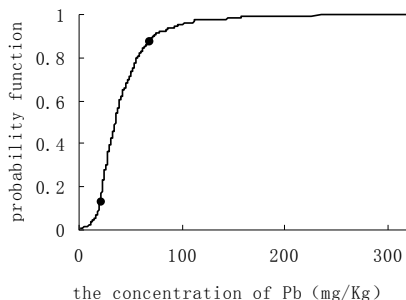


Fig. 14. The probability functions of Pb in surficial soil of Guiyang.

Comprehensively considering the results of calculation using the two kinds of methods, we respectively take 14.8 mg/kg as the baseline values of Pb in topsoil of Guiyang.

4.1.1.6 Establishment of the baselines of Hg in surficial soil

4.1.1.6.1 Relatively accumulative total amount analysis

The double logarithmic figure of RAD to the concentration of the chemical element Hg in topsoil of Guiyang is shown in Fig.15. The inflexion (black points in the figure) is 0.082 mg/kg. So the range of baseline values of Hg in topsoil of Guiyang is 0.031~0.075 mg/kg, i.e., the average value of 0.053mg/kg plus double standard deviation of 0.022 mg/kg less than 0.082mg/kg.

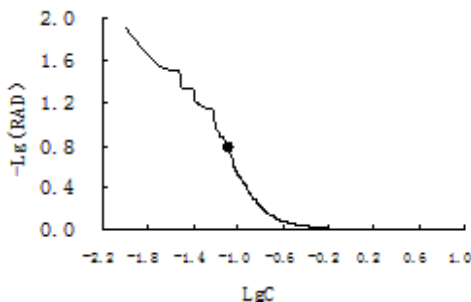


Fig. 15. The logarithm of the concentrations on Hg and the logarithmic curve of relatively accumulative density in surficial soil.

4.1.1.6.2 Relatively accumulative frequency

The figure of relatively accumulative frequency to the concentration of Hg in topsoil of Guiyang is shown in Fig.16. There are two inflexions. One inflexion is 0.072 mg/kg and the other is 0.530 mg/kg. So the first inflexion (0.072mg/kg) represents the upper limit of baseline values of Hg in topsoil of Guiyang. The average of 0.050 mg/kg or the median of 0.045 mg/kg less-than the first inflexion can be regarded as the baseline of Hg in topsoil of Guiyang. The second inflexion (0.530 mg/kg) may regard as represent abnormality, i.e., the influence of human activities.

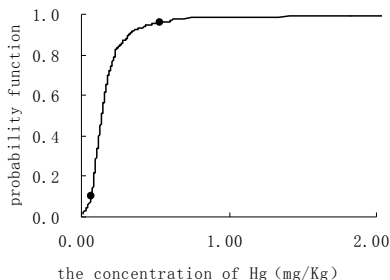


Fig. 16. The probability functions of Hg in surficial soil.

Comprehensively considering the results of calculation using the two kinds of methods, we respectively take 0.045 mg/kg as the baseline values Hg in topsoil of Guiyang.

4.1.1.7 Establishment of the baselines of Cr in surficial soil

4.1.1.7.1 Relatively accumulative total amount analysis

The double logarithmic figure of RAD to the concentration of the chemical element Cr in topsoil of Guiyang is shown in Fig.17. The inflexion (black points in the figure) is 67.8 mg/kg. So the range of baseline values of Cr in topsoil of Guiyang is 31.0~59.8mg/kg, i.e., the average value of 45.4mg/kg plus a double standard deviation of 14.4 mg/kg less than 67.8 mg/kg.

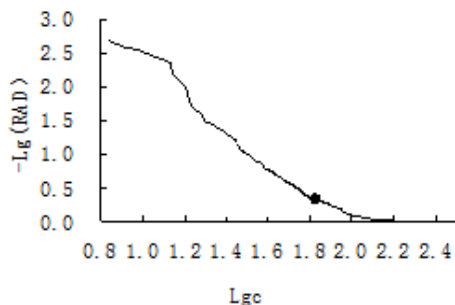


Fig. 17. The logarithm of the concentrations on Cr and the logarithmic curve of relatively accumulative density in surficial soil.

4.1.1.7.2 Relatively accumulative frequency

The figure of relatively accumulative frequency to the concentration of Cr in topsoil of Guiyang is shown in Fig.18. There are two inflexions: one is 63.8 mg/kg and the other is 100.2 mg/kg. So the first inflexion (63.8 mg/kg) represents the upper limit of baseline values of Cr in topsoil of Guiyang. The average of 45.7 mg/kg or the median of 44.0 mg/kg less than the first-inflexion can be regarded as the baseline of Cr in topsoil of Guiyang. The second inflexion (100.2 mg/kg) may represent abnormality, i.e., the influence of human activity.

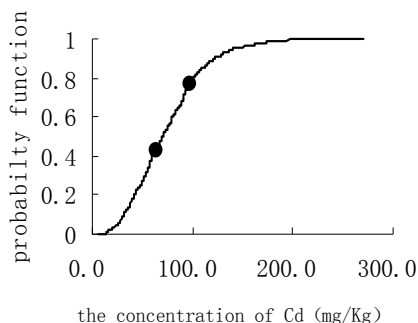


Fig. 18. The probability functions of Cr in surficial soil.

Comprehensively considering the results of calculation using the two kinds of methods, we respectively take 44.0 mg/kg as the baseline values of Cr in topsoil of Guiyang.

4.1.1.8 Establishment of the baselines of Ni in surficial soil

4.1.1.8.1 Relatively accumulative total amount analysis

The double logarithmic figure of RAD to the concentration of the chemical element Ni in topsoil of Guiyang is shown in Fig.19. The inflexion is 27.6 mg/kg. So the range of baseline values of Ni in topsoil of Guiyang is 18.1~26.7 mg/kg, i.e., the average value of 22.4 mg/kg plus double standard deviation of 4.3 mg/kg less than 27.6mg/kg.

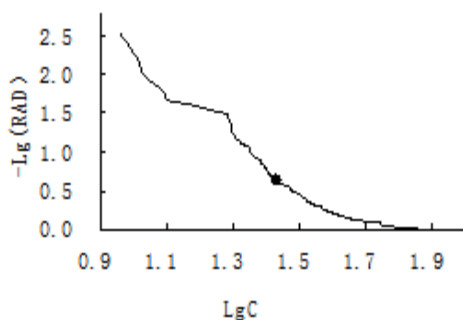


Fig. 19. The logarithm of the concentrations on Ni and the logarithmic curve of relatively accumulative density in surficial soil.

4.1.1.8.2 Relatively accumulative frequency

The figure of relatively accumulative frequency to the concentration of Ni in topsoil of Guiyang is shown in Fig.20. There are two inflexions. One inflexion is 27.8 mg/kg and the other is 57.0 mg/kg. So the first inflexion (27.8 mg/kg) represents the upper limit of baseline values of Ni in topsoil of Guiyang. The average of 19.5 mg/kg or the median of 17.0 mg/kg less-than the first inflexion can be regarded as the baseline of Ni in topsoil of Guiyang. The second inflexion (57.0 mg/kg) may regarded as represent abnormality, i.e., the influence of human activities.

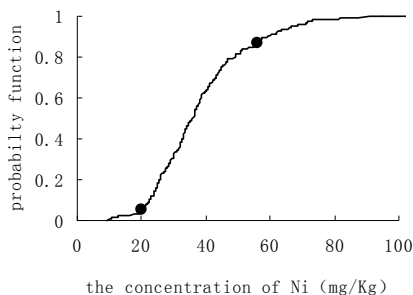


Fig. 20. The probability functions of Ni in surficial soil.

Comprehensively considering the results of calculation using the two kinds of methods, we respectively take 17.0 mg/kg as the baseline values of Ni in topsoil of Guiyang.

4.2 Discussions

4.2.1 Geo-accumulation analysis of heavy metals in surficial soil

Geo-accumulation Index was commonly called Muller Index (Muller, 1969; Forstner & Muller, 1981), was widely used in studying quantitative index for heavy metals pollution in sediments (Forstner et al., 1990; Chen Cuihua et al., 2008; Yi xiu et al., 2010; Hu Mianhao, 2010), and the expression as this.

$$I_{\text{geo}} = \log_2 \left[\frac{C_n}{1.5 \bullet BE_n} \right] \quad (1)$$

C_n represents the concentration of element n in sample. BE_n means the baseline concentration, 1.5 was modified index for characterizing sedimentary characteristics, rocky and other effects.

Geo-accumulation Index can be divided into several levels, e.g. it was divided into seven levels by Forstner (referred to hereafter as F classification), and five levels by Anon (referred to hereafter as A classification). It indicated pollution degrees of heavy metals by different classes of I_{geo} .

F classification			A classification		
I_{geo}	levels	Pollution degrees	I_{geo}	levels	Pollution degrees
<0	1	W.P.	<0	1	W.P. or slight pollution
0~1	2	W.P. to M.P.	0~1	2	M.P.
1~2	3	M.P.	1~3	3	M.P. or S.P.
2~3	4	M.P. to S.P.	3~5	4	S.P.
3~4	5	S.P.	>5	5	S.S.P.
4~5	6	S.P. to S.S.P.			
>5	7	S.S.P.			

W.P.: without pollution; M.P.: mid-pollution; S.P.: strong pollution; S.S.P.: super strong pollution

Table 3. Degrees of pollution by heavy metals indicated by different classes of I_{geo} .

The means of Geo-accumulation indexes of heavy metals in surficial soil of Guiyang city were analyzed (Fig.21 to Fig.28). By the results, we get the surficial soil in 41 per cent of the Guiyang did not suffer the arsenic contaminative, 43 per cent is between without pollution to mid-pollution, 14 per cent mid-pollution, only 2 per cent is between mid-pollution to strong pollution. In 40 per cent did not suffer the cadmium contaminative, 19 per cent between without pollution to mid-pollution, 14 per cent mid-pollution, 19 per cent between mid-pollution to strong pollution, 7 per cent strong pollution, 1 per cent between strong pollution to supper strong pollution. In 46 per cent did not suffer the chromium contaminative, 47 per cent between without pollution to mid-pollution, 6.8 per cent mid-pollution, only 0.2 per cent between mid-pollution to strong pollution. In 38 per cent did not suffer the copper contaminative, 38 per cent between without pollution to mid-pollution, 22 per cent mid-pollution, only 2 per cent between mid-pollution to strong pollution. In 18 per

cent did not suffer the lead contaminative, 47 per cent between without pollution to mid-pollution, 28 per cent mid-pollution, only 3 per cent between mid-pollution to strong pollution. In 12 per cent did not suffer the mercury contaminative, 37 per cent between without pollution to mid-pollution, 36 per cent mid-pollution, 11 per cent between mid-pollution to strong pollution, 2 per cent strong pollution, 1 per cent supper between strong pollution to supper strong pollution, 1 per cent supper strong pollution. In 19.2 per cent did not suffer the nickel contaminative, 63.7 per cent between without pollution to mid-pollution, 16.8 per cent mid-pollution, only 0.3 per cent between mid-pollution to strong pollution. In 41 per cent did not suffer the zinc contamination, 50per cent between without pollution to mid-pollution, 7 per cent mid-pollution, only 2 per cent between mid-pollution to strong pollution.

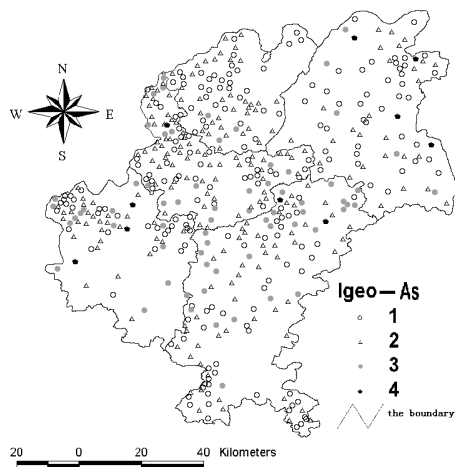


Fig. 21. Distribution of I_{geo} for As in surficial soil.

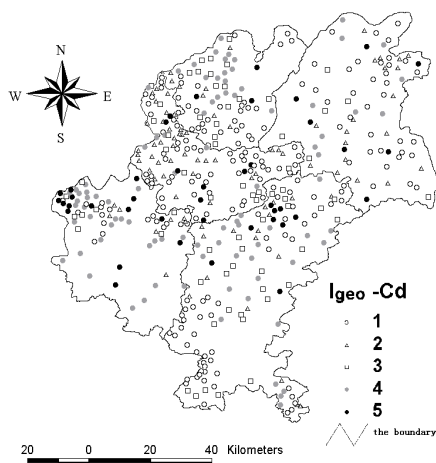


Fig. 22. Distribution of I_{geo} for Cd in surficial soil.

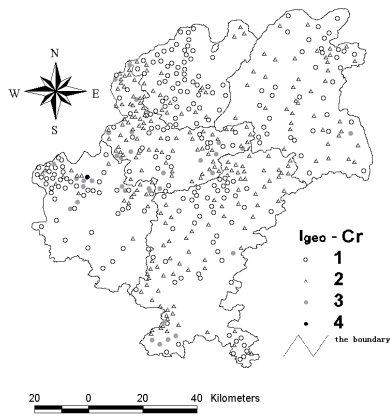


Fig. 23. Distribution of I_{geo} for Cr in surficial soil.

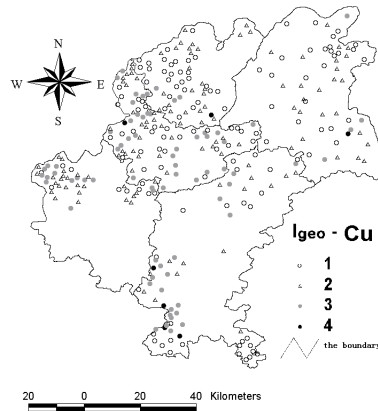


Fig. 24. Distribution of I_{geo} for Cu in surficial soil.

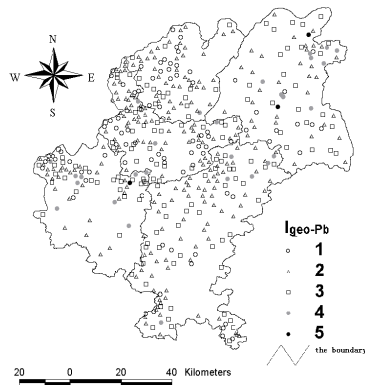


Fig. 25. Distribution of I_{geo} for Pb in surficial soil.

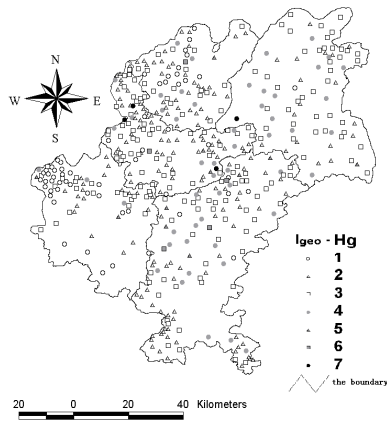


Fig. 26. Distribution of I_{geo} for Hg in surficial soil.

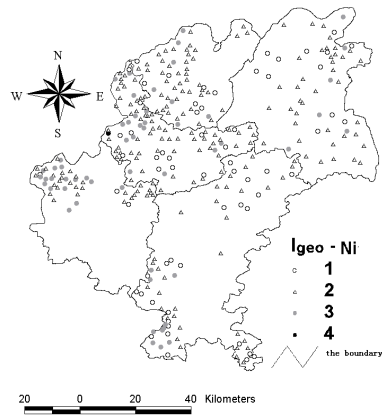


Fig. 27. Distribution of I_{geo} for Ni in surficial soil.

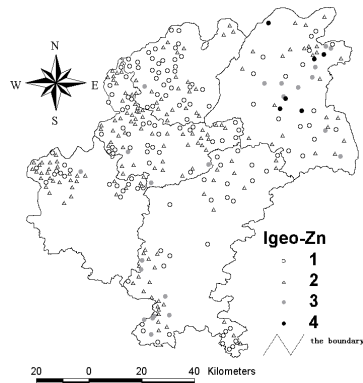


Fig. 28. Distribution of I_{geo} for Zn in surficial soil.

4.2.2 Contamination degree analysis of heavy metals in surficial soil

Contamination Degree (CD) was the most intuitive and commonly used one of the parameters for evaluating heavy metals pollution. The parameter represented the content of heavy metals in soil was over the national standard, and it was expressed as shown.

$$CD = \frac{c_i}{c_A} - 1 \quad (2)$$

c_i represents the analysis value in i sample of an element (the concentration of an element in sample). c_A means the maximum limit of the element concentration in environment, which was commonly the Quality Standard of Soil Environment. The primary standard of national quality standard in soil environment (GB15618-1995) was used to calculate the heavy metals pollution degree for c_A .

The contamination degrees of heavy metals in surficial soil of Guiyang city were analyzed (Table 4 to Table 11). The results indicated that the maximum of arsenic contaminative degree of surficial soil in Guiyang is 4.27. 50.2 per cent surficial soil did not suffer the pollution. The contaminative degree in 97 per cent surficial soil in Guiyang is smaller than 2 and the total contaminative degree is slightly over zero. So the surficial soil of Guiyang suffers the slight pollution. Of cadmium are 12.1. 57.9 per cent surficial soil did not suffer the pollution. 96 per cent is smaller than 4 and the total is over zero. So suffers pollution of Cd. Of chromium are 2.01. 69 per cent did not suffer the pollution, 30.6per cent slight pollution. The total is less than zero. So not suffer pollution of Cr. Of copper are 5.09. 53.2 per cent did not suffer the pollution. The total is slightly over zero. So suffers slight pollution of Cu. Of lead are 8.11. 49.9 per cent did not suffer the pollution. The total is slightly over zero. So suffers slight pollution of Pb. Of mercury are 45.87. 56.1 per cent did not suffer the pollution. The total is over zero. So suffers pollution of Hg. Of nickel is 1.56. 64 per cent did not suffer the pollution. The total is less than zero. So not suffer pollution of Ni. Of zinc are 2.85. 77.8 per cent did not suffer the pollution. The total is less than zero. So not suffer pollution of Zn. Consideration the pollution to join with 8 kinds of heavy metals, 40.2 per cent have no contamination of heavy metal, 15 per cent from no pollution to slight pollution, 36.1 per cent slightly pollution, 7.2 per cent mid-pollution, 1.4 per cent serious pollution in the surficial soil of Guiyang.

CD_{As}	$x \leq 0$	$0 < x \leq 1$	$1 < x \leq 2$
Number	244	187	42
Ratio	50.2%	38.5%	8.6%
CD_{As}	$2 < x \leq 3$	$3 < x \leq 4$	$x > 4$
Number	6	4	3
Ratio	1.2%	0.8%	0.6%
Note: Average: 0.206; Min:-0.81; Max: 4.27			

Table 4. The contamination degree on As in surficial soil of Guiyang city.

CD _{Cd}	x≤0	0< x≤1	1< x≤2	2<x≤3
Number	282	72	48	42
Ratio	57.9%	14.8%	9.9%	8.6%
CD _{Cd}	3< x≤4	4< x≤5	5< x≤6	x>6
Number	22	7	5	9
Ratio	4.5%	1.4%	1.0%	1.9%
Note: Average:0.51; Min:-0.995; Max:12.1				

Table 5. The contamination degree on Cd in surficial soil of Guiyang city.

CD _{Cr}	≤0	0< x≤0.5	0.5< x≤1
Number	337	118	24
Ratio	69.2%	24.3%	4.9%
CD _{Cr}	1<x≤1.5	x>1.5	
Number	7	1	
Ratio	1.4%	0.2%	
Note:Average:-0.16;Min:-0.92; Max:2.01			

Table 6. The contamination degree on Cr in surficial soil of Guiyang city.

CD _{Cu}	≤0	0< x≤1	1< x≤2
Number	177	99	43
Ratio	53.2%	29.7%	12.9%
CD _{Cu}	2<x≤3	x>3	
Number	11	3	
Ratio	3.3%	0.9%	
Note: Average:0.23; Min:-0.94; Max:5.09			

Table 7. The contamination degree on Cu in surficial soil of Guiyang city.

CD _{Pb}	≤0	0< x≤1	1< x≤2
Number	243	189	37
Ratio	49.90%	38.80%	7.60%
CD _{Pb}	2<x≤3	3< x≤4	x>4
Number	7	8	3
Ratio	1.50%	1.60%	0.60%
Note:Average:0.23;Min:-0.98; Max:8.11			

Table 8. The contamination degree on Pb in surficial soil of Guiyang city.

CD _{Hg}	≤0	0 < x ≤ 1	1 < x ≤ 2	2 < x ≤ 3
Number	273	155	33	10
Ratio	56.1%	31.8%	6.8%	2.1%
CD _{Hg}	3 < x ≤ 4	4 < x ≤ 5	x > 5	
Number	6	1	9	
Ratio	1.2%	0.2%	1.8%	
Note: Average:0.48; Min:-0.93; Max:45.87				

Table 9. The contamination degree on Hg in surficial soil of Guiyang city.

CD _{Ni}	≤0	0 < x ≤ 0.5	0.5 < x ≤ 1
Number	213	88	27
Ratio	64.0%	26.4%	8.1%
CD _{Ni}	1 < x ≤ 1.5	x > 1.5	
Number	4	1	
Ratio	1.2%	0.3%	
Note: Average :-0.04; Min:-0.77; Max:1.56			

Table 10. The contamination degree on Ni in surficial soil of Guiyang city.

CD _{Zn}	≤0	0 < x ≤ 0.5	0.5 < x ≤ 1	1 < x ≤ 1.5
Number	259	52	11	5
Ratio	77.8%	15.6%	3.3%	1.5%
CD _{Zn}	1.5 < x ≤ 2	2 < x ≤ 2.5	x > 2.5	
Number	2	2	2	
Ratio	0.6%	0.6%	0.6%	
Note: Average:-0.15; Min:-1.00; Max:2.85				

Table 11. The contamination degree on Zn in surficial soil of Guiyang city.

4.2.3 The correlation of heavy metal elements in surficial soil

The correlation of heavy metals were analyzed and twin-elements that correlation coefficient reached extremely significant level ($P < 0.01$) were As–Pb, Cd–Cr, Ni–Cd, Cu–Cr, Cr–Ni, Cr–Zn, Cu–Ni, Cu–Pb, Cu–Zn, Ni–Zn, Pb–Zn, the twin-elements which correlation was $P < 0.05$ were As–Zn, Cd–Hg, Cd–Zn, Pb–Ni by using SPSS16.0 with CA (Table 12). The correlation between heavy metals mainly because of heavy metal elements between parent rocks associated. For example, the correlation of metalloid element As and Pb reached extremely significant level, of As and Zn reached significant level, for As ore often associated in the sulfide mineral of Pb and Zn, and were produced together with other minerals such as pyrite and sphalerite. The content of As was less than 5-10000 mg/kg in the galena, abnormal area were formed when As were released in the ore mining and smelting

(Liao Z J, 1992). Pb-Zn deposits were mainly distributed in the northeast area, northwest area, south-central area and southwest area (Xu H N and Xu J L, 1996). As and its compound were often accompanied in the non-ferrous metal and precious metal ore, arsenide was distributed in the kinds of intermediate product (Li Q and Mo D L, 1997). The correlation of Cd and Zn reached significant, because there was no separate Cd ore, Cd was often accompanied with Zn ore, Cd was generally existed in the Zn ore as the forms of CdS and CdCO₃, and the concentration of Cd was between 0.01% and 0.5%.

	As	Cd	Cr	Cu	Hg	Ni	Pb	Zn
As	1						** (+)	* (+)
Cd		1	** (-)		* (+)	** (+)		* (-)
Cr			1	** (+)		** (+)		** (+)
Cu				1		** (+)	** (-)	** (+)
Hg					1			
Ni						1	* (-)	** (+)
Pb							1	** (+)
Zn								1

*: significant level(P<0.05); **: extremely significant level(P<0.01);
(+): positive correlation; (-): negative correlation

Table 12. The relativities between contaminating elements in surficial soil of Guiyang.

4.2.4 The influences of soil types in heavy metals pollution

On the basis of measured values in the different characteristics of soil types on heavy metals in surficial soils, the space isoline map and soil type distribution map of Guiyang City were overlaid by using the software ArcView 3.2. The different level concentrations of heavy metals were statistical analyzed according to the different soil types. Meanwhile, to facilitate analysis, soil types within the study area were divided into three types by human impact: man-influenced soil type, soil type by human impact in general and soil type with less human impact.

4.2.4.1 Soils types with stronger human impact: Yellow earths, limestone soils, paddy soils

Yellow soil lands an area of 3.335×10^5 ha for the area of Guiyang City it totally lands 41.5% land area of Guiyang City. Yellow was born in hot and humid environmental conditions, rock weathering and fast weathering by strong leaching, base captions and silicon ions have leached, clay and the formation of secondary minerals constantly, ferric oxide relative aggregation, in which iron oxide by strong hydration, the formation of high water content of goethite (Fe₂O · H₂O), limonite (Fe₂O₃ · 2H₂O), more water, iron oxide (Fe₂O₃·3H₂O), the

yellow hue of the minerals is the main hue(Sun,2002). Lime area 2.021×10^5 ha, accounting for land area of Guiyang City, 25.2%. Guiyang Karst landforms, carbonate rocks are widely distributed, accounting for 80.63% area of Guiyang City, the corrosion - erosion, the erosion severe cases, the carbonate rocks exposed, weathering and limestone soil. Corrosion of carbonate karst weathering process is the release of Ca leaching, the residual calcium carbonate and clay minerals into the soil formed by the lime soil, shallow soil, and more with rock debris, soil properties affected by litho logy great, are rock soil. Limestone soil, with the abundant calcium and substitution of base level is high, the leaching process, due to constantly add calcium carbonate to the soil base to be preserved, weathering alteration of other minerals are also weak, delayed Al-rich off the role of silicon occur so long in a juvenile state. Distribution of lime in the soil and the soil zone boundaries clearly.

Paddy area is 1.156×10^5 ha, accounting for the total land area of Guiyang City, 14.40%. In dam and hills in the valley bottom of the groove, light and heat conditions are good, as the irrigation and drainage conditions are good, the piece of the paddy field in the long-term hydroponics are the formation of the hydromorphic paddy soils that was the advanced stage of development of the paddy soil. As the periodic irrigation and drying, the soil, reduction and oxidation in alternating, the soil of iron, manganese and substances to restore migration, oxidative deposition, mind patterns of soil to form a brown rust, rust, and prism-like structure, which is a typical paddy soil types, is the main farming soil in Guiyang. The development at the initial stage of paddy rice soil infiltration education, are located in higher ground water table is low, almost no groundwater impact position. In the artificial irrigation, the irrigation of the soil affected by seasonal, alternating reduction and oxidation process, iron, manganese and base material was transported, deposited, in the former home territory, based on the formation of more than 20cm percogenic layer, initially with the characteristics of paddy soil. At the same time as soil pollution is not serious.

It shows that the levels of heavy metals were distributed at different levels, but mostly the first level and second level from Table 13 to Table 15. These three categories of soil type are the major soil types in Guiyang. By densely constraints, these three main soil types are local residents using the soil type. Yellow soil that the layer of soil and humus are thicker and soil acidity as well is the top soil for building timber forest and tea orchard. And its natural environment in which conditions is good, so it was open to most of the yellow land. Lime soil with high organic matter content, neutral to slightly alkaline, but the soil is thin, easy to dry; paddy soil water and heat conditions are better in the land after long-term aging and the formation of farming. In the long-term cultivation in the maturation process, human activities on soil heavy metal content of more. Therefore, the heavy metals content in different levels will have the distribution, while not a serious problem due to soil contamination, so in the first level and second level of the majority.

	Cd	Cr	Cu	Hg	Ni	Pb	Zn
1 th level	73.2	20.2	74.2	96.7	37.2	63.7	68.4
2 th level	21.1	61.1	18.9	1.5	45.4	29.0	23.4
3 th level	3.7	16.5	4.1	0.5	12.3	4.8	4.6
4 th level	1.4	1.9	1.8	0.3	4.0	1.7	1.7
5 th level	0.4	0.3	0.5	0.2	0.8	0.5	1.9
6 th level	0.2	0.0	0.5	0.8	0.3	0.3	0

Table 13. The percentage (%) of different concentration levels of heavy metals in Yellow earths of Guiyang.

	Cd	Cr	Cu	Hg	Ni	Pb	Zn
1 th level	61.2	30.4	70.3	97	38.4	69.2	73.8
2 th level	31.9	51.1	20.8	2.0	37.7	26.6	20.4
3 th level	4.8	13.4	5.8	0.4	13.3	2.9	5.1
4 th level	1.1	4.6	2.7	0.3	6.9	1	0.5
5 th level	0.5	0.4	0.4	0.2	3.3	0.1	0.2
6 th level	0.5	0.1	0	0.1	0.4	0.2	0

Table 14. The percentage (%) of different concentration levels of heavy metals in Limestone soils of Guiyang.

	Cd	Cr	Cu	Hg	Ni	Pb	Zn
1 th level	69.6	22.6	74.2	96.8	40	68.3	72.6
2 th level	21.7	58.2	17.4	2.3	39.9	28.1	18.1
3 th level	6.3	16.7	4.9	0.4	13.7	2.6	6.5
4 th level	1.6	2	1.5	0.4	4.7	0.8	1.5
5 th level	0.3	0.5	1.5	0.1	1	0.1	1.3
6 th level	0.5	0	0.5	0	0.7	0.1	0

Table 15. The percentage (%) of different concentration levels of heavy metals in Paddy soils of Guiyang.

4.2.4.2 Soils types with common human impact: Skeleton soils, purplish soils, litho soils, yellow-brown earths

Thick bone was 1.015×10^5 ha of 12.64% total land area in Guiyang city. Thick bone parent rocks were the weathering slope and residual consisting of shale and sand-shale. The soil body of soil type was instability, developed badly, thin soil and serious soil erosion. Phosphorus, potassium content is low. Purple soil area 104 ha, Guiyang 1.20 land area of 1.9%. Purple soil are mainly Jurassic purple red sandstone and mudstone tertiary surface soil after a. Purple rock type soft and crunchy, physical weathering speed, soil erosion is fast. And constantly weathering has added to make purple soil in the early stage of long-term. Purple clay mineral grains by weathering, silicon, carbonate etc iron compounds to form complex was stable in surface film, delaying the chemical weathering, keep the minerals of iron ore, the properties of soil siderite, thus presents. The rock soil due to constantly weathering of supplement, natural fertility soil of natural vegetation, also grew thick.

It can be seen in the heavy metals element content level mainly focus on four levels from Table 16 to Table 19. These four types of soil or natural conditions, using value is not high, Either the area is small, but the natural conditions, so the natural vegetation, soil for use, so not easily by the four types of human influence, but also affect the three types of great influence. Therefore, the four kinds of soil heavy metal content mainly concentrated in the top four.

	Cd	Cr	Cu	Hg	Ni	Pb	Zn
1 th level	71.2	28.3	67.0	96	44.5	68	72.2
2 th level	24.6	43.8	21.2	3.7	34.3	31.8	21.2
3 th level	3.8	25.3	6.0	0.1	12.3	0.2	6.6
4 th level	0.4	2.6	3.9	0.1	8.1	0	0
5 th level	0	0	1.7	0	0.8	0	0
6 th level	0	0	0.2	0.1	0	0	0

Table 16. The percentage (%) of different concentration levels of heavy metals in Skeletal soils.

	Cd	Cr	Cu	Hg	Ni	Pb	Zn
1 th level	68.3	21.1	87.5	91.4	41.8	78.1	68.6
2 th level	22.3	67.1	10.1	6.6	42.2	15.8	26.2
3 th level	7.5	9.9	1.1	0.7	8.2	4.7	4.8
4 th level	1.9	1.9	1.3	0.7	2.5	1.4	0.4
5 th level	0	0	0	0.6	4.3	0	0
6 th level	0	0	0	0	1.0	0	0

Table 17. The percentage (%) of different concentration levels of heavy metals in Purplish soils.

	Cd	Cr	Cu	Hg	Ni	Pb	Zn
1 th level	51.3	37.7	51.4	98.9	21.4	78.5	66.0
2 th level	39.3	38.0	33.1	1.1	42.7	18.5	30.6
3 th level	7.8	11.4	11.1	0	16.9	1.4	3.2
4 th level	1.5	7.0	4.4	0	6.2	1.6	0.2
5 th level	0.1	5.6	0	0	5.1	0	0
6 th level	0	0.3	0	0	7.7	0	0

Table 18. The percentage (%) of different concentration levels of heavy metals in Litho soils.

	Cd	Cr	Cu	Hg	Ni	Pb	Zn
1 th level	52.3	28.5	90.0	79.3	45.2	41.7	78.6
2 th level	42.8	71.1	10.0	13.8	41.5	21.0	16.7
3 th level	4.9	0.4	0	3.1	7.3	25.1	0.7
4 th level	0	0	0	2.2	2.7	10.3	1.4
5 th level	0	0	0	1.3	3.3	0.4	2.6
6 th level	0	0	0	0.3	0	1.5	0

Table 19. The percentage (%) of different concentration levels of heavy metals in Yellow-brown earths.

4.2.4.3 Soils types with less human impact: Mountain meadow soils and bog soils

In Guiyang City, The area of the Bog soils is 902ha, accounting for 0.11% of the total. On the surface of the local ground of the plateau, peal coal was formed by the accumulation of wet plants in the ancient swamp. Crustal movement in the later, ground up-list, swamp marsh

broke off marsh gradually, black peat accumulated, the lower layers was white washing, which is the current peat.

Mountain meadow soil 379ha, accounting only 0.05% of land area of Guiyang. Mountain meadow soil is within the forest line, the gentle mountain top hi wet meadow and meadow shrub coppice Semis formed a class of soil. Such thin layers of soil, and generally contain gravel, grass surface layer with.

As shown in Table 20 to Table 21,the content of heavy metals in these two soil types are mainly concentrated in a Single interval, this phenomenon may be related to less human impact (such as fertilizer), heavy metals content in these soil types are mainly concentrated in the range corresponding their baseline values.

	Cd	Cr	Cu	Hg	Ni	Pb	Zn
1 th level	0	16.8	100	0	100	0	100
2 th level	100	83.2	0	100	0	0	0
3 th level	0	0	0	0	0	17.4	0
4 th level	0	0	0	0	0	82.6	0
5 th level	0	0	0	0	0	0	0
6 th level	0	0	0	0	0	0	0

Table 20. The percentage (%) of different concentration levels of heavy metals in Bog soils.

	Cd	Cr	Cu	Hg	Ni	Pb	Zn
1 th level	100	65.8	98.2	100	0	0	100
2 th level	0	34.2	1.8	0	100	100	0
3 th level	0	0	0	0	0	0	0
4 th level	0	0	0	0	0	0	0
5 th level	0	0	0	0	0	0	0
6 th level	0	0	0	0	0	0	0

Table 21. The percentage (%) of different concentration levels of heavy metals in Meadow solonchaks.

5. Conclusions

1. The mean value, standard deviation and maximum of As separately are 18.09 mg/kg, 11.57 mg/kg and 79.30 mg/kg in the surficial soil in Guiyang, of Cd separately are 0.302mg/kg, 0.363mg/kg, 2.620mg/kg and 95.7 percent smaller than 1.000mg/kg., of Cu separately are 43.1mg/kg, 30.3mg/kg, 213.0mg/kg and 94.6 percent smaller than 100.0mg/kg, of Pb are 43.2mg/kg, 31.3mg/kg, 318.9mg/kg and 95.5 per cent smaller than 100.0mg/kg, of Hg are 0.222mg/kg, 0.531mg/kg, 7.030mg/kg and 98.2 smaller

- than 1.000mg/kg, of Ni are 38.3mg/kg, 14.9mg/kg, 102.5mg/kg and 95.8 percent smaller than 70.0mg/kg, of Zn are 84.7mg/kg, 49.8mg/kg, 385.0mg/kg and 94.3 percent smaller than 150.0mg/kg.
2. Comprehensively considering the results of calculation using the two kinds of methods, we respectively take 9.04mg/kg, 0.068 mg/kg, 18.8 mg/kg, 46.3 mg/kg, 14.8 mg/kg, 0.045 mg/kg, 44.0 mg/kg, 17.0 mg/kg as the baseline values of As, Cd, Cu, Zn, Pb, Hg, Cr and Ni in topsoil of Guiyang.
 3. By the results of Geo-accumulation analysis of heavy metals in surficial soil, we get the surficial soil in 41 per cent of the Guiyang did not suffer the arsenic contaminative, In 40 per cent did not suffer the cadmium contaminative, In 46 per cent did not suffer the chromium contaminative, In 38 per cent did not suffer the copper contaminative, In 18 per cent did not suffer the lead contaminative, In 12 per cent did not suffer the mercury contaminative, In 19.2 per cent did not suffer the nickel contaminative.
 4. By the results of contamination degree analysis, the maximum of arsenic contaminative degree of surficial soil in Guiyang is 4.27. Of cadmium are 12.1. Of chromium are 2.01. Of copper are 5.09. Of lead are 8.11. Of mercury are 45.87. Of nickel is 1.56. Of zinc are 2.85.
 5. The soil types in this area were divided into three types of soil by the human impact degree. The three soil types of yellow soil, limestone soil and paddy soil that were the main soil types in Guiyang city were greatly influenced by human. The four soil types of skeleton soil, purple soil, stone soil and yellow brown soil that were not easily used were certainly influenced by human, the concentration of heavy metals in boggy soil and mountain meadow soil were concentrated on an interval, and tow types of soil (boggy soil and mountain meadow soil) were less influenced by human.

6. References

- [1] Bauer I. and Bor J.1993.Vertikale Bilanzierung von Schwermetallen in Boden Kennzeichnung der Empfindlichkeit der boden gegenüber Schwermetallen unter Berücksichtigung von lithogenem Grundgehalt, pedogener An – und Abreicherung some antheopogener Zusatzbelastung, Teil 2. Texte56, Umweltbundesam, Berlin.
- [2] Bauer I. and Bor J.1995.Lithogene, geonene und anthropogene Schwermetallgehalte von Lobboden an den Beispielen von Cu, Zn, Ni, Pb, Hg und Cd[J]. Mainzer Geowiss Mit. 24, 47-70
- [3] Bauer I., Spernger M. and Bor J.1992.Die Berechnung Lithogener und geonerer Schwermetallgehalte von Lobboden am Beispielen von Cu, Zn und Pb[J]. Mainzer Geowiss Mitt. 21, 47-70
- [4] Chen Cuihua, Ni Shijun, He Binbin, et al.,2008. Spatial-temporal variation of heavy metals contamination in sediments of the dexing mine, Jiangxi province[J]. Acta Geoscientica Sinica,29(5):639-646
- [5] Chen Hangxin, Shen Xiachu, Yan Guangsheng. 1998. Research of experimental unit about international geochemical mapping. Edited by Wang Yanjun[M]. In The Geochemical paper of the 30th international geological meeting. Geological Press. Beijing, China.57-75
- [6] Darnley A G ·1997. A global geochemical reference network: the foundation for geochemical baselines. J Geochemistry Exploration, 60(1):1-5

- [7] Forstner U, Muller G. 1981. Concentrations of heavy metals and polycyclic aromatic hydrocarbons in river sediments: geochemical background, man's influence and environmental impact[J]. *Geojournal*, 5: 417~432.
- [8] Forstner U, Ahlf W, Calmano W, et al. 1990. Sediment criteria development-contributions from environmental geochemistry to water quality management[A]. In: Heling D, Rothe P, Forstner U, et al. *Sediments and environmental geochemistry: selected aspects and case histories*[C]. Berlin Heidelberg: Springer-Verlag, 311~338.
- [9] Hu Mianhao. 2010. Application of index of geo-accumulation in evaluation of heavy metals pollution in Municipal sludge from Nanchang[J]. *Guangdong Weiliang Yuansu Kexue*, 17(3):
- [10] National Environmental Protect Bureau of China, National Technology Supervise Bureau of China. 1995. GB15618-1995 Environmental Quality Standard for Soil [S]. Beijing: Environmental Sciences Press of China (in Chinese)
- [11] National Environmental Protect Bureau of China and National Technology Supervise Bureau of China. 1998. GB/T17134-1997. Environmental Quality Determination of total arsenic-the silver diethyl dithiocarbamate photometric method[S]. Beijing: Environmental Sciences Press of China (in Chinese)
- [12] National Environmental Protect Bureau of China and National Technology Supervise Bureau of China. 1998. GB/T17136-1997. Environmental Quality Determination of total mercury-cold atomic absorption spectrophotometry method[S]. Beijing: Environmental Sciences Press of China (in Chinese)
- [13] National Environmental Protect Bureau of China, National Technology Supervise Bureau of China. 1998. GB17137-1997. Environmental Quality Determination of total chromium-Flame atomic absorption spectrophotometry [S]. Beijing: Environmental Sciences Press of China (in Chinese)
- [14] National Environmental Protect Bureau of China, National Technology Supervise Bureau of China. 1998. GB17138-1997. Environmental Quality Determination of Cu and Zn-Flame atomic absorption spectrophotometry [S]. Beijing: Environmental Sciences Press of China (in Chinese)
- [15] National Environmental Protect Bureau of China, National Technology Supervise Bureau of China. 1998. GB17139-1997. Environmental Quality Determination of Ni-Flame atomic absorption spectrophotometry [S]. Beijing: Environmental Sciences Press of China (in Chinese)
- [16] National Environmental Protect Bureau of China and National Technology Supervise Bureau of China. 1998. GB/T17141-1997. Soil Quality-Determination of Lead and Cadmium: Graphite Furnace Atomic Absorption Spectrophotometry[S]. Beijing: Environmental Sciences Press of China (in Chinese)
- [17] National Environmental Protect Bureau of China, 2004. HJ/T 166-2004. The technical specification for soil environmental monitoring[S]. Beijing Environmental Sciences Press of China (in Chinese)
- [18] Lepeltier C. 1969. A simplified treatment of geochemical data by graphical representation[J]. *Environmental Geology*, 64, 538-550
- [19] Liao Zi Ji. 1992. Environmental chemistry and biological effects of trace elements[M]. Beijing. China Environmental Science Press, 178-253
- [20] Li Qiang, Mo Dalun. 1997. The damage and research progress of As contamination in the soil environment [J]. *Tropical and Subtropical Soil Science*, 6(4): 291 - 295
- [21] Matschullat J., Ottenstein R. and Reimann C. (2000) Geochemical background-can we calculate it[J] *Environmental Geology*, 39, 990-1000

- [22] Muller G. 1969, Index of geoaccumulation in sediments of the Rhine River[J]. *Geojournal*, 2(3): 108~118
- [23] Salminen R, Tarvainen T, 1997. The problem of defining geochemical baseline. A case study of selected elements and geological materials in Finland. *J. Geochemical Exploration*, 60(1): 91-98
- [24] Salminen R, Gregorauskiene V. 2000. Consideration regarding the definition of a geochemical baseline of elements in the surficial materials in areas differing in basic geology. *Applied Geochemistry*, 15: 647-653
- [25] Sun Chengxing. 2002. Red weathering material sources and rare earth elements chemical research in Karst area of Guizhou[D]
- [26] Teng Yanguo, Ni Shijun, Tuo Xianguo et al., 2002. Geochemical baseline and trace metal pollution of soil in Panzhihua mining area[J]. *Chinese Journal of Geochemistry*. 21, 274-281
- [27] Teng Yanguo, Tuo Xianguo, Ni Shijun et al., 2003. Environment geochemical of heavy metal contaminants in soil and stream sediment in Panzhihua mining and smelting area, southwestern China[J]. *Chinese Journal of Geochemistry*, 22, 254-262
- [28] Xu Hong-ning, Xu Jia-lin. 1996. The cause and the distribution of As abnormal area in China [J]. *Soil*, 2:80-84
- [29] Yi Xiu, Gu Xiaojing, Hou Yanqing, et al., 2010. Assessment on soil heavy metals pollution by Geo-accumulation index in Jinghuiqu irrigation district of Shaanxi province[J]. *Journal of Earth Sciences and Environment*, 32(3):288-291

Evaluating the Effects of Radio-Frequency Treatment on Rock Samples: Implications for Rock Comminution

Arthur James Swart
Vaal University of Technology
Republic of South Africa

1. Introduction

“You find remedy in the thorniest tree”. This Arabic proverb well illustrates that scientific solutions to well defined engineering problems are often hard to find, resulting in much frustration and anguish. This has also proved true in the mineral processing industry, where numerous exigent scientific endeavours have sought to improve rock comminution. Comminution may be divided into two steps; the reduction of large materials to a size suitable for grinding (termed crushing) and the reduction of crushed material into powder (termed grinding or milling). Comminution efficiency is currently low and is based on the absolute ratio of energy required to generate new surface area relative to the total mechanical energy input (Tromans, 2008). Current comminution techniques need to be enhanced if a higher efficiency is to be realized.

Mineral liberation efficiency subsequently relates to the amount of energy required to release a certain percentage of valuable minerals from the gangue (waste material) through rock comminution methods. The major source of this energy generation is fossil fuels, coal, natural gas and oil, which are still expected to meet about 84% of energy demand in 2030 (Shafiee & Topal, 2009). However, concerns continue to be raised regarding the burning of fossil fuels as a contributor to rising atmospheric concentrations of carbon dioxide (CO₂), which may contribute to climate change (Wolde-Rufael, 2010). Furthermore, it is estimated that in a mining-intensive country, the minerals processing industry accounts for approximately 18% of the national energy consumption. This process is currently inherently inefficient, with less than 3% of the energy input directly involved in rock breakage and liberation (Moran, 2009). Subsequently, the importance of coal in energy generation and as a possible source of global warming necessitates the use of alternative methods to reduce the amount of energy used by mining industries (increased power efficiency) while at the same time recovering the same (or higher) percentage of valuable minerals (higher throughput) (Wang & Forssberg, 2007). This thorny dilemma continues to frustrate researchers around the globe within the fields of Metallurgical, Mechanical and Electrical Engineering.

Current research studies have found that the mineral liberation process can be enhanced through the use of pulsed power, ultrasound pre-treatment and microwave pre-treatment of

run of mine ore (Gaete-Garretón et al., 2000; Wilson et al., 2006; Jones et al., 2007; Wang & Forssberg, 2007). Ore, from the mining operation, goes through a process that separates the valuable minerals from the gangue. This process usually involves crushing, grinding (or milling), separation and extraction where the gangue is usually discarded in tailings piles (Perkins, 1998). These electrical methods, which are used to enhance the mineral liberation process, each have their own advantages and disadvantages, which are discussed in this chapter. However, this research proposes a different technique involving radio-frequency (RF) power, which may have positive implications for rock comminution and mineral liberation.

The main purpose of this research is to evaluate the effect that RF power exerts on rock samples, with particular focus on textural changes. This evaluation aims to determine if RF power weakens mineral grain boundaries, subsequently leading to improved rock comminution and mineral liberation. This may result in significant reductions of energy consumption of current comminution and mineral liberation equipment. This chapter will firstly define rock comminution and mineral liberation. Rocks used in this research are then presented along with current electrical treatment techniques which are applied to enhance rock comminution. A proposed new technique is substantiated with the practical setup of the equipment being introduced. Results of treating specific rock samples with RF power are presented quantitatively (electrical properties, surface temperature rise, particle screen analysis and SEM photomicrographs).

2. Rock comminution and mineral liberation

The processes used for the purification and enhancement of an ore, to satisfy the needs of downstream applications, are collectively referred to as mineral beneficiation (De Waal, 2007). The aim of mineral beneficiation is to separate ore minerals from gangue minerals, producing as pure as possible a concentrate of ore minerals distinct from tailings. The process is undertaken in steps where the run of mine ore first undergoes comminution followed by separation/concentration.

2.1 Comminution

The aim of comminution is to liberate the ore minerals from the gangue by breaking the rock up into smaller particles until there are loose particles of ore mineral (Wills, 1992; Sadrai et al., 2006). Comminution is essentially the size reduction of the fragments of rock/ore (Wills, 1992). Comminution is effected by compression, impact and abrasion, through crushing or grinding/milling. The process usually involves several steps, each comprising a small reduction ratio of three to six. An example of a mineral processing line is demonstrated in Fig. 1. In this example, a vibrating feeder serves the purpose of making coarse separations of mining ores (200 – 800 mm in diameter) and providing a consistent, even supply of rock material to the jaw crusher. The jaw crusher breaks this material down to a particle size of approximately 10 – 100 mm. The next stage, the ball mill, is used for grinding various ore and other materials down to particle sizes of around 100 μm . The stages which follow (classifier to rotary dryer) are used to separate the valuable minerals from the gangue, and are discussed under section 2.2. The physical properties of minerals that have the most influence on the comminution process are hardness, tenacity, cleavage, fracture and common form.

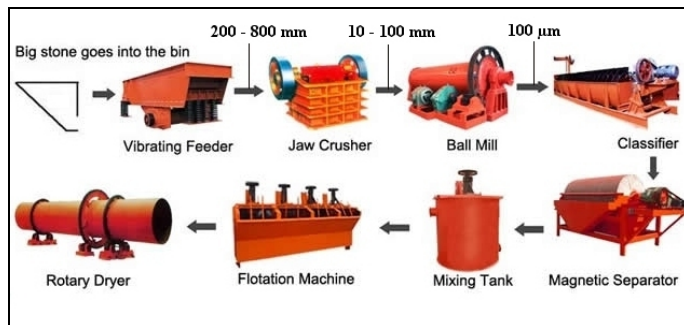


Fig. 1. Mineral processing line (Henan Chuangxin Building-material Equipment Co, 2009)

Hardness is defined as the degree of resistance of a given mineral to scratching, indicating the strength of the bonds that hold the mineral’s atoms together (Skinner & Porter, 1992; Chernicoff & Fox, 1997; Klein, 2002; Thompson & Turk, 2007). The hardness of a mineral is tested by scratching the unknown mineral with a series of minerals or substances with known hardness and is one of the most useful diagnostic properties of minerals (Tarbuck & Lutgens, 1999).

Tenacity is a mineral’s physical reaction to stress such as crushing, bending, breaking, or tearing (Klein, 2002). Certain minerals react differently to each type of stress. Since tenacity is composed of several reactions to various stresses, it is possible for a mineral to have more than one form of tenacity. The different forms of tenacity are (Rapp, 2009):

- Brittle - If a mineral is hammered and the result is a powder or small crumbs, it is considered brittle. Brittle minerals leave a fine powder if scratched, which is the way to test a mineral to see if it is brittle. Majority of all minerals are brittle. Minerals that are not brittle may be referred to as non-brittle minerals.
- Sectile - Sectile minerals can be separated with a knife into thin slices, much like wax (e.g. gold).
- Malleable - If a mineral can be flattened out into thin sheets by pounding it with a hammer, it is malleable. All true metals are malleable (e.g. gold).
- Ductile - A mineral that can be stretched into a wire is ductile. All true metals are ductile.
- Flexible but inelastic - Any minerals that can be bent, but remains in the new position after it is bent are flexible but inelastic. If the term flexible is singularly used, it implies flexible but inelastic (e.g. chlorite).
- Flexible and elastic - When flexible and elastic minerals are bent, they spring back to their original position. All fibrous minerals and some acicular and flaky minerals belong in this category (e.g. mica).

Cleavages occur when some crystals break in one or more smooth plane surfaces, whose orientation is determined by the regular atomic structure of the crystal (Klein, 2002; Wenk & Bulakh, 2004). Certain minerals fracture with an uneven surface when broken, while others split or cleave along distinctive crystallographic planes. Cleavage is thus the ability of a mineral to break, when struck, along preferred directions (Skinner & Porter, 1992; McGeary et al., 2001). Fig. 2 illustrates seven possible types of mineral cleavage which are:

- A – One direction of cleavage;
- B – Two directions of cleavage at 90°;
- C – Two directions of cleavage not at 90°;
- D – Three directions of cleavage at 90°;
- E – Three directions of cleavage not at 90°;
- F – Four directions of cleavage; and
- G – Six directions of cleavage.

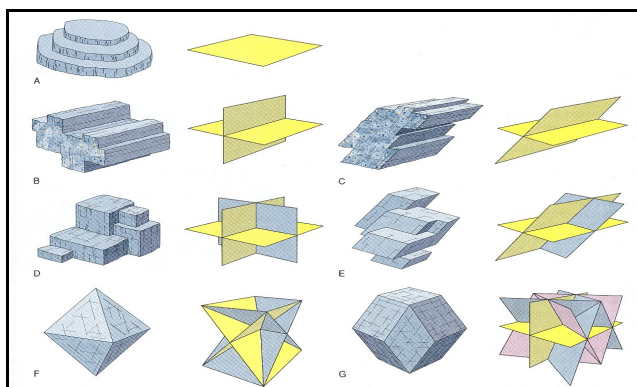


Fig. 2. Seven possible types of mineral cleavage (Wenk & Bulakh, 2004)

Cleavage is tested by striking or hammering a mineral, and is classified by the number of surfaces it produces and the angles between adjacent surfaces (Chernicoff & Fox, 1997). A mineral tends to break along certain planes because the bonding between atoms is weaker there. For example, quartz has equally strong bonds in all directions and would thus have no cleavage, whereas micas are easily split apart into sheets due to the fact that the bonding between adjacent atomic sheets is weak. Cleavage is one of the most useful diagnostic tools because it is identical for a given mineral from one sample to another. It is especially useful for identifying minerals when they appear as small grains in rocks (McGeary et al., 2001).

Some minerals have poorly defined cleavages, while others may not even show any at all. When broken, these minerals cause fractures in that they break on generally irregularly oriented curved surfaces, decided more by stress distribution in the crystal at the time of rupture than by the atomic structure of the mineral (Klein, 2002; Wenk & Bulakh, 2004). Fracture is thus the way a substance breaks when not controlled by cleavage and is the most common type of fracture for minerals (McGeary et al., 2001; Thompson & Turk, 2007). Fracture may appear as a jagged, irregular or rough surface or as a curved, shell-shaped (conchoidal) surface (Chernicoff & Fox, 1997).

Minerals may further be identified by their **common form**. The term form is often used to indicate general outward appearance (Klein, 2002). In crystallography, external shape is denoted by the word habit, whereas the term form is used in a special and restricted sense. Thus a form consists of a group of crystal faces, all of which have the same relation to the elements of symmetry and display the same chemical and physical properties. The term common form is used synonymously to the term habit and refers to the external shape in which a mineral commonly occurs.

2.2 Separation

Automated mineral beneficiation, which essentially involves the separation of specific desired minerals from a crushed/milled mixture of minerals, usually exploits properties such as differences in densities, magnetic susceptibility, electrical conductivity, surface reactivity, refractive index, and fluorescence (Wills, 1992; De Waal, 2007). The most common processes include (Wills, 1992):

- Gravity separation – exploiting the density differences between minerals, and their response to gravity and resistance to motion in a fluid such as water. Typical apparatus includes jigs, Humphries spirals, Reichert cones, sluices, and shaking tables.
- Dense medium separation – exploiting density differences where minerals are introduced to a dense liquid or suspension, in which some minerals will float and others sink, thus effecting separation. A wide variety of separation vessels are employed in industry including some that incorporate a centrifugal aspect to expedite the process.
- Froth flotation – exploiting differences in the surface properties of different types of minerals. Here minerals are exposed to a solution which renders some of the minerals hydrophobic and other hydrophilic. Air is bubbled through the solution in which the minerals are suspended, resulting in separation because the hydrophilic ones settle to the bottom of the solution whereas the hydrophobic minerals can be skimmed off with the soapy froth at the surface.
- Magnetic separation – exploiting the differences in magnetic susceptibility of minerals through use of strong magnetic forces that can be adjusted to separate minerals of differing susceptibility.
- Electrostatic/high tension separation – exploiting differences in electrical conductivity of minerals, in which a charge builds up in non-conductive minerals causing them to stick to charged surfaces, whereas conductive particles do not stick to such surfaces.

Before any of the above separation process can be effective, proper liberation of the ore minerals is essential. Complete liberation is seldom achieved in practice (Wills, 1992; King, 2001), which implies that most particles will comprise both ore and gangue material, with their response to any separation technique being uncertain. The degree of liberation can be described using the following terms:

- A completely liberated particle is one that consists of only one type of mineral, either ore mineral or gangue mineral.
- A middling is a particle that consists of two or more different types of minerals, i.e. it is incompletely liberated.
- Middlings can be further classified into attached mineral (binary, ternary, etc) or enclosed minerals.
- The degree of liberation can also be described in terms of what is called particle grade. For example, a liberated particle comprising 100% ore mineral will have a particle grade of 100%, whereas a middling particle consisting of 25% ore mineral and 75% gangue mineral will have a particle grade of 25%.

3. Rocks used in this research

Rocks are composed of minerals (Chernicoff & Fox, 1997) and are called monomineralic when they contain only one mineral (Best & Christiansen, 2001). Ores are essentially rocks

that contain one or more type of mineral coveted for its metal content or its physical properties for industrial use (Wills, 1992). The coveted minerals in the ores are called ore minerals (if they contain useful metals) or industrial minerals (if they have useful physical properties). Woollacot and Eric (1994) classify mined material into three categories:

- Mined material consisting of useful rock or soil, where the rock/soil has value in its natural form, e.g. as aggregate or filler material.
- Mined material containing industrial minerals, where the value lies in one or more minerals within the rock that must be liberated and separated from the rock, e.g. diamond in kimberlite, crysotile in greenstones, wollastonite in skarn, etc.
- Mined material containing value-bearing minerals, where the value lies in constituents of one or more minerals within the rock (ore) and the constituent (metal) needs to be extracted from the mineral after the latter has been liberated and separated from the rock (ore), e.g. extraction of copper from copper-bearing minerals such as chalcopyrite (CuFeS_2) and bornite (Cu_5FeS_4) occurring as minerals in copper ore.

Rocks may be classified into three groups (see Fig. 3) based on their mode of formation. These are:

- **Igneous rocks:** formed by the solidification/crystallization of mainly molten silicate material called magma or lava (Chernicoff & Fox, 1997; Walther, 2005). These rocks consist of tightly interlocked crystals, where the size of the crystals range from <0.06 mm (as in the case of those crystallized from lava at the surface of the earth) to ± 10 mm (as in the case of those crystallized from slow cooling magma deep in the earth's crust). In addition, there are very coarse-grained igneous rocks (pegmatites) which crystallized from magma containing high proportions of volatile material.
- **Sedimentary rocks:** formed by the solidification of loose material on the earth's surface (Skinner & Porter, 1992; Chernicoff & Fox, 1997). The loose material accumulates through the processes of weathering, erosion and deposition/sedimentation. Solidification takes place by a process called lithification/diagenesis, which involves the compaction, cementation and recrystallisation of sediments that are deeply buried (± 3 km). Sedimentary rocks are also formed by the lithification of chemical precipitates that accumulate as layers of microcrystals on lake floors or subterranean cavities (Thompson & Turk, 2007; Carlson et al., 2008).
- **Metamorphic rocks:** formed by the exposure of rocks to high temperature and/or pressures during magmatic and/or tectonic events (Chernicoff & Fox, 1997). Heat from nearby magmatic intrusions and pressure induced by mountain-building and other tectonic processes causes reactions and recrystallisation of minerals resulting in new sets of minerals within metamorphosed rocks. The process of recrystallisation occurs in the solid state, or in extreme cases, in a partially molten state.

The three rock groups are characterised by important differences in the types of minerals and their textural relationships. These differences are manifest in the physical properties of the rocks, such as strength and elasticity ratios, that affect their behaviour during comminution. Consequently, the physical properties of minerals are not the only controlling factors on the effectiveness of comminution, but more importantly, the mineral assemblage and texture of the rock, which is the reason why three different rocks have been selected for trial in this research (dolerite, sandstone and marble – see Table 1 for selected characteristics of these

rocks). The same is true for different types of ores where the textures ultimately determine the grain-size to which an ore needs to be milled before liberation is properly effected.

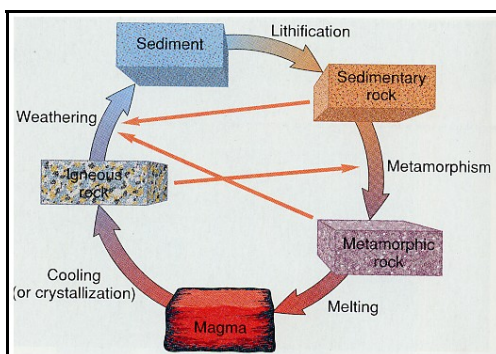


Fig. 3. The rock cycle (Chernicoff & Fox, 1997)

Dolerite is an igneous intrusive rock with medium-sized grains (Aloian, 2010), which was injected as a fluid into older water-laid sedimentary rocks (Leaman, 1973). It was injected under pressure head of at least 700 kg/cm² and caused severe disruptions of pre-existing geological features. As the initially hot fluid was forced into cold sediments, severe thermal gradients were produced during the period of injection and cooling. Dolerite is primarily composed of two essential minerals, termed plagioclase and pyroxene. The mineralogy of dolerite is closely related to the form of the intrusion and the thermal history.

Sandstones are types of sedimentary rocks, which consist particularly of mineral grains, deposited in parallel layers, which have subsequently been cemented together. Sandstones are mostly white, light grey, buff, reddish or yellowish brown in colour. Quartz is the predominant mineral found in most sandstones being chemically stable and physically durable under most weathering and transporting processes (Evans, 1972; Dietrich & Skinner, 1979). Sedimentary rocks formed by the deposition of mineral grains are classified on the basis of grain-size. Sandstones have grain-sizes ranging from 0.0625 mm to 2 mm and generally comprise quartz with or without feldspar and other mineral fragments. In addition, sandstones may also have interstitial finer-grained material such as clay or cementing material which can vary in amount as a percentage of the total rock (< 5 - 25%) (McGeary et al., 2001).

Marble is an example of a metamorphic rock consisting primarily of calcite and/or dolomite. Marble may be snow white, grey, black, buff, yellowish, chocolate, pink, mahogany-red, bluish, lavender or greenish in colour. The grains within marble tend to be of a rather uniform size (Dietrich & Skinner, 1979). Marble forms by the metamorphism of limestone, during which recrystallisation of calcite occurs (Evans, 1972). Completely recrystallised limestone can result in a rock with interlocking calcite crystals and the obliteration of the stratification and other textural characteristics of the parent limestone. Impure parent limestone produces marble that contains other minerals in addition to calcite, with the most common being quartz, anorthite, serpentine, tremolite, diopside, and forsterite. The minerals present depend on the nature of the impurities and the grade of metamorphism.

Characteristic	Dolerite	Sandstone	Marble
Rock type	Igneous (hypabyssal)	Sedimentary	Metamorphic
Texture	Medium grained and smooth	Medium grained and rough	Coarse grained
Principal minerals	Plagioclase and Pyroxene	Quartz	Calcite and dolomite
Principal mineral hardness	Plagioclase: 6; Pyroxene: 6	7	3
Principal mineral breakage	Two good cleavages at 90°	Fracture	Three good cleavages at 75°/105°
Specific gravity	3.00 – 3.05	2.00 – 2.60	2.6 – 2.86
Resistivity ($\Omega\cdot\text{m}$)	20 – 200	8 – 4 000	100 – 250 000 000
Colour	Dark bluish, weathers to brown	White, light grey, buff, reddish or yellowish brown	White, grey, black, buff, yellowish, chocolate, pink, mahogany-red, bluish, lavender or greenish
Porosity	0.1 – 0.5%	5.0 – 25.0%	0.5 – 2.0%

Table 1. Selected characteristics of dolerite, sandstone and marble

The rocks discussed above were selected for this research and were labelled with the text JS (representing James Swart) followed by an alphabetical label as shown in Table 2. This was done to prevent confusion between the different samples which were treated with electrical RF power.

Sample code	Rock family	Rock type
JSA	Igneous	Dolerite
JSB	Metamorphic	Marble
JSD	Sedimentary	Sandstone

Table 2. Rock samples chosen for this research

4. Electrical treatment techniques

Electrical treatment techniques refer to the use of electrical energy in specific ways to achieve desired changes in certain solid and liquid materials. Four specific electrical techniques currently employed include:

- Microwave pre-treatment;
- Ultrasound pre-treatment;
- High voltage electrical pulses; and
- Radio-frequency power.

4.1 Microwave pre-treatment

Numerous studies have shown that microwave pre-treatment is beneficial for:

- Drying of raisins (Kostaropoulos & Saravacos, 1995);
- Accelerating enzymatic hydrolysis of chitin (Roy et al., 2003);
- Improved grindability and gold liberation (Amankwah et al., 2005);
- Improving the moisture diffusion coefficient of wood (Li et al., 2005);
- Enhancement of phosphorus release from dairy manure (Pan et al., 2006);
- Strength reduction in ore samples (Jones et al., 2007);
- Enhancing enzymatic digestibility of switchgrass (Hu & Wen, 2008);
- A higher extractive yield of vegetable oil from Chilean hazelnuts (Uquiche et al., 2008); and
- The liberation of copper carbonatite ore after milling (Scott et al., 2008).

Microwave pre-treatment is found in many other applications where microwaves induce transient motions of free or bound charges, such as electrons or ions or charge complexes such as permanent dipoles. The resistance to these motions causes losses, which result in attenuation of the electric field and increased dissipation of energy in the material (Amankwah et al., 2005).

The most important early work on microwave pre-treatment was that of Chen et al. (1984), who investigated the reaction of 40 minerals to microwave exposure in a waveguide applicator which allowed the mineral samples to be inserted in an area of known high electric field strength. This study showed that microwave heating is dependent on the composition of the minerals.

Walkiewicz et al. (1988) later published data on microwave heating of a number of minerals and speculated on the potential reduction in grinding energy required for minerals with stress fractures induced by microwave heating. Kingman et al. (2004) published an article stating that for the first time microwave-assisted comminution may have the potential to become economically viable. This conclusion was based on significant reductions in strength, coupled with major improvements in liberation of valuable minerals.

The microwave heating system is made up of four basic components: power supply, magnetron, cavity for the heating of the target material and waveguide for transporting microwaves from the generator to the cavity. Commonly, an industrial size microwave heating system is set to a frequency of 915 MHz with a magnetron as high as 75 kW power and an average working life of 6000 hours (Smith, 1993).

Microwave heating is a sophisticated electroheat technology requiring specialist knowledge and expensive equipment if meaningful results are to be obtained (Bradshaw et al., 1998). Included in this is the precision involved in the design and construction of the magnetron and cavity.

4.2 Ultrasound pre-treatment

The use of ultrasound pre-treatment has been applied to:

- Accelerate the anaerobic digestion of sewage sludge (Tiehm et al., 1997);

- Comminution (Gaete-Garretón et al., 2000);
- Titanium tanning of leather (Peng et al., 2007);
- Ammonia steeped switchgrass for enzymatic hydrolysis (Montalbo-Lomboy et al., 2007);
- Two-Minute skin anaesthesia (Spierings et al., 2008); and
- Cassava chip slurry to enhance sugar release for subsequent ethanol production (Nitayavardhana et al., 2008).

The feasibility of the application of ultrasound energy to the grinding process as a viable avenue of study was stated at a meeting of the International Comminution Research Association in Warsaw, 1993 (Gaete-Garretón et al., 2000). One of the most significant reasons for this proposition originated in the accepted fact that inside any material there are a number of inherent cracks and ultrasonic energy has the capacity to produce crack propagation from within the particle to its outer surface, in spite of the very low energy producing an efficient fracture. An ultrasonic grinding machine can be designed in the form of a roller mill constructed over a specially designed ultrasonic transducer (Gaete-Garretón et al., 2003).

Gärtner (1953) was probably the first researcher to have attempted using ultrasonic waves in the fragmentation of particles, obtaining poor results. Leach and Rubin (1988) studied the fragmentation of resonant rocks samples fixed to the tip of an ultrasonic transducer, observing a preferred fracture at the nodes. Yerkovic et al. (1993) made grinding tests comparing standard copper ore with ultrasonic pre-treated samples in a ball mill. The pre-treated ore exhibited a 32% higher grinding rate.

An active roll, which is itself an ultrasonic transducer, is located in front of a passive roll. The vibration in extensional mode combines compression and shear action of the active roll on the mill feed. A funnel feeds the material into the gap by gravity which are then nipped by the rolls. A spring system furnishes the stress applied to the ore and the stress level can be varied by adjusting the spring tension. The rotation of the roll is produced by a variable speed electric motor. The ground ore is collected under the rolls in an iron receiver fed by gravity.

It is evident from the above description of the ultrasound mill that many different parts have to work together in the application of an ultrasonic field in the stressing zone of the material. This setup proves to be very precise and time consuming.

4.3 High voltage pulsed power

High voltage pulsed power has been applied to:

- Enhance coal comminution and beneficiation (Touryan & Benze, 1991);
- Mineral liberation (Andres et al., 2001);
- Metal peening (Zhang & Yao, 2002);
- Rock fragmentation (Cho et al., 2006);
- Recover ferrous and non-ferrous metals from slag waste (Wilson et al., 2006); and
- Convective drying of raisins (Dev et al., 2008).

The history of high voltage pulsed power can be traced back to 1752 when Benjamin Franklin discovered that lightning was a discharge of static electricity (Staszewski, 2010). It

was reported that he raised a kite (with a key attached to his end of the string) which was tied to a post with a silk thread. As time passed, Franklin noticed the loose fibres on the string stretching out; he then brought his hand close to the key and a spark jumped the gap. This electrical discharge across a gap would prove significant in the research of high voltage pulsed power techniques.

In 1924 Erwin Marx described an apparatus, which produced high voltage pulses, and became known as the Marx-Generator (Fontana, 2004). It is a clever technique for generating high-voltage short-duration waveforms by charging a number of capacitors in parallel, then quickly discharging them in series. While originally based upon the use of air-dielectric spark gaps to provide the switching mechanism, solid-state variants utilizing avalanche diodes or other solid-state switching devices have been used to generate nanosecond duration pulses having amplitudes exceeding several thousand volts of direct current (Baker & Johnson, 1993).

There has been intense interest for the last several decades in the use of high-voltage pulse technology for rocks disintegration (Cho et al., 2006). The methods of electric pulse disintegration are mainly electrohydraulics and internal breakdown inside bulk solid dielectrics (Owada et al., 2003). The first method refers to the generation of an intense shock wave in water from the passage of electrical current through water and the crushing and subsequent constituent separation by the impact of that shock wave on the sample. The second method refers to the passage of electrical current through the rock and the separation of the mineral contents from the rock matrix by preferential current flow along the mineral/rock boundary interface. Rock disintegration using the second method consumes substantially less energy than that using the first method and enhanced effect of liberation of mineral constituents of rock aggregates.

A major limiting factor to spark-gap switches used in high voltage pulsed power applications was their short lifetime (Winands et al., 2005). Other shortcomings with spark gaps are related to their limited pulse repetition rate, strong electrode erosion, insulator degradation, high arc inductance, limited hold-off voltage, and costly triggering.

4.4 Radio-frequency power

The application of electrical energy in the RF heating of various materials has been successfully employed in the following:

- Electrical heating along with RF heating was used in the 1970s for the recovery of bitumen from tar sand deposits (Kawala & Atamanczuk, 1998);
- RF treatments can potentially provide an effective and rapid quarantine security protocol against codling moth larvae in walnuts as an alternative to methyl bromide fumigation (Wang et al., 2001);
- RF heating was successfully used to increase the temperature of human blood without incurring cell destruction (Pienaar, 2002);
- Treating fruit in immersion water of selected salt concentration and RF power may be used to develop an effective alternative quarantine method for fruit (Ikediala et al., 2002);
- RF power in conjunction with conventional hot water treatment can be used to develop feasible heat treatments to combat codling moths in apples (Wang et al., 2006);

- RF-based dielectric heating was used in the alkali pre-treatment of switchgrass to enhance its enzymatic digestibility (Hu et al., 2008); and
- Dielectric heating of soil using radio waves (RW) can be applied to support various remediation techniques, namely biodegradation and soil vapor extraction, under in situ or ex situ conditions (Roland et al., 2008).

Dielectrics have two important properties (Jones et al., 2002):

- They have very few free charge carriers. There is very little charge carried through the material matrix when an external electrical field is applied.
- The molecules or atoms comprising the dielectric exhibit a dipole movement.

The principle of dielectric heating basically involves the absorption of energy by dipoles (Chee et al., 2005). A dipole is essentially two equal and opposite charges separated by a finite distance. An example of this is the stereochemistry of covalent bonds in a water molecule, giving the water molecule a dipole movement. Water is the typical case of a non-symmetric molecule. Dipoles may be a natural feature of the dielectric or they may be induced (Kelly & Rowson, 1995). Distortion of the electron cloud around non-polar molecules or atoms through the presence of an external electric field can induce a temporary dipole movement. This movement generates friction inside the dielectric and the power is dissipated subsequently as heat. The interaction of dielectric materials with electromagnetic radiation in a given frequency band results in energy absorbance (Wang et al., 2001; Jones et al., 2002). The power coupled into a sample is nearly constant when the electric field intensity and dielectric loss factor do not vary at a given frequency. The heat generated per unit volume (P in W/m^3) in a dielectric material when exposed to RF power can be expressed as (Nelson, 1996):

$$P = 5.56 \times 10^{-11} \times f \times E^2 \times \varepsilon \quad W/m^3 \quad (1)$$

Where

$f \equiv$ frequency of radiation in Hertz (Hz)

$E \equiv$ the electric field intensity in Voltage per meter (V/m)

$\varepsilon \equiv$ the permittivity of the material

Moreover, the amount of heat (Q) required to change the temperature of a given material is proportional to the mass of the material and to the temperature change as given by Giancoli (2005):

$$Q = C \times m \times \Delta T \quad J \quad (2)$$

Where

$\Delta T \equiv$ temperature change in degrees Celsius ($^{\circ}C$)

$m \equiv$ the sample mass in kilogram (kg)

$C \equiv$ specific heat capacity in Joules per kilogram per degrees Celsius ($J/kg/^{\circ}C$)

Subsequently, temperature rise within the sample due to absorbed electromagnetic energy is really a function of the heating time. The temperature increase can be estimated by assuming that the electric field is uniform and the dielectric properties are relatively

constant. The temperature increase (ΔT in $^{\circ}\text{C}$) of the sample during RF heating can furthermore be expressed as (Halverson et al., 1996):

$$\Delta T = \frac{k \times P}{C \times m} \times \Delta t \quad ^{\circ}\text{C} \quad (3)$$

Where

$k \equiv$ coupling coefficient

$P \equiv$ input power (W)

$\Delta t \equiv$ RF heating time in seconds (s)

The practical setup used to achieve the transfer of RF power to a dielectric sample is shown in Fig. 4, and consists of a transformer, rectifier, oscillator, an inductance-capacitance pair commonly referred to as the 'tank circuit', and the work circuit (Wang et al., 2001). The transformer raises the voltage to 9 kV and the rectifier provides a direct current which is then converted by the oscillator into RF power at 27 MHz. This frequency is determined by the values of the inductance and capacitor in the tank circuit. The parallel-plate electrodes, with sample in-between, act as the capacitor in the work circuit. The gap of the electrode plates can be changed to adjust RF power coupled to the sample between the two plates.

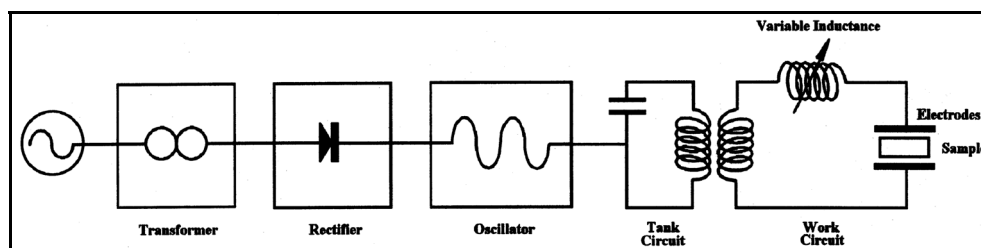


Fig. 4. Practical setup used in the dielectric heating of a material (Wang et al., 2001)

Three (microwave, ultrasound and high voltage pulsed power) of the four electrical treatment techniques noted above have been successful in weakening the mineral grain boundaries of rocks, thereby enhancing mineral liberation within the rock comminution process. This is accomplished by the generation of stress within the material, which gives rise to fractures and breakages. The weakening of mineral grain boundaries may yet be achieved by using RF power.

5. Proposed new treatment: RF power

Emanating from the above scientific literature on the use of electrical energy in various treatment techniques, the following hypotheses are made:

- The successful transfer of RF power to specific rocks through dielectric heating may exhibit positive effects on the textural characteristics of these samples; and
- These textural changes may further contribute to enhancing the rock comminution process, thereby increasing the percentage of valuable liberated minerals.

As far as could be established, no current literature exists substantiating these hypotheses. A novel electrical treatment technique of rock samples involving RF power within the very-high frequency (VHF) range (30-300 MHz) is subsequently presented.

A high power RF amplifier may be connected to a rock sample (acting as a dielectric material) by means of a suitable coupling device. RF power is transferred from the amplifier to the rock sample at the resonating frequency. Confirmation of power transfer may be determined through the following results:

- Temperature increase on the surface of the rock sample;
- Surface colour change of the sample;
- Screening of particles from pre-treated and non-treated sample;
- Scanning electron microscope (SEM) analysis of pre-treated and non-treated samples; and
- Power consumption analysis of pre-treated and non-treated samples in a ball mill.

The practical setup of this experiment is shown in Fig. 5. A commercial RF transceiver (ICOM IC-V8000) may be used in conjunction with two RF amplifiers (MIRAGE PAC30-130B) to generate the power required at the resonating frequency. However, the output impedance of the RF amplifiers is 50 Ω while the input impedance of the rock samples may vary dramatically from a few hundred ohm to a few thousand ohm (determined by a practical setup discussed by Swart et al. (2005)). This necessitates the use of a matching network and a coupling device, which are presented next.

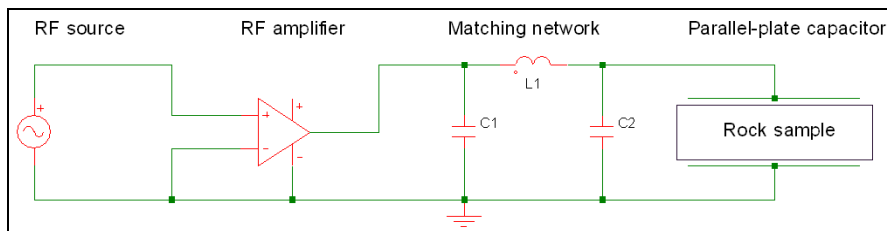


Fig. 5. Practical setup of the experiment based on research by Wang et al. (2001)

6. Innovative coupling technique

Two RF measurement coupling techniques currently exist for connecting RF equipment to dielectric materials, namely the cylindrical capacitor with coaxial electrodes and the parallel-plate capacitor (PPC) with disk electrodes.

Numerous articles list the usefulness of the **cylindrical capacitor** in measuring electrical impedances (Levitskaya & Sternberg, 2000; Bagdassarov & Slutskii, 2003; Azimi & Golnabi, 2009). A cylindrical capacitor consists of a three-part coaxial capacitance sensor in which the middle one acts as the main sensing probe (Azimi & Golnabi, 2009). The outer conductor is considered to be a guard ring in order to reduce stray capacitance and error measurements. Aluminium material is often used for manufacturing the capacitor tube electrodes (Rutschlin et al., 2006). The cylindrical capacitor extends the frequency limit of measurements to 1 GHz for materials with a dielectric permittivity of less than 25 (Levitskaya & Sternberg, 2000). However, cutting a sample of marble (dielectric permittivity

of 8) into a cylindrical form with exact diameter spacing proves cumbersome and difficult in the absence of a core-drill. For this reason the PPC was reviewed as a coupling device.

A PPC with disk electrodes is formed when a dielectric material or sample is sandwiched between two conducting plates (see Fig. 6). These conducting plates (made from copper due to its good conductivity (Zaghloul, 2008) are connected to relevant test equipment via standard RF connectors and coaxial cables. Swart et al. (2009) suggests that high frequency measurements (up to 950 MHz) using PPCs are easier on dielectric material samples with small widths (<5 mm) and low dielectric permittivities (around 8). Subsequently, all rock samples were cut to a width of 4 mm (using a laboratory rock cutter) and sandwiched within a PPC connected to a matching network housed in a novel wooden jig.

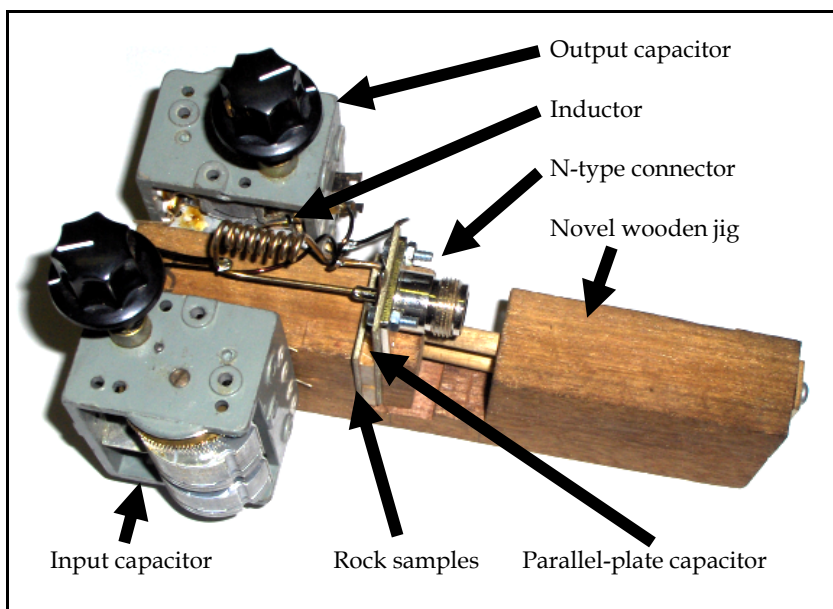


Fig. 6. Two rock samples inside a PPC with the matching network

The matching network ensures maximum power transfer to the rock samples and was made from mechanical plate trimmer capacitors (5-100 pf) and an inductor constructed from silver wire (silver solder). Silver has a lower resistivity ($1.624 \times 10^{-8} \Omega\text{-cm}$) than that of copper ($1.728 \times 10^{-8} \Omega\text{-cm}$) at 20 °C and is therefore a better conductor with less attenuation (Hutchinson, 2001). Hence, it will not heat up as quickly as copper will, which could weaken the soldering joints. Pozar (2005) substantiates this claim by noting that the conductivity of silver ($6.173 \times 10^7 \text{ S/m}$ at 20 °C) is higher than that of copper ($5.813 \times 10^7 \text{ S/m}$ at 20 °C).

7. Practical setup of the equipment

The matching network’s performance was evaluated using two RF amplifiers (MIRAGE PAC30-130B) driven by a commercial RF transceiver (ICOM IC-V8000). The RF transceiver generated a 3.2 W RF signal which was amplified by the first RF amplifier to approximately

32 W, and in turn, to approximately 113 W by the second RF amplifier. This was necessary because the RF transceiver was not capable of providing more than 70 W of RF power. The input to the RF amplifiers was limited to 35 W to ensure correct operation of the driver stages. The practical setup is shown in Fig. 7.

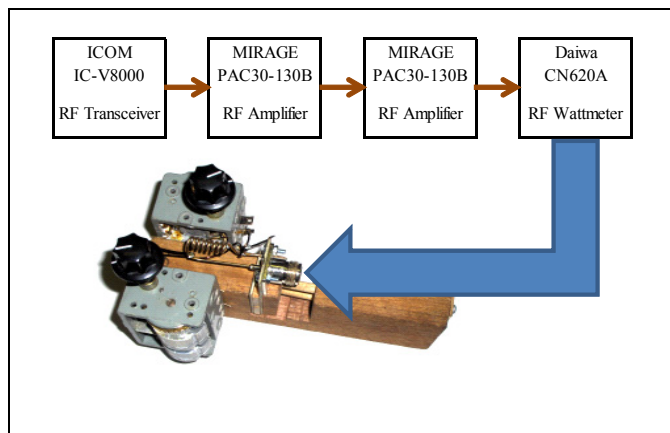


Fig. 7. Practical setup to determine the efficacy of the matching network

The output of the RF transceiver was first connected straight to the matching network through a RF wattmeter to determine the standing wave ratio (SWR) of the circuit. The reason for this is to ensure that the SWR value remain as close as possible to one, in order to prevent an excess of reflected power damaging the output stage of the RF amplifier. With the two RF amplifiers bypassed, the RF transceiver was activated (keyed) to generate a 3.2 W signal at 160 MHz (approximate centre of the VHF range which extends from 30 – 300 MHz). The trimmer capacitors were then fine-tuned to obtain the lowest possible SWR. The RF amplifiers were then switched on (thus connecting the amplifiers directly into the circuit between the RF transceiver and the matching network). The RF transceiver was keyed again and approximately 113 W of forward power was measured with the wattmeter. Two different wattmeters were used to verify the reliability of the measurements. The reflected power measured approximately 1.8 W resulting in a SWR reading of 1.308. The successful transfer of RF power (82 W) to the rock samples was further collaborated by a significant rise in surface temperature, as described in the following results section.

8. Results of treating rock sample with RF power

Rock samples of specific size which have been exposed to a known amount of RF power at a given frequency are referred to as treated samples, while those which were not exposed are termed untreated samples. Possible changes that were considered include textural, phase, grindability, colour, temperature and electrical property changes. Textural changes (changes in grain size and inter-grain boundary relationships) were considered using polarizing optical microscopy on polished thin sections of the rock samples. Geological type samples are often cut into thin slices, using diamond type saws, and then fixed onto glass slides using a strong adhesive (Tiedt & Pretorius, 2002). The mount is then polished, and subsequently coated with a conductive layer. These thin sections were also used to determine phase changes (changes in

mineral assemblage) using polarizing optical microscopy. The textural and phase changes were analyzed with a Phillips model XL30 DX41 scanning electron microscope. Grindability, being the changes in the power consumption during grinding and changes in the particle size distribution after grinding, was determined by measuring the power consumption during milling (using a HIOKI 3286-20 clamp on power meter) and by performing particle size analyses (sieve tests of screen sizes 250 μm , 150 μm , 90 μm and 38 μm). Surface colour changes were visually observed while surface temperature changes were measured (using a LUTRON TM-2000 digital thermometer and K-type thermocouples pressed firmly against the surface of the rock samples). Contrasts between the electrical properties (resonating frequencies and impedances obtained from a HP 8752C network analyzer) of the untreated and treated samples are further indicated. The results from the above considerations were interpreted in terms of the mineralogical and chemical composition of the samples.

8.1 SEM analysis of photomicrographs

A comparison of the photomicrographs of the untreated and treated rock samples reveals no significant differences in grain size, grain shape, minerals present or inter-granular textures. No visible cracks or fractures exist along the mineral grain boundaries of the treated rock samples, as shown in Fig. 8 – 10.

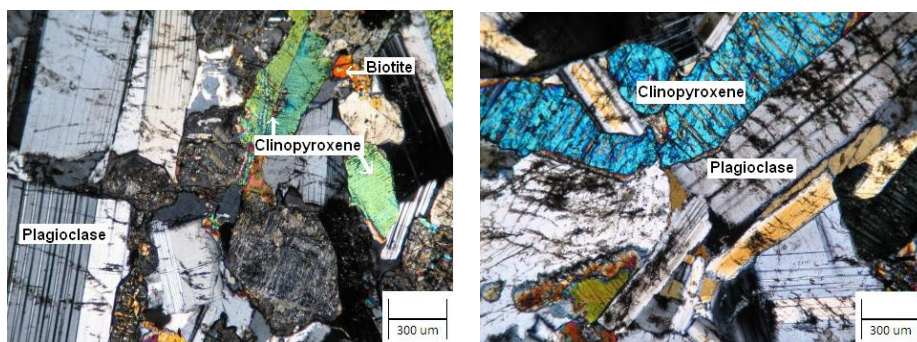


Fig. 8. Photomicrographs of the untreated (left) and treated (right) JSA rock sample taken under cross-polarized light

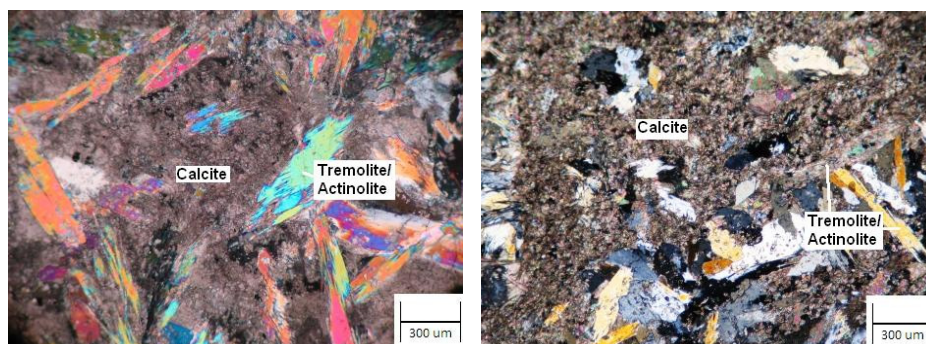


Fig. 9. Photomicrographs of the untreated (left) and treated (right) JSB rock sample taken under cross-polarized light

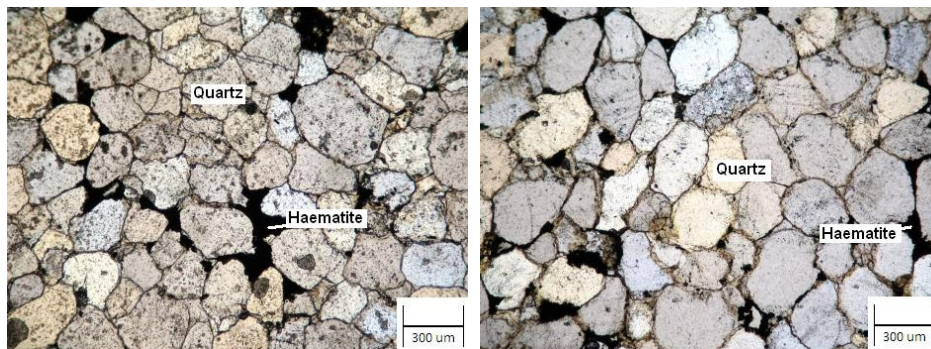


Fig. 10. Photomicrographs of the untreated (left) and treated (right) JSD rock sample taken under plane-polarized light

8.2 Particle screen analysis

Determination of the relative grindability of the untreated and treated samples was done by measuring the power consumption during grinding and comparing the particle size distribution after the grinding process. The untreated and treated samples were ground down to powder form in a laboratory swing mill, which consists of a shallow cylinder; two internal rings and a heavy disc. These mills are designed for reduction of materials to extremely fine powders for preparation of samples for spectra analysis. All samples were milled for 2 minutes with corresponding power measurements taken of the power consumed. A small brush was used to clean out the grounded samples (in the form of powder or dust) from the pot, which were then weighed with a digital scale.

The powder samples were next transferred to particle screening sieves (250 µm, 150 µm, 90 µm and 38 µm screens placed on top of each other). This screen combination was placed in an ENDECOTTS EFL2000 shaker for 5 minutes. Rock sample particles left behind in each screen was weighed individually. These weightings were converted into percentages by dividing each weighting by the total mass and cumulative mass percentages by adding successive mass percentages. The results of this evaluation are shown in Fig. 11 – 13, where the untreated samples are shown by means of a triangle or cross. The treated samples are indicated by means of a diamond or square. The left sketch indicates the particle size distribution to cumulative mass, while the right hand sketch shows the frequency of occurrence for each grain size. Four samples were used in the analysis of the JSA and JSD rock samples, to ensure repeatability and reliability of the results. Three JSB rock samples were used in this analysis, as it showed little or no variation in post-grinding particle size distribution between the untreated and treated rock samples.

However, JSA and JSD revealed minor to major variations. The treated JSA sample (right hand graph) shows a significant coarser grain size distribution with a mode value of 90 µm, whereas it is 38 µm for the untreated samples. Similarly, the d_{80} (nominal sieve size allowing 80% of the powered sample to pass through – left hand graph) is approximately 85 µm for the treated ones, but less than 38 µm for the untreated samples. This means that for the same amount of grinding (2 minutes) the treated samples were reduced in size to a lesser extent than the untreated samples, suggesting reduced grindability. This may also indicate that

fewer fines (smaller particles) are generated and therefore over-grinding is reduced. A similar situation is evident for the JSD sample, which is a sandstone with granular textures in which sand grains are cemented with matrix material such as haematite, whereas the JSA sample has a typical igneous texture of interlocking crystals.

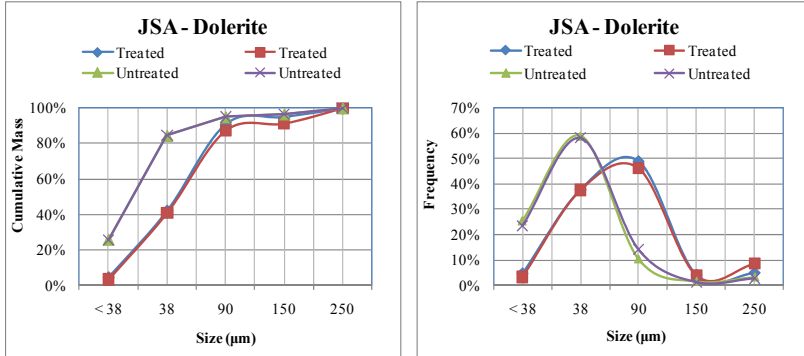


Fig. 11. Particle screen results for the untreated and treated JSA sample

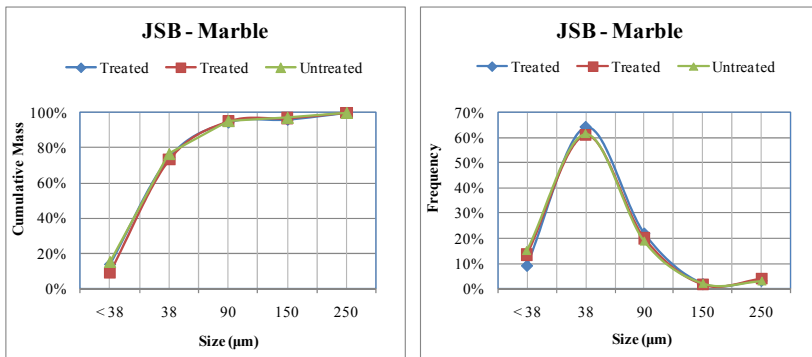


Fig. 12. Particle screen results for the untreated and treated JSB sample

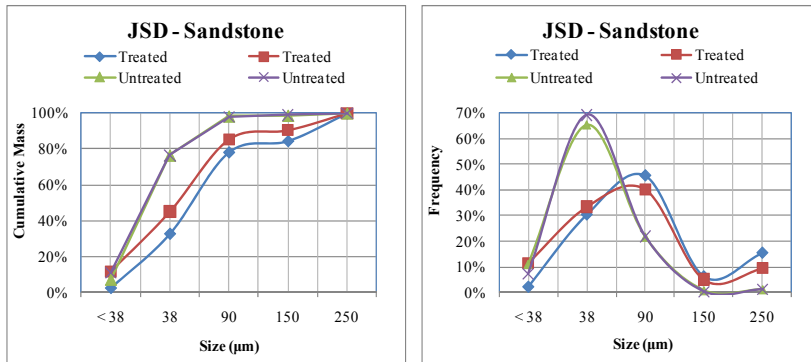


Fig. 13. Particle screen results for the untreated and treated JSD sample

Polished sections of the powdered samples were obtained to check for textural changes with regard to particle sizes of the untreated and treated samples (see Fig. 14 - 16). The size of the mineral grains is indicated, revealing no significant reduction in size between the untreated and treated samples.

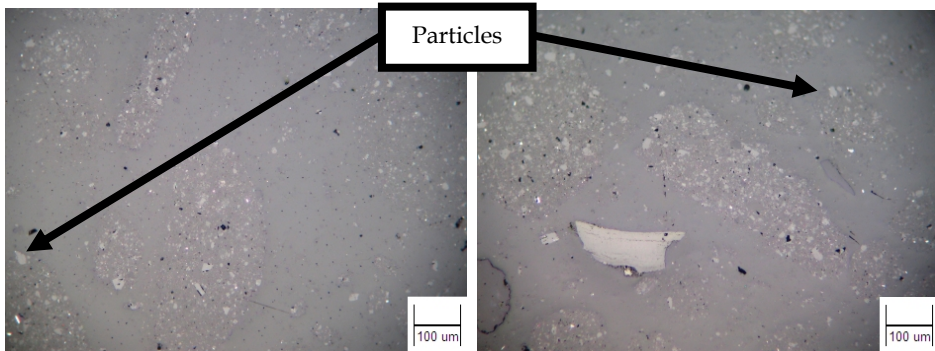


Fig. 14. Photomicrographs of the untreated (left) and treated (right) JSA sample

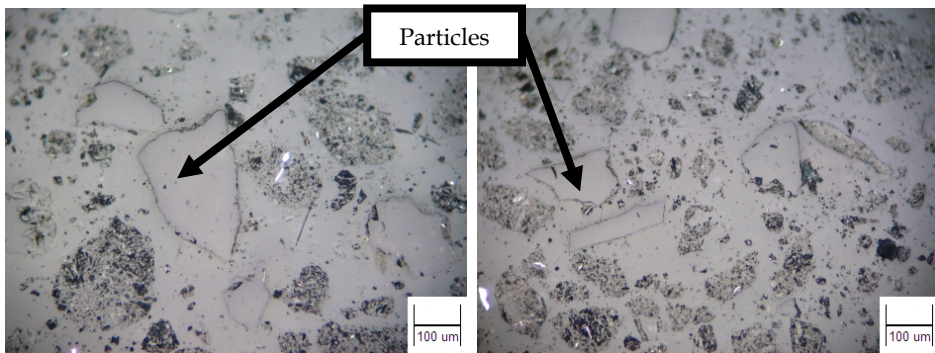


Fig. 15. Photomicrographs of the untreated (left) and treated (right) JSB sample

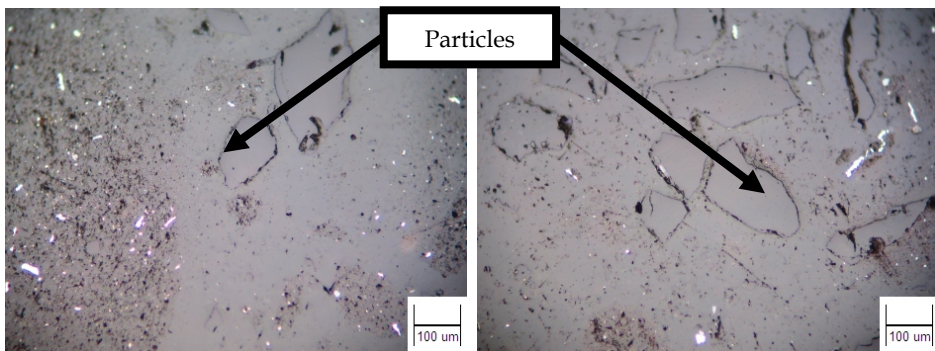


Fig. 16. Photomicrographs of the untreated (left) and treated (right) JSD sample

8.3 Electrical properties and surface colour changes

The transfer of RF power to the rock samples resulted in a surface temperature rise due to RF heating of the dielectric material. Table 3 presents visual effects of RF heating on the three rock samples (JSA, JSB and JSD), as well as the temperature reached after a specified time of RF treatment.







Sample code and type	Maximum temperature (degrees Celsius)	Time (min)	Screen change	Colour change	Untreated sample	Treated sample
JSA 30 x 19 x 4 mm Dolerite Igneous	151	4	Yes	No		
	Frequency / resistance				160.14 MHz / 1264 Ω	164.37 MHz / 1319 Ω
	Power consumption				1419 W	1420 W
JSB 31 x 19 x 4 mm Marble Metamorphic	107	2	No	Yes		
	Frequency / resistance				162.58 MHz / 1325 Ω	161.57 MHz / 1467 Ω
	Power consumption				1357 W	1356 W
JSD 30 x 19 x 4 mm Sandstone Sedimentary	55	5	Yes	No		
	Frequency / resistance				170.08 MHz / 1169 Ω	169.86 MHz / 1292 Ω
	Power consumption				1357 W	1358 W

Table 3. Surface colour changes and maximum temperatures reached for samples JSA, JSB and JSD (untreated on the left and treated on the right)

Colour changes and maximum temperature reached with 82 W of RF power at 160 MHz is indicated. S-parameters (in the form of Cartesian Coordinates) for the rock samples were obtained from a network analyser, from which the resonating frequencies and resistances were calculated for the untreated and treated rock samples. No significant variations were

observed between the untreated and treated samples with regard to two of their electrical properties, being the resonating frequencies and resistances. The power consumption (sum of the power consumed by the RF equipment and milling machine) of the untreated and treated samples also reveals no significant variations.

9. Conclusion

One of the primary aims of this research was to design and develop a suitable coupling device to connect relevant electronic equipment (test instruments and amplifiers) to various rock samples. Maximum power transfer to the rock sample at a specific frequency was achieved with the use of a PPC and matching network housed in a novel wooden jig. Inserting specific sized rock samples into this coupling device proved simple and effective, being neither time consuming or difficult.

Only two of the three samples (JSA and JSD) revealed a notable change in their particle size distribution. The fact that the percentage of larger sized particles increased (from 38 μm to 90 μm) suggests that the rock was **strengthened** rather than weakened (see Fig. 11 and Fig. 13). A possible application could be the prevention of over-grinding during comminution, which may have benefits during mineral processing. Moreover, RF power could further be used in the colouring of rock surfaces (see Table 3).

Evaluating the effects of RF power treatment on rocks has brought to light that mineral grain boundaries within specified rock samples are not significantly weakened by RF treatment. This was firstly confirmed by the similar electrical properties of the untreated and treated samples, where consistent values for the resonating frequency were obtained from a network analyser. Secondly, the SEM analysis of the untreated and treated rock samples revealed no significant changes in the form of fractures or breakages along the mineral grain boundaries. Photomicrographs of the thin sections of the two rock samples were used in this analysis. The particle size distribution of both samples further revealed no weakening or softening of the rock, as the percentage of smaller sized particles did not increase in the treated samples. It may therefore be stated that treating rock samples with RF power within the VHF range will not significantly improve rock comminution and mineral liberation.

10. Acknowledgment

I acknowledge Prof. Christo Pienaar (Director of the Telkom Centre of Excellence) for his specific guidance relating to the methodology employed in this research. I also would like to acknowledge Prof. Peter Mendonidis (Principal Lecturer in Metallurgical Engineering at Vaal University of Technology) for explaining difficult terms and principles relating to rock comminution. I further acknowledge my colleague, Ruaan Schoeman, who often provided a listening ear to my concerns and battles regarding this research. Appreciation is also extended to the Central Research Committee at VUT for their financial contribution to this research.

11. References

Aloian, M. (2010). *What are igneous rocks*. New York: Crabtree Publishing Company.

- Amankwah, R. K., Khan, A. U., Pickles, C. A., & Yen, W. T. (2005). Improved grindability and gold liberation by microwave pretreatment of a free-milling gold ore. *International Journal of Mineral Processing and Extractive Metallurgy Review*, Vol. 114, No. C, pp. 30-36, ISSN 0882-7508
- Andres, U., Timoshkin, I., & Soloviev, M. (2001). Energy consumption and liberation of minerals in explosive electrical breakdown of ores. *Mineral Processing and Extractive Metallurgy: Transactions of the Institute of Mining and Metallurgy, Section C*, Vol. 110, No., pp. 149-157, ISSN 0371-9553
- Azimi, P., & Golnabi, H. (2009). Precise formulation of electrical capacitance for a cylindrical capacitive sensor. *Journal of Applied Science*, Vol., No. 9, pp. 1556-1561, ISSN 1812-5654
- Bagdassarov, N. S., & Slutskii, A. B. (2003). Phase transformations in calcite from electrical impedance measurements. *Phase Transitions: A Multinational Journal*, Vol. 76, No. 12, pp. 1015 - 1028, ISSN 0141-1594
- Baker, R. J., & Johnson, B. P. (1993). Applying the Marx bank circuit configuration to power MOSFETs. *Electronics Letters*, Vol. 29, No. 1, pp. 56-57, ISSN 0013-5194
- Best, M. G., & Christiansen, E. H. (2001). *Igneous Petrology*. Massachusetts: Blackwell Science.
- Bradshaw, S. M., van Wyk, E. J., & de Swardt, J. B. (1998). Microwave heating principles and the application to the regeneration of granular activated carbon. *The Journal of The South African Institute of Mining and Metallurgy*, Vol. July/August, No., pp. 201-210, ISSN 0038-223X
- Carlson, D. H., Plummer, C. C., & McGeary, D. (2008). *Physical Geology: Earth Revealed* (7th ed.). New York: McGraw-Hill.
- Chee, S. N., Johansen, A. L., Gu, L., Karlsen, J., & Heng, P. W. S. (2005). Microwave Drying of Granules Containing a Moisture-Sensitive Drug: A Promising Alternative to Fluid Bed and Hot Air Oven Drying. *Chemical & Pharmaceutical Bulletin*, Vol. 53, No. 7, pp. 770-775, ISSN 0009-2363
- Chen, T. T., Dutrizac, J. E., Haque, K. E., Wyslouzil, W., & Kashyap, S. (1984). The relative transparency of minerals to microwave radiation. *Canadian Metallurgical Quarterly*, Vol. 23, No. 3, pp. 349-351, ISSN 0008-4433
- Chernicoff, S., & Fox, H. A. (1997). *Essential of Geology*. New York: Worth Publishers.
- Cho, S. H., Mohanty, B., Ito, M., Nakamiya, Y., Owada, S., Kubota, S., et al. (2006). *Dynamic fragmentation of rock by high-voltage pulses*. Paper presented at the The 41st U.S. Symposium on Rock Mechanics (USRMS), Golden, Colorado. June 17-21
- De Waal, P. (2007). *Tomorrow's Technology - Out of Africa - Today*. Paper presented at the The Fourth Southern African Conference on Base Metals, Swakopmund, Namibia. 23-25 July
- Dev, S. R. S., Padmini, T., Adedeji, A., Garipey, Y., & Raghavan, G. S. V. (2008). A comparative study on the effect of chemical, microwave, and pulsed electric pretreatments on convective drying and quality of raisins. *Drying Technology*, Vol. 26, No. 10, pp. 1238-1243, ISSN 07373937
- Dietrich, R. V., & Skinner, B. J. (1979). *Rocks and rock minerals*. New York: John Wiley and Sons.
- Evans, I. O. (1972). *Rocks, Minerals & Gemstones*. London: The Hamlyn Publishing Group.

- Fontana, R. J. (2004). Recent System Applications of Short-Pulse Ultra-Wideband (UWB) Technology. *IEEE Transactions on Microwave Theory and Techniques*, Vol. 52, No. 9, pp. 2087-2104, ISSN 0018-9480
- Gaete-Garretón, L., Vargas-Hernandez, Y., Chamayou, A., Dodds, J. A., Valderama-Reyes, W., & Montoya-Vitini, F. (2003). Development of an ultrasonic high-pressure roller press. *Chemical Engineering Science*, Vol. 58, No. 19, pp. 4317-4322, ISSN 0009-2509
- Gaete-Garretón, L. F., Vargas-Hermández, Y. P., & Velasquez-Lambert, C. (2000). Application of ultrasound in comminution. *Ultrasonics*, Vol. 38, No. 1-8, pp. 345-352, ISSN 0041-624X
- Gärtner, W. (1953). Über die Möglichkeit der zerkleinerung suspendierter stoffe durch ultrashall. *Acustica*, Vol. 3, No., pp. 124-128, ISSN 1610-1928
- Giancoli, D. C. (2005). *Physics - principles with applications* (6th Ed ed.). New Jersey: Pearson Prentice Hall.
- Halverson, S. L., Burkholder, W. E., Bigelow, T. S., Norsheim, E. V., & Misenheimer, M. E. (1996). High-power microwave radiation as an alternative insect control method for stored products. *J. Econ. Entomol.*, Vol. 89, No., pp. 1638-1648, ISSN 0022-0493
- Henan Chuangxin Building-material Equipment Co. (2009). Retrieved 6 November 2009, from <http://www.enchuangxin.com/Mineral%20Processing%20Equipment/>
- Hu, Z., Wang, Y., & Wen, Z. (2008). Alkali (NaOH) pretreatment of switchgrass by radio frequency-based dielectric heating. *Applied Biochemistry and Biotechnology*, Vol. 148, No. 1-3, pp. 71-81, ISSN 0273-2289
- Hu, Z., & Wen, Z. (2008). Enhancing enzymatic digestibility of switchgrass by microwave-assisted alkali pretreatment. *Biochemical Engineering Journal*, Vol. 38, No. 3, pp. 369-378, ISSN 1369-703X
- Hutchinson, C. (Ed.). (2001). *The ARRL Handbook for Radio Amateurs* (78th ed.). Newington: ARRL.
- Ikediala, J. N., Hansen, J. D., Tang, J., Drake, S. R., & Wang, S. (2002). Development of a saline water immersion technique with RF energy as a postharvest treatment against codling moth in cherries. *Postharvest Biology and Technology*, Vol. 24, No., pp. 209-221, ISSN 0925-5214
- Jones, D. A., Kingman, S. W., Whittles, D. N., & Lowndes, I. S. (2007). The influence of microwave energy delivery method on strength reduction in ore samples. *Chemical Engineering and Processing*, Vol. 46, No. 4, pp. 291-299, ISSN 0255-2701
- Jones, D. A., Lelyveld, T. P., Mavrofidis, S. D., Kingman, S. W., & Miles, N. J. (2002). Microwave heating applications in environmental engineering--a review. *Resources, Conservation and Recycling*, Vol. 34, No. 2, pp. 75-90, ISSN 0921-3449
- Kawala, Z., & Atamanczuk, T. (1998). Microwave-enhanced thermal decontamination of soil. *Environmental Science and Technology*, Vol. 32, No. 17, pp. 2602-2607, ISSN 0013-936X
- Kelly, R. M., & Rowson, N. A. (1995). Microwave reduction of oxidised ilmenite concentrates. *Minerals Engineering*, Vol. 8, No. 11, pp. 1427-1438, ISSN 0892-6875
- King, R. P. (2001). *Modelling and simulation of mineral processing systems*. Oxford: Butterworth-Heinemann.

- Kingman, S. W., Jackson, K., Cumbane, A., Bradshaw, S. M., Rowson, N. A., & Greenwood, R. (2004). Recent developments in microwave-assisted comminution. *Int. J. Min. Proc.*, Vol. 74, No. 1-4, pp. 71-83, ISSN 1478-6478
- Klein, C. (2002). *The 22nd edition of the manual of Mineral Science*. New York: John Wiley & Sons.
- Kostaropoulos, A. E., & Saravacos, G. D. (1995). Microwave Pre-treatment for Sun-Dried Raisins. *Journal of Food Science*, Vol. 60, No. 2, pp. 344-347, ISSN 1750-3841
- Leach, M. F., & Rubin, G. A. (1988). *Fragmentation of Rocks Under Ultrasonic Loading*. Paper presented at the Ultrasonic Symp of the IEEE, Chicago, USA. 2-5 October
- Leaman, D. E. (1973). *The engineering properties of Tasmanian dolerite, with particular reference to the route of the Bell Bay Railway*, Tasm. Dep. Mines. Tech. Rept.
- Levitskaya, T. M., & Sternberg, B. K. (2000). Laboratory measurement of material electrical properties: extending the application of lumped-circuit equivalent models to 1 GHz. *Radio Science*, Vol. 35, No. 2, pp. 371-383, ISSN 0048-6604
- Li, X., Zhang, B., Li, W., & Li, Y. (2005). Research on the effect of microwave pretreatment on moisture diffusion coefficient of wood. *Wood Science and Technology*, Vol. 39, No. 7, pp. 521-528, ISSN 0043-7719
- McGeary, D., Plummer, C. C., & Carlson, D. (2001). *Physical Geology EARTH REVEALED* (4th ed.). New York: WCB/McGraw-Hill.
- Montalbo-Lombay, M., Srinivasan, G., Raman, D. R., Anex Jr, R. P., & Grewell, D. (2007). *Influence of ultrasonics in ammonia steeped switchgrass for enzymatic hydrolysis*. Paper presented at the 2007 ASABE Annual International Meeting, Technical Papers, Minneapolis, MN, United states. 17-20 June
- Moran, C. (2009). *Submission to the Australian Government Energy White Paper*. Retrieved 7 July 2011. From <http://www.ret.gov.au/energy/Documents/ewp/pdf/EWP%200047%20DP%20Submission%20-%20Sustainable%20Minerals%20Institute.pdf>.
- Nelson, S. O. (1996). Review and assessment of RF and microwave energy for stored-grain insect control. *Trans. ASAE*, Vol. 39, No., pp. 1475-1484, ISSN 0001-2351
- Nitayavardhana, S., Rakshit, S. K., Grewell, D., Van Leeuwen, J., & Khanal, S. K. (2008). Ultrasound pretreatment of cassava chip slurry to enhance sugar release for subsequent ethanol production. *Biotechnology and Bioengineering*, Vol. 101, No. 3, pp. 487-496, ISSN 0006-3592
- Owada, S., Ito, M., Ota, T., Nishimura, T., Ando, T., Yamashita, T., et al. (2003). *Application of electrical disintegration to coal*. Paper presented at the 22th International Mineral Processing Congress, Cape Town, South Africa. 28 September - 3 October
- Pan, S., Lo, K. V., Ping, H. L., & Schreier, H. (2006). Microwave pretreatment for enhancement of phosphorus release from dairy manure. *Journal of Environmental Science and Health - Part B Pesticides, Food Contaminants, and Agricultural Wastes*, Vol. 41, No. 4, pp. 451-458, ISSN 0360-1234
- Peng, B., Shi, B., Sun, D., Chen, Y., & Shelly, D. C. (2007). Ultrasonic effects on titanium tanning of leather. *Ultrasonics Sonochemistry*, Vol. 14, No. 3, pp. 305-313, ISSN 1350-4177
- Perkins, D. (1998). *Mineralogy*. New Jersey: Prentice Hall.

- Pienaar, H. C. (2002). *Design and development of a class E dielectric blood heater*. DTech, Vaal Triangle Technikon, Vanderbijlpark.
- Pozar, D. M. (2005). *Microwave Engineering* (3rd ed.). Massachusetts: John Wiley & Sons.
- Rapp, G. (2009). Properties of Minerals. In B. Herrmann & G. A. Wagner (Eds.), *Archaeomineralogy* (pp. 17-43): Springer Berlin Heidelberg.
- Roland, U., Buchenhorst, D., Holzer, F., & Kopinke, F. D. (2008). Engineering Aspects of Radio-Wave Heating for Soil Remediation and Compatibility with Biodegradation. *Environmental Science & Technology*, Vol. 42, No. 4, pp. 1232-1237, ISSN 0013-936X
- Roy, I., Mondal, K., & Gupta, M. N. (2003). Accelerating Enzymatic Hydrolysis of Chitin by Microwave Pretreatment. *Biotechnology Progress*, Vol. 19, No. 6, pp. 1648-1653, ISSN 8756-7938
- Rutschlin, M., Cloete, J. H., & Palmer, K. D. (2006). A guarded cylindrical capacitor for the non-destructive measurement of hard rock core samples. *Measurement Science and Technology*, Vol. 17, No. 6, pp. 1390-1398, ISSN 0957-0233
- Sadrai, S., Meech, J. A., Ghomshei, M., Sassani, F., & Tromans, D. (2006). Influence of impact velocity on fragmentation and the energy efficiency of comminution. *International Journal of Impact Engineering*, Vol. 33, No. 1-12, pp. 723-734, ISSN 0734-743X
- Scott, G., Bradshaw, S. M., & Eksteen, J. J. (2008). The effect of microwave pretreatment on the liberation of a copper carbonatite ore after milling. *International Journal of Mineral Processing*, Vol. 85, No., pp. 121-128, ISSN 0301-7516
- Shafiee, S., & Topal, E. (2009). When will fossil fuel reserves be diminished? *Energy Policy*, Vol. 37, No. 1, pp. 181-189, ISSN 0301-4215
- Skinner, B. J., & Porter, S. C. (1992). *The Dynamic Earth an introduction to physical geology* (2nd ed.). New York: John Wiley & Sons.
- Smith, R. D. (1993). *Large industrial microwave power supplies*. Paper presented at the Proc. Microwave-Induced reactions workshops, Pacific Grove, California. April
- Spierings, E. L. H., Brevard, J. A., & Katz, N. P. (2008). Two-Minute Skin Anesthesia Through Ultrasound Pretreatment and Iontophoretic Delivery of a Topical Anesthetic: A Feasibility Study. *Pain Medicine*, Vol. 9, No. 1, pp. 55-59, ISSN 1526-2375
- Staszewski, L. (2010). *Lightning Phenomenon – Introduction and Basic Information to Understand the Power of Nature*. Paper presented at the International Conference Environment and Electrical Engineering 2010, Prague, Czech Republic. 16-19 May
- Swart, A. J., Pienaar, H. C. v., & Mendonidis, P. (2005). *Radio frequencies effect on rock comminution*. Paper presented at the Annual Faculty Research Seminar, Vaal University of Technology, Emfuleni Conference Centre, Vanderbijlpark. July 2005
- Swart, J., Mendonidis, P., & Pienaar, C. (2009). The Electrical Properties of Chlorite Tremolite Marble measured for a range of Radio-Frequencies. *Mineral Processing and Extractive Metallurgy Review: An International Journal*, Vol. 30, No. 4, pp. 307 - 326, ISSN 0882-7508
- Tarback, E. J., & Lutgens, F. K. (1999). *Earth An introduction to physical geology* (6th ed.). New Jersey: Prentice Hall.
- Thompson, G. R., & Turk, J. (2007). *Earth Science and the Environment* (4th ed.). Belmont: Thompson Brooks/Cole.

- Tiedt, L. R., & Pretorius, W. E. (2002). An introduction to electron microscopy and x-ray microanalysis [Electronic Version]. *Laboratory for Electron Microscopy*, North-West University.
- Tiehm, A., Nickel, K., & Neis, U. (1997). The use of ultrasound to accelerate the anaerobic digestion of sewage sludge. *Water Science and Technology*, Vol. 36, No., pp. 121-128, ISSN 0273-1223
- Touryan, K. J., & Benze, J. W. (1991). *Enhanced Coal Comminution And Beneficiation using Pulsed Power Generated Shocks*. Paper presented at the Pulsed Power Conference, 8th IEEE International, San Diego, California. 16-19 June
- Tromans, D. (2008). Mineral comminution: Energy efficiency considerations. *Minerals Engineering*, Vol. 21, No. 8, pp. 613-620, ISSN 0892-6875
- Uquiche, E., Jerez, M., & Ortiz, J. (2008). Effect of pretreatment with microwaves on mechanical extraction yield and quality of vegetable oil from Chilean hazelnuts (Gevuina avellana Mol). *Innovative Food Science and Emerging Technologies*, Vol. 9, No. 4, pp. 495-500, ISSN 1466-8564
- Walkiewicz, J. W., Kazonich, G., & McGill, S. L. (1988). Microwave heating characteristics of selected minerals and compounds. *Minerals and Metallurgical Processing*, Vol., No., pp. 39-42, ISSN 0747-9182
- Walther, J. V. (2005). *Essentials of geochemistry*. Massachusetts: Jones & Bartlett Publishers.
- Wang, S., Birla, S. L., Tang, J., & Hansen, J. D. (2006). Postharvest treatment to control codling moth in fresh apples using water assisted radio frequency heating. *Postharvest Biology and Technology*, Vol. 40, No. 1, pp. 89-96, ISSN 0925-5214
- Wang, S., Ikediala, J. N., Tang, J., Hansen, J. D., Mitcham, E., Mao, R., et al. (2001). Radio frequency treatments to control codling moth in in-shell walnuts. *Postharvest Biology and Technology*, Vol. 22, No., pp. 29-38, ISSN 0925-5214
- Wang, Y., & Forsberg, E. (2007). Enhancement of energy efficiency for mechanical production of fine and ultra-fine particles in comminution. *China Particuology*, Vol. 5, No. 3, pp. 193-201, ISSN 1672-2515
- Wenk, H. R., & Bulakh, A. (2004). *Minerals their Constitution and Origin*. Cambridge: Cambridge University Press.
- Wills, B. A. (1992). *Mineral processing technology* (5th ed.). Oxford: Pergamon Press.
- Wilson, M. P., Balmer, L., Given, M. J., MacGregor, S. J., Mackersie, J. W., & Timoshkin, I. V. (2006). Application of electric spark generated high power ultrasound to recover ferrous and non-ferrous metals from slag waste. *Minerals Engineering*, Vol. 19, No. 5, pp. 491-499, ISSN 0892-6875
- Winands, G. J. J., Liu, Z., Pemen, A. J. M., van Heesch, E. J. M., & Yan, K. (2005). Long lifetime, triggered, spark-gap switch for repetitive pulsed power applications. *Review of Scientific Instruments*, Vol. 76, No. 8, pp. 085107-085106, ISSN 0034-6748
- Wolde-Rufael, Y. (2010). Coal consumption and economic growth revisited. *Applied Energy*, Vol. 87, No. 1, pp. 160-167, ISSN 0306-2619
- Woollacott, L. C., & Eric, R. H. (1994). *Mineral and metal extraction: an overview*. Johannesburg: The South African Institute of Mining and Metallurgy.
- Yerkovic, C., Menacho, J., & Gaete, L. (1993). Exploring the ultrasonic comminution of copper ores. *Minerals Engineering*, Vol. 6, No. 6, pp. 607-617, ISSN 0892-6875

- Zaghloul, M. R. (2008). A simple theoretical approach to calculate the electrical conductivity of nonideal copper plasma. *Physics of Plasmas*, Vol. 15, No. 4, pp. 701-705, ISSN 1070-664X
- Zhang, W., & Yao, Y. L. (2002). Micro scale laser shock processing of metallic components. *Journal of Manufacturing Science and Engineering Transactions of ASME*, Vol. 124, No., pp. 369-378, ISSN 1087-1357

Evolution of Calciocarbonatite Magma: Evidence from the Sövite and Alvikite Association in the Amba Dongar Complex, India

S. G. Viladkar

*Carbonatite Research Centre, Amba Dongar, Kadipani, District Vadodara
India*

1. Introduction

CaCO₃-rich carbonatites seem to be the most common and abundant carbonatite in many complexes. The Amba Dongar complex too, is dominantly composed of sövite. Its dike equivalent-(alvikite I and II), though volumetrically less abundant, occur in association with sövite. Majority of sövites samples are composed essentially of CaCO₃ and MgO content is low (0.99% average) and goes up to maximum 3% in phlogopite-sövite. A small fraction of periclase was reported earlier from some sövite samples by Viladkar and Wimmenauer, [4]. In this paper I propose that sövites are crystallized from calciocarbonatite magma. Trace elements and REE distribution patterns suggest that sövite fractionated to Alvikite I and II. The C and O isotope data provides evidence to supports the mantle derivation of the carbonatite magma at Amba Dongar.

2. General geology

Amba Dongar carbonatite-alkalic rock diatreme is located on the western periphery of the Deccan flood basalt province in Gujarat State, Western India. This sub-volcanic diatreme consisting of different phases of carbonatites, nephelinites and phonolites, has intruded into the Bagh sandstone and overlying Deccan basalts sequence and has been dated at 65.5 Ma [1].

The outstanding geological feature of the Amba Dongar complex is the bold exposures and clear intrusive relationship between different carbonatite units. Sövite is the predominant type of carbonatite and forms a ring dike around the inner rim of carbonatite breccia (Fig.1). Apart from major ring dike, sövite also forms large and small plugs within the Bagh sandstone terrain. Ankeritic carbonatite intrudes sövite at several places as dikes and large oval plugs while, last in the differentiation sequence, sideritic carbonatite phase intrudes the ankeritic carbonatite as thin dikes, in the southwestern part of the ring structure. Alvikite (phase I), dikes equivalents of sövite, are widespread within as well as outside the ring structure. Alvikite phase II intrude sövite at some places along the ring dike. Nephelinite plugs and phonolite dikes occur in the outer periphery of the ring structure. Large reserves of hydrothermal fluorite deposits (11.5 million tones) are associated with the carbonatites. A

vertical zonation of fenitization developed with strongly sodic and sodi-potassic fenites at deeper levels and potassic fenites at higher levels [2] [3]. The central part of the ring structure is occupied by intrusive basalt which replaced the original plug of carbonatite breccia. This youngest intrusive event seems to have occurred at 41.7 Ma [3].

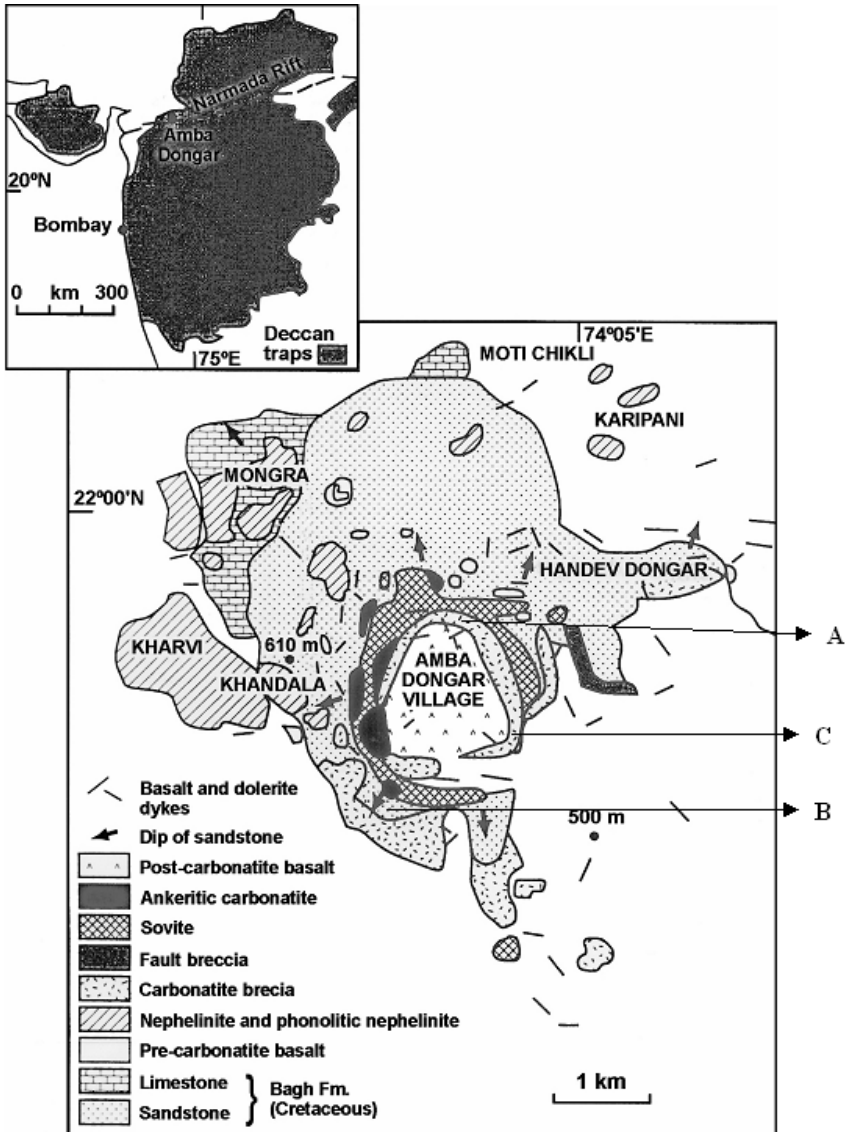


Fig. 1. Geological map of the Amba Dongar carbonatite diatreme with locations of Alvikite centres within sövite ring and outside the ring. A and C are in carbonatite breccia, B in Bagh sandstone.

It has been possible to establish the different phases of sövite intrusion with each phase marked by characteristic texture and mineralogy [3] [4]. The texture of sövite varies from coarse grained in the inner part of the ring in contact with carbonatite breccias to very fine grained in the outermost part of the ring in contact with the sandstone. Sövite also reveals excellent flow structure, and at several places large blocks of fenites are caught up within the flowage structure.

Early crystallization (segregations) of magnetite, apatite, pyrochlore and Nb-zirconolite occur as bands within sövite (Fig. 2). Silico-sövites (phlogopite-sövite and pyroxene-sövite) are not exposed at present level of erosion, however; many xenoliths of these rocks were encountered at deeper levels during mining operations and also in a tunnel driven through the sövite exposure.



Fig. 2. Banding (shown by an arrow) in sövite.

The alvikites vary in thickness from several centimeters to almost a meter. Detailed field investigation of numerous dikes suggests that there are at least two distinct intrusive phases; one either predating or contemporaneous with the main phase of sövite intrusion while the second (alvikite II) clearly postdates the sövite intrusion. In general, alvikites do not show any particular trend in their disposition and, they are located all over the central ring structure as well as outside the ring structure in sandstones and basalts. Three main centres of alvikite (Fig. 1) have been located in and around the ring dike of sövite. Alvikites of phase I intrude mainly carbonatite breccia (Fig. 3), sandstone and basalts while those of the second phase intrude sövite and fenite outcrops. Apart from these exposures alvikites were also exposed in fluorite mine workings and along road cuttings.

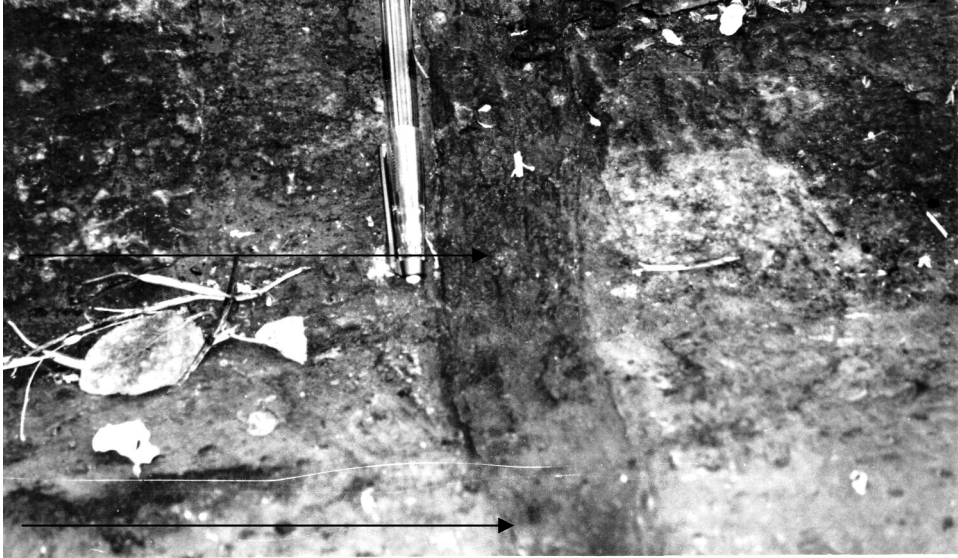


Fig. 3. Alvikite I (shown by an arrow) in carbonatite breccia.

The majority of phase I alvikites show thin chilled contacts with the host rocks. In some dikes grain size variation from margin (smaller grains) to center (larger grains) is observed. However, the most conspicuous feature observed around alvikite dikes of this phase (whenever they intrude sandstone) is the feldspathization of country rock sandstone. The fenitization effects along alvikite-basalt contact are not so conspicuous except for a small increase in K (formation of K-feldspar), modal apatite and calcite in the host basalt.



Fig. 4. Alvikite II (shown by an arrow) in sövite.

Second generation alvikites (phase II) intrude sövite (Fig. 4) in the ring dike and some are located in exposures of fenites. Mineral zonation is clearly developed in some of these alvikites with margins exclusively rich in calcite while concentration of magnetite and pyrochlore in the central part of the dikes.

In Amba Dongar, along with intrusive phase of calciocarbonatite, the extrusive phase also occurs in the form of tuff (Fig.5) in the western part at Mongra [20].



Fig. 5. Carbonatite tuff beds (shown by an arrow) in Mongra, West of Amba Dongar.

3. Petrography and mineralogy

Sövite shows various textures such as coarse grained, medium grained and, fine grained porphyritic [6]. In porphyritic types, the euhedral calcite phenocrysts are embedded in fine grained groundmass calcite of a later generation. In silico-sövites primary phlogopite is the most abundant silicate mineral while diopsidic augite is next in abundance. Phlogopite occurs as euhedral to sub-hedral crystals which locally show resorption by surrounding calcite. Occasionally phlogopite forms thin bands with individual crystals showing parallel orientation. The majority of phlogopite crystals are homogenous and do not show any zoning. Accessory minerals in order of decreasing abundance are apatite, magnetite, fluorite, barite, galena, pyrochlore, niobian-zirconolite, zircon, bastnaesite and monazite.

Alvikites, on the other hand, are medium to fine grained equigranular with anhedral grains of calcite and ankeritic calcite (in alvikite II) showing interlocking texture. Porphyritic texture is not uncommon. Some dikes show good flow texture with platy calcite crystals aligned along the direction of flow. All alvikite dikes of phase I have mineralogy broadly similar to coarse sövites whereas the post-sövite alvikites (phase II) are characterized by

abundance of phlogopitic-biotite displaying strong zoning with pale brown core and dark brown rims. Oscillatory zoning is not uncommon. Dark brown to reddish brown tetraferriphlogopite occurs as small isolated flakes as well as rims of some strongly zoned crystals [7]. Octahedral magnetite is very common; sometimes it also forms a thin rim around pyrochlore.

Micas from sövites and alvikites were investigated in detail earlier and the details of their evolutionary history from sövite to alvikite are discussed in earlier publication [7]. The chemical differences shown by the two types of micas (Mg-rich in sövite and Fe-rich in alvikite II) and their evolution trends from sövite to Alvikite II are thought to reflect the chemical evolution of the calciocarbonatite magma from which they crystallized.

4. Analytical method

Major and trace elements were determined by X-ray fluorescence using a Philips PW 1450/20 instrument at the Mineralogische-Petrographisches Institute of the Albert-Ludwigs University, Freiburg im Br. Germany. Rare earth elements were determined by the Neutron Activation method at the B.A.R.C., Trombay, Mumbai (Note: where only Ce, La and Nd values mentioned in the analytical tables, these are the XRF analyses. Other REE analyses (La-Lu) are by the Neutron Activation method).

C and O isotopes were determined at the Biogeochemistry section of the Max-Planck Institute, Mainz, Germany using following method

Finely powdered (200 mesh-size) carbonatite samples were reacted for 72 hours with anhydrous (100%) phosphoric acid at 250 C [8] [9] to ensure quantitative reaction of dolomite and ankerite components. Carbon and oxygen isotope ratios were determined for CO₂ on a VG PRISM mass spectrometer equipped with a three-collector system allowing the simultaneous collection of the masses 44, 45, and 46. Results were corrected for ¹⁷O after Craig [9] and are reported as δ¹³C and δ¹⁸O values relative to the Pee Dee Belemnite (PDB) and Standard Mean Ocean Water (SMOW) standards, respectively, with

$$\delta^{13}\text{C} = \left\{ \left[\left(\frac{^{13}\text{C}}{^{12}\text{C}} \right)_{\text{sa}} / \left(\frac{^{13}\text{C}}{^{12}\text{C}} \right)_{\text{st}} \right] - 1 \right\} * 1000(\text{‰})$$

and

$$\delta^{18}\text{O} = \left\{ \left[\left(\frac{^{18}\text{O}}{^{16}\text{O}} \right)_{\text{sa}} / \left(\frac{^{18}\text{O}}{^{16}\text{O}} \right)_{\text{st}} \right] - 1 \right\} * 1000(\text{‰})$$

were sa = sample and st = standard. Standard deviations of the measurements were usually smaller than ± 0.1 ‰.

5. Geochemistry

The present section is aimed mainly to show how the parent calciocarbonatite magma at Amba Dongar fractionated. Geochemical differences between sövite and alvikite (phases I and II) during their evolution are brought out using spidergram for trace elements and the chondrite normalized REE patterns. Representative major, trace and rare earth elements analyses of sövite, alvikite (phase I) and alvikite (phase II) are given in tables 1, 2 and 3 respectively.

Sample	1201SOV	1244SOV	1250SOV	1270SOV	187SOV	195SOV	Ave.	SD	CV%
SiO ₂	2.33	7.19	0.68	3.82	4.82	2.62	2.97	3.167	0.949
TiO ₂	0.96	0.15	0	0	0.41	0	0.09	0.182	1.889
Al ₂ O ₃	0.26	0.18	0	0.17	0.58	0.18	0.16	0.187	1.232
Fe ₂ O ₃	2.22	2.08	1.66	1.1	5.25	1.74	2.63	2.468	0.955
MnO	0.59	0.53	0.73	0.44	0.15	0.66	0.5	0.429	0.826
MgO	0.26	0.16	3.08	0.16	2.05	1.16	0.99	0.972	1.067
CaO	50	47.84	50.57	51.9	47.19	50	49.34	3.511	0.071
Na ₂ O	0	0.15	0	0.12	0	0	0.04	0.066	1.516
K ₂ O	0	0	0	0	0.16	0	0.06	0.066	1.232
P ₂ O ₅	0.6	3.47	0.45	1.04	3.99	0.19	1.69	1.469	0.855
CO ₂	41.89	36.3	41.52	40.2	33.32	41.74	39.76	2.814	0.071
Total	99.31	98.05	98.69	98.95	97.92	98.29	92.95		
Ba	770	3860	6580	920	980	4130	4080	3125	0.786
Sr	6100	3630	2560	5515	6310	2260	6871	6402	1.018
Nb	1070	250	190	110	80	490	535.88	1179	0.636
Zr	80	110	70	35	260	80	101.51	151.58	2.204
Y	50	230	60	130	80	110	124	77.64	1.427
Th	120	130	60	30	80	40	59	56.64	0.796
U	10	45	0	50	30	0	13.97	30.12	1.988
V	10	0	65		115	50	110.14	157	1.483
La	290	1110	662	1830	666	1080	1040.44	894.4	0.903
Ce	879	2460	1660	2980	1350	2800	2581.14	2697	1.117
Nd	233	550	375	410	446	695	572.05	459	0.862
Sm	34	125	47	44	58	177			
Eu	9.23	19.9	11.3	10.4	14.3	25.3			
Tb	3.09	8.61	3.59	4.32	4.15	7.95			
Yb	4.28	16	3.5	12.7	4.2	8.83			
Lu	0.55	2.33	0.4	1.78	0.55	0.87			

Table 1. Representative analyses of sövitte from different parts of ring dike and plugs.

	1	2	3	4	5	6	
Sample	1272AD(I)	1292AD(I)	79AD(I)	86/A/48(I)	BH/15 /ALV	V/alk/ 68	Ave
SiO ₂	1.64	2.48	1.44	3.78	1.56	6.22	3.65
TiO ₂	0.00	0.00	0.11	0.02	0.11	0.13	0.09
Al ₂ O ₃	0.37	0.00	0.11	0.21	0.07	1.78	0.75
Fe ₂ O ₃	1.20	0.40	2.11	1.03	3.19	1.29	1.84
MnO	0.44	0.20	0.85	0.28	0.16	0.37	0.28
MgO	0.17	0.80	0.24	0.60	0.42	1.46	0.75
CaO	51.68	53.26	50.10	51.65	50.49	48.52	49.42
Na ₂ O	0.20	0.10	0.18	0.06	0.05	0.54	0.16
K ₂ O	0.00	0.00	0.00	0.10	0.00	0.59	0.37
P ₂ O ₅	0.30	0.00	0.47	0.15	3.24	0.09	0.87
CO ₂	42.04	42.10	40.78	41.50	39.80	38.90	40.48
Total	98.54	97.34	96.39	99.38	100.49	99.91	
Ba	2815.00	*	9850.00	211.00	485.00	210.00	2960.3
Sr	16410.00	*	5210.00	2407.00	4295.00	1282.00	6610
Nb	40.00	*	160.00	70.00	135.00	10.00	87.9
Zr	20.00	*	80.00	44.00	220.00	78.00	161.5
Y	175.00	*	155.00	70.00	40.00	33.00	226.8
Th	120.00	*	130.00	10.00	40.00	0.00	59.4
U	20.00	*	20.00	0.00	10.00	0.00	62.44
V	*	*	*	33.00	85.00	40.00	23.3
La	1070.00	354.00	1830.00	823.00	310.00	60.00	634.18
Ce	2140.00	680.00	3340.00	1430.00	690.00	120.00	1237.455
Nd	445.00	181.00	612.00	230.00	200.00	45.00	265
Sm	*	30.00	73.00	64.00	*	14.00	
Eu	16.30	7.51	16.20	7.93	*	4.00	
Tb	6.57	2.93	6.65	2.10	*	2.00	
Yb	11.80	6.37	8.60	1.70	*	1.50	
Lu	1.41	0.79	1.22	0.34	*	2.00	

Table 2. Representative analyses of alvikite I.

Sample	1 1246/AD/II	2 1268(II)	3 1269AD(II)*	4 1288(II)	Ave
SiO ₂	8	4.77	5.19	1	4.11
TiO ₂	0.1	0.15	0.12	0.23	0.17
Al ₂ O ₃	0	0.05	0.04	0.04	0.07
Fe ₂ O ₃	8	10.21	7.9	9.3	8.19
MnO	1.5	0.74	1.43	0.5	0.84
MgO	0.6	0.41	0.45	0.8	0.5
CaO	45	40.2	44.48	46.3	45.08
Na ₂ O	0.1	0.12	0.15	0	0.07
K ₂ O	0.2	0	0	0	0.03
P ₂ O ₅	2.1	1.12	0.49	1.6	1.01
CO ₂	37.6	40.5	38.2	39	38.43
Total	100.2	98.27	98.45	98.77	98.26
Ba	12800	10810	8730	8200	8438
Sr	17510	3910	3210	6570	6059
Nb	1600	1890	580	1670	956
Zr	*	140	80	200	91
Y	180	120	130	80	112
Th	40	50	20	110	99
U	*	25	40	5	13
V	1055	200	135	0	269
La	2070	2140	2360	770	1508
Ce	8370	6010	5870	2250	4051
Nd	935	1050	1310	460	826
Sm	*	*	216	*	
Eu	*	*	34.6	*	
Tb	*	*	9.4	*	
Yb	*	*	3.5	*	
Lu	*	*	0.83	*	

Table 3. Representative analyses of Alvikite II.

On the CaO-MgO-Fe⁺ + MnO plot (Fig 6) there is clear separation between sövite and alvikite II (alvikite I plot in the same field as sövites). The alvikite II are richer in Fe on account of presence of ankeritic calcite in them. Most sövites and alvikites in Amba Dongar show MgO content below 1 wt % while those with MgO more than 1 wt% have either phlogopitic mica or periclase in them. Higher Fe₂O₃ contents of one sövite is due to high modal magnetite in this rock while the high Fe₂O₃ content of phase II alvikites can be attributed to a small amount of oxidized ankeritic calcite present in them.

The fractionation from sövite to alvikites (I and II) can be brought out more clearly on the spidergram for trace elements and chondrite normalized REE patterns. Plotting of average values of trace elements in sövites, alvikite (I) and (II) (Fig.7) show that incompatible trace elements gradually increase from alvikite I → sövite → alvikite (II), and as compared to alvikite I and sövites, alvikite II is enriched in all trace elements except Sr, Zr and Y.

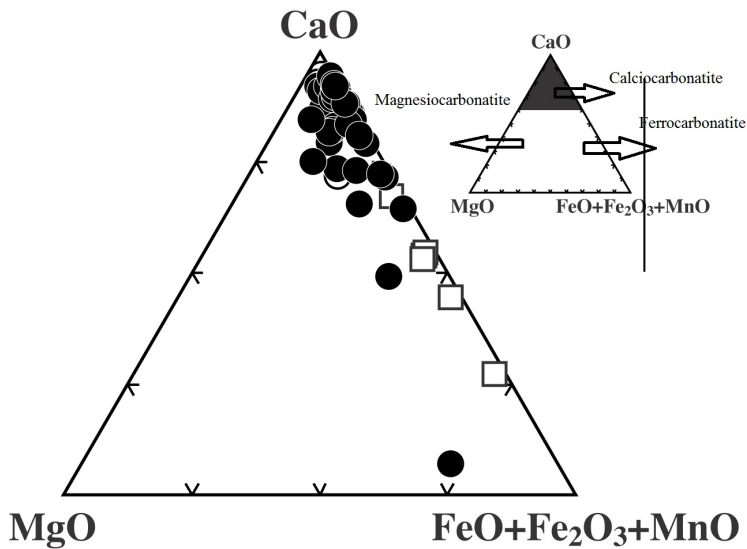


Fig. 6. Amba Dongar sövites (filled circles), Alvikite I (open circles) and Alvikite II (open squares) plotted on CaO-MgO-FeO+Fe₂O₃+MnO.

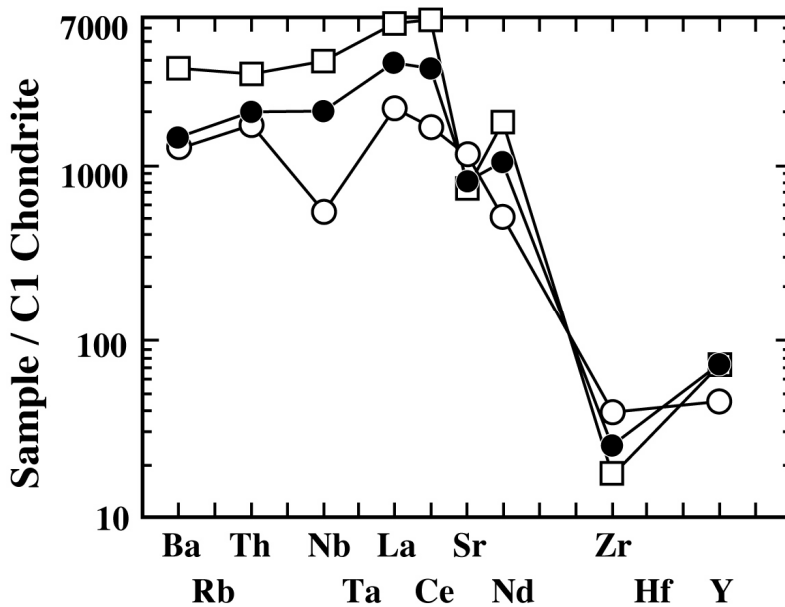


Fig. 7. Spidergram showing trace element variation in averages of Amba Dongar Alvikite I (open circle), Alvikite II (open square) and sövites (filled circle).

Chondrite normalized plots of sövikite (two different phases, coarse and fine grained) and alvikites (I and II) of Amba Dongar are shown in Fig. 8. Alvikite II is strongly enriched in all REE in comparison to Alvikite I and sövikites. Steep slope of LREE/HREE, similar and parallel REE patterns point to fractionation during evolution of these two types of carbonatites in Amba Dongar.

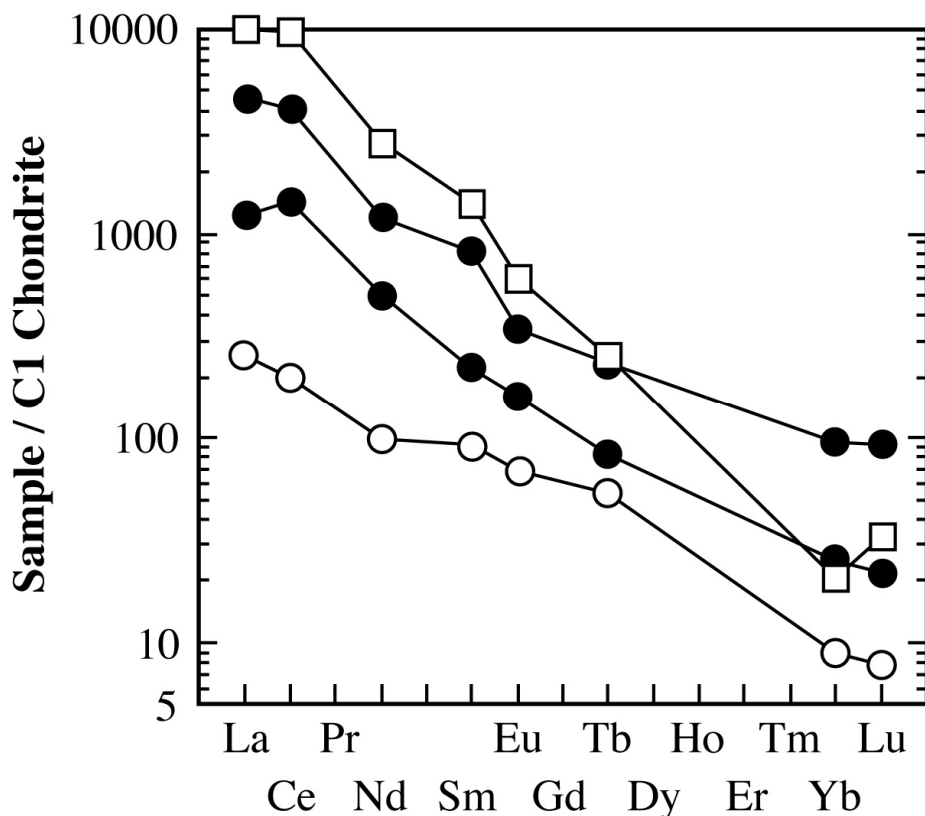


Fig. 8. Chondrite normalized REE distribution patterns of Amba Dongar sövikites and alvikites; Open circle – Phase I alvikite, Open square -- Phase II alvikite, Filled circle – 2 phases of sövikites (coarse and fine grained).

6. C and O isotopes

Stable isotopes of carbon and oxygen have proved useful in differentiating primary igneous carbonatites from marine carbonates. Relative to the PDB standard, mantle derived carbon has a $\delta^{13}\text{C}$ range of -7 to -5 ‰, and relative to the SMOW standard, mantle oxygen has a $\delta^{18}\text{O}$ range of $+5$ to $+8$ ‰ [10] [11]. However, various types of carbonatites (e.g., calcitic, dolomitic, ankeritic) may have evolved from a set of source values typical of the above range, and have undergone fractional crystallization and subsequent magmatic hydrothermal or meteoric alteration in diverse environments subsequent to their

emplacement. Therefore, it is customary to divide carbonatites broadly into two categories, primary and secondary. In the former variety, variations in both the isotope ratios (viz., $\delta^{13}\text{C}$ and $\delta^{18}\text{O}$) occur mainly due to fractional crystallization; the $\delta^{13}\text{C}$ values range from -9 to -1 ‰, while $\delta^{18}\text{O}$ ranges from $+5$ to $+15$ ‰ [12] [10]. In the second (altered) variety, the $\delta^{18}\text{O}$ values can increase up to $+30$ ‰, close to that of marine carbonates [13].

The data obtained on C and O isotopes of sövite, alvikites (I & II) supports the observation that calciocarbonatite magma at the Amba Dongar carbonatites complex, is mantle derived as majority of sövite samples and a few alvikites have retained the primary mantle signature. Accordingly, it is seen that the majority of sövite samples and few alvikite I and II plot in the field of mantle derived primary carbonatites in Fig. 9 [14]. Two samples of alvikite I fall within the mantle box while, remaining plot close to the box. Majority of alvikite II plot outside the box and this trend can be explained by process of fractionation. The sövite samples which lie farther away from the mantle box are mostly medium to fine grained sövites. The arrow shows the relation between phenocryst in sövite (star) and the

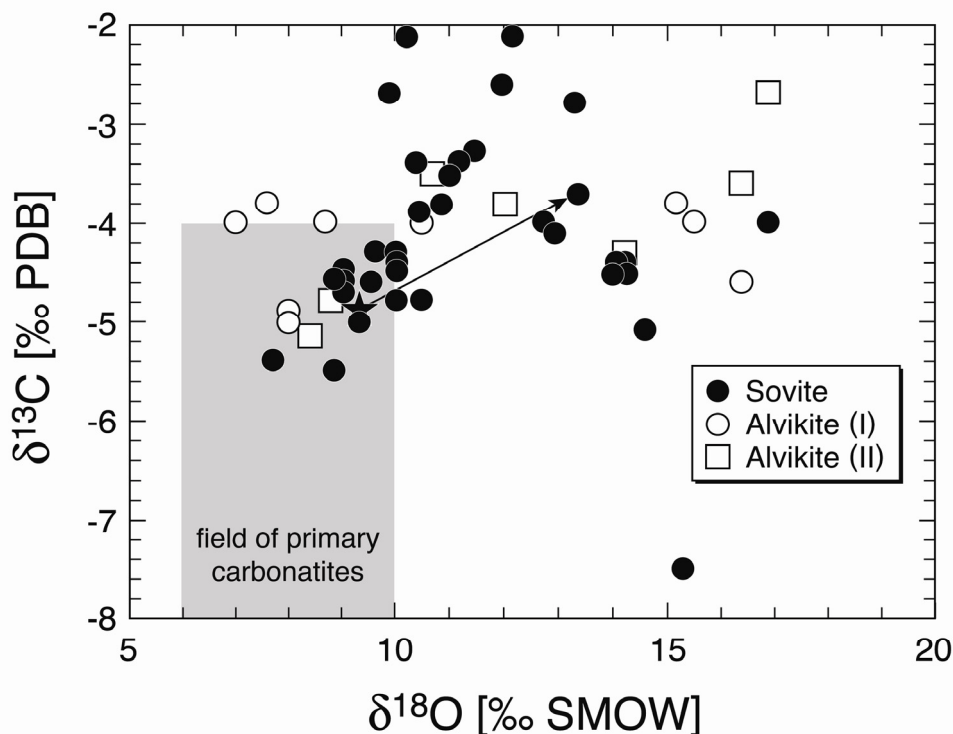


Fig. 9. C and O compositions of sövite, alvikite I and alvikite II of Amba Dongar complex. Open circle – Phase I alvikite, Open square -- Phase II alvikite, Filled circle – 2 phases of sövites (coarse and fine grained).

groundmass sövite. Coarse-grained sövite, in general, has lower $\delta^{13}\text{C}$ and $\delta^{18}\text{O}$ values compared to fine grained ones, indicating that the fractional crystallization of the carbonatite magma initiated with the crystallization of coarse-grained sövite. As fractionation proceeded, the magma continuously became enriched in water (i.e., the $\text{CO}_2/\text{H}_2\text{O}$ ratio decreased), at which time crystallization of fine-grained sövites started, thus explaining their higher $\delta^{13}\text{C}$ and $\delta^{18}\text{O}$ values.

It thus can be concluded that the primary carbonatites of Amba Dongar are interpreted to have evolved from a carbonatite parent magma of $\delta^{18}\text{O} = 8\text{‰}$ and $\delta^{13}\text{C} = -5.3\text{‰}$. The initial molar ratio of H_2O to CO_2 that best explains the trend is ~ 0.9 , with a crystallization temperature of $\sim 800^\circ\text{C}$. The secondary carbonatites in Amba Dongar appear to be altered mainly by a hydrothermal fluid with $\text{H}_2\text{O}/\text{CO}_2$ ratio between 0.001 and 0.1 at temperatures between 100 and 200°C . This model also applies to the secondary carbonatites found in carbonatite dikes from Amba Dongar [15].

7. Discussion

There has been an ongoing debate for many years about whether calciocarbonatite magmas exist or whether calcitic carbonatites are cumulate rocks derived from the crystallization of dolomitic carbonatite magma. While this may be true in some cases the present study of Amba Dongar dikes argues very strongly for the existence of a calcitic carbonatite magma (calciocarbonatite) magma, although somewhat magnesian in its early stages.

In Amba Dongar field relations between sövite and two phases of alvikites and petrographic observations such as tabular plates of calcite aligned along flowage, porphyritic texture with phenocrysts of calcite provide convincing evidence to assume that these carbonatites are crystallized from CaCO_3 -rich melt. The surface exposures of different generations of carbonatites are very clear and injection of alvikite II into sövite provides indisputable evidence of their origin that they being younger than the main sövite intrusion. With the help of geochemistry of major, trace and rare earth elements the fractionation of calciocarbonatite magma from sövite to two generations alvikite is well documented in the earlier section.

Early experimental studies of Wyllie and Tuttle [16] showed that calcite can crystallize as a liquidus phase at a temperature around 650°C at 0.1 GPa pressure.

According to Gittins [17] and Bailey [18] carbonatites can be precipitated from primary calciocarbonatite magma. Bailey listed 8 examples effusive calciocarbonatite [18], (Table 2, p. 6) and majority of them erupted from mantle as primary melt. Mariano and Roedder [19] studied products of Kerimasi carbonatite volcano and concluded that calcite was a primary phase in some flows. It is worth mentioning here that in Amba Dongar too an extrusive phase of calciocarbonatite magma occurs in the form of well bedded tuff and C and O isotopes of an unaltered tuff plots in field of mantle derived primary carbonatites [20]. Jago and Gittins [21] and Gittins and Jago [22] suggest, from experimental evidence, that a small amount of fluorine in carbonatite magma can reduce the temperature of crystallization of calcite which allows crystallization of calcite at atmospheric pressure

and conclude that the most of the calcite in extrusive carbonatite is primary magmatic. Dalton and Wood [23] demonstrated experimentally the formation of primary calciocarbonatite magma at low pressure. This is further supported by experimental results of Wyllie and Lee [24]. Additional evidence of existence of primary calciocarbonatite comes from occurrence of globules of calcite in mantle xenoliths which has been considered as evidence for the formation of immiscible CaCO_3 -rich melts in the mantle [25].

It thus appears that calciocarbonatite magma was the primary magma in Amba Dongar and during its evolution differentiated to alvikite I and II. That such calciocarbonatite magma was initially more magnesian is evident from the presence of phlogopite-sövite and periclase bearing sövite [4].

8. Acknowledgements

I am grateful to John Gittins for discussions, comments and suggestions on the manuscript. I thank: R. Ramesh of PRL, Ahmedabad for discussions on stable isotope data, Mrs Schegel formerly at Mineralogisches-petrographisches Institute, Freiburg, Germany for technical assistance. Dr. P.B. Pawaskar, formerly at BARC, Trombay, Mumbai for the REE analytical work. Part of the analytical work was done during the tenure of an Alexander von Humboldt fellowship in 1980 for which I thank the AvH Foundation, Germany. For the stable isotope determination I thank Mr. Georg Josten and Hedi Oberhansli for help during the laboratory work and Professor Schidlowski for guidance and discussions. I also gratefully acknowledge receipt of a Max-Planck Fellowship for conducting this investigation.

9. References

- [1] Ray, J.S., Kanchan Pande and Venkatesan, T.R. (2000) Emplacement of Amba Dongar carbonatite alkalic complex at Cretaceous/Tertiary boundary: Evidence from $^{40}\text{Ar}/^{39}\text{Ar}$ chronology. *Proc. Ind. Aca. Sci. (Earth Planet.Sci)* 109 : 39- 47.
- [2] Viladkar, S.G. (1986) Fenitization at the Amba Dongar carbonatite alkalic complex. *Proce. Sympo. NEMIRAM, Czechoslovakia*: pp170-189
- [3] Viladkar, S.G. (1996) Geology of the Carbonatite-Alkalic Diatreme of Amba Dongar Gujarat. *GMDC Sci. and Research Centre, Ahmedabad* : pp1-74
- [4] Viladkar, S.G. and Wimmenauer, W. (1992). Geochemical and Petrological studies on the Amba Dongar carbonatites (Gujarat, India). *Chem. Erde.* 52:277-291.
- [5] Viladkar, S.G., Ramesh, R., Avasia, R.K. and Pawaskar, P.B. (2005). Extrusive phase of Carbonatite-Alkalic activity in Amba Dongar complex, Chhota Udaipur, Gujarat. *Geol. Soc. India.* 66: 273-276.
- [6] Viladkar, S.G., (1981): The carbonatites of Amba Dongar, Gujarat, India. *Bull. Geol. Soc. Finland.* 53: 17-28
- [7] Viladkar, S. G. (2000) Phlogopite as indicator of magmatic differentiation in the Amba Dongar carbonatite, Gujarat, India. *N. Jb.Mineral. Mh.* 7: 302-314.

- [8] McCrea, J. M. (1950) The isotopic chemistry of carbonates and a palaeotemperature scale. *J. Chem. Phys.* 18: 849-857
- [9] Craig, H., (1957) Isotopic standards for carbon and oxygen and correction factors for mass spectrometric analysis of carbon dioxide. *Geochim. Cosmochim. Acta.* 12: 133-149.
- [10] Deines, P. (1989) Stable isotope variations in carbonatites, In: *Carbonatites: genesis and evolution* editor K. Bell. Unwin Hyman, London pp301-359.
- [11] Keller, J. and Hoefs, J. (1995) Stable isotope characteristics of recent natrocarbonatite from Oldoinyo Lengai, In: *Carbonatite Volcanism: Oldoinyo Lengai and the Petrogenesis of Natrocarbonatites*, Editors K. Bell and J. Keller, IAVCE I, *Proc. Volcanol.* 4: pp113-123.
- [12] Plyusnin, G. S., Samoylov, V.S., and Gol'shev, S.I.(1980) The $\delta^{13}\text{C}$, $\delta^{18}\text{O}$ isotope pair method and temperature facies of carbonatites, *Doklady Akademi Nank USSR, Seriya Geologiya.* 254:1241-1245.
- [13] Ray, J. S. and Ramesh, R., 1999. Evolution of carbonatite complexes of Deccan Flood Basalt province: stable carbon and oxygen isotopic constraints *J. Geophys. Res.*B12, 104, 29471-29483.
- [14] Taylor, H.P. Jr. French, J. and E.T. Degens (1967) Oxygen and carbon isotope studies of carbonatites from the Laacher See district, West Germany and the Alnö district, Sweden. *Geochim Cosmochim Acta.* 31: 407-430
- [15] Viladkar, S.G. and R. Ramesh Stable Isotope geochemistry of some Indian carbonatites: Implications for post-emplacement hydrothermal alteration processes (in preparation)
- [16] Wyllie, P.J. and O.F. Tuttle (1960a) The system $\text{CaO-CO}_2\text{-H}_2\text{O}$ and the origin of Carbonatites. *J. Petrol.* 1: 1-96.
- [17] Gittins, J. (1989) The origin and evolution of carbonatite magmas. In *Carbonatites: Genesis and evolution* Editor K. Bell. London, Unwin Hyman : pp580-600.
- [18] Bailey, D.K. (1993) Carbonatite magmas. *J. Geol. Soc.* 150 : 637-651.
- [19] Mariano, A. N. and P.L. Roedder (1977) Kermasi: a neglected carbonatite volcano. *J. Geol.* 91: 449-455.
- [20] Viladkar, S.G., Ramesh, R., Avasia, R.K. and Pawaskar, P.B. (2005). Extrusive phase of Carbonatite-Alkalic activity in Amba Dongar complex, Chhota Udaipur, Gujarat. *Geol. Soc. India.* 66: 273-276.
- [21] Jago, B.C. and Gittins, I. (1991) The role of fluorine in carbonatite magma evolution. *Nature.* 349: 56-58.
- [22] Gittins, J and B.C. Jago (1991) Extrusive carbonatites: their origins reappraised in the light of new experimental data. *Geol Mag.* 128, 4: 301-305.
- [23] Dalton J.A. and Wood B.J. (1993) The compositions of primary carbonate melts and their evolution through wall rock reactions in the mantle. *Earth & Plan. Sci Lett* 119: 511-525.
- [24] Wyllie, P. J. and Lee, W.J. (1998) Model system controls on conditions for formation of magnesiocarbonatite and calciocarbonatite magmas from the mantle. *J. petrol.* 39 : 1885-1893.

- [25] Kogarko, L.N., C.N.B. Henderson and H. Pacheko (1995) Primary Ca-rich carbonatite Magma and carbonate-silicate-sulphide liquid immiscibility in the upper mantle. *Contr. Miner. Petrol.* 121: 267-274.